Syntheses and Functional Studies of Cationic Metal-organic Frameworks (MOFs) toward Light Hydrocarbons Separation and Environmental Pollutants Remediation

A Thesis

Submitted in Partial Fulfillment of the Requirements for the

Degree of

Doctor of Philosophy

by

Subhajit Dutta
Reg. ID: 20163456

Indian Institute of Science Education and Research (IISER), Pune

2022

Dedicated to

Maa, Baba and Didivai

Indian Institute of Science Education and Research (IISER), Pune

Certificate

It is hereby certified that the work described in this thesis entitled *"**Syntheses and Functional Studies of Cationic Metal-organic Frameworks (MOFs) toward Light Hydrocarbons Separation and Environmental Pollutants Remediation**"* submitted by *Mr. Subhajit Dutta* was carried out by the candidate, under my supervision. The work presented here or any part of it has not been included in any other thesis submitted previously for the award of any degree or diploma from any other university or institution.

Date: 06.06.2022

Dr. Sujit K. Ghosh
Research Supervisor
Email: sghosh@iiserpune.ac.in
Contact No.:+91(20)25908076

Declaration

I declare that this written submission represents my ideas in my own words and wherever other's ideas have been included; I have adequately cited and referenced the original sources. I also declare that I have adhered to all principles of academic honesty and integrity and have not misrepresented or fabricated or falsified any idea/ data/ fact/ source in my submission. I understand that violation of the above will cause for disciplinary action by the Institute and can also evoke penal action from the sources which have thus not been properly cited or from whom proper permission has not been taken when needed.

Date: 06.06.2022

Subhajit Dutta

Reg. ID: 20163456

Acknowledgement

I would like to take this opportunity to convey my deepest gratitude for my PhD supervisor **Prof. Sujit K. Ghosh** for his continuous guidance, encouragement and support for shaping me as an all-round researcher over the last five years. He has been a diligent mentor and source of constant motivation who imbibed appropriate work ethics required for development of scientific aptitude and temperament. It has been an absolute honour for me to work under his mentorship. I feel his motivating guidance has truly assisted me in effectively designing and executing several research projects. Thank you very much Sir for having trust in me, keeping a positive outlook in all situations and most importantly for being such an encouraging supervisor.

I sincerely acknowledge the former director of IISER Pune, Prof. K. N. Ganesh and the present director Prof. J. B. Udgaonkar for providing such world class facilities and having a lively research environment. I am also extremely grateful to my research advisory committee (RAC) members, Dr. Sakya Sen (NCL, Pune) and Dr. Partha Hazra (IISER, Pune) for their insights and valuable suggestions during the annual RAC meetings. I am also thankful to former chair chemistry Prof. M. Jayakannan and present chair chemistry Prof. H. N. Gopi and all other faculty members of the department of chemistry for fostering a vibrant scientific environment in the department and being reachable for any queries. I sincerely thank all the collaborators - especially Dr. Ravichandar Babarao (RMIT, Australia), Dr. Mandar M. Shirolkar (Symbiosis international (Deemed University)), Dr. Omid T. Qazvini (University of Manchester, UK), Dr. Arvind K. Gupta (Lund University, Sweden) who assisted me in completion of different projects. I would like to convey my sincere gratitude to Ma'am (Dr. Sudarshana Mukherjee) for her valuable advices and I wish both Suvan and Suyosh all the best for their future.

It has been a great honour and experience for me to be a part of the 'Microporous Materials Lab' and I am extremely thankful to all the past and present members of the extraordinary team. I would like to thank all of them (Dr. Biplab Joarder, Dr. Soumya Mukherjee, Dr. Avishek Karmakar, Dr. Aamod V. Desai, Dr. Partha Samanta, Dr. Samraj Mollick, Dr. Shivani Sharma, Dr. Tarak Nath Mandal, Dr. Sreenu Bhanoth, Shilpa Sonar, Yogeshwar More, Prateek Agrawal, Sumanta Let, Writakshi Mandal, Sahel Fajal, Debanjan Mahato, Gourab Kumar Dam, Satyam Saurabh, Priyanshu Chandra, Arkendu

Roy and Depanjan Majumder). Thank you very much all for your significant contribution, help and providing friendly environment in the lab. Of them, I would like to sincerely thank to Arunabha for introducing me to the lab along with Soumya da and Avishek Da for their valuable guidance and immense support during my initial PhD days. My sincere thanks go out for all my seniors: Soumya da, Avishek da, Tarak da, Aamod da, Partha da, Yogesh bhaiya, Samraj da and Shivani di for their guidance, support and valuable suggestions. Particularly, I would like to convey my sincere gratitude for Aamod da and Partha da for their continuous guidance, care and support throughout this long journey of doctoral research. It was really an amazing experience to work with all of you and I feel I have learnt a lot of things from you guys. Apart from their mentorship, I have been fortunate to have developed a strong personal equation with each of them. I would also like to express my special appreciation to all my current lab members, because without them this journey would not have been as exciting and memorable as it has been. I would consider myself lucky to have a batch-mate and friend like Sumanta, with whom I had maximum overlap in lab, which was a long, memorable partnership of sharing highs and lows and driving each other to achieve full potential. I am grateful to him for his wonderful friendship and contributions in my researches. I would like to specially mention about two juniors who worked with me over a long period – Debanjan and Gourab, for their enthusiastic involvement and optimistic ideas. I wish to acknowledge the prompt and unconditional assistance from Sahel, Writakshi, Dipanjan, and Satyam whenever required. I thank Tarak da for providing a timely advice and perspective. I especially thank Aamod da and Soumya Da for their invaluable support and encouragement during the last phase of my PhD.

For the smooth progress in a long course, the support of administrative and technical staff is equally important. I thank Anuradha and Dr. Umeshareddy Kacherki for library assistance, technical staff of the institute - Parveen Nasa, Ravinder Malothu, Mahesh Jadhav, Nilesh Dumbre, Anil Jadhav, Yatish, Ganesh Dimbar, Suresh Prajapat, Sandeep Kanade, Nitin Dalvi, Megha, Deepali and administrative staff - Mayuresh, Nayana, Tushar, Vrushali, Suresh, Prabhas, Priyadarshani for their prompt assistance at multiple occasions. I also express my deep gratitude to IISER Pune for research fellowship for the entire tenure in IISER. I thank John Wiley & Sons (Wiley-VCH), Royal Society of Chemistry (RSC), American Chemical Society (ACS), Elsevier for publishing several research and

review articles.

I would convey my regards towards my school and college teachers who have encouraged me throughout different stages of life. I would also thank Dr. Chinmoy Choudhury for his guidance and support during my school days. I am also very much thankful to Dr. Arogyavaram Saha, Dr. Prasanta Ghosh, Dr. Amit Saharoy, Dr. Pulak Ganguly, Dr. Hrisikesh Chatterjee, Dr. Bikashbaran Ghosh, Dr. Bimal Kumar Sadhukhan and Dr. Rathindranath Ghosh of Ramkrishna Mission Residential College, Narendrapur (University of Calcutta) for teaching me and generating the love inside me for Chemistry. I would pay my deepest regards to Swami Suparnananda (Satya da) for his guidance, care and support in various stage of my life.

I wish to thank all my friends for their support and help at different stages of my life. I particularly wish to thank my friend Rashmi Sharma for her constant support and encouragements during the long discussions over tea and coffee throughout the last 5 years in both highs and lows, which kept driving the motivation to sustain the long terrain. I would like to thank each and every member of Prof. Pinaki Talukders' group (past and present) for their constant support and understanding in allowing us to access UV-vis and fluorescence spectrometer freely. I would like to thank all my batch-mates (PhD batch August-2016) and wish all the success in the future. I was a part of the integral part of Chemphilic Team -2019 which was indeed a memorable experience. Also, I would like to mention about my friends in campus Saptashwa, Krishnendu, Indra, Ruma, Padmini, Jyoti, Puneet and Pulak for sharing innumerable rejoicing moments. I also thank my seniors Dr. Sagar Satpati, Dr. Debanjan Chakrabarty, Dr.Soumendu Roy and Dr. Aditi Nandy for their help. Also, I would like to mention about our institute cricket "Dadagiri", of which I was a integral for the last five years, and I wish all of the members the best of luck in the years ahead. I also wish to thank my my B.Sc. batchmates Aishik, Palash and Arpan for their constant support and encouragements. I am indebted to my family (Maa, Baba, Didibhai, Bui, Meso, Sonai, Rishi) for being the invisible backroom support, without whom this could not have been completed.

- Subhajit Dutta

Contents

1	**Introduction**	
1.1	Metal-Organic Frameworks (MOFs)	1.1
1.2	Applications of MOFs	1.10
1.3	Light hydrocarbon separation	1.11
1.4	Toxic aquatic pollutants remediation	1.14
1.5	Thesis Overview	1.16
1.5	References	1.18
	Part-I: Functional Cationic MOFs for Efficient Industrially Relevant Light Hydrocarbon Separation	I.1
2.	**Three-in-one C_2H_2 Selectivities Guided adsorptive separation across an isoreticular family of cationic square lattice MOFs**	
2.1	Introduction	2.1
2.2	Experimental	2.3
2.3	Results and discussion	2.7
2.4	Conclusions	2.12
2.5	Appendix section	2.12
2.6	References	2.22
3.	**C_2H_2 Induced Structural Dynamism Driven Efficient C_2H_2/CO_2 Separation by a Water-Stable Cationic Metal-organic framework**	
3.1	Introduction	3.1
3.2	Experimental	3.3
3.3	Results and discussion	3.6
3.4	Conclusions	3.13
3.5	Appendix section	3.14
3.6	References	3.37
	Part-II: Water Stable Cationic MOFs for Toxic Aquatic Pollutants Remediation	II.1

4. A Luminescent Cationic MOF for Bimodal Recognition of Chromium and Arsenic based Oxo-anions in Water

4.1 Introduction 4.1

4.2 Experimental 4.2

4.3 Results and discussion 4.6

4.4 Conclusions 4.13

4.5 Appendix section 4.14

4.6 References 4.34

5. A Stable Cationic MOF For Rapid and Efficient Scavenging of Toxic Oxo-anions from Water

5.1 Introduction 5.1

5.2 Experimental 5.2

5.3 Results and discussion 5.5

5.4 Conclusions 5.10

5.5 Appendix section 5.11

5.6 References 5.28

6. Summary and Perspectives 6.1

Synopsis

The prime motivation of this thesis work is to design, syntheses and functional studies of neutral N-donor linker based cationic metal-organic frameworks (MOFs) towards their potential application for industrially relevant light hydrocarbon separation and efficient remediation of toxic aquatic pollutants. Metal-organic frameworks (MOFs) have come forth as the most important subset of functional porous materials owing to their several advantages over the traditional porous materials. Generally, MOFs are classified into ionic and neutral frameworks, depending upon the residual charge on the framework backbone. Distinct terminal donor groups have been employed for synthesis of MOFs such as N-heterocyclic aromatic rings, carboxylates, phosphonates, sulfonates, etc. Among them, neutral N-donor based ligands possess several advantages likewise other donating groups and it can render formation of cationic MOFs with counter anions free inside the pores. Whereas the counter anions can act as the extra-framework functionalities for cationic MOFs, the organic building blocks can also be custom-designed via pre- or post-synthetic functionalization to introduce desired functional groups. Although cationic MOFs have been employed toward several applications like catalysis, sensing, ion-conduction etc., its' utility toward extremally challenging light hydrocarbon separation and selective aquatic pollutant remediation is still to be explored. In this context, one of the prime objectives of this thesis work is functional studies of cationic MOFs toward selective separation of industrially relevant light hydrocarbons. To archive this, attempts were made to design and synthesize several functional cationic MOFs with both different inorganic and organic anions inside the pores as extra-framework functionalities. Apart from light hydrocarbon separation, water pollution from toxic industrial as well as radioactive wastes is another major concern which requires urgent attention. In this context, functional cationic MOFs were synthesized and employed toward selective recognition and removal of such hazardous substances from water based on principles of host guest interactions and ion exchange.

Chapter 1. Introduction

At the outset, a brief discussion about MOFs and the scope in terms of structural diversity and methodology is included. Role of judicious choice of the building blocks as well as metal nodes in synthesizing functional MOFs has been presented. Particularly, contribution of various types of organic ligands in preparation of MOFs have been discussed in details and the scope for neutral N-donor ligand-based MOFs is presented. In addition, classification of MOFs based on the structural diversity (generations of MOFs) and the residual framework charge (ionic and neutral) is discussed in details. Further, different routes of synthesizing ionic MOFs have been discussed in details. A summary of the diverse applications of ionic MOFs has been included, particularly in the field of light hydrocarbon

separation and toxic aquatic pollutants remediation. In this context, several industrially challenging light hydrocarbons and their importance in petrochemical industries has been discussed in details. In addition, water pollutions by toxic and hazardous pollutants have been discussed thoroughly. As the focus of the current work is utilization of cationic MOFs toward industrial and environmental applications, a brief state-of-art overview has been provided. In particular, as the tunability of functional anions inside the cationic MOFs is the prime focus, the strategies for synthesis of cationic MOFs along-with the role of anions have been briefly summarized.

Part-I: Functional Cationic MOFs for efficient Industrially Relevant Low Hydrocarbon Separation

Light hydrocarbons, such as acetylene, ethylene, ethane, propane etc. are the backbone of the petroleum-based commodity industries. The global annual production of these light hydrocarbons is estimated as more than 200 million tons with a gigantic market valuation of $254.6 billion in 2016, which is expected to touch $475.8 billion by 2023. The state-of-the-art separation process such as cryogenic and/or fractional distillation, solvent extraction etc. are extremely energy-intensive as it involves a gigantic ~ 230 gigawatts of energy consumption per day globally, accounting for ~ 40% of total global industrial energy consumption. To address this issue, new type of sorbent material is required for the efficient and selective separation of these light hydrocarbons with a lesser energy and capital requisite. In this section, we devoted our effort toward pore-engineering of stable cationic MOFs via tuning the functional uncoordinated anions inside the pore. This section of the thesis is separated into two chapters, chapter-2 and chapter-3. In chapter-2, the very first example of light hydrocarbon separation in a cationic MOF series has been demonstrated across a previously unreported pre-functionalized platform of isoreticular cationic metal-organic frameworks. While in chapter-3, the practical issue of lack of chemical stability in cationic MOFs have been address along with utilization of bulky organic sulfonic acid ligands for efficient and selective C_2H_2 separation from its' industrial impurity CO_2.

Chapter 2. Three-in-one C_2H_2 Selectivities Guided Adsorptive Separation across an Isoreticular Family of Cationic Square Lattice MOFs

Purification of C_2H_2 from other light hydrocarbons such as C_2H_4, CO_2 and CH_4 by selective adsorption is an important process in commodity chemical industries. In this chapter, we present a novel approach to address this challenge by a series of three new isostructural cationic metal-organic frameworks (MOFs),

namely iMOF-nC (n = 5, 6, 7) featuring multiple functionalities with strong binding affinities toward C_2H_2. All three MOFs exhibited higher adsorption uptake for C_2H_2 than the other three light hydrocarbons in single component measurements. Ideal Adsorbed Solution Theory (IAST) and simulated breakthrough experiments demonstrated the excellent selectivity of iMOF-nC for C_2H_2 and high-efficiency in purification of C_2H_2 from other light hydrocarbons at room temperature. Moreover, dynamic column breakthrough with the best performing material, i.e. iMOF-6C confirmed its' potential towards real-time applicability. In addition, Density Functional Theory (DFT) calculations further revealed the various functional interaction sites inside the MOF frameworks which preferentially interact with C_2H_2 than other three light hydrocarbons. This report provides an alternative approach for development of functional cationic materials for efficient separations of light hydrocarbons.

Reference: S. Dutta,† S. Mukherjee,† O. T. Qazvini, A. K. Gupta, S. Sharma, D. Mahato, R. Babarao, S. K. Ghosh, *Angew. Chem. Int. Ed.* **2021**, 61, e202114132.

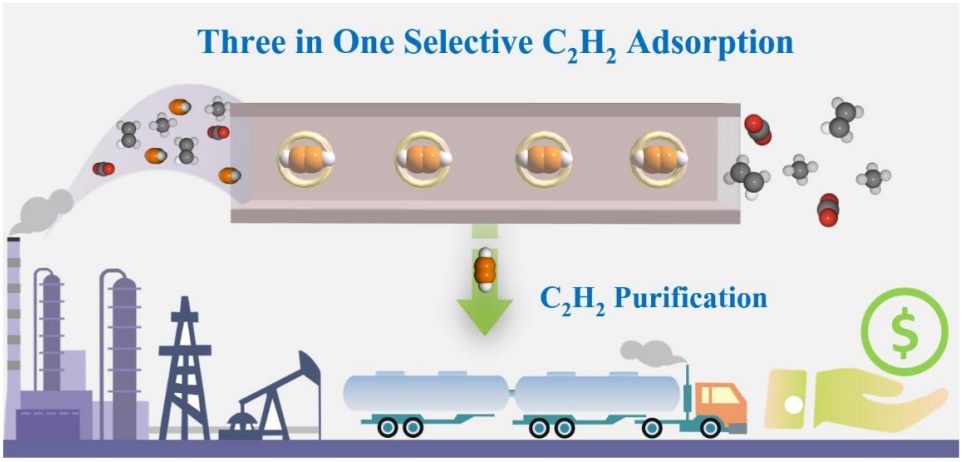

Chapter 3. C_2H_2 Induced Structural Dynamism Driven Efficient C_2H_2/CO_2 Separation by a Water-stable Cationic Metal-organic framework

Extending the idea of exploration of cationic MOFs for light hydrocarbon separation utilizing various functional anions inside the framework, a novel cationic MOF (iMOF-8C) having free sulfonic acid moiety as counter anions were synthesized. Further, iMOF-8C found to exhibit a rare guest-induced anion-dynamism-based gate-opening behavior towards C_2H_2. Further, the single component adsorption isotherms revealed excellent selectivity for C_2H_2 over its' industrial impurity, i.e. CO_2. Additionally, IAST calculations, simulated breakthrough studies and dynamic column breakthrough experiments corroborated well with the high efficiency of iMOF-8C in the purification of C_2H_2 from C_2H_2/CO_2

mixtures, which is recognized as very crucial but challenging task in industrial separation. Moreover, theoretical studies confirmed the structural dynamism upon incremental loading of C2H2 molecules inside iMOF-8C framework. (*Manuscript under revision*)

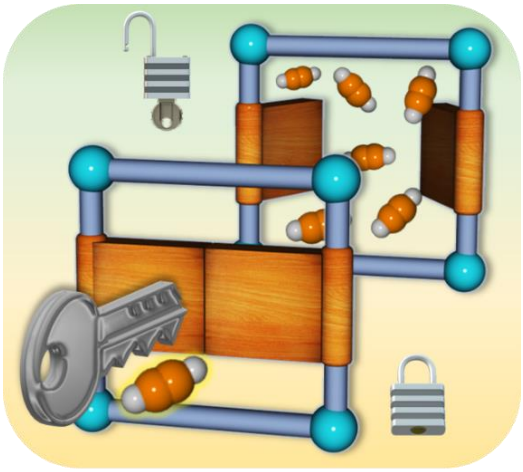

Part-II: Sensing and Capture of Toxic Aquatic Pollutants by Water Stable Cationic MOFs

Growing industries is a part of growth of modern civilization and urbanization. But release of their toxic effluents, which are generated from those industries, directly into the mainstream water bodies has resulted into the heavily increasing environmental pollution. To address this issue, we devote our effort toward synthesis and functional studies of water stable cationic MOFs toward efficient remediation of toxic and hazardous aquatic pollutants. This section is also divided into two chapters, chapter-4 and chapter-5. In chapter-3, we have utilized a water stable luminescent cationic MOF for selective recognition of toxic oxo-anions (CrO_4^{2-}, $Cr_2O_7^{2-}$, $HAsO_4^{2-}$, $HAsO_3^{2-}$) from water via a bimodal recognition process. While in chapter 5, we have utilized a chemically stable cationic MOF having hydrophobic pore surface for efficient sequestration of heavy metal based oxo-anion (chromate and perrhenate) from water.

Chapter 4. A Luminescent Cationic MOF for Bimodal Recognition of Chromium and Arsenic based Oxo-anions in Water

In this chapter, a Zinc based water stable luminescent cationic MOF (iMOF-4C) was synthesized formulated on rational choice of organic building block to afford chemical stability as well as ionic nature. iMOF-4C exhibited excellent luminescence quenching behavior toward toxic industrial pollutants such as CrO_4^{2-} and $Cr_2O_7^{2-}$ oxo-anions in water. On the flipside, it showed a rare luminescence turn-on

response toward toxic arsenic based oxo-anions, i.e. $HAsO_4^{2-}$, $HAsO_3^{2-}$. Such bimodal recognition behavior in a stand-alone material is indeed rare in the domain of MOFs. Further, the "turn-off" and "turn-on" efficiency of iMOF-4C was found to be comparable with the highest reported values in the domain of porous materials, highlighting its' potential toward practical applicability. In addition, the theoretical calculations confirmed the alteration in electronic properties of iMOF-4C upon interacting with different toxic oxo-anions and indicate the origin of distinctive fluorescence responses.

Reference: S. Dutta, † S. Let, † M. M. Shirolkar, A. V. Desai, P. Samanta, S. Fajal, Y. D. More, S. K. Ghosh, *Dalton Trans.* **2021**, *50*, 10133–10141.

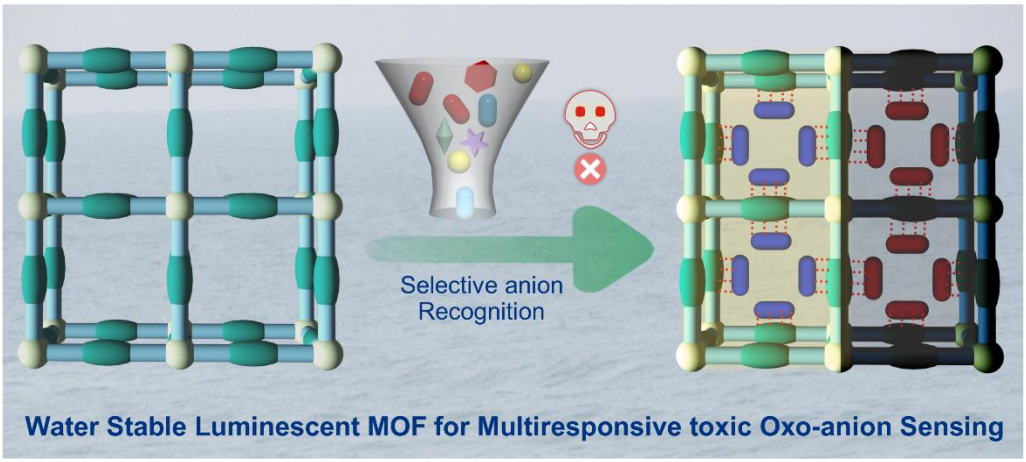

Chapter 5. A Stable Cationic MOF For Rapid and Efficient Scavenging of Toxic Oxo-anions from Water

In this chapter, we have synthesized a robust cationic MOF (iMOF-2C) with hydrophobic pore surface toward efficient remediation of toxic industrial waste e.g., CrO_4^{2-} and radioactive waste TcO_4^- (ReO_4^- anion was used as the surrogating anion of radioactive TcO_4^- anion). iMOF-2C showed excellent capture efficiency via ion-exchange toward these oxo-anions as the saturation uptake capacity values were found to be among the highest values reported in the literature. In addition, it showed excellent selectivity as well as recyclability up to 10 cycles, rendering its' potential toward real-time applicability. Further, theoretical calculation studies revealed the preferential oxo-anion binding sites inside iMOF-2C, resulting in such high efficiency in oxo-anion removal.

Reference: S. Dutta, P. Samanta, B. Joarder, S. Let, D. Mahato, R. Babarao, S. K. Ghosh, *ACS Appl. Mater. Interfaces 2020, 12, 41810−41818.*

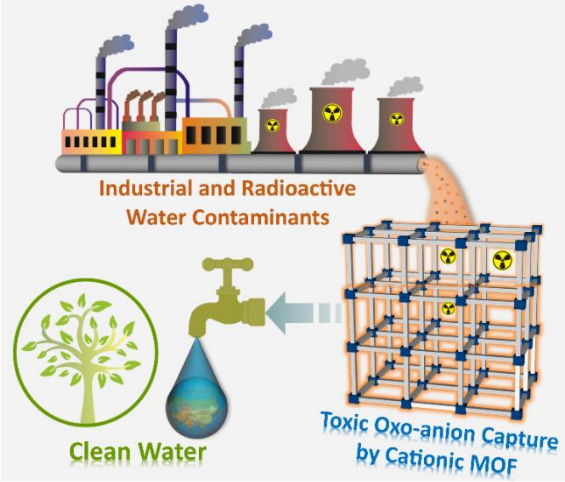

Chapter 6. Summary and Perspectives

In conclusion, a brief synopsis of the understandings acquired by the library of cationic MOFs presented in chapters 2-5 has been provided. This work primarily focuses on systematic design, synthesis and functional studies of cationic MOFs to address the challenging industrial separation as well as environmental pollution issues. An overview on the influence of counter anions (both inorganic and organic anions) in pore-engineering of functional cationic MOFs to direct the structure-property correlation for targeted applications have been discussed. The outcomes from this thesis work in the domain of cationic MOFs for efficient separation of light hydrocarbons and remediation of environmental pollutants has been discussed with regard to state-of-art. Such studies based on functional cationic MOFs for light hydrocarbon separation and water pollutants remediation could provide new avenues to develop next generation ionic materials to address the concerning industrial and environmental issues in near future.

Abbreviations

Anal.	Analysis
Calc.	Calculated
CCDC	Cambridge Crystallographic Data Centre
DMF	N,N'-dimethylformamide
DCM	Dichloromethane
EtOH	Ethanol
FT-IR	Fourier transform infra-red spectroscopy
g	Gram
MeOH	Methanol
mg	Milligram
min	Minutes
mL	Milliliter
mM	Millimolar
mmol	Milli moles
MOF	Metal-Organic Framework
PCP	Porous Coordination Polymer
PXRD	Powder X-Ray Diffraction
RT	Room Temperature
SCXRD	Single-Crystal X-Ray Diffraction
TGA	Thermogravimetric Analysis
UV	Ultraviolet
FE-SEM	Field Emission Scanning Electron Microscopy
MeCN	Acetonitrile
NMR	Nuclear Magnetic Resonance
iMOF	Ionic Metal-Organic Framework
EDX	Energy Dispersive X-ray Analysis
ICP-AES	Inductively Coupled Plasma Atomic Emission Spectroscopy
cMOF	Cationic Metal-Organic Framework

Rights and Permissions

Chapter 2:

Reprinted (adapted) with permission from *Angew. Chem. Int. Ed.* **2022**, *61, e202114132.* Copyright 2022: John Wiley and Sons. (*License Number:* ***5318681116102***)

Chapter 4:

Reprinted (adapted) with permission from *Dalton Trans.,* **2021***, 50, 10133-10141*. Copyright 2021: Royal Society of Chemistry.

Chapter 5:

Reprinted (adapted) with permission from *ACS Appl. Mater. Interfaces,* **2020***, 12, 41810–41818*. Copyright 2020: American Chemical Society.

Research Publications

(† - indicates equal contribution)

Included in Thesis:

1. Recognition and Sequestration of Toxic Inorganic Water Pollutants with Hydrolytically Stable Metal-organic Frameworks (Review).
   Subhajit Dutta, Sumanta Let, Shivani Sharma, Debanjan Mahato and Sujit K. Ghosh.
   Chem. Rec., **2021**, *21*, 1666– 1680.
2. Post-synthetic Modification Approaches in Metal-organic Frameworks for Sensing and Capture of Water Pollutants (Review).
   Soumya Mukherjee,† **Subhajit Dutta,**† Sahel Fajal and Sujit K. Ghosh.
   Dalton Trans. **2021**, 50, 17832-17850.
3. Three-in-one C_2H_2 selectivities guided adsorptive separation across an isoreticular family of cationic square lattice MOFs.
   Subhajit Dutta,† Soumya Mukherjee,† Omid T. Qazvini, Shivani Sharma, Debanjan Mahato, Ravichandar Babarao and Sujit K. Ghosh.
   Angew. Chem. Int. Ed., **2022**, 61, e202114132.
4. C_2H_2 induced structural dynamism driven efficient C_2H_2/CO_2 separation of in a water-stable cationic metal-organic framework.
   Subhajit Dutta,† Shivani Sharma,† Omid T. Qazvini, Gourab K. Dam, Ravichandar Babarao, Soumya Mukherjee and Sujit K. Ghosh.
   (Manuscript Submitted).
5. A Luminescent Water-Stable Cationic MOF for Bimodal Recognition of Cr (VI) and As (V & III) Oxo-anions in Water.
   Subhajit Dutta,† Sumanta Let,† Mandar M. Shirolkar, Aamod V. Desai, Partha Samanta, Sahel Fajal, Yogeshwar D. More and Sujit K. Ghosh.
   Dalton Trans., **2021**, *50*, 10133-10141.
6. A Water Stable Cationic MOF with Hydrophobic Pore Surface as Efficient Scavenger of Oxo-anion Pollutants from Water.
   Subhajit Dutta, Partha Samanta, Biplab Joarder, Sumanta Let, Debanjan Mahato, Ravichandar Babarao and Sujit K. Ghosh.
   ACS Appl. Mater. Interfaces, **2020**, *12*, *37*, 41810–41818.

Not Included in Thesis:

7. Imidazolium functionalized chemically robust ionic porous organic polymers (iPOPs) toward toxic oxo-pollutants capture from water.
   Arunabha Sen,† **Subhajit Dutta,**† Gourab K. Dam, Partha Samanta, Sumanta Let, Shivani Sharma, Mandar M. Shirolkar and Sujit K. Ghosh.
   Chem. Eur. J., 2021, 27, 1 –9.
8. Synthesis and structural elucidation of neutral N-donor linker based bi-porous isostructural cationic metal-organic frameworks.
   Subhajit Dutta, Aamod V. Desai, Partha Samanta and Sujit K. Ghosh.
   Inorganica Chimica Acta., 2019, 486, 401-405.
9. An Amide Functionalized Ultramicroporous MOF for Triple Selectivity in C2H2 Adsorption..
   Subhajit Dutta,† Soumya Mukherjee,† Tarak Nath Mandal, Omid T. Qazvini, Avishek Karmakar, Matthias Vandichel, Debanjan Mahato and Sujit K. Ghosh.
   (Manuscript Submitted).
10. Partha Samanta,† **Subhajit Dutta,**† Sumanta Let, Arunabha Sen, Mandar Shirolkar and Sujit K. Ghosh.
    Cost-effective Route to Dual Phase Scavenger of Iodine with Chemically Stable Hydroxy-functionalized Hyper-cross-linked Polymers (HCPs).
    (Manuscript Submitted).
11. Chemically Stable Ionic Viologen-Organic Network: An Efficient Scavenger of Toxic Oxo-anions from Water.
    Partha Samanta, Priyanshu Chandra,† **Subhajit Dutta,**† Aamod V. Desai and Sujit K. Ghosh.
    Chem. Sci., 2018, 9, 7874–7881.
12. Post-synthetically modified magnetic hyper crosslinked microporous polymers (HCPs) for toxic water pollutants capture.
    Sumanta Let, **Subhajit Dutta**, Partha Samanta, Shivani Sharma and Sujit K. Ghosh.
    (Manuscript Under minor revision in ACS Appl. Mater. Interfaces).
13. MOFs for Detection of Explosive and related toxic Nitro-aromatic compounds (NAC) (Book Chapter).
    Partha Samanta, **Subhajit Dutta** and Sujit K. Ghosh.
    (DOI: 10.1016/B978-0-12-814633-0.00002-8).
14. Neutral nitrogen donor-based MOFs for sensing based applications (Review).
    Shivani Sharma, **Subhajit Dutta**, Gourab K. Dam and Sujit K. Ghosh.
    Chem Asian J., 2021, 16, 1 – 20.
15. Fluorescent “Turn-on” Sensing Based on Metal-organic Frameworks (MOFs) (Review).

Avishek Karmakar, Partha Samanta, **Subhajit Dutta** and Sujit K. Ghosh.
Chem. Asian J., 2019, 14, 4506- 4519 (Cover Page).

16. A Dye@MOF Composite as Luminescent Sensory Material for Selective and Sensitive Recognition of Fe(III) ions in Water.
    S Sumanta Let, Partha Samanta, **Subhajit Dutta** and Sujit K. Ghosh.
    Inorganica Chimica Acta, 2019, 500, 119205.
17. Selective and sensitive recognition of Fe^{3+} ion by a Lewis basic functionalized chemically stable metal-organic framework (MOF).
    Sahel Fajal, Partha Samanta, **Subhajit Dutta** and Sujit K. Ghosh.
    Inorganica Chimica Acta, 2019, 500, 1193592
18. Functionalized ionic porous organic polymers exhibiting remarkable iodine uptake from both vapor and aqueous medium.
    Arunabha Sen, Shivani Sharma, **Subhajit Dutta**, Mandar M. Shirolkar, Gourab K. Dam, Sumanta Let and Sujit K. Ghosh.
    ACS Appl. Mater. Interfaces, 2021, 13, 29, 34188–34196
19. Advances in adsorptive separation of benzene and cyclohexane by metal-organic framework adsorbents (Review).
    Soumya Mukherjee, Debobroto Sensharma, Omid T. Qazvini, **Subhajit Dutta**, Lauren K. Macreadie, Sujit K. Ghosh and Ravichandar Babarao.
    Coord. Chem. Rev., 2021, 437, 213852.
20. Rapid, selective capture of toxic oxo-anions of Se (IV), Se (VI) and As(V) from water by an ionic metal-organic framework (iMOF).
    Shivani Sharma, Sumanta Let, Aamod V. Desai, **Subhajit Dutta**, Gopalsamy Karuppasamy, Mandar M. Shirolkar, Ravichandar Babarao and Sujit K. Ghosh.
    J. Mater. Chem. A, 2021,9, 6499-6507.
21. Metal-organic Frameworks (MOFs) Based Luminescent Sensory Probes for the Recognition of Cationic Water Pollutants (Review).
    Partha Samanta, Sumanta Let, Writakshi Mandal, **Subhajit Dutta** and Sujit K. Ghosh.
    Inorg. Chem. Front., 2020, 7, 1801.
22. Post-synthetically modified metal-organic framework as a scaffold for selective bisulphite recognition in water.
    Arunabha Sen, Aamod V. Desai, Partha Samanta, **Subhajit Dutta**, Sumanta Let and Sujit K. Ghosh.
    Polyhedron 2018, 156, 1-5.
23. Luminescent Metal-Organic Frameworks as Chemical Sensors (Book Chapter).

Yogeshwar D. More, Sahel Fajal, **Subhajit Dutta** and Sujit K. Ghosh.

(Manuscript Submitted).

24. Adsorption of CO_2 by high performance porous carbon derived from cotton stalk crop-residue collected across diverse geographical locations in India.

    Manpreet Singh, Nitin Borkhatariya, **Subhajit Dutta**, Sujit K. Ghosh, Pratyush Maiti, Subhadip Neogi and Subarna Maiti.

    J. CO2 Util. 2022, DOI: 10.1016/j.jcou.2022.101975.

25. Metal-organic framework based 'Molecular Nose' for selective recognition of toxic VOC-styrene.

    Arunabha Sen, Sahel Fajal, **Subhajit Dutta**, Aamod V. Desai, Writakshi Mandal and Sujit K. Ghosh.

    (Manuscript Submitted).

26. Unprecedented Boosting of Luminescence Property of a Hybrid Blue Perovskite via Loading into Metal-Organic Polyhedra Matrix.

    Samraj Mollick, Satyam Saurabh, Yogeshwar D. More, Writakshi Mandal, Sahel Fajal, Tarak Nath Mandal, Mandar M. Shirolkar, **Subhajit Dutta** and Sujit K. Ghosh.

    (Manuscript Submitted).

27. Atomically Dispersed Pd (II)- tethered N-Heterocyclic carbene on a Porous Polymer – A Heterogeneous catalyst for C-C coupling at Room Temperature.

    Sumanta Let, Gourab K. Dam, Sahel Fajal, Partha Samanta, **Subhajit Dutta** and Sujit K. Ghosh.

    (Manuscript Submitted).

28. A Hydrolytically Stable Luminescent Cationic MOF for Selective Detection of Toxic Organic Arsenic in Water.

    Gourab K. Dam, **Subhajit Dutta**, Sahel Fajal, Sumanta Let, Pratibha Agarwala, and Sujit K. Ghosh.

    (Manuscript Submitted).

29. Highly Stable and End-Group Tuneable Metal-organic Framework UiO-66/PVDF Composite for Superior Triboelectric Nanogenerator Application.

    Yogeshwar D. More, Satyam Saurabh, Samraj Mollick, Sachin Kumar Singh, **Subhajit Dutta**, Sahel Fazal, Anil Shetty, Mandar M. Shirolkar, Suresh Panchal, Minal Wable, Satishchandra Ogale and Sujit K. Ghosh.

    (Manuscript Submitted).

Chapter 1

Introduction

1. Introduction

1.1 Metal-organic frameworks (MOFs):

The domain of porous materials has seen a meteoric surge throughout scientific community over the last few decades owing to their widespread utility across a variety of fields.[1] Amongst its sub-classes, metal-organic frameworks (MOFs) or porous coordination polymers (PCPs) have come forth as a new research hotspot on account of their tremendous potential as next generation inorganic-organic hybrid materials.[2] MOFs are solid-state porous crystalline materials encompassing potential voids, constructed from bi-/multi-dentate organic struts which extend infinitely through metal nodes in a periodic manner to form a framework structure (Figure 1.1). The void space inside the framework typically remain preoccupied by the solvent molecules utilized during the synthesis process, counter ions and unreacted ligands.[3] Generally, depending upon the pore-aperture size, MOFs are categorized as (i) ultramicroporous MOFs (pore size < 0.7 nm), (ii) microporous MOFs (pore size < 2 nm) and Mesoporous MOFs (pore size > 2 nm). The liberty of designing and tailor-made syntheses of MOFs with a vast range of organic ligands and metal cations bestow

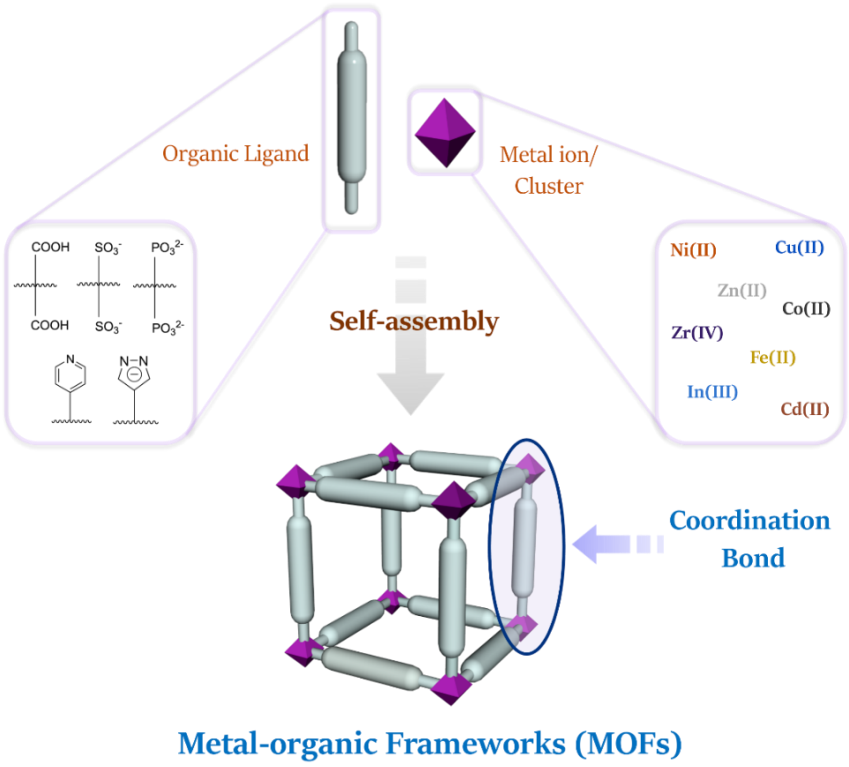

Figure 1.1 Schematic representation illustrating the general protocol to synthesize metal-organic frameworks (MOFs).

probability of infinite combinations of networked structures which are proven to be frontrunners in the fields of gas adsorption, sensing, ion conduction, catalysis, environmental pollutant capture, drug-delivery etc.[4-8]

1.1.1 Building blocks of MOFs:

Typically, 3d transition metal cations are preferred choice for the preparation of MOFs along with different kinds of organic ligand systems. Selection of these first row transition metal cations have certainly become crucial as they offer range of advantages, e.g., Fe(II) can impart magnetic property, Zn(II) or Cd(II) [d^{10} cations] can impart fluorescence properties in the system. On the other hand, certain metal ions such as Zn(II) cation (for dynamic coordination sphere) and Cu(II) (for Jahn-Teller distortion) have shown promises toward developing dynamic MOFs.[9-14] In pursuit of synthesizing new materials, chemical stability has become a crucial challenge both in terms of compound synthesis and for its subsequent real-time implementation. When it comes to MOFs, the framework stability is directly correlated with the metal-ligand bond strength, which underscore the importance of judicious choice of the metal cations in designing and synthesis of the MOFs.[15-18]

On the other hand, the library of organic ligands consists of a wide range of diverse functionalities, in terms of both terminal binding moieties as well as nature of the core or backbone.[19-21] The organic ligands can be broadly classified as (a) Oxygen-donor ligands [e.g. carboxylates(R-COOH), sulfonates(R-SO_3H), phosphonates (R-$PO(OH)_2$) etc.] and (ii) Nitrogen-donor ligands having N-heterocyclic aromatic groups as terminal binding unit (pyridine, imidazole, triazole, adenine, pyrazine etc.). From the inception of MOFs, carboxylate-based ligands are been utilized for the synthesis of majority of the MOFs because of their strong binding ability with most of the metal cations. On the contrary, albeit N-donor ligands have been commonly utilized as the co-ligand with carboxylate-terminal linkers, the domain of standalone MOFs built from N-donor ligands is yet to investigated thoroughly.[22-25] Further, N-donor ligands can be broadly classified into two, (i) neutral and (ii) ionic ligands depending upon their charge. Ionic N-donor linkers with N-heterocyclic aromatic groups such as pyrazolate, imidazolate, tetrazolate etc. can form strong coordination bond with the metal center owing to their higher pKa values, imparting higher resistance to hydrolysis. Typically, neutral N-donor moieties such as imidazole, pyridine, triazole etc. have been utilized for the synthesis of cationic MOFs and as a co-ligand they are used to increase the porosity or provide extra functional sites. Despite the fact that the field of MOF has witnessed the growing supremacy of O-donor ligand-based MOFs and have been investigated for numerous applications, N-donor ligand-based MOFs are also catching up with potential solutions in a variety of disciplines.

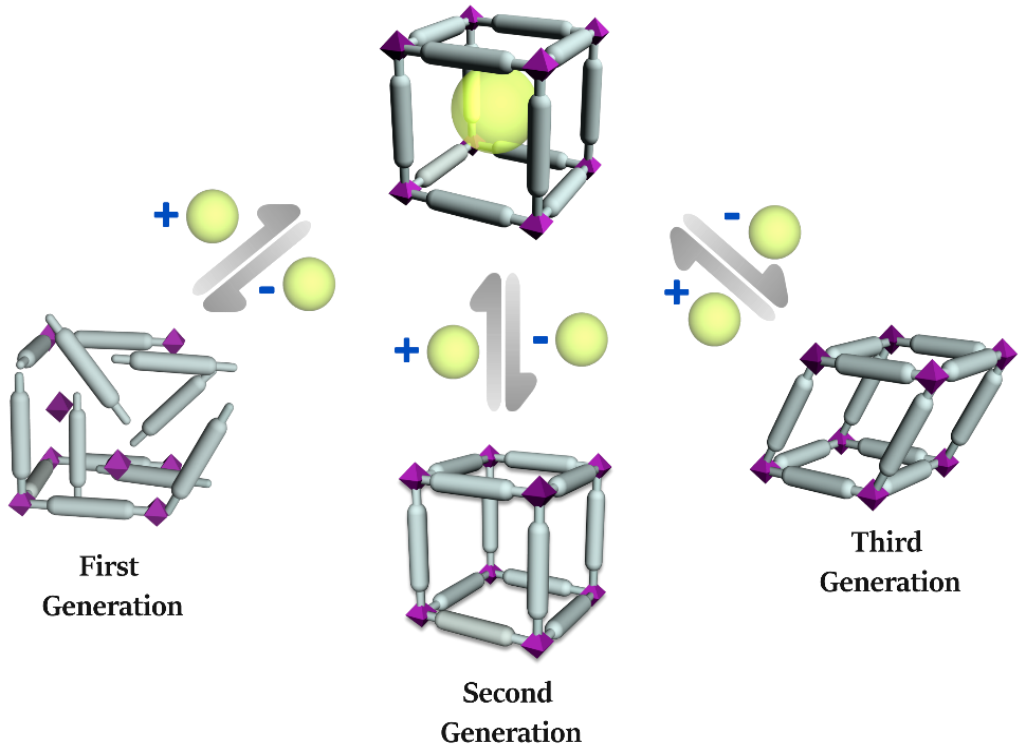

Figure 1.2 Generation-wise classification of MOFs depending upon the fate of the compound after the evacuation of guest molecules.

1.1.2 Types of MOFs:

1.1.2.1 Classification of MOFs based on structural aspect:

Generally, it is observed that the structural rigidity of the MOF can alter upon removal or desolvation of the occluded guest solvent molecules from the voids. On this basis, MOFs can be broadly classified into 3 generations (Figure 1.2).[26] The 1st generation MOFs are known to undergo complete disintegration of the framework upon removal of solvent molecules. The 2nd generation MOFs known to be rigid and retain their structural integrity after guest removal. The 3rd generation MOFs are known as the dynamic MOFs which can alter their structural rigidity upon guest removal and can come back to its' initial phase upon antagonistic stimulus. MOFs.

1.1.2.2 Classification of MOFs based on charge: Neutral MOFs and ionic-MOFs:

The Apart from the structural aspect, depending upon the residual charge of the framework backbone, MOFs are generally classified into two, i.e. neutral MOFs and ionic MOFs (Figure 1.3).[27-28] In case of

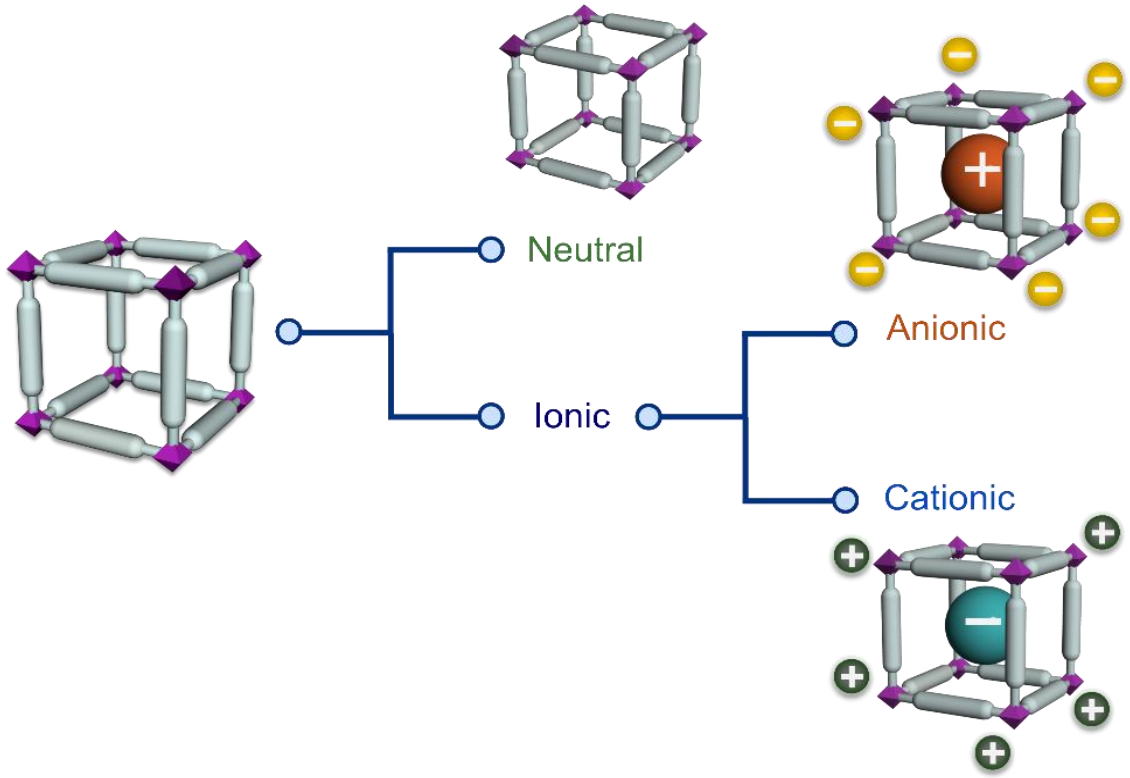

Figure 1.3 Classification of MOFs on the basis of the charge of the framework backbone.

neutral MOFs, the positive charge of the metal center is typically balanced out either by various charge balancing moieties such as negative charge of the counter anions or negatively charged coordinating ligands. On the other hand, the framework backbone of ionic MOFs (iMOFs) have a residual uncompensated charge (positive or negative) thereby resulting in cationic/anionic frameworks with some extra framework counter-ions. The preparation of ionic or neutral MOFs can be achieved with various approaches and the synthetic protocols are guided by the fundamentals of coordination chemistry which directly underscore the significant role of choice of organic ligands and metal ions.

1.1.2.2a Neutral MOFs:

The literature of MOFs has witnessed a clear predominance of reported electronically neutral MOFs in which the positive charges on the metal center are fully balanced by the coordinating moieties itself. In such cases the electronic charge is counterbalanced by the anionic linkers (mostly carboxylates-based ligands) or negatively charged anions of the metal salts coordinated to the metal center (Figure 1.4a).[29-31]

1.1.2.2b Ionic MOFs:

Typically, ionic MOFs form due to presence of uncompensated framework charge and therefore necessitating extra framework ions either negative or positive to maintain the overall charge neutrality. On the basis of the residual charge of the framework backbone, ionic MOFs are classified into two, anionic and cationic MOFs. The framework backbone of cationic MOFs possesses a net positive charge which is counterbalanced by the uncoordinated anions present inside the pores. In case of anionic MOFs, the framework backbone bears a residual anionic charge which is balanced by the uncoordinated cations (Figure 1.4b-1.4c). Although, the partial occupation of the uncoordinated ions can cause pore blocking and complete accessibility to the surface area, but the free counter-ions offer extra ionic functionality which are found to be extremely suitable for different applications.[32-34]

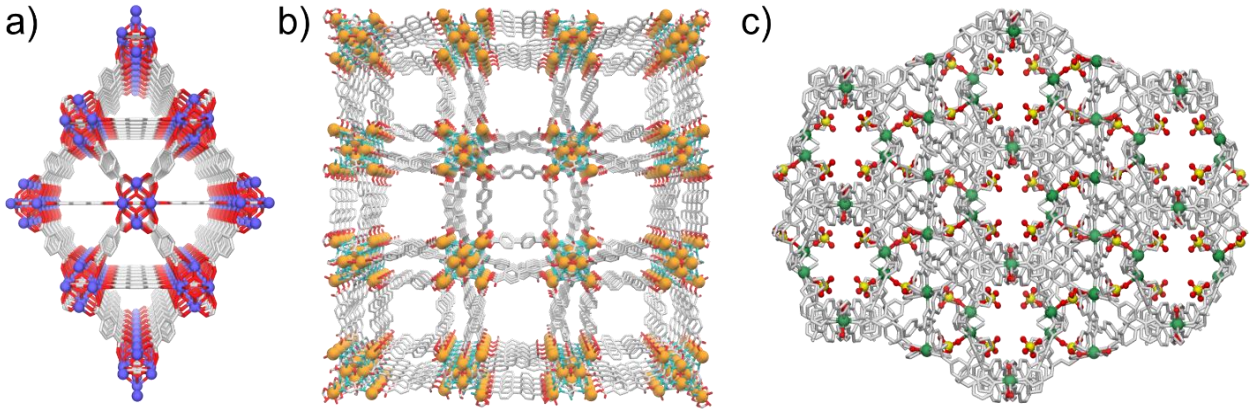

Figure 1.4 Packing diagrams of few benchmark MOFs with different charge of the framework backbone, a) neutral MOF, b) anionic MOF and c) cationic MOF. The corresponding crystal structure data have been reproduced with permission from reference 17, 18 and 116 respectively. (Color code: C, grey; O, red; N, blue; Zr, navy blue; Zn, yellow; Ni, dark green. H-atoms have been omitted for clarity).

1.1.2.2b.1 Anionic MOFs:

An anionic MOF is primarily consisting of a negatively charged framework backbone with extra uncoordinated counter cations to neutralize the overall charge. Typically, metal cations having higher coordination numbers are commonly used to prepare anionic MOFs which yield in ionic character when a higher number of organic ligands concentrate around the metal nodes. In such cases, the compound show enhanced chemical stability as the central metal node gets protected with the higher number of ligands.[35-38]

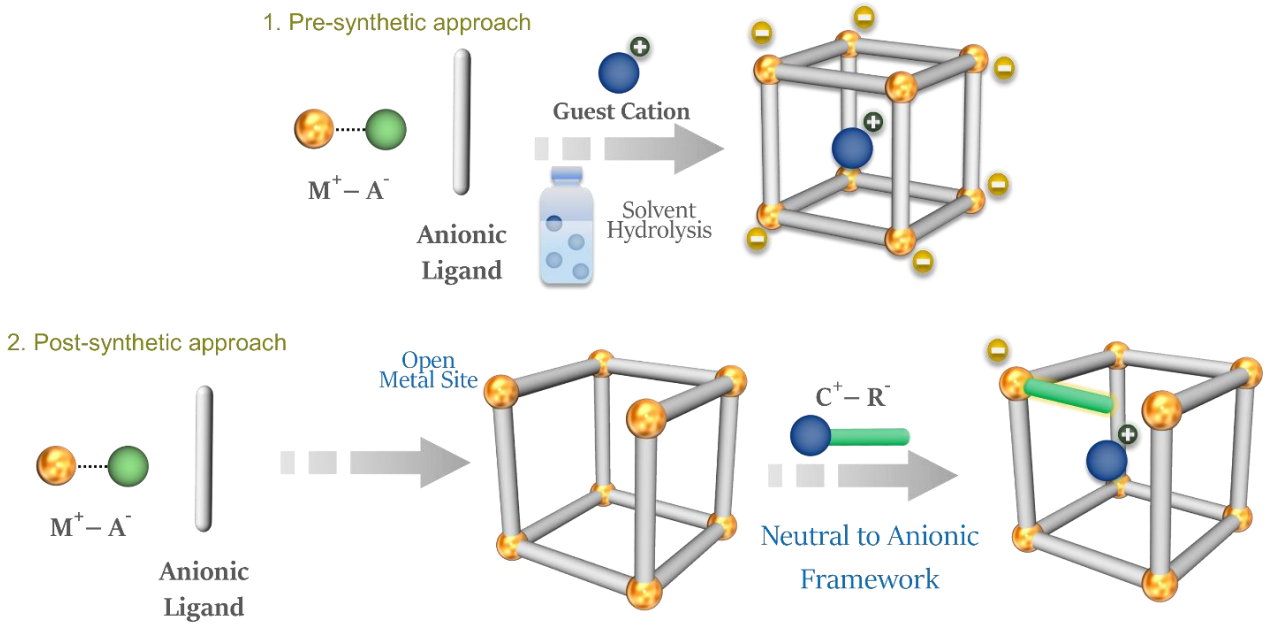

Figure 1.5 Schematic representation of routes to synthesize anionic MOFs via pre-synthetic and post-synthetic methods.

The routes for constructing anionic MOFs are challenging since they are mostly accidental. However, few organic solvents like N, N-dimethylacetamide (DMA), N, N diethyl formamide (DEF), N, N-dimethylformamide (DMF) etc. can undergo hydrolysis and subsequent decarbonylation in solvothermal conditions to generate $[NH_2Et_2]^+$ or $[NH_2Me_2]^+$ cations, yielding in the formation of anionic frameworks (Figure 1.5).[35-38]

1.1.2.2b.2 Cationic MOFs:

Likewise, cationic MOFs are primarily consisting of a positively charged framework backbone with extra uncoordinated anions to neutralize the overall framework charge. The counter anions typically remain free inside the porous channels of the framework or can coordinate to the mental centre via weak electrostatic interactions. In recent years, cationic MOFs have exhibited extraordinary potential toward applications like sensing, environmental pollutant capture, catalysis etc. Owing to its' several advantages such as pre-functionalized cationic framework backbone, uncoordinated polar functional anions inside the pores etc., cationic MOFs are regarded as the next generation anion exchange material for various environmental applications.[27]

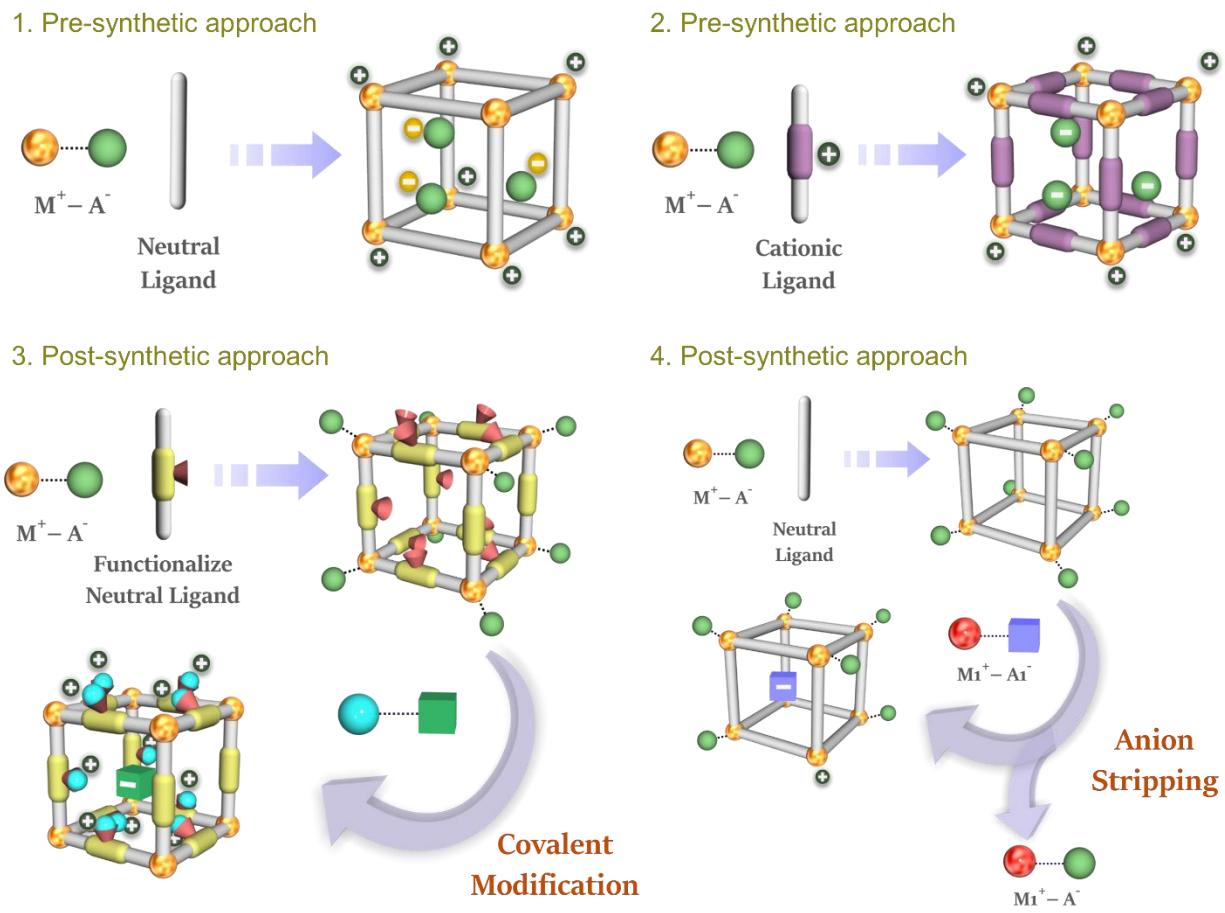

Figure 1.6 Schematic representation of routes to synthesize cationic MOFs via pre-synthetic and post-synthetic methods.

Despite of such huge potential, exploration of cationic MOFs in the domain of industrial separation and aquatic remediation is at very nascent phase which is the prime object of this thesis work.

1.1.2.2b.3 Design and Fabrication of Functional Cationic MOFs:

Cationic MOFs can be synthesized either by pre-synthetic approach or by post-synthetic modifications of a secondary functionality in a neutral framework. [39-46] The rational synthetic strategies of cationic MOFs are summarized in Figure 1.6. The main design strategy of cationic MOFs is based on pre-synthetic ligand designing in which neutral N-heterocyclic donor moiety linked ligands are mainly utilized. Representative examples of such N-donor ligands are presented in Figure 1.7. In this regard, five-member terminal donating groups such as imidazole, triazole, pyrazole etc. are preferred owing to smaller size and

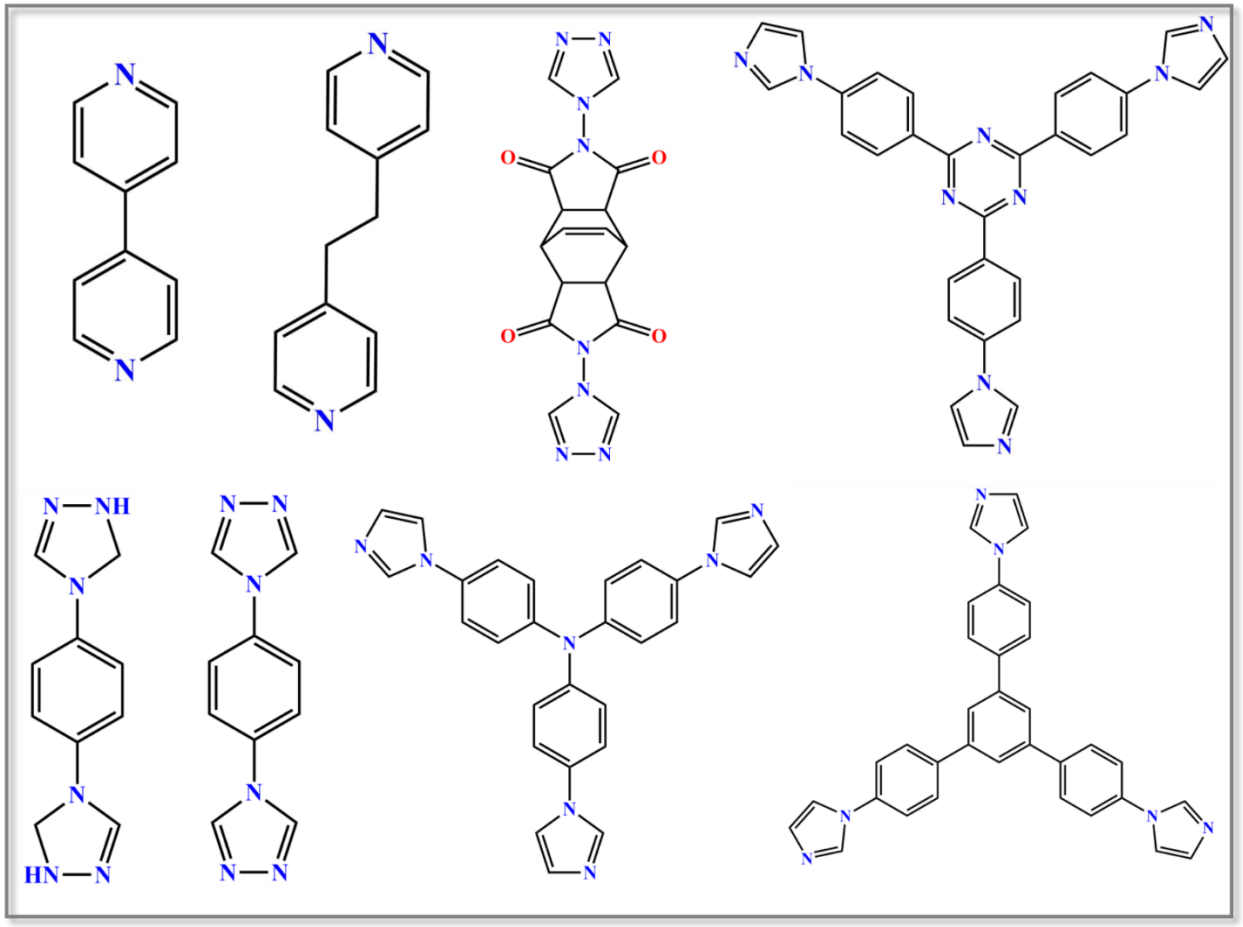

Figure 1.7 Schematic representation of list of organic ligands to be used for synthesis of ionic MOFs.

stronger binding ability over the six membered heterocycles such as pyridine, pyrazine etc. The vicinity of the coordination sphere of the central metal will be strengthen by using such lesser bulky 5-membered N-heterocyclic moieties which can result into a higher density of the ligand moieties around the central metal centers, enabling hexa-coordination to the metal nodes and shielding from the influence of external species. Further, the coordination number of the particular metal ion gets satisfied by solely the functional ligands and the metal center gets covered by the high number of 5-membered rings, which acts as shield here from water molecules, imparting hydrolytic stability in the MOF. Another approach to synthesize cationic MOFs via pre-synthetic approach is to utilize cationic imidazolium moieties in the ligand backbone. Such ligands comprise of positively charged nitrogen atom which intrinsically impart cationic nature to the framework.

Moreover, Carboxylic acid-based ligands are also employed to synthesize cationic MOF *via* pre-functionalization approach. In this method, the carboxylic acid ligands having nitrogen heteroatom (e.g. pyridine moiety) appended can be reacted with alkyl halide (R-X) moieties via nucleophilic substitution which yield in $N\text{-}R^{+}X^{-}$ moiety, having the halide (X^{-}) anions uncoordinated inside the pores. On the other hand, postsynthetic modification (PSM) of neutral MOFs is another effective technique of synthesize cationic MOFs. For example, PSM-based approach can be employed for oxidation of metal centres such as Fe^{2+} to convert into oxidised metal centre Fe^{3+}, which will result in a requirement of extra negative charge to balance the overall framework's charge. Oxidation of such MOFs can result in generation of cationic frameworks containing extra-framework anions to balance overall charge.

1.1.2.2b.4 Advantages of Cationic MOFs:

Cationic MOFs have shown enormous promise to become the frontrunner as the next generation cationic/ anion-exchange materials owing to its' several supreme features including tunable architecture, bimodal functionalization in terms of both framework backbone and uncoordinated functional anions, surface functionalization, ease in ion-exchange processes and so on. Strategic functionalization of cationic MOFs has resulted in the emergence of critical features such as physicochemical stability and tunable pore size both of which are required for the development of advanced ionic materials. In addition, cationic MOFs can be tuned both in terms of framework building units and appended functionality for their applicability for selective anion exchange and enhancing the overall interactions of guest anions with the framework. Particularly, the tunability of the uncoordinated anions as the extra-framework functionality has proven to be game changer in various applications such as environmental pollutant sensing and capture, catalysis, optoelectronic based applications etc. These anions can be varied depending upon the demand of the application and offer a wide range of library of functional anions such as: NO_3^{-}, ClO_4^{-}, Cl^{-}, Br^{-}, BF_4^{-}, SO_4^{-}, SiF_6^{-} etc. Apart from these inorganic anions, organic moieties with carboxylic acid (-COOH), sulfonic acid ($-SO_3H$) or phosphonic acid ($-PO_3H$) groups can also serve as the extra framework anion to balance the overall charge of the cationic framework. The additional advantage of these uncoordinated anions is the pore size of the cationic framework can also be tuned by varying these anions. Hence, the cationic framework nanospace can be functionalized as well as tuned by these functional anions for target specific applications. Moreover, in case of ion-exchange based applications, cationic MOFs enable to exchange the targeted guest anions via ion-exchange process which ensures no leaching of the incoming anions. Thus, cationic MOFs can impart selectivity with high efficiency in ion-exchange based applications.

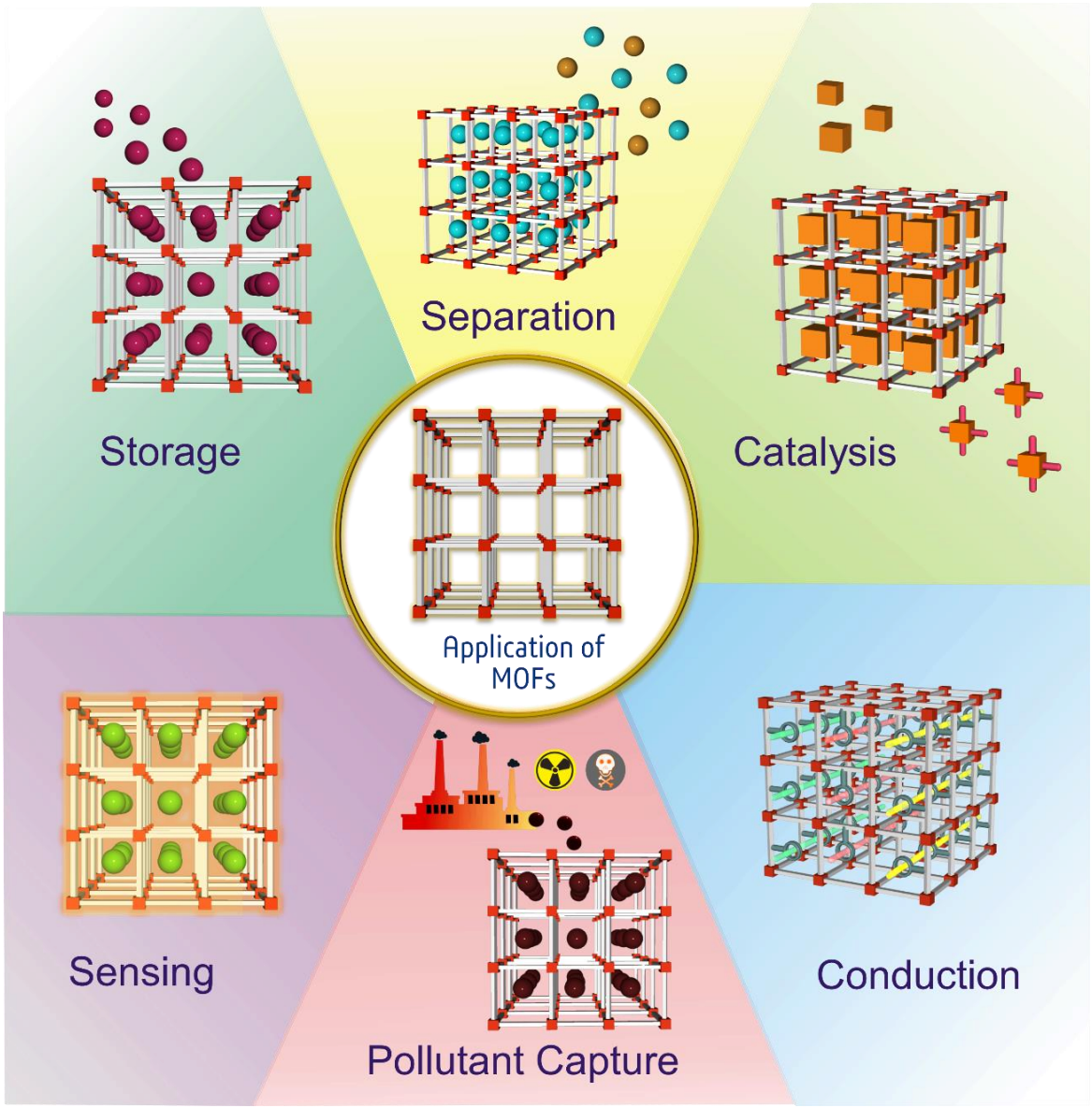

Figure 1.8 Schematic representation illustrating the diverse potential applications of MOFs.

1.2 Applications of ionic MOFs:

Thanks to the numerous structural and characteristic advantages of MOFs, they have proven suitable toward tackling of several real-world applications (Figure 1.8), such as, sensing of environmentally toxic species, gas separation and storage, industrially relevant light hydrocarbon separation, fuel cell applications, ion conduction, removal of toxic and hazardous waste, heterogeneous catalysis, magnetism etc.[47-55] The insight

of structure-property correlation has a huge impact in rapid progress of MOFs toward these emerging applications. Furthermore, the functional networks can be tuned to meet the needs of any target-specific applications. On account of such huge potential, advancement of the MOFs continues as an eminent crystalline porous material which, in the next few years, will strive significant attention in terms of real-time applicability. In this current thesis, we focus on design, synthesis and functional studies of neutral N-donor ligand based cationic MOFs toward exclusively selective separation of industrially relevant light hydrocarbons and remediation of toxic aquatic pollutants, which are discussed herein:

1.3 Light hydrocarbon separation:

Energetically efficient as well as cost-effective separation and purification of light hydrocarbons are of the most fundamental challenges in petrochemical industries globally.[56-64] Every year, millions of tons of C2 light hydrocarbons are generated from petroleum, coal, and natural gas via an interconnected network of chemical processes and purification methods. Light hydrocarbons like acetylene (C_2H_2) and ethylene (C_2H_4) have been regarded as the key components of various commodity chemicals, such as fibers, plastics, rubber, acrylic acid derivatives, vinyl compounds, ethynyl alcohols and so on. Among them, acetylene is one of the most crucial raw chemicals in electronic as well as petrochemical industries.[65-67] However, industrial production of C_2H_2 inevitably yield some impurities such as CO_2, C_2H_4, CH_4 etc. which are very difficult to separate due to their almost similar physical properties and can degrade the purity of C_2H_2

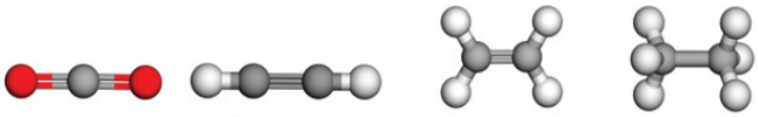

Adsorbate molecules	CO_2	C_2H_2	C_2H_4	C_2H_6
Boiling point (K)	194.7	188.4	169.4	184.5
Quadrupole moment (x 10^{26} e.s.u. cm^2)	4.3	3.0	1.5	0.65
Polarisability (x 10^{-25} cm^3)	29.1	33.3-39.3	42.5	44.3-44.7
Kinetic diameter (Å)	3.3	3.3	4.16	4.44

Figure 1.9 Schematic representation illustrating selective light hydrocarbon separation by cationic MOFs.

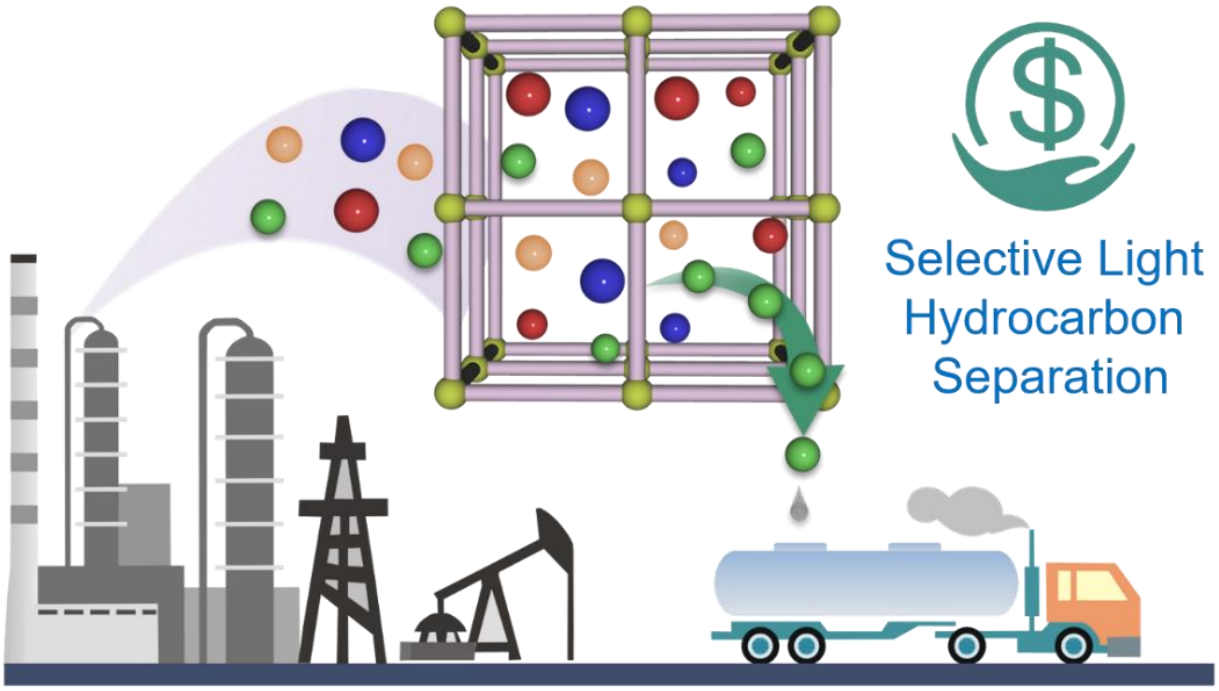

Figure 1.10 Schematic representation illustrating selective light hydrocarbon separation by cationic MOFs.

significantly (Figure 1.9). Thus, C_2H_2 purification is crucial from two distinct aspects: selective separation of trace amount of C_2H_2 from its $C_2H_4/CO_2/CH_4$ mixtures and elimination of any other contaminants to produce ultra pure C_2H_2.[68-70] Traditional separation and purification techniques for C_2H_2 involve cryogenic distillation, solvent extraction, chemical reactions etc. which possess several drawbacks. Solvent absorption methods typically involve higher energy consumption and low selectivities in the regeneration process. Moreover, with the usage of volatile organic solvents, these methods induce environmental pollution and rapid degradation. Similarly, cryogenic distillation bears a huge energy-expensive footprint and a high-energy penalty owing to the similar physiochemical properties (e.g. boiling points) of C_2H_2, CO_2, C_2H_4 etc. Hence, significant challenges still remain in the development of sustainable, effective and energy-efficient techniques for separation and purification of C_2H_2.[71-78] On the other hand, C_2H_4 is primarily generated from steam cracking of naphtha and ethane (C_2H_6) along with hydrogenation of C_2H_2. Typically, C_2H_4 is the major product during C_2H_6 production, and hence C_2H_4/C_2H_6 separation is required to remove unwanted C_2H_6 from the mixture of incomplete conversion. A highly complex and energy-intensive process is involved for production and purification of C_2H_4 from its' naphtha creaking by-products such as propylene and other C2–C6 olefins. Moreover, similar physiochemical properties of these light

hydrocarbons such as molecular sizes and shapes, boiling points etc. make these separation processes highly challenging and energy-expensive, which necessitate alternative separation methods with lesser energy-footprints and higher efficiency. For example, the most traditionally utilized method, cryogenic distillation, is highly energy-demanding as it requires operational pressures of 7−28 bar along with the temperatures of 183−258 K combined with high reflux ratios (e.g. 2.5–4 for C_2H_4/C_2H_6) and high tray numbers (>100) to achieve the purity of polymer-grade C_2H_4. Given the massive market for light hydrocarbons, even minor betterments in separation performance will make a substantial impact both in terms of reducing the operating costs and lowering the carbon footprint.[79-84]

In this regard, adsorption driven separation processes offer enormous promise as viable alternatives which can facilitate a transition from conventional cryogenic distillation technologies to energy-efficient light hydrocarbons purification. This process affords both hydrocarbon purification as well as separation via adsorbing either the trace or major component, respectively. Typically, the conventional porous materials like activated carbon or zeolites fail to perform efficiently both in terms of selectivity and efficacy. Under this backdrop, ultramicroporous MOFs in particular have shown tremendous potential toward these highly challenging separations. Such materials offer unique advantages such as: (1) designability: enabling the prospective design of the target compound with enhanced structural predictability which subsequently yield in control over the structures-property correlation; (2) tunability: the porous void can be delicately tuned by the appropriate choice of metal cations and organic ligands; (3) ease of functionalization: various functional moieties can be conveniently incorporated inside the pore of MOFs to enable specific interactions with the incoming gas molecules, enhancing their separation capabilities (Figure 1.10).[85-95] Hitherto, most of the studies of MOFs based gas separations are primarily focused on the methods to tune the framework functionalities and pore dimensions to improve the separation performance toward a targeted sorbent molecule. Although, till date several MOFs have been utilized towards such separation, but the domain of ionic MOFs still remains rarely explored in this regard. Particularly, cationic MOFs are very well suited for selective sorption and separation of such light hydrocarbons owing to their pre-functionalized ionic framework backbone along with contribution of the functional counter anions in preferential interaction with the incoming gas molecules. Tunability in building block functionality as well as uncoordinated anions renders huge opportunities to design and synthesis of novel functional cationic MOFs with optimum pore-aperture and appropriate functionalities to address this challenging industrial issue of light hydrocarbon separation.

1.4 Toxic aquatic pollutants remediation:

Water is the essential resource to all living beings and according to the united nations (UN), the water consumption is estimated to increase by 20-55% by 2050.[69-97] In this regard, water pollution has become the most serious environmental crisis globally in the twenty-first century, causing the massive deterioration to the marine ecosystem as well as human beings.[98-100] The escalating impact of rapidly expanding industrialization and urban sectors throughout the globe is the primary cause of water contamination. Consequently, dumping of waste water from various industries as well as radioactive waste from nuclear power plants are among the prime contributors toward water pollution.[101-102] In addition, the major chemical water contaminants include both organic and inorganic pollutants (Figure 1.11).[103-107] The organic contaminants include antibiotics, pesticides, herbicides, pharmaceuticals, toxic dyes etc. On the other hand,

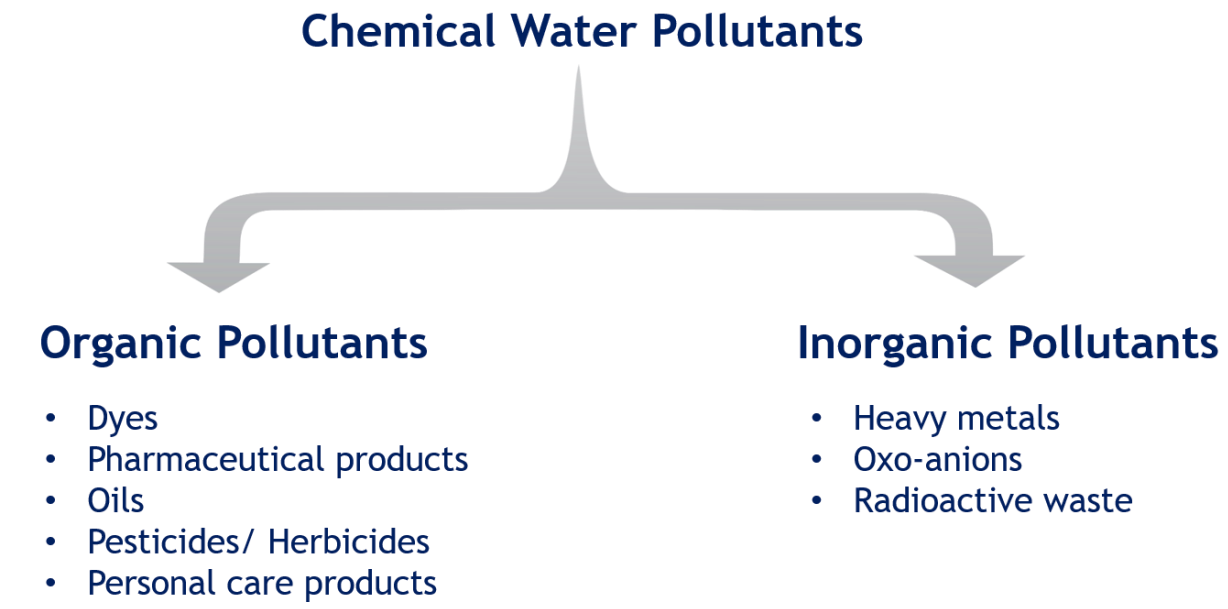

Figure 1.11 Schematic representation illustrating classification of the chemical water pollution.

inorganic contaminants can be classified into two, (1) cationic pollutants and (2) anionic pollutants. The cationic inorganic pollutants include toxic heavy-metal ions comprising of lead (Pb^{2+}), mercury (Hg^{2+}), cadmium (Cd^{2+}) along with several ionic radionuclides such as uranium (UO_2^{2+}), cesium (Cs^{+}), strontium (Sr^{2+}) cations. The anionic counterpart consists of heavy-metal oxo-anions such as CrO_4^{2-}, $Cr_2O_7^{2-}$, AsO_4^{3-}, SeO_3^{2-}, SeO_4^{2-} along with different radioactive anions, e.g. pertechnetate ($^{99}TcO_4^{-}$). Many of these pollutants feature in the "Priority pollutant list" by environmental protection agency (U.S.). All these toxic and

hazardous pollutants possess extreme threat to ecological symbiosis and thus, safe disposal of such contaminants is of paramount scientific as well as industrial interest. On account of this, selective sensing and sequestration of the toxic aquatic pollutants has been regarded as the primary steps toward complete remediation of the pollutants. In this context, the protype material should possess few key features such as hydrolytic stability for a long period of time for enhanced efficiency. Another important factor is simple, rapid and precise response toward the targeted pollutants. Among the state-of-the art sensory techniques, the photoluminescence method-based signal transduction in MOFs has attracted huge scientific attention because of its several advantages such as: (i) quick response time, (ii) High sensitivity and selectivity (iii) Heterogeneous phase (ii) very low limit of detection range etc.[108-111] Apart from sensing, effective removal and degradation of aquatic pollutants from the natural water bodies is regarded as a viable solution toward remediation of these toxic pollutants. Such demand necessitates development of new functional materials which offer some key features like stability, kinetics, uptake capacity etc. for its real-time applicability. In this regard, ionic MOFs have shown tremendous promise owing to their unique shape-memory effect as well as shape-template effect which can be introduce easily in such systems by judicious choice of cationic/anionic components.[112-114] Thus introduced features distinctly enhances the interactions between

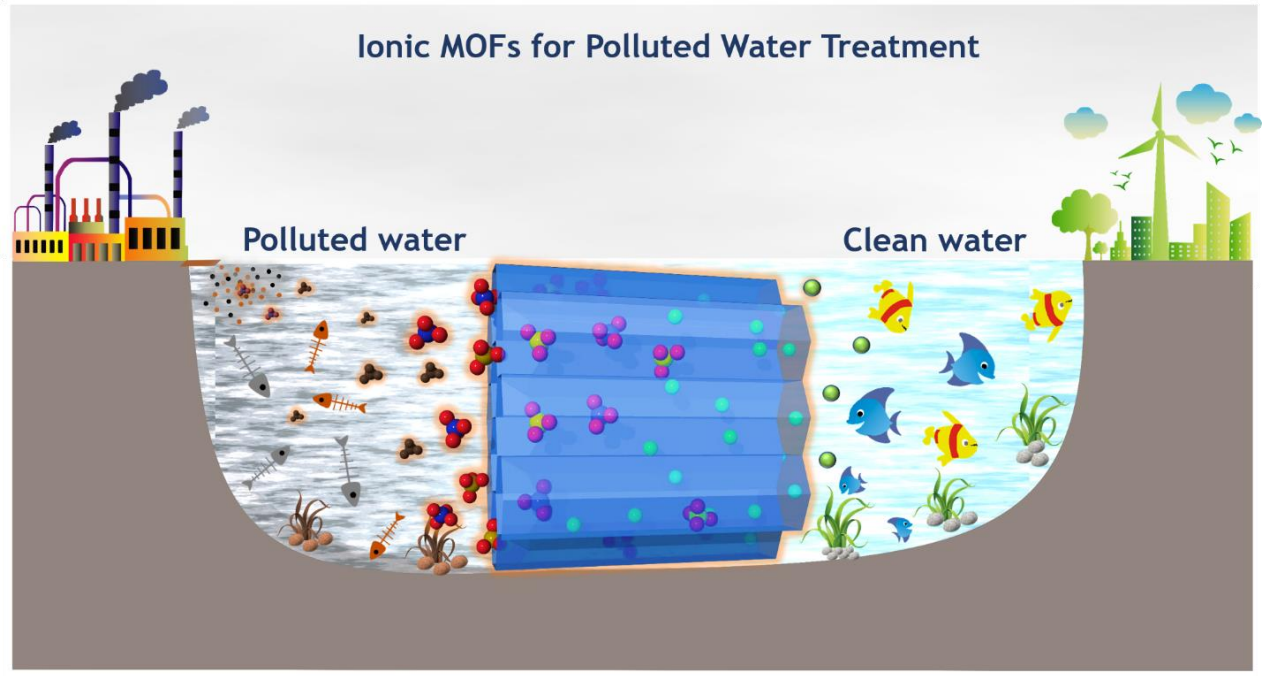

Figure 1.12 Schematic representation illustrating remediation of toxic and hazardous water pollutants by MOFs.

the ionic framework backbone and incoming toxic pollutants thereby improving selectivity (Figure 1.12). Moreover, ionic MOFs enable the mode of sequestration via ion-exchange which plays very crucial role in removal kinetics and selectivity toward the pollutants. In the field of MOFs, several neutral MOFs (NU-1000, UiO-66 etc.) with different functionalities such as zirconium clusters as building units have been utilized for removal of these aquatic pollutants, specially the heavy-metal based oxo-anions.[114] However, ionic MOFs, particularly the cationic MOFs are very rarely explored toward the capture of oxo-anions with lower charge density.[115] Hence, in order to fast-track the development and explore the huge potential of ionic MOFs, our effort have been devoted toward selective sequestration of the toxic oxo-anions via cationic MOFs.

1.5 Thesis Overview:

Herein, the work accomplished in this thesis has focused on the design and synthesis of neutral N-donor based cationic MOFs for energy and environmental applications. Although cationic MOFs are recently getting attention in various application fields, but they have rarely been explored toward efficient light hydrocarbon separation and selection remediation of toxic aquatic pollutants. The entire thesis divided in two parts and each part further consists of two chapters each. In part-I, efficient separation of industrially relevant light hydrocarbons by several functional cationic MOFs were described in details, while in part-II selective sensing and capture of toxic aquatic pollutants by novel water stable cationic MOFs have been addressed and described in details.

In the second chapter (Chapter 2), a series of novel iso-structural cationic MOFs were synthesized by varying the uncoordinated inorganic anions (ClO_4^-, BF_4^-, NO_3^-) inside the pore. Further, all these MOFs were found to show excellent adsorptive separation of industrially relevant light hydrocarbons (C_2H_2, CO_2, C_2H_4, CH_4). This work demonstrates the first example of a cationic MOF series delivering such challenging and efficient hydrocarbon separation even in dynamic conditions. The knowledge acquired regarding the technicalities and real-time applicability of cationic MOFs was then further applied to prepare a series of novel water-stable, cationic MOF with different functional organic anions inside the MOFs (Chapter 3). Further, the MOFs showed excellent selective separation of C_2H_2 from its industrial impurity CO_2 in an efficient manner. Interestingly, one of these MOFs (iMOF-8C) showed very rare temperature dependent adsorptive gate opening behavior towards C_2H_2. This work marks the first example of a cationic MOF exhibiting such stepped isotherms towards C_2H_2, resulting in a huge separation performance between C_2H_2/CO_2.

We further continued our effort to develop and explore water stable cationic MOFs toward selective recognition and sequestration of toxic environmental pollutants, which can serve as the next generation

alternative to tackle environmental pollution. On account of that, in the fourth chapter (Chapter 4) a novel Zn(II) based water stable cationic MOF was synthesized and employed toward selective detection of several heavy metal based toxic oxo-anions (CrO_4^{2-}, $Cr_2O_7^{2-}$,$HAsO_4^{2-}$, and $HAsO_3^{2-}$). The compound was found to exhibit a very rare dual turn off/on fluorescence response toward these oxo-anions. It showed a rapid quenching behavior with excellent limit of detection values toward chromium based oxo-anions CrO_4^{2-}, $Cr_2O_7^{2-}$. On the other hand, it showed fluorescence enhancement toward arsenic based oxo-anions $HAsO_4^{2-}$, and $HAsO_3^{2-}$. Further in the fifth chapter (Chapter 5), we focused on to integrate robustness and chemical stability to cationic MOFs to be suited for real-world problems. Along this line, we have synthesized a Ni(II) based robust, water stable cationic MOF with hydrophobic pore surface. The central metal node was strategically protected by hydrophobic shielding which yielded in high chemical stability of the material. Further, the material showed excellent removal of toxic CrO_4^{2-} anions both in terms of kinetics and saturation uptake capacity and showed selective removal of CrO_4^{2-} anions even in presence of competing anions such as NO_3^-, Cl^-, NO_3^- etc. Environmental pollution due to radioactive waste, particularly by another oxo-anion, TcO_4^- ion, has been a huge concern because of the abundance of its radioactive isotope technetium (^{99}Tc). Due to its safety handling issue in common laboratory, the capture of TcO_4^- anions were carried out by using its surrogating anion ReO_4^-, in which the material registers a very high saturation uptake capacity value. In addition, the material showed excellent recyclability toward both the oxo-anions, showing its potential as a real-time applicable material.

1.4 References

[1] A. G. Slater, A. I. Cooper, *Science* **2015**, *348*, aaa8075.

[2] S. Kitagawa, R. Kitaura, S.-i. Noro, *Angew. Chem. Int. Ed.* **2004**, *43*, 2334-2375.

[3] H. Li, M. Eddaoudi, M. O'Keeffe, O. M. Yaghi, *Nature* **1999**, *402*, 276-279.

[4] H. Furukawa, K. E. Cordova, M. O'Keeffe, O. M. Yaghi, *Science* **2013**, *341*, 1230444.

[5] O. M. Yaghi, M. O'Keeffe, N. W. Ockwig, H. K. Chae, M. Eddaoudi, J. Kim, *Nature* **2003**, *423*, 705-714.

[6] J.-R. Li, R. J. Kuppler, H.-C. Zhou, *Chem. Soc. Rev.*, **2009**, *38*, 1477-1504.

[7] J.-R. Li, J. Sculley, H.-C. Zhou, *Chem. Rev.* **2012**, *112*, 869–932.

[8] N. Stock, S. Biswas, *Chem. Rev.* **2012**, *112*, 933–969.

[9] X. Liu, Y. Zhou, J. Zhang, L. Tang, L. Luo, G. Zeng, *ACS Appl. Mater. Interfaces* **2017**, *9*, 20255-20275.

[10] M. D. Allendorf, C. A. Bauer, R. K. Bhakta, R. J. T. Houk, *Chem. Soc. Rev.* **2009**, *38*, 1330-1352.

[11] W. P. Lustig, S. Mukherjee, N. D. Rudd, A. V. Desai, J. Li, S. K. Ghosh, *Chem. Soc. Rev.* **2017**, *46*, 3242-3285.

[12] Espallargas, G. M.; Coronado, E., *Chem. Soc. Rev.* **2018**, *47*, 533-557.

[13] A. Schneemann, V. Bon, I. Schwedler, I. Senkovska, S. Kaskel, R. A. Fischer, *Chem. Soc. Rev.* **2014**, *43*, 6062-6096.

[14] Z. Chang, D.-H. Yang, J. Xu, T.-L. Hu, X.-H. Bu, *Adv. Mater.* **2015**, *27*, 5432-5441.

[15] N. C. Burtch, H. Jasuja, K. S. Walton, *Chem. Rev.* **2014**, *114*, 10575-10612.

[16] S. Yuan, L. Feng, K. Wang, J. Pang, M. Bosch, C. Lollar, Y. Sun, J. Qin, X. Yang, P. Zhang, Q. Wang, L. Zou, Y. Zhang, L. Zhang, Y. Fang, J. Li, H.-C. Zhou, *Adv. Mater.* **2018**, *30*, 1704303.

[17] J. H. Cavka, S. Jakobsen, U. Olsbye, N. Guillou, C. Lamberti, S. Bordiga, K. P. Lillerud, *J. Am. Chem. Soc.* **2008**, *130*, 13850-13851

[18] J. An, S. J. Geib, N. L. Rosi, *J. Am. Chem. Soc.* **2009**, *131*, 8376- 8377.

[19] C. N. R. Rao, S. Natarajan, R. Vaidhyanathan, *Angew. Chem. Int. Ed.* **2004**, *43*, 1466-1496.

[20] J. Gu, M. Wen, X. Liang, Z. Shi, M. V. Kirillova, A. M. Kirillov, *Crystals* **2018**, *8*, 83.

[21] A. Schoedel, M. Li, D. Li, M. O'Keeffe, O. M. Yaghi, *Chem. Rev.* **2016**, *116*, 12466-12535.

[22] G. K. H. Shimizu, R. Vaidhyanathan, J. M. Taylor, *Chem. Soc. Rev.* **2009**, *38*, 1430-1449.

[23] J. E. Reynolds, S. G. Dunning, C. M. McCulley, S. M. Humphrey, A Survey of Metal-Organic Frameworks Based on Phosphorus and Sulfur-Containing Building Blocks (Elaboration and Applications of Metal-Organic Frameworks; Eds. S. Ma, J. A. Perman), **2018**, 37-141, DOI: 10.1142/9789813226739_0002.

[24] J.-P. Zhang, Y.-B. Zhang, J.-B. Lin, X.-M. Chen, *Chem. Rev.* **2012**, *112*, 1001-1033.

[25] B. Manna, A. V. Desai, S. K. Ghosh, *Dalton Trans.* **2016**, *45*, 4060-4072.

[26] S. Horike, S. Shimomura, S. Kitagawa, *Nat. Chem.* **2009**, *1*, 695-704.

[27] A. Karmakar, A. V. Desai, S. K. Ghosh, *Coord. Chem. Rev.* **2016**, *307*, 313-341.

[28] J. A. Johnson, X. Zhang, X. Zhang, J. Zhang, *Current Organic Chemistry*, **2014**, *18*, 1973-2001.

[29] C. Mao, R. A. Kudla, F. Zuo, X. Zhao, L. J. Mueller, X. Bu, P. Feng, *J. Am. Chem. Soc.* **2014**, *136*, 7579-7582.

[30] T. Chen, C. Zhang, Y. Qin, H. Yang, P. Zhang, F. Ye, *Materials* **2017**, DOI: 10.3390/ma10080879.

[31] B. M. Wiers, M.-L. Foo, N. P. Balsara, J. R. Long, *J. Am. Chem. Soc.* **2011**, *133*, 14522-14525.

[32] S. R. J. Oliver, *Chem. Soc. Rev.* **2009**, *38*, 1868-1881.

[33] D. Banerjee, D. Kim, M. J. Schweiger, A. A. Kruger, P. K. Thallapally, *Chem. Soc. Rev.* **2016**, *45*, 2724-2739.

[34] P. Kumar, A. Pournara, K.-H. Kim, V. Bansal, S. Rapti, M. J. Manos, *Prog. Mater. Sci.* **2017**, *86*, 25-74.

[35] J. An, C. M. Shade, D. A. Chengelis-Czegan, S. Petoud, N. L. Rosi, *J. Am. Chem. Soc.* **2011**, *133*, 1220-1223.

[36] L. Li, X. Wang, J. Liang, Y. Huang, H. Li, Z. Lin, R. Cao, *ACS Appl. Mater. Interfaces* **2016**, *8*, 9777-9781.

[37] P. Li, N. A. Vermeulen, X. Gong, C. D. Malliakas, J. F. Stoddart, J. T. Hupp, O. K. Farha, *Angew. Chem. Int. Ed.* **2016**, *55*, 10358-10362.

[38] H.-F. Ma, Q.-Y. Liu, Y.-L. Wang, S.-G. Yin, *Inorg. Chem.* **2017**, *56*, 2919-2925.

[39] S.-i. Noro, R. Kitaura, M. Kondo, S. Kitagawa, T. Ishii, H. Matsuzaka, M. Yamashita, *J. Am. Chem. Soc.* **2002**, *124*, 2568-2583

[40] H. Fei, L. Paw U, D. L. Rogow, M. R. Bresler, Y. A. Abdollahian, S. R. J. Oliver, *Chem. Mater.* **2010**, *22*, 2027-2032

[41] I. R. Colinas, K. K. Inglis, F. Blanc, S. R. J. Oliver, *Dalton Trans.* **2017**, *46*, 5320-5325.

[42] Y.-Q. Chen, G.-R. Li, Z. Chang, Y.-K. Qu, Y.- H. Zhang, X.-H. Bu, *Chem. Sci.* **2013**, *4*, 3678-3682.

[43] X. Li, H. Xu, F. Kong, R. Wang, *Angew. Chem. Int. Ed.* **2013**, *52*, 13769-13773.

[44] X. Li, Y. Gong, H. Zhao, R. Wang, *Inorg. Chem.* **2014**, *53*, 12127-12134.

[45] M. Guo, H. Guo, S. Liu, Y. Sun, X. Guo, *RSC Adv.* **2017**, *7*, 51021-51026.

[46] D. Sheng, L. Zhu, C. Xu, C. Xiao, Y. Wang, Y. Wang, L. Chen, J. Diwu, J. Chen, Z. Chai, T. E. Albrecht-Schmitt, S. Wang, *Environ. Sci. Technol.* **2017**, *51*, 3471-3479.

[47] Y. Cui, Y. Yue, G. Qian, B. Chen, *Chem. Rev.* **2012**, *112*, 1126-1162.

[48] E. Coronado, G. M. Espallargas, *Chem. Soc. Rev.* **2013**, *42*, 1526-1539.

[49] Z. Zhang, Z.-Z. Yao, S. Xiang, B. Chen, *Energy Environ. Sci.* **2014**, *7*, 2868-2899.

[50] P. Ramaswamy, N. E. Wong, G. K. H. Shimizu, *Chem. Soc. Rev.* **2014**, *43*, 5913-5932.

[51] E. Barea, C. Montoro, J. A. R. Navarro, *Chem. Soc. Rev.* **2014**, *43*, 5419- 5430.

[52] C. Wang, X. Liu, N. K. Demir, J. P. Chen, K. Li, *Chem. Soc. Rev.* **2016**, *45*, 5107-5134

[53] Z. Bao, G. Chang, H. Xing, R. Krishna, Q. Ren, B. Chen, *Energy Environ. Sci.* **2016**, *9*, 3612-3641.

[54] W. Wang, X. Xu, W. Zhou, Z. Shao, *Adv. Sci.* **2017**, *4*, 1600371.

[55] Y.-B. Huang, J. Liang, X.-S. Wang, R. Cao, *Chem. Soc. Rev.* **2017**, *46*, 126-157.

[56] S. Yang, A. J. Ramirez-Cuesta, R. Newby, V. Garcia-Sakai, P. Manuel, S. K. Callear, S. I. Campbell, C. C. Tang, M. Schröder, *Nat. Chem.* **2015**, *7*, 121−129.

[57] M. du Plessis, V. I. Nikolayenko, L. J. Barbour, *J. Am. Chem. Soc.* **2020**, *142*, 4529–4533.

[58] Y. Chai, X. Han, W. Li, S. Liu, S. Yao, C. Wang, W. Shi, I. d.-Silva, P. Manuel, Y. Cheng, L. D. Daemen, A. J. R.-Cuesta, C. C. Tang, L. Jiang, S. Yang, N. Guan, L. Li, *Science* **2020**, *368*, 1002–1006

[59] S. Liu, X. Han, Y. Chai, G. Wu, W. Li, J. Li, I. d.-Silva, P. Manuel, Y. Cheng, L. L. Daemen, A. J. R.-Cuesta, W. Shi, N. Guan, S. Yang, L. Li, *Angew. Chem. Int. Ed.* **2021**, *60*, 6526−6532.

[60] D. S. Sholl, R. P. Lively, *Nature* **2016**, *532*, 435–437.

[61] M. Peplow, *Nature* **2015**, *520*, 148–150.

[62] J. R. Li, R. J. Kuppler, H. C. Zhou, *Chem. Soc. Rev.* **2009**, *38*, 1477–1504.

[63] S. Sen, N. Hosono, J.-J. Zheng, S. Kusaka, R. Matsuda, S. Sakaki, S. Kitagawa, *J. Am. Chem. Soc.* **2017**, *139*, 18313−18321.

[64] H. Wang, Y. Liu, J. Li, *Adv. Mater.* **2020**, *32*, 2002603.

[65] T. Ren, M. Patel, K. Blok, *Energy* **2006**, *31*, 425−451.

[66] P. Pässler, W. Hefner, K. Buckl, H. Meinass, H.-J. Wernicke, G. Ebersberg, R. Müller, J. Bässler, H. Behringer, D. Mayer, in Ullmann's Encyclopedia of Industrial Chemistry, Wiley-VCH Verlag GmbH & Co. KGaA, 2000

[67] Y. L. Peng, T. Pham, P. Li, T. Wang, Y. Chen, K. J. Chen, K. A. Forrest, B. Space, P. Cheng, M. J. Zaworotko, Z. Zhang, *Angew. Chem. Int. Ed.* **2018**, *57*, 10971–10975.

[68] S. Mukherjee, D. Sensharma, K. J. Chen, M. J. Zaworotko, *Chem. Commun.* **2020**, *56*, 10419–10441.

[69] H. Molero, B. F. Bartlett, W. T. Tysoe, *J. Catal.* **1999**, *181*, 49–56.

[70] O. T. Qazvini, L. K. Macreadie, S. G. Telfer, *Chem. Mater.* **2020**, *32*, 6744–6752.

[71] B. R. Barnett, M. I. Gonzalez, J. R. Long, *Trends Chem.* **2020**, *2*, 159–171.

[72] S. Mukherjee, Y. He, D. Franz, S.-Q. Wang, W.-R. Xian, A. A. Bezrukov, B. Space, Z. Xu, J. He, M. J. Zaworotko, *Chem. Eur. J.* **2020**, *26*, 4923–4929.

[73] O. T. Qazvini, R. Babarao, Z.-L. Shi, Y.-B. Zhang, S. G. Telfer, *J. Am. Chem. Soc.* **2019**, *141*, 5014−5020.

[74] O. T. Qazvini, R. Babarao, S. G. Telfer, *Chem. Mater.* **2019**, *31*, 4919–4926.

[75] 2019 Report of The International Council of Chemical Associations, https://icca-chem.org/news/chemical-industry-contributes-5-7-trillion-to-global-gdp-and-supports-120-million-jobs-new-report-shows/, accessed on 05-02-2021.

[76] S. Mukherjee, N. Kumar, A. A. Bezrukov, K. Tan, T. Pham, K. A. Forrest, K. A. Oyekan, O. T. Qazvini, D. G. Madden, B. Space, M. J. Zaworotko, *Angew. Chem. Int. Ed.* **2021**, *60*, 10902–10909.

[77] D. S. Sholl, R. P. Lively, *Nature* **2016**, *532*, 435–437.

[78] S. Kitagawa, *Angew. Chem. Int. Ed.* **2015**, *54*, 10686–10687.

[79] J. J. McKetta Jr, *Encyclopedia of Chemical Processing and Design: Volume 20 - Ethanol as Fuel*, CRC Press, **1984**.

[80] J. H. Kang, E. W. Shin, W. J. Kim, J. D. Park, S. H. Moon, *Catal. Today* **2000**, *63*, 183–188

[81] S. Sircar, *Ind. Eng. Chem. Res.* **2006**, *45*, 5435–5448.

[82] J.-R. Li, R. J. Kuppler, H.-C. Zhou, *Chem. Soc. Rev.* **2009**, *38*, 1477–1504

[83] D. R. Lide, *CRC handbook of chemistry and physics*, CRC Press, **2004**.

[84] M. Neelis, M. Patel, K. Blok, W. Haije, P. Bach, *Energy* **2007**, *32*, 1104–1123.

[85] Z. R. Herm, E. D. Bloch and J. R. Long, *Chem. Mater.*, **2014**, *26*, 323–338.

[86] Z. B. Bao, G. G. Chang, H. B. Xing, R. Krishna, Q. L. Ren, B. Chen, *Energy Environ. Sci.* **2016**, *9*, 3612–3641.

[87] R. B. Lin, S. C. Xiang, H. B. Xing, W. Zhou, L. Chen, *Coord. Chem. Rev.*, **2019**, *378*, 87–103.

[88] J. P. Zhang, H. L. Zhou, D. D. Zhou, P. Q. Liao, X. M. Chen, *Natl. Sci. Rev.*, **2018**, *5*, 907–919.

[89] X. Zhao, Y. X. Wang, D. S. Li, X. H. Bu, P. Y. Feng, *Adv. Mater.* **2018**, *30*, 1705189.

[90] H. Li, K. C. Wang, Y. J. Sun, C. T. Lollar, J. L. Li and H. C. Zhou, *Mater. Today* **2018**, *21*, 108–121.

[91] L. F. Yang, S. H. Qian, X. B. Wang, X. L. Cui, L. Chen, H. B. Xing, *Chem. Soc. Rev.*, **2020**, *49*, 5359–5406.

[92] Y. B. He, F. L. Chen, B. Li, G. D. Qian, W. Zhou, L. Chen, *Coord. Chem. Rev.*, **2018**, *373*, 167–198.

[93] H. Li, L. b. Li, R. B. Lin, W. Zhou, Z. J. Zhang, S. C. Xiang, B. Chen, *Energy Chem*, **2019**, *1*, 100006.

[94] R.-B. Lin, S. C. Xiang, W. Zhou, B. Chen, *Chem*, **2020**, *6*, 337–363.

[95] S. Mukherjee, M. J. Zaworotko, *Trends Chem.*, **2020**, *2*, 506–518.

[96] World Population Prospects: The 2015 Revision, Methodology of the United Nations Population Estimates and Projections; Working Paper No. ESA/P/WP.242; Department of Economic and Social Affairs, Population Division, United Nations, 2015.

[97] P. Samanta, A. V. Desai, S. Let, S. K. Ghosh, *ACS Sustainable Chem. Eng.* **2019**, *7*, 7456–7478.

[98] P. C. D. Milly, J. Betancourt, M. Falkenmark, R. M. Hirsch, Z. W. Kundzewicz, D. P. Lettenmaier, R. J. Stouffer, *Science* **2008**, *319*, 573–574.

[99] S. Rojas, P. Horcajada, *Chem. Rev.* **2020**, *120*, 8378–8415.

[100] Resolution A/RES/64/292; United Nations General Assembly, July **2010**.

[101] P. A. Kobielska, A. J. Howarth, O. K. Farha, S. Nayak, *Coord. Chem. Rev.* **2018**, *358*, 92–107.

[102] P. Samanta, P. Chandra, S. Dutta, A. V. Desai, S. K. Ghosh, *Chem. Sci.* **2018**, *9*, 7874–7881.

[103] R. Iranpour, M. Stenstrom, G. Tchobanoglous, D. Miller, J. Wright, M. Vossoughi, *Science* **1999**, *285*, 706–711.

[104] M. W. Skougstad, M. J. Fishman, *Toxicol. Environ. Chem. Rev.* **1978**, *2*, 219–236.

[105] C. Grandclement, I. Seyssiecq, A. Piram, P. Wong-Wah-Chung, G. Vanot, N. Tiliacos, N. Roche, P. Doumenq, *Water Res.* **2017**, *111*, 297–317.

[106] K. C. Jones, P. de Voogt, *Environ. Pollut.* **1999**, *100*, 209–221.

[107] N. Bolong, A. F. Ismail, M. R. Salim, T. Matsuura, *Desalination* **2009**, *239*, 229–246.

[108] L. E. Kreno, K. Leong, O. K. Farha, M. Allendorf, R. P. Van Duyne, J. T. Hupp, *Chem. Rev.* **2012**, *112*, 1105-1125.

[109] M. D. Allendorf, C. A. Bauer, R. K. Bhakta, R. J. T. Houk, *Chem. Soc. Rev.* **2009**, *38*, 1330-1352.

[110] Y. Cui, Y. Yue, G. Qian, B. Chen, *Chem. Rev.* **2012**, *112*, 1126-1162.

[111] J. Li, G. Zhao, C. Chen, Z. Chai, A. Alsaedi, T. Hayat, X. Wang, *Chem. Soc. Rev.* **2018**, *47*, 2322-2356.

[112] J. Li, H. Wanga, X. Yuan, J. Zhang, J. W. Chew, *Coord. Chem. Rev.* **2020**, *404*, 213116.

[113] M. Mon, R. Bruno, J. Ferrando-Soria, D. Armentano, E. Pardo, *J. Mater. Chem. A* **2018**, *6*, 4912–4947.

[114] Q. Gao, J. Xu, X.-H. Bu, *Coord. Chem. Rev.* **2018**, *378*, 17-31.

[115] S. Dutta, S. Let, S. Sharma, D. Mahato, S. K. Ghosh, *Chem. Rec.* **2021**, *21*, 1666– 1680.

[116] Desai, A. V.; Manna, B.; Karmakar, A.; Sahu, A.; Ghosh, S. K., *Angew. Chem. Int. Ed.* **2016**, *55*, 7811-7815.

Part-I

Functional Cationic MOFs for Efficient Industrially Relevant Light Hydrocarbon Separation

With the rapid growth in industrialization across the globe during last few decades, hydrocarbon-based compounds evolved as the most vital chemicals and energy resources, with a huge demand and wide utilization even in our daily life.[1] For example, acetylene (C_2H_2) is widely exploited as key commodity and important raw material for industrial production of several important chemicals and as a fuel. Olefins such as ethylene, propylene, butadiene etc. are essential commodity chemicals for industrial manufacture of different polymers, e.g., polyethylene, polyvinyl chloride, polypropylene, polystyrene, polyester etc. as well as other organic chemicals.[2] The global annual production of these light hydrocarbons are estimated as more than 200 million tons with a gigantic market valuation of $254.6 billion in 2016, which is expected to touch $475.8 billion by 2023.[3] Separation of such hydrocarbon mixtures into their pure single components is a vital process as they are further employed to manufacture high-quality gasoline, polymers, plastics in the petrochemical industry. Generally, during the industrial production, all these hydrocarbons contain a significant amount of impurities, resulting in lower-purity crude material for further processes. The similar physiochemical properties (size, boiling points, kinetic diameters etc.) and reactivity typically render a great difficulty in separation of these hydrocarbon mixtures (Figure 1).[4] Current separation and purification methods in the petrochemical industry mainly relies upon cryogenic distillation-based separation, chemisorption and solvent extraction, fractional distillation etc. which are highly capital and energy-intensive process (~ 230 gigawatts of energy consumption per day globally).[4] The energy footprint of such separation and purification processes accounting for ca. 40% of overall industrial energy consumption 15% of total global energy consumption.[1,5] Hence, developing alternative separation methods which can reduce the energy costs significantly is extremely enticing. In this regard, Metal–organic frameworks (MOFs) or porous coordination polymers (PCPs) have attracted tremendous attention owing to its' advantages like high surface area, tunable porosity and pore surface, structure property correlation etc. Particularly, cationic MOFs, being a significant subclass of ionic MOFs, have shown tremendous potential in the field of sensing, catalysis, pollutant capture etc. Although recent years have witnessed the emergence of functional MOFs as physisorbent materials for separation of various gases and light hydrocarbons, but ionic MOFs are yet to be explored in this domain.

This section consists of two chapters i.e. chapter 2 and chapter 3. In chapter 2, an iso-structural series of cationic MOFs with different functional anions (ClO_4^-, BF_4^- and NO_3^-) inside the porous channels as extra-framework functionality was utilized for selective separation of light hydrocarbon for the first time in the domain of ionic MOFs. While in chapter 3, two water stable cationic MOFs with π-electron rich bulky organic sulfonic acid anions have been employed toward selective C_2H_2 sorption and separation. Both the chapters primarily focus on designing and functionalization of cationic MOFs as ultramicroporous sorbent material for selective light hydrocarbon separation.

References:

[1] D. S. Sholl and R. P. Lively, *Nature*, **2016**, 532, 435–437.

[2] M. Peplow, Materials science: The hole story, *Nature*, **2015**, 520, 148-150.

[3] Y. Wang, S. B. Peh and D. Zhao, *Small*, **2019**, 15, 1900058.

[4] S. Mukherjee, D. Sensharma, K.-J. Chen and M. J. Zaworotko, *Chem. Commun.*, **2020**, 56, 10419--10441.

[5] S. Kitagawa, *Angew. Chem., Int. Ed.*, **2015**, 54, 10686–10687.

Chapter 2

Three-in-one C_2H_2 Selectivities Guided Adsorptive Separation across an Isoreticular Family of Cationic Square Lattice MOFs

2.1 Introduction

Under the backdrop of the current industrial energy consumption accounting for *ca.* 15% of the global energy landscape, and the fact that *ca.* 40% of this industrial energy is used just for commodity separations and purifications imply the high societal need to lower the energy footprint of purifications.[1] Besides, the demand for commodities is estimated to be tripled by 2050.[2] This underscores the need to replace the existing energy-intensive purification technologies that majorly suffer from high energy footprint. These include state-of-the-art methods: chemisorption, solvent extraction, azeotropic and/or fractional and/or cryogenic distillation, and therefore need to be replaced with energy-efficient alternatives such as recyclable/regenerable physisorption.[3]

Separation and purification of light hydrocarbons in an energy-efficient manner is of fundamental relevance to petrochemical industries.[4,5] Typically, light hydrocarbons such as acetylene (C_2H_2) and ethylene (C_2H_4) are utilized to produce several commodity chemicals, such as plastics, fibres, rubber, vinyl compounds, acrylic acid derivatives, α-ethynyl alcohols, among others.[6,7] Industrial production of C_2H_2 continue to rely upon energy-intensive state-of-the-art, including methane (CH_4) combustion and/or steam cracking of naphtha. Exacerbating the energy footprint and producing waste, these processes often co-produce other C_2-C_1 gases such as CH_4, C_2H_4 and carbon dioxide (CO_2).[8] Even when present in trace concentrations, C_2H_2 is a catalytic poison in C_2H_4 polymerization, therefore its presence blocks the desired C_2H_4 flow, inadvertently leading to explosions. Flammability of C_2H_2, with the widest range among flammables, 2.5-81 %, compounds this problem.[9] In this context, it is rather unsurprising to notice the recent upsurge in research interest to develop porous physisorbents for energy-efficient C_2H_2 capture driven adsorptive separation from mixtures of industrial relevance, including but not limited to C_2H_2/CO_2, C_2H_2/C_2H_4, C_2H_2/CH_4.[10] Despite recent advances, the oft-encountered handicaps to achieve such small molecule separations primarily stems from their close physicochemical properties, such as similar kinetic diameters and boiling/melting points.[11] In this context, porous framework solids, metal-organic frameworks (MOFs) have recently emerged with benchmark early performance indicators for C_2H_2 separation.[12] Nevertheless, combining multiple binary selectivities to achieve C_2H_2 separation from more than one gas mixtures is a task yet unaddressed by MOFs, despite the high efficiency entailed. Considering C_2H_2/CO_2, C_2H_2/C_2H_4, C_2H_2/CH_4 mixtures, hereinafter denoted as C2-C1 separations, MOFs have established several new benchmarks in the past few years.[13] Thanks to their compositional modularity i.e. amenability to crystal engineering principles, controlled pore environments could elicit

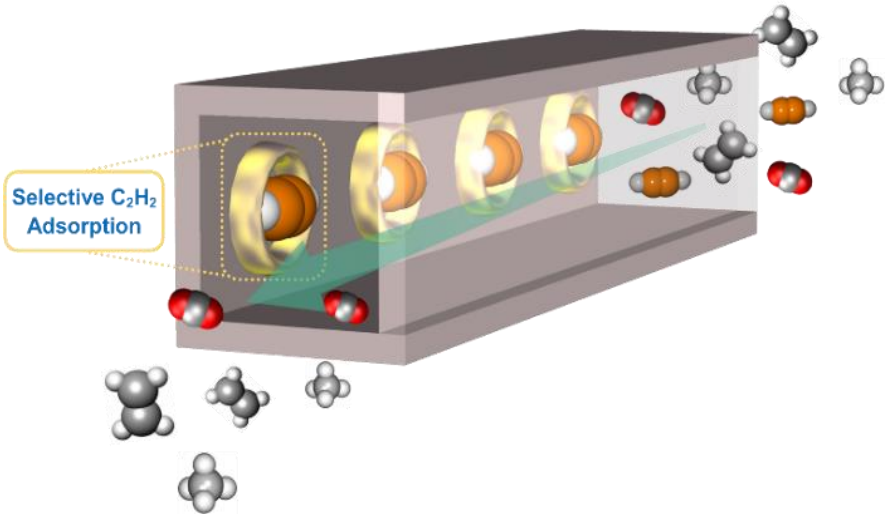

Figure 2.1. Schematic representation of the design principle leading to iMOF-nC series; design of the cationic pore environment enables C_2H_2 selectivity over other C2-C1 gases. (colour codes: grey or gold – C, White – H, red – O).

just the right pore sizes, electrostatics and diffusion barriers, reflected in their optimal sorption thermodynamics and kinetics for these gas sorbates.[14, 15] Recently, ionic metal-organic frameworks (iMOFs) have emerged as promising lead candidates in several applications.[16] Cationic MOFs, a subclass of ionic MOFs integrating dual features *viz.* cationic backbone and free counter anions have delivered record-high performances in the fields of water pollutant capture, heterogeneous catalysis, molecular recognition and sensing.[17, 18] Here we envision that upon systematic fine-tuning of the uncoordinated anions alongside the use of a pre-functionalized organic ligand can facilitate selective MOF−C_2H_2 interactions, despite leveraging simple and one of the most abundant network topologies, square lattice (**sql**). Whereas organic ligands functionalized with polar substituents, such as −F, −Cl, −OH, −NH_2, −CO_2H are known to promote C_2H_2 specific interactions by inducing additional electronic polarization on the MOF pore surfaces, modulation of pore environments to maximize C_2H_2 selectivity guided binary C2/C1 separations is an approach we introduce herein.

Despite some recent reports demonstrating the utility of cationic MOFs as adsorbents, these simple, modular porous solids remain underexplored to an extent that our literature survey could only find one prototypical cationic MOF (ZJU-48a; $[Zn_8O(EDDA)_4(ad)_4.(HEDDA)_2.6DMF.27H_2O]$; H_2EDDA = (E)-4,4'-(ethene-1,2-diyl)dibenzoic acid; ad = adenine) to exhibit adsorption selectivity among the C2/C1 light hydrocarbons.[19] Considering these aspects, herein we introduce a new cationic isoreticular family

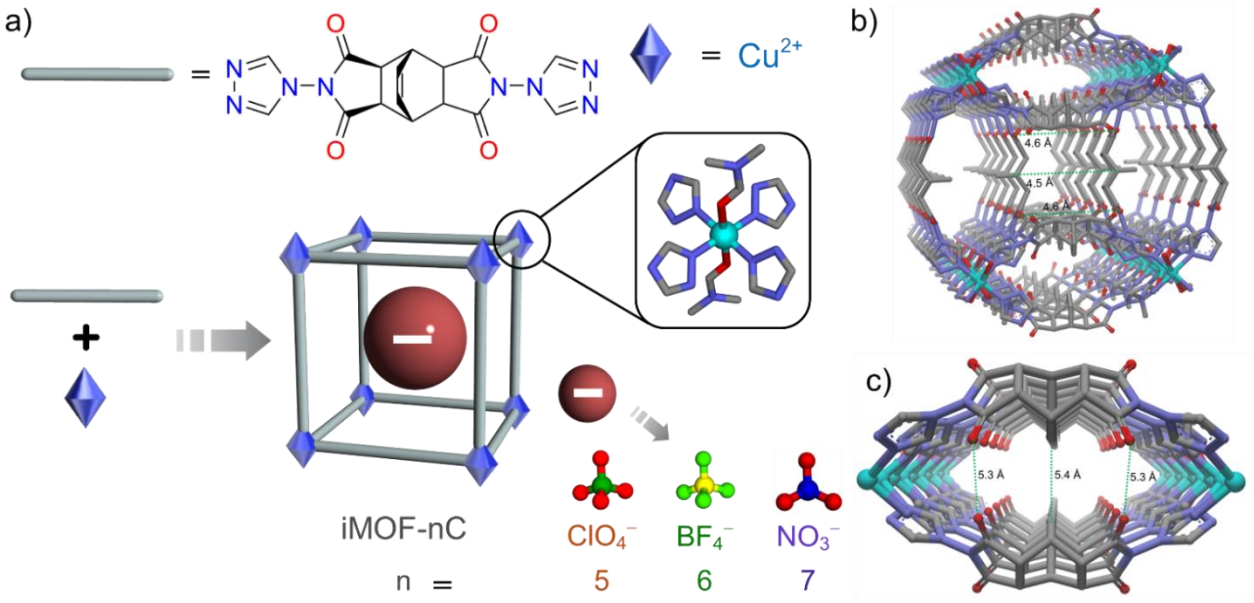

Figure 2.2. (a) Schematic representation of the synthetic protocol leading to isoreticular iMOF-nC series, by varying the uncoordinated anions within its pores; (b, c) Perspective view of iMOF- 5C showing its bi-porous nature with two types of ultramicroporous channels sustaining the framework (colour codes: grey – C, blue – N, red – O, cyan – Cu)..

of three two-dimensional (2D) ultramicroporous (< 7 Å) MOFs, namely iMOF-nC. Crafted with a flexible, pre-functionalized neutral N-donor linker L, N,N'-bicyclo[2.2.2]oct-7-ene-2,3,5,6-tetracarboxdiimidebi(1,2,4-triazole), the iMOF-nC series contains three different uncoordinated counter anions (ClO_4^-, BF_4^-, NO_3^-) inside the porous channels to afford iMOF-5C, iMOF-6C and iMOF-7C, respectively. Strategic choice of the electronically polarized dianhydride core-based ligand (L) equipped with additional functionalities, such as carbonyl oxygen atoms, coordinated N,N-dimethyl formamide (DMF) molecule, unsaturated π-electron cloud and free N-termini of the triazole groups, appear promising as a C_2H_2 selective supramolecular scaffold, leading us to examine them thoroughly as adsorbents (Scheme 1).

2.2 Experimental

2.2.1 Materials and measurements.

All solvents and reagents were commercially available and used without any purification.

2.2.2 Synthesis

Synthesis of Ligand *N*,*N*′-bicyclo[2.2.2]oct-7-ene-2,3,5,6-tetracarboxdiimide bi(1,2,4-triazole), L. A previously reported protocol was followed to synthesize the ligand (L).[20] A mixture of BTD (bicyclo[2.2.2]oct-7-ene-2,3,5,6-tetracarboxylic dianhydride) (5 g, 20 mmol) and 4-amino-1,2,4-triazole (5.04 g., 60 mmol) were dissolved in 75 mL acetic acid. The mixture was heated to reflux at 120 °C for 72 h under N_2 atmosphere. Upon cooling to room temperature, the reaction mixture was centrifuged,

filtered, and washed thrice with *N*,*N*-dimethylformamide (DMF), water and ether to remove the excess acetic acid from the final crude product. After vacuum-drying the solid residue for a few hours, white powder form of ligand L was obtained.

Synthesis of iMOF-5C. iMOF-5C was synthesised by slow diffusion based crystallization. 1 mL DMF solution of the ligand L (0.05 mmol, 19 mg) was poured into a cylindrical glass tube. On top of this ligand solution layer, 1 mL benzene was added as a layer. This was followed by adding another layer of 1 mL methanolic solution of $Cu(ClO_4)_2.6H_2O$ (0.05 mmol, 18.57 mg). The triple layered diffusion system was kept isolated without any disturbance. Deep blue coloured crystals were obtained after 15 days. **iMOF-5C** crystals were collected by filtration, washed with DMF and methanol for several times. Single crystals of **iMOF-5C** were obtained in ~ 45% yield (based on Cu(II) content). Followed by CH_3CN exchange, activation was conducted under high vacuum at 60 °C to obtain the guest free phase **iMOF-5C**. Highly disordered free ClO_4^- anion and guest molecules inside **iMOF-5C** were not located by low temperature single crystal X-ray diffraction; PLATON SQUEEZE analysis and thermogravimetric analysis leads us to determine the molecular formula of **iMOF-5C** as $\{[CuL_2(DMF)_2](ClO_4)_2.xG\}_n$ (G = disordered guest molecules).

Synthesis of iMOF-6C. iMOF-6C was synthesised by slow diffusion based crystallization. 1 mL DMF solution of the ligand L (0.05 mmol, 19 mg) was poured into a cylindrical glass tube. On top of this ligand solution layer, 1 mL benzene was added as a layer. This was followed by adding another layer of 1 mL methanolic solution of $Cu(BF_4)_2.xH_2O$ (0.05 mmol, 11.9 mg). The triple layered diffusion system was kept isolated without any disturbance. Rod shaped blue coloured crystals were obtained after 15 days. **iMOF-6C** crystals were collected by filtration, washed with DMF and methanol for several times. Single crystals of **iMOF-6C** were obtained in ~ 45% yield (based on Cu(II) content). Followed by CH_3CN exchange, activation was conducted under high vacuum at 60 °C to obtain the guest free phase **iMOF-6C**.

Highly disordered free BF_4^- anion and guest molecules inside **iMOF-6C** were not located by low temperature single crystal X-ray diffraction; PLATON SQUEEZE analysis and thermogravimetric analysis leads us to determine the molecular formula of **iMOF-5C** as $\{[CuL_2(DMF)_2](BF_4)_2.xG\}_n$ (G = disordered guest molecules).

Synthesis of iMOF-7C. Similarly, **iMOF-7C** was synthesised by slow diffusion based crystallization. 1 mL DMF solution of the ligand L (0.05 mmol, 19 mg) was poured into a cylindrical glass tube. On top of this ligand solution layer, 1 mL benzene was added as a layer. This was followed by adding another layer of 1 mL methanolic solution of $Cu(NO_3)_2.3H_2O$ (0.05 mmol, 12.2 mg). The triple layered diffusion system was kept isolated without any disturbance. Deep blue coloured crystals were obtained after 15 days. **iMOF-7C** crystals were collected by filtration, washed with DMF and methanol for several times. Single crystals of **iMOF-7C** were obtained in ~ 45% yield (based on Cu(II) content). Followed by CH_3CN exchange, activation was conducted under high vacuum at 60 °C to obtain the guest free phase **iMOF-7C**. Unfortunately, despite of several attempts, we were unable to solve the structure of **iMOF-7C** framework crystallographically. Furthermore, comparison between the as-synthesized powder X-ray diffraction (PXRD) patterns of **iMOF-6C** and **iMOF-7C** revealed their isostructural nature (Appendix 2.15).

2.2.3 Physical Measurements.

PXRD patterns were recorded on a Bruker D8 Advanced X-Ray diffractometer using Cu K radiation (λ= 1.5406 Å) in a 2θ range 5° to 40°, with a scan speed of 0.6° min^{-1}. All infra-red (IR) spectra were recorded using a NICOLET 6700 FT-IR spectrophotometer, using KBr pellets in the range of 400– 4000 cm^{-1}. Thermogravimetric analysis (TGA) traces were recorded on a Perkin-Elmer STA 6000 TGA analyser under N_2 atmosphere, with a heating rate of 10° C min^{-1}. Field emission scanning electron microscopy (FESEM) images were captured using a FEI Quanta 3D dual beam ESEM at 30 kV. Ultraviolet (UV) spectra were acquired on a Shimadzu UV 2600 Spectrophotometer.

2.2.4 X-ray structural studies.

Single-crystal X-ray data of **iMOF-nC** were collected at 150 K on a Bruker D8 Venture Duo X-ray diffractometer equipped with Microfocus X-ray source (operated at 50 W; 50 kV/1 mA), graded multilayer optics for monochromatic Mo Kα radiation (λ = 0.71073 Å) focused X-ray beam and Photon 100 CMOS chip-based detector system. Crystal was on nylon CryoLoops (Hampton Research) with

Paraton-N (Hampton Research). The data integration and reduction were processed with SAINT software. [21] A multi-scan absorption correction was applied to the collected reflections. The structure was solved by the direct method using SHELXTL [22] and was refined on F^2 by full matrix least-squares technique using the SHELXL-97[23] program package within the WINGX [24] program. All non-hydrogen atoms were refined anisotropically. All hydrogen atoms were located in successive difference Fourier maps, and they were treated as riding atoms using SHELXL default parameters. The structures were examined using the Adsym subroutine of PLATON [25] to ensure that no additional symmetry could be applied to the models. Guest molecules in **iMOF-5C** and **iMOF-6C** are highly disordered and could not be modelled properly, so the diffused electron densities resulting from them were masked by the Olex2 programme [26] similar to the SQUEEZE/PLATON [27] and the results were appended in the CIF files. The SQUEEZE option was used to eliminate the contribution of disordered guest molecules. Crystallographic data for **iMOF-5C** and **iMOF-6C**: CCDC 2058422 and 2058428 contains the supplementary crystallographic data for this paper (Tables S7 and S8).

2.2.5 Gas sorption measurements.

N_2 adsorption−desorption isotherms from 0 to 1 bar at 77 K with liquid nitrogen were measured by a Micrometrics ASAP 2460 volumetric gas adsorption analyzer. The measurements of gas adsorption of hydrocarbons from 273 to 313 K precisely controlled through a LAUDR RP890 recirculating control system with absolute ethyl alcohol were carried out by a Micrometrics ASAP 2020M volumetric gas adsorption analyzer.

2.2.6 Calculation of BET surface areas.

We determined BET surface areas from CO_2 adsorption isotherms at 195 K according to the following procedures[28,29]:

1) A section of the adsorption isotherm branch was selected where $v\left(1-\frac{P}{P_0}\right)$ increases versus $\left(\frac{P}{P_0}\right)$, where v is the amount of CO_2 adsorbed.

2) Within this section, sequential data points that led to a positive intercept in the plot of $\left[\frac{\left(\frac{P}{P_0}\right)}{v\left(1-\frac{P}{P_0}\right)}\right]$ against (P/P_0), were identified. This plot results in a slope a, and a positive intercept b. The amount of CO_2 adsorbed in the initial monolayer is $v_m = \frac{1}{a+b}$

3) The BET surface area was determined based on the following equation:

$$A_{BET} = v_m\,(cm^3 g^{-1}) \times \frac{1(mol)}{22400(cm^3)} \times \sigma_0\,(\text{Å}^2) \times N_A(mol^{-1}) \times 10^{-20}\left(\frac{m^2}{\text{Å}^2}\right)$$

Where N_A is Avogadro's constant (6.023×10^{23} mol^{-1}) and σ_0 is the cross-sectional area of a CO_2 molecule, which is 17.0 Å^2. [30]

2.2.7 Q_{st} Calculation for iMOF-nC (n = 5, 6, 7).

A virial-type expression of the below form was used to fit the combined 273 and 298 K isotherm data of C_2H_2 for **iMOF-nC** compounds (n = 5, 6 and 7 corresponding to ClO_4^-, BF_4^- and NO_3^-), where P is the pressure described in Pa, *N* is the adsorbed amount in mmol g^{-1}, T is the temperature in K, a_i and b_i are virial coefficients, and *m* and *n* are the number of coefficients used to describe the isotherms. Q_{st} is the coverage-dependent enthalpy of adsorption and R is the universal gas constant. All fitting was performed using Origin Pro 2016. [31] Fitting parameters thus obtained for the three **iMOF-nC** adsorbents can be found in Appendix 2.49–S51.

$$\ln P = \ln N + \sum_{i=0}^{m} a_i N_i + \sum_{i=0}^{n} \binom{n}{k} b_i N_i$$

Q_{st} was calculated from the virial model using the equation below.

$$-Q_{st} = -R\sum_{i=0}^{m} a_i N_i$$

2.2.8 Adsorption selectivity from IAST.

The selectivities for the adsorbate mixture composition of interest were calculated from the single-component adsorption isotherms using Ideal Adsorbed Solution Theory (IAST), using a modified version of the program pyIAST. [32] First, the single-component isotherms for the gas sorbates at 298 K were fitted to the dual-site Langmuir-Freundlich (DSLF) equation. [33]

$$n(P) = \frac{q_1(k_1P)^{n_1}}{1+(k_1P)^{n_1}} + \frac{q_2(k_2P)^{n_2}}{1+(k_2P)^{n_1}}$$

In this equation, q_i is the amount adsorbed per unit mass of material (in cm^3 g^{-1}), *P* is the total pressure (in bar) of the bulk gas at equilibrium with the adsorbed phase, q_1 and q_2 are the saturation uptakes (in cm^3 g$^-$

[1]) for sites 1 and 2 respectively, k_1 and k_2 are the affinity coefficients (in bar^{-1}) for sites 1 and 2 respectively, and n_1^{-1} and n_2^{-1} represent the deviations from the ideal homogeneous surface (unit-less) for sites 1 and 2 respectively. Selectivity for adsorbate *i* relative to adsorbate *j* was calculated using the following equation.

$$S_{i/j} = \frac{(x_i/x_j)}{(y_i/y_j)}$$

Here, x_i and x_j are the mole fractions of components *i* and *j*, respectively, in the adsorbed phase, and y_i and y_j are the mole fractions of components *i* and *j*, respectively, in the gas phase. DSLF fitting plots thus obtained for the three **iMOF-nC** sorbents can be found in the parameters included in (S52-S54).

2.2.9 Breakthrough Curve Simulation Details.

Mathematical Modelling.

Considering a fixed bed adsorption column of length L filled with **iMOF-nC** (n = 5, 6 and 7 corresponding to ClO_4^-, BF_4^- and NO_3^-), following assumptions were made to develop a mathematical model [34-37] that could be solved using proper numerical methods to calculate the concentration of gasses at different elapsed times along the bed.

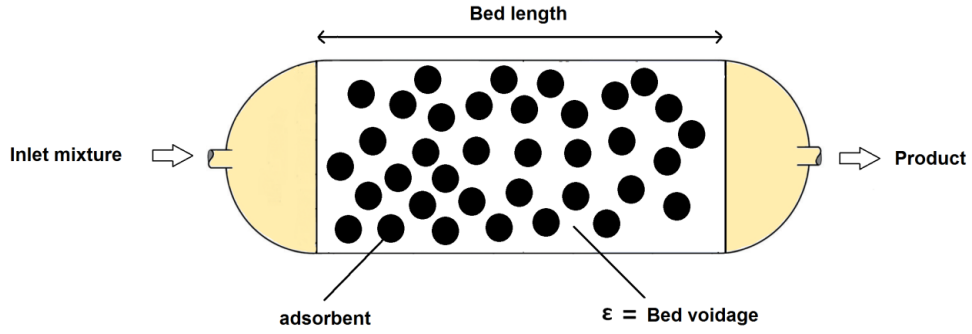

Figure 2.3. Schematic diagram of a fixed adsorption bed

The following assumptions were made:

- The dynamic behaviour of the fluid obeys an axially dispersed plug flow model.
- The gradient of the concentration along the radial and angular directions were neglected.

- The flow velocity is varied along the bed and it is calculated from the total mass balance equation.
- The gas property is described by the Peng-Robinson equation of state.
- Adsorption kinetics into the particles are assumed to obey instant adsorption model (equilibrium model), where adsorbates are adsorbed instantly with no resistance.
- The pressure drop is considered along the bed using the Ergun equation.
- The adsorption columns operate under isothermal conditions.
- Mixed gas isotherms are calculated by Extended Single-Site Langmuir Freundlich (SSLF) method. [38]

Based on the preceding assumptions, the component and overall mass balances in the bulk phase of the adsorption column are written as follow:

$$\varepsilon \frac{\partial C_i}{\partial t} = -\frac{\partial (uC_i)}{\partial z} + \varepsilon D_{ax,i} \frac{\partial^2 C_i}{\partial z^2} - (1-\varepsilon)\rho_s \frac{\partial q_i}{\partial t}$$

$$\varepsilon \frac{\partial C}{\partial t} = -\frac{\partial (uC)}{\partial z} - (1-\varepsilon)\rho_s \sum_{1}^{n_c} \left(\frac{\partial q_i}{\partial t}\right)$$

Where C_i and q_i are, respectively, concentration of components in the gas phase and in the adsorbed phase, z is the axial coordinate in the bed, D_{ax} is the effective axial dispersion coefficient, u is the superficial gas velocity, ρ_s is the adsorbent density, n_c is the number of the adsorbed components in the mixture and ε is the bed voidage. The value of D_{ax} was calculated through the following equation [39]:

$$\frac{\varepsilon D_{ax,i}}{D_{m,i}} = 20 + 0.5\, Sc_i\, Re$$

Where Re is the Reynolds number and Sc is the Schmidt number and $D_{m,i}$ is the molecular diffusivity of component i in the mixture which was calculated by following equation:

$$D_{m,i} = \frac{1-y_i}{\sum_{x=j}^{n} \frac{y_i}{D_{i,x}}}$$

Where y_i is the mole fraction of component i and $D_{i,x}$ is molecular diffusivity of component i in component x which was calculated by Wile-Lee equation [40]. An instant adsorption model (equilibrium model) were assumed, where adsorbates are adsorbed rapidly with no transfer resistance. This means q_i in equation 1 can be replaced with q_i^*: [42,43]

$$q_i = q_i^*$$

q_i^* is then related to concentration in the gas phase through isotherms. The Extended Single-Site Langmuir Freundlich method was used to predict the isotherm of gases in the mixture as below: [24]

$$q_i^* = \frac{abP^{1/t}}{1 + \sum_{j=1}^{n} bP^{1/t}}$$

Where a, b, and t are constants. To calculate these constants, single gas isotherms were fitted by Single-Site Langmuir Freundlich model as shown in Appendix 2.52, 2.53 and 2.54.

$$q = \frac{abP^{1/t}}{1 + bP^{1/t}}$$

The pressure drop is defined by the Ergun's equation as: [44]

$$\frac{\partial P}{\partial z} = -\left(\frac{37.5\,(1-\varepsilon)^2 \mu u}{\left(r_p \varphi\right)^2 \varepsilon^3} + 0.875\rho\,\frac{(1-\varepsilon)u^2}{r_p \varphi \varepsilon^3}\right) \qquad (6)$$

Where P is the local pressure at the z axial coordinate, μ is the gas viscosity, φ is the shape factor (assumed 1 in this work) and ρ is the gas density.

Breakthrough curves were then calculated for a mixture of 50/50 C_2H_2/CO_2, C_2H_2/C_2H_4 and C_2H_2/CH_4 at 298 K and 1.05 bar for three beds packed with the iMOFs. The bed was initially pressurized with helium. An equimolar or 1/99 mixture of C_2H_2/CO_2 or C_2H_2/C_2H_4 or C_2H_2/CH_4 was introduced to the system. This mixture with a total flowrate of 1.6 cm^3/min at 298 K and 1.05 bar was passed through an adsorption column packed with 0.3 gram of material. A summary of bed and feed characteristics are presented in Table S1:

Table 1. Adsorption column parameters and feed characteristics used for the simulations.

Adsorption bed	***Feed***
Length: 38 mm	Total Flow rate: 1.6 cm^3/min
Diameter: 6 mm	Temperature: 298 K
Amount of adsorbent in the bed: 0.3 g	Pressure: 1.05 bar
Adsorbent average radius: 0.2 mm	

Numerical Methods.

Numerical solutions of the nonlinear parabolic PDEs derived from mass and momentum balance were conducted by an implicit method of lines using finite difference method for the spatial derivatives. Firstly, the second and first space derivatives were discreted by central and upwind- differential scheme (backward), respectively. In this way, the sets of partial equations were transformed to the sets of ODEs with respect to the time derivative terms. The length of the bed was divided to 50 increments and the set of equations were solved by the Implicit Euler method with a time step of one second. [45]

2.2.10 Experimental Breakthrough experiments. In a typical breakthrough experiment, ~ 0.3 g of pre-activated (evacuated at room temperature in Micromeritics SmartVacPrep™ using dynamic vacuum) **iMOF-6C** was placed in a quartz tube (8 mm internal diameter; 8 mm x 6 mm x 400 mm) to form a packed adsorbent bed. First, the bed was purged by a 20 cm^3 min^{-1} flow of He gas at 298 K for 60 min prior to each of the breakthrough experiments. The gas flow was switched to the binary equimolar gas mixtures (C_2H_2/CO_2, C_2H_2/C_2H_4 and C_2H_2/CH_4), maintained at a total flow rate of 1.6 cm^3 min^{-1}. In each experiment, the outlet composition was continuously monitored by a SRI Instruments 8610C gas chromatograph until complete breakthrough was achieved.

2.2.11 Molecular Modelling Details.

Simulated annealing.

Based on the experimental crystallographic data of the **iMOF-6C** structure, the initial location of different gas molecules were obtained from the classical simulated annealing technique using classical force field as implemented in sorption module in *Materials Studio*. [46] The interactions of anion-adsorbent and anion-anion were modelled as a combination of pairwise site-site Lennard-Jones (LJ) and Coulombic potentials.

The LJ potential parameters for both the framework atoms and the adsorbates are adopted from the Universal force field (UFF). [47] The charges for the framework atoms were assigned based on the Qeq charges as implemented in *Materials Studio* package.

In the simulated annealing method, the temperature was lowered stepwise, allowing the gas molecule to reach a desirable configuration based on different moves such as rotation, translation and repositioning with preset probabilities of occurrence. This process of heating and cooling the system was repeated in several heating cycles to find the local minima. Forty heating cycles were performed where the maximum temperature and the final temperature were 10^5 K and 100 K, respectively.

DFT calculations.

Periodic geometric optimization and the static binding energies for gas molecule including C_2H_2, C_2H_4, CO_2 and CH_4 with the **iMOF-6C** framework was calculated using density functional theory (DFT) as implemented in the software package VASP 5.4.4. [48] It is well-known that standard DFT methods based on generalized gradient approximation do not fully account for the long-range dispersion interactions between the framework and the bound adsorbates. To accurately estimate static binding energies for each gas molecule with the framework, we implemented dispersion corrections using DFT-D3 method.[49] Electron exchange and correlation were described using the generalized gradient approximation Perdew, Burke, and Ernzerhof (PBE) [50] form and the projector-augmented wave potentials were used to treat core and valence electrons. [51] In all cases, we used a plane-wave kinetic energy cutoff of 600 eV and a Gamma-point mesh with kpoints (2 x 2 x 1) for sampling the Brillouin zone. The ionic coordinates and the cell parameters were fully relaxed until the Hellman-Feynman ionic forces were less than 0.02 eV/Å.

Binding energies.

The initial preferential location of each gas molecule in the primitive cell of corresponding MOF structures were obtained from the classical simulated annealing technique as described above. Static binding energies (ΔE) at 0 K in vacuum were calculated using the following expression

$$\Delta E = E_{MOF+Gas} - E_{MOF,def} - E_{Gas}$$

where E_x refers, respectively, to the total energies of the MOF + gas complex, the deformed MOF alone in its adsorbed state, and the gas molecule respectively.

2.3 Results and discussion

Structural analysis.

Single crystals of the three iMOF-nC variants were prepared at room temperature via slow diffusion technique (details in the supporting information). X-ray diffraction quality crystals for iMOF-5C and iMOF-6C were synthesised by reacting L with $Cu(ClO_4)_2.6H_2O$ and $Cu(BF_4)_2.xH_2O$ respectively in a solvent combination of DMF, benzene and methanol (Figure 2.1a). Single crystal X-ray diffraction (SC-XRD) studies revealed similar unit cell parameters as well as an identical coordination environment for iMOF-5C and iMOF-6C, indicative of their isoreticular nature. Powder X-ray diffraction (PXRD) patterns were found to be in agreement, confirming isoreticularity (Appendix 2.12). Both MOFs were found to crystallize in orthorhombic Cmcm space group (Appendix Tables 2.6, 2.7). The asymmetric unit of iMOF-5C is found to comprise of one Cu(II), two half L ligands and one DMF molecule coordinated to the Cu(II) flanked by three free ClO_4^- anions. On the flipside, in iMOF-6C, the asymmetric unit consists of one Cu(II), two half ligands (L) and one DMF molecule coordinated to the central Cu(II) that comprises three free BF_4^- anions (Appendix 2.1- Appendix 2.4). In both iMOF-5C and iMOF-6C, Cu(II) is octahedrally coordinated by four independent L ligands and two independent DMF molecules, which further extends to form a 2D sheet like structure typical of **sql** topology networks free from any interpenetration (Appendix 2.5, 2.6, 2.11). The residual positive charges of these networks were found to be neutralized by the tetrahedral ClO_4^- and BF_4^- anions residing freely inside the voids of iMOF-5C and iMOF-6C, respectively. The overall 2D structures are found to be bi-porous in nature having ultramicroporous channels of dimension 4.5×4.6 Å^2 and 5.3×5.4 Å^2 (Figure 2.1 b,c). PLATON analysis revealed that iMOF-5C and iMOF-6C possess large guest-accessible voids of 4085 Å^3 and 4198 Å^3 respectively, omitting the solvent molecules which represent 31.2% and 32.1% of the corresponding unit cell volumes. The one-dimensional channels in these iMOFs are decorated with polar carbonyl oxygens, while unsaturated π-electron cloud endow the Connolly surfaces with potential ability to engage in host-guest interactions (Appendix 2.7-2.9). Moreover, the triazole N-termini of the ligands coordinate to the Cu(II) centres, allowing the other N's to remain free, thereby acting as a complementary functionality (Appendix 2.5, 2.6). Employing a similar synthetic strategy while altering the metal salt to $Cu(NO_3)_2.3H_2O$, another isoreticular MOF, iMOF-7C was obtained where the pores were occluded with NO_3^- anions (Figure 2.1a). Due to poor crystallinity, despite several attempts, single crystal structure of iMOF-7C could not be determined. PXRD patterns of both iMOF-5C and iMOF-6C indicate bulk phase purity and high crystallinity (Appendix 2.13, 2.14). Slight differences observed between the simulated

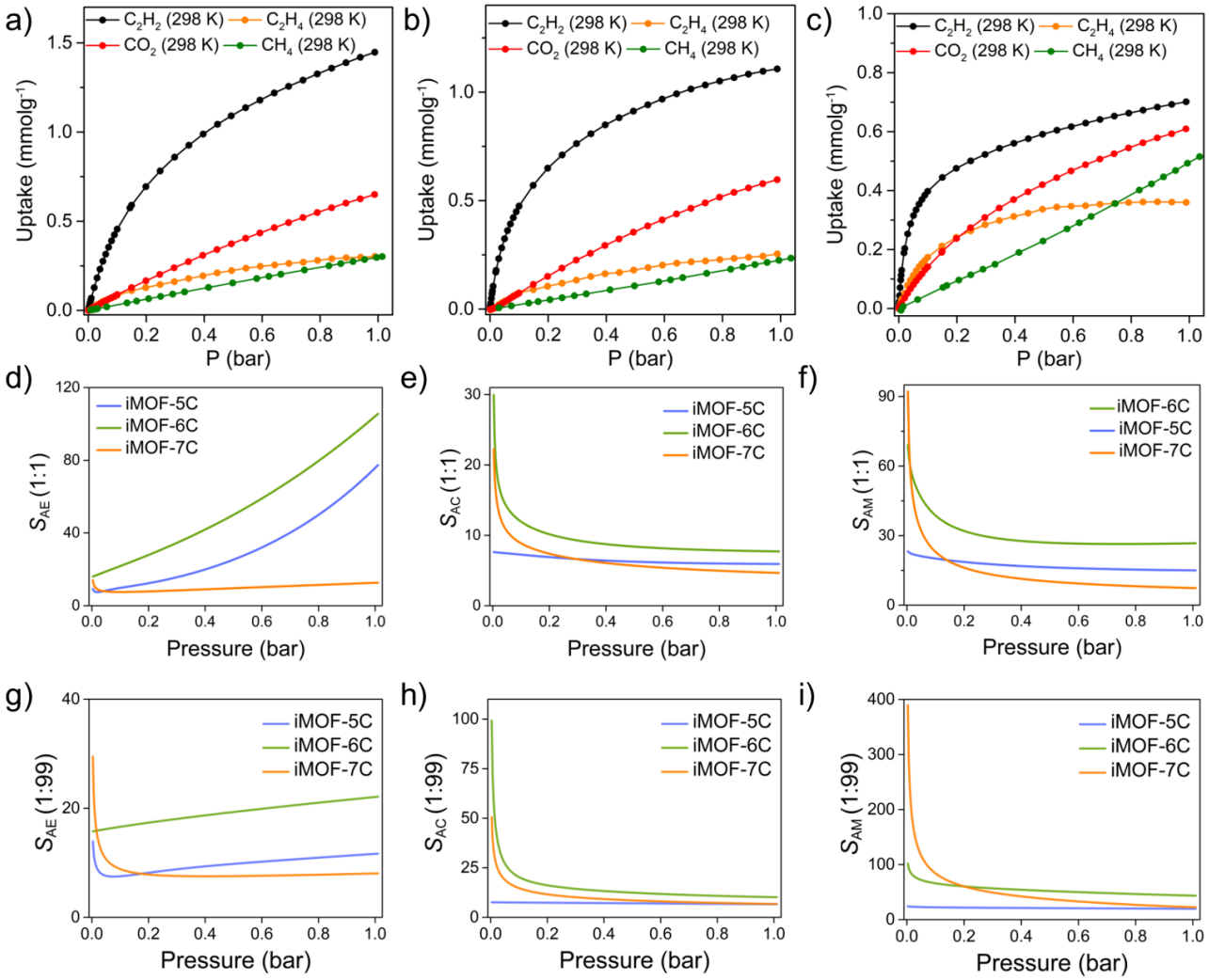

Figure 2.4. Single-component C2-C1 adsorption isotherms at 298K for (a) iMOF-5C; (b) iMOF-6C; (c) iMOF-7C; IAST selectivities of all the iMOF-nC for (d) C_2H_2/C_2H_4 mixtures (1/1, v/v); (e) C_2H_2/CO_2 mixtures (1/1, v/v); (f) C_2H_2/CH_4 mixtures (1/1, v/v); (g) C_2H_2/C_2H_4 mixtures (1/99, v/v); (h) C_2H_2/CO_2 mixtures (1/99, v/v); (i) C_2H_2/CH_4 mixtures (1/99, v/v) . (colour codes: black – C_2H_2, orange – C_2H_4, red – CO_2, green – CH_4).

and as-synthesised patterns can be attributed to the evaporation of low-boiling solvent molecules occluded inside the 2D frameworks of iMOF-5C and iMOF-6C. This is aligned with routine observations among layered MOFs in which the 2D sheets tend to slip from their original positions, resulting in slight changes to the as-synthesised structures. Nevertheless, the overall framework integrity remains

unaltered.[52] Moreover, comparison of the PXRD patterns of as-synthesised iMOF-6C and iMOF-7C established their isoreticular nature (Appendix 2.15). Thermogravimetric analysis (TGA) profiles of the activated iMOF-5C, iMOF-6C and iMOF-7C recorded under N_2 atmosphere revealed guest-free nature until 573 K (Appendix 2.17-2.19). FT-IR spectra of the MOFs confirmed the presence of characteristic ligand peaks along with a peak at ~ 1100 cm^{-1} for iMOF-5C corresponding to the uncoordinated ClO_4^-; a peak at ~ 1200 cm^{-1} for iMOF-6C corresponding to the uncoordinated BF_4^- and a peak at ~ 1400 cm^{-1} for iMOF-7C corresponding to NO_3^- anions (Appendix 2.20). Field emission scanning electron microscopy images of iMOF-nC crystals revealed rod shaped morphologies and EDX spectral data was in agreement with the respective elemental compositions (Appendix 2.21-2.26, Appendix Table 2.6).

Gas sorption studies.

Substantiating permanent microporosity, low-temperature (195 K) CO_2 adsorption recorded upon the iMOFs revealed typical Type 1 isotherms, registering uptakes of 80 $cm^3\ g^{-1}$, 100 $cm^3\ g^{-1}$ and 45 $cm^3\ g^{-1}$ for iMOF-5C, iMOF-6C and iMOF-7C respectively (Appendix 2.27-2.29). Only insignificant uptakes for N_2 (77 K) were noted, which is in agreement with the presence of free counter anions partially occluding the pores of iMOF-nC, an oft-encountered feature in ionic MOFs. Brunauer−Emmett−Teller (BET) surface areas were determined from the CO_2 (195 K) isotherms following Rouquerol criteria: 242, 330 and 109 $m^2\ g^{-1}$ for iMOF-5C, iMOF-6C and iMOF-7C, respectively (Appendix 2.30-2.32).[53] Pore size distribution analysis based on the Horvath-Kawazoe model from CO2 (195 K) data validated ultramicroporosity (~ 5–6 Å) along the iMOF-nC series, which is consistent with the pore dimensions derived from X-ray structural analysis (Figures 2.2b, 2c, Appendix 2.33).

C_2H_2, C_2H_4, CO_2 and CH_4 adsorption experiments were recorded on all three iMOFs at 298 K. For these four sorbates, all iMOF-nC analogues exhibited the highest saturation uptakes for C_2H_2 (Figure 2.2 a-c). At 298 K and 1 bar, the saturation uptake trend in iMOF-5C is: C_2H_2 (1.45 mmol g^{-1}) > CO_2 (0.65 mmol g^{-1}) > C_2H_4 (0.30 mmol g^{-1}) > CH_4 (0.29 mmol g^{-1}), the most preliminary signature of C_2H_2 selectivity (Figure 2.2a). Likewise, the saturation uptake trend in iMOF-6C was found to be: C_2H_2 (1.11 mmol g^{-1}) > CO_2 (0.59 mmol g^{-1}) > C_2H_4(0.25 mmol g^{-1}) > CH_4 (0.23 mmol g^{-1}) (Figure 2.2b). Further, for iMOF-7C, the trend appeared to be: C_2H_2 (0.70 mmol g^{-1}) > CO_2 (0.61 mmol g^{-1}) > CH_4 (0.51 mmol g^{-1}) > C_2H_4 (0.35 mmol g^{-1}) (Figure 2.2c). Importantly, iMOF-nC MOFs exhibit rapid C_2H_2 uptakes in the low-pressure region at 298 K, as low as 3000 ppm, i.e. 3 mbar: iMOF-5C (0.86 mmol g^{-1}) > iMOF-6C (0.77

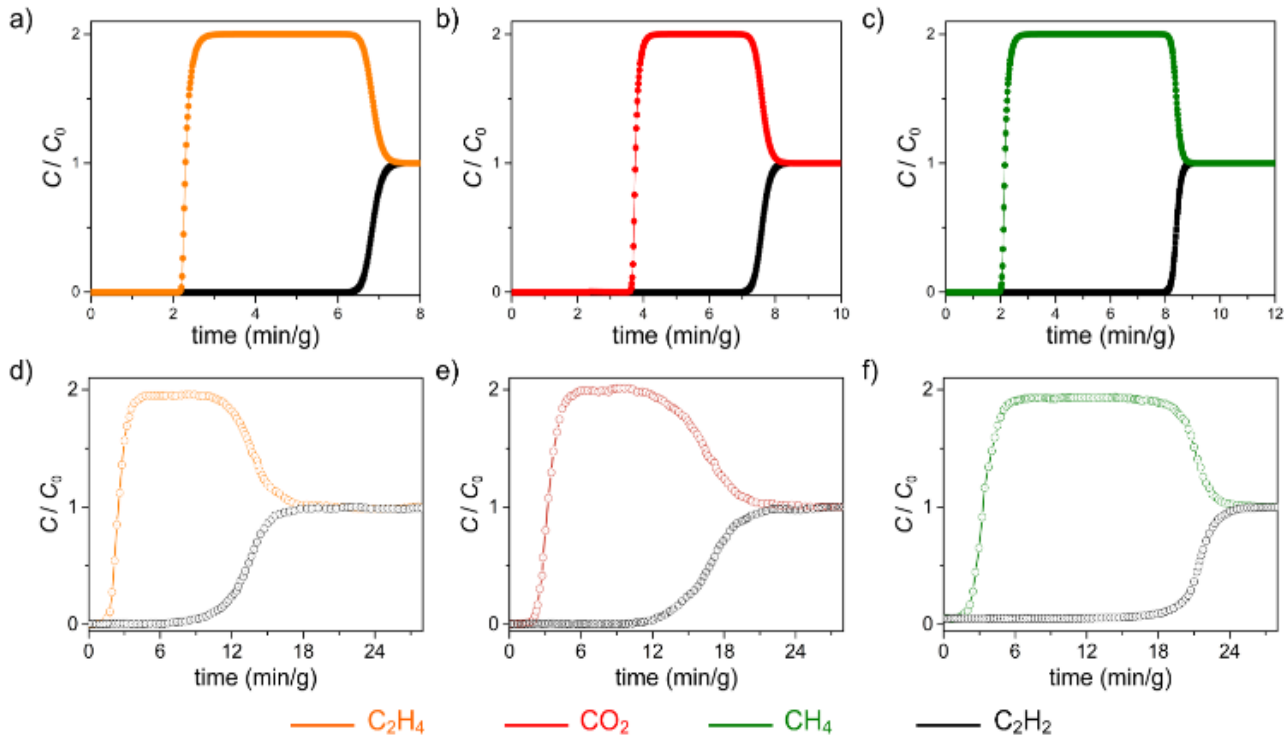

Figure 2.5. For iMOF-6c, simulated dynamic column breakthrough curves for equimolar mixtures of C_2H_2/C_2H_4 (a), C_2H_2/CO_2 (b) and C_2H_2/CH_4 (c) (total flow rate: 1.6 cm^3 min^{-1}); experimental dynamic column breakthrough curves for equimolar mixtures of C_2H_2/C_2H_4 (d), C_2H_2/CO_2 (e) and C_2H_2/CH_4 (f) (total flow rate: 1.6 cm^3 min^{-1}). (a-f) each maintained at 298 K and 1 bar. Filled symbols: simulated breakthrough profiles; open symbols: experimental breakthrough profiles. (colour codes: black – C_2H_2, orange – C_2H_4, red – CO_2, green – CH_4).

mmol g^{-1}) > iMOF-7C (0.52 mmol g^{-1}) (Appendix 2.34-2.36). Conversely, the three competing C2/C1 gases registered negligible uptakes under identical conditions. A similar adsorption selectivity trend was followed by iMOF-nC at 273 K (Appendix 2.37-2.39). The isosteric enthalpies of adsorption (Q_{st}) for iMOF-nC were calculated from fitting the 298 K and 273 K isotherms to dual-site Langmuir Freundlich isotherm model. The low-coverage $Q_{st}(C_2H_2)$ were found to follow the trend: 38 $kJmol^{-1}$ (iMOF-6C) > 35.5 $kJmol^{-1}$ (iMOF-5C) > 35 $kJmol^{-1}$ (iMOF-7C) (Appendix 2.40-2.43). The favourable thermodynamics between the iMOF-nC frameworks and C_2H_2 molecules was evident from their $Q_{st}(C_2H_2)$ at low coverage, which is one of the prime qualifying criterion in terms of leveraging sorption selectivity (Q_{st} ~ 35–50 $kJmol^{-1}$), generally regarded an optimal range in gas adsorption thermodynamics to potentially induce any adsorptive separation.[54] Fitting the 298 K pure gas isotherms to dual-site Langmuir-Freundlich equation,

clear differences among the fractional uptakes of C_2H_2 and the three other gases could be noted. These differences imply comprehensive C_2H_2/C_2H_4, C_2H_2/CO_2 and C_2H_2/CH_4 selectivities (Appendix 2.44, 2.45).

Ideal Adsorbed Solution Theory (IAST) Calculations.

To mimic the real-world gas separation conditions and to understand the applicability of these iMOFs, IAST selectivities for the binary mixtures of C_2H_2/CO_2, C_2H_2/C_2H_4 and C_2H_2/CH_4 (1/1 and 1/99; v/v) were determined using experimental single-component adsorption isotherms at 298 K under 1 bar (Figure 2.2 d-i). The IAST selectivity trend for C_2H_2/C_2H_4 (1/1, v/v) was 105 (iMOF-6C) > 78 (iMOF-5C) > 12 (iMOF-7C) and for C_2H_2/C_2H_4 (1/99, v/v), it was evaluated as: 25 (iMOF-6C) > 14 (iMOF-5C) > 8 (iMOF-7C) (Figure 2.2 d,g) (all values refer to IAST selectivities at the saturation pressure of 1 bar). This indicates a clear order of C_2H_2 adsorption selectivity in iMOF-nC: iMOF-6c > iMOF-5c > iMOF-7c. Importantly, upon excluding molecular sieves, the C_2H_2/C_2H_4 IAST selectivities for iMOF-5C and iMOF-6C (1/1, v/v) are comparable to the benchmark physisorbents including MOFs (Appendix Table 2.1). IAST selectivities for C_2H_2/CO_2 (1/1, v/v) mixture (iMOF-6C) > 6 (iMOF-5C) > 4 (iMOF-7C) and for (1/99, v/v) C_2H_2/CO_2: 15 (iMOF-6C) > 9 (iMOF-5C) > 8 (iMOF-7C) (Figure 2.2 e,h). These high values are also found comparable to the current benchmark MOF sorbents (Appendix Table 2.2). Further, this trend remains unaltered for C_2H_2/CH_4 (1/1, v/v) at 1 bar: 27 (iMOF-6C) > 15 (iMOF-5C) > 8 (iMOF-7C) and for (1/99 v/v) C_2H_2/CH_4: 38 (iMOF-6C) > 19 (iMOF-5C) > 16 (iMOF-7C) (Figure 2.2 f-i). Notably, these values of iMOF-nC found to be comparable with some benchmark MOFs reported in literature (Appendix Table 2.3). IAST results disclose that the C2-C1 selectivity across iMOF-nC platform of sorbents is set at iMOF-6C > iMOF-5C > iMOF-7C, which unsurprisingly agrees with the observed trend in $Q_{st}(C_2H_2)$.

Simulated breakthrough separation studies.

Building on these results, we then demonstrated the feasibility of using iMOFs for C_2H_2/C_2H_4, C_2H_2/CO_2 and C_2H_2/CH_4 separations under dynamic conditions encountered in industrial processes. Breakthrough curve simulation using a fixed adsorbent bed containing 0.3 g of the iMOFs were conducted at room temperature and atmospheric pressure using a previously reported methodology (details in the Supporting information).[55] Equimolar mixtures of these mixtures were used as feeds to mimic a range of industrial process conditions. For the case of C_2H_2/C_2H_4, as evident in Figures 2.3a, Appendix 2.46a, 2.46d, C_2H_4 eluted through the bed first in case of all three iMOF-nC to yield an outflow of pure gas. Conversely,

because C_2H_2 is more strongly adsorbed, it breaks through following a substantial time lapse. Similarly, iMOF-nC exhibited excellent separation performances for C_2H_2/CO_2 and C_2H_2/CH_4 mixtures as in both the cases CO_2 and CH_4 broke through first, while the signal for C_2H_2 was not detected over a significant time (Figure 2.3b-c: Appendix 2.46b-2.46c, 2.46e-2.46f). These simulation breakthrough results underscore the utility of iMOF-nC for addressing the pressing challenge of separating industrially

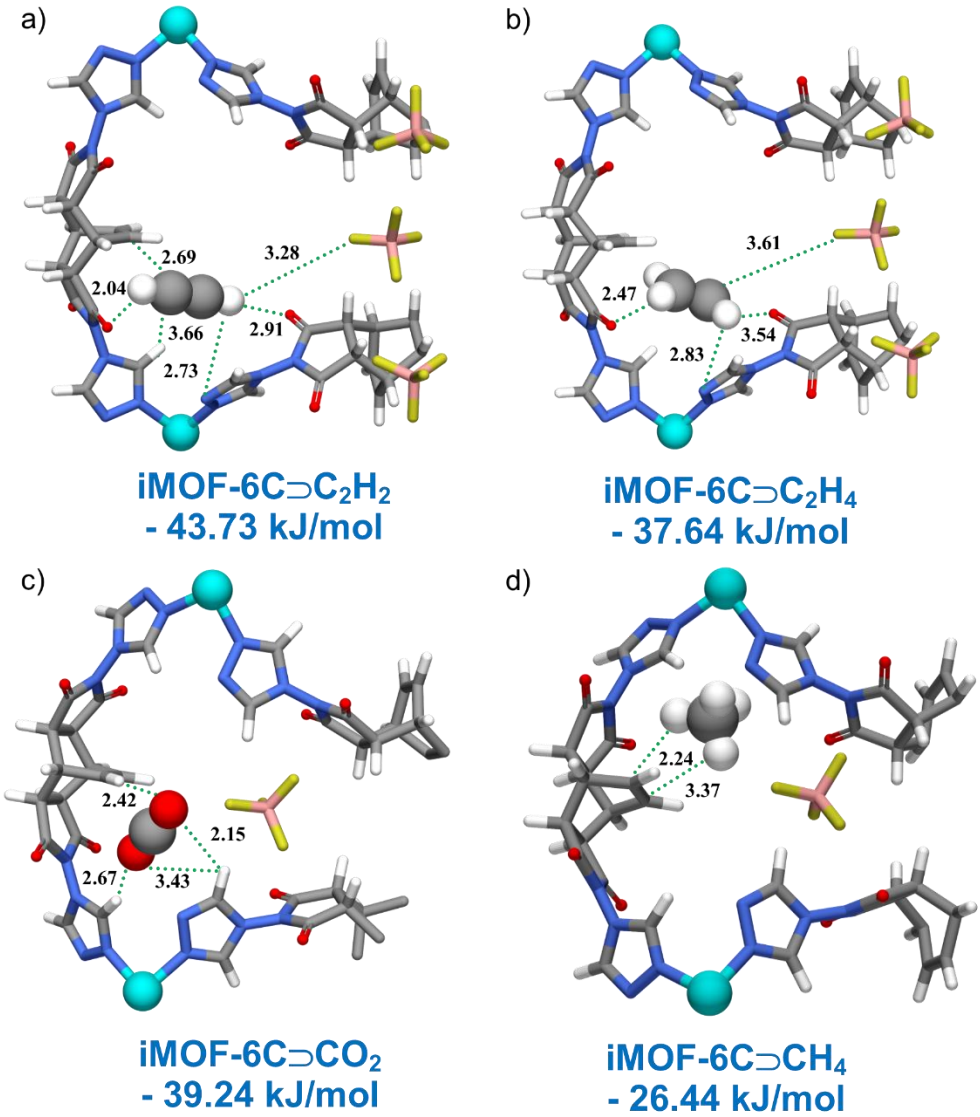

Figure 2.6. DFT optimisation based energy-optimised binding sites: (a) C_2H_2; (b) C_2H_4; (c) CO_2; (d) CH_4 in iMOF-6C, each. (colour codes: grey – C, blue – N, red – O, cyan – Cu, pink- B, yellow- F).

important C2-C1 gases such as C_2H_2/C_2H_4, C_2H_2/CO_2 and C_2H_2/CH_4.

Experimental breakthrough separation performance.

The promising isotherms based IAST selectivities and simulated breakthrough curve results prompted us to study the C_2H_2/CO_2, C_2H_2/C_2H_4, C_2H_2/CH_4 separation performances for the best-performing MOF, iMOF-6C, using a total flow rate of 1.6 cm^3/min (see details in the Supporting information, Appendix 2.48). Under ambient temperature and pressure (298 K and 1 bar), dynamic column breakthrough (DCB) experiments with three gas mixtures as aforementioned were carried out while the eluted components were continuously monitored through gas chromatography. Figure 2.3d-f reveal that in each case, C_2H_2 breakthrough occurred significantly later in comparison to CO_2 (13.0 versus 2.0 min g^{-1} for C_2H_2/CO_2), C_2H_4 (10.1 versus 1.4 min g^{-1} for C_2H_2/C_2H_4) and CH_4 (17.6 versus 1.3 min g^{-1} for C_2H_2/CH_4). For iMOF-6C, C_2H_2 saturation uptakes calculated from the C_2H_2/CO_2, C_2H_2/C_2H_4, C_2H_2/CH_4 DCB profiles are 19.8, 19.1 and 20.1 cm^3 g^{-1} respectively, are in good agreement with the single‑component C_2H_2 isotherm‑based uptake at half‑coverage (21.1 cm^3 g^{-1} under ambient equilibrium conditions). Moreover, iMOF-6C maintained phase purity and acetylene uptake capacity as the initial DCB cycle in subsequent cycles (Appendix 2.55, 2.56).

Theoretical calculations.

To understand the superior adsorption performances of iMOF-nC towards C_2H_2 and to delve deeper into the mechanism of gas adsorption, both density functional theory (DFT) and Monte Carlo simulations were performed (See SI for details on molecular modelling). First, based on the DFT optimized model of iMOF-6C, NVT simulated annealing using Monte Carlo approach were performed to recognize the most preferable site of various gas molecules within the porous framework. Secondly, the binding energies between the MOF structure and different gas molecules were calculated based on periodic model using the dispersion corrected DFT method (DFT-D3) as implemented in the software package VASP 5.4.4.[56] The preferential lowest energy binding sites identified from classical NVT simulated annealing is considered as the initial position for further DFT optimization. Figure 2.6 shows the optimized structure and the favourable binding location of C_2H_2, C_2H_4, CH_4 and CO_2 in iMOF-nC.

Consistent with the adsorption isotherms shown in Figure 2.2a, the calculated static binding energy follows the order C_2H_2 (–43.73 kJ/mol), CO_2 (–39.24 kJ/mol), C_2H_4 (–37.64 kJ/mol) and CH_4 (–26.44 kJ/mol) in iMOF-6C (Figure 2.6 a-d, Appendix Table 2.4), agreeing qualitatively with the experimental

adsorption enthalpies at low loading. The observed trend in binding energies can be explained on account of multiple factors. These include the likelihood of realising optimal binding between the ideally shaped/sized sorbate molecules and the narrow-pore MOF channels. As shown in Figure 2.6a, iMOF-6C exhibits several C_2H_2 binding sites. Strong interactions were found between (HC≡CH···O=C(MOF)), (HC≡CH···F–B (uncoordinated anion)) and (HC≡CH ···N–C (triazole unit)) whereas π–π interactions sustain the binding between π electron rich bicyclo-unit and C_2H_2 molecules. In contrary, significantly weaker interactions found for other gases (C_2H_4, CO_2 and CH_4) result in relatively low binding energies. This further corroborates with IAST predicted C_2H_2 selectivities against C_2H_4, CO_2 and CH_4.

2.4 Conclusion

Exploiting crystal engineering design across one of the simplest topologies (*viz.*, sql) and fine-tuning the pore environments by anion modulation, for the first time, herein a cationic MOF series delivers light hydrocarbon separation performance. Thanks to its multiple functionalities (carbonyl oxygen atoms, coordinated DMF molecules, unsaturated π-electron cloud etc.) along the pore including three different anions occluding the channels, compositional modularity directly impacts separation performances as anticipated. In addition, the tetrafluoroborate variant, iMOF-6C, emerges as the lead sorbent to register new benchmarks in three-in-one C_2H_2 adsorption selectivity (unifying C_2H_2/C_2H_4, C_2H_2/CO_2 and C_2H_2/CH_4) driven adsorptive separation under dynamic conditions, a rarity among all physisorbents hitherto documented, including zeolites, silica and activated carbon. Moreover, theoretical studies further corroborated well with the high affinity and selectivity of iMOF-nC frameworks toward C_2H_2 (in terms of favourable interactions and binding energies) over C_2H_4, CO_2 and CH_4.

This work not only inaugurates any systematic study of light hydrocarbon separation among cationic MOFs, but perhaps more importantly, the combination of three binary separation performances in iMOF-6C validated by multiple experiments and theoretical calculations underscores the pressing need to explore this class of modular physisorbents in future. C_2H_2 selective binding sites, as computationally determined herein, also indicate the yet untapped potentials of ionic supramolecular scaffolds, rather abundant in today's MOF literature. Development of such *multiple-in-one* separating sorbents able to remove several impurities (gases/vapors) at one step stands out in terms of cost and energy efficiency of commodity purifications. In hindsight, the current design approach might potentially hold a key to mitigate the existing environmental footprints of the state-of-the-art technologies.

2.5 Appendix section

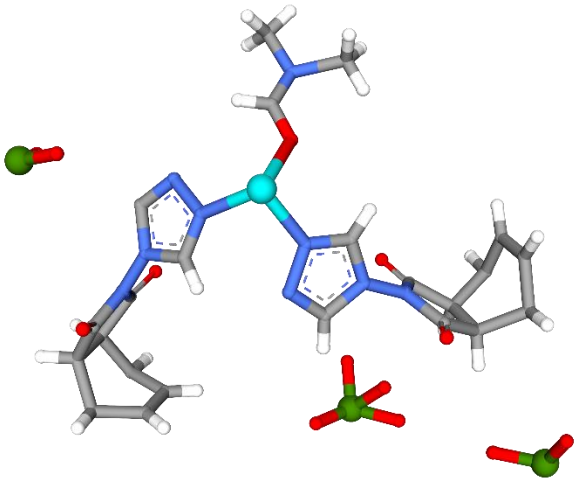

Appendix 2.1. Asymmetric unit of **iMOF-5C** (colour codes: grey - C, blue - N, red – O, cyan – Cu, green – Cl, colourless - hydrogen).

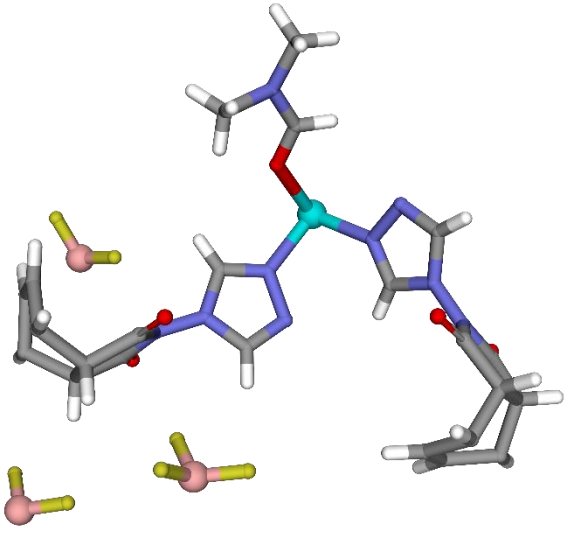

Appendix 2.2. Asymmetric unit of **iMOF-6C** (colour codes: grey - C, blue - N, Red – O, cyan – Cu, yellow – F, pink – B, colourless - hydrogen).

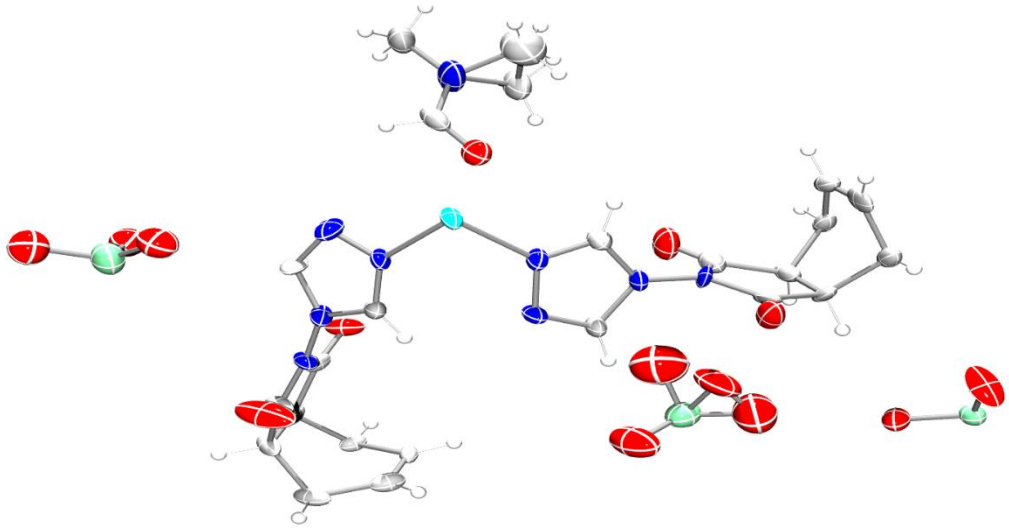

Appendix 2.3. ORTEP diagram of asymmetric unit of **iMOF-5C** presented in thermal ellipsoids (50% probability).

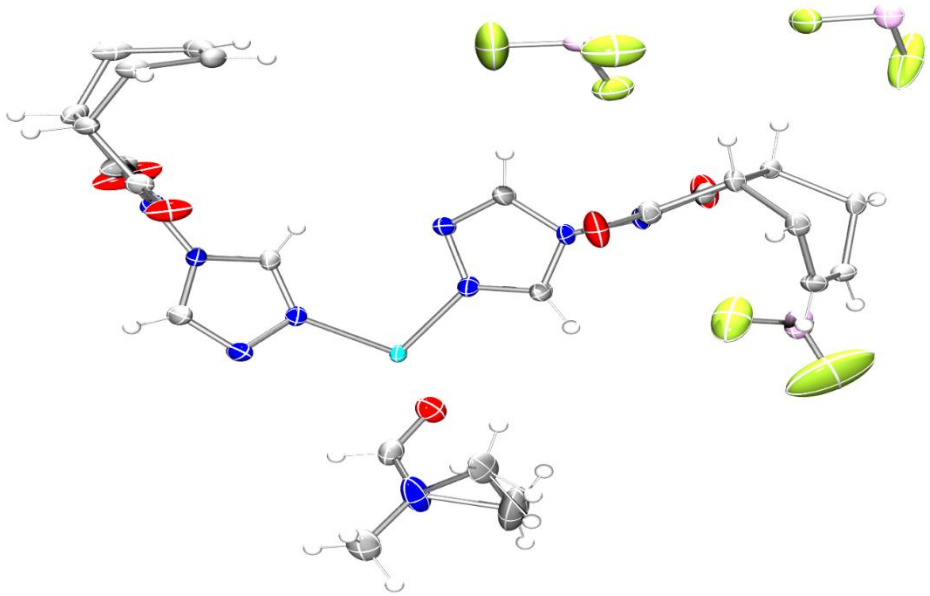

Appendix 2.4. ORTEP diagram of asymmetric unit of **iMOF-6C** presented in thermal ellipsoids (50% probability).

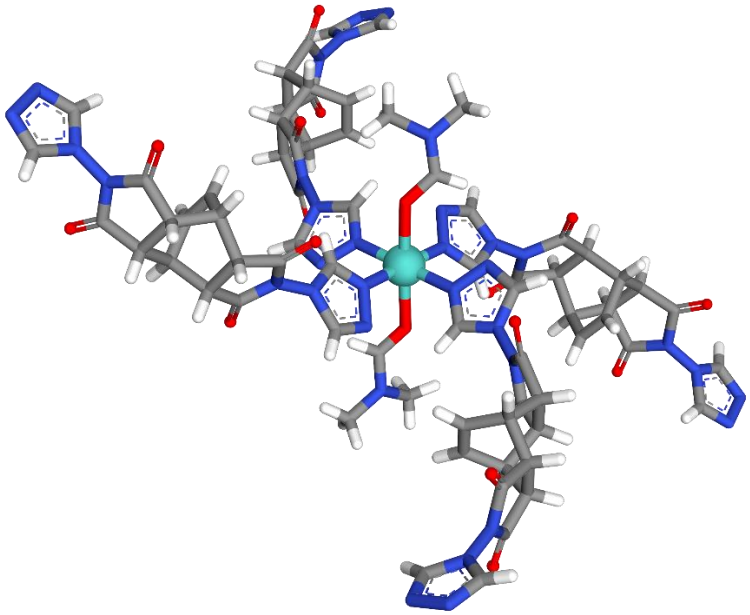

Appendix 2.5. Coordination environment of **iMOF-5C** (colour codes: grey - C, blue - N, red – O, cyan – Cu, colourless - hydrogen).

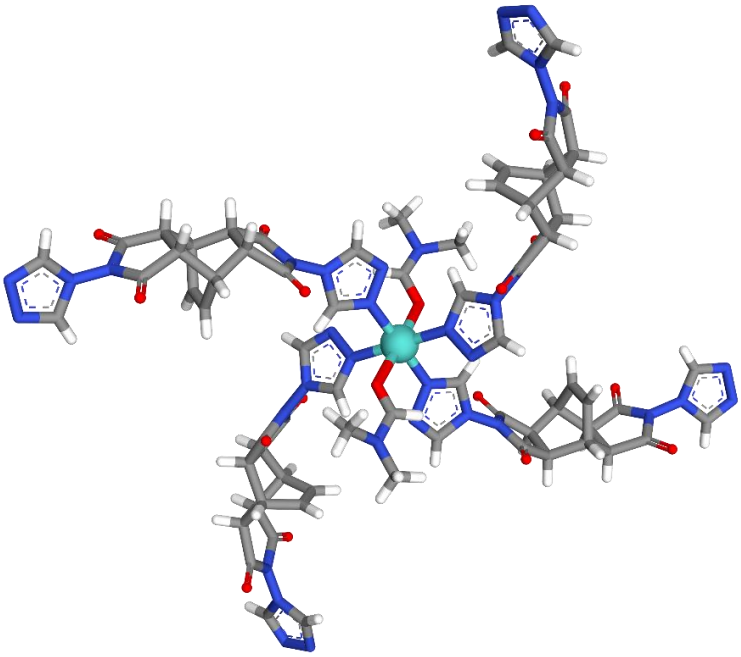

Appendix 2.6. Coordination environment of **iMOF-6C** (colour codes: grey - C, blue - N, red – O, cyan – Cu, colourless - hydrogen).

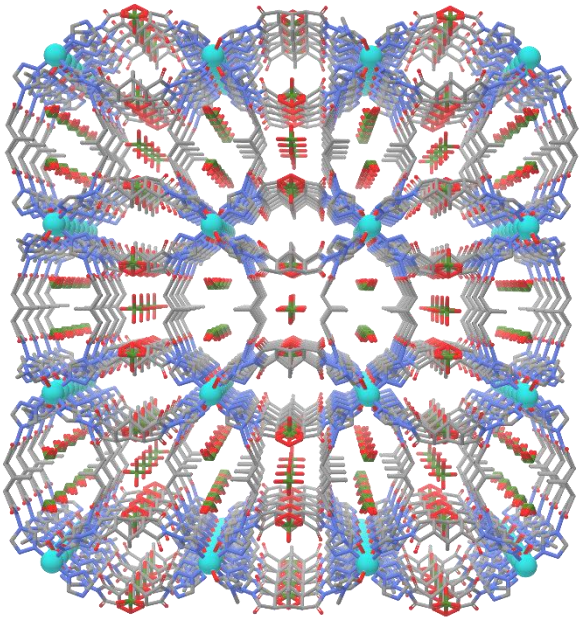

Appendix 2.7. Perspective packing view of **iMOF-5C** along *c* axis. (colour codes: grey - C, blue - N, red – O, cyan – Cu, colourless - hydrogen).

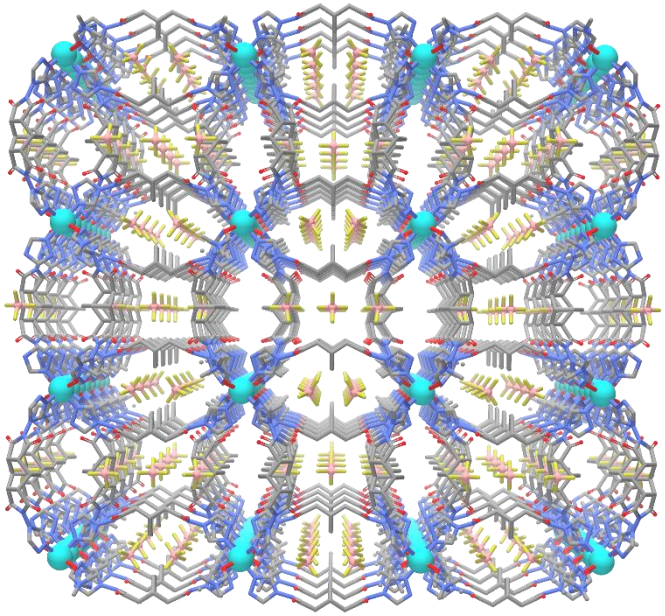

Appendix 2.8. Perspective packing view of **iMOF-6C** along *c* axis. (colour codes: grey - C, blue - N, red – O, cyan – Cu, colourless - hydrogen).

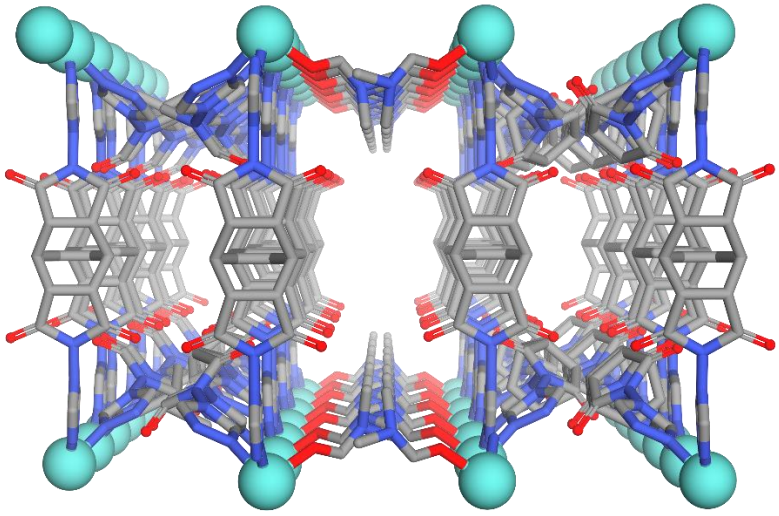

Appendix 2.9. Perspective packing view of **iMOF-5C** along *b* axis; (colour codes: grey - C, blue - N, red – O, cyan – Cu), ClO_4^- anions and H atoms omitted for clarity.

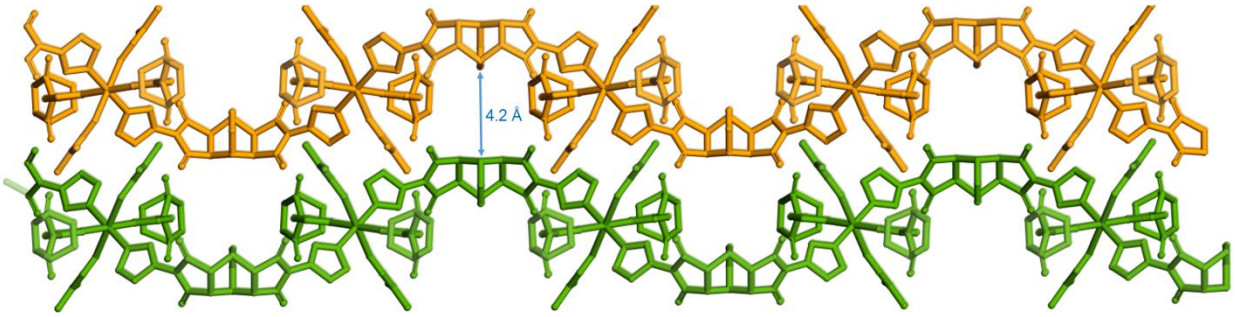

Appendix 2.10. Interplanar distance in **iMOF-5C** between two consecutive layers as shown in orange and green (ClO_4^- anions and H atoms omitted considering crystallographic disorder and clarity).

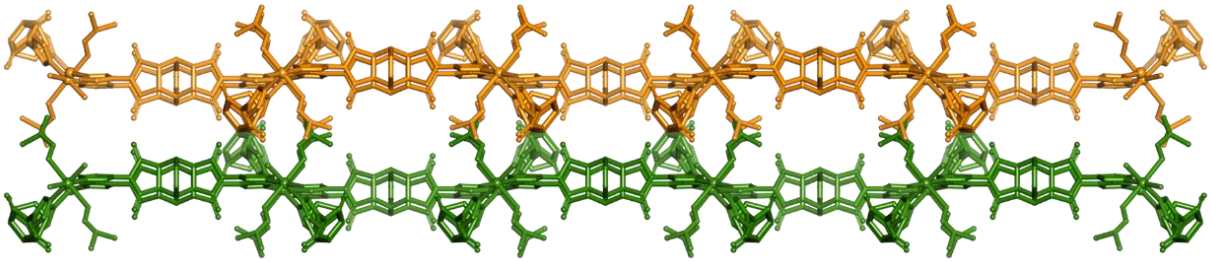

Appendix 2.11. sql topology of **iMOF-5C**; two consecutive undulating layers are shown in orange and green (ClO_4^- anions and H atoms omitted considering crystallographic disorder and clarity).

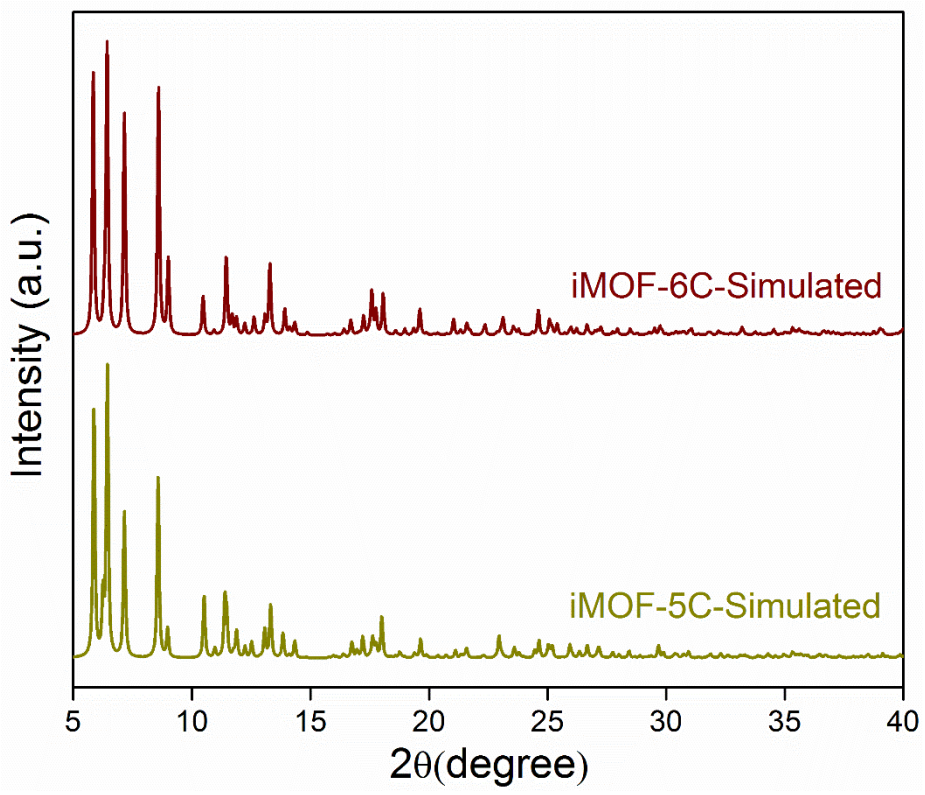

Appendix 2.12. Simulated PXRD patterns of **iMOF-5C** and **iMOF-6C**.

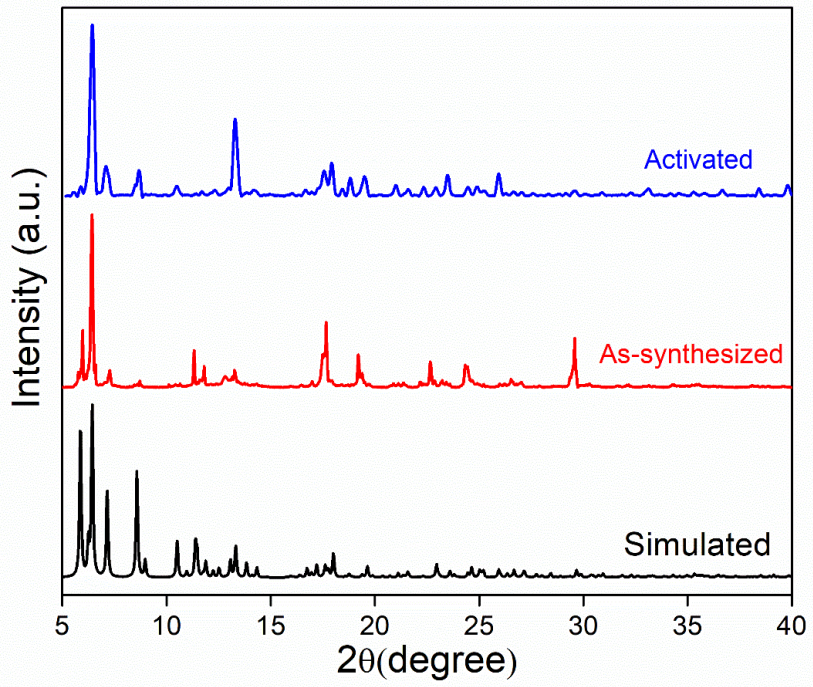

Appendix 2.13. Powder X-ray diffraction patterns of **iMOF-5C**.

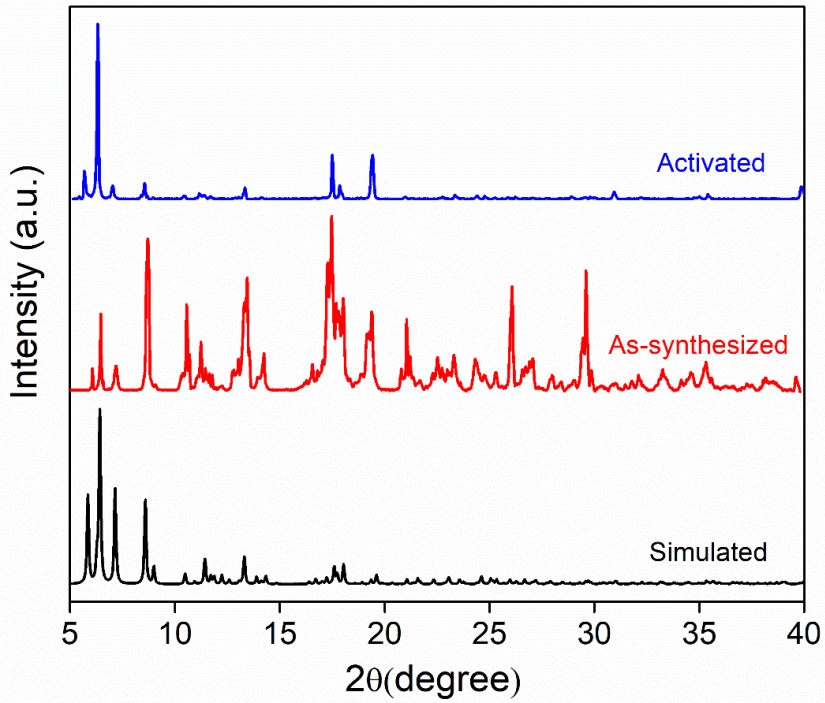

Appendix 2.14. PXRD patterns of **iMOF-6C**.

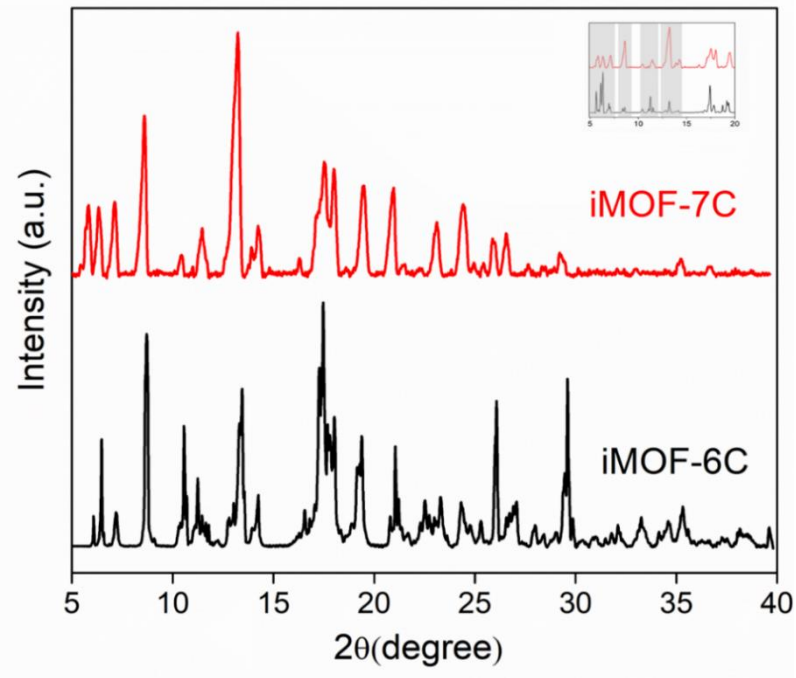

Appendix 2.15. PXRD patterns of as-synthesized **iMOF-6C** and **iMOF-7C**. Inset shows the PXRD patterns zoomed at low angle.

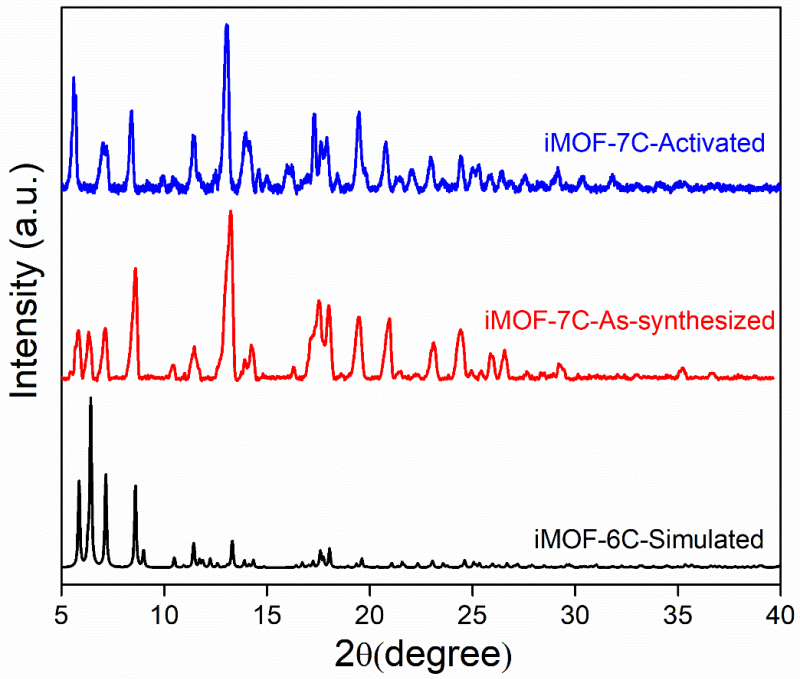

Appendix 2.16. PXRD patterns of **iMOF-7C**, compared to the simulated pattern of **iMOF-6C**.

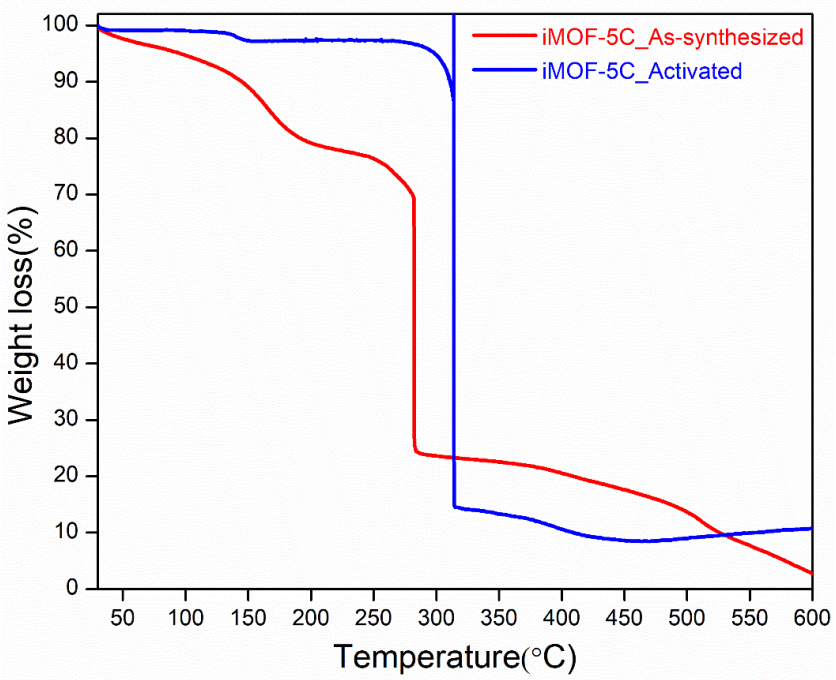

Appendix 2.17. TGA profiles for **iMOF-5C**.

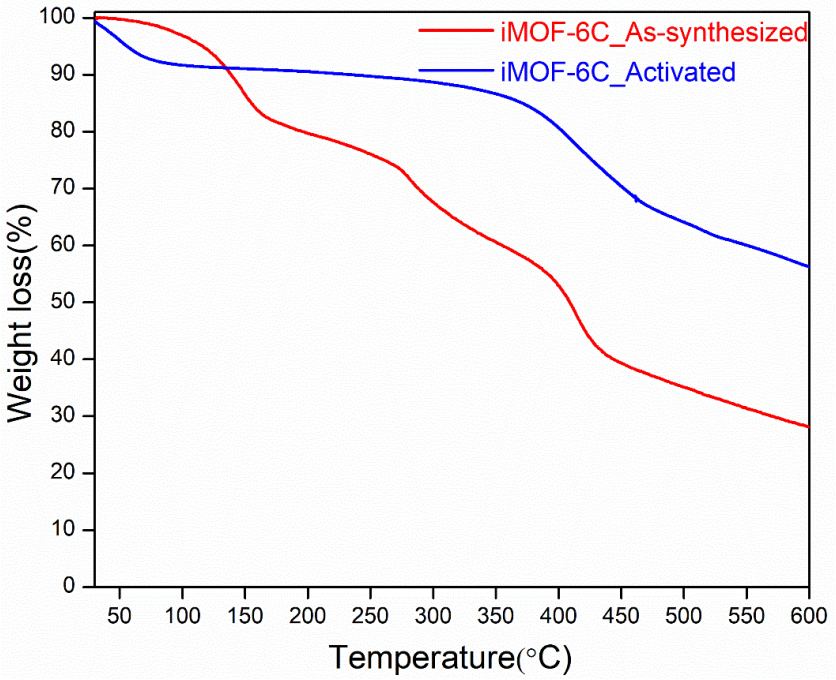

Appendix 2.18. TGA profiles for **iMOF-6C**.

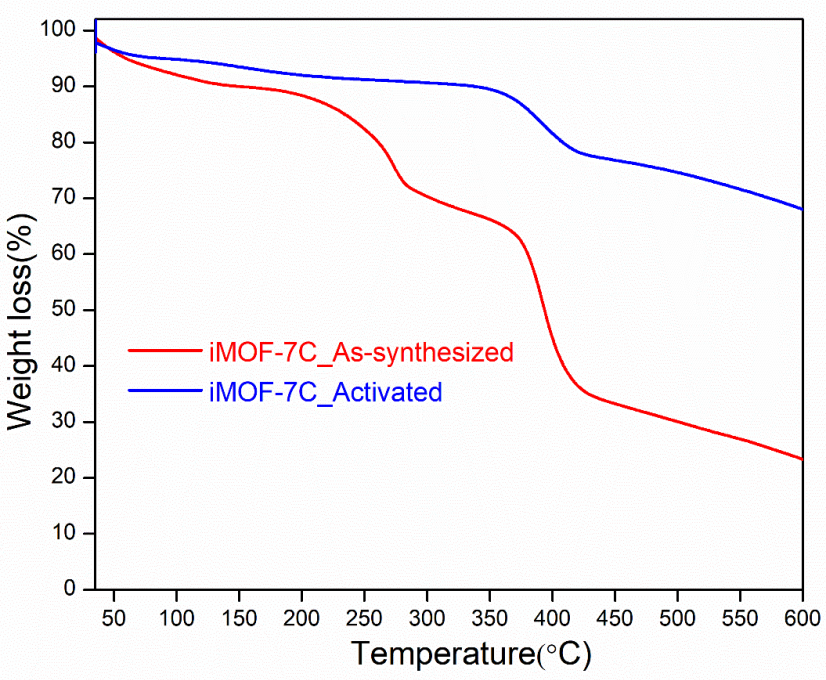

Appendix 2.19. TGA profiles for **iMOF-7C**.

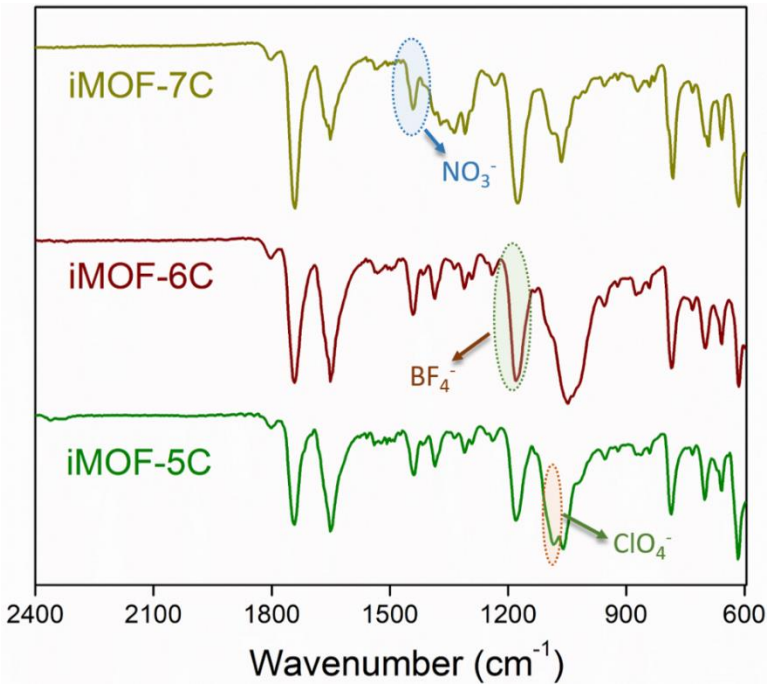

Appendix 2.20. IR spectra of **iMOF-5C** (green), **iMOF-6C** (wine red) and **iMOF-7C** (dark yellow).

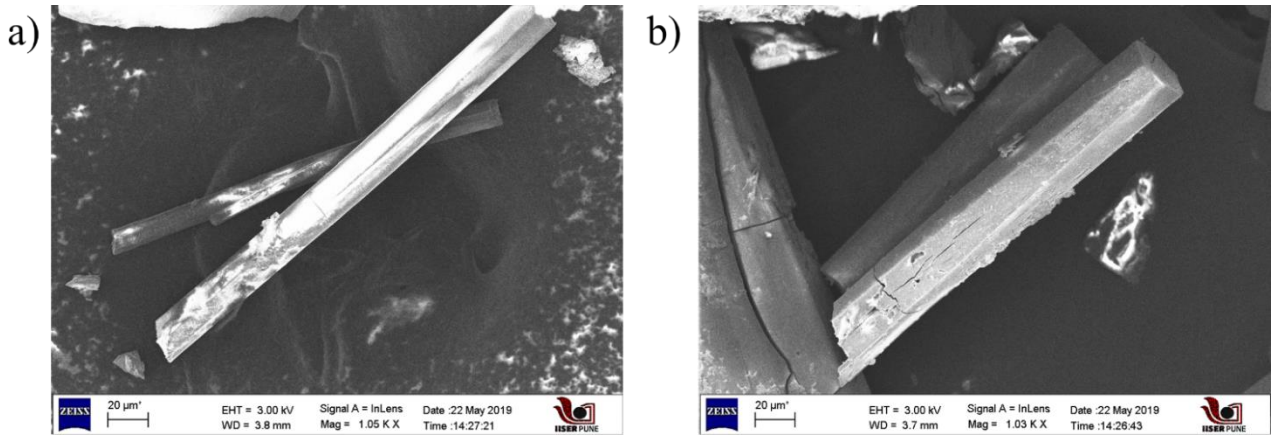

Appendix 2.21. FESEM images of **iMOF-5C** crystals.

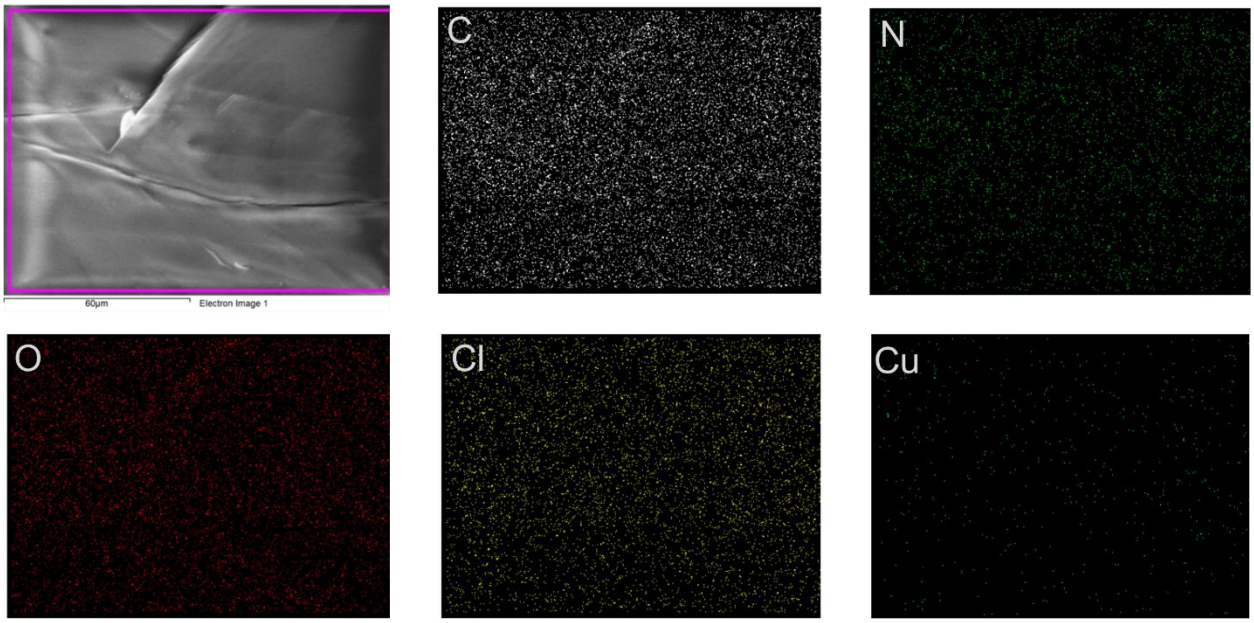

Appendix 2.22. Elemental mapping recorded on **iMOF-5C** crystals.

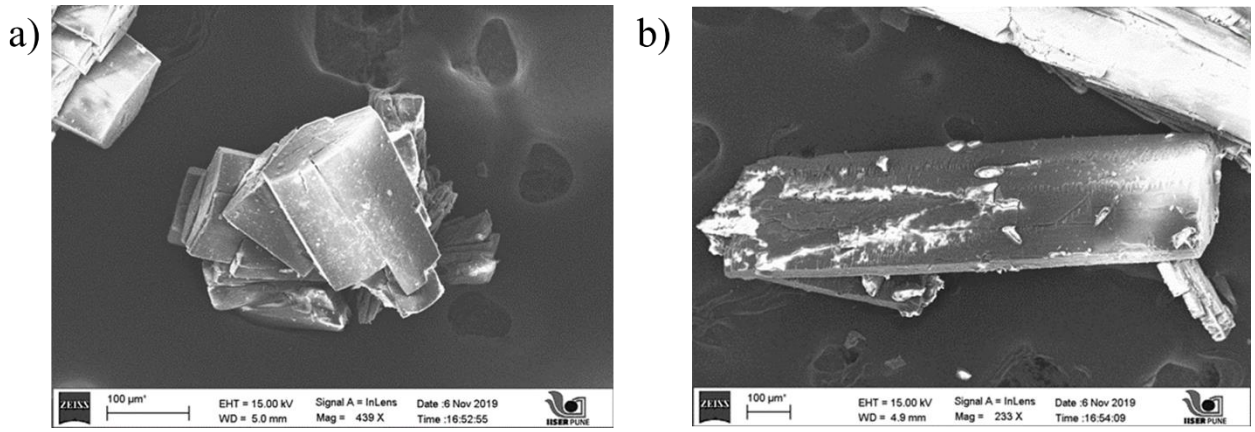

Appendix 2.23. FESEM images of **iMOF-6C** crystals.

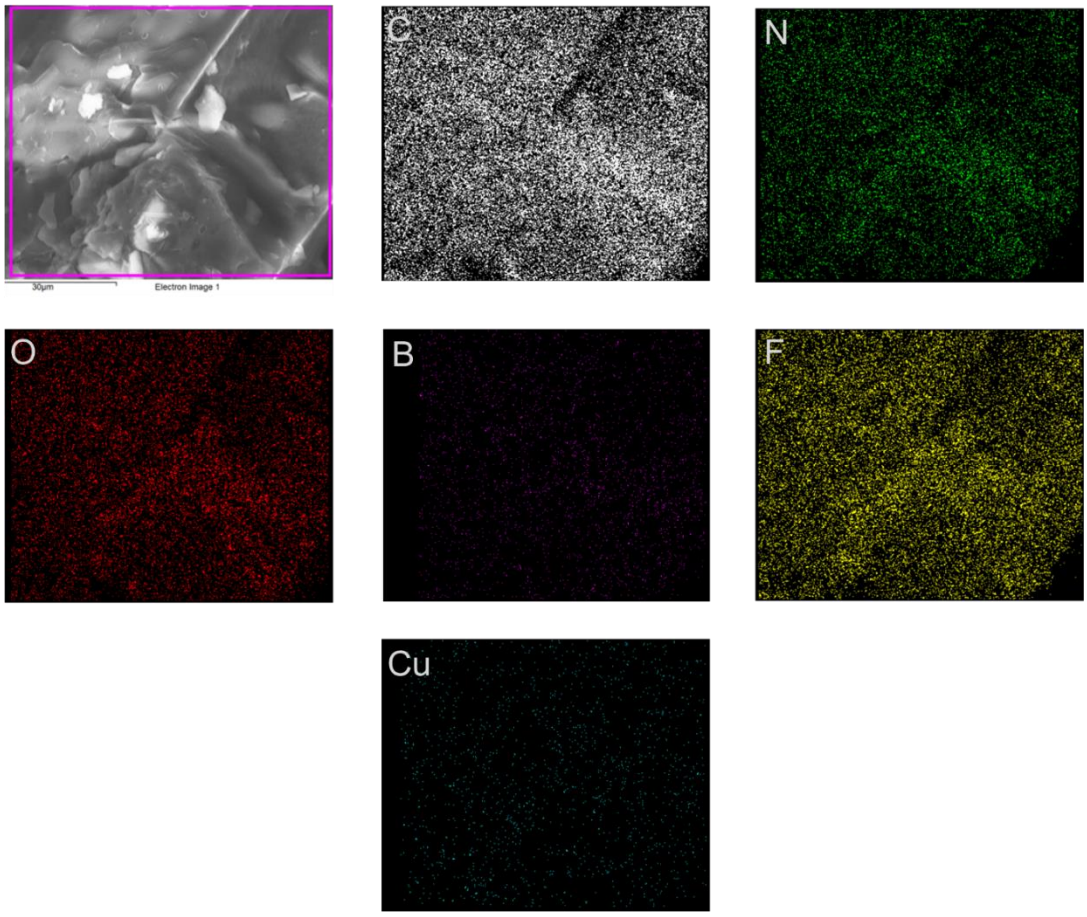

Appendix 2.24. Elemental mapping recorded on **iMOF-6C** crystals.

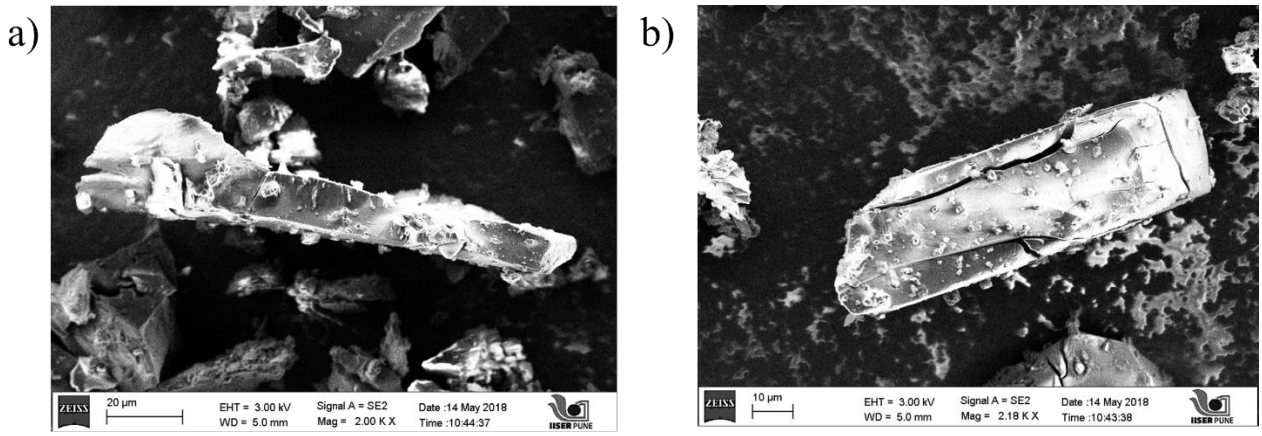

Appendix 2.25. FESEM images of **iMOF-7C** crystals.

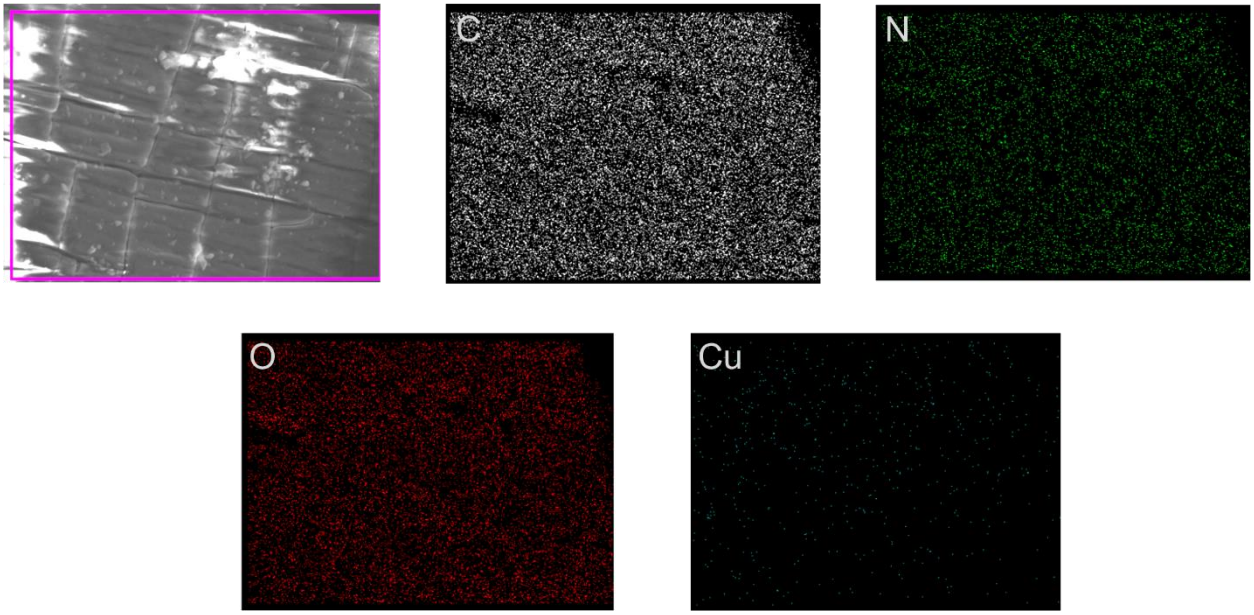

Appendix 2.26. Elemental mapping recorded on **iMOF-7C** crystals.

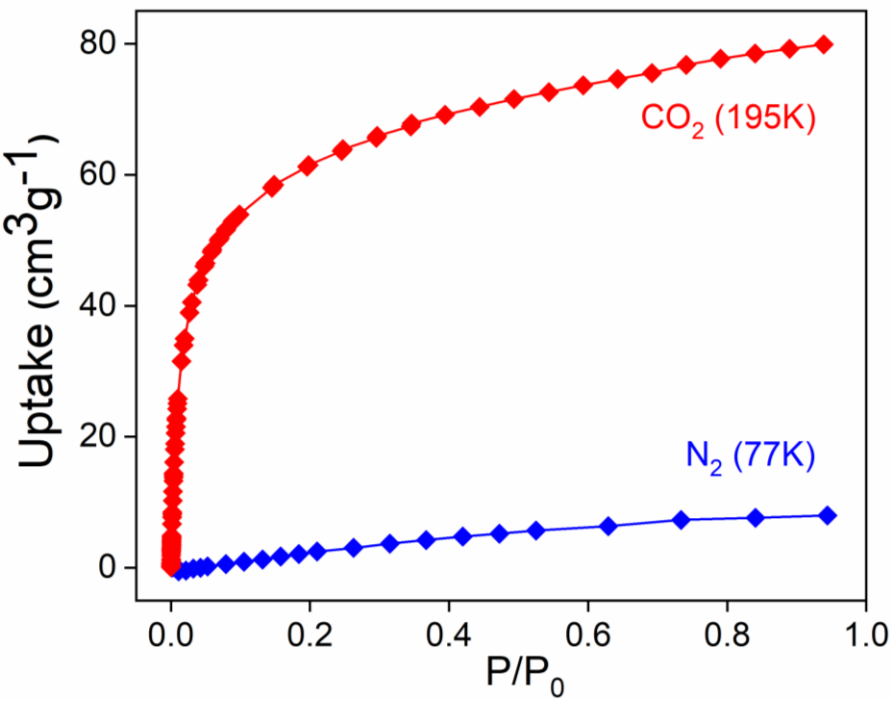

Appendix 2.27. Low temperature adsorption isotherms of **iMOF-5C**.

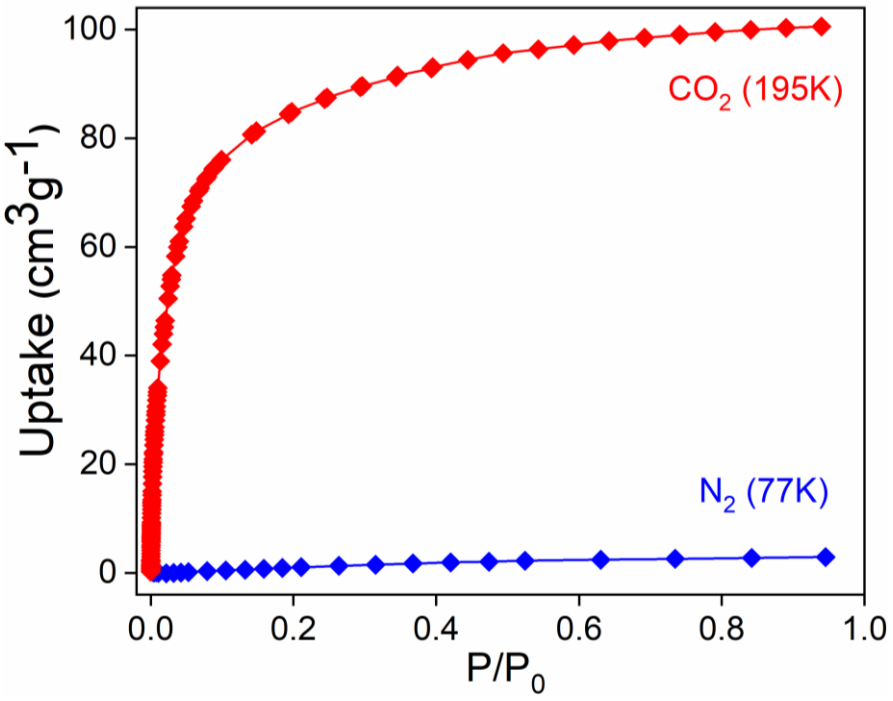

Appendix 2.28. Low temperature adsorption isotherms of **iMOF-6C**.

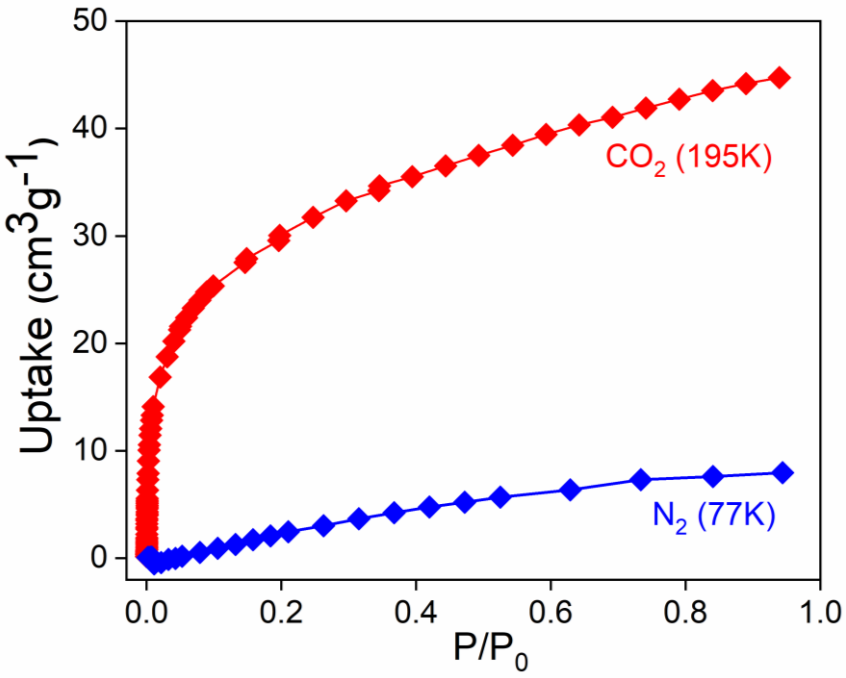

Appendix 2.29. Low temperature adsorption isotherms of **iMOF-7C**.

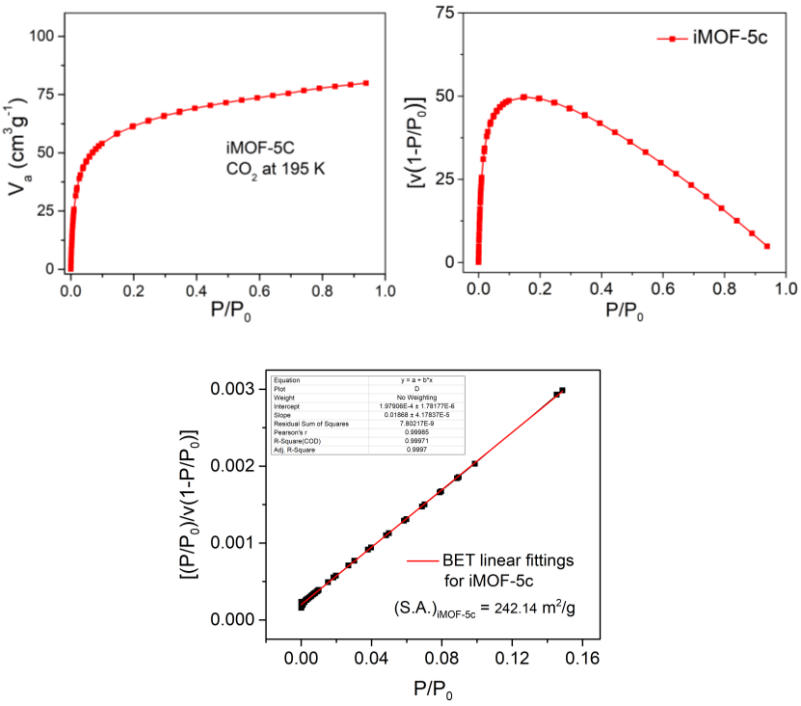

Appendix 2.30. CO_2 adsorption isotherm at 195 K and BET surface area plots for **iMOF-5C**.

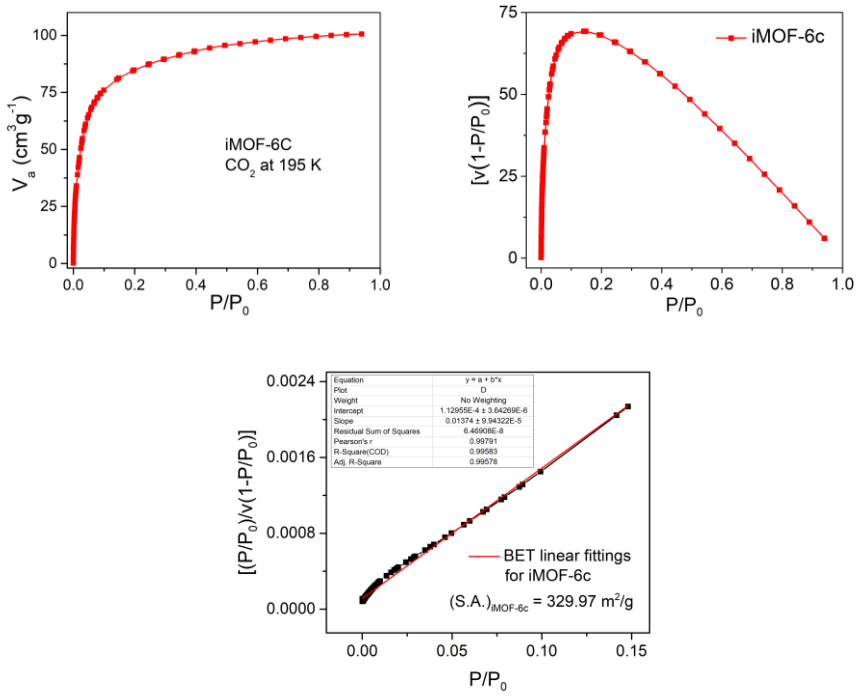

Appendix 2.31. CO_2 adsorption isotherm at 195 K and BET surface area plots for **iMOF-6C**.

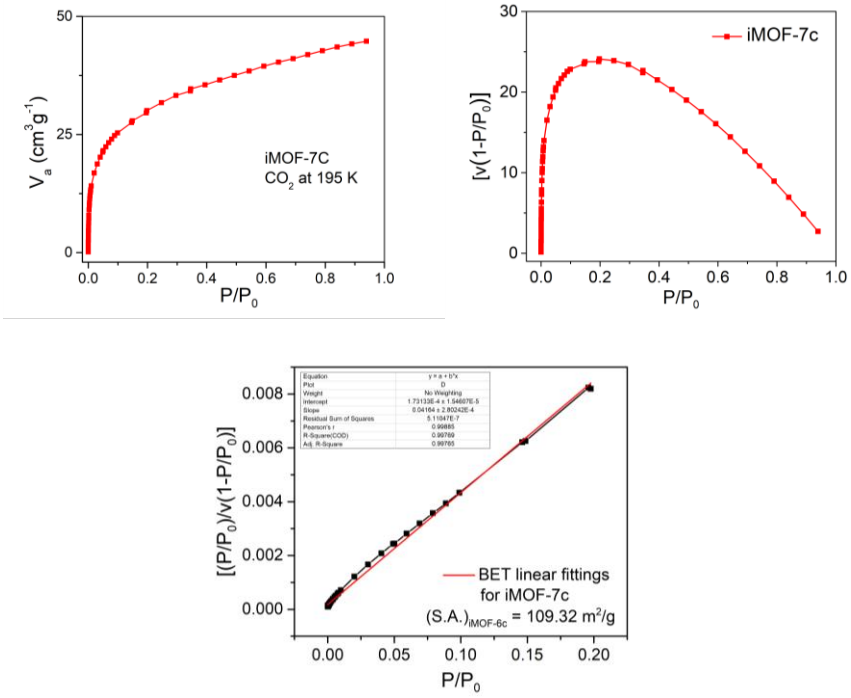

Appendix 2.32. CO_2 adsorption isotherm at 195 K and BET surface area plots for **iMOF-7C**.

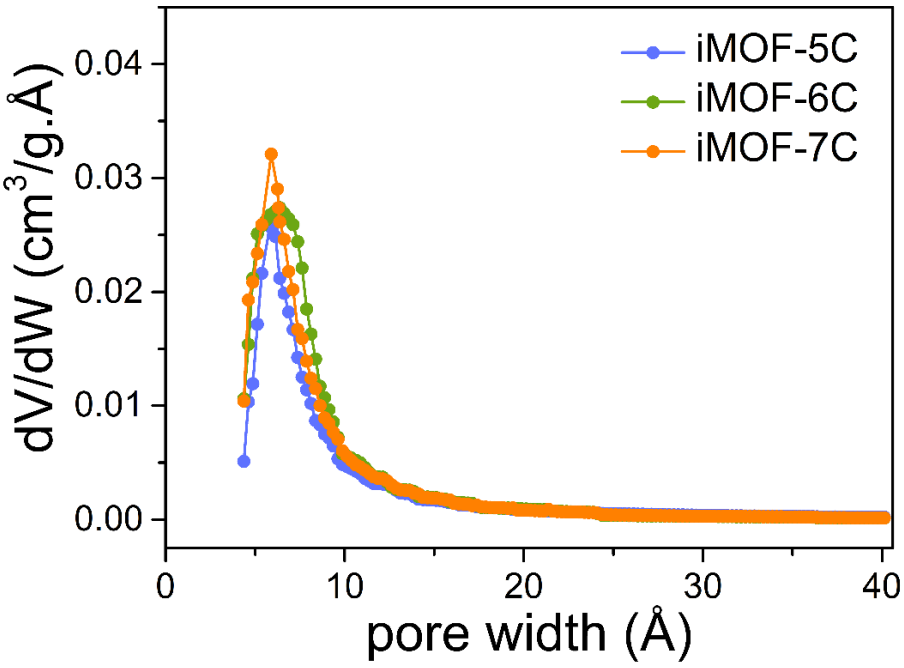

Appendix 2.33. Pore size distribution plots for **iMOF-nC**.

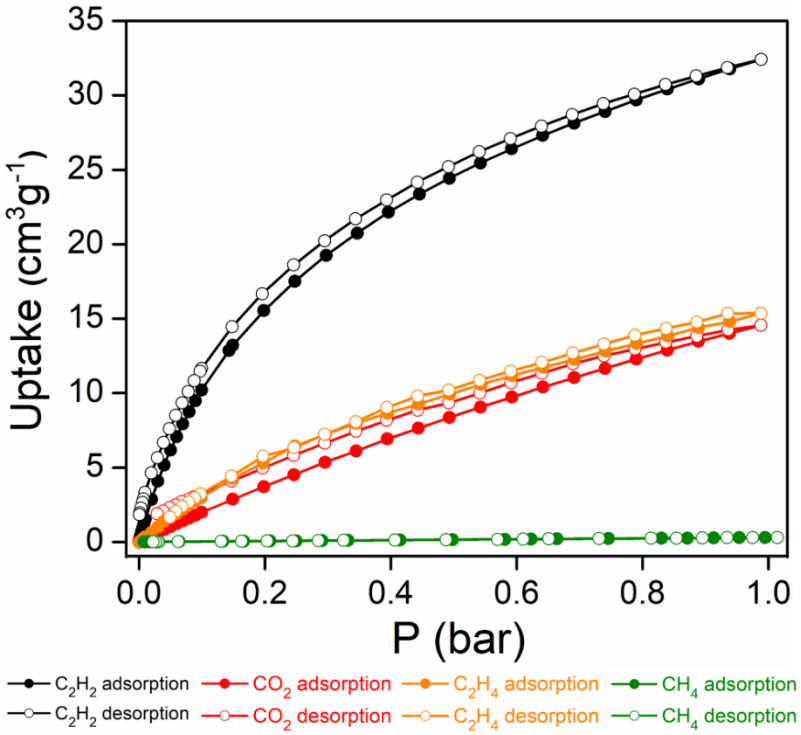

Appendix 2.34. Single-component adsorption isotherms for **iMOF-5C** recorded at 298 K.

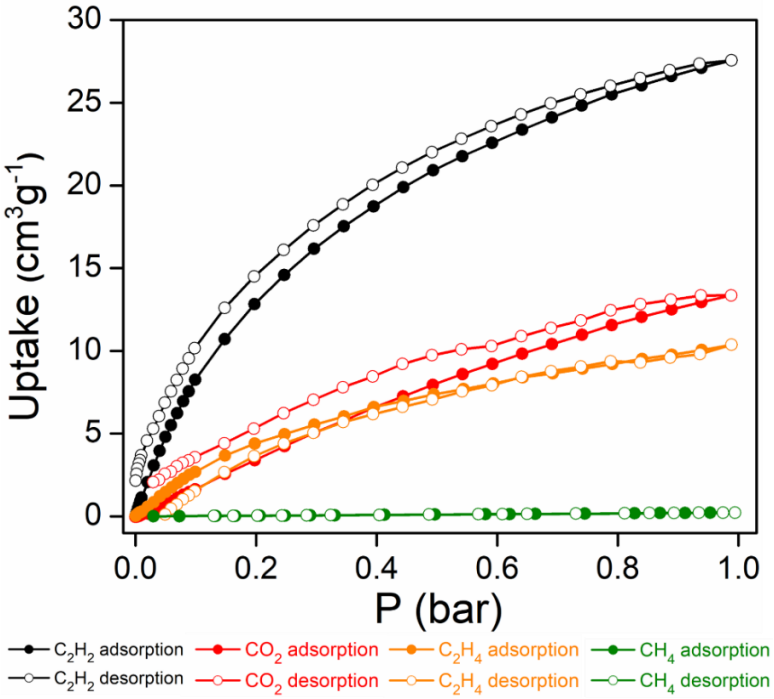

Appendix 2.35. Single-component adsorption isotherms for **iMOF-6C** recorded at 298 K.

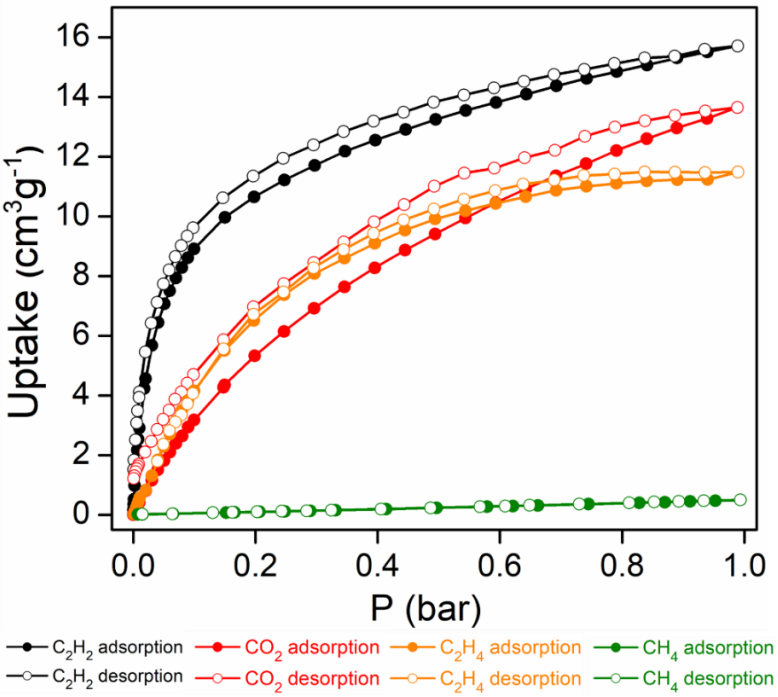

Appendix 2.36. Single-component adsorption isotherms for **iMOF-7C** recorded at 298 K.

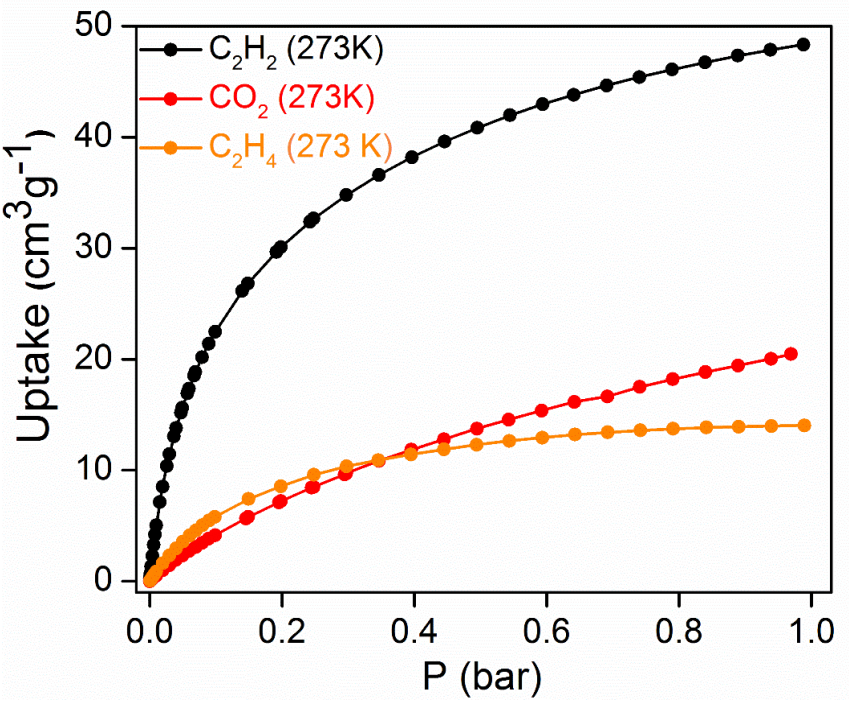

Appendix 2.37. Single-component adsorption isotherms for **iMOF-5C** recorded at 273 K.

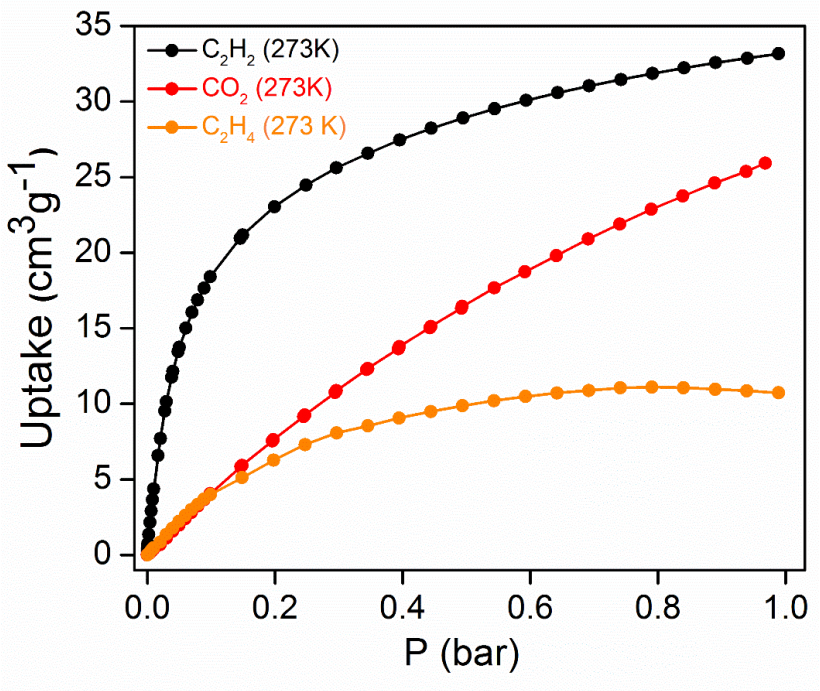

Appendix 2.38. Single-component adsorption isotherms for **iMOF-6C** recorded at 273 K.

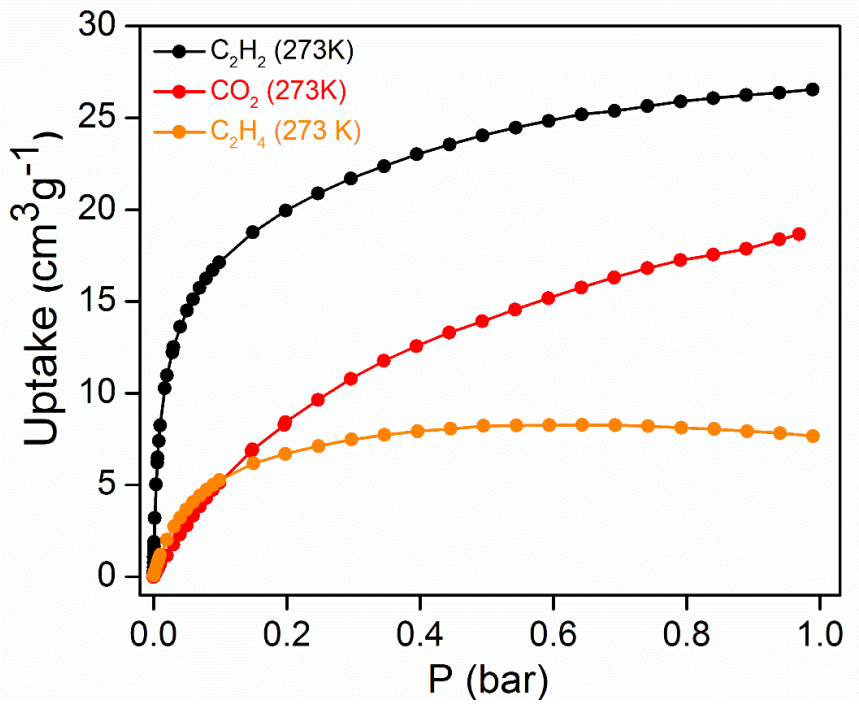

Appendix 2.39. Single-component adsorption isotherms for **iMOF-7C** recorded at 273 K.

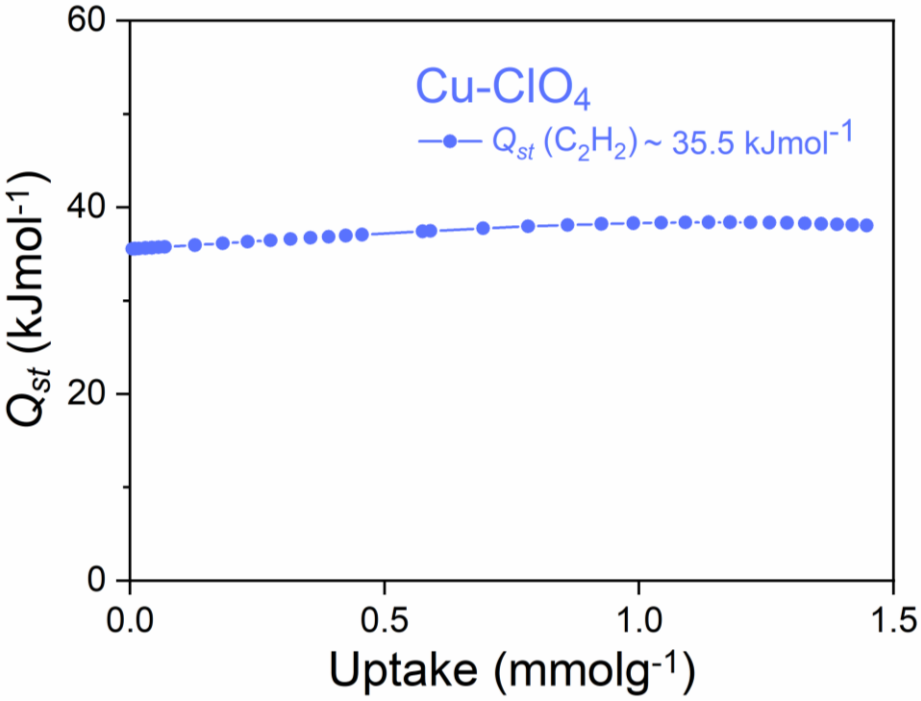

Appendix 2.40. Isosteric enthalpy of adsorption profile of C_2H_2 for **iMOF-5C**.

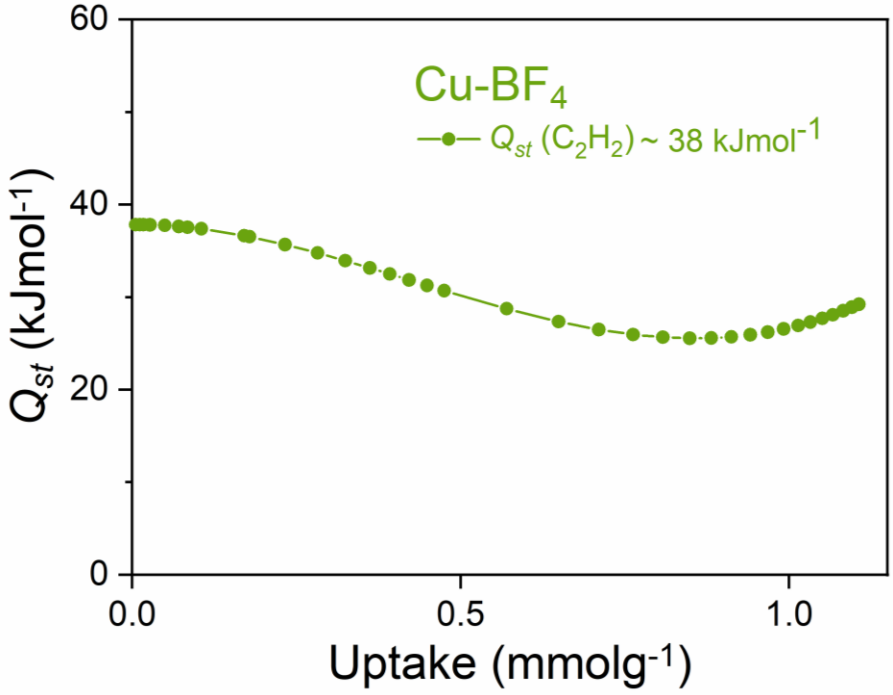

Appendix 2.41. Isosteric enthalpy of adsorption profile of C_2H_2 for **iMOF-6C**.

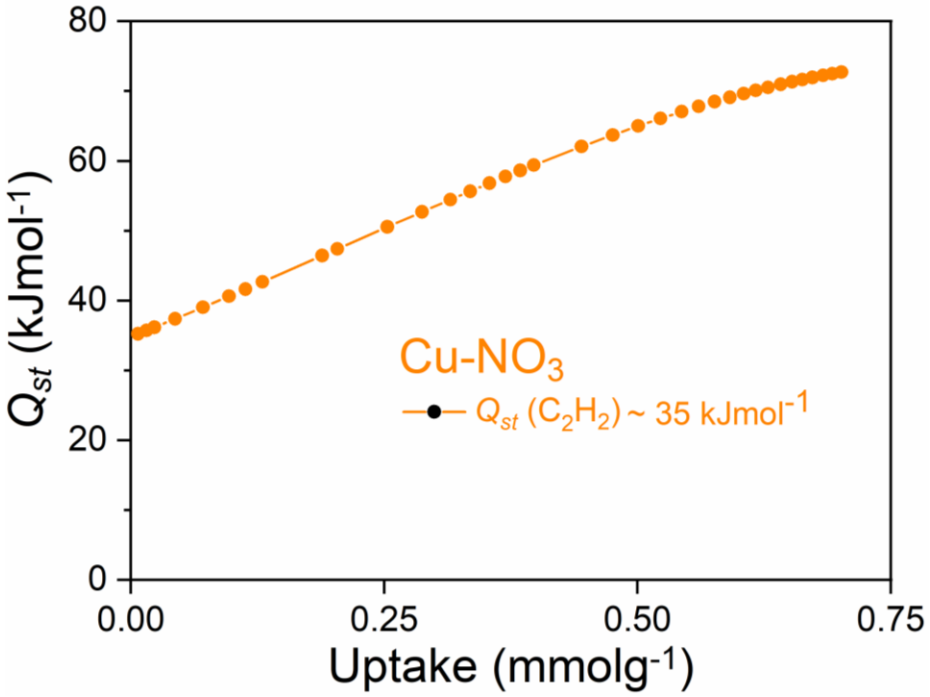

Appendix 2.42. Isosteric enthalpy of adsorption profile of C_2H_2 for **iMOF-7C**.

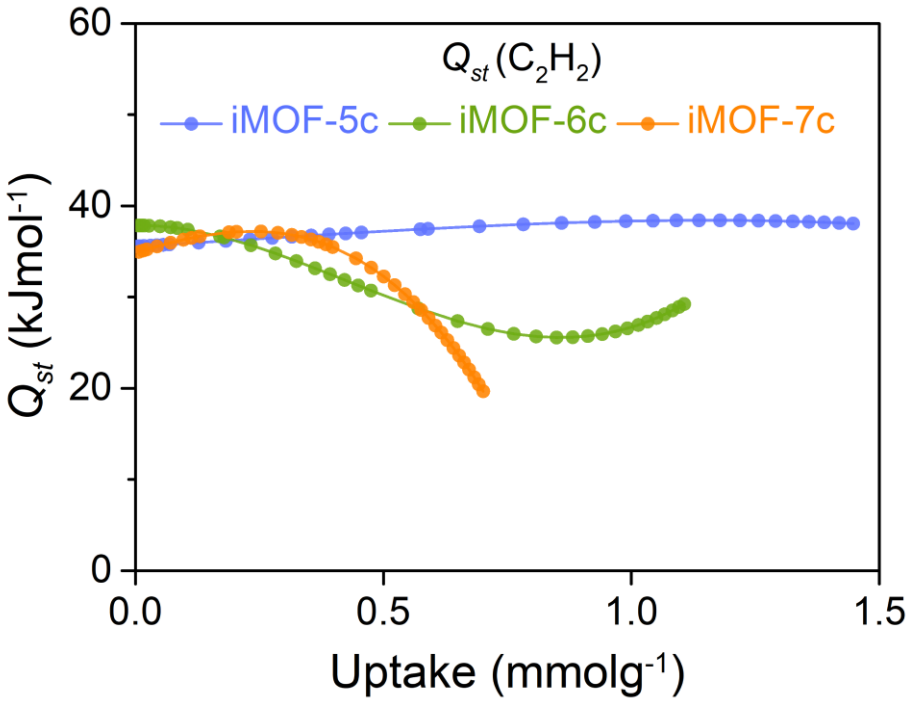

Appendix 2.43. Isosteric enthalpy of adsorption profiles for C_2H_2 in **iMOF-nC** adsorbents.

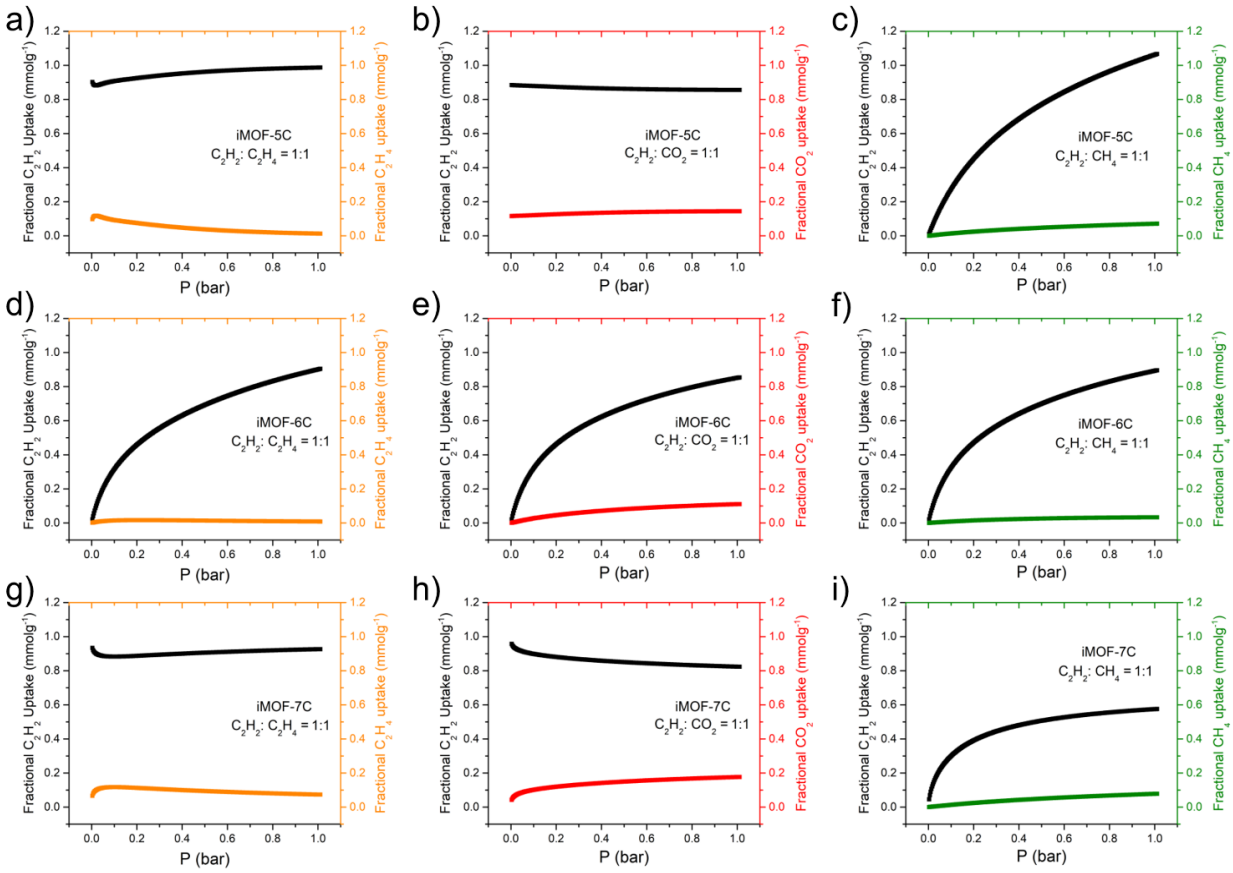

Appendix 2.44. Fractional uptake adsorption isotherms (v/v, 1:1) at 1 bar and 298 K of (a) C_2H_2/C_2H_4 for iMOF-5C, (b) C_2H_2/CO_2 for **iMOF-5C**, (c) C_2H_2/CH_4 for **iMOF-5C**, (d) C_2H_2/C_2H_4 for **iMOF-6C**, (e) C_2H_2/CO_2 for **iMOF-6C**, (f) C_2H_2/CH_4 for **iMOF-6C**, (g) C_2H_2/C_2H_4 for **iMOF-7C**, (h) C_2H_2/C_2H_4 for iMOF-7C, (i) C_2H_2/CH_4 for **iMOF-7C**.

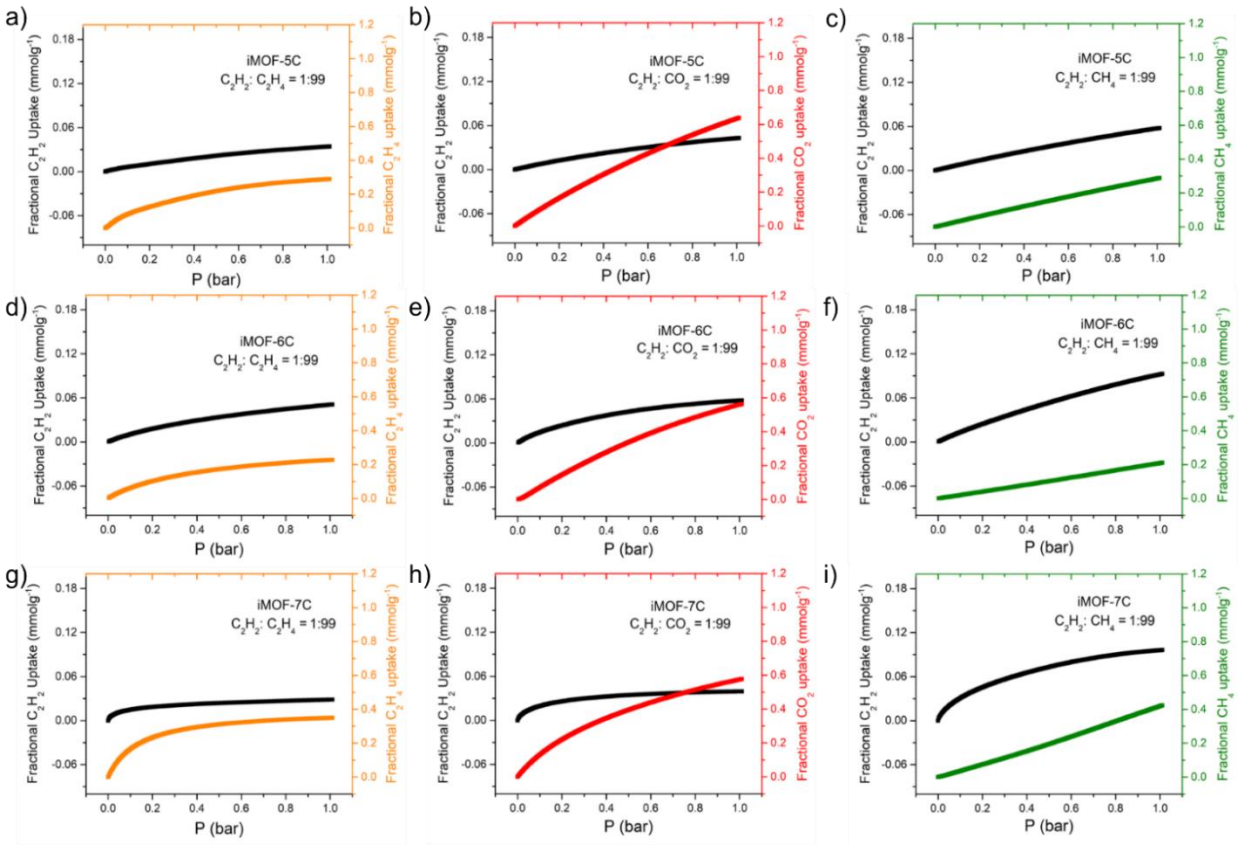

Appendix 2.45. Fractional uptake adsorption isotherms (v/v, 1:99)at 1 bar and 298 K of (a) C_2H_2/C_2H_4 for **iMOF-5C**, (b) C_2H_2/CO_2 for **iMOF-5C**, (c) C_2H_2/CH_4 for **iMOF-5C**, (d) C_2H_2/C_2H_4 for **iMOF-6C**, (e) C_2H_2/CO_2 for **iMOF-6C**, (f) C_2H_2/CH_4 for **iMOF-6C**, (g) C_2H_2/C_2H_4 for **iMOF-7C**, (h) C_2H_2/C_2H_4 for **iMOF-7C**, (i) C_2H_2/CH_4 for **iMOF-7C**.

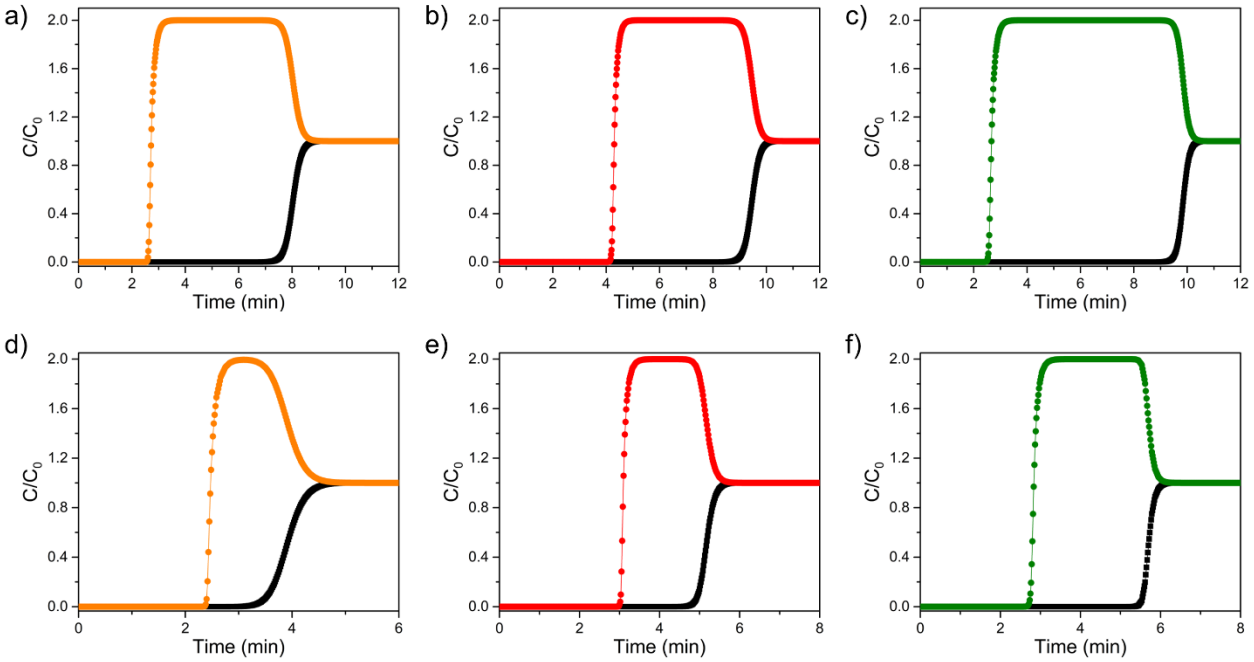

Appendix 2.46. Simulated breakthrough curves for equimolar mixtures of C_2H_2/C_2H_4, C_2H_2/CO_2 and C_2H_2/CO_2 with a flowrate of 1.6 cm^3/g at 298 K and 1 bar in fixed-bed columns packed with 0.3 g each of **iMOF-5C** (a-c) and **iMOF-7C** (d-f).

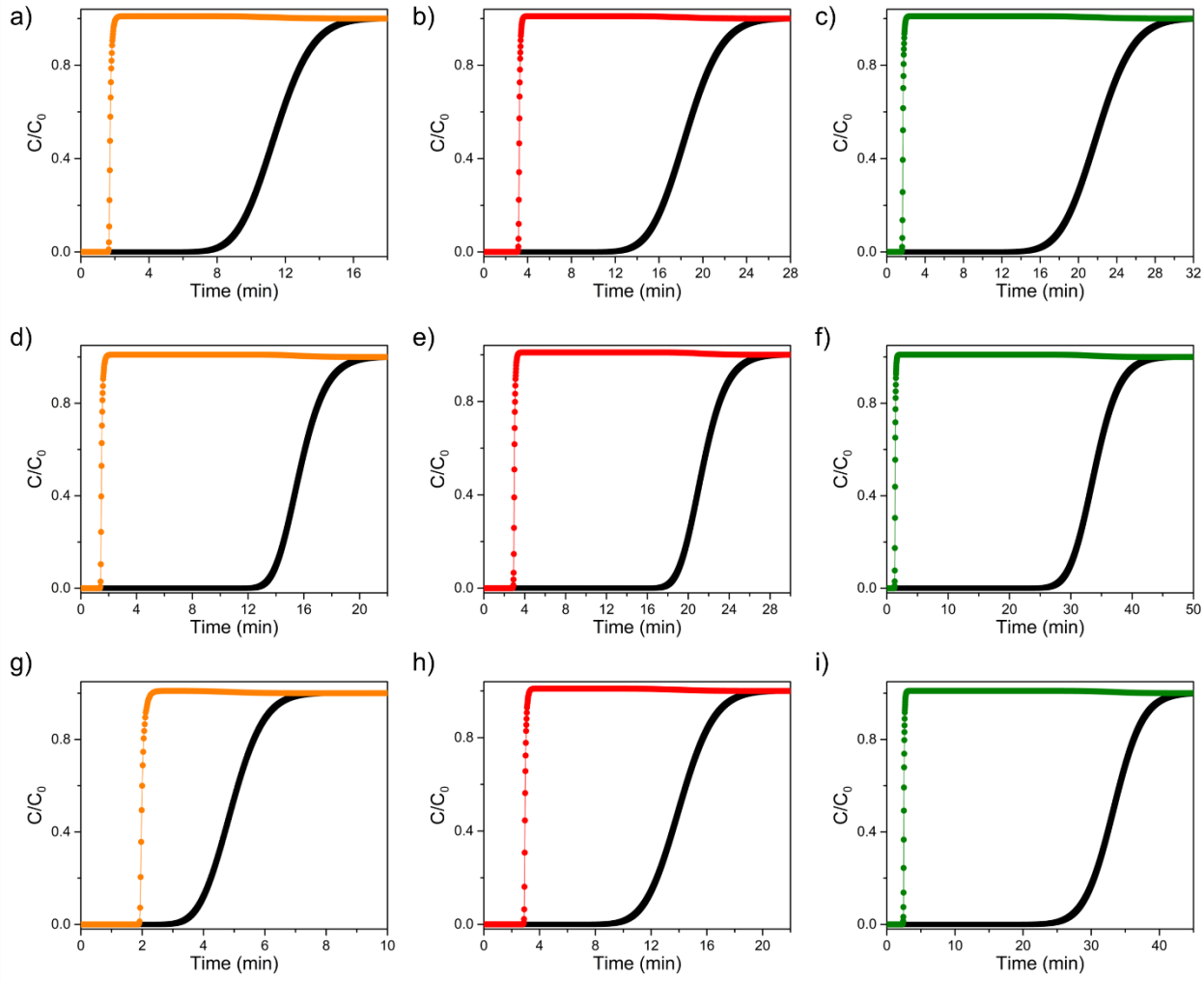

Appendix 2.47. Simulated breakthrough curves for 1:99 mixtures of C_2H_2/C_2H_4, C_2H_2/CO_2 and C_2H_2/CO_2 with a flowrate of 1.6 cm^3/g at 298 K and 1 bar in fixed-bed columns packed with 0.3 g each of **iMOF-5C** (a-c), **iMOF-6C** (d-f) and **iMOF-7C** (g-i).

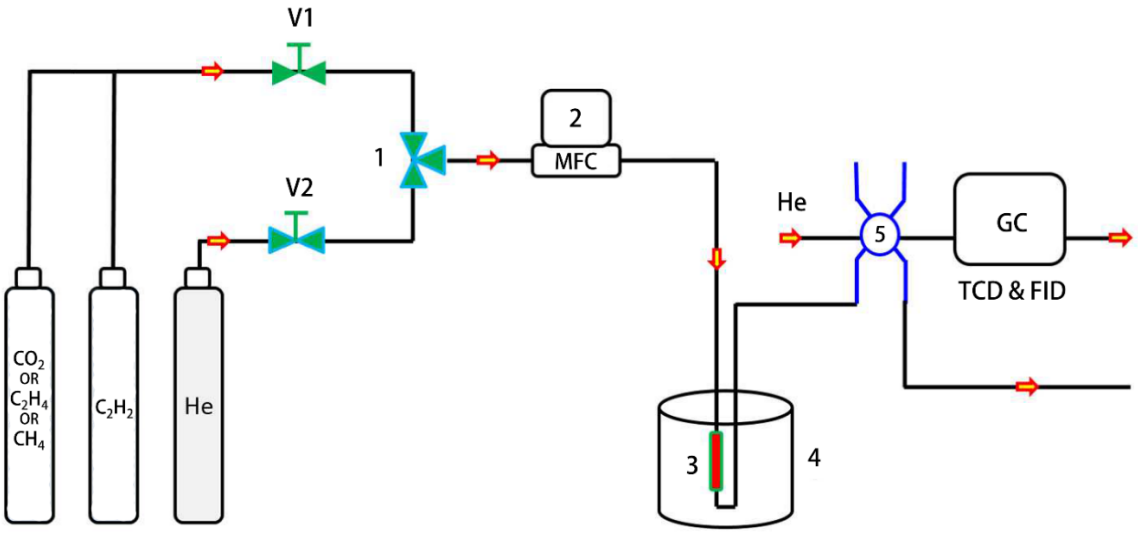

Appendix 2.48. Schematic of gas mixing unit, gravimetric gas uptake analyser and gas separation analyser for breakthrough experiments (1. 3-way valve; 2. mass flow controller; 3. packed MOF column; 4. water bath; 5. 6-way valve).

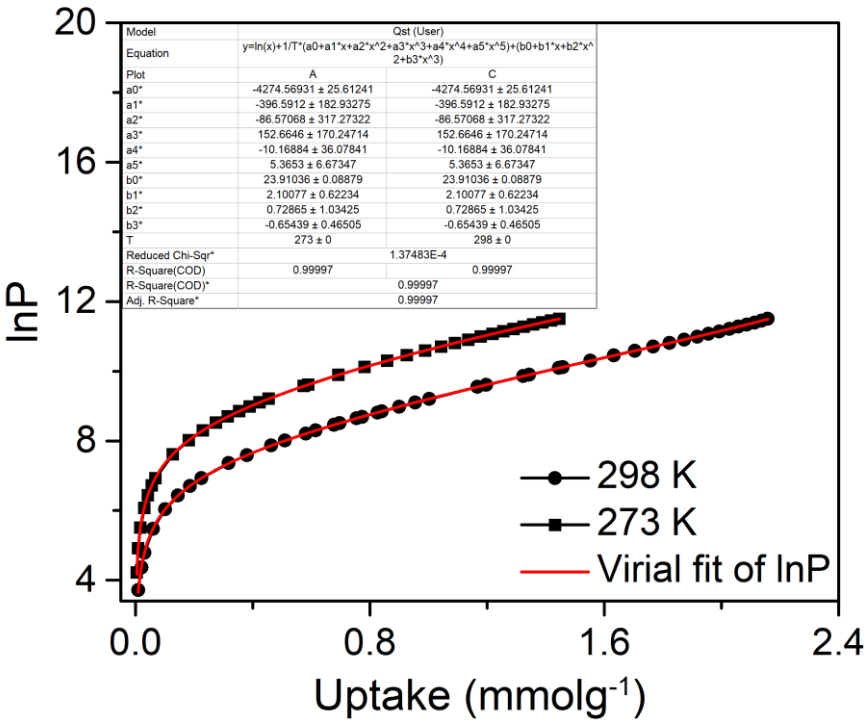

Appendix 2.49. Fitting of the C_2H_2 isotherm data for **iMOF-5C** to the virial equation.

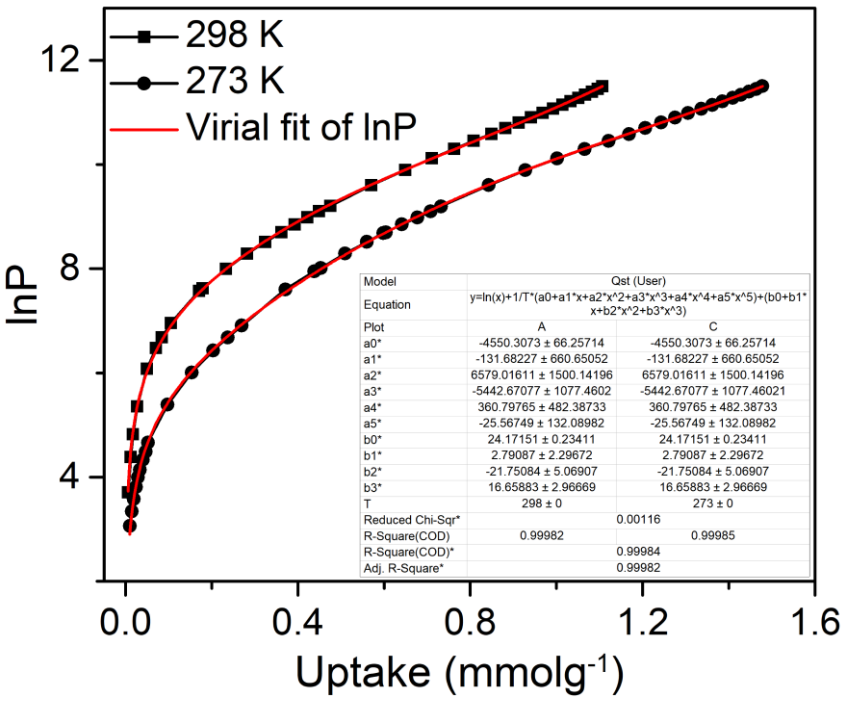

Model	Qst (User)	
Equation	y=ln(x)+1/T*(a0+a1*x+a2*x^2+a3*x^3+a4*x^4+a5*x^5)+(b0+b1*x+b2*x^2+b3*x^3)	
Plot	A	C
a0*	-4550.3073 ± 66.25714	-4550.3073 ± 66.25714
a1*	-131.68227 ± 660.65052	-131.68227 ± 660.65052
a2*	6579.01611 ± 1500.14196	6579.01611 ± 1500.14196
a3*	-5442.67077 ± 1077.4602	-5442.67077 ± 1077.46021
a4*	360.79765 ± 482.38733	360.79765 ± 482.38733
a5*	-25.56749 ± 132.08982	-25.56749 ± 132.08982
b0*	24.17151 ± 0.23411	24.17151 ± 0.23411
b1*	2.79087 ± 2.29672	2.79087 ± 2.29672
b2*	-21.75084 ± 5.06907	-21.75084 ± 5.06907
b3*	16.65883 ± 2.96669	16.65883 ± 2.96669
T	298 ± 0	273 ± 0
Reduced Chi-Sqr*	0.00116	
R-Square(COD)	0.99982	0.99985
R-Square(COD)*	0.99984	
Adj. R-Square*	0.99982	

Appendix 2.50. Fitting of the C_2H_2 isotherm data for **iMOF-6C** to the virial equation.

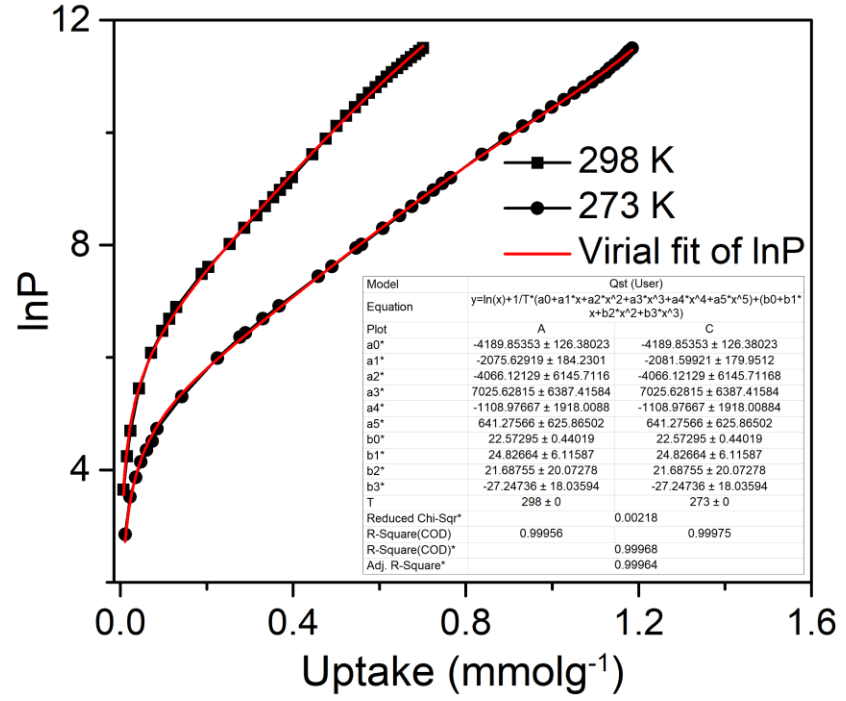

Model	Qst (User)	
Equation	y=ln(x)+1/T*(a0+a1*x+a2*x^2+a3*x^3+a4*x^4+a5*x^5)+(b0+b1*x+b2*x^2+b3*x^3)	
Plot	A	C
a0*	-4189.85353 ± 126.38023	-4189.85353 ± 126.38023
a1*	-2075.62919 ± 184.2301	-2081.59921 ± 179.9512
a2*	-4066.12129 ± 6145.7116	-4066.12129 ± 6145.71168
a3*	7025.62815 ± 6387.41584	7025.62815 ± 6387.41584
a4*	-1108.97667 ± 1918.0088	-1108.97667 ± 1918.00884
a5*	641.27566 ± 625.86502	641.27566 ± 625.86502
b0*	22.57295 ± 0.44019	22.57295 ± 0.44019
b1*	24.82664 ± 6.11587	24.82664 ± 6.11587
b2*	21.68755 ± 20.07278	21.68755 ± 20.07278
b3*	-27.24736 ± 18.03594	-27.24736 ± 18.03594
T	298 ± 0	273 ± 0
Reduced Chi-Sqr*	0.00218	
R-Square(COD)	0.99956	0.99975
R-Square(COD)*	0.99968	
Adj. R-Square*	0.99964	

Appendix 2.51. Fitting of the C_2H_2 isotherm data for **iMOF-7C** to the virial equation.

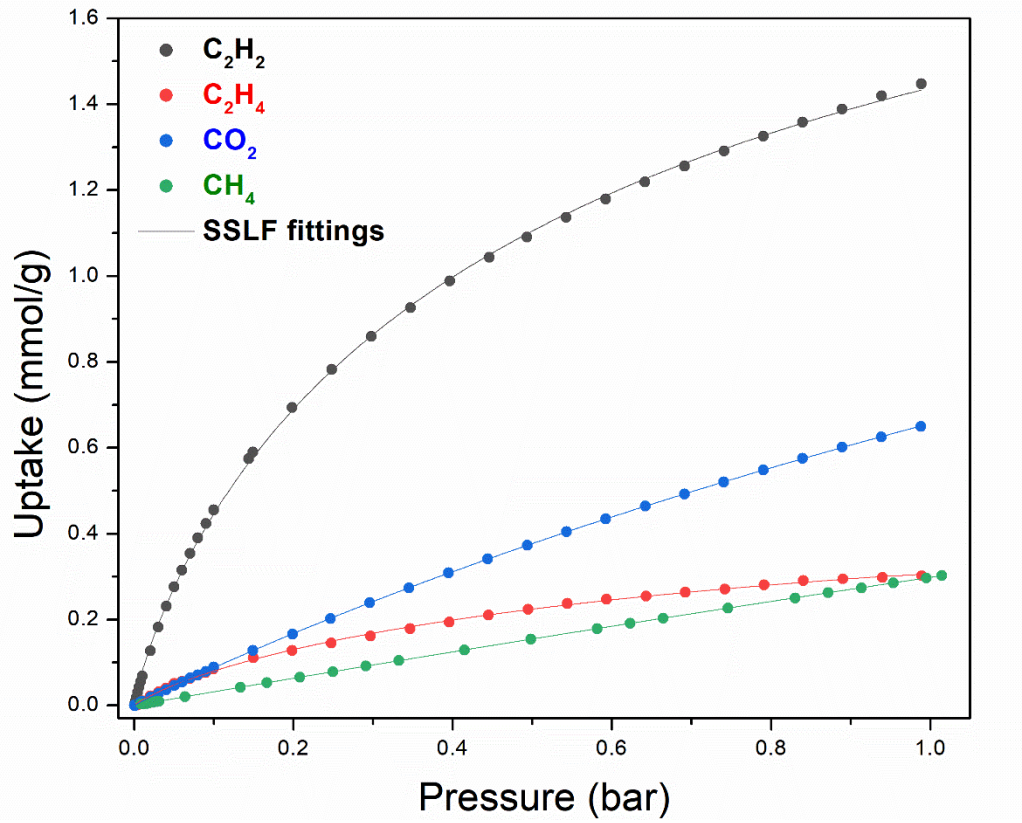

Model	SSLF			
Equation	a*b*x^(1/t)/(1+b*x^(1/t))			
Plot	C2H2 (298K)	C2H4 (298K)	CO2 (298K)	CH4 (298K)
a	2.36479 Â± 0.05161	0.57144 Â± 0.03111	2.82247 Â± 0.04944	3.8079 Â± 0.16403
b	1.55261 Â± 0.0789	1.16514 Â± 0.12767	0.30326 Â± 0.00678	0.08491 Â± 0.00396
t	1.21388 Â± 0.01646	1.1705 Â± 0.03129	1.02595 Â± 0.00277	0.99498 Â± 0.00211
Reduced Chi-Sqr	6.6763E-5	1.11924E-5	3.57597E-7	2.9395E-8
R-Square (COD)	0.99976	0.99912	0.99999	1
Adj. R-Square	0.99974	0.99906	0.99999	1

Appendix 2.52. Single-Site Langmuir Freundlich fits of **iMOF-5C** from single-component gas adsorption isotherms recorded at 298 K.

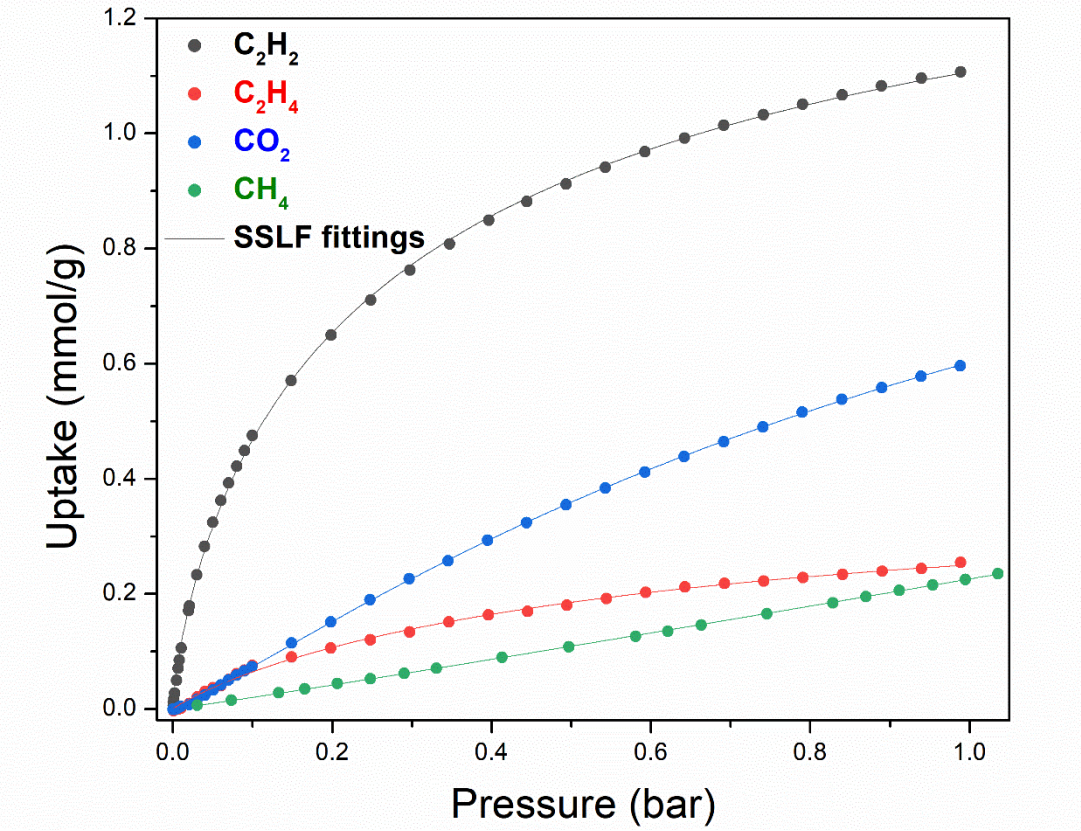

Model	SSLF			
Equation	a*b*x^(1/t)/(1+b*x^(1/t))			
Plot	C2H2 (298K)	C2H4 (298K)	CO2 (298K)	CH4 (298K)
a	1.57486 Â± 0.02375	0.41867 Â± 0.03112	1.35636 Â± 0.03024	19.02769 Â± 47.25123
b	2.36997 Â± 0.10594	1.49285 Â± 0.25212	0.79852 Â± 0.03034	0.012 Â± 0.03014
t	1.33696 Â± 0.01729	1.09199 Â± 0.04825	0.872 Â± 0.00707	0.9424 Â± 0.01691
Reduced Chi-Sqr	4.23246E-5	2.17496E-5	3.17981E-6	9.92069E-7
R-Square (COD)	0.99975	0.99761	0.99993	0.99985
Adj. R-Square	0.99973	0.99746	0.99993	0.99983

Appendix 2.53. Single-Site Langmuir Freundlich fits of **iMOF-6C** from single-component gas adsorption isotherms recorded at 298 K.

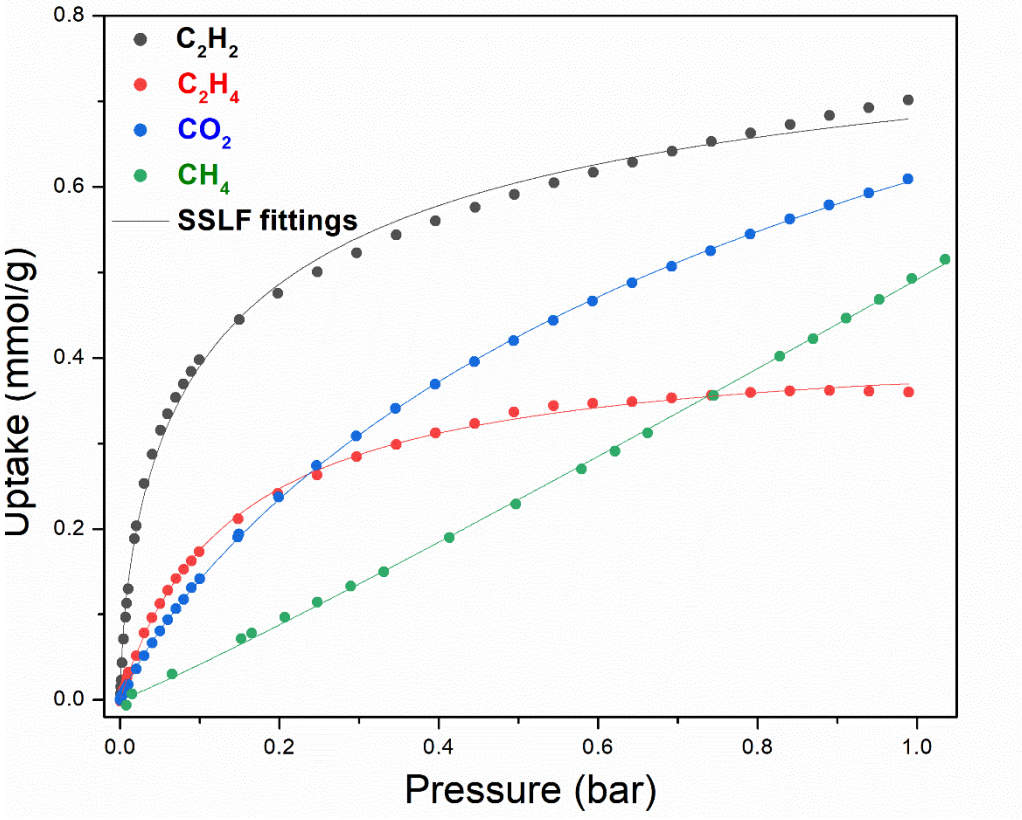

Model	SSLF			
Equation	a*b*x^(1/t)/(1+b*x^(1/t))			
Plot	C2H2 (298K)	C2H4 (298K)	CO2 (298K)	CH4 (298K)
a	0.87633 Â± 0.02974	0.42482 Â± 0.00542	1.28616 Â± 0.02361	70.34329 Â± 622.08679
b	3.46989 Â± 0.4472	6.83551 Â± 0.50883	0.89992 Â± 0.02962	0.00704 Â± 0.0627
t	1.57484 Â± 0.06303	1.0133 Â± 0.02233	1.15748 Â± 0.00842	0.9324 Â± 0.03504
Reduced Chi-Sqr	1.69279E-4	1.63484E-5	3.0586E-6	2.00352E-5
R-Square (COD)	0.99701	0.99919	0.99994	0.99939
Adj. R-Square	0.99683	0.99913	0.99993	0.99932

Appendix 2.54. Single-Site Langmuir Freundlich fits of **iMOF-7C** from single-component gas adsorption isotherms recorded at 298 K.

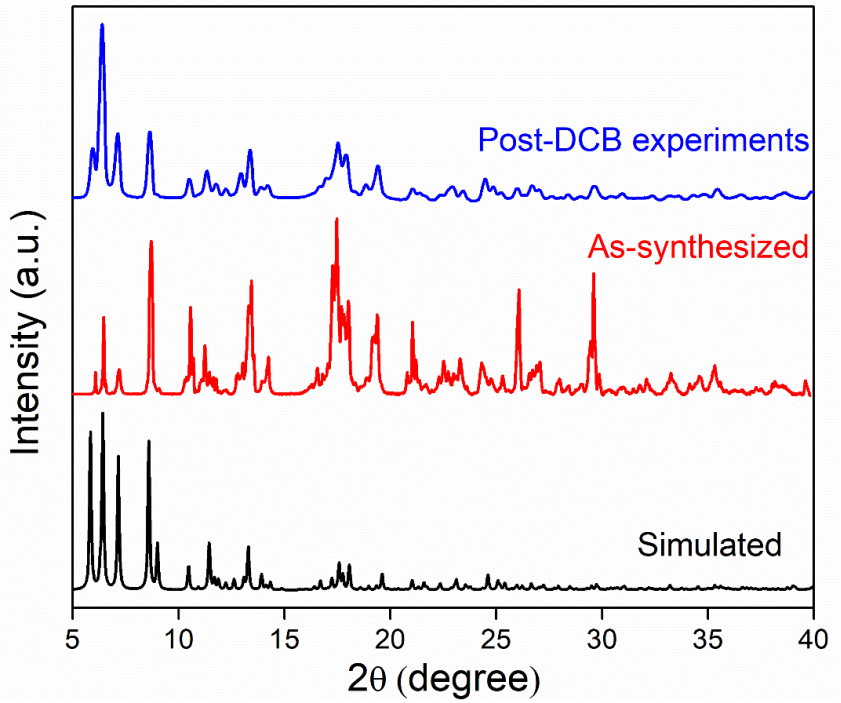

Appendix 2.55. PXRD patterns of **iMOF-6C**, comparison *versus* post-breakthrough experiments.

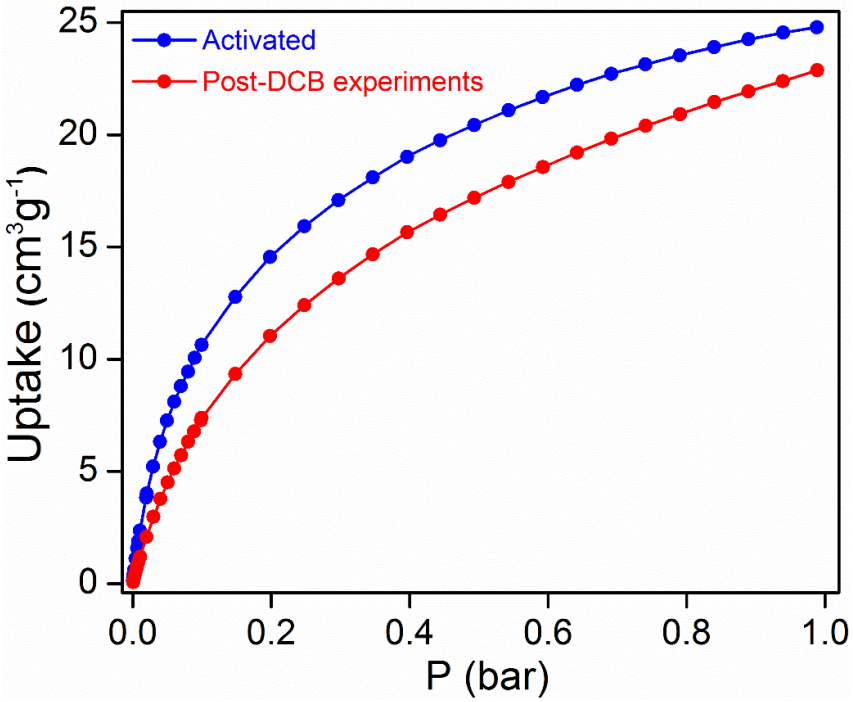

Appendix 2.56. C_2H_2 (298 K) adsorption isotherms of **iMOF-6C**.

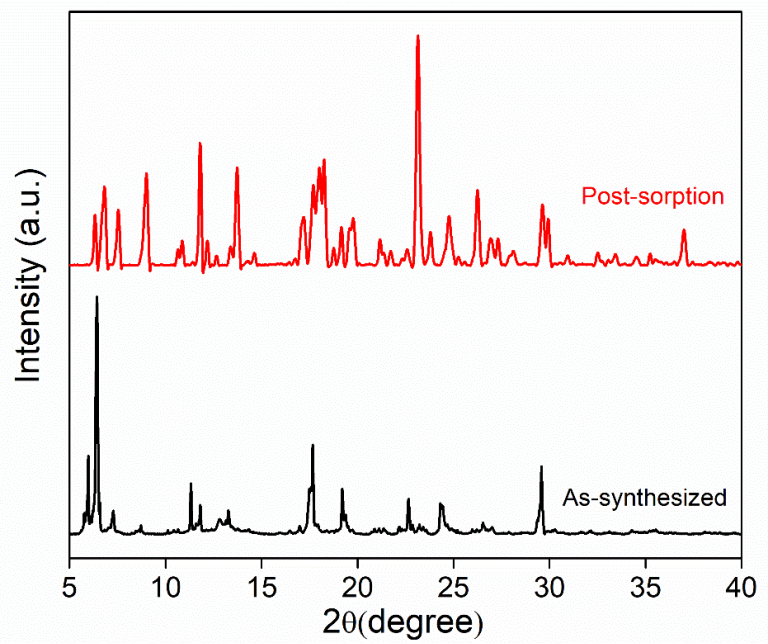

Appendix 2.57. Comparative analysis of the PXRD patterns of **iMOF-5C**: as-synthesized plotted against the phase obtained post-sorption experiments.

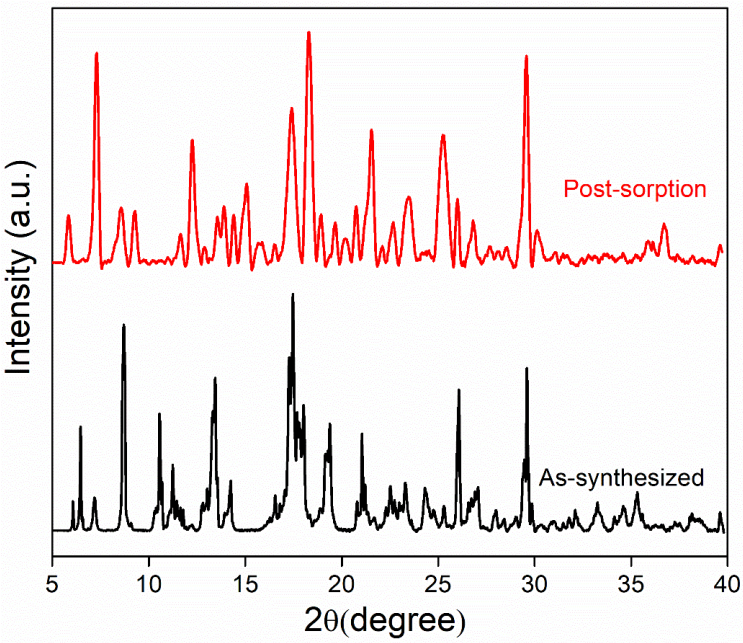

Appendix 2.58. Comparative analysis of the PXRD patterns of **iMOF-6C**: as-synthesized plotted against the phase obtained post-sorption experiments.

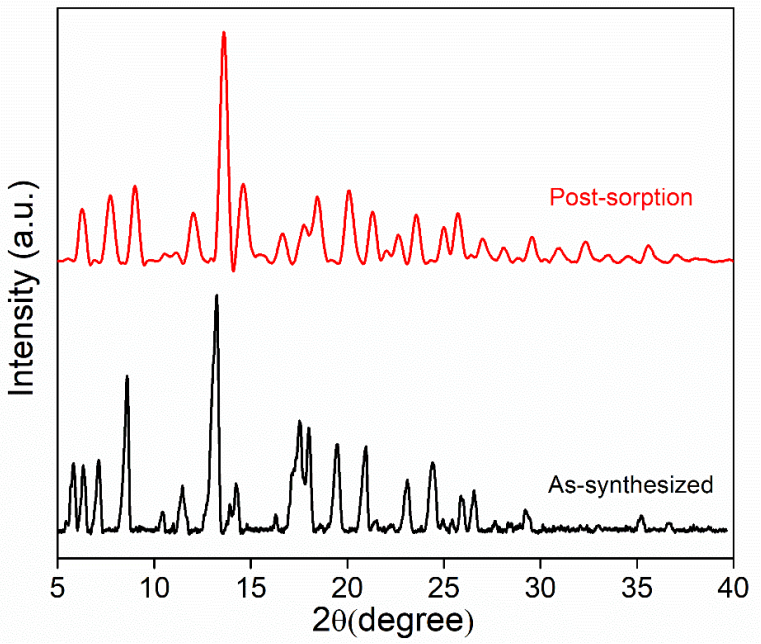

Appendix 2.59. Comparative analysis of the PXRD patterns of **iMOF-7C**: as-synthesized plotted against the phase obtained post-sorption experiments.

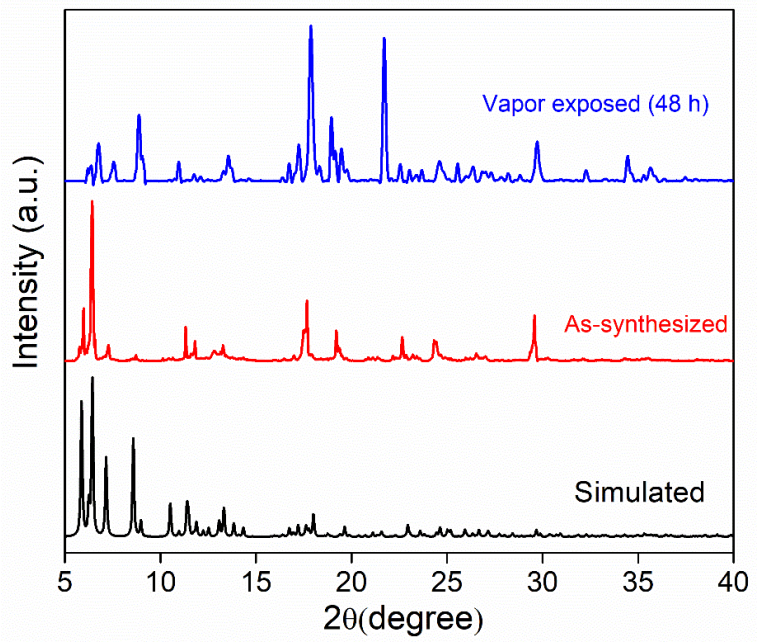

Appendix 2.60. Comparative analysis of the PXRD patterns of **iMOF-5C**: simulated, as-synthesized, and the phase obtained after humidity exposure.

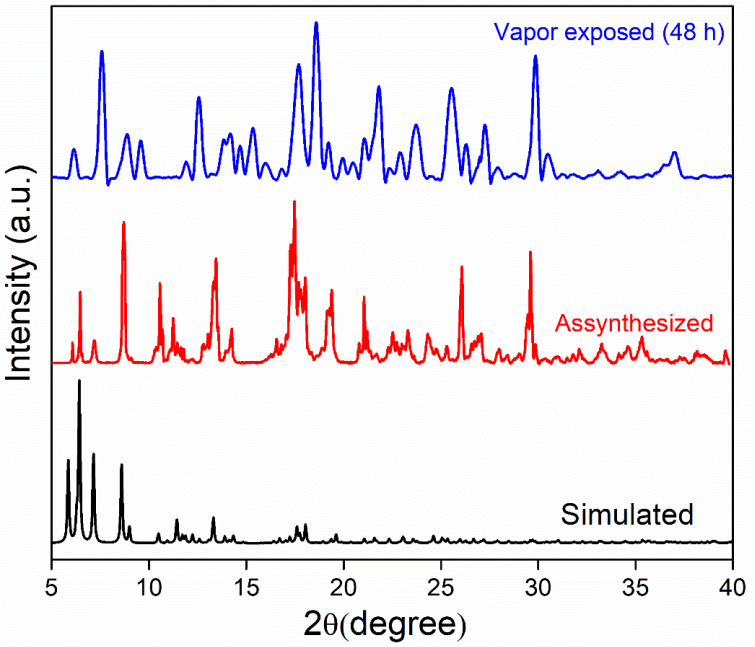

Appendix 2.61. Comparative analysis of the PXRD patterns of **iMOF-6C**: simulated, as-synthesized, and the phase obtained after humidity exposure.

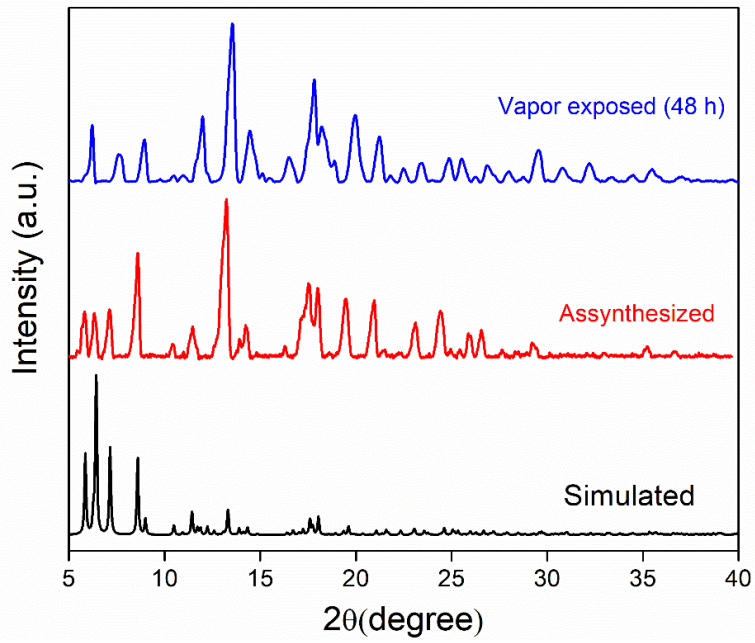

Appendix 2.62. Comparative analysis of the PXRD patterns of **iMOF-7C**: simulated, as-synthesized, and the phase obtained after humidity exposure.

Appendix Table 2.1. Summary of adsorption uptakes, adsorption enthalpies (Q_{st}) and IAST selectivity at 298K 1 bar for 1:1 (v/v) C_2H_2/C_2H_4) for C_2H_2 selective sorbents.

Adsorbent, network dimensionality (nD)	**S_{BET} / m^2g^{-1}**	**Pore size (Å)**	**C_2H_2 uptake at 1 bar, mmol g^{-1}**	**C_2H_4 uptake at 1 bar, mmol g^{-1}**	**$Q_{st}(C_2H_2)$ at low loading, kJ mol^{-1}**	**S_{AE}**	**Ref**
TIFSIX-17-Ni	237.6	3.59 × 3.59	3.135	2.935×10^{-13}	38.8	670.9	57
SIFSIX-17-Ni	229.2	3.51 × 3.51	3.303	1.293	37.0	506.4	58
TIFSIX-2-Cu-i, 3D	685	5.1 × 5.1	3.9	2.1	46	212.2	58
iMOF-6C, 2D	330	4.6 × 4.5; 5.3 × 5.4	1.2	0.25	38	105	This Work
iMOF-5C, 2D	242	4.6 × 4.5; 5.3 × 5.4	1.5	0.31	35.5	78	This Work
SIFSIX-2-Cu-i, 3D	503	5.2 × 5.2	4.02	2.19	52.9	41.01	59
NKMOF-1-Ni, 3D	382	5.8 × 5.8	2.72	2.14	58	30	60
APPT-Cd-ClO_4^-, 3D	205	11 × 11	1.75	0.44	28.6	14.71	61
CPL-2, 3D	495	9.0 × 6.0	3.13	1.86	30.8	12	62
iMOF-7C, 2D	109	4.6 × 4.5; 5.3 × 5.4	0.7	0.35	35	12	This Work
SIFSIX-1-Cu, 3D	1178	8.0 × 8.0	8.5	4.11	30/37	8.37	59
UTSA-220, 3D	577	4.5 × 4.1 ; 2.1 × 5.0	3.4	2.53	29	8.8	35
SIFSIX-3-Zn, 3D	250	4.2 × 4.2	3.64	2.24	21/31	13.72	59
JCM-1, 3D	550	3.9 × 12.5	3.34	1.56	36.9	8.1	63

ZJU-198a, 3D	343.1	3.6 × 4.1; 2.1 × 5.0	3.25	2.95	26.1	7.2	64
SIFSIX-2-Cu, 3D	1881	10.5 × 10.5	5.38	2.02	26.3	4.95	59
NbU-1, 3D	368	3.8[g]	3.64	2.07	38.3	5.9	65
SIFSIX-3-Ni, 3D	368	4.2 × 4.2	3.3	1.75	20.5	5.98	59
HUST-6, 3D	645.3	NA[h]	3.49	2.38	31.1	3.8	66

Appendix Table 2.2. Summary of adsorption uptakes, adsorption enthalpies (Q_{st}) and IAST selectivity at 298K 1 bar for 1:1 (v/v) C_2H_2/CO_2) for C_2H_2 selective sorbents.

Adsorbent, network dimensionality (nD)	**S_{BET} / m^2g^{-1}**	**Pore size (Å)**	**C_2H_2 uptake at 1 bar, mmol g^{-1}**	**CO_2 uptake at 1 bar, mmol g^{-1}**	**$Q_{st}(C_2H_2)$ at low loading, kJ mol^{-1}**	**S_{AC}**	**Ref**
UTSA-300a, 2D	311	2.4 × 3.3	3.3	0.2	57.6	10^3	67
ZJU-74a, 3D	64	3.6 × 3.8	3.83	3.08	44.5	36.5	68
NKMOF-1-Ni, 3D	382	5.8 × 5.8	2.7	2.3	60.3	30	69
sql-16-Cu-NO_3-α′	179	4.6 × 5.0	1.33	0.38	38.6	27.8	70
FeNi-M'MOF, 3D	383	4.15 × 4.27; 3.94 × 4.58	4.29	2.72	27	24	71
$[Ni_3(HCOO)_6]_n$, 3D	289	4.3 × 4.3	2.4	1.6	40.9	22	72
TIFSIX-17-Ni	237.6	3.59 × 3.59	3.135	2.935×10^{-13}	38.8	20.9	57
TCuCl, 3D	167	3.69 × 3.69	3.0	2.0	41	16.9	73
pacs-CoMOF-2a	196	5.8, 6.6	5.40	2.81	34.2	13	74
SIFSIX-17-Ni	229.2	3.51 × 3.51	3.303	1.293	37.0	11.7	57
ZJU-40a, 3D	2858	10.2, 9.6 ×	9.64	3.34	34.5	11.5	75

		22.3					
Co-MOF, 3D	973	NM	6.47	2.68	33	11	76
JCM-1, 3D	550	12.5 × 3.9	3.3	1.7	36.9	10	77
ZJUT-2a, 3D	350	3.2 × 3.2	3.4	2.2	41.5	10	78
TCuBr, 3D	173	3.59 × 3.59	2.8	2.0	36.6	9.5	73
UTSA-74a, 3D	830	8.0 × 8.0	4.8	3.2	31	9	79
iMOF-6C, 2D	330	4.6 × 4.5; 5.3 × 5.4	1.2	0.68	38	8	This Work
SNNU-150-Al, 3D	NM	8.5	4.33	1.98	29	7.27	80
UTSA-83a, 2D	70	3.5 × 6.6	0.53	0.17	24.4	6.2	81
iMOF-5C, 2D	242	4.6 × 4.5; 5.3 × 5.4	1.5	0.71	35.5	6	This Work
MUF-17, 3D	247	4.7 × 4.8	2.7	2.2	49.5	6	82
CPM-107op, 3D	319	NM	4.35	1.55	37	5.7	83
ZJNU-13, 3D	1352	6.8, 11.8	5.28	3.92	33.5	5.64	84
TCuI, 3D	250	3.66 × 3.66	2.2	1.6	38.4	5.3	75
UPC-110, 3D	1384.3	6	3.27	1.08	24.6	5.1	85
JXNU-5, 3D	406	4.6, 6.7	2.5	1.55	32.9	5	86
iMOF-7C, 2D	109	4.6 × 4.5; 5.3 × 5.4	0.7	0.61	35	4	This Work
SNNU-45, 3D	1006	4.5	5.98	4.33	40	4.5	87
UTSA-220, 3D	577	4.5-5.5; 3.1-4.8	3.40	3.38	29	4.4	88
FJU-90a, 3D	1572	5.4 × 5.1	8.0	4.6	25.1	4.3	89
$Cu_2(ade)_2(PA)_2$, 3D	401	2 × 6	2.19	1.5	26.8	4.2	90
Hex-Zn-MOF 1a, 3D	770.3	8.6, 9.8	3.18	2.21	39	4	91
mot-Cu(Br-BDC) MOF, 3D	303	4.2 × 4.7; 12 × 24.1	1.53	1.08	26.1	3.9	92

Cu−CPAH, 3D	880	6-9	5.88	3.93	35.4	3.6	93
UPC-200(Al)-F-BIM, 3D	2212.8	7 × 11	6.2	2.5	20.5	3.15	94
JNU-1, 3D	818	16.3 × 6.6	2.7	2.2	13	3	95
Cu-tztp MOF 1a, 3D	798.9	5.4-8.6	5.02	3.35	38.3	2.7	96
Zn-MOF-74, 3D	1360	11 × 11	5.5	5.4	22.1	2	90

Appendix Table 2.3. Summary of adsorption uptakes, adsorption enthalpies (Q_{st}) and IAST selectivity at 298K 1 bar for 1:1 (v/v) C_2H_2/CH_4) for C_2H_2 selective sorbents.

Adsorbent	**S_{BET} / m^2g^{-1}**	**Pore size (Å)**	**C_2H_2 uptake at 1 bar, mmol g^{-1}**	**CH_4 uptake at 1 bar, mmol g^{-1}**	**$Q_{st}(C_2H_2)$ at low loading, kJ mol^{-1}**	**S_{AM}**	**Ref**
ZJU-198a	343	3.6 × 4.1; 2.1 × 5.0	3.07	0.36	26.1	391.1	97
PMOF-3	1378	4.0- 8.4	4.94	0.73	21.9	156.5	98
SNNU-65-Cu-Ga	1918.0	3.9 × 7.7; 10.8 ×14. 7; 11.2 × 14.0	2.43	0.55	31.7	120.6	99
SNNU-65-Cu-Sc	2089.2	NM	3.91	0.68	44.9	115.5	99
UTSA-121a	1081	5.0 × 6.2; 7.1 ×14. 5	3.01	0.25	22.6	96	100
JLU-MOF66	471	3.4 × 5; 4.6 × 11.8	2.30	0.39	35.6	86.2	101
SNNU-65-Cu-In	1936.2	NM	3.13	0.56	23.4	69.5	101
BUT-70A	460	5.5 - 6.5, 5.8- 6.9	3.1	0.39	23.9-25.6	66.6	102
UTSA-85	558	5 × 5	2.32	0.39	22.9	64	103

[Cu-THBA][x]	1755	10, 9.4 × 22	5.82	0.78	39.7	49-56	104
BSF-1	535	10.0 ×13.6 × 13.6	2.21	0.43	31	46.9	105
ZJNU-13	1352	5.5, 11.4	4.99	1.03	33.5	43.3	106
Tb-N	NM	NM	0.91	0.12	29.6	43	107
ZJNU-19	2165	NM	8.64	0.86	30	42.2	108
SNNU-65-Cu-Fe	2112.0	NM	3.26	0.62	28.2	37.3	99
FJU-99a	802.5	NM	3.57	0.62	28	34.8	109
ZJNU-69	1655	NM	7.24	0.81	31.2	34.5	110
([Cu(TDYPT)].DMA)*	1599	9 × 9.5	4.53	0.64	35.3	33.7	111
ZJNU-8	1015	NM	3.89	1.23	32.4	30.6	62
ZJNU-70	1748	NM	7.78	0.94	NM	28	110
ZJNU-71a	1860	NM	8.45	0.99	NM	27.6	110
ZJU-199	987	4.7 × 7.8; 8 ×8.4; 4 ×8.4	5.39	0.59	38.5	27.3-33.5	113
iMOF-6C		4.6 × 4.5; 5.3 × 5.4	1.2	0.15	38	27	This Work
ZJU-15a	1660	3 × 7.5; 2.5 ×6.5; 6.8 × 6.8	4.21	0.49	20	25.5	112
In-MOF-1[a]	307	6.65 × 16.26	2.23	0.69	36	24.6	115
BUT-70B	695	5.5 - 6.5, 5.8- 6.9	3.9	0.39	23-27	23.3-47.9	114
[Co_EA-TBP][b]	NM	8.1 × 6.0	1.58	0.31	32	23.7	116
[Zn(Cp-TBP)][c]	770	8.6 × 8.6	3.00	1.25	39	22.4	117
UTSA-33a	660	3.1 × 4.8	4.09	0.374	32	16	118
UTSA-222a	703	9.3 × 5.1	3.56	0.55	26	16-19	119
iMOF-5C		4.6 × 4.5; 5.3 × 5.4	1.5	0.19	35.5	15	This Work

SNNU-63	1719.8	11 × 11	3.84	0.42	21.6	12.9	120
iMOF-7C		4.6 × 4.5; 5.3 × 5.4	0.7	0.15	35	7.6	This Work
ZJU-195	1721.9	5.6 × 8.2; 4.4 × 4.4; 6.4 × 8.9;	9.09	1.0	29.9	4.7– 12.4	121
*([Cu(TDYPT)].DMA) = ([$Cu_6(L)_3(H_2O)_4(HCOO)$]·$Me_2NH_2^+$.20DMF); (TDYPT = 5,5′- (triazole-2,5-diyl) diisophthalate), [a]In-MOF-1 = $(Me_2NH_2)_{1.5}[In_{1.5}(FBDC)(BDC)]$·2.5NMF·$CH_3CN$; ($H_4$FBDC = 2,5- di(2′,5′-dicarboxylphenyl)-difluorobenzene), [b][Co_EA-TBP] = {$[Co_6$(5-EIA)$_5$(tmbpy)$(OH)_2(H_2O)_2]$·$4(H_2O)\}_n$; (5-H_2EIA = 5-ethoxy-isophthalic acid; tmbpy = 3,3' -dimethyl-4,4' -bipyridine), [c][Zn(Cp-TBP)] = $[Zn(cpna)_3(tmbpy)]_n$·4DMF; (H_2cpna = 6-(4-carboxyphenyl)nicotinic acid), [x][Cu-THBA] = $[Cu_2THBA(H_2O)_2]$·$(C_3H_7NO)_{12}$·$(H_2O)_{10}$,((H_4THBA = p-terphenyl-3,2",3",5,5",5'"-hexcarboxylic acid)							

Appendix Table 2.4. Interaction energies of the studied adsorbate molecules with **iMOF-6C** determined by DFT – D3 optimisation.

MOFs	Interaction Energies, ΔE_{def} (kJ/mol)			
	C_2H_2	C_2H_4	CO_2	CH_4
iMOF-6C	-43.73	-37.64	-39.24	-26.44

Table S6. EDX analysis of as-synthesized phases of **iMOF-nC**.

iMOF-5C		iMOF-6C		iMOF-7C	
Element	**% Weight**	**Element**	**% Weight**	**Element**	**% Weight**
C	55.26	C	47.45	C	55.09
N	17.14	N	14.82	N	13.67
O	21.55	B	18.13	O	26.77
Cl	3.84	O	8.08	Cu	4.47
Cu	2.21	F	7.71	Total	100
Total	100	Cu	3.81		
		Total	100		

Appendix Table 2.5. Crystallographic data for **iMOF-5C**.

Crystal data	
Chemical formula	$2(Cl_{0.5}O_2)\cdot 2(ClO_{4.5})\cdot C_{76}H_{72}Cu_2N_{36}O_{20}\cdot 0.25(Cl_4O_{12})$
M_r	2334.57
Crystal system, space group	Orthorhombic, *Cmcm*
Temperature (K)	293
a, *b*, *c* (Å)	30.2145 (5), 15.3354 (4), 28.1785 (5)
V (Å^3)	13056.5 (5)
Z	4
Radiation type	Mo *K*α
μ (mm^{-1})	0.49
Crystal size (mm)	0.18 × 0.13 × 0.12
Data collection	
Diffractometer	Bruker *APEX3* Photon 100 CMOS chip
Absorption correction	Multi-scan multi-scan absorption correction
No. of measured, independent and observed [$I > 2\sigma(I)$] reflections	112070, 6003, 4667
R_{int}	0.103
$(\sin\theta/\lambda)_{max}$ (Å^{-1})	0.595
Refinement	
$R[F^2 > 2\sigma(F^2)]$, $wR(F^2)$, S	0.121, 0.297, 1.05
No. of reflections	6003
No. of parameters	418
No. of restraints	129
H-atom treatment	H-atom parameters constrained
	$w = 1/[\sigma^2(F_o^2) + (0.078P)^2 + 393.8063P]$ where $P = (F_o^2 + 2F_c^2)/3$
$\Delta\rho_{max}$, $\Delta\rho_{min}$ (e Å^{-3})	1.34, −0.74

Appendix Table 2.6. Crystallographic data for **iMOF-6C**.

Crystal data	
Chemical formula	$4(BF_4)\cdot C_{76}H_{76}Cu_2N_{36}O_{20}$
M_r	2288.04
Crystal system, space group	Orthorhombic, *Cmcm*
Temperature (K)	293
a, *b*, *c* (Å)	30.1696 (3), 15.4430 (2), 28.0909 (3)
V (Å^3)	13087.8 (3)
Z	4
Radiation type	Mo *K*α
μ (mm^{-1})	0.41
Crystal size (mm)	0.18 × 0.13 × 0.12
Data collection	
Diffractometer	Bruker *APEX3* Photon 100 CMOS chip
Absorption correction	Multi-scan multi-scan absorption correction
No. of measured, independent and observed [$I > 2\sigma(I)$] reflections	113789, 6698, 5248
R_{int}	0.059
$(\sin \theta/\lambda)_{max}$ (Å^{-1})	0.617
Refinement	
$R[F^2 > 2\sigma(F^2)]$, $wR(F^2)$, S	0.063, 0.200, 1.08
No. of reflections	6698
No. of parameters	395
No. of restraints	21
H-atom treatment	H-atom parameters constrained
	$w = 1/[\sigma^2(F_o^2) + (0.1211P)^2 + 35.2876P]$ where $P = (F_o^2 + 2F_c^2)/3$
$\Delta\rho_{max}$, $\Delta\rho_{min}$ (e Å^{-3})	1.91, −0.60

Computer programs: Bruker *APEX3*, Bruker *SAINT*, *SHELXT* 2014/5 (Sheldrick, 2014), *SHELXL2018*/1 (Sheldrick, 2018), Bruker *SHELXTL*.

2.6 References

[1] (a) 2019 Report of The International Council of Chemical Associations, https://icca-chem.org/news/chemical-industry-contributes-5-7-trillion-to-global-gdp-and-supports-120-million-jobs-new-report-shows/, accessed on 05-02-2021; (b) S. Kitagawa, *Angew. Chem. Int. Ed.* **2015**, *54*, 10686–10687; (c) D. S. Sholl, R. P. Lively, *Nature* **2016**, *532*, 435–437.

[2] S. Kitagawa, *Angew. Chem. Int. Ed.* **2015**, *54*, 10686–10687.

[3] (a) Z. Bao, G. Chang, H. Xing, R. Krishna, Q. Ren, B. Chen, *Energy Environ. Sci.* **2016**, *9*, 3612-3641; (b) S. Mukherjee, A. V. Desai, S. K. Ghosh, *Coord. Chem. Rev.* **2018**, *367*, 82−126.; (c) H. Wang, Y. Liu, J. Li, *Adv. Mater*. **2020**, *32*, 2002603.

[4] (a) S. Yang, A. J. Ramirez-Cuesta, R. Newby, V. Garcia-Sakai, P. Manuel, S. K. Callear, S. I. Campbell, C. C. Tang, M. Schröder, *Nat. Chem.* **2015**, *7*, 121−129; (b) M. du Plessis, V. I. Nikolayenko, L. J. Barbour, *J. Am. Chem. Soc.* **2020**, *142*, 4529–4533; (c) Y. Chai, X. Han, W. Li, S. Liu, S. Yao, C. Wang, W. Shi, I. d.-Silva, P. Manuel, Y. Cheng, L. D. Daemen, A. J. R.-Cuesta, C. C. Tang, L. Jiang, S. Yang, N. Guan, L. Li, *Science* **2020**, *368*, 1002–1006; (d) S. Liu, X. Han, Y. Chai, G. Wu, W. Li, J. Li, I. d.-Silva, P. Manuel, Y. Cheng, L. L. Daemen, A. J R.-Cuesta, W. Shi, N. Guan, S. Yang, L. Li, *Angew. Chem. Int. Ed.* **2020**, 60, 6526−6532.

[5] (a) D. S. Sholl, R. P. Lively, *Nature* **2016**, *532*, 435-437; (b) M. Peplow, *Nature* **2015**, *520*, 148–150; (c) J. R. Li, R. J. Kuppler, H. C. Zhou, *Chem. Soc. Rev.* **2009**, *38*, 1477–1504; (d) S. Sen, N. Hosono, J.-J. Zheng, S. Kusaka, R. Matsuda, S. Sakaki, S. Kitagawa, *J. Am. Chem. Soc.* **2017**, *139*, 18313−18321; (e) H. Wang, Y. Liu, J. Li, *Adv. Mater.* **2020**, *32*, 2002603.

[6] T. Ren, M. Patel, K. Blok, *Energy* **2006**, *31*, 425−451.

[7] (a) P. Pässler, W. Hefner, K. Buckl, H. Meinass, H.-J. Wernicke, G. Ebersberg, R. Müller, J. Bässler, H. Behringer, D. Mayer, *Ullmann's Encyclopedia of Industrial Chemistry, Wiley-VCH, Weinheim*, **2000**; (b) Y. L. Peng, T. Pham, P. Li, T. Wang, Y. Chen, K. J. Chen, K. A. Forrest, B. Space, P. Cheng, M. J. Zaworotko, Z. Zhang, *Angew. Chem. Int. Ed.* **2018**, *57*, 10971 –10975.

[8] (a) S. Mukherjee, D. Sensharma, K. J. Chen, M. J. Zaworotko, *Chem. Commun.* **2020**, *56*, 10419-10441.

[9] (a) H. Molero, B. F. Bartlett, W. T. Tysoe, *J. Catal.* **1999**, *181*, 49–56; (b) O. T. Qazvini, L. K. Macreadie, S. G. Telfer, *Chem. Mater*., **2020**, *32*, 6744-6752.

[10] (a) B. R. Barnett, M. I. Gonzalez, J. R. Long, *Trends Chem.* **2020**, *2*, 159-171; (b) S. Mukherjee, Y. He, D. Franz, S.-Q. Wang, W.-R. Xian, A. A. Bezrukov, B. Space, Z. Xu, J. He, M. J. Zaworotko, *Chem. Eur. J.* **2020**, *26*, 4923-4929; (c) O. T. Qazvini, R. Babarao, Z.-L. Shi, Y.-B. Zhang, S. G. Telfer, *J. Am. Chem. Soc.* **2019**, *141*, 5014−5020; (d) O. T. Qazvini, R. Babarao, S. G. Telfer, *Chem. Mater.* **2019**, *31*, 4919-4926.

[11] (a) S. Sircar, *Ind. Eng. Chem. Res.* **2006**, *45*, 5435–5448; (b) J.-R. Li, R. J. Kuppler, H.-C. Zhou, *Chem. Soc. Rev.* **2009**, *38*, 1477–1504.

[12] (a) S. Mukherjee, D. Sensharma, K.-J. Chen, M. J. Zaworotko, *Chem. Commun.* **2020**, *56*, 10419-10441; (b) R.-B. Lin, S. Xiang, W. Zhou, B. Chen, *Chem* **2020**, *6*, 337-363, (c) S. Mukherjee, N. Sikdar, D. O'Nolan, D. M. Franz, V. Gascón, A. Kumar, N. Kumar, H. S. Scott, D. G. Madden, P. E. Kruger, B. Space, M. J. Zaworotko, *Sci. Adv.* **2019**, *5*, eaax9171.

[13] (a) K. J. Chen, H. S. Scott, D. G. Madden, T. Pham, A. Kumar, A. Bajpai, M. Lusi, K. A. Forrest, B. Space, J. J. Perry, M. J. Zaworotko, *Chem* **2016**, *1*, 753–765; (b) J. Pei, K. Shao, J. Wang, H. Wen, Y. Yang, Y. Cui, R. Krishna, B. Li, G. Qian, *Adv. Mat.* **2020**, *32*, 1908275; (c) X. Cui, K. Chen, H. Xing, Q. Yang, R. Krishna, Z. Bao, H. Wu, W. Zhou, X. Dong, Y. Han, B. Li, Q. Ren, M. J. Zaworotko, B. Chen, *Science* **2016**, *353*, 141–144; (d) Y. Zhang, B. Li, R. Krishna, Z. Wu, D. Ma, Z. Shi, T. Pham, K. Forrest, B. Space, S. Ma, *Chem. Commun*. **2015**, *51*, 2714–2717; (e) P. Q. Liao, W. X. Zhang, J. P. Zhang, X. M. Chen, *Nat. Commun.* **2015**, *6*, 1–9; (f) O. T. Qazvini, R. Babarao, S. G. Telfer, *Nat. Commun.* **2021**, *197*, 1–8.

[14] (a) R. J. Kuppler, D. J. Timmons, Q.-R. Fang, J.-R. Li, T. A. Makal, M. D. Young, D. Yuan, D. Zhao, W. Zhuan, H. C. Zhou, *Coord. Chem. Rev.* **2009**, *253*, 3042− 3066; (b) P. Nugent, Y. Belmabkhout, S. D. Burd, A. J. Cairns, R. Luebke, K. Forrest, T. Pham, S. Ma, B.

Space, L. Wojtas, M. Eddaoudi, M. J. Zaworotko, *Nature* **2013**, *495*, 80–84.; (c) N. S. Bobbitt, M. L. Mendonca, A. J. Howarth, T. Islamoglu, J. T. Hupp, O. K. Farha, R. Q. Snurr, *Chem. Soc. Rev.* **2017**, *46*, 3357−3385.

[15] (a) D. Tian, J. Xu, Z.-J. Xie, Z.-Q. Yao, D.-L. Fu, Z. Zhou, X.-H. Bu, *Adv. Sci.* **2015**, *3*, 1500283; (b) F.-M. Zhang, L.-Z. Dong, J.-S. Qin, W. Guan, J. Liu, S.-L. Li, M. Lu, Y.-Q. Lan, Z.-M. Su, H.-C. Zhou, *J. Am. Chem. Soc.* **2017**, *139*, 6183–6189; (c) S. Yuan, L. Feng, K. C. Wang, J. D. Pang, M. Bosch, C. Lollar, Y. J. Sun, J. S. Qin, X. Y. Yang, P. Zhang, Q. Wang, L. F. Zou, Y. M. Zhang, L. L. Zhang, Y. Fang, J. L. Li, H.-C. Zhou, *Adv. Mater.* **2018**, *30*, 1704303; (d) P. Lama, L. J. Barbour, *J. Am. Chem. Soc.* **2018**, *140*, 2145−2150.

[16] (a) A. Karmakar, A. V. Desai, S. K. Ghosh, *Coord. Chem. Rev.* **2016**, *307*, 313–341; (b) Y.-Q. Chen, G.-R. Li, Z. Chang, Y.-K. Qu, Y.-H. Zhang, X.-H. Bu, *Chem. Sci.* **2013**, *4*, 3678–3682; (c) S.-S. Bao, G. K.H. Shimizu, L.-M. Zheng, *Coord. Chem. Rev.* **2019**, *378*, 577-594; (d) C. Healy, L. Hermanspahn, P. E. Kruger, *Coord. Chem. Rev.* **2021**, *432*, 213756.

[17] (a) A. V. Desai, B. Manna, A. Karmakar, A. Sahu, S. K. Ghosh, *Angew. Chem. Int. Ed.* **2016**, *55*, 7811–7815; (b) S. Sharma, S. Let, A. V. Desai, S. Dutta, G. Karuppasamy, M. M. Shirolkar, R. Babarao, S. K. Ghosh, *J. Mater. Chem. A* **2021**, *9*, 6499-6507.

[18] (a) H. Fei, D. L. Rogow, S. R. J. Oliver, *J. Am. Chem. Soc.* **2010**, *132*, 7202–7209; (b) A. Schoedel, L. Wojtas, S. P. Kelley, R. D. Rogers, M. Eddaoudi, M. J. Zaworotko, *Angew. Chem. Int. Ed.* **2011**, *50*, 11421–11424; (c) J.-P. Ma, Y. Yu, Y.-B. Dong, *Chem. Commun.* **2012**, *48*, 2946−2948; (d) B. Manna, B. Joarder, A. V. Desai, A. Karmakar, S. K. Ghosh, *Chem. Eur. J.* **2014**, *20*, 12399–12404; (e) D.-m. Chen, W. Shi, P. Cheng, *Chem. Commun.* **2015**, *51*, 370 –372; (f) S. Sharma, A. V. Desai, B. Joarder, S. K. Ghosh, *Angew. Chem. Int. Ed.* **2020**, *59*, 7788-7792; (g) B.-Q. Song, X.-L. Wang, Y.-T. Zhang, X.- S. Wu, H.-S. Liu, K.-Z. Shao, Z.-M. Su, *Chem. Commun.* **2015**, *51*, 9515–9518; (h) G. Brunet, K. Robeyns, R. P. S. Huynh, J.-B. Lin, S. P. Collins, G. A. Facey, G. K. H. Shimizu, T. K. Woo, M. Murugesu, *ACS Appl. Mater. Interfaces* **2019**, *11*, 3181−3188; (i) W. P. Lustig, S. Mukherjee, N. D. Rudd, A. V. Desai, J. Li, S. K. Ghosh, *Chem. Soc. Rev.* **2017**, *46*, 3242−3285.

[19] H. Xu, J. Cai, S. Xiang, Z. Zhang, C. Wu, X. Rao, Y. Cui, Y. Yang, R. Krishna, B. Chen, G. Qian, *J. Mater. Chem. A* **2013**, *1*, 9916–9921.

[20] S. Dutta, A.V. Desai, P. Samanta, S.K. Ghosh, *Inorg. Chim. Acta* **2019**, *486*, 401–405.

[21] SAINT Plus, version 7.03; Bruker AXS Inc.: *Madison, WI,* **2004**.

[22] G. M. Sheldrick, SHELXTL, Reference Manual, version 5.1; Bruker AXS Inc.: *Madison, WI,* 1997.

[23] G. M. Sheldrick, *Acta. Crystallogr., Sect. A* **2008**, *64*, 112-122.

[24] L. Farrugia, WinGX, version 1.80.05; University of Glasgow: Glasgow, Scotland, **2009**.

[25] A. L. Spek, PLATON, a Multipurpose Crystallographic Tool; Utrecht University: Utrecht, The Netherlands, **2005**.

[26] O. V. Dolomanov, L. J. Bourhis, R. J. Gildea, J. A. K. Howard, H. Puschmann, *J. Appl. Crystallogr.* **2009**, *42*, 339-341.

[27] A. L. Spek, *J. Appl. Crystallogr.* **2003**, *36*, 7-13.

[28] K. S. Walton, R. Q. Snurr, *J. Am. Chem. Soc.* **2007**, *129*, 8552-8556.

[29] A. J. Howarth, A. W. Peters, N. A. Vermeulen, T. C. Wang, J. T. Hupp, O. K. Farha, *Chem. Mater.* **2017**, *29*, 26-39.

[30] W. Yang, A. J. Davies, X. Lin, M. Suyetin, R. Matsuda, A. J. Blake, C. Wilson, W. Lewis, J. E. Parker, C. C. Tang, M. W. George, P. Hubberstey, S. Kitagawa, H. Sakamoto, E. Bichoutskaia, N. R. Champness, S. Yang, M. Schröder, *Chemical Science* **2012**, *3*, 2993-2999.

[31] Origin(Pro), Version 2016. OriginLab Corporation, Northampton, MA, USA.

[32] A. L. Myers, J. M. Prausnitz, *AIChE J.* **1965**, *11*, 121-127.

[33] R. T. Yang, Gas separation by adsorption processes, Butterworth-Heinemann, **2013**.

[34] O. T. Qazvini, S. Fatemi, *Sep. Purif. Technol.* **2015**, *139*, 88-103.

[35] M. Mehdipour, S. Fatemi, *Sep. Sci. Technol.* **2012**, *47*, 1199-1212.

[36] M. H. Chahbani, D. Tondeur, *Sep. Purif. Technol.* **2000**, *20*, 185-196.

[37] O. T. Qazvini, R. Babarao, Z.-L. Shi, Y.-B. Zhang, S. G. Telfer, *J. Am. Chem. Soc.* **2019**, *141*, 5014-5020.

[38] D. D. Do, Adsorption analysis: equilibria and kinetics. *Imperial college press London:* **1998**; Vol. 2.

[39] R. B. Bird, Transport phenomena. *Applied Mechanics Reviews* **2002**, *55*, R1-R4.

[40] R. Perry, D. Green, J. Maloney, *Chemical engineers handbook. 8th edition ed.; The McGraw Hill Companies, Inc:* **2008**.

[41] S. Farooq, D. M.Ruthven, *Chem. Eng. Sci.* **1990**, *45*, 107-115.

[42] L. Joss, M. Gazzani, M. Hefti, D. Marx, M. Mazzotti, *Ind. Eng. Chem. Res.* **2015**, *54*,3027-3038.

[43] A. D. Ebner, J. A. Ritter, *AIChE J.* **2002**, *48*, 1679-1691.

[44] R. T. Yang, *Gas separation by adsorption processes. Butterworth-Heinemann:* **2013**.

[45] J. Kiusalaas, *Numerical methods in engineering with Python 3. Cambridge university press:* **2013**.

[46] Dassault Systèmes BIOVIA, Material Studio, San Diego: Dassault Systèmes, **2019**.

[47] A. K. Rappe, C. J. Casewit, K. S. Colwell, W. A. Goddard, W. M. Skiff, J. Am. Chem. Soc. **1992**, *114*, 10024-10035.

[48] G. Kresse, J. Hafner, *Phys. Rev. B* **1993**, *48*, 13115-13118.

[49] S. Grimme, S. Ehrlich, L. *J.* Goerigk, *Comp. Chem.* **2011**, *32*, 1456-1465.

[50] J. P. Perdew, K. Burke, M. Ernzerhof, *Phys. Rev. Lett.* **1996**, ***77***, 3865-3868.

[51] G. Kresse, D. Joubert, *Phys. Rev. B* **1999**, *59*, 1758-1775.

[52] (a) S. Krause, N. Hosono, S. Kitagawa, *Angew. Chem. Int. Ed*. **2020**, *59*, 15325–15341; (b) Y. Jiang, L. Cao, X. Hu, Z. Ren, C. Zhang, C. Wang, *Inorg. Chem*. **2018**, *57*, 15123−15132; (c) S. Dutta, P. Samanta, B. Joarder, S. Let, D. Mahato, R. Babarao, S. K. Ghosh, *ACS Appl. Mater. Interfaces* **2020**, *12*, 41810–41818; (d) A. J. Howarth, A. W. Peters, N. A. Vermeulen, T. C. Wang, J. T. Hupp, O. K. Farha, *Chem. Mater.* **2017**, *29*, 26−39.

[53] K. S. Walton, R. Q. Snurr, *J. Am. Chem. Soc.* **2007**, *129*, 8552–8556.

[54] M. Oschatz, M. Antonietti, *Energy Environ. Sci.* **2018**, *11*, 57--70.

[55] (a) O. T. Qazvini, S. G. Telfer, *J. Mater. Chem. A* **2020**, *8*, 12028–12034; (b) Z. Tohidi, S. Fatemi, Omid Taheri Qazvini, *J. Nat. Gas. Sci. Eng.* **2015**, *26*, 758-769; (c) L. K. Macreadie, R. Babarao, C. J. Setter, S. J. Lee, O. T. Qazvini, A. J. Seeber, J. Tsanaktsidis, S. G. Telfer, S. R. Batten, M. R. Hill, *Angew. Chem. Int. Ed.* **2020**, *59*, 6090–6098; (d) S. Mukherjee, D. Sensharma, O. T. Qazvini, S. Dutta, L. K. Macreadie, S. K. Ghosh, R. Babarao, *Coord. Chem. Rev*. **2021**, *437*, 213852

[56] (a) G. Kresse, J. Hafner, *Phys. Rev. B* **1993**, *48*, 13115-13118; (b) N. Kumar, S. Mukherjee, N. C. Harvey-Reid, A. A. Bezrukov, K. Tan, V. Martins, M. Vandichel, T. Pham, L. M. v. Wyk, K. Oyekan, A. Kumar, K. A. Forrest, K. M. Patil, L. J. Barbour, B. Space, Y. Huang, P. E. Kruger, M. J.Zaworotko, *Chem* **2021**, *7*, 1–14.

[57] S. Mukherjee, N. Kumar, A. A. Bezrukov, K. Tan, T. Pham, K. A. Forrest, K. A. Oyekan, O. T. Qazvini, D. G. Madden, B. Space, M. J. Zaworotko, *Angew. Chem. Int. Ed.* **2021**, DOI: 10.1002/anie.202100240.

[58] K.-J. Chen, H. S. Scott, D. G. Madden, T. Pham, A. Kumar, A. Bajpai, M. Lusi, K. A. Forrest, B. Space, J. J. Perry, Michael J. Zaworotko, *Chem* **2016**, *1*, 753-765.

[59] X. Cui, K. Chen, H. Xing, Q. Yang, R. Krishna, Z. Bao, H. Wu, W. Zhou, X. Dong, Y. Han, B. Li, Q. Ren, M. J. Zaworotko, B. Chen, *Science* **2016**, *353*, 141-144.

[60] Y. L. Peng, T. Pham, P. Li, T. Wang, Y. Chen, K. J. Chen, K. A. Forrest, B. Space, P. Cheng, M. J. Zaworotko, *Angew. Chem. Int. Ed.* **2018**, *57*, 10971-10975.

[61] G.-X. Jin, X. Niu, J. Wang, J.-P. Ma, T.-L. Hu, Y.-B. Dong, *Chem. Mater.* **2018**, *30*, 7433-7437.

[62] F. Zheng, L. Guo, B. Gao, L. Li, Z. Zhang, Q. Yang, Y. Yang, B. Su, Q. Ren, Z. Bao, *ACS Appl. Mater. Interfaces* **2019**, *11*, 28197-28204.

[63] J. Lee, C. Y. Chuah, J. Kim, Y. Kim, N. Ko, Y. Seo, K. Kim, T. H. Bae, E. Lee, *Angew. Chem. Int. Ed.* **2018**, *57*, 7869-7873.

[64] L. Zhang, X. Cui, H. Xing, Y. Yang, Y. Cui, B. Chen, G. Qian, *RSC Adv.* **2017**, ***7***, 20795-20800.

[65] J. Li, L. Jiang, S. Chen, A. Kirchon, B. Li, Y. Li, H.-C. Zhou, *J. Am. Chem. Soc.* **2019**, *141*, 3807-3811.

[66] F. Yu, B.-Q. Hu, X.-N. Wang, Y.-M. Zhao, J.-L. Li, B. Li, H.-C. Zhou, *J. Mater. Chem. A* **2020**, *8*, 2083-2089.

[67] R.-B. Lin, L. Li, H. Wu, H. Arman, B. Li, R.-G. Lin, W. Zhou, B. Chen, *J. Am. Chem. Soc.* **2017**, *139*, 8022-8028.

[68] J. Pei, K. Shao, J.-X. Wang, H.-M. Wen, Y. Yang, Y. Cui, R. Krishna, B. Li, G. Qian, *Adv. Mater.* **2020**, *32*, 1908275.

[69] Y. L. Peng, T. Pham, P. Li, T. Wang, Y. Chen, K. J. Chen, K. A. Forrest, B. Space, P. Cheng, M. J. Zaworotko, *Angew. Chem. Int. Ed.* **2018**, *57*, 10971-10975.

[70] N. Kumar, S. Mukherjee, A. A. Bezrukov, M. Vandichel, M. Shivanna, D. Sensharma, A. Bajpai, V. Gascón, K.-i. Otake, S. Kitagawa, M. J. Zaworotko, *SmartMat.* **2020**, *1*, e1008.

[71] J. Gao, X. Qian, R.-B. Lin, R. Krishna, H. Wu, W. Zhou, B. Chen, *Angew. Chem. Int. Ed.* **2020**, *59*, 4396-4400.

[72] L. Zhang, K. Jiang, J. Zhang, J. Pei, K. Shao, Y. Cui, Y. Yang, B. Li, B. Chen, G. Qian, *ACS Sustain. Chem. Eng.* **2019**, ***7***, 1667-1672.

[73] S. Mukherjee, Y. He, D. Franz, S.-Q. Wang, W.-R. Xian, A. A. Bezrukov, B. Space, Z. Xu, J. He, M. J. Zaworotko, *Chem. Eur. J.* **2020**, *26*, 4923-4929.

[74] D.-M. Chen, C.-X. Sun, N.-N. Zhang, H.-H. Si, C.-S. Liu, M. Du, *Inorg. Chem.* **2018**, *57*, 2883-2889.

[75] H.-M. Wen, H. Wang, B. Li, Y. Cui, H. Wang, G. Qian, B. Chen, *Inorg. Chem.* **2016**, *55*, 7214-7218.

[76] D.-M. Chen, X.-H. Liu, J.-Y. Tian, J.-H. Zhang, C.-S. Liu, M. Du, *Inorg. Chem.* **2017**, *56*, 14767-14770.

[77] J. Lee, C. Y. Chuah, J. Kim, Y. Kim, N. Ko, Y. Seo, K. Kim, T. H. Bae, E. Lee, *Angew. Chem. Int. Ed.* **2018**, *57*, 7869-7873.

[78] H.-M. Wen, C. Liao, L. Li, L. Yang, J. Wang, L. Huang, B. Li, B. Chen and J. Hu, *Chem. Commun.* **2019**, *55*, 11354-11357.

[79] F. Luo, C. Yan, L. Dang, R. Krishna, W. Zhou, H. Wu, X. Dong, Y. Han, T.-L. Hu, M. O'Keeffe, L. Wang, M. Luo, R.-B. Lin, B. Chen, *J. Am. Chem. Soc.* **2016**, *138*, 5678-5684.

[80] H.-J. Lv, Y.-P. Li, Y.-Y. Xue, Y.-C. Jiang, S.-N. Li, M.-C. Hu, Q.-G. Zhai, *Inorg. Chem.* **2020**, *59*, 4825-4834.

[81] H. Cui, S. Chen, H. Arman, Y. Ye, A. Alsalme, R.-B. Lin, B. Chen, *Inorg. Chim. Acta* **2019**, *495*, 118938.

[82] O. T. Qazvini, R. Babarao, S. G. Telfer, *Chem. Mater.* **2019**, *31*, 4919-4926.

[83] H. Yang, T. X. Trieu, X. Zhao, Y. Wang, Y. Wang, P. Feng and X. Bu, *Angew. Chem. Int. Ed.* **2019**, *58*, 11757-11762.

[84] T. Xu, Z. Jiang, P. Liu, H. Chen, X. Lan, D. Chen, L. Li, Y. He, *ACS Appl. Nano Mater.* **2020**, *3*, 2911-2919.

[85] W. Fan, X. Wang, X. Liu, B. Xu, X. Zhang, W. Wang, X. Wang, Y. Wang, F. Dai, D. Yuan, D. Sun, *ACS Sustain. Chem. Eng.* **2019**, ***7***, 2134-2140.

[86] R. Liu, Q.-Y. Liu, R. Krishna, W. Wang, C.-T. He, Y.-L. Wang, *Inorg. Chem.* **2019**, *58*, 5089-5095.

[87] Y.-P. Li, Y. Wang, Y.-Y. Xue, H.-P. Li, Q.-G. Zhai, S.-N. Li, Y.-C. Jiang, M.-C. Hu, X. Bu, *Angew. Chem. Int. Ed.* **2019**, *58*, 13590-13595.

[88] H. Li, L. Li, R.-B. Lin, G. Ramirez, W. Zhou, R. Krishna, Z. Zhang, S. Xiang, B. Chen, *ACS Sustain. Chem. Eng.* **2019**, ***7***, 4897-4902.

[89] Y. Ye, Z. Ma, R.-B. Lin, R. Krishna, W. Zhou, Q. Lin, Z. Zhang, S. Xiang, B. Chen, *J. Am. Chem. Soc.* **2019**, *141*, 4130-4136.

[90] H. Li, H. Bonduris, X. Zhang, Y. Ye, A. Alsalme, R.-B. Lin, Z. Zhang, S. Xiang, B. Chen, *J. Solid State Chem.* **2020**, *284*, 121209.

[91] P. Yan, J. Yang, X. Hao, Z. Chen, G. Shen, Y. Zhao, D. Ma, J. Zhu, *CrystEngComm*. **2020**, *22*, 275-282.

[92] H. Cui, Y. Ye, H. Arman, Z. Li, A. Alsalme, R.-B. Lin, B. Chen, *Cryst. Growth Des.* **2019**, *19*, 5829-5835.

[93] L. Meng, L. Yang, C. Chen, X. Dong, S. Ren, G. Li, Y. Li, Y. Han, Z. Shi. S. Feng, *ACS Appl. Mater. Interfaces* **2020**, *12*, 5999-6006.

[94] W. Fan, S. Yuan, W. Wang, L. Feng, X. Liu, X. Zhang, X. Wang, Z. Kang, F. Dai, D. Yuan, D. Sun, H.-C. Zhou, *J. Am. Chem. Soc.* **2020**, *142*, 8728-8737.

[95] H. Zeng, M. Xie, Y.-L. Huang, Y. Zhao, X.-J. Xie, J.-P. Bai, M.-Y. Wan, R. Krishna, W. Lu, D. Li, *Angew. Chem. Int. Ed.* **2019**, *58*, 8515-8519.

[96] X.-Y. Li, Y.-Z. Li, L.-N. Ma, L. Hou, C.-Z. He, Y.-Y. Wang, Z. Zhu, *J. Mater. Chem. A* **2020**, *8*, 5227-5233.

[97] L. Zhang, X. Cui, H. Xing, Y. Yang, Y. Cui, B. Chen, G. Qian, *RSC Adv.* **2017**, *7*, 20795–20800.

[98] O. Alduhaish, H. Wang, B. Li, T.-L. Hu, H. D. Arman, K. Alfooty, B. Chen, *ChemPlusChem* **2016**, *81*, 770 – 774.

[99] J. -W. Zhang, M.-C. Hu, S.-N. Li, Y.-C. Jiang, P. Qu, Q.-G. Zhai, *Chem. Commun.* **2018**, *54*, 2012-2015.

[100] O. Alduhaish, R.-B. Lin, H. Wang, B. Li, H. D. Arman, T.-L. Hu, B. Chen, *Cryst. Growth Des.* **2018**, *18*, 4522−4527.

[101] L. Kan, G. Li, Y. Liu, *ACS Appl. Mater. Interfaces* **2020**, *12*, 18642−18649.

[102] Z.-J. Guo, J. Yu, Y.-Z. Zhang, J. Zhang, Y. Chen, Y. Wu, L.-H. Xie, J.-R. Li, *Inorg. Chem.* **2017**, *56*, 2188−2197.

[103] O. Alduhaish, H. Wang, B. Li, H. D. Arman, V. Nesterov, K. Alfooty, B. Chen, *ChemPlusChem* **2016**, *81*, 764 – 769.

[104] X. Duan, R. Lv, S. Li, J. Tang, J. Ge, D. Zhao, *Z. Anorg. Allg. Chem.* **2019**, *645*, 955–959.

[105] Y. Zhang, L. Yang, L. Wang, S. Duttwyler, H. Xing, *Angew. Chem. Int. Ed.* **2019**, *58*, 8145 –8150.

[106] T. Xu, Z. Jiang, P. Liu, H. Chen, X. Lan, D. Chen, L. Li, Y. He, *ACS Appl. Nano Mater.* **2020**, *3*, 2911−2919.

[107] W. Wang, N. Gong, H. Yin, B. Zhang, P. Guo, B. Liu, Y.-Y. Wang, *Inorg. Chem.* **2019**, *58*, 10295−10303.

[108] T. Xu, L. Fan, Z. Jiang, P. Zhou, Z. Li, H. Lu, Y. He, *Dalton Trans*. **2020**, *49*, 7174–7181.

[109]T. Chen, Y. Ye, M. Yin, L. Chen, Z. Ke, J. Guo, M. Zhang, Z. Yao, Z. Zhang and S. Xiang, *Cryst. Growth Des.* **2020**, *20*, 2099−2105.

[110] F. Chen, Y. Wang, D. Bai, M. He, X. Gao, Y. He, *J. Mater. Chem. A* **2018**, *6*, 3471–3478.

[111] Z. Liu, L. Lv, Y. He, Y. Feng, *CrystEngComm* **2017**, *19*, 2795–2801.

[112] X. Gao, H. Zhong, Y. Zhang, Y. Yao, D.-l. Chen, Y. He, Eur. J. *Inorg. Chem*. **2020**, 1683–1689.

[113] L. Zhang, C. Zou, M. Zhao, K. Jiang, R. Lin, Y. He, C.-D. Wu, Y. Cui, B. Chen, G. Qian, *Cryst. Growth Des*. **2016**, *16*, 7194−7197.

[114] X. Duan, Y. Zhou, R. Lv, B. Yu, H. Chen, Z. Ji, Y. Cui, Y. Yang, G. Qian, *Journal of Solid State Chemistry* **2018**, *260*, 31–33.

[115] Q. Chu, B. Zhang, H. Zhou, B. Liu, L. Hou, Y.-Y. Wang, *Inorg. Chem.* **2020**, *59*, 2853−2860.

[116] P. Yan, J. Yang, D. Ma, S. Zhang, S. Zeng, L. Feng, S. Zhan, Q. Lin, *Microporous and Mesoporous Materials* **2020**, *293*, 109777.

[117] P. Yan, J. Yang, X. Hao, Z. Chen, G. Shen, Y. Zhao, D. Ma, J. Zhu, *CrystEngComm* **2020**, *22*, 275–282.

[118] Y. He, Z. Zhang, S. Xiang, F. R. Fronczek, R. Krishna, B. Chen, *Chem. Eur. J.* **2012**, *18*, 613 – 619.

[119] J.-x. Ma, J. Guo, H. Wang, B. Li, T. Yang, B. Chen, *Inorg. Chem.* **2017**, *56*, 7145−7150.

[120] Y.-T. Li, J.-W. Zhang, H.-J. Lv, M.-C. Hu, S.-N. Li, Y.-C. Jiang, Q.-G. Zhai, *Inorg. Chem.* **2020**, *59*, 10368−10373.

[121] L. Zhang, K. Jiang, Y. Li, D. Zhao, Y. Yang, Y. Cui, B. Chen, G. Qian, *Cryst. Growth Des.* **2017**, *17*, 2319−2322.

Chapter 3

C_2H_2 Induced Structural Dynamism Driven Efficient C_2H_2/CO_2 Separation by a Water-stable Cationic Metal-organic framework

3.1 Introduction

The annual revenue of chemical industries is ~$5.7 trillion, accounting for almost 7% of the global gross domestic product.[1] Its' energy impact is much expensive as the chemical commodity separation and purification processes accounting for > 40% of industrial energy usage. This highlights the social need for energy-efficient and sustainable chemical manufacturing techniques, considering the fact that this energy footprint accounts for approximately 15% of worldwide energy consumption.[2-3] Furthermore, it has been estimated that the demand for chemical commodities would be tripled by 2050. In this context, acetylene (C_2H_2), an important feedstock chemical and a vital fuel gas, is typically manufactured either by incomplete methane combustion or separation of steam cracking distillates generated in the petroleum refining.[4-6] The state-of-the-art technologies for C_2H_2 purification from its' gas mixtures are mainly based on organic solvent extraction, which in-course produce a huge amount of waste solvent and involve highly energy-intensive processes.[7-10] Hence, developing new separation technologies which enable efficient C_2H_2 recovery from its' major industrial impurities e.g. carbon dioxide (CO_2) is reckoned as an urgent priority.[11-12] In this context, physisorbents with superior adsorptive potential towards C_2H_2 are regarded as a more energy efficient and environmentally friendly alternative to solvent extractions.[13-15] Traditional porous sorbent materials such as zeolite, activated carbons etc. found to exhibit lower adsorption capacities toward these gas mixtures. However, physisorption based separation methods are certainly handicapped due to the inflexible upper pressure processing limit of pure C_2H_2 (2 bar). In addition, the physicochemical similarities of CO_2 and C_2H_2 in terms of linear molecular shapes (3.18 × 3.33 × 5.36 $Å^3$ and 3.32 × 3.34 × 5.7 $Å^3$ for CO_2 and C_2H_2, respectively) and similar boiling points [194.7 K (CO_2) and 189.3 K (C_2H_2)] render significant challenges in separation and purification.[16-21]

In this light, adsorptive separation by porous solids are regarded as promising and energy-efficient alternatives for industrial separation.[22-26] As an significant material class, metal-organic frameworks (MOFs) have been investigated extensively towards gas separation and storage, sensing, catalysis, drug delivery, pollutant capture, ion conduction etc.[27-35] Further, on account of the charge of the framework backbone, MOFs are generally classified into two classes, viz. neutral MOFs and ionic MOFs (iMOFs). Furthermore, ionic MOFs are ctagorized into two, anionic and cationic MOFs.[36-43] Amongst, cationic MOFs featured with a synergy of cationic framework backbone and uncoordinated counter anions are a special subclass of ionic MOFs which have already shown tremendous promise in several diverse applications.[44-52] Although uncoordinated anions are not a direct component of the framework backbone in such MOFs, their selection is also very crucial in the preparation. Systematic tuning of the uncoordinated anions inside the pores along with pre-functionalized organic ligands can play vital role in selective host−guest interactions

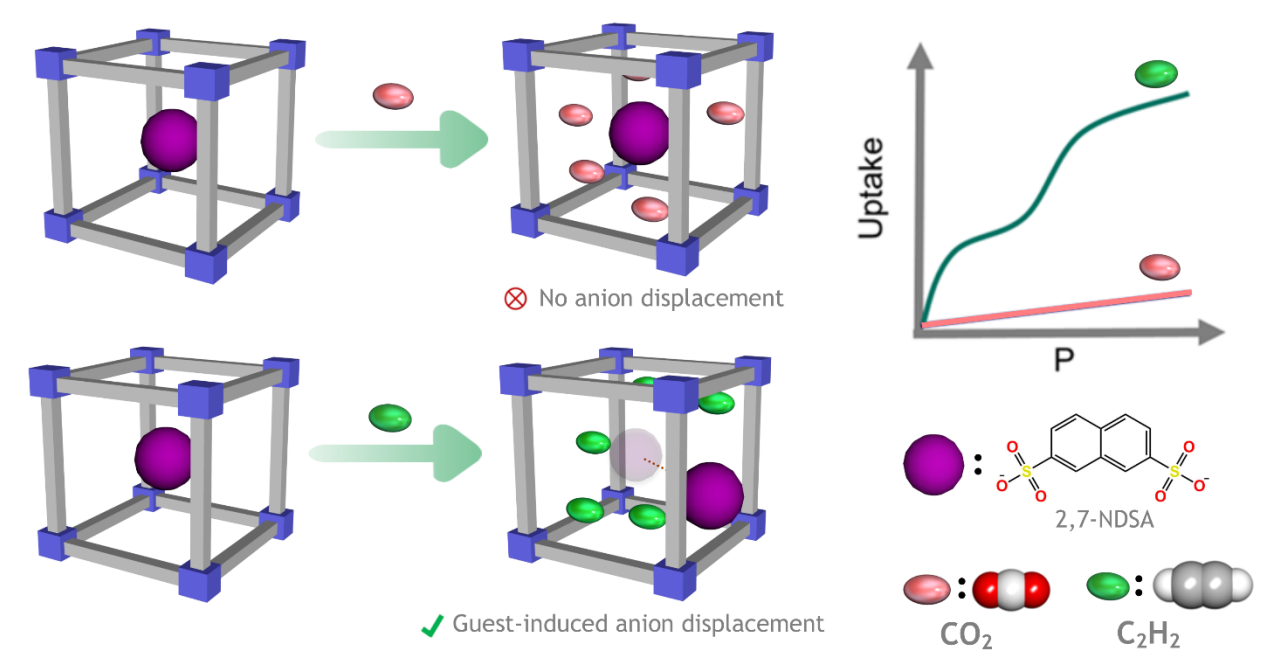

Sorbent-induced anion displacement in a water-stable cationic MOF

Scheme 3.1. Schematic representation of the design principle leading to **iMOF-8C** series; design of the cationic pore environment enables C_2H_2 selectivity over other C2-C1 gases. (colour codes: grey or gold – C, White – H, red – O).

between the MOF and the incoming guest molecules specially in the application of hydrocarbon separation. It is noteworthy to mention that although cationic MOFs are utilized for several applications in recent years, but separation of light hydrocarbons utilizing cationic MOFs is still at its' nascent stage and to best of our knowledge, there is only few reports in literature of separation of light hydrocarbons by cationic MOFs.

Accounting all these aspects, herein we introduce a novel two dimensional (2D) cationic ultramicroporous (< 7 Å) MOF, namely **iMOF-8C**, formulated with a neutral N-donor semi flexible ligand {namely, -tris(4-(1H-imidazol-1-yl) phenyl) amine} and uncoordinated 2,7-naphthalenedisulfonic acid (2,7-NDSA) molecules as bulky organic anionic templets inside the pores. The strategic choice of semi flexible ligand (L) and the presence of polar oxygen atoms of the sulfonic acid groups can be decisive in selective interaction and sorption of C_2H_2. Further, the role of the uncoordinated organic anions in selective adsorption of C_2H_2 at ambient temperature is established by utilizing two different organic sulfonic acid anions, viz. 4,4'-biphenyldisulfonic acid (BPSA) and 2,7-NDSA. Interestingly, **iMOF-8C** showed very

rare guest induced dynamism driven multi-stepped adsorption isotherms towards C_2H_2, resulting in benchmark adsorptive separation between C_2H_2 and CO_2 (Scheme 3.1).

3.2 Experimental

3.2.1 Materials:

The solvents and reagents used in this work were available from commercial sources and were further used directly.

3.2.2 Synthesis:

Synthesis of Ligand {tris(4-(1H-imidazol-1-yl)phenyl)amine}: A reported protocol was followed to synthesize the ligand.[53] A mixture of imidazole (6.22 mmol, 423 mg), tris(4-bromophenyl)amine (1.04 mmol, 500 mg), K_2CO_3 (4.15 mmol, 573 mg) and $CuSO_4$ (0.041 mmol, 6.5 mg) was allowed to heat at 160°C under inert atmospheric conditions for 72 hours. Once it is cooled to ambient condition, the resultant mixture was allowed to dissolve in CH_2Cl_2 (100 ml) and simultaneously washed with water for several times. The CH_2Cl_2 layer was further allowed to be dried, which yielded in a white powdered material. The ligand (L) was subsequently recyrstallized in a 1:1mixture of CH_2Cl_2: MeOH in yield of 60%.

Synthesis of Compound iMOF-8C: A mixture of the linker (0.02 mmol, 8.86 mg), $NiSO_4 \cdot xH_2O$ (0.02 mmol, 5.60 mg), 1,5-napthalenedisulfonic acid tetrahydrate (0.025 mmol, 9.00 mg) in a combination of solvent of 2 ml water and 1 ml N,N-dimethylformamide (DMF) was placed in a teflon vial, and heated at 130°C for 48 hours and subsequently allowed to cooldown to room temperature (Appendix 3.1). The single crystals of **iMOF-8C** were collected by filtration and cautiously washed with water and methanol several times. Single crystals of **iMOF-8C** viz. $[\{Ni(L)_2\}\cdot(2,7\text{-NDSA})\cdot xG]_n$ were collected with ~40% yield. Further, the crystals of **iMOF-8C** were allowed to dip in MeOH for exchanging the trapped DMF and water molecules. The MeOH exchanged phase of **iMOF-8C** was further heated at 75°C maintaining vacuum to obtain the activated phase of **iMOF-8C**. We would like to point out that the highly disordered uncoordinated anions and guest solvents inside the framework were unable to be located crystallographically. Employing the SQUEEZE function of PLATON the formula for the guest-free phase of the MOF was estimated to be $[\{Ni(L)_2\}\cdot(BPSA)]_n$. Anal. Calcd.: C/N, 4.02; N/S, 3.04; C/S, 12.41. Found: C/N, 3.88; N/S, 3.12; C/S, 12.65. Crystallographic data for **iMOF-8C**: CCDC 2176569 contains the crystallographic supplementary data for this chapter (Tables S9).

Synthesis of Compound IPM-MOF-201: IPM-MOF-201 was synthesized following a previously reported protocol which is almost similar as above, except using 4,4'-biphenyldisulfonic acid instead of

1,5-napthalenedisulfonic acid tetrahydrate as the counter-anion.[53] A mixture of ligand (0.02 mmol, 8.86 mg), $NiSO_4 \cdot xH_2O$ (0.02 mmol, 5.60 mg), 4,4'-biphenyldisulfonic acid [H_2BPSA] (9.45 mg, 0.03 mmol), in a solvent combination of 2 ml water and 1 ml DMF was placed in a teflon vial, and allowed to be heated at 130°C for 48 hours and subsequently allowed to cooldown to ambient temperature. The single crystals of IPM-MOF-201 were collected by filtration and carefully washed with methanol and water several times.

3.2.3 Water Stability Test: The activated **iMOF-8C (**~100 mg**)** crystals were dipped in deionised water (50 ml) at room temperature and kept for 24 hours. The crystalline powder was subsequently collected by filtration and allowed for air dry. The residual supernatant was carefully stored for further Inductively coupled plasma atomic emission spectroscopy (ICP-AES) analysis.

3.2.4 Physical Measurements: PXRD patterns were collected with the Bruker D8 X-Ray diffractometer using Cu Kα radiation (λ= 1.5406 Å) with a scan speed of 0.6° min^{-1} in the 2θ range of 5° to 40°. Thermogravimetric analysis (TGA) traces were collected with the heating rate of 10°C min^{-1} on a Perkin-Elmer STA 6000 TGA analyser maintaining N_2 atmosphere. All IR spectra were taken using a NICOLET 6700 FT-IR spectrophotometer, having KBr pellets in the 400–4000 cm^{-1} range. Field emission scanning electron microscopy (FESEM) images were acquired with a FEI Quanta 3D dual beam ESEM at 30 kV.

3.2.5 X-ray Structural Studies: Single-crystal X-ray diffraction data of **iMOF-8C** were recorded on a Bruker D8 Venture Duo X-ray diffractometer at 100K crafted with Microfocus X-ray source (operated at 50W; 50 kV/1 mA) along with a Photon 100 CMOS chip based detector system and graded multilayer optics for monochromatic focused X-ray beam Mo Kα radiation (λ = 0.71073 Å). Hexagonal single crystal was kept on nylon Cryo-Loops (Hampton Research) along with Paraton-N (Hampton Research). SAINT software[54] was used to conduct the data integration and reduction. The gathered reflections were subjected to a multi-scan absorption correction. The structure was solved using SHELXTL[55] direct approach, and then refined on F2 using the SHELXL-97[56] software package within the WINGX[57] program's complete matrix least-squares methodology. Anisotropic refinement was used on all non-hydrogen atoms. Using SHELXL default settings, all hydrogen atoms were found in consecutive difference Fourier maps and handled as riding atoms. To guarantee that no extra symmetry could be given to the models, the Adsym subroutine of PLATON[58] was used to investigate the structures. Because the guest and anion molecules in iMOF-8C are very disordered and couldn't be correctly modelled, the diffused electron densities that resulted from them were eliminated using PLATON's SQUEEZE[59] programme, and the results were appended to the CIF files. To reduce the contribution of disordered guest molecules, the SQUEEZE option was employed.

Gas sorption measurements: A BELSORP-Max instrument (BEL Japan) volumetric gas adsorption analyzer was used to collect N_2 sorption isotherms from 0 to 1 bar at 77 K. A BELSORP-Max instrument (BEL Japan) volumetric gas adsorption analyzer was used to collect the adsorption isotherms of different hydrocarbons in the temperature range of 273-313 K, accurately regulated using a Julabo F25-MC recirculating control system with 60:40 ethylene glycol and deionized water.

Breakthrough Curve Simulation Details

Mathematical Modelling

Considering a fixed bed adsorption column of length L filled with iMOF-8C, following assumptions were made to develop a mathematical model[60-63] that could be solved using proper numerical methods to calculate the concentration of gasses at different elapsed times along the bed.

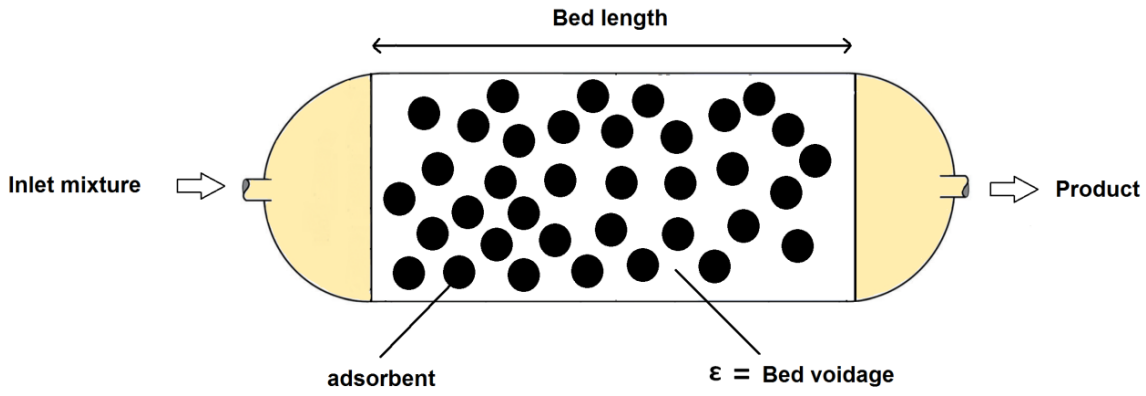

Figure S1. Schematic diagram of a fixed adsorption bed.

The following assumptions were made:

- The dynamic behaviour of the fluid obeys an axially dispersed plug flow model.
- The concentration gradient along the radial and angular directions was ignored.
- The flow velocity is calculated using the total mass balance equation and varies along the bed.
- The gas property is described by the Peng-Robinson equation of state.
- Adsorption kinetics into the particles are assumed to obey instant adsorption model (equilibrium model), where adsorbates are adsorbed rapidly with no resistance.
- The Ergun equation is used to calculate the pressure drop along the bed.

- The adsorption columns operate under isothermal conditions.
- Mixed gas isotherms are calculated by Extended Dual-Site Langmuir Freundlich (DSLF) method.[64]

The component and overall mass balances in the bulk phase of the adsorption column are written as follows, based on the preceding assumptions:

$$\varepsilon \frac{\partial C_i}{\partial t} = -\frac{\partial (uC_i)}{\partial z} + \varepsilon D_{ax,i} \frac{\partial^2 C_i}{\partial z^2} - (1-\varepsilon)\rho_s \frac{\partial q_i}{\partial t}$$

$$\varepsilon \frac{\partial C}{\partial t} = -\frac{\partial (uC)}{\partial z} - (1-\varepsilon)\rho_s \sum_{1}^{n_c} \left(\frac{\partial q_i}{\partial t}\right)$$

Where C_i is concentration of components in the gas phase and q_i is concentration of components in the adsorbed phase respectively. z is denoted as the axial coordinate in the bed, u is the superficial gas velocity, D_{ax} is the effective axial dispersion coefficient, ρ_s is the adsorbent density, ε is the bed voidage, and n_c is the number of the adsorbed components in the mixture. The following equation has been used to calculate the value of D_{ax} [65]:

$$\frac{\varepsilon D_{ax,i}}{D_{m,i}} = 20 + 0.5\, Sc_i\, Re$$

Where Sc is the Schmidt number, Re is the Reynolds number and $D_{m,i}$ is the molecular diffusivity of component i in the mixture which was calculated by following equation:

$$D_{m,i} = \frac{1 - y_i}{\sum_{x=j}^{n} \frac{y_i}{D_{i,x}}}$$

Where y_i is the mole fraction of component i and $D_{i,x}$ is molecular diffusivity of component i in component x which was calculated by Wile-Lee equation[66]. The solid linear driving force (LDF) model is used to describe the mass transfer rate of the gas and solid phases based on the assumptions[67]:

$$\frac{\partial q_i}{\partial t} = k_i (q_i^* - q_i)$$

Where k_i is the overall mass transfer coefficient, q_i^* is the equilibrium concentration of *i*th component in the adsorbed phase. An instant adsorption model (equilibrium model) were assumbed, where adsorbates are adsorbed rapidly with no transfer resistance. This means q_i in equation 1 can be replaced with q_i^*:[68,69]

$$q_i = q_i^*$$

q_i^* is then related to concentration in the gas phase through isotherms. The Extended Dual-Site Langmuir Freundlich method was used to predict the isotherm of gases in the mixture as below:[64]

$$q_i^* = \frac{q_1 b_1 {P_i}^{1/t_1}}{1 + \sum_{j=1}^{n} b_1 {P_j}^{1/t_1}} + \frac{q_2 b_2 {P_i}^{1/t_2}}{1 + \sum_{j=1}^{n} b_2 {P_j}^{1/t_2}}$$

Where q, b, and t are constants. To calculate these constants, single gas isotherms were fitted by Dual-Site Langmuir Freundlich model as shown in Figures S2.

$$q_i^* = \frac{q_1 b_1 {P_i}^{1/t_1}}{1 + b_1 {P_i}^{1/t_1}} + \frac{q_2 b_2 {P_i}^{1/t_2}}{1 + b_2 {P_i}^{1/t_2}}$$

The pressure drop is defined by the Ergun's equation as:[70]

$$\frac{\partial P}{\partial z} = -\left(\frac{37.5\,(1-\varepsilon)^2 \mu u}{\left(r_p \varphi\right)^2 \varepsilon^3} + 0.875 \rho \, \frac{(1-\varepsilon) u^2}{r_p \varphi \varepsilon^3} \right)$$

Where P is the local pressure at the z axial coordinate, μ is the gas viscosity, φ is the shape factor (assumed 1 in this work) and ρ is the gas density.

Table S1. Adsorption column parameters and feed characteristics used for the simulations.

Adsorption bed	***Feed***
Length: 400 mm	Total Flow rate: 11.6 mL_N/min
Diameter: 6 mm	Temperature: 273 K and 298 K

Amount of adsorbent in the bed: 0.3 g	Pressure: 1 bar
	Carrier gas (He) flow rate: 10 mL_N/min

Breakthrough curves were then calculated for a mixture of 50/50 C_2H_2/CO_2 at 273 K and 298 K at 1 bar for a bed packed with 0.3 g of iMOF-8C. The bed was initially pressurized with helium. A 50/50 mixture of C_2H_2/CO_2 with helium as carrier gas was introduced to the system. These mixture with a total flowrate of 11.6 ml_N/min (including 10 ml_N/min of helium) at 273 K and 298 K and 1 bar was passed through the adsorption column. A summary of bed and feed characteristics are presented in Table S1:

Numerical Methods

The implicit method of lines was used to solve the nonlinear parabolic PDEs derived from mass and momentum balance using the finite difference method for the spatial derivatives. First, the central and upwind differential schemes (backward) were used to discretize the second and first space derivatives, respectively. With respect to the time derivative terms, the sets of partial equations were transformed into sets of ODEs in this way. The length of the bed was divided into 50 increments, and the set of equations was solved with a one-second time step using the Implicit Euler method.[71]

Molecular Modelling Details.

Simulated annealing.

The starting position of distinct gas molecules was determined through the traditional simulated annealing approach utilising the classical force field as implemented in Materials Studio's sorption module, based on the experimental crystallographic data of the iMOF-8C structure.[72] Pairwise site-site Lennard-Jones (LJ) and Coulombic potentials were used to represent anion-adsorbent and anion-anion interactions. The Universal force field is used to determine the LJ potential parameters for both the framework atoms and the adsorbates (UFF).[73] The framework atoms' charges were assigned using the Q_{eq} charges implemented in the Materials Studio package.

The temperature was gradually dropped in the simulated annealing approach, allowing the gas molecule to achieve a preferred configuration based on various actions such as rotation, translation, and repositioning with predetermined probability of occurrence. To discover the local minima, this procedure

of heating and cooling the system was performed numerous times. A total of forty heating cycles were carried out, with the maximum and final temperatures being 10^5 K and 100 K, respectively.

DFT calculations.

Density functional theory (DFT) as implemented in the software programme VASP 5.4.4.[74] was used to determine periodic geometric optimization and static binding energies for gas molecules including C_2H_2 and CO_2 with the iMOF-8C framework. Standard DFT approaches based on generalised gradient approximation are widely recognised for failing to account for long-range dispersion interactions between the framework and bound adsorbates. We used the DFT-D3 approach to incorporate dispersion corrections to precisely estimate static binding energies for each gas molecule with the framework.[75] The generalised gradient approximation Perdew, Burke, and Ernzerhof (PBE)[76] form was utilised to represent electron exchange and correlation, and projector augmented wave potentials were employed to address core and valence electrons.[77] For sampling the Brillouin zone, we employed a plane-wave kinetic energy cutoff of 600 eV and a Gamma-point mesh of k-points (2x2x1) in all cases. The Hellman-Feynman ionic forces were less than 0.02 eV/ until the ionic coordinates and cell parameters were totally relaxed.

Binding energies.

The traditional simulated annealing approach, as mentioned above, was used to determine the initial favoured placement of each gas molecule in the primitive cell of matching MOF structures. Static binding energies (ΔE) at 0 K in vacuum were calculated using the following expression

$$\Delta E = E_{MOF+Gas} - E_{MOF,def} - E_{Gas}$$

where E_x refers, respectively, to the total energies of the MOF + gas complex, the deformed MOF alone in its adsorbed state, and the gas molecule respectively.

3.3 Results and discussion

Following a reported protocol while altering the bulky organic anion from 4,4′-biphenyldisulfonic acid (BPSA) to 2,7-naphthalenedisulfonic acid (2,7-NDSA), we have synthesized an iso-structural cationic MOF (**iMOF-8C**) with previously reported **IPM-MOF-201**.[53] Single crystals of **iMOF-8C** were prepared via solvothermal reaction of $NiSO_4 \cdot xH_2O$, 2,7-naphthalenedisulfonic acid (2,7-NDSA) and ligand (L) (1:1.5:1) in a solvent combination of DMF and water (2:1) at 130°C (Appendix 3.1). SC-XRD studies revealed that the hexagonal-shaped crystals crystallized in *R-3* space group. In addition, the unit cell parameters of **iMOF-8C** found to be similar with **IPM-MOF-201**, substantiating the iso-structural nature to each other (Appendix 3.3). The asymmetric unit contains one Ni(II), one ligand (L) molecule and disordered organic anions and solvent molecules (Figure 3.1a). The presence of the 2,7-NDSA was

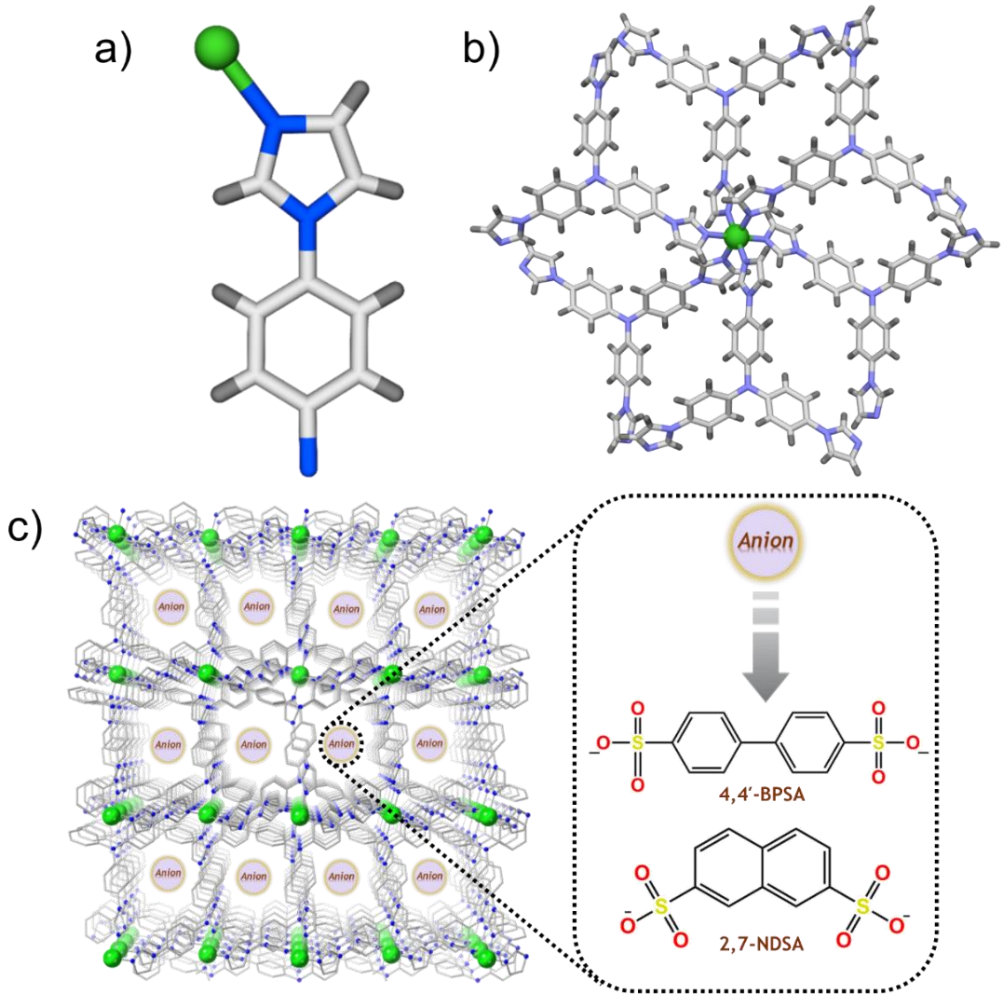

Figure 3.1 (a) Asymmetric unit of **iMOF-8C**, (b) Coordination environment in of **iMOF-8C** (c) Perspective packing view of **iMOF-8C** along *c* axis (colour - C: grey, N: blue, Ni: green).

corroborated via ^{1}H-NMR studies for which the as-synthesized MOF was digested in D_3PO_4/D_2O and neutralization with NaOD (Appendix 3.8). The Ni(II) center is octahedrally coordinated to six individual ligand units which lead to form an extended 2D sheet-structure (Figure 3.1b). The topology further revealed that **iMOF-8C** possess binodal **kgd** topology with (3,6)-connection.[53] The residual charge of the cationic framework is neutralized by the uncoordinated 2,7-NDSA anions populating inside the framework (Figure 3.1c). The solvent accessible void calculated from the PLATON calculations in **iMOF-8C** is found to be 2754 Å^3 (49%), considering only the cationic network. The one-dimensional channels of **iMOF-8C** are furnished with π-electron rich surface as well as the functional 2,7-NDSA anions which endow the polar sulfonic acid groups with potential ability to preferentially interact with the incoming guest molecules (Figure 3.1c, Appendix 3.5-3.6). All the basic characterizations of **iMOF-8C** were carried out before the subsequent studies. The bulk phase purity and high crystallinity of **iMOF-8C**

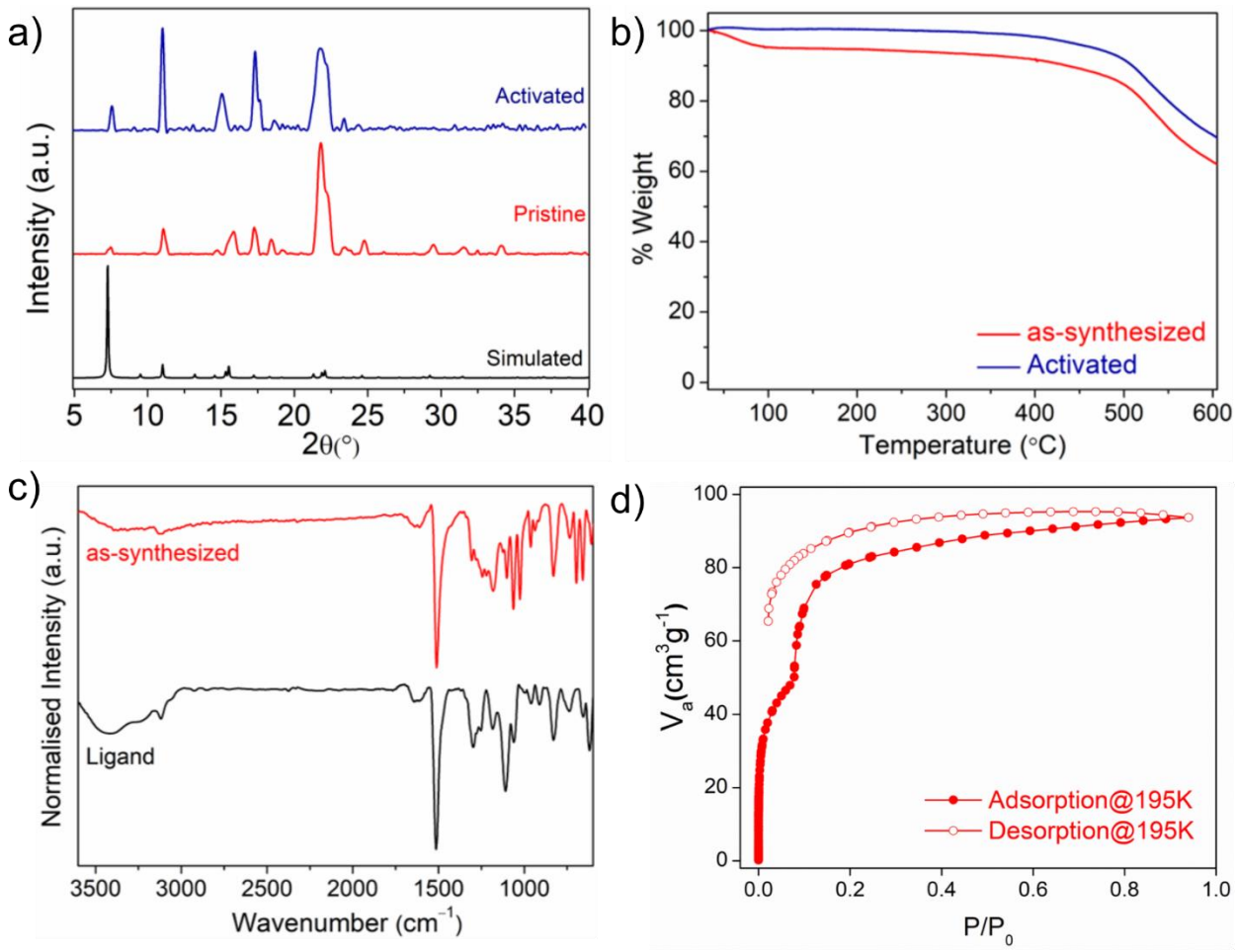

Figure 3.2 (a) PXRD patterns of **iMOF-8C**, (b) TGA traces for **iMOF-8C**, (c) IR spectra of **iMOF-8C**, (d) Low temperature (195K) CO_2 adsorption profile of **iMOF-8C**.

was validated from the PXRD patterns (Figure 3.2a). TGA traces of **iMOF-8C** suggested initial weight loss of guest water and DMF molecules, but excellent thermal stability upto ~500°C (Figure 3.2b). The FT-IR spectrum of **iMOF-8C** affirmed the presence of all characteristic peaks related to the ligand moiety along with the peak corresponding to S-O stretching frequency of the sulfonate anion (Figure 3.2c). FE-SEM images of **iMOF-8C** revealed the hexagonal shaped morphology of the single crystals and the EDX spectrums substantiated the homogeneous distribution of all the elements over **iMOF-8C** crystals (Appendix 3.9-3.11). Moreover, **iMOF-8C** exhibited excellent hydrolytic stability as the PXRD patterns confirmed the retention of all pecks (Appendix 3.12-3.13). The steric shielding of the metal centres with six imidazole units result in fulfilment of all coordination sites of Ni(II) nodes, imparting such hydrolytic stability (Appendix 3.4). To substantiate permanent porosity, we have recorded low-temperature (195 K) CO_2 adsorption of **iMOF-8C** which exhibited a type-1 isotherm with a step-wise gate-opening behavior having an uptake of 95 $cm^3\ g^{-1}$ (Figure 3.2d). The Brunauer-Emmett-Teller (BET) surface area of **iMOF-**

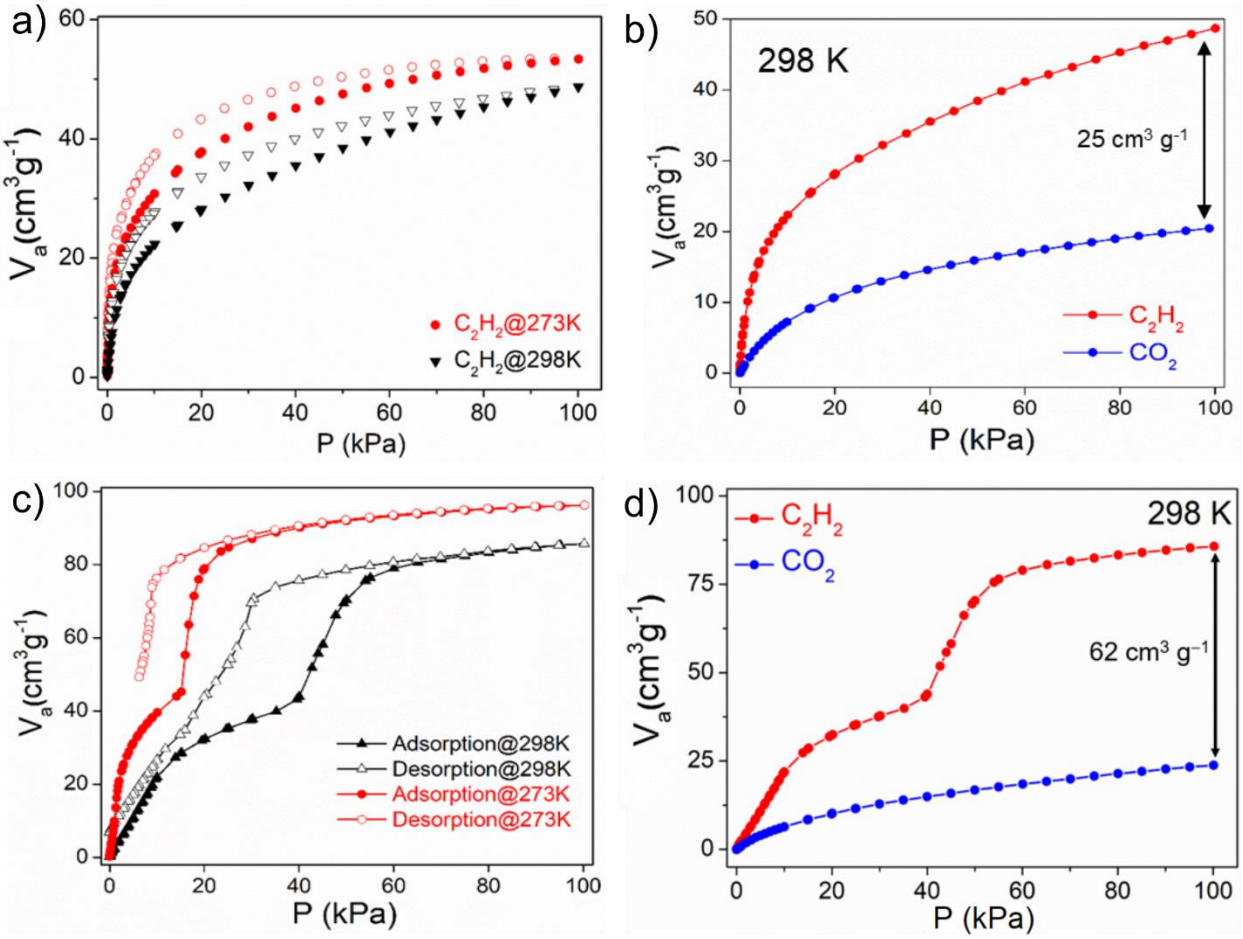

Figure 3.3 (a) Single-component C_2H_2 adsorption isotherms at both 273K and 298 K for **IPM-MOF-201**, (b) Adsorptive separation of C_2H_2 and CO_2 by **IPM-MOF-201** at 298K, (c) Single-component C_2H_2 adsorption isotherms at both 273K and 298 K for **iMOF-8C**, (d) Adsorptive separation of C_2H_2 and CO_2 by **iMOF-8C** at 298K.

8C was found to be 189.23 m^2 g^{-1} calculated from the CO_2 (195 K) isotherm adopting Rouquerol.[60] The N_2 adsorption profile at 77K showed negligible uptake which is corroborates well with the partial pore-blocking due to presence of the uncoordinated organic anions (Appendix 3.21). Pore size distribution analysis from CO_2 (195 K) data substantiated the ultra-microporosity of **iMOF-8C**, which was found to be in good agreement with the pore dimensions derived from X-ray structural analysis (Appendix 3.22). All the basic characterizations were also carried out for **IPM-MOF-201** prior to the adsorption studies (Appendix 3.14-3.20). The bulk phase purity and high crystallinity of **IPM-MOF-201** was confirmed from PXRD patterns whereas the TGA traces of **IPM-MOF-201** corroborated well with the initial weight loss of guest solvent molecules, but excellent thermal stability up to ~500°C (Appendix 3.14-3.15).

Next, we recorded the single component sorption isotherms of CO_2 and C_2H_2 for both **IPM-MOF-201** and **iMOF-8C** at 273 and 298 K under 1 bar to delve into their potency for light hydrocarbon adsorption and separation (Figure 3.3a-3d). **IPM-MOF-201** registered the saturation C_2H_2 uptake of 49 mlg^{-1} at

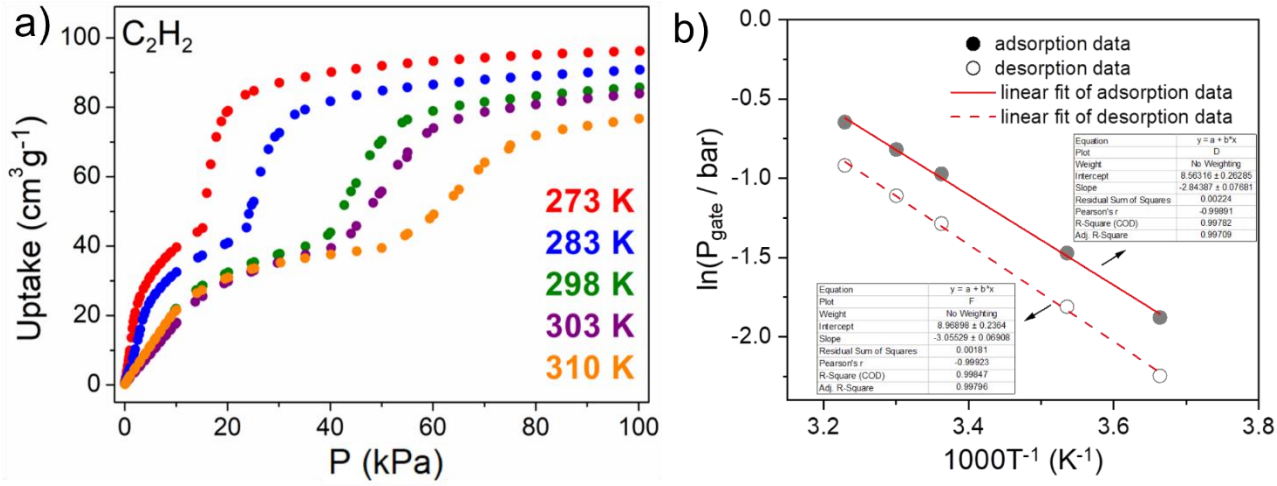

Figure 3.4 (a) Temperature dependent C_2H_2 adsorption isotherms for **iMOF-8C**, (b) The temperature and gate opening/closing pressures of C_2H_2-sorption were fitted with the Clausius– Clapeyron equation for **iMOF-8C**.

298K and 1 bar. On the flipside, the CO_2 uptake was 20.6 mlg^{-1}, resulting in significant adsorptive separation of C_2H_2/CO_2 at room temperature (Figure 3.3a-3b). Interestingly, **iMOF-8C** exhibited a multi-step-gate-opening behaviour toward C_2H_2 with a high saturation C_2H_2 uptake of 86 mlg^{-1} at 298K and 96 mlg^{-1} at 273K and 1 bar whereas the CO_2 uptake was 20.6 mlg^{-1}, affording an excellent adsorptive C_2H_2/CO_2 separation of ~60 ml at room temperature (Figure 3.3c-3d). The loading of the gas molecules per formula unit was also found to be much higher in case of C_2H_2 (5) than CO_2 (1) indicating clear selectivity toward C_2H_2 (Appendix 3.24). Moreover, the first and second gate opening pressure ($P_{ga}1$ and $P_{ga}2$) for C_2H_2 at 273 K are found to be 15 kPa and 25 kPa respectively, whereas $P_{ga}1$ and $P_{ga}2$ at 298K are 36 kPa and 55 kPa respectively (Figure 3.3c). Such variation in P_{ga} with change in temperature propelled us to explore the C_2H_2-sorption behaviour of **iMOF-8C** at different temperatures. The temperature dependent adsorption isotherm profiles show that the gate-opening pressure range can vary from 15 kPa to 50 kPa by varying the adsorption temperature from 273K to 310K (Figure 3.4a). Such dynamic adsorption behaviour can be directly corelated with pressure-induced anion movement inside the pores of **iMOF-8C** (Figure 3.7). Further, the gate opening/closing pressures and the adsorption temperatures were fitted via Clausius–Clapeyron equation[78] which revealed that the formation enthalpy of the clathrate Δ_fH, is ca. 23.6 kJ mol^{-1} and the dissociation enthalpy, Δ_dH, to be ca. 25.4 kJ mol^{-1}(Figure 3.4b). These values are indicative of higher affinity and stronger preferential interaction between C_2H_2 molecules and **iMOF-8C** framework.

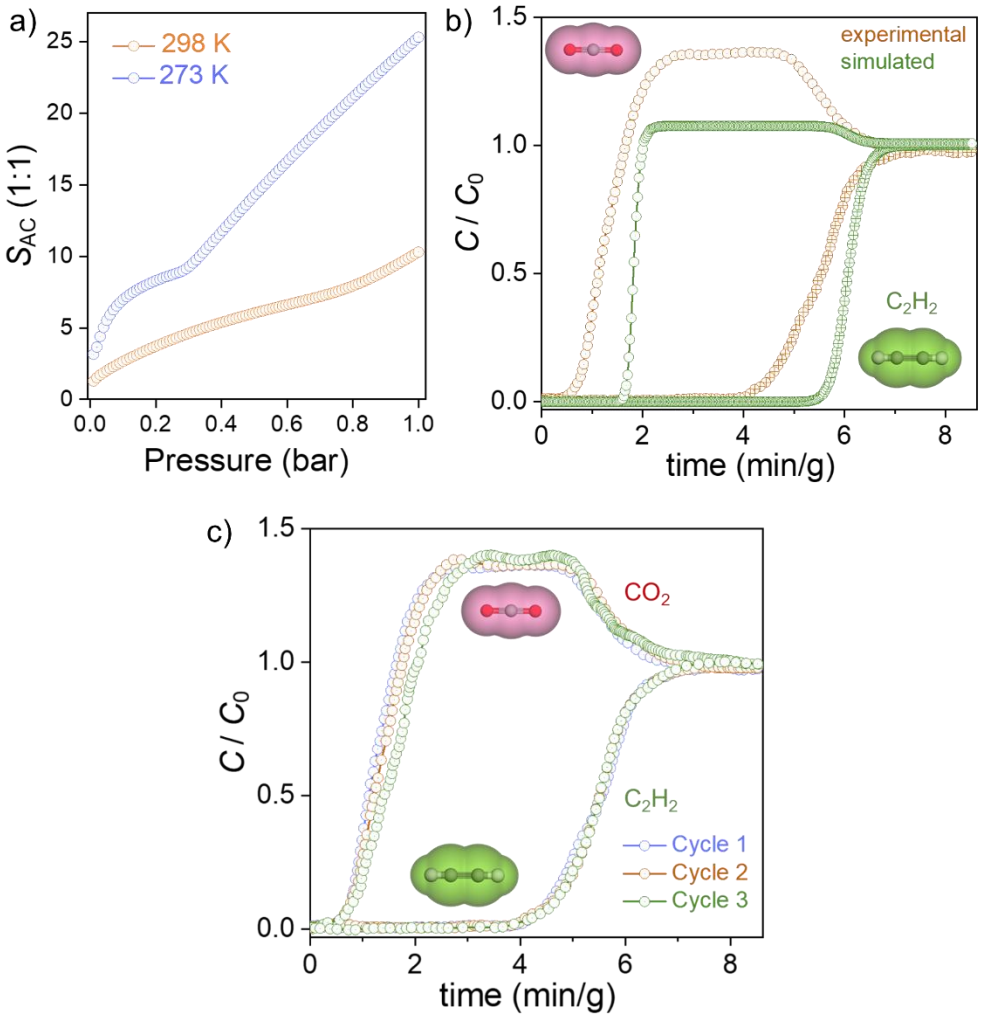

Figure 3.5 (a) IAST selectivities of the **iMOF-8C** for C_2H_2/CO_2 at different temperatures, (b) Comparison between simulated and dynamic column breakthrough curves of iMOF-8C for equimolar mixtures of C_2H_2/CO_2, (c) Experimental dynamic column breakthrough curves for equimolar mixtures of C_2H_2/CO_2 for iMOF-8C recorded for 3 cycles.

To simulate the real-time separation predicament and to understand the potency of **iMOF-8C**, we have determined the IAST selectivity for the binary mixtures of C_2H_2/CO_2 (1/1; v/v) employing single-component experimental adsorption isotherms obtained at 298 K under 1 bar (Figure 3.5a). **iMOF-8C** found to exhibit an adsorption selectivity of 10 for the mixture of C_2H_2/CO_2 (1/1; v/v) at 298K whereas it showed an adsorption selectivity of 26 at 273K. Notably, **iMOF-8C** found to exhibit highest IAST selectivity value in the domain of ionic MOFs for C_2H_2/CO_2 (1/1; v/v) separation (Appendix Table S1). Such encouraging values are indicative of the true potential of **iMOF-8C** towards real-time C_2H_2/CO_2 separation.

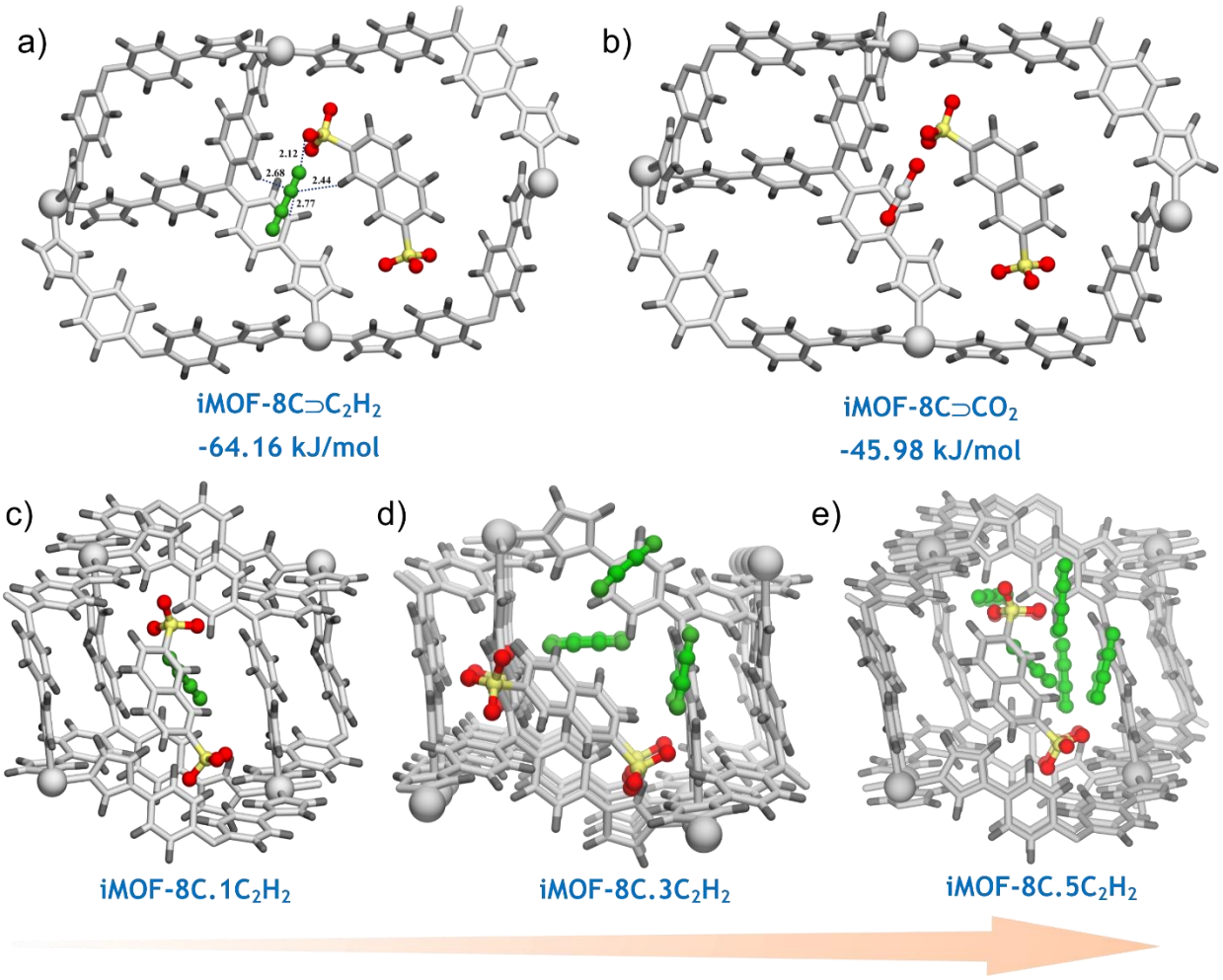

Figure 3.6 (a) DFT optimization-based energy-optimized binding sites in **iMOF-8C** for: (a) C_2H_2; (b) CO_2, (c-e) Gradual increase of C_2H_2 loading up to the saturation loading limit in **iMOF-8C** and simultaneous structural as well as lattice parameter change as a function of loading.

To assess the combined contributions of the uptake capacity and sorption selectivity accurately, we executed the simulated breakthrough experiments. The simulated breakthrough demonstrates the concentration differences of C_2H_2/CO_2 eluting from the adsorber packed with **iMOF-8C** as a function of time (min). As evident in (figure 3.5b), CO_2 came out first from the adsorber bed for **iMOF-8C** and the retention of C_2H_2 within the bed continued for a significant time until C_2H_2 reached its saturation and broke through. Therefore, such excellent simulation performance reflects on the exceptional potential of **iMOF-8C** towards combating the crucial challenge of separation of light hydrocarbons such as C_2H_2/CO_2.

To validate separation potency of **iMOF-8C** in real-time situations, dynamic column breakthrough (DCB) studies has been performed in which the C_2H_2/CO_2 (1/1; v/v) mixture was allowed to flow through a fixed

bed of 300mg **iMOF-8C** with a total flow of cm^3min^{-1} at 298K. As described in Figure 3.5b, the C_2H_2 breakthrough took place significantly later in comparison with CO_2 (18.0 versus 2.0 min g^{-1} for C_2H_2/CO_2 (1/1; v/v)). **iMOF-8C** exhibited a saturation C_2H_2 uptake of 2.79 mmol g^{-1} in the DCB profile which is in accordance with the experimental single-component saturation uptake from C_2H_2 isotherm at half-coverage (3.14 mmol g^{-1} under ambient equilibrium conditions). In addition, **iMOF-8C** found to maintain its' breakthrough performance up to 3 cycles, revealing its' true potential in real-time applications (Figures 3.5c).

To acquire further insights regarding the mechanism of such preferential C_2H_2 adsorption performances of **iMOF-8C**, both Monte Carlo simulations (MCS) and density functional theory (DFT) were carried out. First, NVT simulated annealing using MCS technique was performed on the basis of the DFT optimized model structure of **iMOF-8C** to identify the most favourable binding sites for C_2H_2 and CO_2 molecules

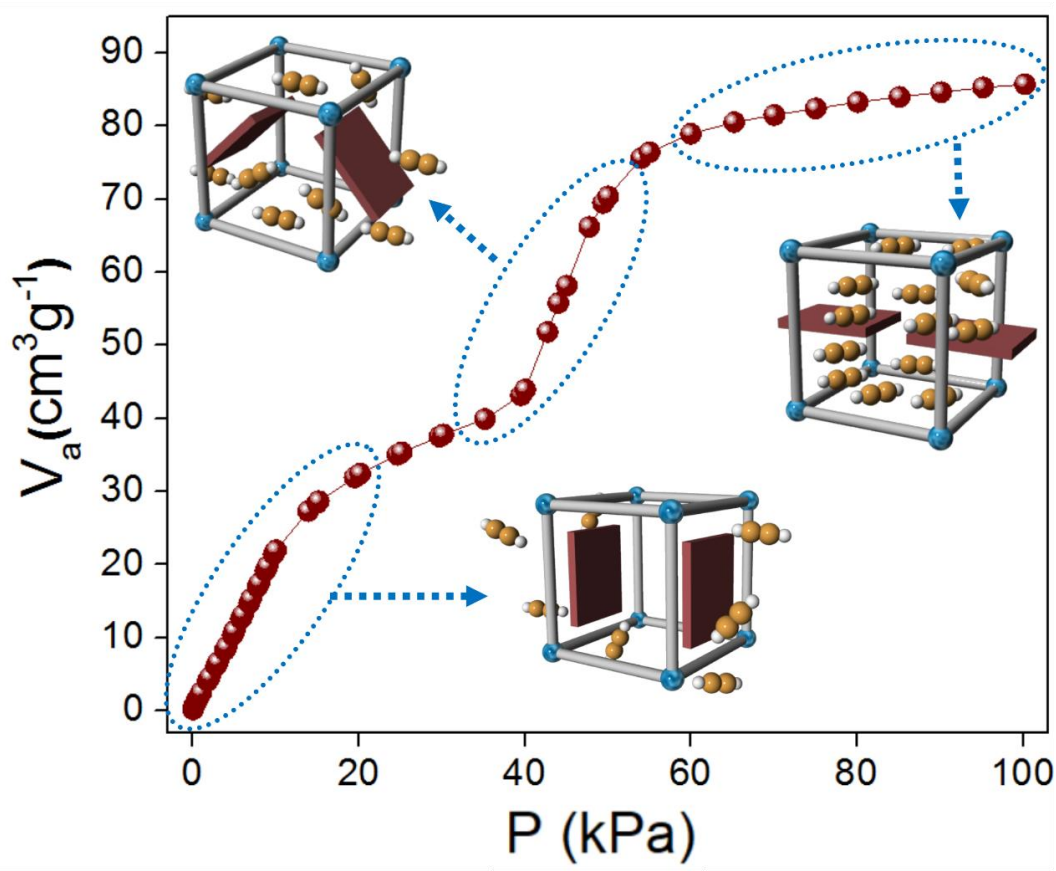

Figure 3.7 Schematic representation of probable mechanism of C_2H_2 induced anion movement resulting in multistep adsorption isotherms.

within the **iMOF-8C** framework. Secondly, employing the DFT method (DFT-D3) with dispersion correction, the binding energies between the different gas molecules and the **iMOF-8C** framework were

evaluated on the basis of the periodic model as employed in the software VASP 5.4.4 package. The favourable binding sites in terms of lowest energy were recognized from classical NVT simulated annealing which were regarded as the preliminary DFT optimization positions. As described in Figure 3.6a-6b, the favourable binding locations of incoming C_2H_2 and CO_2 molecules inside the optimized structure iMOF- 8C. Both DFT and MCS methods has been utilized to understand such dynamism in C_2H_2 adsorption isotherms exhibited by **iMOF-8C**. In this study, we have gradually increased the loading the of C_2H_2 in the primitive cell of DFT optimized **iMOF-8C** model to understand the selectivity mechanism and effect of guest loading. The classical NVT simulated annealing studies revealed the preferential binding sites with lowest energy which were further considered as the initial position for further DFT optimization. As revealed by Figure 3.6, in all the C_2H_2 loading range, the C_2H_2 molecules found to occupy the 1D channels as well as the interlayer space of **iMOF-8C**. As shown in Figure 3.6a, **iMOF-8C** exhibits different binding sites toward C_2H_2. Strong interactions were observed between (HC≡CH···O=S (uncoordinated anions)), (HC≡C···H-C (MOF)) and (HC≡C···π (MOF)). Moreover, incremental loading of C_2H_2 in the primitive cell of **iMOF-8C** revealed a significant structural change as the distance between 2,7-NDSA molecule and **iMOF-8C** framework is gradually changing (Figure 3.6c-6e, Appendix 3.29). Additionally, the alteration in torsion angles as well as the bond angles of ligand L can be directly corelated with the structural dynamism upon incremental C_2H_2 loading inside **iMOF-8C (**Appendix 3.30-3.31). The calculated binding energies are also found to be in well alignment with the experimental adsorption selectivity: C_2H_2 (-64.16 kJ mol^{-1}) > CO_2 (45.98 kJ mol^{-1}).

3.4 Conclusion

In conclusion, herein we have developed a novel cationic ultramicroporous MOF (**iMOF-8C**) with functional sulfonic acids as counter anions favoring the selective adsorption of C_2H_2. **iMOF-8C** exhibited a rare guest-induced anion-dynamism-based gate-opening behavior towards C_2H_2 which is for the first time utilized for challenging separation of C_2H_2/CO_2. Further, the single component adsorption isotherms revealed excellent selectivity for C_2H_2 over its' industrial impurity, i.e. CO_2. Such selectivity is predominantly attributed to the existence of several functional groups e.g., polar sulfonic acid groups, unsaturated π-electron cloud in framework backbone etc. In addition, IAST calculations and simulated breakthrough experiments revealed the high efficiency of **iMOF-8C** in the purification of C_2H_2 from C_2H_2/CO_2mixtures, which is recognized as very crucial but challenging task in industrial separation. Moreover, theoretical calculations further comprehensively supported the high affinity of **iMOF-8C** toward C_2H_2 over CO_2. This work not only demonstrate systematic exploration of functional sulfonic acid anions in

a cationic MOF for such hydrocarbon separation for the first time but also provides a new direction to the development of cationic MOFs and rational designing of functional porous materials for the pressing industrial challenges of light hydrocarbon separation.

3.5 Appendix section

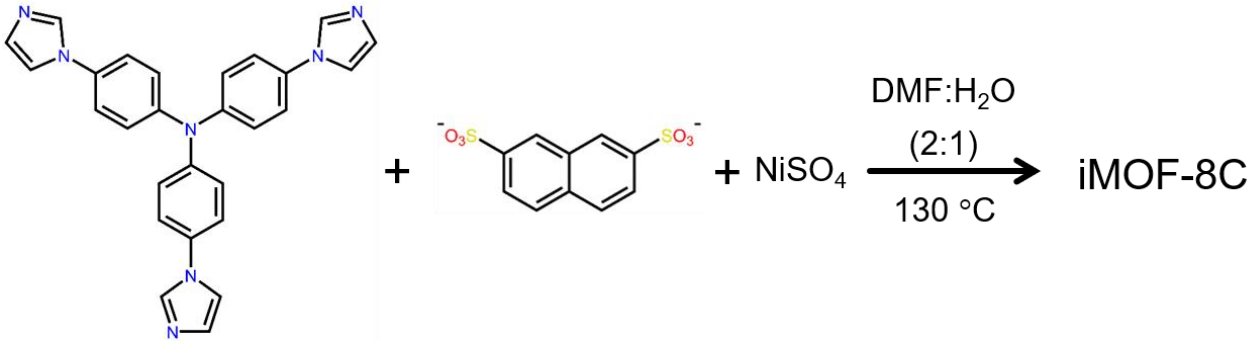

Appendix 3.1 Synthetic protocol leading to the synthesis of **iMOF-8C**.

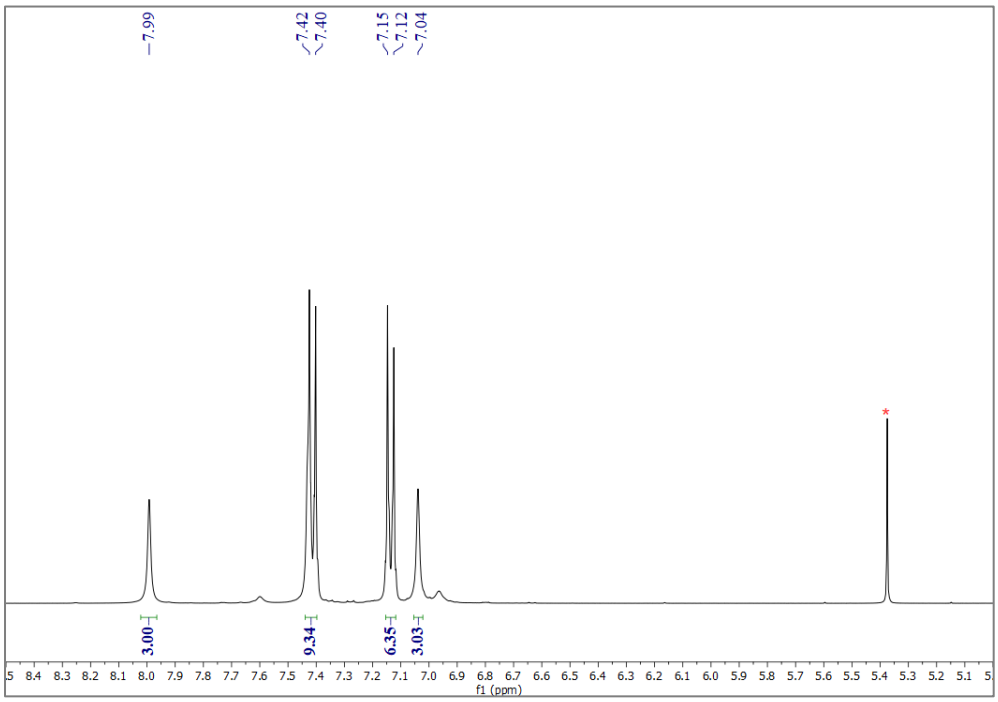

Appendix 3.2. ^{1}H NMR spectra of ligand (L).

Parameters	*a* (Å)	*b* (Å)	*c* (Å)	α (°)	β (°)	γ (°)	V (Å^3)	Space Group
IPM-MOF-201	16.04 (10)	16.04 (10)	25.00 (18)	90	90	120	5574.9 (8)	*R*-3
iMOF-8C	15.98 (0.04)	15.98 (0.04)	25.08 (0.09)	90	90	120	5540.5 (3)	*R*-3

Appendix 3.3. A comparison table of cell parameters of previously reported **IPM-MOF-201** and **iMOF-8C**.

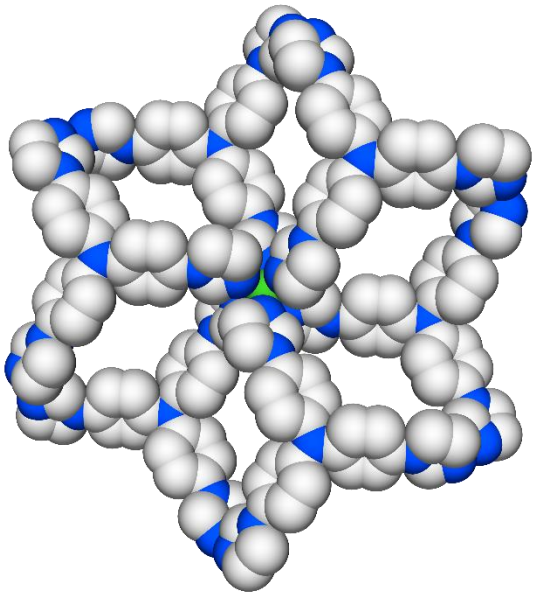

Appendix 3.4. Coordination environment of **iMOF-8C** (colour codes: grey - C, blue - N, green – Ni).

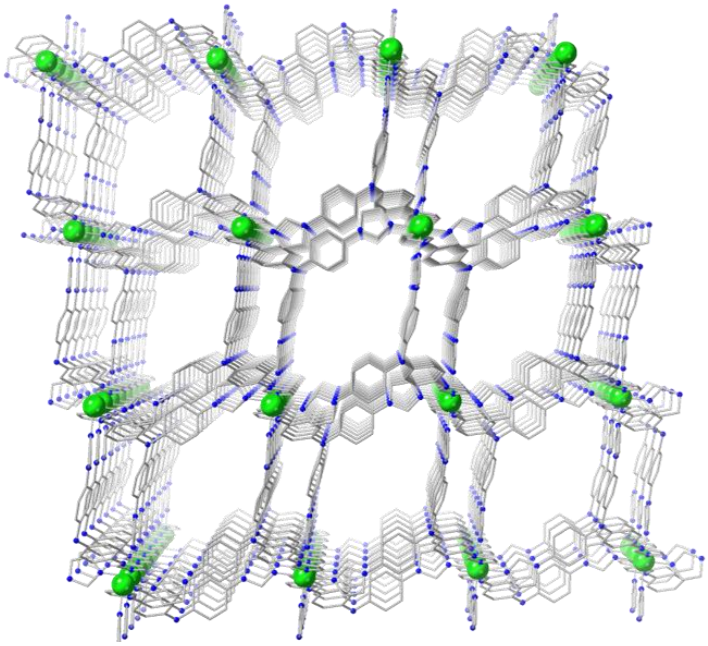

Appendix 3.5. Perspective view of overall packing of **iMOF-8C** along c-axis (colour codes: grey - C, blue - N, green – Ni).

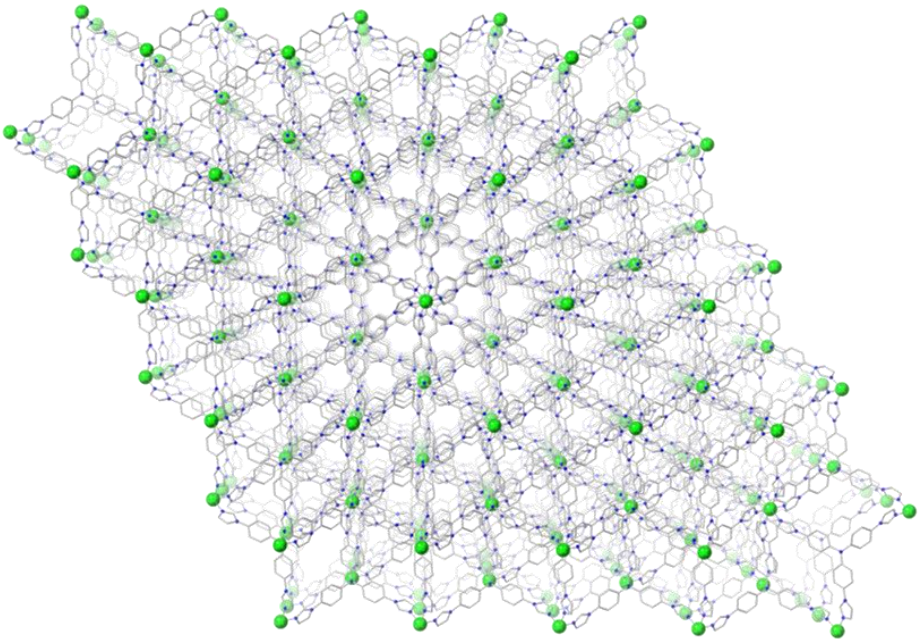

Appendix 3.6. Packing diagram of **iMOF-8C** showing the coordination environment of the metal node (colour codes: grey - C, blue - N, green – Ni).

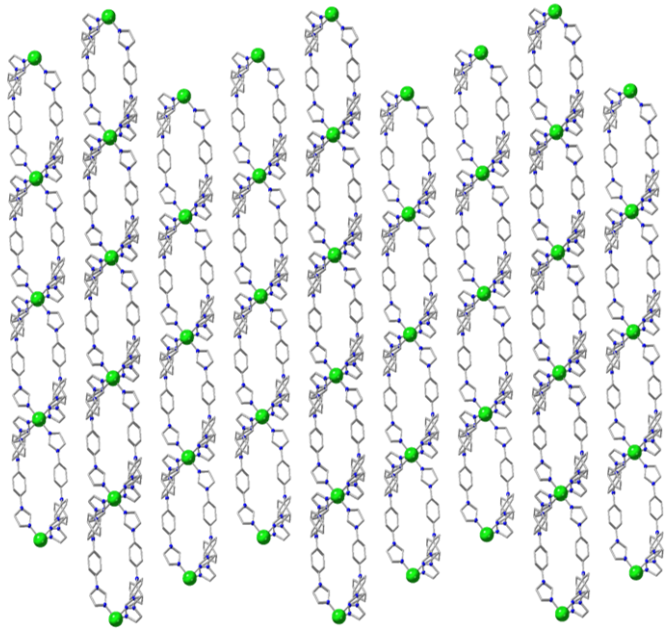

Appendix 3.7. Packing diagram showing construction of a 2D nonplanar sheet like structure of **iMOF-8C**.

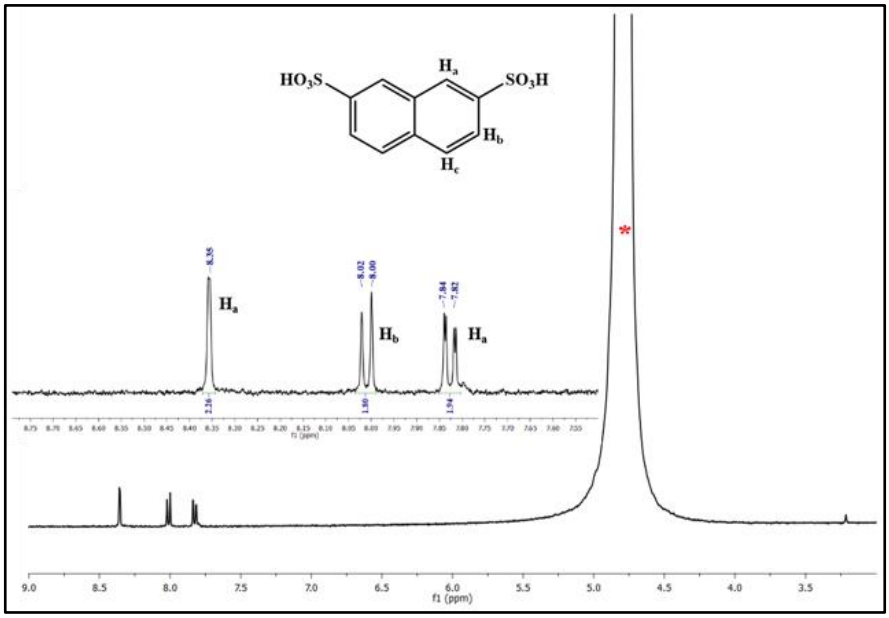

Appendix 3.8. ^{1}H-NMR after digesting **iMOF-8C** in D_3PO_4/D_2O followed by neutralization with NaOD.

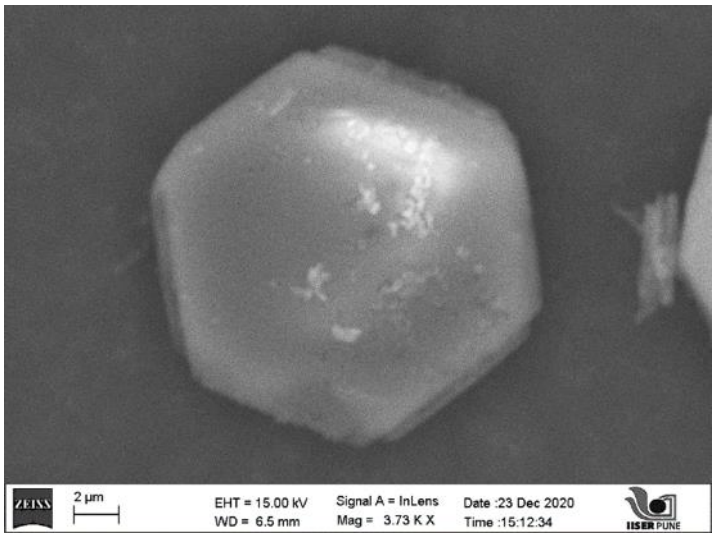

Appendix 3.9. FESEM images of **iMOF-8C** crystals.

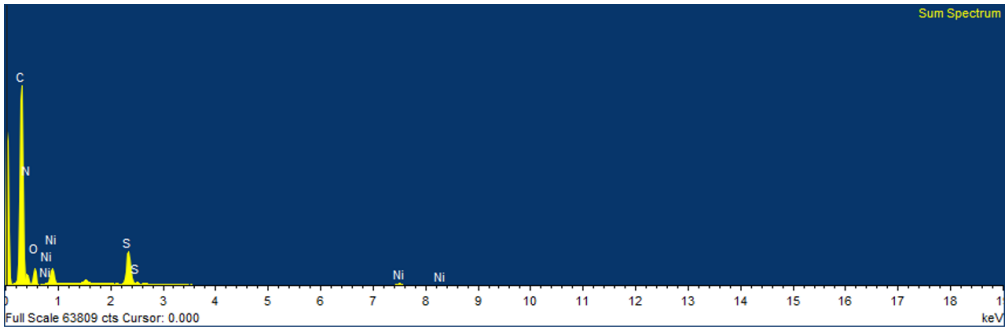

Element	Weight %
C	63.61
N	16.56
O	11.58
S	4.75
Ni	3.50

Appendix 3.10. EDX analysis of **iMOF-8C**.

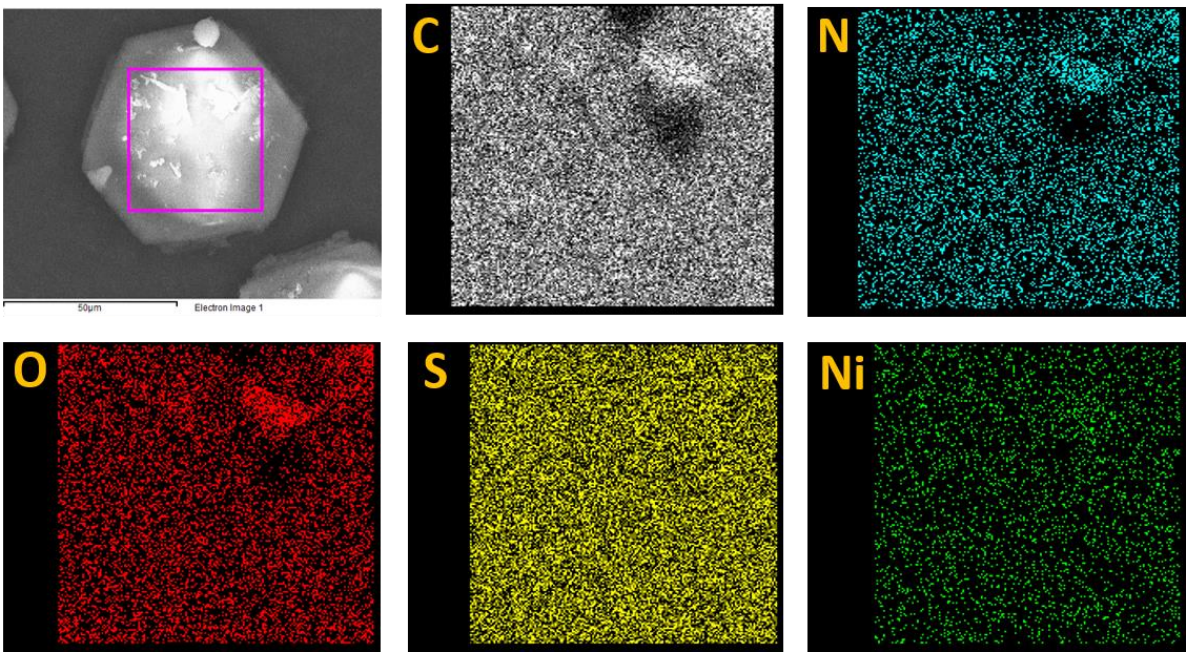

Appendix 3.11. Elemental mapping recorded on **iMOF-8C** crystals.

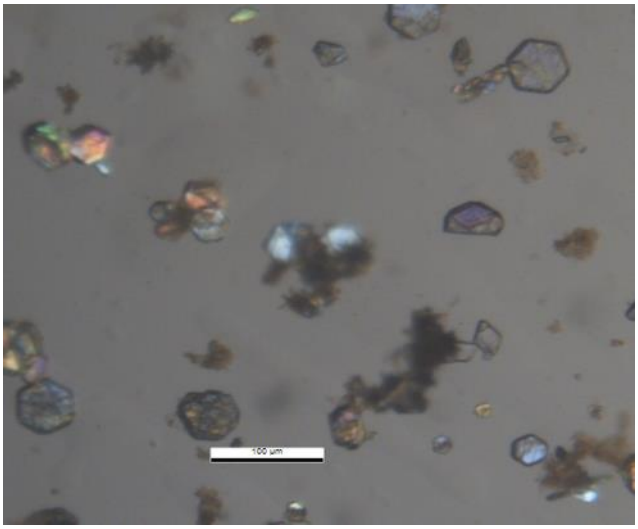

Appendix 3.12. Image of single crystals of **iMOF-8C** after dipped in water for 7 days.

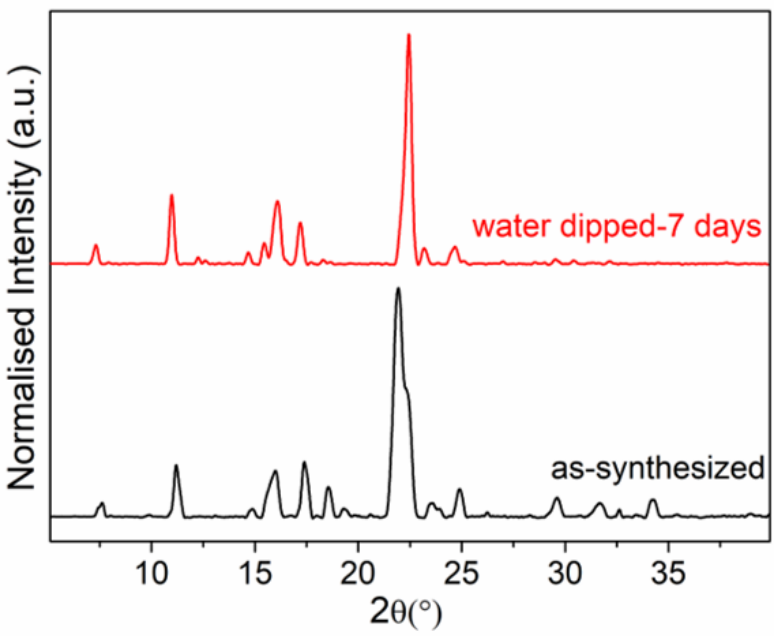

Appendix 3.13. Powder X-ray diffraction patterns of **iMOF-8C**; as-synthesized (black), water dipped (red).

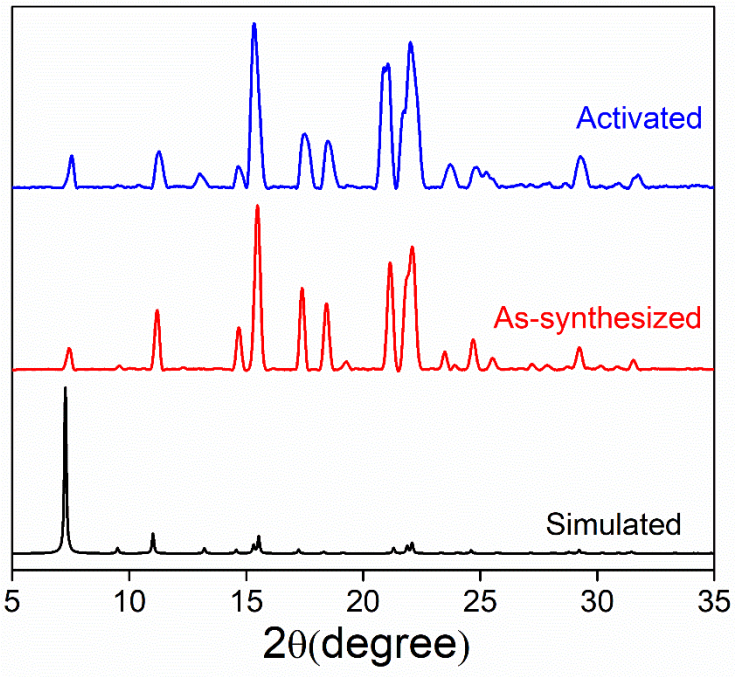

Appendix 3.14. Powder X-ray diffraction patterns of **IPM-MOF-201**; simulated (black), as-synthesized (red), activated (blue).

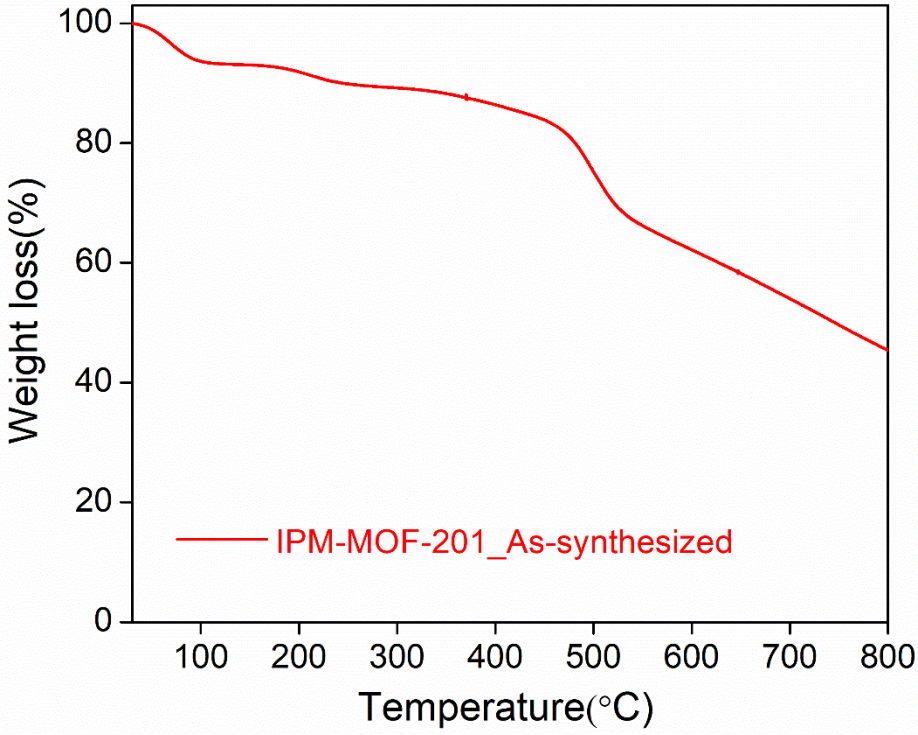

Appendix 3.15. TGA traces for the as-synthesized phase of **IPM-MOF-201**.

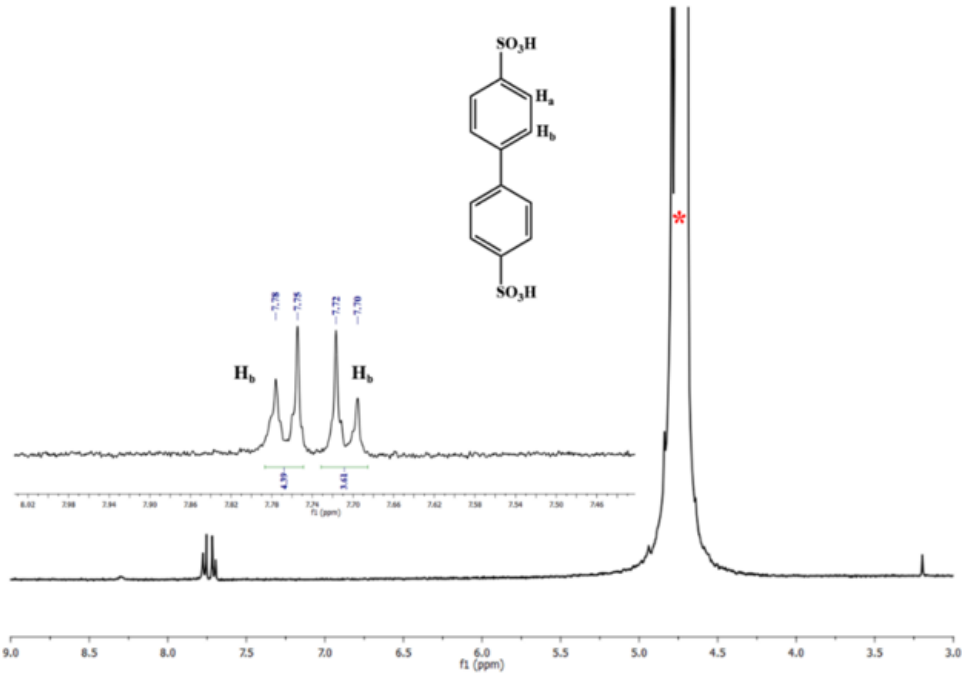

Appendix 3.16. ^{1}H-NMR after digesting **IPM-MOF-201** in D_3PO_4/D_2O followed by neutralization with NaOD.

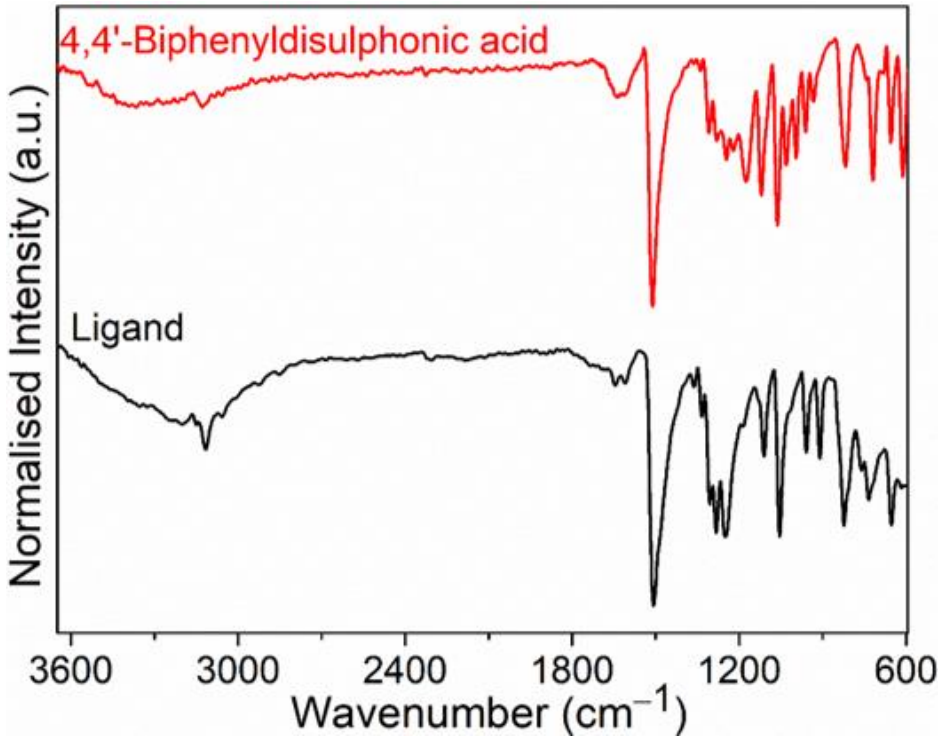

Appendix 3.17. IR spectra of **IPM-MOF-201**.

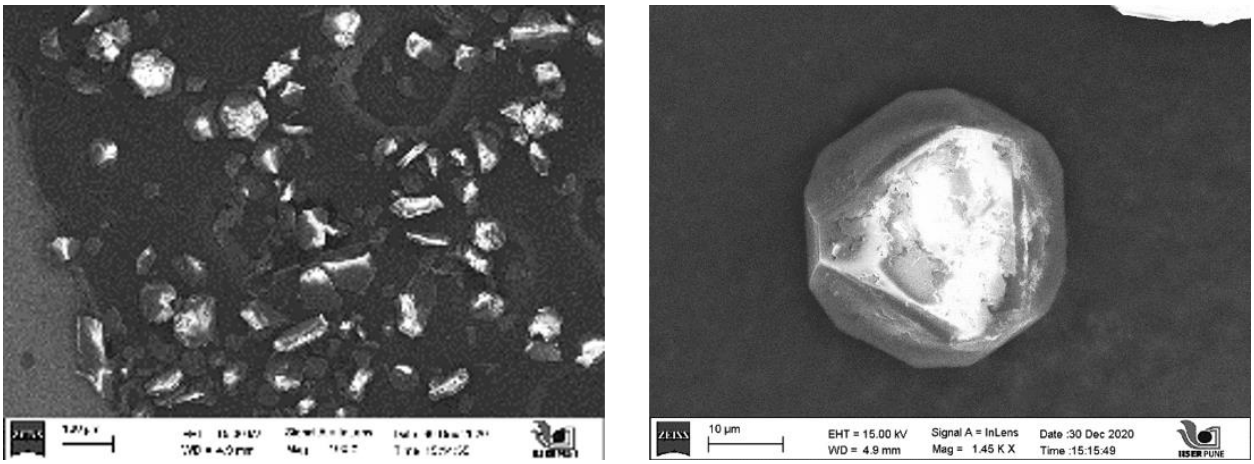

Appendix 3.18. FESEM images of **IPM-MOF-201**.

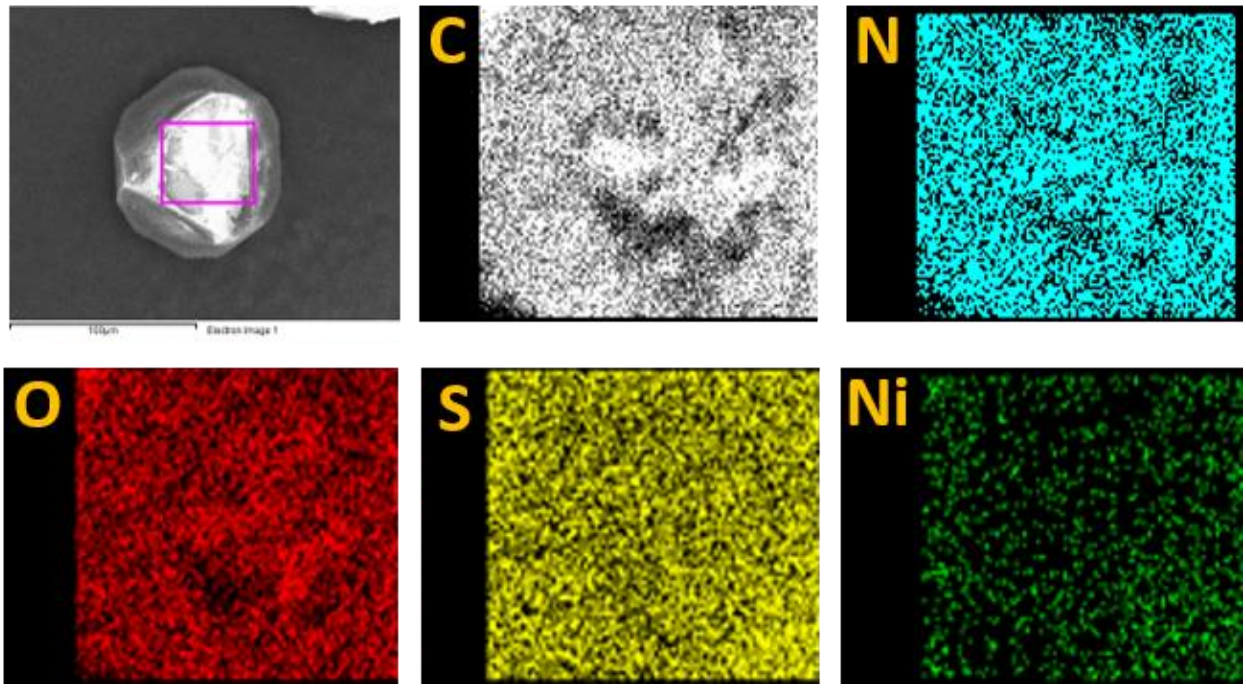

Appendix 3.19. Elemental mapping recorded on **IPM-MOF-201**.

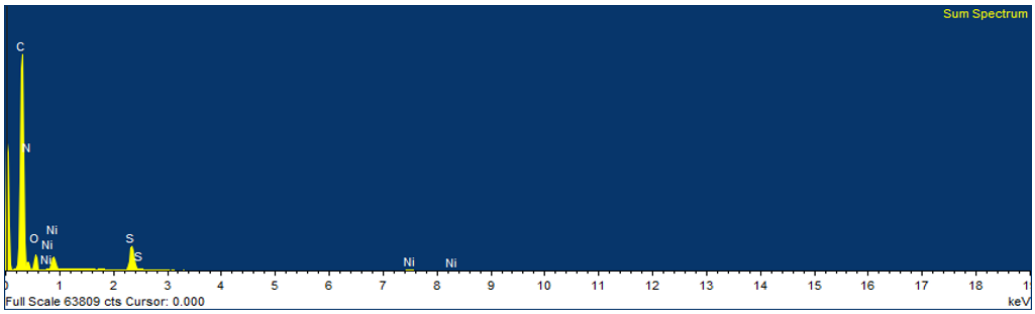

Element	Weight %
C	64.69
N	18.35
O	12.97
S	3.16
Ni	0.82

Appendix 3.20. EDX analysis of **IPM-MOF-201**.

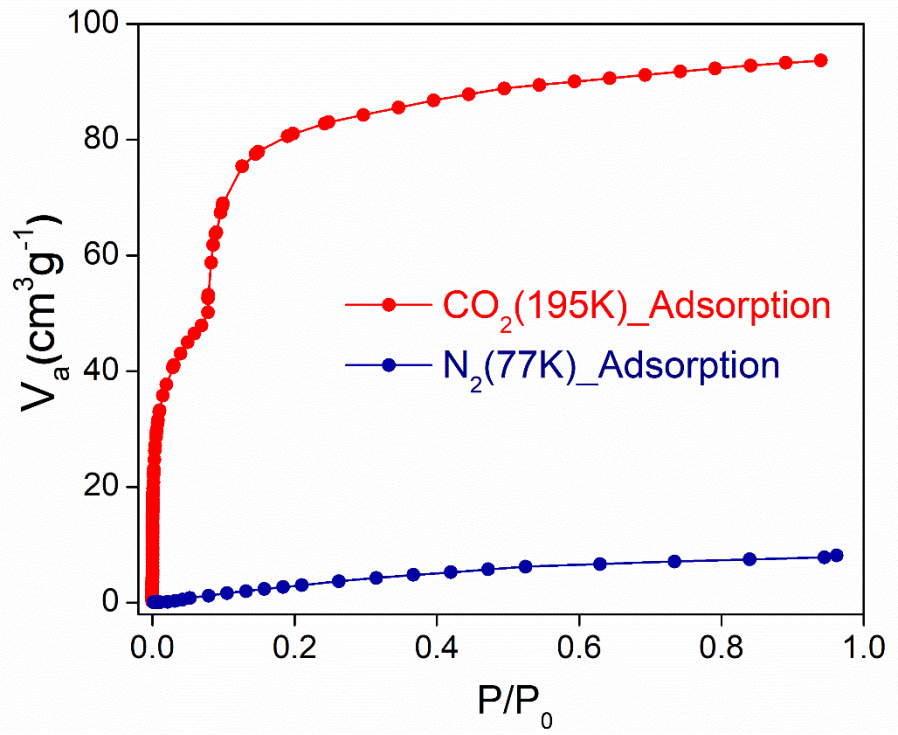

Appendix 3.21. Low temperature adsorption isotherms for **iMOF-8C**.

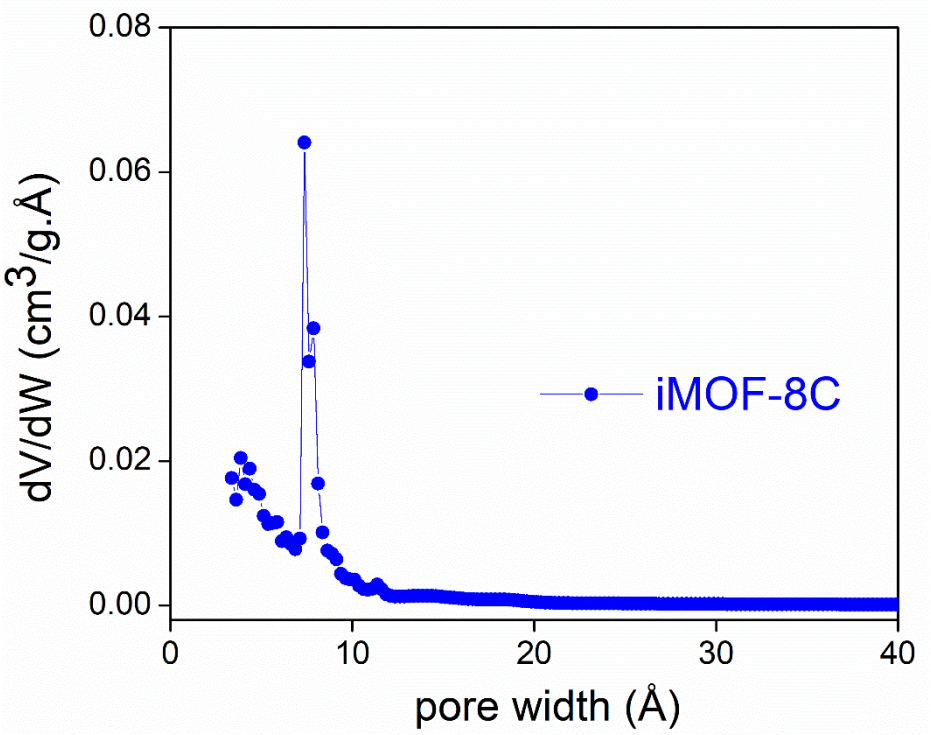

Appendix 3.22. Pore size distribution plots for **iMOF-8C**.

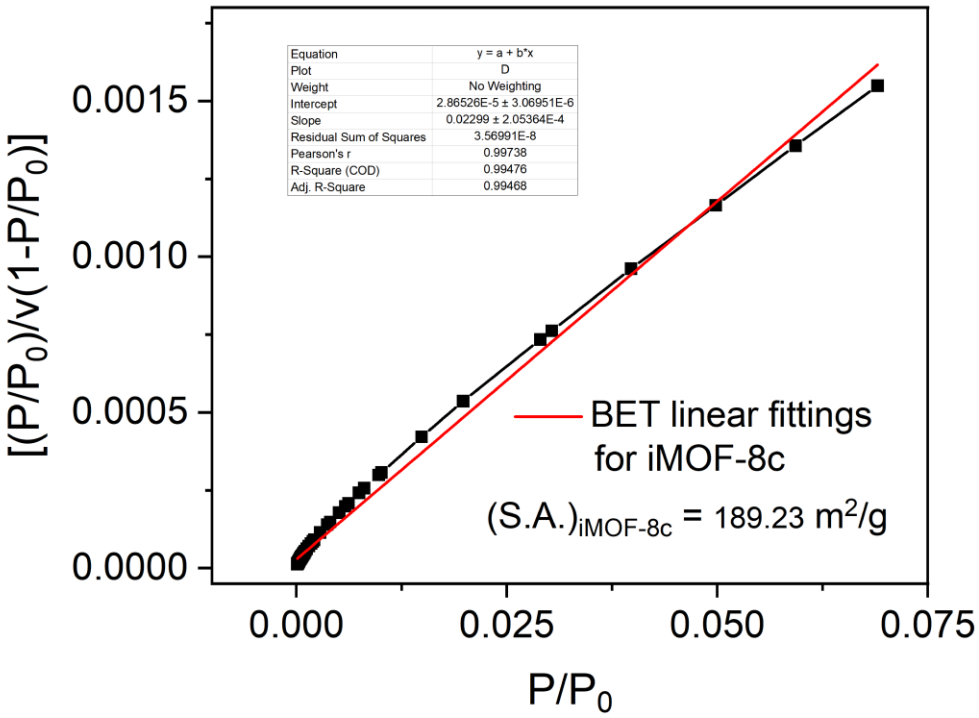

Appendix 3.23. BET surface area plots for **iMOF-8C**.

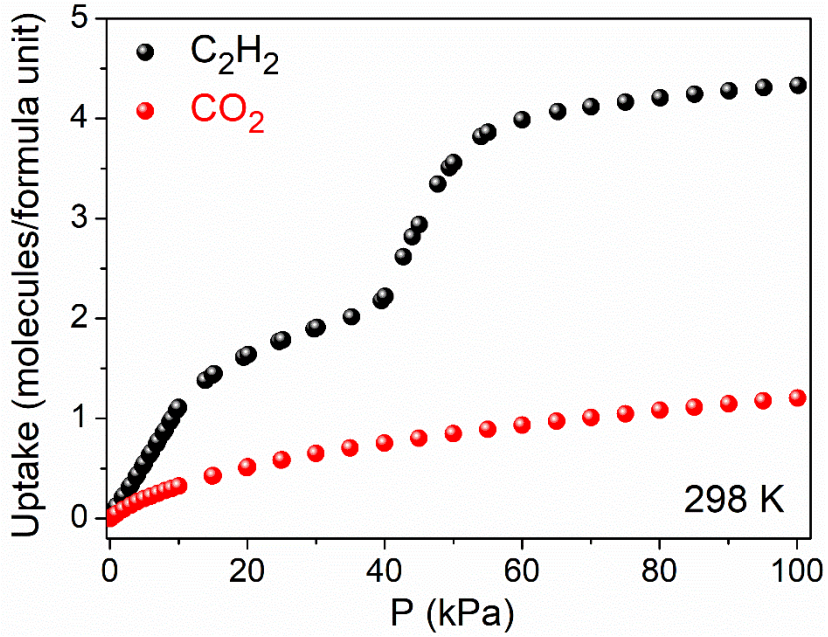

Appendix 3.24. Respective loading of C_2H_2 and CO_2 molecules per unit cell of **iMOF-8C** (colour codes: black – C_2H_2, red – CO_2).

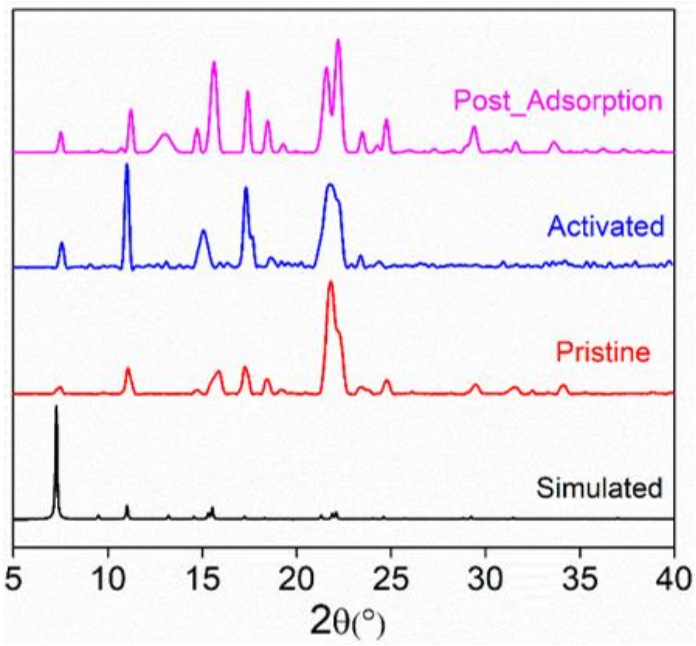

Appendix 3.25. Powder X-ray diffraction patterns of **iMOF-8C**; simulated (black), as-synthesized (red), activated (blue), Post-adsorption (pink).

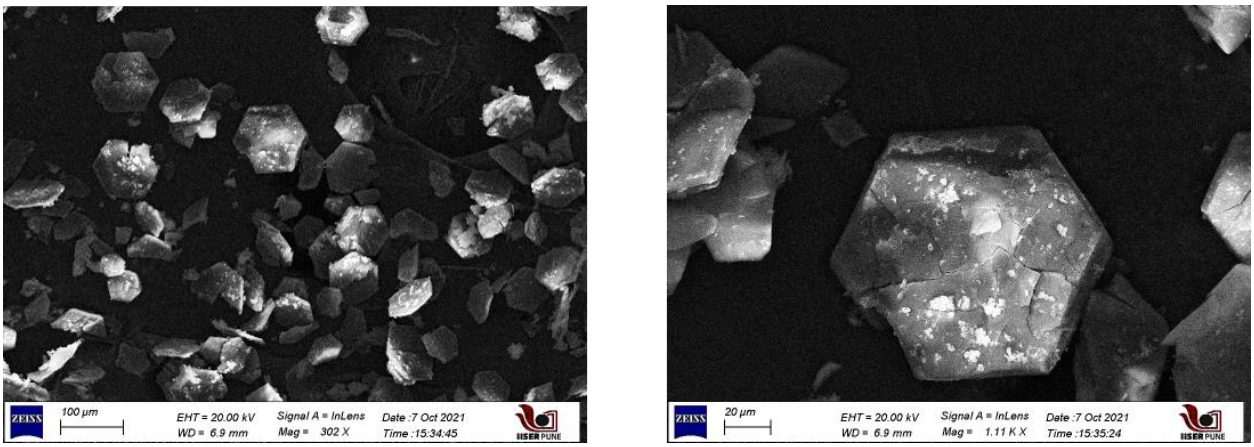

Appendix 3.26. FESEM images of post-sorption **iMOF-8C** crystals.

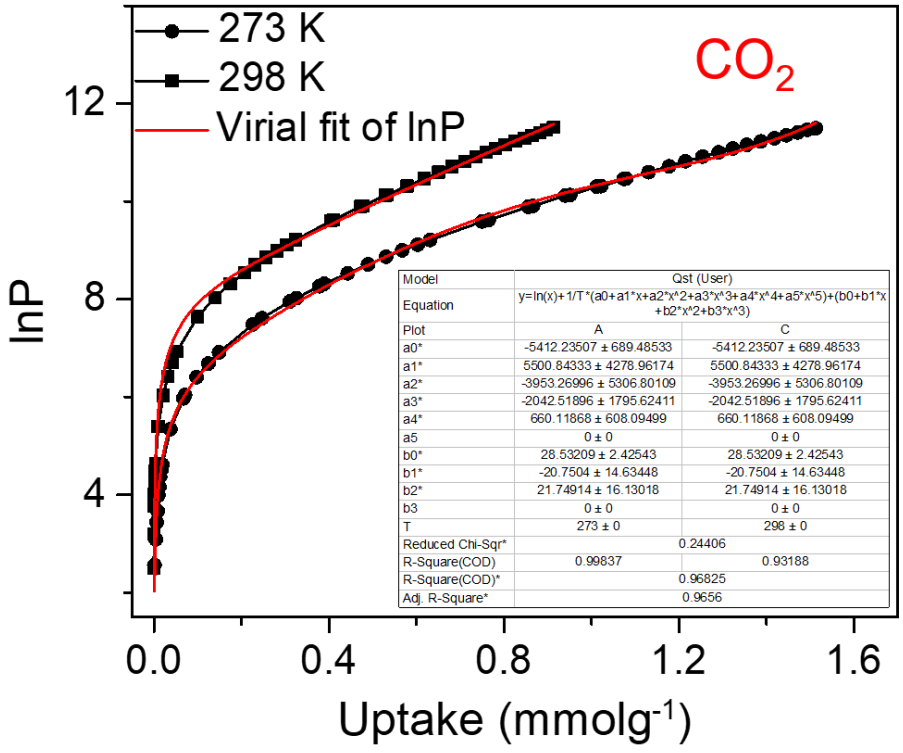

Model	Qst (User)	
Equation	y=ln(x)+1/T*(a0+a1*x+a2*x^2+a3*x^3+a4*x^4+a5*x^5)+(b0+b1*x+b2*x^2+b3*x^3)	
Plot	A	C
a0*	-5412.23507 ± 689.48533	-5412.23507 ± 689.48533
a1*	5500.84333 ± 4278.96174	5500.84333 ± 4278.96174
a2*	-3953.26996 ± 5306.80109	-3953.26996 ± 5306.80109
a3*	-2042.51896 ± 1795.62411	-2042.51896 ± 1795.62411
a4*	660.11868 ± 608.09499	660.11868 ± 608.09499
a5	0 ± 0	0 ± 0
b0*	28.53209 ± 2.42543	28.53209 ± 2.42543
b1*	-20.7504 ± 14.63448	-20.7504 ± 14.63448
b2*	21.74914 ± 16.13018	21.74914 ± 16.13018
b3	0 ± 0	0 ± 0
T	273 ± 0	298 ± 0
Reduced Chi-Sqr*	0.24406	
R-Square(COD)	0.99837	0.93188
R-Square(COD)*	0.96825	
Adj. R-Square*	0.9656	

Appendix 3.27. Fitting of the CO_2 isotherm data for **iMOF-8C** to the virial equation.

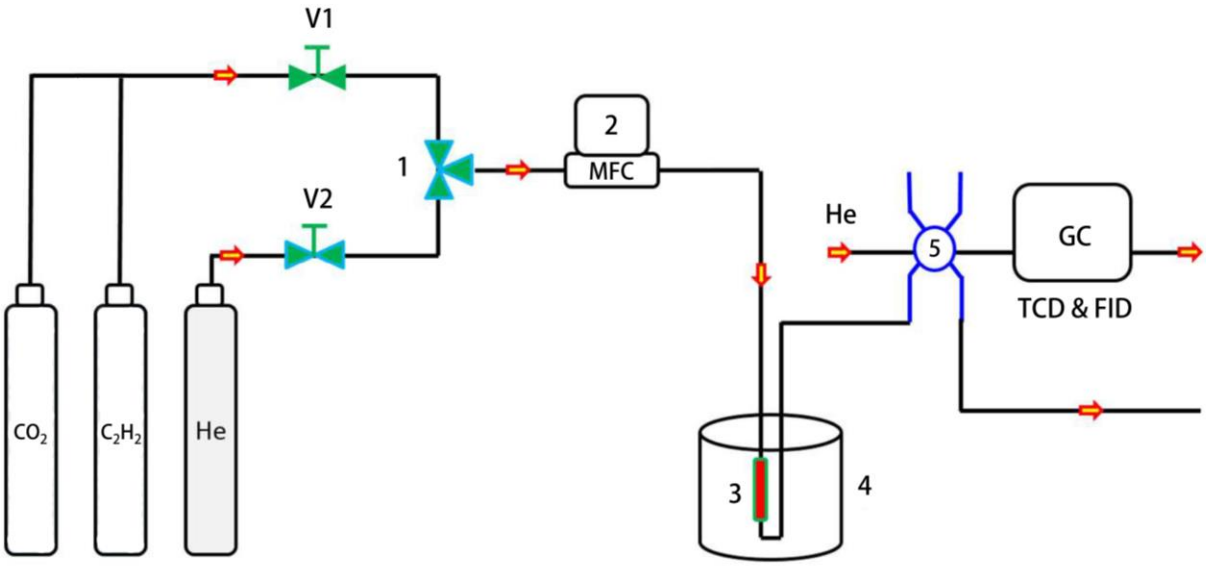

1) 3-way valve; 2) Mass flow controller; 3) Packed MOF column; 4) Water bath; 5) 6-way valve
(TCD: thermal conductivity detector; FID: flame ionisation detector in GC (gas chromatograph; MFC: mass flow controller)

Appendix 3.28. Schematic of gas mixing unit, gravimetric gas uptake analyser and gas separation analyser for breakthrough experiments.

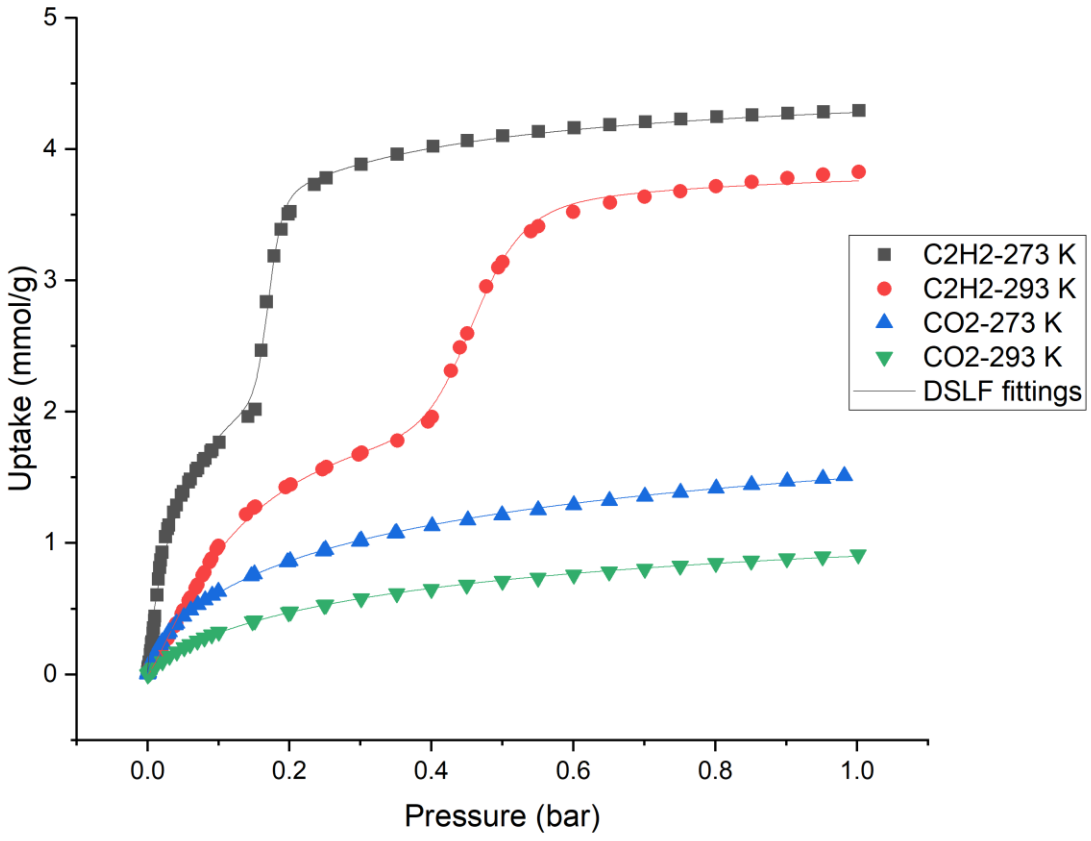

Model	DSLF (User)			
Equation	q1*b1*x^(1/t1)/(1+b1*x^(1/t1))+q2*b2*x^(1/t2)/(1+b2*x^(1/t2))			
Plot	C2H2-273	C2H2-293	CO2-273	CO2-293
q1	3.08952 ± 0.11563	2.27458 ± 0.09384	1.15637 ± --	0.6815 ± --
b1	9.98779 ± 1.33538	13.063 ± 2.54471	1.83923 ± 34953.32023	1.95156 ± 14295.69654
t1	1.17523 ± 0.03736	0.78675 ± 0.03194	1.42908 ± --	1.23406 ± --
q2	1.47044 ± 0.06496	1.64473 ± 0.05448	1.15637 ± --	0.6815 ± --
b2	9.80222E13 ± 1.89739E14	35437.67505 ± 18567.23469	1.83923 ± 34950.65555	1.95157 ± 14292.93341
t2	0.05489 ± 0.00327	0.07393 ± 0.00373	1.42904 ± --	1.23398 ± --
Reduced Chi-Sqr	0.00411	0.00117	1.29906E-4	4.63302E-5
R-Square (COD)	0.99852	0.9994	0.99958	0.99962
Adj. R-Square	0.99839	0.99934	0.99954	0.99957

Appendix 3.29. Dual-Site Langmuir Freundlich fits of the iMOF-8C single gas isotherms at 273K and 298 K.

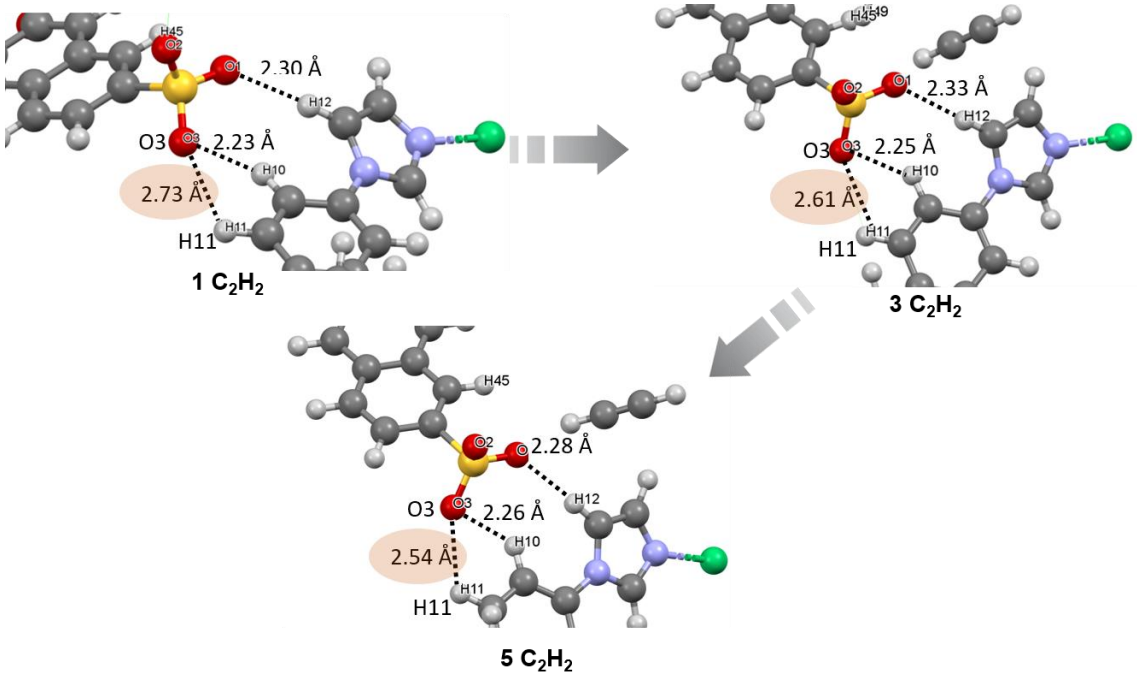

Appendix 3.30. Structural change due to gradual increase of C_2H_2 molecules in **iMOF-8C** from 1 to 3 to 5 molecules per unit cell of iMOF-8C.

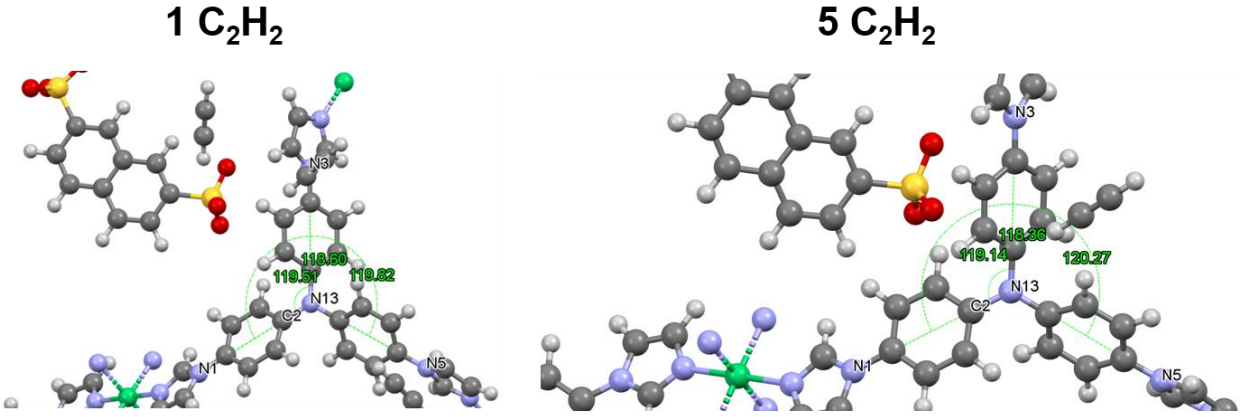

Appendix 3.31. Tortion angle change in iMOF-8C framework due to gradual increase of C_2H_2 molecules from 1 to 3 to 5 molecules per unit cell of iMOF-8C.

Optimised Structure	Lattice Parameters		
	a	***b***	***c***
iMOF-8C	12.51042	12.01905	11.59511
iMOF-8C@1-C_2H_2	12.5864	11.68315	11.82509
iMOF-8C@3-C_2H_2	12.33373	12.14429	11.88847
iMOF-8C@6-C_2H_2	12.62497	12.96245	11.13519
iMOF-8C@8-C_2H_2	12.43898	12.05462	11.43202

Appendix 3.32. Comparison of lattice parameters of simulated iMOF-8C structure with incremental loading of C_2H_2.

Table S1. Summary of adsorption uptakes, adsorption enthalpies (Q_{st}) and IAST selectivity at 298K 1 bar for 1:1 (v/v) C_2H_2/CO_2) for C_2H_2 selective sorbents.

Type of Adsorbent	Adsorbent, network dimensionality (nD)	S_{BET} / m^2g^{-1}	Pore size (Å)	C_2H_2 uptake at 1 bar, mmol g^{-1}	CO_2 uptake at 1 bar, mmol g^{-1}	$Q_{st}(C_2H_2)$ at low loading, kJ mol^{-1}	S_{AC}	Ref
Ionic	**iMOF-8C, 2D**	330	4.6 × 4.5; 5.3 × 5.4	1.2	0.68	38	10	This work
	iMOF-6C, 2D	330	4.6 × 4.5; 5.3 × 5.4	1.2	0.68	38	8	79
	iMOF-5C, 2D	242	4.6 × 4.5; 5.3 × 5.4	1.5	0.71	35.5	6	79
	iMOF-7C, 2D	109	4.6 × 4.5; 5.3 × 5.4	0.7	0.61	35	4	79
	JCM-1, 3D	550	12.5 × 3.9	3.3	1.7	36.9	10	80
Neutral	**UTSA-300a, 2D**	311	2.4 × 3.3	3.3	0.2	57.6	10^3	81
	ZJU-74a, 3D	64	3.6 × 3.8	3.83	3.08	44.5	36.5	82
	NKMOF-1-Ni, 3D	382	5.8 × 5.8	2.7	2.3	60.3	30	83
	sql-16-Cu-NO_3-α′	179	4.6 × 5.0	1.33	0.38	38.6	27.8	84
	FeNi-M'MOF, 3D	383	4.15 × 4.27; 3.94 × 4.58	4.29	2.72	27	24	85
	$[Ni_3(HCOO)_6]_n$, 3D	289	4.3 × 4.3	2.4	1.6	40.9	22	86
	TIFSIX-17-Ni	237.6	3.59 × 3.59	3.135	2.935×10^{-13}	38.8	20.9	87
	TCuCl, 3D	167	3.69 × 3.69	3.0	2.0	41	16.9	88
	pacs-CoMOF-2a	196	5.8, 6.6	5.40	2.81	34.2	13	89
	SIFSIX-17-Ni	229.2	3.51 × 3.51	3.303	1.293	37.0	11.7	87
	ZJU-40a, 3D	2858	10.2, 9.6 × 22.3	9.64	3.34	34.5	11.5	90
	Co-MOF, 3D	973	NM	6.47	2.68	33	11	91
	ZJUT-2a, 3D	350	3.2 × 3.2	3.4	2.2	41.5	10	92
	TCuBr, 3D	173	3.59 × 3.59	2.8	2.0	36.6	9.5	88
	UTSA-74a, 3D	830	8.0 × 8.0	4.8	3.2	31	9	93
	SNNU-150-Al, 3D	NM	8.5	4.33	1.98	29	7.27	94

	UTSA-83a, 2D	70	3.5 × 6.6	0.53	0.17	24.4	6.2	95
	MUF-17, 3D	247	4.7 × 4.8	2.7	2.2	49.5	6	96
	CPM-107op, 3D	319	NM	4.35	1.55	37	5.7	97
	ZJNU-13, 3D	1352	6.8, 11.8	5.28	3.92	33.5	5.64	98
	TCuI, 3D	250	3.66 × 3.66	2.2	1.6	38.4	5.3	90
	UPC-110, 3D	1384.3	6	3.27	1.08	24.6	5.1	99
	JXNU-5, 3D	406	4.6, 6.7	2.5	1.55	32.9	5	100
	SNNU-45, 3D	1006	4.5	5.98	4.33	40	4.5	101
	UTSA-220, 3D	577	4.5-5.5; 3.1-4.8	3.40	3.38	29	4.4	102
	FJU-90a, 3D	1572	5.4 × 5.1	8.0	4.6	25.1	4.3	103
	$Cu_2(ade)_2(PA)_2$, 3D	401	2 × 6	2.19	1.5	26.8	4.2	104
	Hex-Zn-MOF 1a, 3D	770.3	8.6, 9.8	3.18	2.21	39	4	105
	mot-Cu(Br-BDC) MOF, 3D	303	4.2 × 4.7; 12 × 24.1	1.53	1.08	26.1	3.9	106
	Cu−CPAH, 3D	880	6-9	5.88	3.93	35.4	3.6	107
	UPC-200(Al)-F-BIM, 3D	2212.8	7 × 11	6.2	2.5	20.5	3.15	108
	JNU-1, 3D	818	16.3 × 6.6	2.7	2.2	13	3	109
	Cu-tztp MOF 1a, 3D	798.9	5.4-8.6	5.02	3.35	38.3	2.7	110
	Zn-MOF-74, 3D	1360	11 × 11	5.5	5.4	22.1	2	104

Table S9. Crystallographic data for **iMOF-8C**.

Crystal data	
Chemical formula	$C_{54}H_{42}N_{14}Ni$
M_r	993.78
Crystal system, space group	Trigonal, *R-3:H*
Temperature (K)	100(2) K
a, *b*, *c* (Å)	16.075(3), 16.075(3), 24.907(6)
V (Å^3)	5574(3)
Z	3
Radiation type	Mo *K*α
μ (mm^{-1})	0.30
Crystal size (mm)	0.17 × 0.12 × 0.10
Data collection	
Diffractometer	Bruker *APEX3* Photon 100 CMOS chip
Absorption correction	Multi-scan multi-scan absorption correction
Theta range for data collection	2.194 to 25.238°.
Index ranges	-19<=h<=19, -18<=k<=19, -29<=l<=29
Reflections collected	43930
Independent reflections	2239 [R(int) = 0.1411]
Completeness to theta = 25.238°	99.2 %
Absorption correction	Semi-empirical from equivalents
Refinement method	Full-matrix least-squares on F^2
Data / restraints / parameters	2239 / 18 / 105
Goodness-of-fit on F^2	1.859
Final R indices [I>2sigma(I)]	R1 = 0.1692, wR2 = 0.4593
R indices (all data)	R1 = 0.2308, wR2 = 0.4928
Extinction coefficient	n/a
Largest diff. peak and hole	1.294 and -0.774 e.Å^{-3}

Computer programs: Bruker *APEX3*, Bruker *SAINT*, *SHELXT* 2014/5 (Sheldrick, 2014), *SHELXL2018*/1 (Sheldrick, 2018), Bruker *SHELXTL*.

3.6 References

[1] S. Mukherjee, D. Sensharma, K.-J. Chen and M. J. Zaworotko, *Chem. Commun.*, **2020**, 56, 10419--10441.

[2] S. Kitagawa, Angew. Chem., Int. Ed., **2015**, 54, 10686–10687.

[3] D. S. Sholl and R. P. Lively, Nature, **2016**, 532, 435–437.

[4] T. Ren, M. Patel, K. Blok, *Energy* **2006**, *31*, 425−451.

[5] Y. L. Peng, T. Pham, P. Li, T. Wang, Y. Chen, K. J. Chen, K. A. Forrest, B. Space, P. Cheng, M. J. Zaworotko, Z. Zhang, *Angew. Chem. Int. Ed.* **2018**, *57*, 10971–10975.

[6] P. Pässler, W. Hefner, K. Buckl, H. Meinass, H.-J. Wernicke, G. Ebersberg, R. Müller, J. Bässler, H. Behringer, D. Mayer, in *Ullmann's Encyclopedia of Industrial Chemistry, Wiley-VCH Verlag GmbH & Co. KGaA*, **2000.**

[7] Z. Bao, G. Chang, H. Xing, R. Krishna, Q. Ren and B. Chen, Energy Environ. Sci., 2016, 9, 3612–3641.

[8] D. G. Madden, D. O'Nolan, K.-J. Chen, C. Hua, A. Kumar, T. Pham, K. A. Forrest, B. Space, J. J. Perry and M. Khraisheh, Chem. Commun., 2019, 55, 3219–3222.

[9] W.-G. Cui, T.-L. Hu and X.-H. Bu, Adv. Mater., 2020, 32, 1806445.

[10] T. Ren, M. K. Patel and K. Blok, Energy, 2008, 33, 817–833.

[11] S. Dutta, S. Mukherjee, O. T. Qazvini, A. K. Gupta, S. Sharma, D. Mahato, R. Babarao and S. K. Ghosh, Angew. Chem. Int. Ed. 2022, 61, e202114132.

[12] S. Sharma, S. Mukherjee, A. V. Desai, M. Vandichel, G. K. Dam, A. Jadhav, G. Kociok-Köhn, M. J. Zaworotko and S. K. Ghosh, Chem. Mater. 2021, 33, 14, 5800–5808.

[13] S. Kitagawa, R. Kitaura and S.-I. Noro, Angew. Chem., Int. Ed., 2004, 43, 2334-2375.

[14] H.-C. Zhou, J. R. Long and O. M. Yaghi, Chem. Rev., 2012, 112, 673.

[15] H. Furukawa, K. E. Cordova, M. O'Keeffe and O. M. Yaghi, Science, 2013, 341, 974.

[16] J.-R. Li, R. J. Kuppler, H.-C. Zhou, Chem. Soc. Rev. 2009, 38, 1477.

[17] D. S. Sholl, R. P. Lively, Nature 2016, 532, 435.

[18] Materials for Separation Technology: Energy and Emission Reduction Opportunities 1218755, O. R. N. Laboratory, Oak Ridge, TN 2005.

[19] R. B. Eldridge, Ind. Eng. Chem. Res. 1993, 32, 2208.

[20] R. L. Burns, W. J. Koros, J. Membr. Sci. 2003, 211, 299.

[21] R. Faiz, K. Li, Desalination 2012, 287, 82.

[22] a) R. Schoellner, U. Mueller, *Adsorpt. Sci. Technol.* **1986**, *3*, 167.

[23] V. R. Choudhary, S. Mayadevi, A. P. Singh, *J. Chem. Soc., Faraday Trans.* **1995**, *91*, 2935.

[24] J. Padin, R. T. Yang, *Chem. Eng. Sci.* **2000**, *55*, 2607.

[25] A. Jayaraman, R. T. Yang, C. L. Munson, D. Chinn, *Ind. Eng. Chem. Res.* **2001**, *40*, 4370.

[26] *Adsorption and Diffusion*, Springer, Berlin **2008**.

[27] O. M. Yaghi, G. Li and H. Li, Nature, 1995, 378, 703–706.

[28] H. Li, M. Eddaoudi, T. L. Groy and O. M. Yaghi, J. Am. Chem. Soc., 1998, 120, 8571–8572.

[29] M. Kondo, T. Yoshitomi, K. Seki, H. Matsuzaka and S. Kitagawa, Angew. Chem., Int. Ed. Engl., 1997, 36, 1725–1727.

[30] B. C. Hughes, C. R. Murdock and D. M. Jenkins, Inorg. Chem. Front., 2015, 2, 1001–1005.

[31] M. T. Wharmby, J. P. S. Mowat, S. P. Thompson and P. A. Wright, J. Am. Chem. Soc., 2011, 133, 1266–1269.

[32] O. Delgado Friedrichs, M. O'Keeffe and O. M. Yaghi, Solid State Sci., 2003, 5, 73–78.

[33] M. Eddaoudi, J. Kim, N. Rosi, D. Vodak, J. Wachter, M. O'Keeffe and O. M. Yaghi, Science, 2002, 295, 469–472.

[34] H. Furukawa, Y. B. Go, N. Ko, Y. K. Park, F. J. Uribe-Romo, J. Kim, M. O'Keeffe and O. M. Yaghi, Inorg. Chem., 2011, 50, 9147–9152.

[35] C. Orellana-Tavra, E. F. Baxter, T. Tian, T. D. Bennett, N. K. H. Slater, A. K. Cheetham and D. Fairen-Jimenez, Chem. Commun., 2015, 51, 13878–13881.

[36] A. Karmakar, A. V. Desai, S. K. Ghosh, *Coord. Chem. Rev.* **2016**, *307*, 313–341.

[37] Y.-Q. Chen, G.-R. Li, Z. Chang, Y.-K. Qu, Y.-H. Zhang, X.-H. Bu, *Chem. Sci.* **2013**, *4*, 3678–3682.

[38] S. Dutta, S. Let, S. Sharma, D. Mahato, S. K. Ghosh, *Chem. Rec*. **2021**, *21*, 1666–1680.

[39] S. Sharma, S. Dutta, G. Dam, S. K. Ghosh, *Chem. Asian J.* **2021**, *16*, 2569–2587.

[40] S. Dutta, S. Let, M. M. Shirolkar, A. V. Desai, P. Samanta, S. Fajal, Y. D. More, S. K. Ghosh, *Dalton Trans*. **2021**, *50*, 10133–10141.

[41] S.-S. Bao, G. K.H. Shimizu, L.-M. Zheng, *Coord. Chem. Rev.* **2019** *378*, 577–594.

[42] H. He, L. Hashemi, M.-L. Hua, A. Morsali, *Coord. Chem. Rev.* **2018**, *376*, 319–347.

[43] C. Healy, L. Hermanspahn, P. E. Kruger, *Coord. Chem. Rev.* **2021**, *432*, 213756.

[44] H. Fei, D. L. Rogow, S. R. J. Oliver, *J. Am. Chem. Soc.* **2010**, *132*, 7202–7209.

[45] A. Schoedel, L. Wojtas, S. P. Kelley, R. D. Rogers, M. Eddaoudi, M. J. Zaworotko, *Angew. Chem. Int. Ed.* **2011**, *50*, 11421–11424.

[46] J.-P. Ma, Y. Yu, Y.-B. Dong, *Chem. Commun.* **2012**, *48*, 2946−2948.

[47] B. Manna, B. Joarder, A. V. Desai, A. Karmakar, S. K. Ghosh, *Chem. Eur. J.* **2014**, *20*, 12399–12404.

[48] D.-m. Chen, W. Shi, P. Cheng, *Chem. Commun.* **2015**, *51*, 370–372.

[49] S. Sharma, A. V. Desai, B. Joarder, S. K. Ghosh, *Angew. Chem. Int. Ed.* **2020**, *59*, 7788–7792.

[50] B.-Q. Song, X.-L. Wang, Y.-T. Zhang, X.- S. Wu, H.-S. Liu, K.-Z. Shao, Z.-M. Su, *Chem. Commun.* **2015**, *51*, 9515–9518.

[51] G. Brunet, K. Robeyns, R. P. S. Huynh, J.-B. Lin, S. P. Collins, G. A. Facey, G. K. H. Shimizu, T. K. Woo, M. Murugesu, *ACS Appl. Mater. Interfaces* **2019**, *11*, 3181−3188.

[52] W. P. Lustig, S. Mukherjee, N. D. Rudd, A. V. Desai, J. Li, S. K. Ghosh, *Chem. Soc. Rev.* **2017**, *46*, 3242−3285.

[53] A. V. Desai, A. Roy, P. Samanta, B. Manna and S. K. Ghosh, *iScience*, 2018, **3**, 21-30.

[54] SAINT Plus, version 7.03; Bruker AXS Inc.: Madison, WI, 2004.

[55] G. M. Sheldrick, SHELXTL, Reference Manual, version 5.1; Bruker AXS Inc.: Madison, WI, 1997.

[56] G. M. Sheldrick, Acta. Crystallogr., Sect. A 2008, 64, 112-122.

[57] L. Farrugia, WinGX, version 1.80.05; University of Glasgow: Glasgow, Scotland, 2009.

[58] A. L. Spek, PLATON, a Multipurpose Crystallographic Tool; Utrecht University: Utrecht, The Netherlands, 2005.

[59] A. L. Spek, J. Appl. Crystallogr. 2003, 36, 7-13.

[60] O. T. Qazvini, S. Fatemi, Sep. Purif. Technol. 2015, 139, 88-103.

[61] M. Mehdipour, S. Fatemi, Sep. Sci. Technol. 2012, 47, 1199-1212.

[62] M. H. Chahbani, D. Tondeur, Sep. Purif. Technol. 2000, 20, 185-196.

[63] O. T. Qazvini, R. Babarao, Z.-L. Shi, Y.-B. Zhang, S. G. Telfer, J. Am. Chem. Soc. 2019, 141, 5014-5020.

[64] D. D. Do, Adsorption analysis: equilibria and kinetics. Imperial college press London: 1998; Vol. 2

[65] R. B. Bird, Transport phenomena. Applied Mechanics Reviews 2002, 55, R1-R4

[66] R. Perry, D. Green, J. Maloney, Chemical engineers handbook. 8th edition ed.; The McGraw Hill Companies, Inc: 2008

[67] S. Farooq, D. M. Ruthven, Chem. Eng. Sci. 1990, 45, 107-115

[68] L. Joss, M. Gazzani, M. Hefti, D. Marx, M. Mazzotti, Ind. Eng. Chem. Res. 2015, 54, 3027-3038

[69] A. D. Ebner, J. A. Ritter, AIChE J. 2002, 48 (8), 1679-1691

[70] Yang, R. T., Gas separation by adsorption processes. Butterworth-Heinemann: 2013.

[71] Kiusalaas, J., Numerical methods in engineering with Python 3. Cambridge university press: 2013.

[72] Dassault Systèmes BIOVIA, Material Studio, San Diego: Dassault Systèmes, 2019.

[73] A. K. Rappe, C. J. Casewit, K. S. Colwell, W. A. Goddard, W. M. Skiff, J. Am. Chem. Soc. 1992, 114, 10024-10035.

[74] G. Kresse, J. Hafner, Phys. Rev. B 1993, 48, 13115-13118.

[75] S. Grimme, S. Ehrlich, L. J. Goerigk, Comp. Chem. 2011, 32, 1456-1465.

[76] J. P. Perdew, K. Burke, M. Ernzerhof, Phys. Rev. Lett. 1996, 77, 3865-3868.

[77] G. Kresse, D. Joubert, Phys. Rev. B 1999, 59, 1758-1775.

[78] A. Nuhnen and C. Janiak, Dalton Trans., 2020, 49, 10295–10307.

[79] S. Dutta, S. Mukherjee, O. T. Qazvini, A. K. Gupta, S. Sharma, D. Mahato, R. Babarao and S. K. Ghosh, Angew. Chem. Int. Ed. 2022, 61, e202114132.

[80] J. Lee, C. Y. Chuah, J. Kim, Y. Kim, N. Ko, Y. Seo, K. Kim, T. H. Bae, E. Lee, Angew. Chem. Int. Ed. 2018, 57, 7869-7873.

[81] R.-B. Lin, L. Li, H. Wu, H. Arman, B. Li, R.-G. Lin, W. Zhou, B. Chen, J. Am. Chem. Soc. 2017, 139, 8022-8028.

[82] J. Pei, K. Shao, J.-X. Wang, H.-M. Wen, Y. Yang, Y. Cui, R. Krishna, B. Li, G. Qian, Adv. Mater. 2020, 32, 1908275.

[83] Y. L. Peng, T. Pham, P. Li, T. Wang, Y. Chen, K. J. Chen, K. A. Forrest, B. Space, P. Cheng, M. J. Zaworotko, Z. Zhang, Angew. Chem. Int. Ed. 2018, 57, 10971-10975.

[84] N. Kumar, S. Mukherjee, A. A. Bezrukov, M. Vandichel, M. Shivanna, D. Sensharma, A. Bajpai, V. Gascón, K.-i. Otake, S. Kitagawa, M. J. Zaworotko, SmartMat. 2020, 1, e1008.

[85] J. Gao, X. Qian, R.-B. Lin, R. Krishna, H. Wu, W. Zhou, B. Chen, Angew. Chem. Int. Ed. 2020, 59, 4396-4400.

[86] L. Zhang, K. Jiang, J. Zhang, J. Pei, K. Shao, Y. Cui, Y. Yang, B. Li, B. Chen, G. Qian, ACS Sustain. Chem. Eng. 2019, 7, 1667-1672.

[87] S. Mukherjee, N. Kumar, A. A. Bezrukov, K. Tan, T. Pham, K. A. Forrest, K. A. Oyekan, O. T. Qazvini, D. G. Madden, B. Space, M. J. Zaworotko, Angew. Chem. Int. Ed. 2021, 60, 10902-10909.

[88] S. Mukherjee, Y. He, D. Franz, S.-Q. Wang, W.-R. Xian, A. A. Bezrukov, B. Space, Z. Xu, J. He, M. J. Zaworotko, Chem. Eur. J. 2020, 26, 4923-4929.

[89] D.-M. Chen, C.-X. Sun, N.-N. Zhang, H.-H. Si, C.-S. Liu, M. Du, Inorg. Chem. 2018, 57, 2883-2889.

[90] H.-M. Wen, H. Wang, B. Li, Y. Cui, H. Wang, G. Qian, B. Chen, Inorg. Chem. 2016, 55, 7214-7218. [84] D.-M. Chen, X.-H. Liu, J.-Y. Tian, J.-H. Zhang, C.-S. Liu, M. Du, Inorg. Chem. 2017, 56, 14767-14770.

[91] H.-M. Wen, C. Liao, L. Li, L. Yang, J. Wang, L. Huang, B. Li, B. Chen and J. Hu, Chem. Commun. 2019, 55, 11354-11357.

[92] F. Luo, C. Yan, L. Dang, R. Krishna, W. Zhou, H. Wu, X. Dong, Y. Han, T.-L. Hu, M. O'Keeffe, L. Wang, M. Luo, R.-B. Lin, B. Chen, J. Am. Chem. Soc. 2016, 138, 5678-5684.

[93] H.-J. Lv, Y.-P. Li, Y.-Y. Xue, Y.-C. Jiang, S.-N. Li, M.-C. Hu, Q.-G. Zhai, Inorg. Chem. 2020, 59, 4825-4834.

[94] H. Cui, S. Chen, H. Arman, Y. Ye, A. Alsalme, R.-B. Lin, B. Chen, Inorg. Chim. Acta 2019, 495, 118938.

[95] O. T. Qazvini, R. Babarao, S. G. Telfer, Chem. Mater. 2019, 31, 4919-4926.

[96] H. Yang, T. X. Trieu, X. Zhao, Y. Wang, Y. Wang, P. Feng and X. Bu, Angew. Chem. Int. Ed. 2019, 58, 11757-11762.

[97] T. Xu, Z. Jiang, P. Liu, H. Chen, X. Lan, D. Chen, L. Li, Y. He, ACS Appl. Nano Mater. 2020, 3, 2911-2919.

[98] W. Fan, X. Wang, X. Liu, B. Xu, X. Zhang, W. Wang, X. Wang, Y. Wang, F. Dai, D. Yuan, D. Sun, ACS Sustain. Chem. Eng. 2019, 7, 2134-2140.

[99] R. Liu, Q.-Y. Liu, R. Krishna, W. Wang, C.-T. He, Y.-L. Wang, Inorg. Chem. 2019, 58, 5089-5095. [100] Y.-P. Li, Y. Wang, Y.-Y. Xue, H.-P. Li, Q.-G. Zhai, S.-N. Li, Y.-C. Jiang, M.-C. Hu, X. Bu, Angew. Chem. Int. Ed. 2019, 58, 13590-13595.

[101] H. Li, L. Li, R.-B. Lin, G. Ramirez, W. Zhou, R. Krishna, Z. Zhang, S. Xiang, B. Chen, ACS Sustain. Chem. Eng. 2019, 7, 4897-4902.

[102] Y. Ye, Z. Ma, R.-B. Lin, R. Krishna, W. Zhou, Q. Lin, Z. Zhang, S. Xiang, B. Chen, J. Am. Chem. Soc. 2019, 141, 4130-4136.

[103] H. Li, H. Bonduris, X. Zhang, Y. Ye, A. Alsalme, R.-B. Lin, Z. Zhang, S. Xiang, B. Chen, J. Solid State Chem. 2020, 284, 121209.

[104] P. Yan, J. Yang, X. Hao, Z. Chen, G. Shen, Y. Zhao, D. Ma, J. Zhu, CrystEngComm. 2020, 22, 275-282.

[105] H. Cui, Y. Ye, H. Arman, Z. Li, A. Alsalme, R.-B. Lin, B. Chen, Cryst. Growth Des. 2019, 19, 5829-5835.

[106] L. Meng, L. Yang, C. Chen, X. Dong, S. Ren, G. Li, Y. Li, Y. Han, Z. Shi. S. Feng, ACS Appl. Mater. Interfaces 2020, 12, 5999-6006.

[107] W. Fan, S. Yuan, W. Wang, L. Feng, X. Liu, X. Zhang, X. Wang, Z. Kang, F. Dai, D. Yuan, D. Sun, H.-C. Zhou, J. Am. Chem. Soc. 2020, 142, 8728-8737.

[108] H. Zeng, M. Xie, Y.-L. Huang, Y. Zhao, X.-J. Xie, J.-P. Bai, M.-Y. Wan, R. Krishna, W. Lu, D. Li, Angew. Chem. Int. Ed. 2019, 58, 8515-8519.

[109] X.-Y. Li, Y.-Z. Li, L.-N. Ma, L. Hou, C.-Z. He, Y.-Y. Wang, Z. Zhu, J. Mater. Chem. A 2020, 8, 5227-5233..

Part-II

Water Stable Cationic MOFs for Toxic Aquatic Pollutants Remediation

Growing industries is a part of growth of modern civilization and urbanization. But release of their toxic effluents, which are generated from those industries, directly into the mainstream water bodies has resulted into the heavily increasing environmental pollution.[1] Such increasing water pollution due to various organic and inorganic contaminants has earned tremendous attention. Freshwater resources are becoming increasingly limited across the world as a result of rising population and water pollution.[2] According to United Nations estimates, the global population will reach ten billion people by 2050, and as many as one billion people may face extreme difficulty in accessing clean water even by 2025.[3,4] As a consequence of increasing threats to the living systems, huge attention has been devoted to the selective and sensitive detection of those toxic water pollutants. In this regard, metal-organic frameworks (MOFs) have emerged as the next generation sequestration material toward efficient remediation of various environmental pollutants.[5] Among them, cationic MOFs have attracted tremendous attention owing to their extra functionalities in the form of counter functional anions inside the pores, which has proven to be the game changer in selective sensing and capture of environmental pollutants.6 Although several neutral and ionic MOFs have been utilized towards such pollutant remediation, but dual/bimodal sequestration of these pollutants by multifunctional cationic MOFs is still very rare and challenging.[7]

There are two chapters in this section: chapter 4 and chapter 5. In chapter 4, a water stable luminescent cationic MOF was utilized for dual recognition of heavy-metal based oxo-anionic pollutants, i.e. CrO_4^{2-}, $Cr_2O_7^{2-}$, $HAsO_4^{2-}$ and $HAsO_3^{2-}$ in water. In chapter 5, another water stable cationic MOF with hydrophobic pore surface has been designed and utilized toward remediation of chromate (CrO_4^{2-}) and perrhenate (ReO_4^-) anions. Chromate is considered as one of the priority pollutant by US- Environment protection agency (US-EPA) owing to its hazardous effects while perrhenate anions are used as surrogate anions for radioactive pertechnatate (TcO_4^-) anion which is highly soluble in water with a high half-life ($t_{1/2}$=2.1x10^5 years) produced from nuclear fission activities.

References:

[1] M. A. Shannon, P. W. Bohn, M. Elimelech, J. G. Georgiadis, B. J. Mariñas, A. M. Mayes, *Nature* **2008**, 452, 301–310.

[2] P. C. D. Milly, J. Betancourt, M. Falkenmark, R. M. Hirsch, Z. W. Kundzewicz, D. P. Lettenmaier, R. J. Stouffer, *Science*, **2008**, 319, 573–574.

[3] World Population Prospects: The 2015 Revision, Methodology of the United Nations Population Estimates and Projections; Working Paper No. ESA/P/WP.242; Department of Economic and Social Affairs, Population Division, United Nations, **2015**.

[4] P. Samanta, A. V. Desai, S. Let, S. K. Ghosh, *ACS Sustainable Chem. Eng.*, **2019**, 7, 7456–7478.

[5] S. Mukherjee, D. Sensharma, O. T. Qazvini, S. Dutta, L. K. Macreadie, S. K. Ghosh, R. Babarao, *Coord. Chem. Rev.*, **2021**, 437, 213852.

[6] A. Karmakar, A. V. Desai, S. K. Ghosh, *Coord. Chem. Rev.* **2016**, 307, 313–341.

[7] N. C. Burtch, H. Jasuja, K. S. Walton, *Chem. Rev.* **2014**, *114*, 10575‑10612.

Chapter 4

A Luminescent Cationic MOF for Bimodal Recognition of Chromium and Arsenic based Oxo-anions in Water

4.1 Introduction

Water pollution has become a pressing problem in the 21st century to global population.[1] The access to clean and fresh aquatic systems is acknowledged as indispensable to entirely discern human rights.[2] Compelling upsurge in world population in combination with increasing urbanization and energy consumption possess a direct threat to sustainable life on earth for generations to come.[3] Consequently, the generation of enormous hazardous wastes and overexploitation of natural resources are apparent on earth's ecosystem as well as water bodies.[4] Acknowledging this fact, universal accessibility to clean freshwater remains the main objective of the "Sustainable Development Agenda" of the United Nations.[5] In particular, water pollution from heavy metals (density > 5 g cm^{-3}) and their corresponding oxo-anions (e.g., AsO_4^{3-}, CrO_4^{2-}, SeO_3^{2-}) has come forth as a persisting problem that leads to acute toxicity when accumulated in living organisms.[6] Chromium (Cr), on account of its hard and corrosion resistance ability, is of huge industrial relevance, and is extensively utilized in electroplating, metallurgy and printing.[7] In waste water, the usual abundance of chromium is in its highly soluble hexavalent oxo-anionic forms (CrO_4^{2-} and $Cr_2O_7^{2-}$) depending upon the pH.[8] It is a well known fact that these anions are mutagenic and carcinogenic in nature being highly toxic to living organisms and environments. To this end, pollution due to chromium has caught considerable attention amongst researchers worldwide.

On the other hand, Arsenic (As), noted as slow death mineral stands tall among the most carcinogenic and lethal elements,[9] and is largely abundant in waters, soils, atmosphere and organisms.[10] Inorganic arsenic [As (III) & As (V)] generally accumulates in keratin-rich tissues, viz., hair, skin, body fluids, [11-12] and impede ATP production, energy transduction reactions along with endothelial damage.[13] The toxicity is punctuated by the fact that the U.S. EPA (Environmental Protection Agency, United States) and WHO has lowered the maximum contaminant level (MCL) from 50 to 10 ppb for arsenic in drinking water.[9] Keeping in mind the extreme toxicity both chromium and arsenic present, it is topical to develop potent sensors toward recognition of these oxo-anions. To mitigate the prevailing magnitude of arsenic water contamination and toxicity, tremendous effort has been put forward in pursuit of efficient technologies aimed at efficacious detection and sequestration of these toxic anions. Instrumental techniques like inductively coupled plasma mass spectrometry (ICP-MS), ion chromatography, high-performance liquid chromatography coupled with atomic absorption spectrometry are suitable for qualitative as well as quantitative recognition while distinct approaches such as adsorption, flocculation–coagulation, chemical oxidation and electrochemical detection have also been probed.[14-18] These methods are reliable albeit pitfalls like sophisticated equipment requirement, intensive operational time and sample pre-treatment adds to the complexity of measurement. That being said, on a parallel approach,

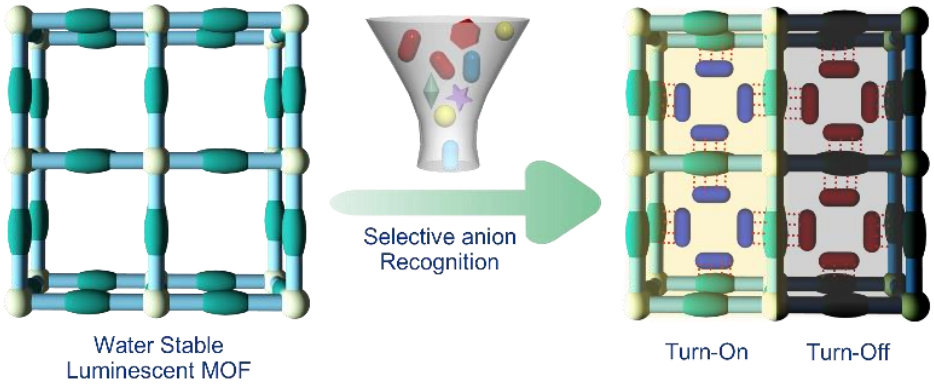

Scheme 4.1. Schematic representation of the design principle leading to iMOF-nC series; design of the cationic pore environment enables C_2H_2 selectivity over other C2-C1 gases. (colour codes: grey or gold – C, White – H, red – O).

fluorogenic and colorimetric techniques are advantageous due to fast response time, sensitivity and also requiring no or very less sample pre-treatment pertaining to feasibility.[19] Additionally, bi-functional materials offering synergistic detection and removal proves to be a significant advancement in addressing the issue whereby adsorption allows preconcentration of the analytes leading to an increased sensitivity.

Fabricated from a combination of organic linkers and metal ions/clusters held together periodically, metal organic frameworks (MOFs) are an emergent class of crystalline materials bearing potential voids. Since its advent, MOFs have found their potential in a broad range of applications. In fact, by virtue of their π-rich bridging organic ligands along with metal nodes/clusters as well as adsorbed or functionalized luminous guest molecules, MOFs can exhibit excellent luminescence property.[20] In recent years, luminescent MOFs (L-MOFs) have established their potential in variety of applications including environmental issues.[21] As a new paradigm for chemical sensing, plentiful L-MOFs have been documented as efficient sensory probes toward small molecules,[22] heavy metal ions[23] and toxic gases.[24] Hitherto, the manifestation of L-MOFs designed for anion recognition are few and far between.[25] One of the reasoning behind this might be the requirement of stable porous cationic L-MOFs, which are still limited in MOF community.[26] To address this issue, we have adopted the strategic utilization of a π-electron rich organic linker with rigid and conjugated aromatic skeleton. The highly conjugated nature of the ligand makes the MOF highly emissive in nature mainly through ligand centered emission. Also, based on HSAB principle, the neutral tripodal linker used for the construction of the MOF has smaller five-membered imidazole units as the terminal moieties that enables maximum coordination leading to chemically robust cationic framework through the metal center shielding.[27] Overall, the judicious choice of d^{10} metal system in synergism with highly conjugated linker and metal ion shielding

consequently produces chemically robust positively charged luminous nano-spaces abundant with multiple binding sites for incoming anionic guest molecules. In this report, we present a water stable highly luminescent cationic MOF (iMOF-4C), built from a tripodal neutral N-donor linker (1,1'-(5'-(4-(1H-imidazol-1-yl)phenyl)-[1,1':3',1''-terphenyl]-4,4''-diyl)bis(1H-imidazole) and d^{10} metal ion system for simultaneous detection and removal of environmentally toxic oxo-anions (CrO_4^{2-}, $Cr_2O_7^{2-}$, $HAsO_4^{2-}$, $HAsO_3^{2-}$) in water medium. The MOF based sensory probe displayed precise and sensitive recognition of these anions via a unique "off-on" fluorogenic signal output with extremely fast response time. Moreover, the limit of detection (LOD) was found to be among the lowest in MOF based sensors.

4.2 Experimental

Caution: Benzene is a highly volatile compound with severe toxicity and carcinogenic nature towards humans. Thus, it should be handled with appropriate safety measures and very carefully.

4.2.1 Materials: All the required solvents and reagents were acquired commercially and further used without any laboratory purification.

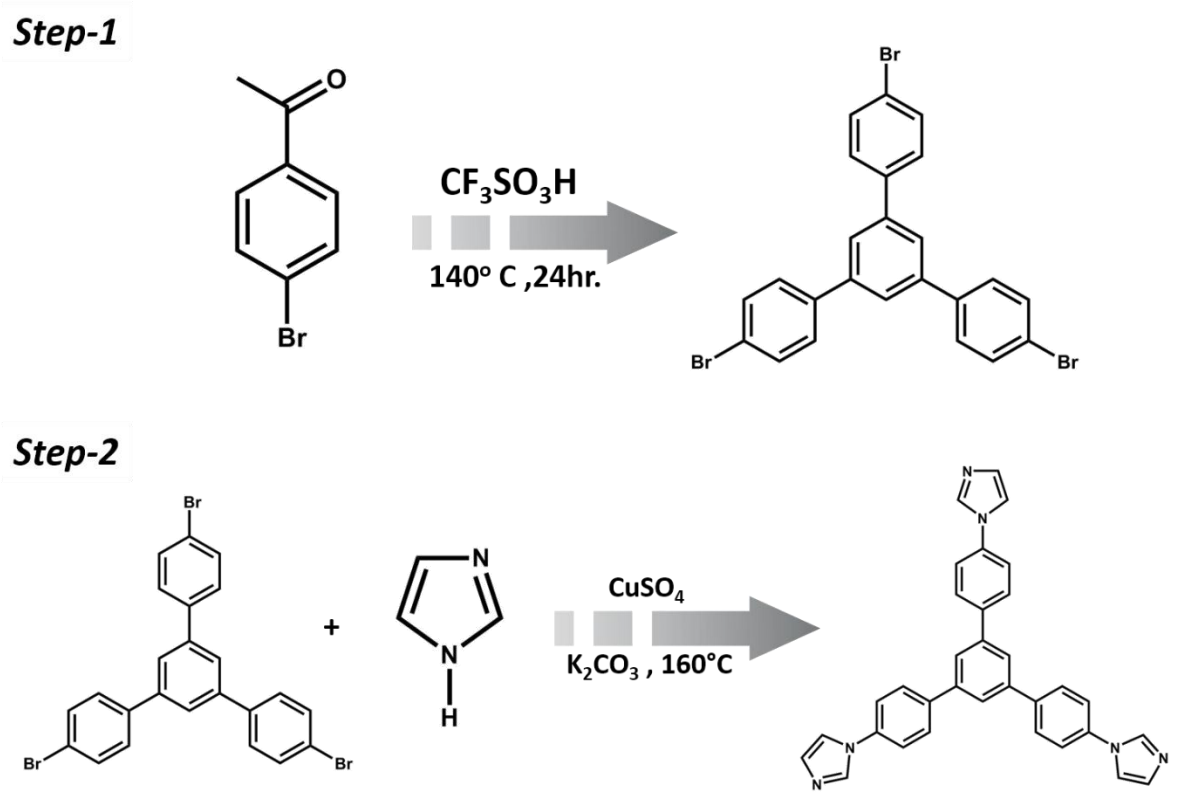

Scheme 4.2. Representation of the protocol employed for the synthesis of ligand (L).

4.2.2 Synthesis

Synthesis of Linker 1,1'-(5'-(4-(1H-imidazol-1-yl)phenyl)-[1,1':3',1''-terphenyl]-4,4''-diyl)bis(1H-imidazole): The linker was synthesized via adapting a previously reported protocol (Scheme 4.2).[28a]

Synthesis of iMOF-4C: The MOF was synthesized by a slow diffusion crystallization method. A N,N'-dimethylformamide (DMF) solution was prepared of the linker L (0.02 mmol, 10.15 mg, and 1 mL) and poured into a cylindrical glass tube. On the top of the layer of the ligand solution, another layer of (1 ml) benzene was added followed by addition of another layer of the 1 mL solution of metal salt, $Zn(ClO_4)_2.6H_2O$ (7.45 mg, 0.02 mmol) in methanol. The triple layered diffusion system was kept isolated without any disturbance. Hexagonal shaped colourless crystals were obtained after 10 days. The compound was collected by filtration and washing with methanol for several times. Pure single crystals of iMOF-4C were obtained with ~40% yield. Subsequently, the iMOF-4C crystals were dipped in CH_3CN for 24 hours to exchange the free solvent molecules inside the pores and activated under high vacuum at 60°C to obtain the guest free activated phase. In addition, we could not locate the highly disordered uncoordinated ClO_4^- anions and guest molecules inside the framework crystallographically. From PLATON SQUEEZE function, the formula of iMOF-4C was found to be $\{[Zn_1(L)_1](ClO_4)_2.x(G)\}_n$ (G = disorder guest molecules).

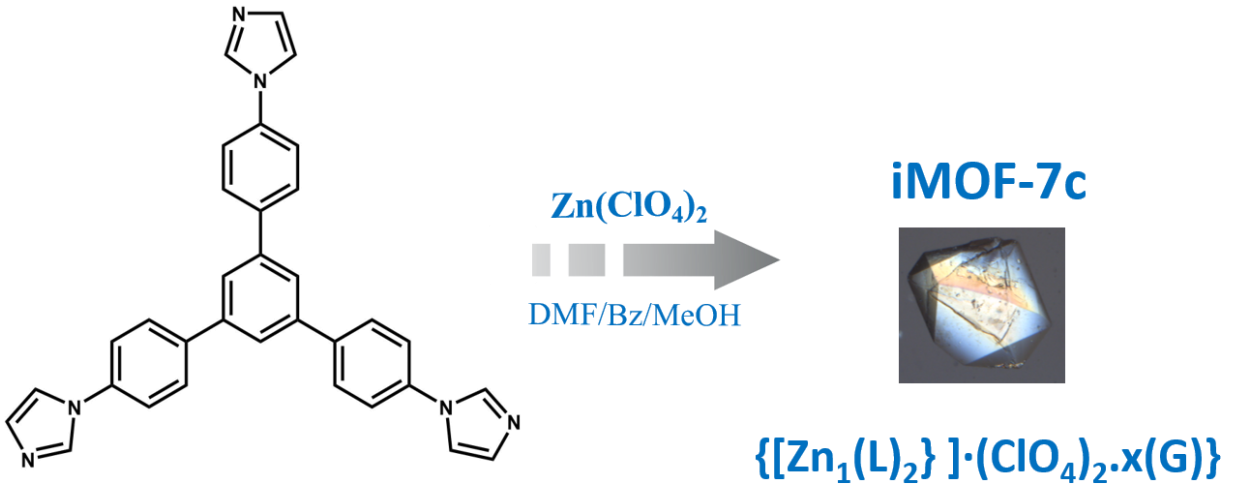

Scheme 4.3. Representation of the protocol employed for the synthesis of iMOF-4C.

4.2.3 Physical measurements: Powder X-ray diffraction (PXRD) patterns were acquired from a Bruker D8 Advanced X-ray diffractometer in a 5° to 40° 2θ range by using Cu Kα radiation (λ = 1.5406 Å) with a scan speed of 0.9° min^{-1}. The Fourier transform infrared spectra (FT-IR) spectra were collected from

Bruker spectrometer. The fluorescence spectroscopic studies were performed with Jobin Yvon Fluoromax-4 spectrofluorometer. The thermogravimetric analysis (TGA) were collected from a TGA analyzer (Perkin-Elmer STA6000) under N_2 atmosphere keeping the heating rate constant at 10 °C min^{-1}. The field emission scanning electron microscopy (FESEM) studies and energy dispersive X-ray (EDX) analysis data were acquired from a FEI Quanta 3D dual beam ESEM. The fluorescence imaging experiments were performed on Leica DM6B EPI-Fluorescence instrument.

4.2.4 X-ray structural studies: Single-crystal X-ray data of iMOF-4C was acquired at 150 K from Bruker D8 Venture Duo X-ray diffractometer equipped with a Microfocus X-ray source (operated at 50 W; 50 kV/1 mA) and graded multilayer optics for monochromatic Mo Kα radiation (λ = 0.71073 Å) with a focused X-ray beam and a Photon 100 CMOS chip based detector system. The crystal was mounted on nylon CryoLoops (Hampton Research) with Paraton-N (Hampton Research). The data integration and reduction were processed with SAINT software.[29] A multi-scan absorption correction was applied to the collected reflections. [30] The structure was solved by a direct method using SHELXTL[31,32] and was refined on F^2 with a full-matrix least-squares technique using the SHELXL-2014/7[33] program package within the WINGX[29] programme. All of the hydrogen atoms were refined anisotropically. All of the hydrogen atoms were located in successive difference Fourier maps and they were treated as riding atoms using SHELXL default parameters. The structures were examined using the Adsym subroutine in PLATON to assure that no additional symmetries could be applied to the models. The SQUEEZE option[35] was used to eliminate the contribution from the disordered guest molecules. CCDC number: 2073931 for iMOF-4C contains the supplementary crystallographic data for this paper.

4.2.5 Water Stability Test: Roughly 40 mg of the activated iMOF-4C was dipped in 10 mL of deionized water at room temperature and kept as it is for 24 h. Thereafter, the compound was collected by filtration and air dried at room temperature for further characterization.

4.2.6 Analyte preparation: First, stock solutions of all the anions were prepared from their respective sodium and potassium salts in water of concentration 0.5mM. Cr(VI) and As(V & III) based anion solutions were further diluted 10 times to prepare 0.05mM stock solution in water.

4.2.7 Fluorescence measurements: To execute the sensing experiments, finely grinded powdered form of activated crystals of iMOF-4C (1 mg) were allowed to disperse in 2 ml of water and 1 mM aqueous stock solution of CrO_4^{2-}, $Cr_2O_7^{2-}$, $HAsO_4^{2-}$ and $HAsO_3^{2-}$ (20−200 μL) were added individually. The corresponding gradual change in fluorescence spectra were monitored under stirring condition.

4.2.8 Detection Limit Calculation: For calculating detection limit, Cr(VI), As(V) and As(III) (20 – 200μL, 0.05mM stock solutions) were added to probe (desolvated iMOF-4C) (1mg, in 2mL water) and

fluorescent intensity was recorded. By plotting fluorescence intensity with increasing concentration of the oxo-anions, slope (m) of graph were calculated from there. Further, the standard deviation (σ) was calculated from five blank measurements of probe. Detection limit is calculated according to the formula:[36]

Detection limit: (3σ /m)

4.2.9 Titration with CrO_4^{2-}, $Cr_2O_7^{2-}$, $HAsO_4^{2-}$, $HAsO_3^{2-}$ and other competing anions with iMOF-4C: 1mg desolvated iMOF-4C was taken in a cuvette and 2mL water has been added to that. Initial luminescence spectra of iMOF-4C in water has been recorded by exciting at 330nm (spectra recorded in the range of 350-650nm). Then to the dispersed MOF in water, we have added stock solution of Cr(VI) ions in water (20µL to 200µL) and spectra were for each addition. With each addition of Cr(VI) anion, we found quenching in the fluorescence emission of iMOF-4C. Similar procedure was followed for titration of As(V) and As(III) based oxo-anions. With each addition of As(V) and As(III) anions, we found enhancement in the fluorescence emission of iMOF-4C individually. For competing studies, we have taken SO_4^{2-}, Cl^-, Br^-, ClO_4^-, NO_3^- and SCN^- ions in water. In a typical way, for initial study we have taken 1mg of iMOF-4C in 2mL of water. To the dispersed MOF we have added 200µL of the competing anion from the stock solution and recorded the corresponding spectra to check the response of MOF towards other anions (which we have provided in a bar diagram profile). Later, in a similar way to the dispersed MOF (1mg) in water medium (2mL) we have added 200µL of competing anions and followed by the addition of 200µL individual oxo-anionic solutions from the stock as prepared earlier. We have recorded both responses of MOF in presence of competing anions and in presence of both competing anions and respective oxo-anions. By combining two responses, we got the sensitivity of iMOF-4C towards these oxo-anions in presence of other competing anions.

4.2.10 Oxo-anion capture study: iMOF-4C (1mg) was immersed in an 2mL aqueous solution of 0.5mM CrO_4^{2-} and subsequently UV-Vis absorbance spectra were recorded with different time intervals. Further, the percentage removal of the oxo-anion and decrement in concentration was calculated by using the following equation:

$$\boldsymbol{D_t = \frac{C_0 - C_t}{C_0} \text{ x } 100\% = \frac{A_0 - A_t}{A_0} \text{ x } 100\%}$$

Where, D_t is the exchange capacity, C_0 and A_0 are initial concentration and absorbance of the oxo-anion solution respectively, C_t and A_t, are concentration and absorbance of the oxo-anion solution at specific times respectively.

4.2.11 Structure simulation studies

The structural simulations studies were performed using Materials Studio software suite 2017 (Accelrys).[37] Initially, the framework structure of the single MOF unit cell was totally relaxed employing DMOL3 code and B3LYP hybrid exchange correlation function by keeping Multiplicity factor to Auto mode, Double Numeric Plus Polarizing (DNP+) as Basis set and water as solvent. The calculations were performed with Global orbital cutoff scheme (medium quality). For the geometry relaxation of MOF unit cell, force, energy and displacement parameters were set to 0.004 Ha/Å, 2×10^{-5} Ha and 0.005 Å respectively. On this geometry relaxed MOF unit cell the structural simulation was acquired via Universal force field with a high calculation level. The Connolly surface was constructed using atom, surface, and volumes tools available in Materials Studio, having a fine grid resolution of 0.25 Å with Connolly radius 1.0 Å. Using the Sorption module, the possible interaction sites of various guest and anion molecules were introduced in MOF unit cell and modelled. The calculations were executed via Metropolis algorithm with high quality grid calculations at 298 K temperature on single MOF unit cell as well as 3×3×3 supercell.

Determination of binding energy of interactions, electrostatic – potential surface (ESP) and binding sites: Using Discovery Studio 2016 (Accelrys) we obtained interactions between MOF unit and guest molecules in terms of the binding energy of interactions, electrostatic – potential surface (ESP) and binding sites. [37] All calculations were performed at fine quality calculation level. These interactions were evaluated considering HOMO – LUMO (HOMO: “Highest Occupied Molecular Orbital” of the MOF; and LUMO: “Lowest Unoccupied Molecular Orbital” of the MOF) energy levels for single MOF unit and interaction of guest molecule. Firstly, using DMOL and B3LYP hybrid function the framework of the MOF unit was allowed to relax fully. During calculations, the Multiplicity factor was kept in Auto mode with double numeric plus polarizing (DNP+) basis set and water as solvent. Successively, structural simulation was performed on the relaxed structure to locate possible interaction site of the anion within the relaxed MOF unit was located using simulated annealing technique. The electrostatic potential (ESP) on the van der Waals (VDW) surfaces (isodensity = 0.001 a.u.) of MOF unit was derived based on its ground state electron density.

Optical properties simulation: The optical characteristics simulation were performed using CASTEP code and the calculations on above obtained geometry optimized framework unit cell. We constructed 3×3×3 supercell with framework unit cell. To simulate optical properties following parameters were considered, Koelling–Harmon relativistic treatment, B3LYP as exchange correlation function with Norm

conserving pseudopotentials, 600 eV energy cutoff, 2×2×2 Monkhorst–Pack grid and self–consistent dipole correction.

4.3 Results and discussion

Structural description of iMOF-4C: Hexagonal shaped crystals of iMOF-4C were obtained via a slow diffusion of ligand (L) and $Zn(ClO_4)_2.6H_2O$ with a solvent mixture of DMF/MeOH/Benzene at room temperature (Scheme 4.3). Single crystal X-ray diffraction (SC-XRD) studies disclosed that the two dimensional framework of iMOF-4C crystallized in *R*-3 space group (Appendix Table 4.2). The asymmetric unit is comprised of one Zn(II) cation having 1/6 occupancy, connected with 1/3 of one ligand (L) unit and disordered solvent molecules and free ClO_4^- anions (Figure 4.1a). The lesser steric hindrance from terminal imidazole units allowed six individual nitrogen atoms of six ligand units to coordinate with the central Zn(II) center affording an octahedral geometry around the Zn(II) center (Figures 4.1b, Appendix 4.2). The average Zn−N bond length was measured to be 2.171 Å. Crafted with a

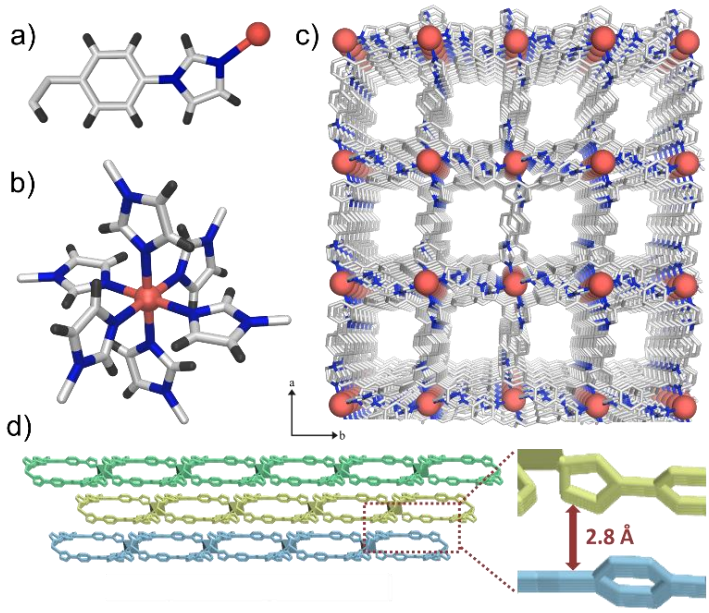

Figure 4.1. Structural representation of iMOF-4C illustrating (a) asymmetric unit (b) coordination environment of the central Zn(II) ion; (c) Perspective view along c-axis showing its one dimensional ultramicroporous channels sustaining the framework; (colour codes: grey – C, blue – N, maroon – Zn, hydrogen atoms are omitted for clarity); (d) Packing diagram of iMOF-4C showing the distance between successive two 2D layers.

highly hydrophobic ligand, iMOF-4C was found have biporous architecture with one large and one small pore (Figures 4.1c, Appendix 4.3-4.5). Such inherent functionality is known to be beneficial towards preferential interaction with heavy-metal based oxo-anions with lower charge density.[28] The residual framework positive charge was balanced by the uncoordinated tetrahedral perchlorate (ClO_4^-) anions residing free inside the porous channels. However, due to high disorder, we were unable to locate the free ClO_4^- anions crystallographically but were corroborated by Energy Dispersive X-Ray analysis (EDX), elemental mapping studies and Fourier transform infrared spectra (FTIR). The compound found to possess a binodal kgd topology with (3,6)- connectivity which ensures intrinsical porosity of the compound originates from the 2D sheets (Appendix 4.6-4.7). The total accessible volume of iMOF-4C (without anions) was found to be 3834 $Å^3$ from PLATON calculation study, which represents almost 54.6% of the total pore volume. Powder X-ray diffraction (PXRD) analysis of iMOF-4C showed retention of bulk phase crystallinity accompanied with a slight alteration arising due to evaporation of labile solvent molecules occluded inside the framework but affirmed the overall structural integrity and purity in bulk phase (Appendix 4.8). Thermogravimetric analysis (TGA) of the as-synthesized phase validated initial weight loss corresponding to the occluded guest molecules, water and DMF inside the framework (Appendix 4.9). The FTIR studies of iMOF-4C revealed the existence of all the characteristic peaks of the ligand along with a new peak at ~1100 cm^{-1} corresponding to the uncoordinated ClO_4^- anions within the pore (Appendix 4.10). Field emission scanning electron microscopy (FESEM) images of iMOF-4C corroborated well with the Hexagonal shape of the single crystals of iMOF-4C, and EDX spectra affirmed the abundance of all elements with proper ratio (Appendix 4.11−4.13). Moreover, the shielding of the Zn(II) metal node with six imidazole units imparted hydrolytic stability to iMOF-4C as implied by the PXRD patterns (Appendix 4.14-4.15). Low temperature (77 K) N_2 adsorption was carried out to check the porosity of iMOF-4C. It showed a very little uptake of N_2, which is indicative of the presence of free ClO_4^- anions contributing in partial blocking the pores of iMOF-4C (Appendix 4.16).

Photoluminescent studies: Judicious combination of electronically noble d^{10} metal cations (Zn^{2+}, Cd^{2+} etc.) along with π-conjugated luminescent linkers can lead to the integration of luminescent MOFs. Owing to the luminescent as well as cationic nature of iMOF-4C, we speculate that the incoming guest oxo-anions can be entrapped and have selective interactions with the framework, which may result in the alteration of photoluminescence properties of the framework. Both solid-state as well as aqueous phase luminescence spectra of iMOF-4C were acquired at room temperature. Upon excitation at 330 nm, iMOF-4C exhibited intense broad single emission spectra with a peak at 378 nm, which can be assigned to the ligand centered luminescence or emission due to ligand-to ligand charge transfer (LLCT) (Appendix 4.17).[20a, 21b]

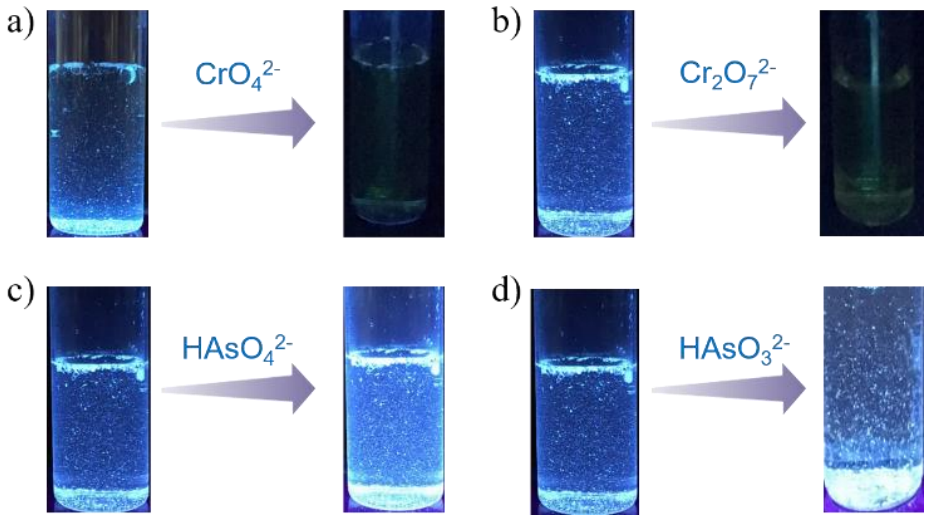

Figure 4.2. Photographs of change in emission intensities of iMOF-4C in water under UV-vis light upon addition of (a) aqueous solution of CrO_4^{2-}, (b) aqueous solution of $Cr_2O_7^{2-}$ showing quenching in emission intensity; and (c) aqueous solution of $HAsO_4^{2-}$ (d) aqueous solution of $HAsO_3^{2-}$ showing enhancement in emission intensity.

Cr (VI) sensing studies: The prominent hydrolytic stability and strong luminescence properties of iMOF-4C advocated its promising potential as an aqueous phase chemosensor. To evaluate its sensing performance towards toxic heavy metals e.g. Cr (VI) based oxo-anions, we have carried out fluorescence experiments with both chromate (CrO_4^{2-}) and dichromate ($Cr_2O_7^{2-}$) anions in water medium as both of the uncoordinated tetrahedral perchlorate (ClO_4^-) anions residing free inside the porous channels. them are interconvertible depending upon the pH of the solution. 1mg of the powdered sample was dispersed in a 2 ml water and the aqueous solution of CrO_4^{2-} and $Cr_2O_7^{2-}$ (0.05 mM) were added individually. As anticipated, with incremental addition of Cr(VI) ions, a gradual quenching of fluorescence intensity was observed (Figure 4.2a-4.2b, 4.3a-4.3b). The quenching process was found to be more rapid in case of $Cr_2O_7^{2-}$ over CrO_4^{2-} owing to its more electron deficient nature (Appendix 4.18-4.19). Further, to quantify the quenching process, the acquired experimental data were investigated via the Stern– Volmer (SV) equation, ($I_0/I = 1 + K_{SV}\cdot[Q]$), where I_0 and I represent the luminescence intensity of the dispersed iMOF-4C before and after addition of Cr(VI) oxo-anions, [Q] is the concentration of the respective Cr(VI) oxo-anion and K_{SV} is the Stern Volmer Constant μM and 4.1 μM respectively (details in supporting information) (Appendix 4.20-4.21).

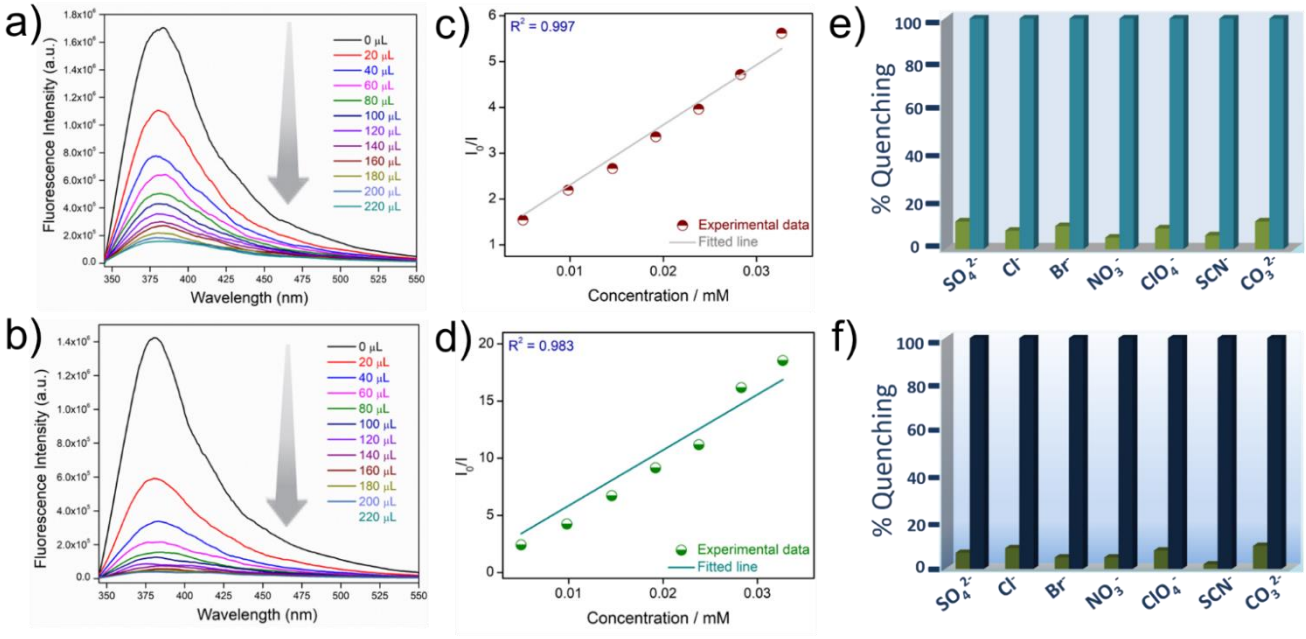

Figure 4.3. Fluorescence turn-off response of iMOF-4C upon incremental addition of (a) CrO_4^{2-}, (b) $Cr_2O_7^{2-}$; Stern–Volmer plot for iMOF-4C quenched by (c) CrO_4^{2-}, (d) $Cr_2O_7^{2-}$; %Quenching for competing ion alone (green) and response in presence of 1:1 binary mixture with (e) CrO_4^{2-} and (f) $Cr_2O_7^{2-}$.

High selectivity of a sensory material is another major aspect towards its real-time applicability. Considering this aspect, we have recorded the fluorescence response of iMOF-4C toward other competing anions (SO_4^{2-}, Cl^-, Br^-, ClO_4^-, NO_3^-, SCN^- and CO_3^{2-}) having same concentration as of Cr(VI) anions. Interestingly, no significant change in fluorescence response was observed in case of the other anions (Appendix 4.22-4.23). Enthused from these results, we further proceeded to check the efficacy of the material to sense these oxo-anions in presence of other anions. For this experiment, 1 mg of the MOF was allowed to disperse in water and subsequently aqueous solution of a particular competing anion was added to it. After 2 minutes of equilibration time, fluorescence spectra was recorded and later Cr(VI) anion was added to the solution and the fluorescence spectra of the solution was measured again. In this case, the respective competing anions did not show any significant change in fluorescence intensity, but the addition of Cr(VI) anions yielded a strong quenching in the emission intensity (Figure 4.3e-4.3f). Thus, it can be inferred that iMOF-4C can maintain its' high sensitivity and selectivity towards these toxic Cr(VI) oxo-anions even in presence of concurrent anions.

As (V) and As (III) sensing studies: As we discussed earlier also, water pollution due to arsenic has attracted tremendous scientific attention due to its' lethal nature and carcinogenic effects on living beings.

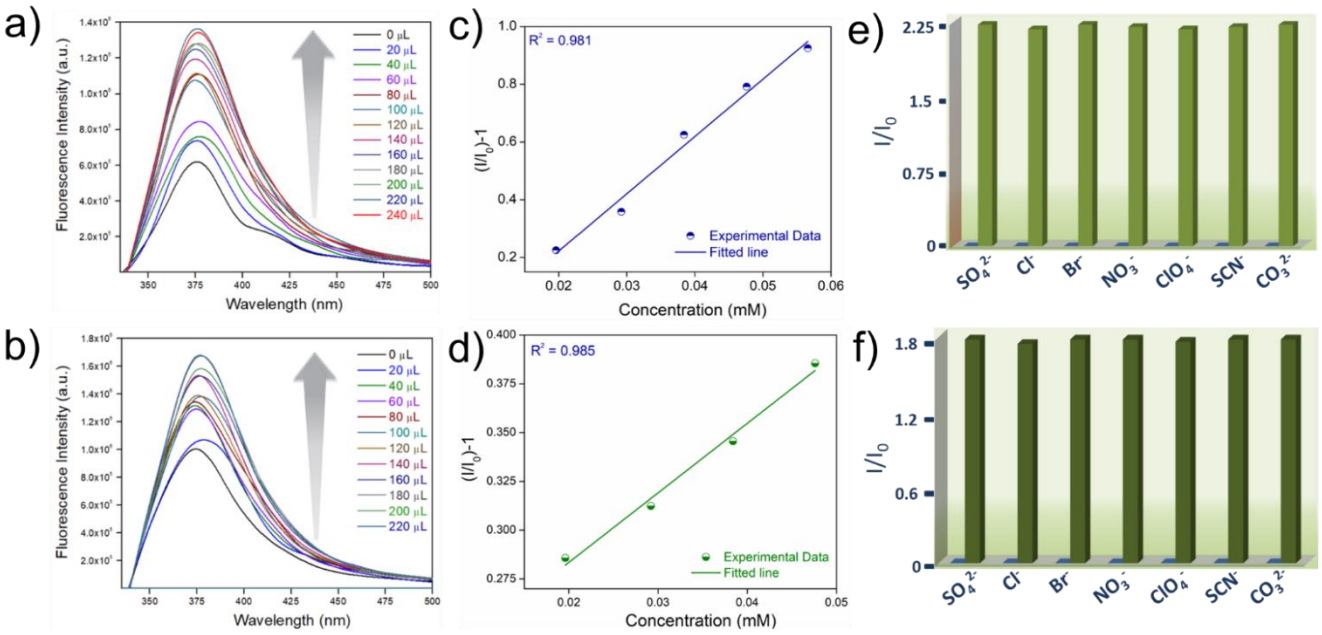

Figure 4.4. Fluorescence turn-on response of iMOF-4C upon incremental addition of (a) $HAsO_4^{2-}$, (b) $HAsO_3^{2-}$; Linear fit of (I_0/I -1) vs concentration of the analyte for iMOF-4C at low concentration region in case of (c) $HAsO_4^{2-}$, (d) $HAsO_3^{2-}$; comparison of fluorescence response of iMOF-4C in presence of other competing anions toward (e) $HAsO_4^{2-}$ and (f) $HAsO_3^{2-}$.

Hence, we have continued our effort further to check the sensitivity of iMOF-4C towards arsenic based oxo-anions (both As(III) and As(V). Similar experimental procedure as stated before was followed for these sensing studies. Surprisingly, iMOF-4C exhibited enhancement in luminescence intensity under UV-vis light and also a fluorescence "turn-on" response upon incremental addition of both $HAsO_4^{2-}$ and $HAsO_3^{2-}$ (Figure 4.2c-4.2d, 4.4a-4.4b). In order to quantify the fluorescence enhancement process and to establish the relationship between luminescence enhancement and the concentration of the anions, we have calculated the luminescence enhancement coefficient (K_{ec}) with the following equation; ($I/I_0 = 1 + K_{ec}\cdot[M]$), where I_0 and I represent the luminescence intensity of the dispersed iMOF-4C before and after addition of $HAsO_4^{2-}$ and $HAsO_3^{2-}$, [M] is the concentration of the anions.[38] A very good linear relationship between the amount of the anions and luminescence intensity was observed in the low concentration range (Figure 4.4c-4.4d). The K_{ec} of iMOF-4C toward $HAsO_4^{2-}$ and $HAsO_3^{2-}$ were found to be 1.98×10^4 M^{-1} and 3.56×10^3 M^{-1} respectively. The LOD of iMOF-4C toward $HAsO_4^{2-}$ and $HAsO_3^{2-}$ were calculated to be as low as 8.3 µM and 9.9 µM respectively (Figure 4.3c-4.3d). The SV plots corroborated well with the linear relationship between the emission intensities of iMOF-4C and the amount of the oxo-anions in the low concentration range. The K_{SV} for iMOF-4C toward CrO_4^{2-} and $Cr_2O_7^{2-}$ were calculated as 1.31×10^5 M^{-1} and 4.85×10^5 M^{-1}, which are found to be among the highest values reported in literature (Appendix Table 1). The limit of detection (LOD) of iMOF-4C toward CrO_4

$^{2-}$ and $Cr_2O_7^{2-}$ were found to be as low as 3 (Appendix 4.24-4.25). In addition, similar binary studies were performed as described previously in which iMOF-4C was found to show almost unaltered recognition efficiency toward both $HAsO_4^{2-}$ and $HAsO_3^{2-}$ even in presence of other competing anions (Figure 4.4e-4.4f). The oxo-anion treated phases of iMOF-4C were further characterised with PXRD, solid-state UV, FESEM, elemental analysis and confocal fluorescence imaging. The almost unaltered PXRD patterns of the treated phases corroborated well with the retention of structural integrity of iMOF-4C post sensing the MOF procedure (Appendix 4.26). The FESEM images of treated phases affirmed the retention of morphology of whereas the elemental analysis confirmed the homogeneous distribution of

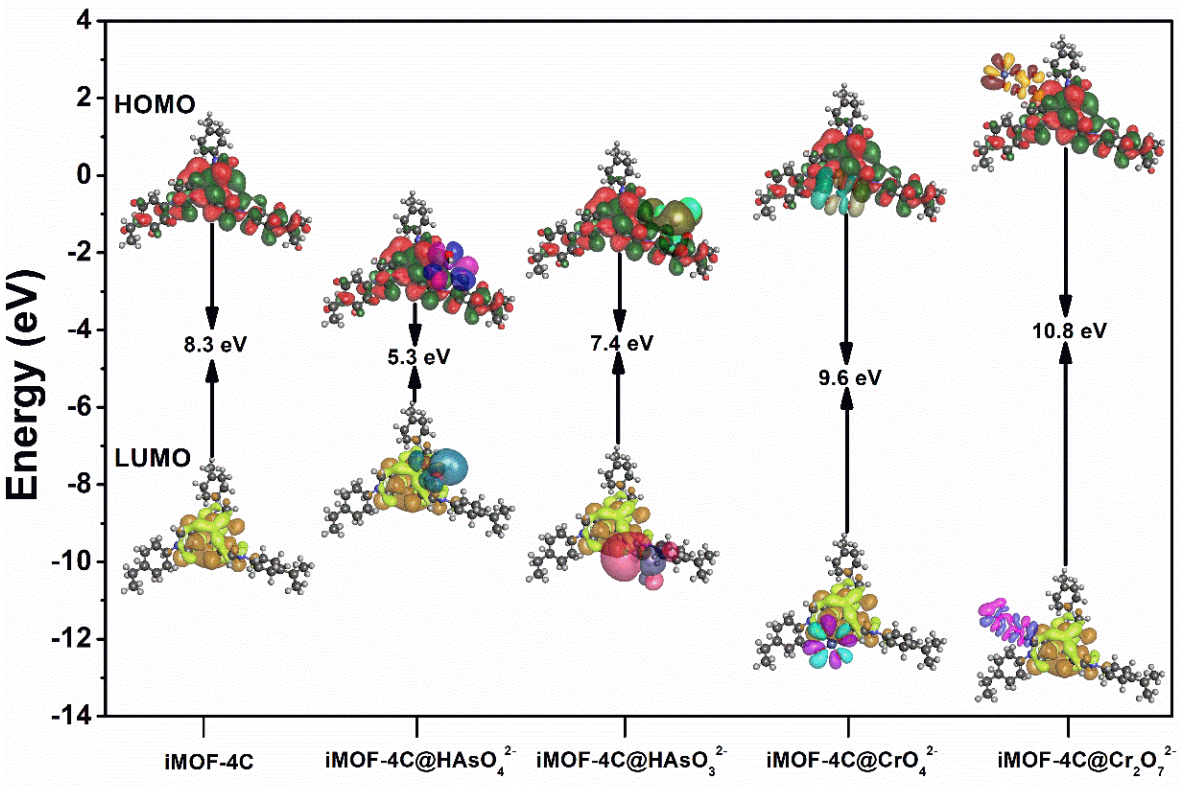

Figure 4.5. HOMO-LUMO molecular energy gap obtained for the interactions between iMOF-4C (single unit) and different oxo-anions.

chromium and arsenic along with the other elements inside the framework (Appendix 4.27-4.32).

Furthermore, we have probed the sensing phenomenon via confocal fluorescence imaging in which the single crystals of iMOF-4C were kept under confocal microscope and the effect of the oxo-anions were monitored. To our delight, single crystals of iMOF-4C exhibited excellent fluorescence quenching as well as fluorescence enhancement upon addition of Cr (VI) and As (V, III) based oxo-anions respectively

(Appendix 4.34). This experiment provides a direct visualization of the fluorescence turn-off/on behaviour within the MOF single crystals.

Sensing mechanism and theoretical insights: To get more insights about such rare fluorescent turn off/on phenomenon in a single material, we have performed DFT calculations. We have selected a characteristic fragment of iMOF-4C for the theoretical modelling consists of the one Zn^{2+} cation and six partial ligands. The HOMO–LUMO energy gaps were investigated to correlate the experimental results (Figure 4.5). This quantum mechanical information is very important to estimate the overall electronic interactions between iMOF–4C and oxo-anions. Overall, the electron donation ability of a specific molecule is governed by HOMO energy level, while LUMO energy level unveils electron acceptance ability. Hence, the active sites of iMOF–4C and oxo-anions responsible for HOMO and LUMO primarily control the electron exchange process and also govern the physicochemical properties. The calculated HOMO–LUMO energy gap for iMOF–4C and oxo-anions is shown in Figure 4.5. Employing Koopman's theorem and frontier molecular orbital theory,[39] we deduced the results obtained from simulation. It can be seen that the quantum mechanical parameter, viz., global hardness for iMOF–4C is 8.4 eV, which decreases to 5.3 eV upon interaction with $HAsO_4^{2-}$, while due to interaction with $HAsO_3^{2-}$, it increases to 7.4 eV. Interestingly, interaction of iMOF–4C with CrO_4^{2-} and $Cr_2O_7^{2-}$ increases global hardness to 9.6 eV and 10.8 eV respectively, which is above pure iMOF–4C. These results are also supported by ESP distribution map (Appendix 4.40), which shows that interaction sites exhibit energy maxima. Thus, incorporation of different oxo-anions has different effect on the electronic property of iMOF-4C, which can be directly correlated to sensing due to anion exchange processes. These results correlate several key features observed experimentally. The quenching or turn–off features observed for iMOF–4C@CrO_4^{2-} and iMOF–4C@$Cr_2O_7^{2-}$ could be attributed to higher ΔE, which hinders electronic transition and eventually quenching of the fluorescence emission intensity. On the other hand, ΔE parameters for iMOF-4C@$HAsO_4^{2-}$ and iMOF-4C@$HAsO_3^{2-}$ are much lower than that of iMOF-4C, which can ease the electron transition pathway and result in enhancement in emission intensity. The fluorescence- quenching phenomenon of iMOF-4C upon addition of Cr (VI) based oxo-anions can be directly attributed to the possible inner filter effect as there is significant overlap between the absorption spectra of CrO_4^{2-}/$Cr_2O_7^{2-}$ and the emission of iMOF-4C (Appendix 4.39). Moreover, the theoretically predicted fluorescence emission patterns were found to be in close agreement with the experimentally acquired patterns (Appendix 4.41). Additionally, anion-π interactions in supramolecular assemblies leading to change in optical properties is well known in literature, which plays pivotal role in emanating such dual fluorescence response.

4.4 Conclusions

In summary, we have developed a new stable 2D cationic fluorescent MOF, iMOF-4C, which exhibits a rare multi-responsive (turn off/on) recognition response toward toxic oxo-anions (such as CrO_4^{2-}, $Cr_2O_7^{2-}$, $HAsO_4^{2-}$ and $HAsO_3^{2-}$) in water. Further, iMOF-4C was found to exhibit excellent selectivity toward such oxo-anions even in presence of several concurrent anions. The quenching constant toward CrO_4^{2-} and $Cr_2O_7^{2-}$ for iMOF-4C were found to be among the highest values reported in the regime of MOF, whereas the low limit of detection values established the potential of iMOF-4C in real-time applications. The cationic nature of the MOF was exploited towards sequestration of such toxic oxo-anions from water. Further, the theoretical studies evidently reveal the change in electronic properties of the MOF toward different oxo-anions and points out the origin of different fluorescence response. We believe that this work promises to open new avenues in rational designing and development of water stable cationic luminescent MOFs to address the pressing environmental issues of selective recognition and efficient remediation of toxic pollutants in water.

4.5 Appendix section

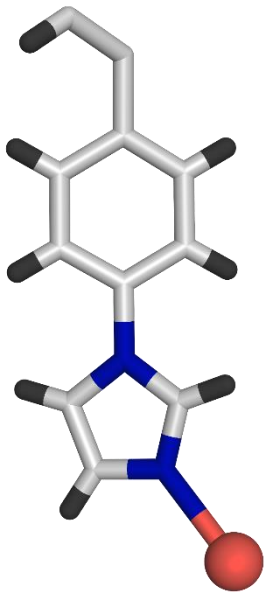

Appendix 4.1. Asymmetric unit of iMOF-4C (Hydrogen atoms have been omitted for clarity, (color: Gray - C, Blue - N, Maroon - Zn), ClO_4^- anions have been omitted because of crystallographic disorder and clarity.

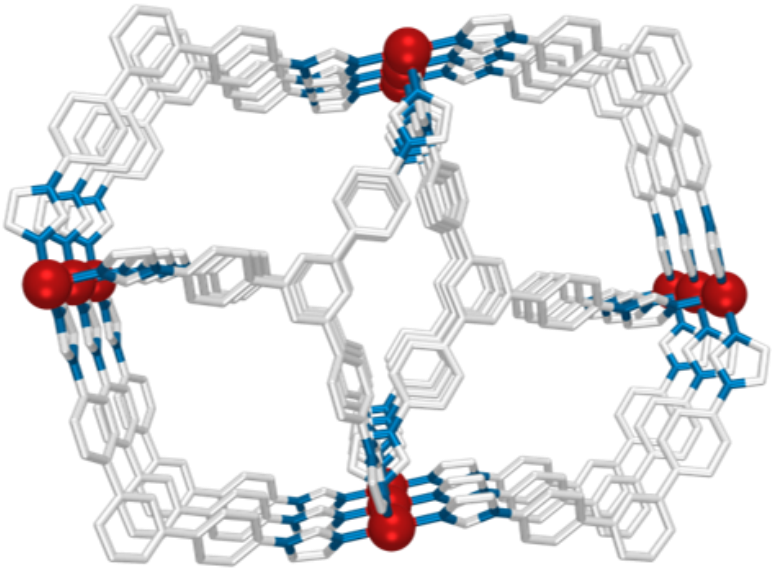

Appendix 4.2. Coordination environment of iMOF-4C (Hydrogen atoms have been omitted for clarity, (color: Gray - C, Blue - N, Red - Zn).

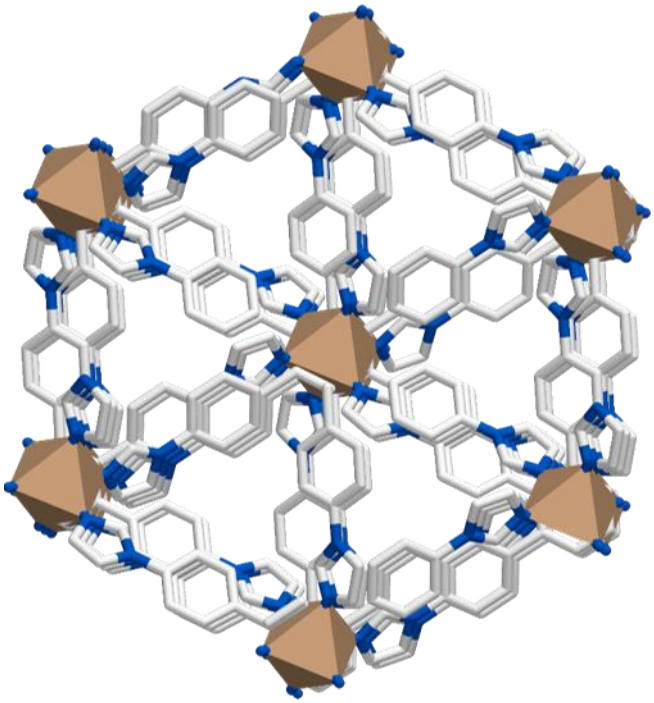

Appendix 4.3. Orthographic view of overall packing of iMOF-4C. (Hydrogen atoms have been omitted for clarity, (color: Gray - C, Blue - N, Brown - Zn), ClO_4^- anions have been omitted because of crystallographic disorder and clarity.

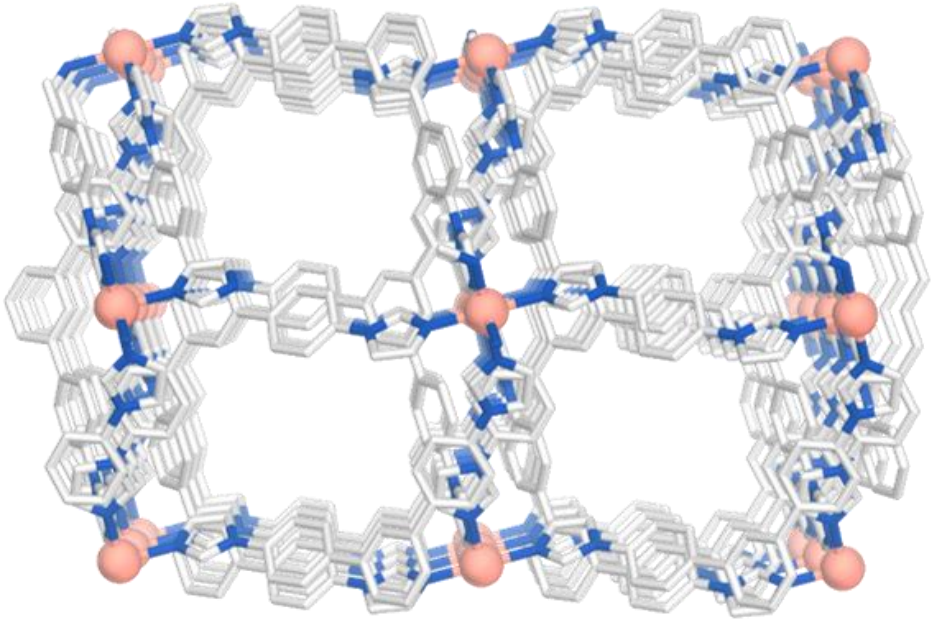

Appendix 4.4. Perspective view of overall packing of iMOF-4C along c-axis. (Hydrogen atoms have been omitted for clarity, (color: Gray - C, Blue - N, Red - Zn), ClO_4^- anions have been omitted because of crystallographic disorder and clarity.

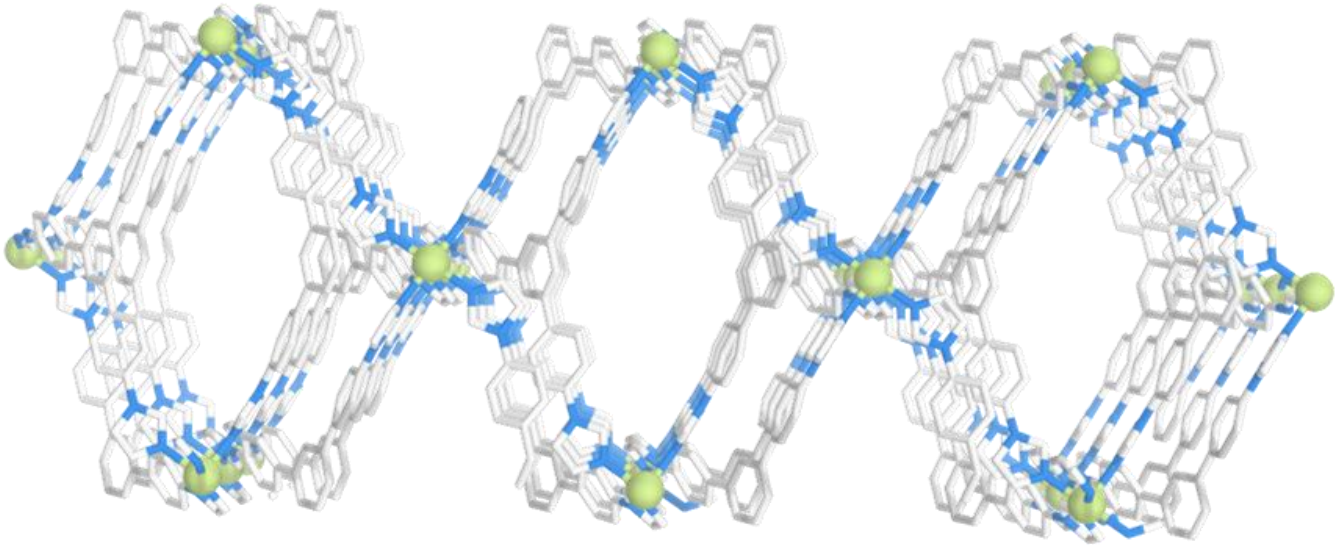

Appendix 4.5. Perspective view of overall packing of iMOF-4C along c-axis. (Hydrogen atoms have been omitted for clarity, (color: Gray - C, Blue - N, Green - Zn), ClO_4^- anions have been omitted because of crystallographic disorder and clarity.

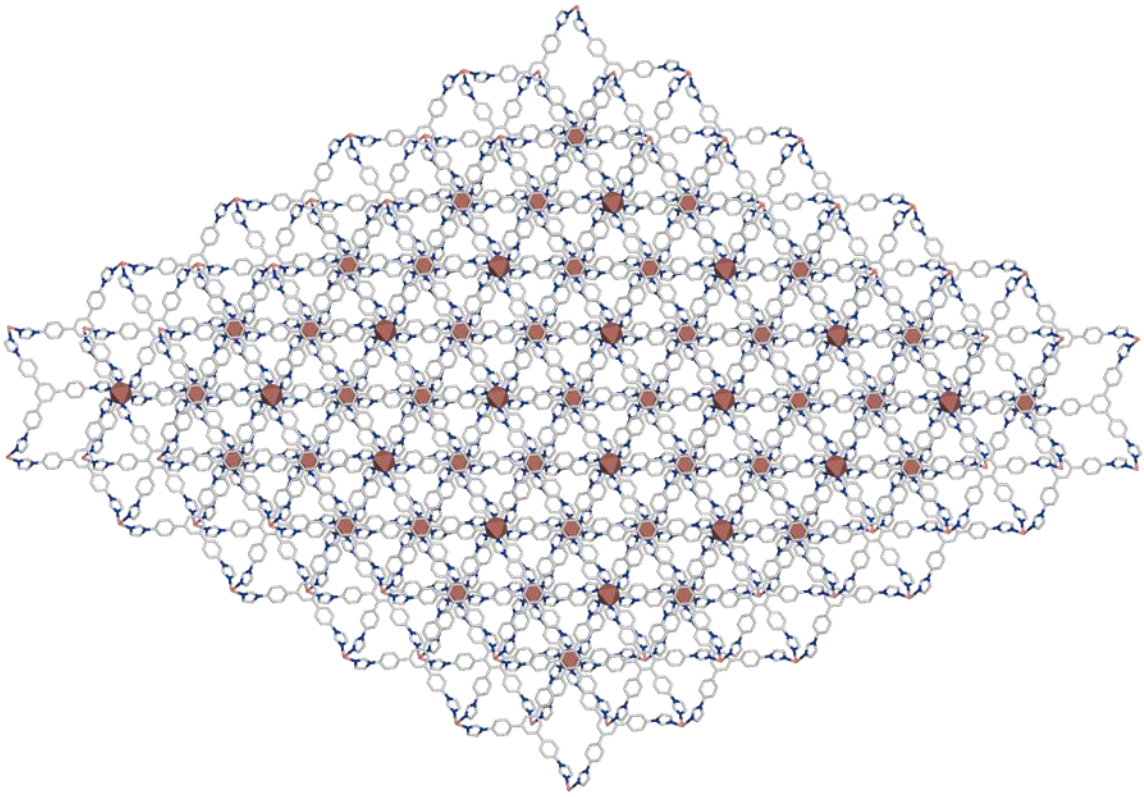

Appendix 4.6. Orthographic view of overall packing of iMOF-4C. (Hydrogen atoms have been omitted for clarity, (color: Gray - C, Blue - N, Brown - Zn), ClO_4^- anions have been omitted because of crystallographic disorder and clarity.

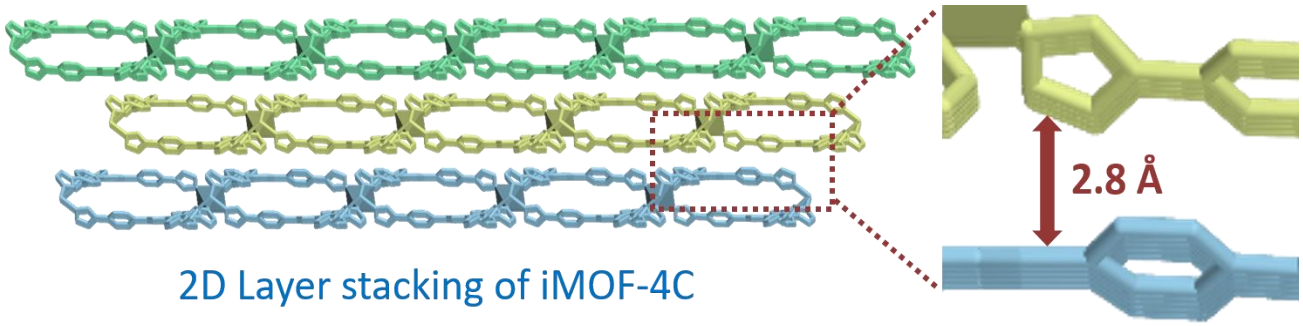

Appendix 4.7. Packing diagram of iMOF-4C showing the distance between successive two 2D layers.

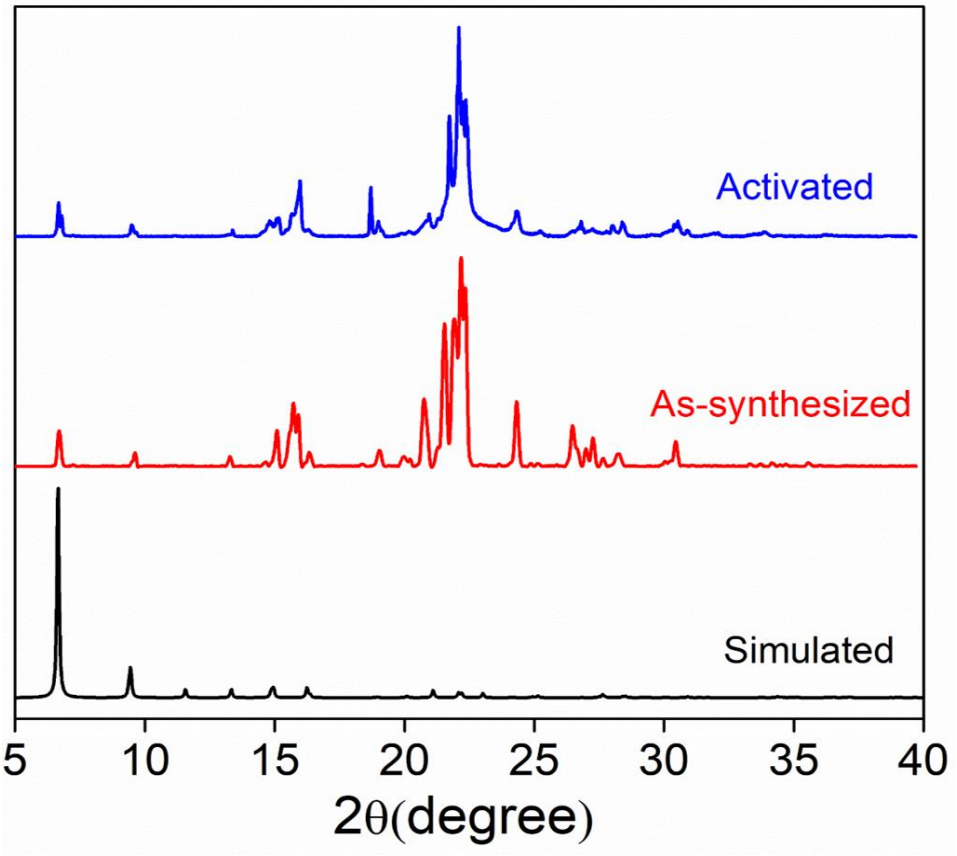

Appendix 4.8. Powder X-ray diffraction patterns of iMOF-4C.

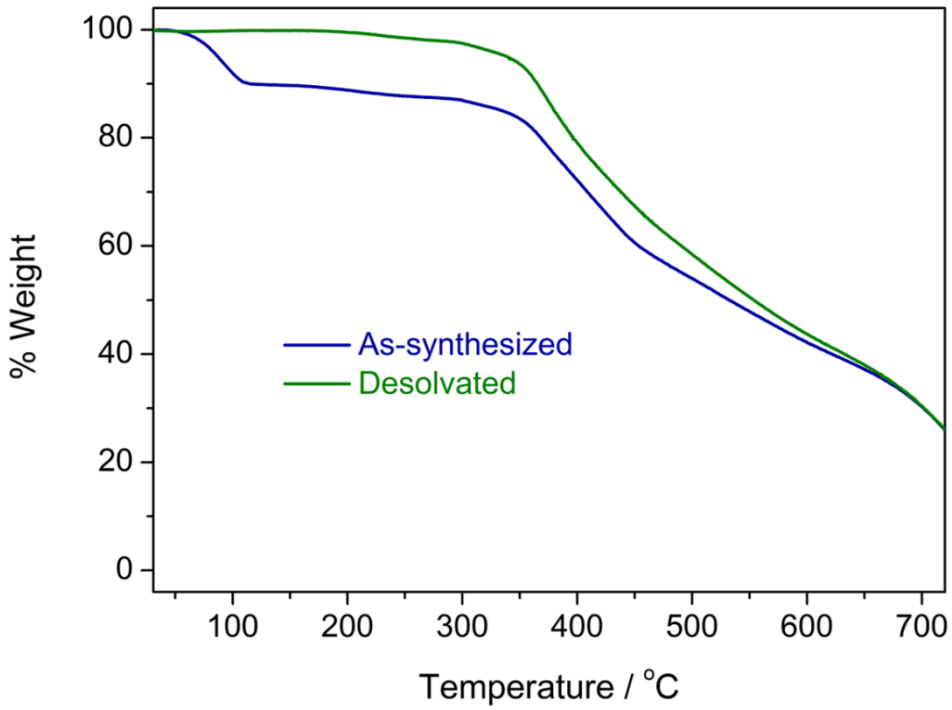

Appendix 4.9: TGA profiles for compound iMOF-4C.

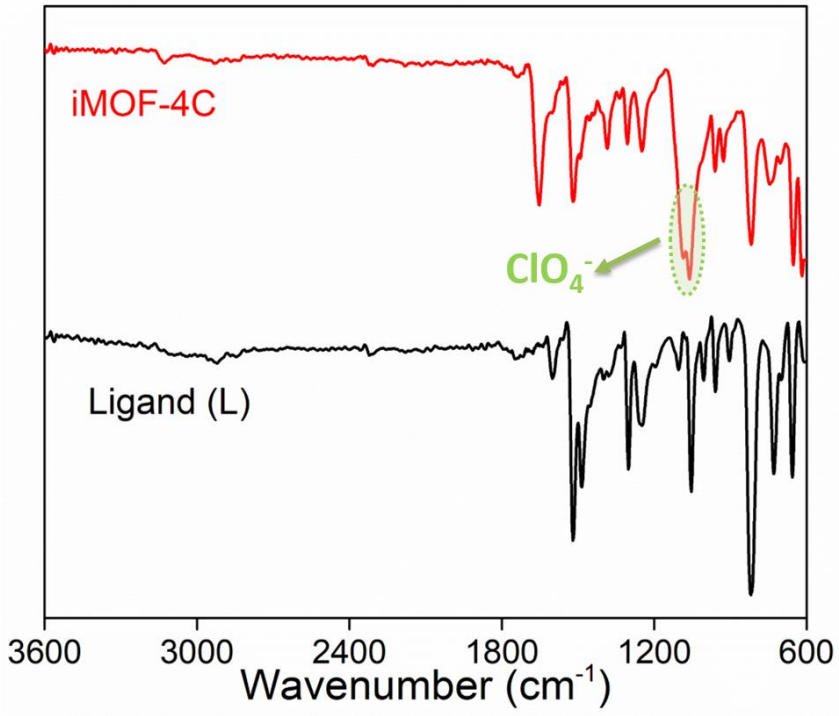

Appendix 4.10. Infra-red (IR) spectroscopy of iMOF-4C showing the characteristic peaks of the framework anlong with the ClO_4^- anions.

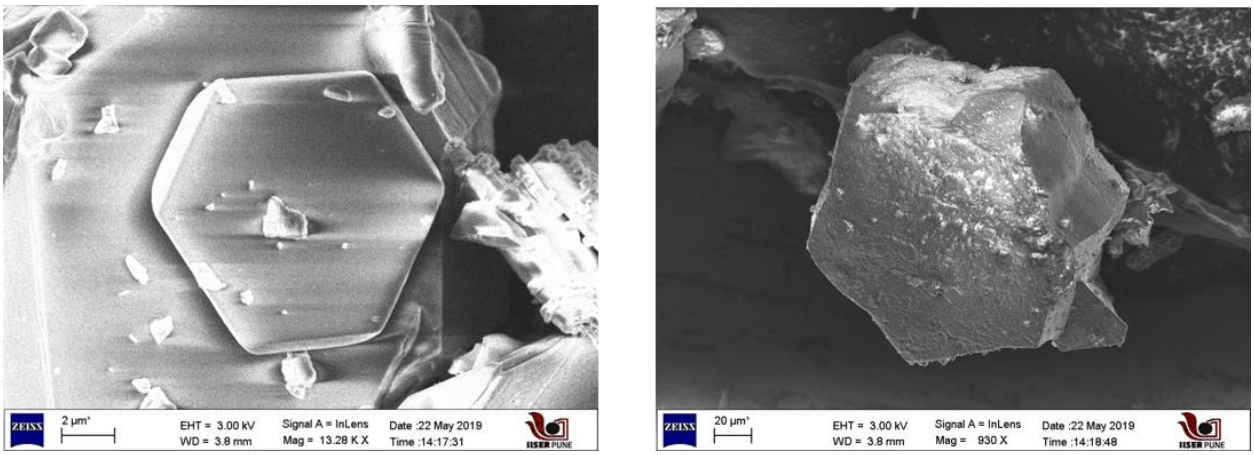

Appendix 4.11. FESEM images of iMOF-4C.

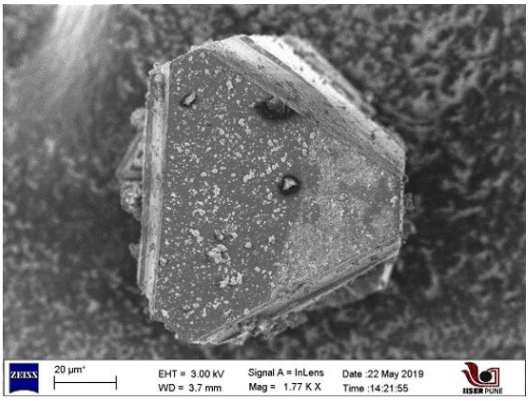

Element	Weight%	Atomic%
C K	62.47	71.34
N K	15.98	15.65
O K	11.82	10.13
Cl K	4.76	1.84
Zn L	4.97	1.04
Totals	100.00	

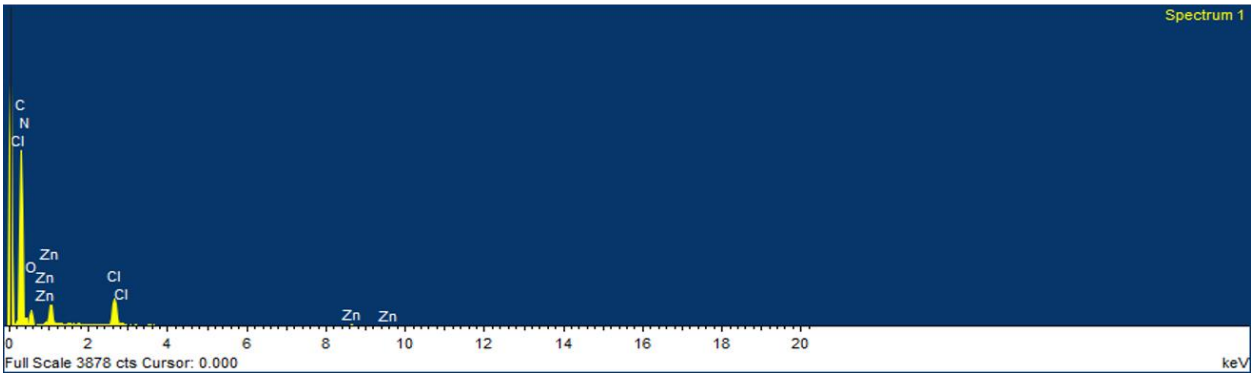

Appendix 4.12. EDX analysis of iMOF-4C.

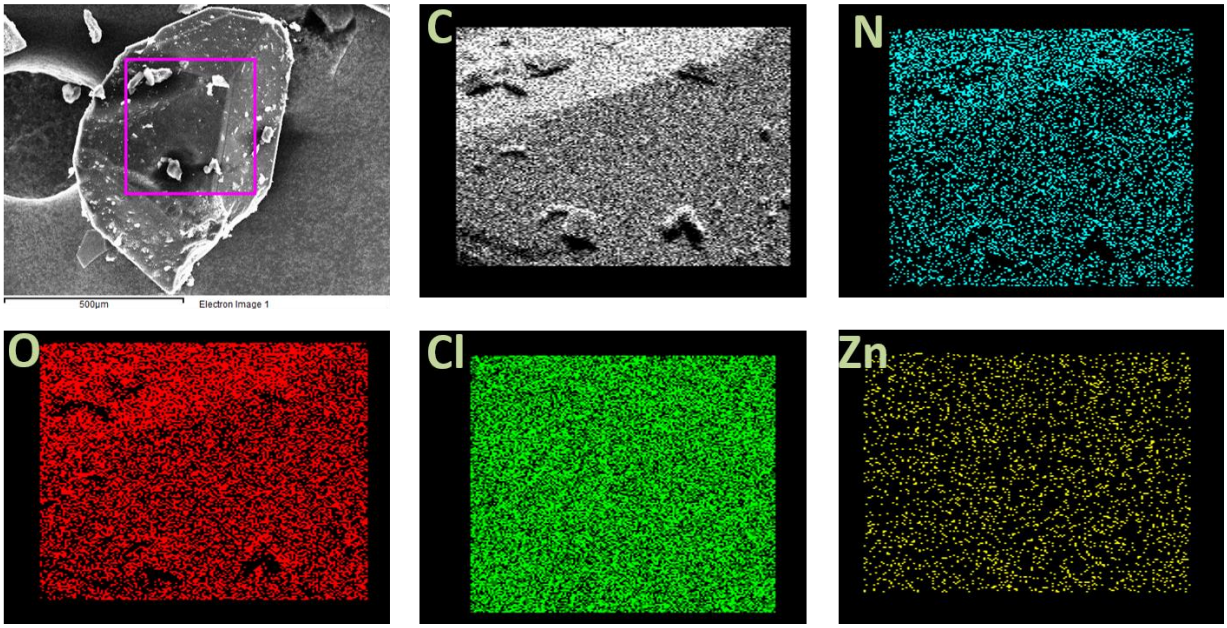

Appendix 4.13. Elemental mapping of iMOF-4C.

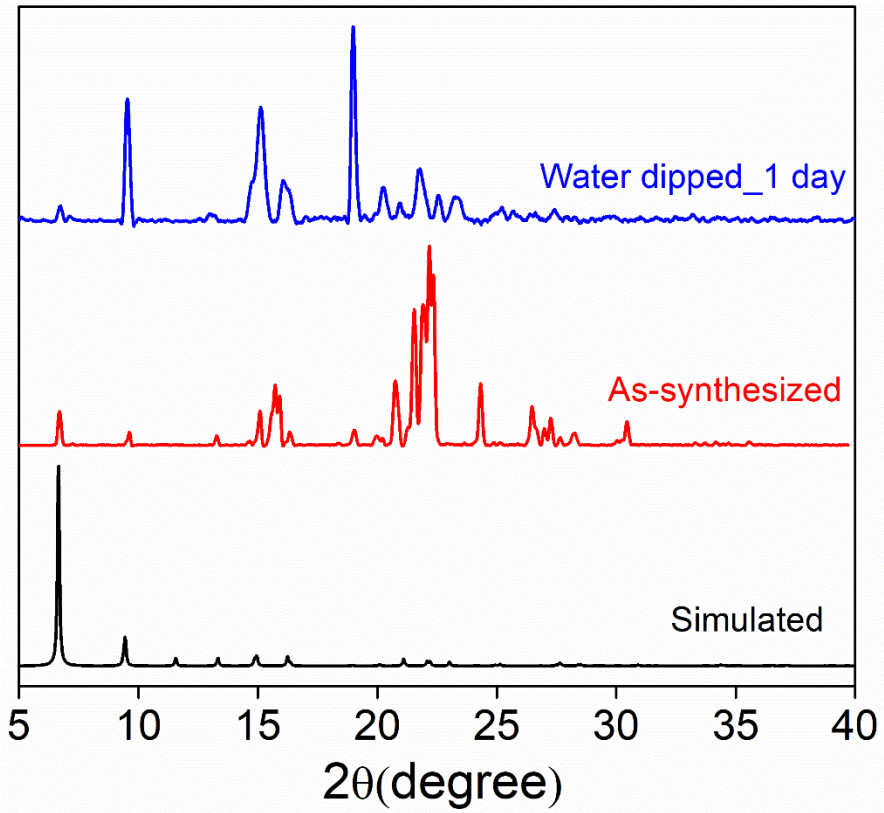

Appendix 4.14. Powder X-ray diffraction patterns of iMOF-4C illustrating hydrolytic stability of the framework.

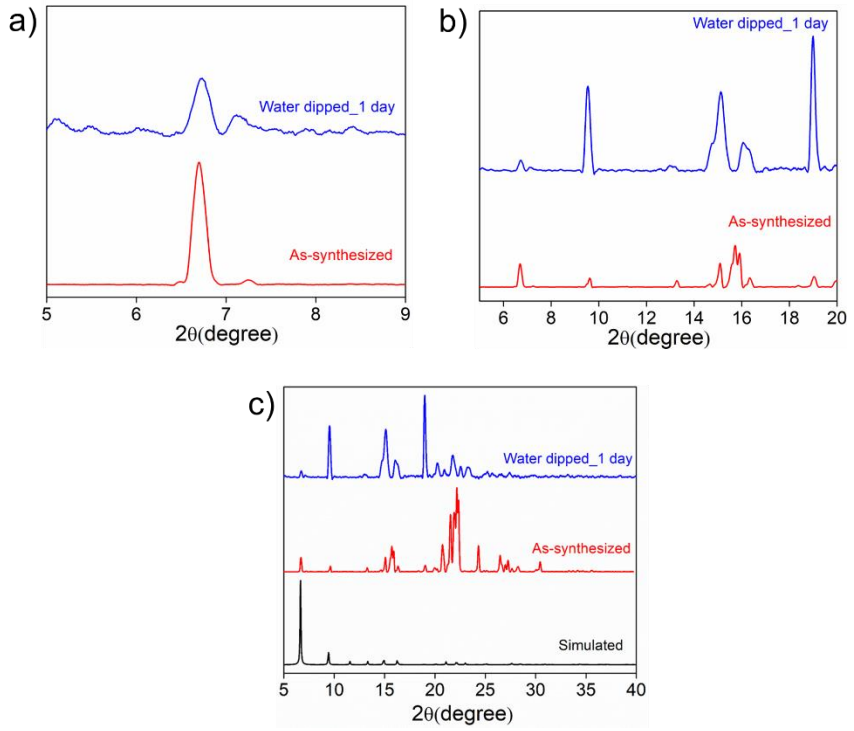

Appendix 4.15. Powder X-ray diffraction patterns of iMOF-4C (a), (b) with zoomed view of the PXRD spectra. (c) PXRD spectra of pristine and water dipped phases.

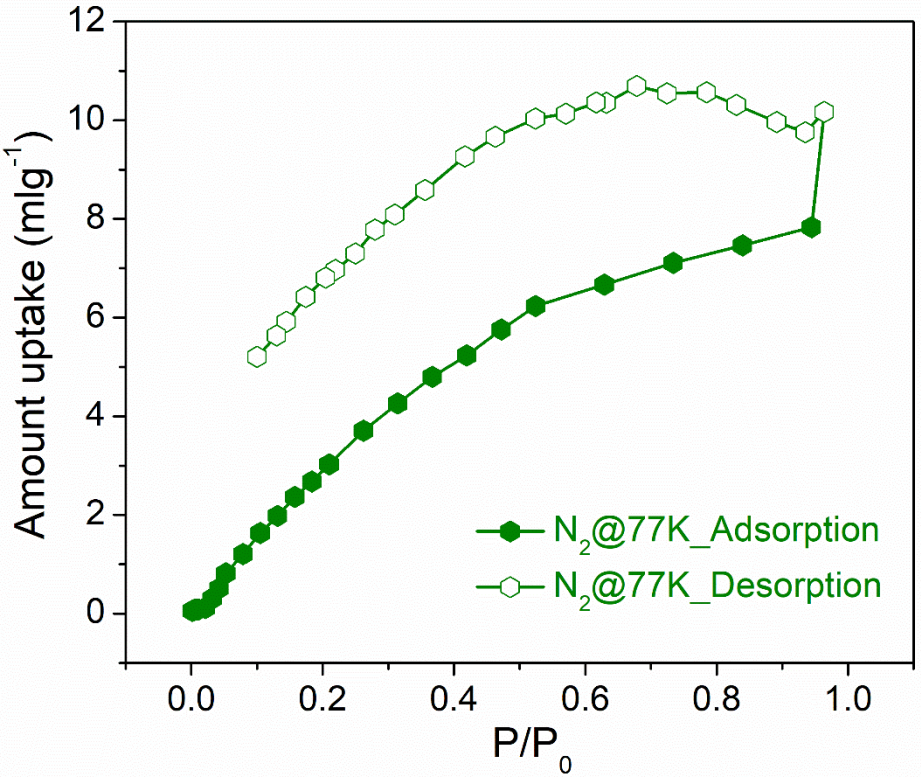

Appendix 4.16. N_2 (77 K) adsorption isotherm of iMOF-4C.

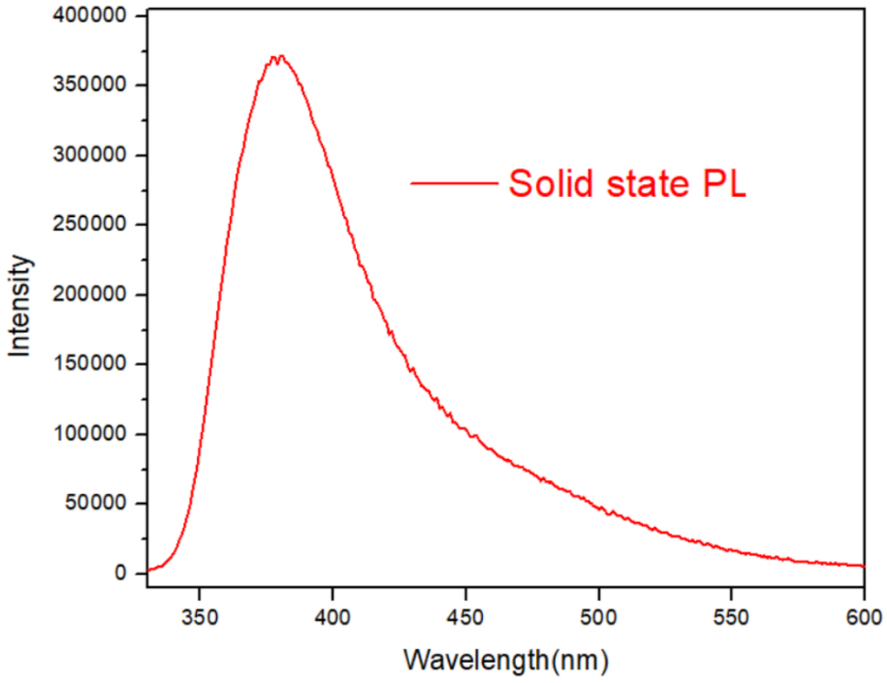

Appendix 4.17. Solid state fluorescence spectra of iMOF-4C (λ_{ex}= 330nm).

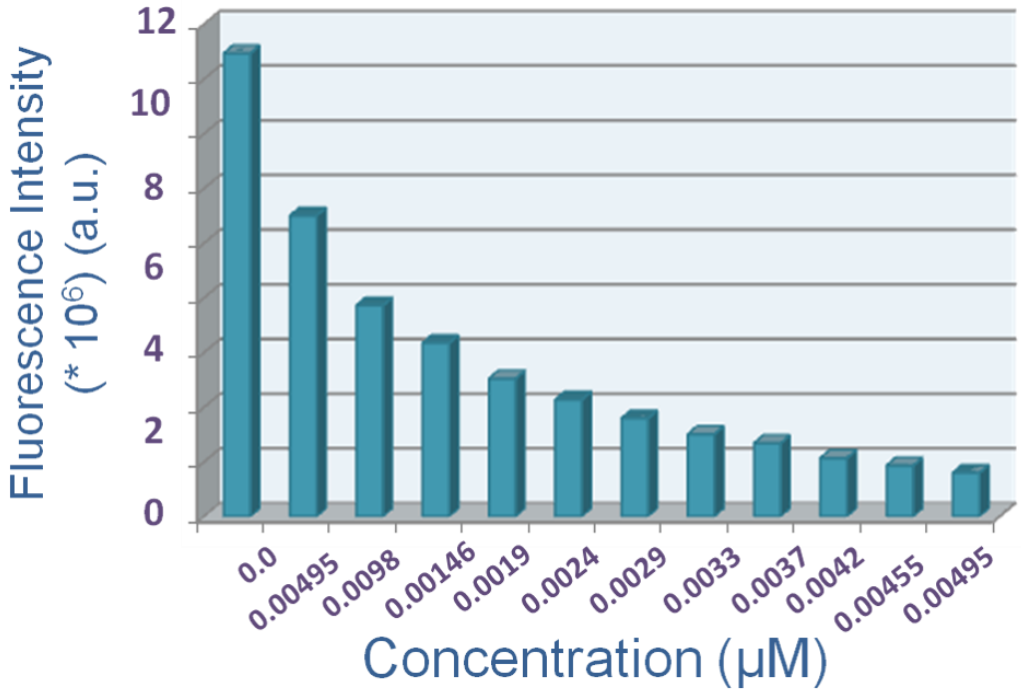

Appendix 4.18. Change in the fluorescence intensity of iMOF-4C in water medium with increasing concentration of the CrO_4^{2-} anions at 378 nm.

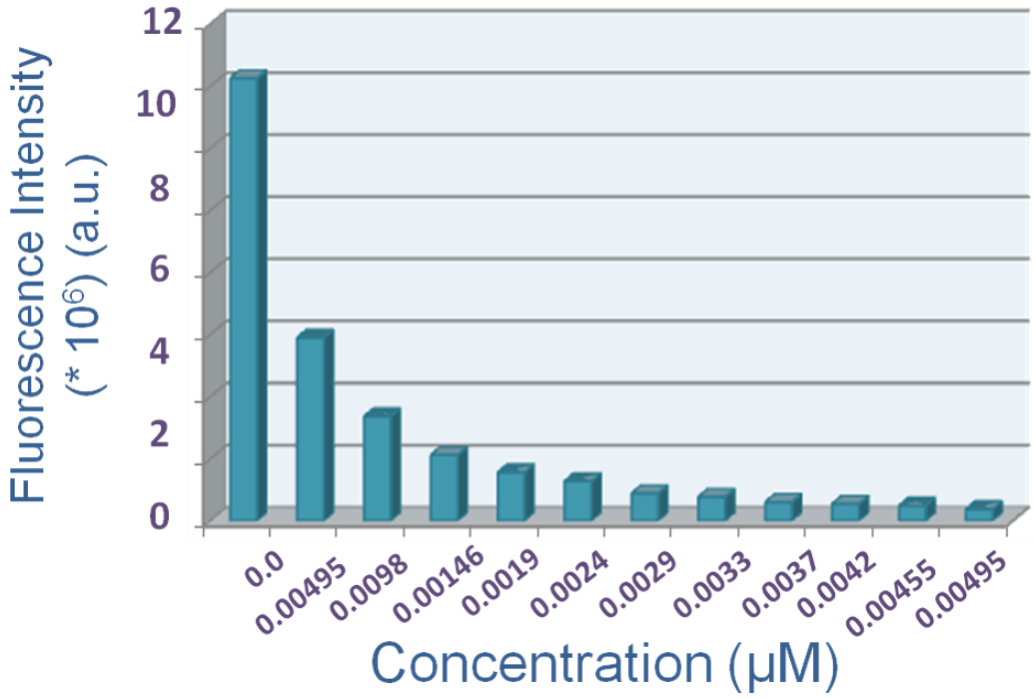

Appendix 4.19. Change in the fluorescence intensity of iMOF-4C in water medium with increasing concentration of the $Cr_2O_7^{2-}$ anions at 378 nm.

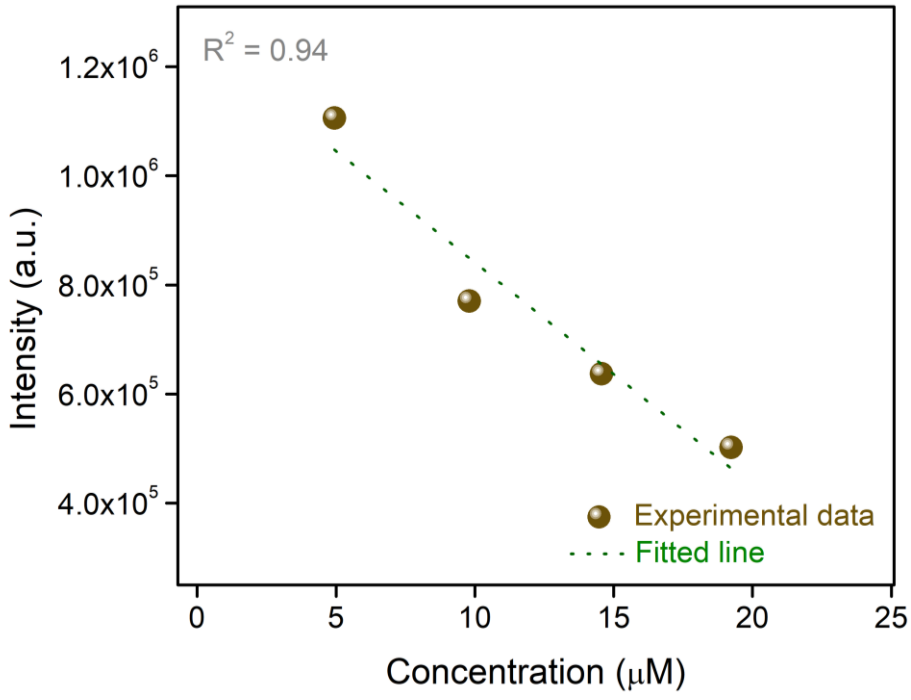

Appendix 4.20. Linear region of fluorescence intensity of probe upon addition of CrO_4^{2-}; λ_{em}= 378 nm (upon excitation at 330 nm).

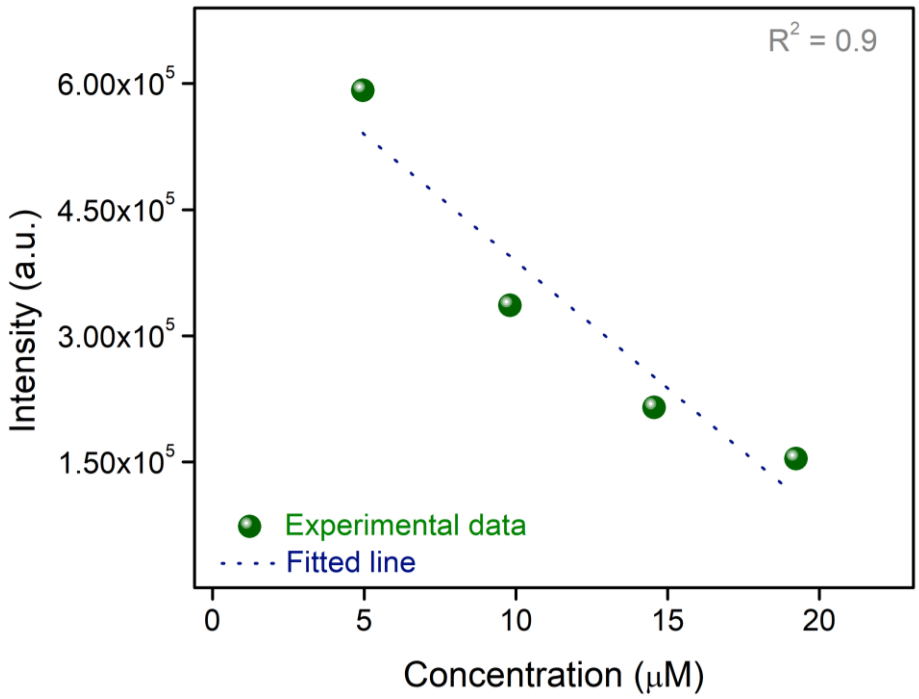

Appendix 4.21. Linear region of fluorescence intensity of probe upon addition of $Cr_2O_7^{2-}$; λ_{em}= 378 nm (upon excitation at 330 nm).

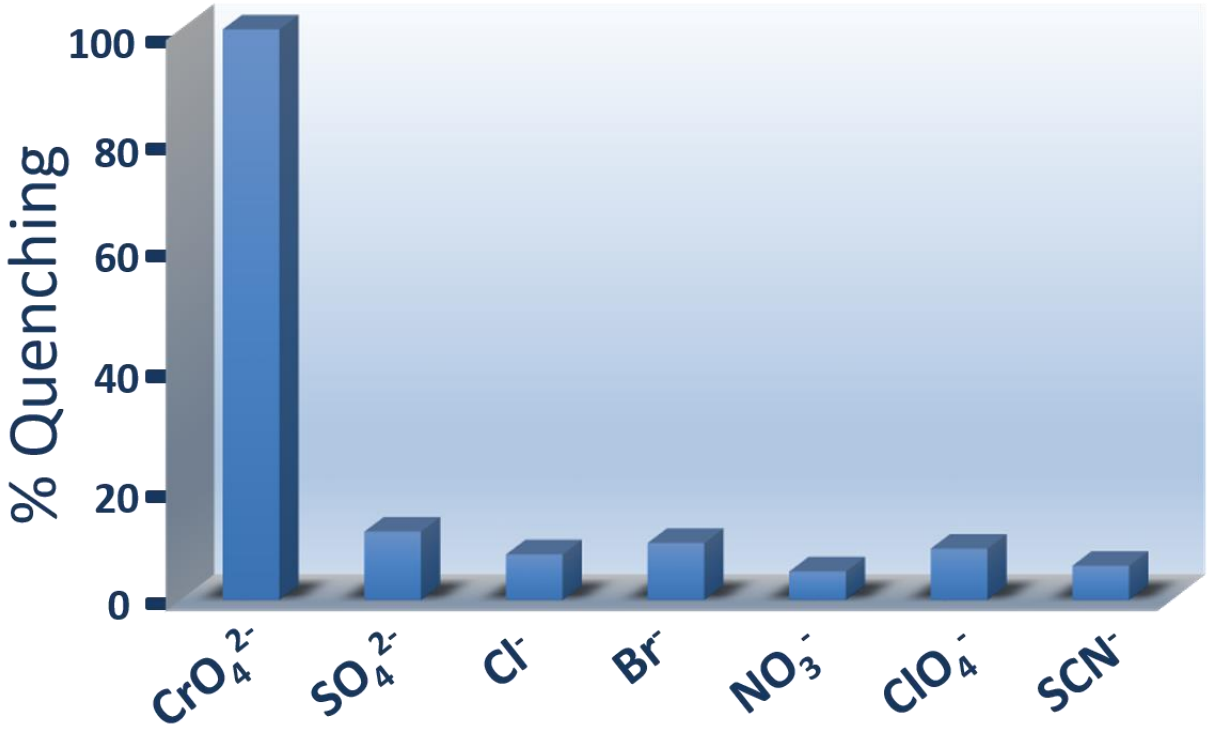

Appendix 4.22. Percentage quenching of fluorescence emission of iMOF-4C toward CrO_4^{2-} and other competing anions.

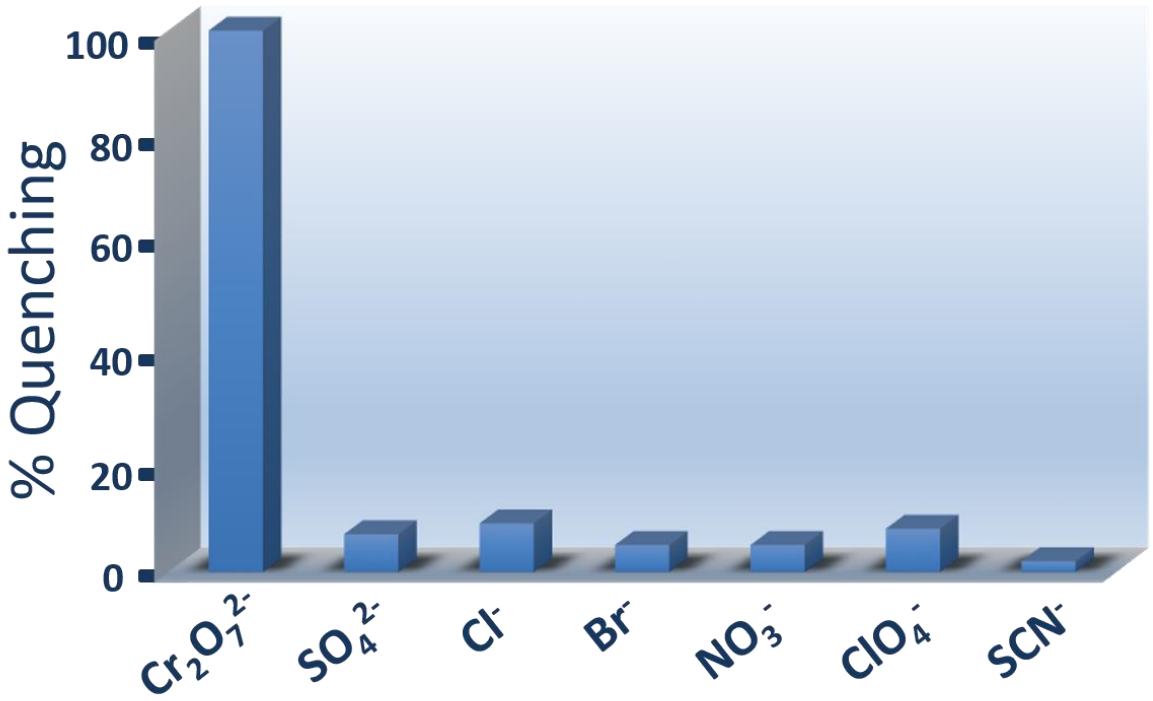

Appendix 4.23. Percentage quenching of fluorescence emission of iMOF-4C toward $Cr_2O_7^{2-}$ and other competing anions.

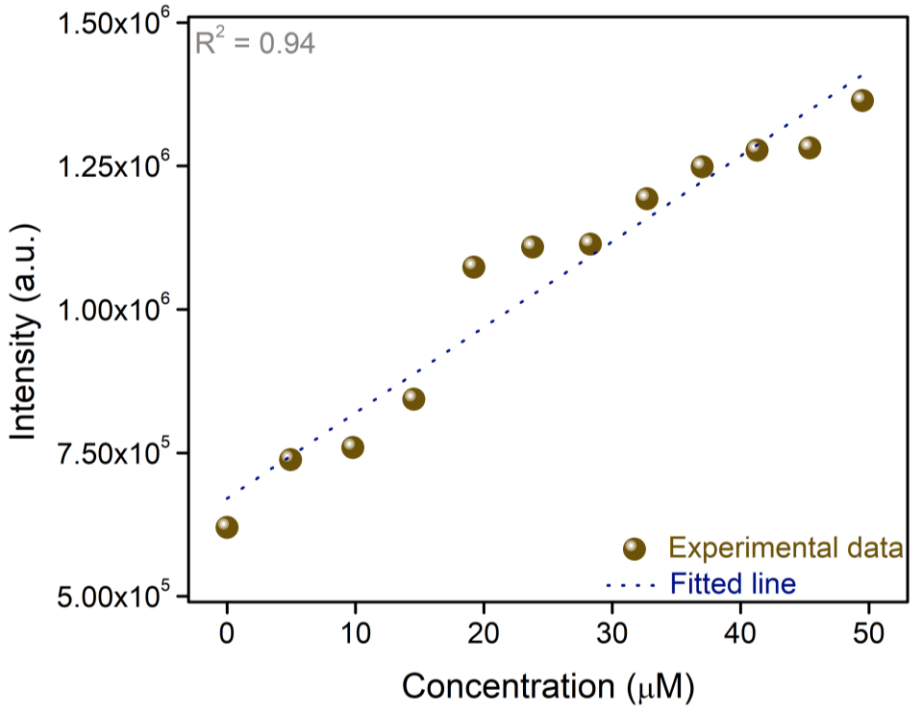

Appendix 4.24. Linear region of fluorescence intensity of probe upon addition of $HAsO_4^{2-}$; λ_{em}= 378 nm (upon excitation at 330 nm).

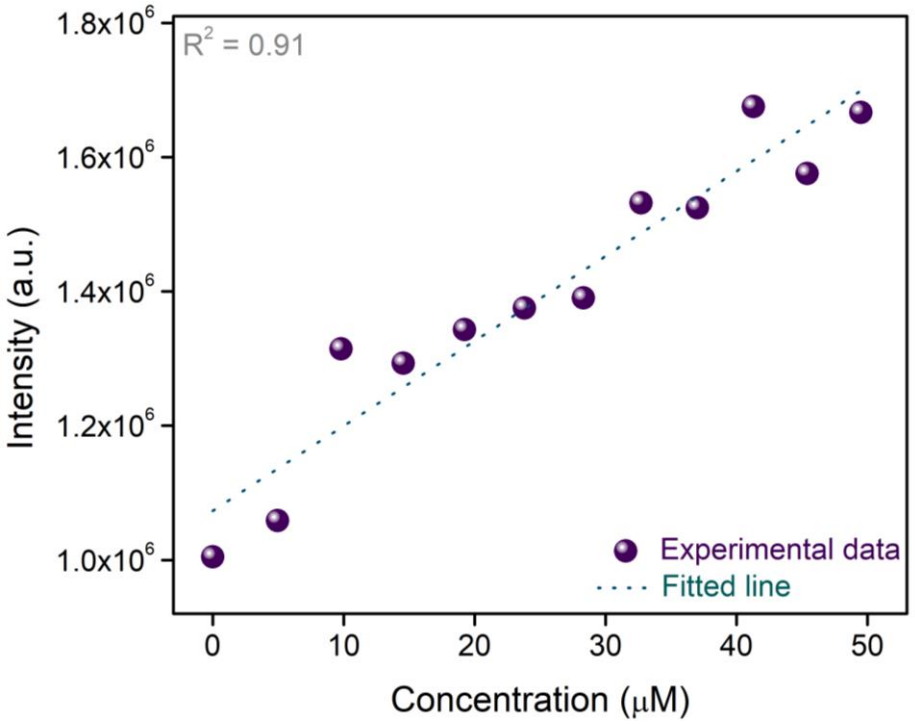

Appendix 4.25. Linear region of fluorescence intensity of probe upon addition of $HAsO_3^{2-}$; λ_{em}= 378 nm (upon excitation at 330 nm).

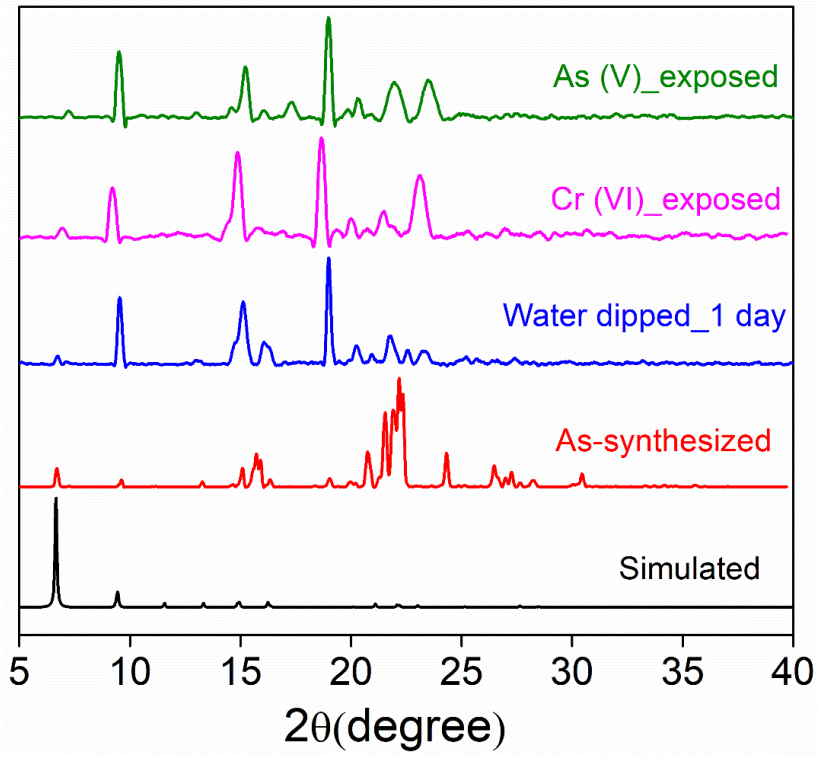

Appendix 4.26. Powder X-ray diffraction patterns of iMOF-4C.

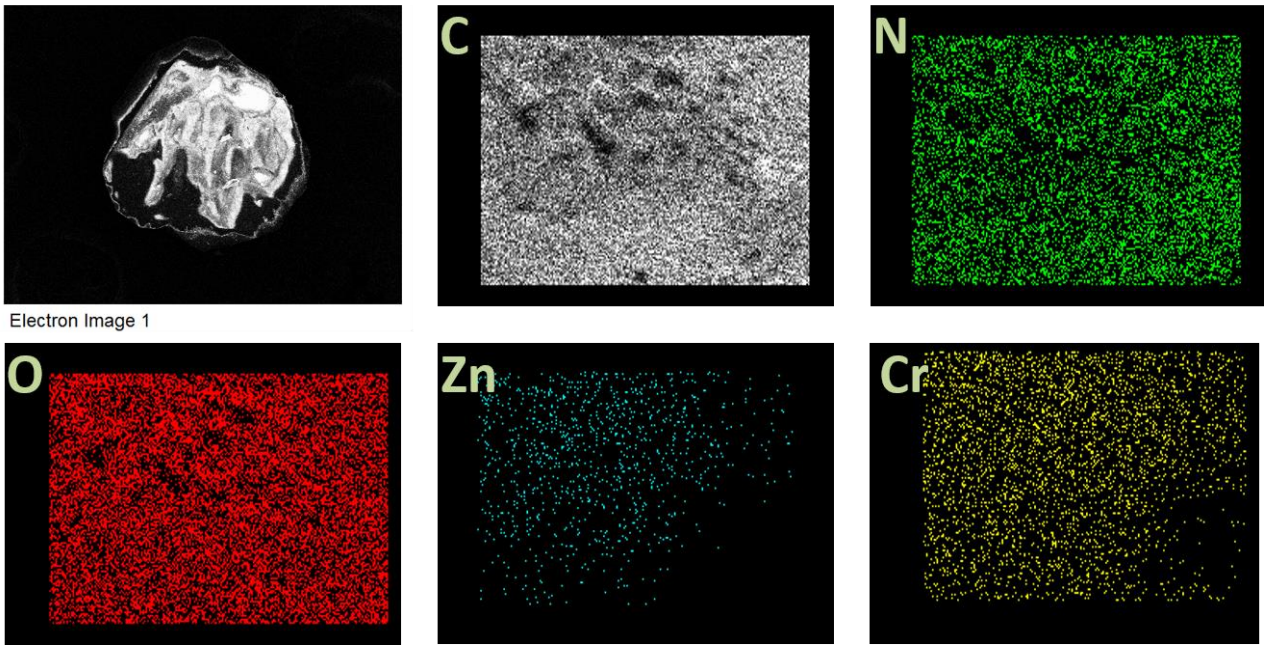

Appendix 4.27. Elemental mapping of iMOF-4C@CrO_4^{2-}.

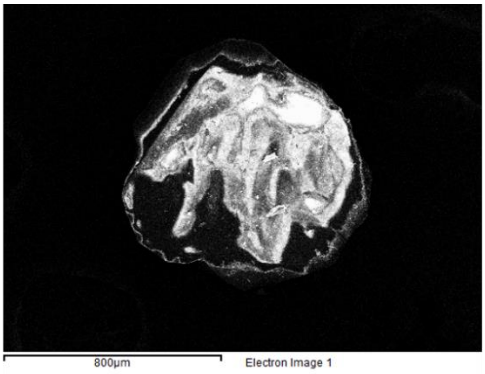

Element	Weight%	Atomic%
C K	60.76	69.64
N K	14.84	14.59
O K	16.26	13.99
Cr K	1.34	0.35
Zn L	6.80	1.43
Totals	100.00	

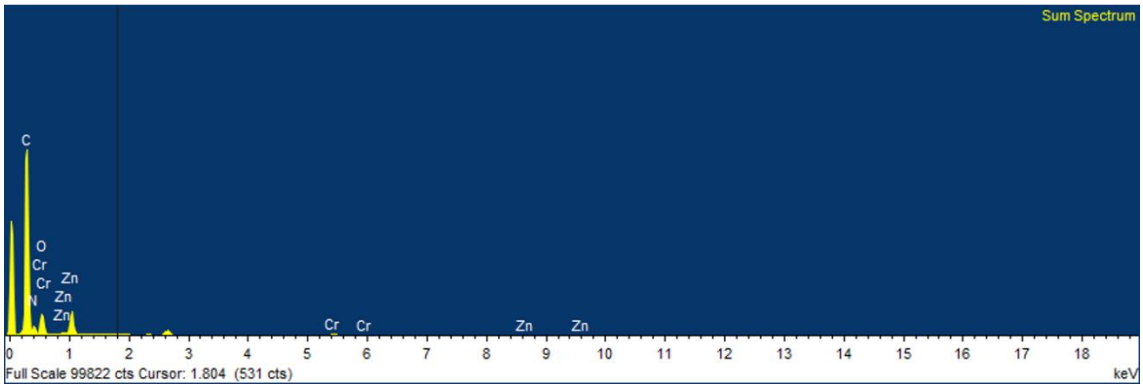

Appendix 4.28. EDX analysis of iMOF-4C.@CrO_4^{2-}.

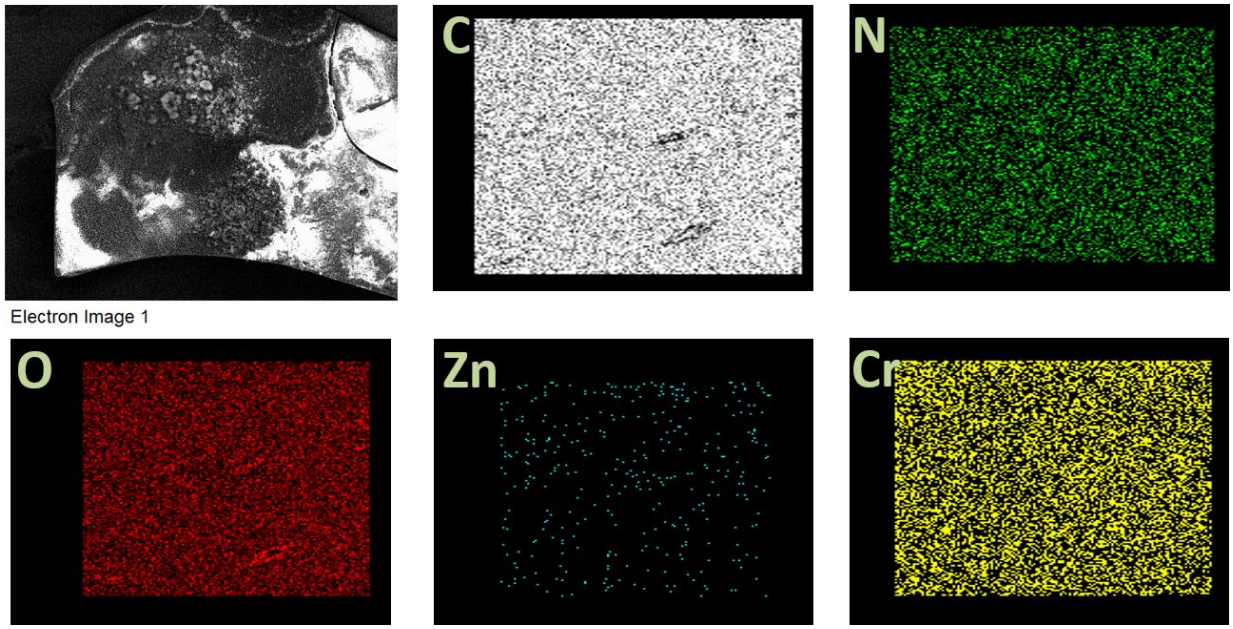

Appendix 4.29. Elemental mapping of iMOF-4C@$Cr_2O_7^{2-}$.

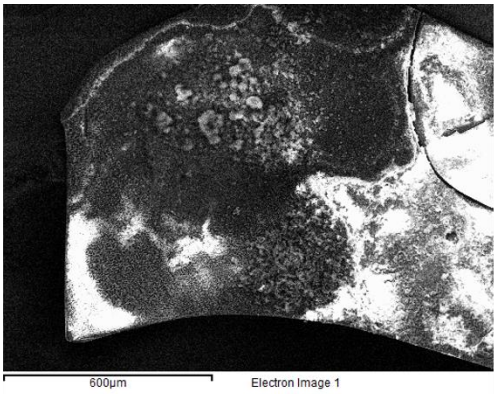

Element	Weight%	Atomic%
C K	55.80	65.05
N K	12.60	12.60
O K	23.21	20.31
Cr K	4.49	1.21
Zn L	3.90	0.83
Totals	100.00	

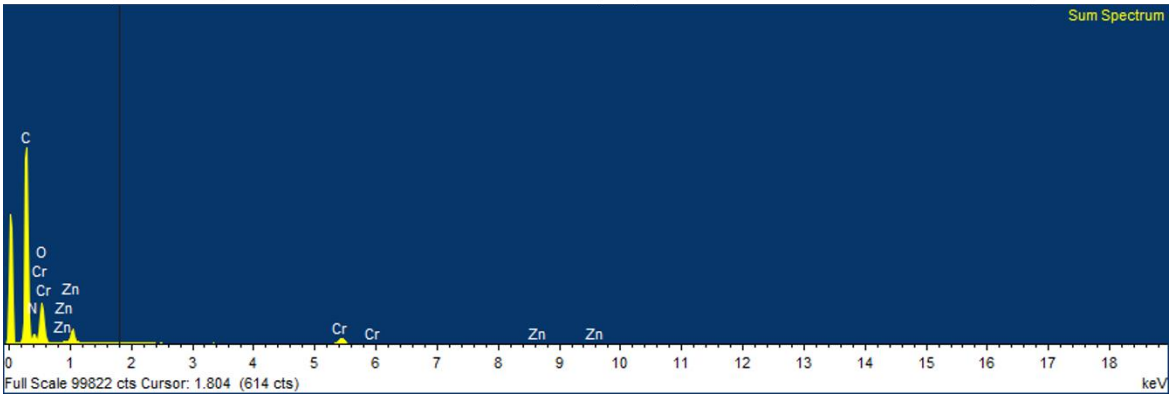

Appendix 4.30. EDX analysis of iMOF-4C.@$Cr_2O_7^{2-}$.

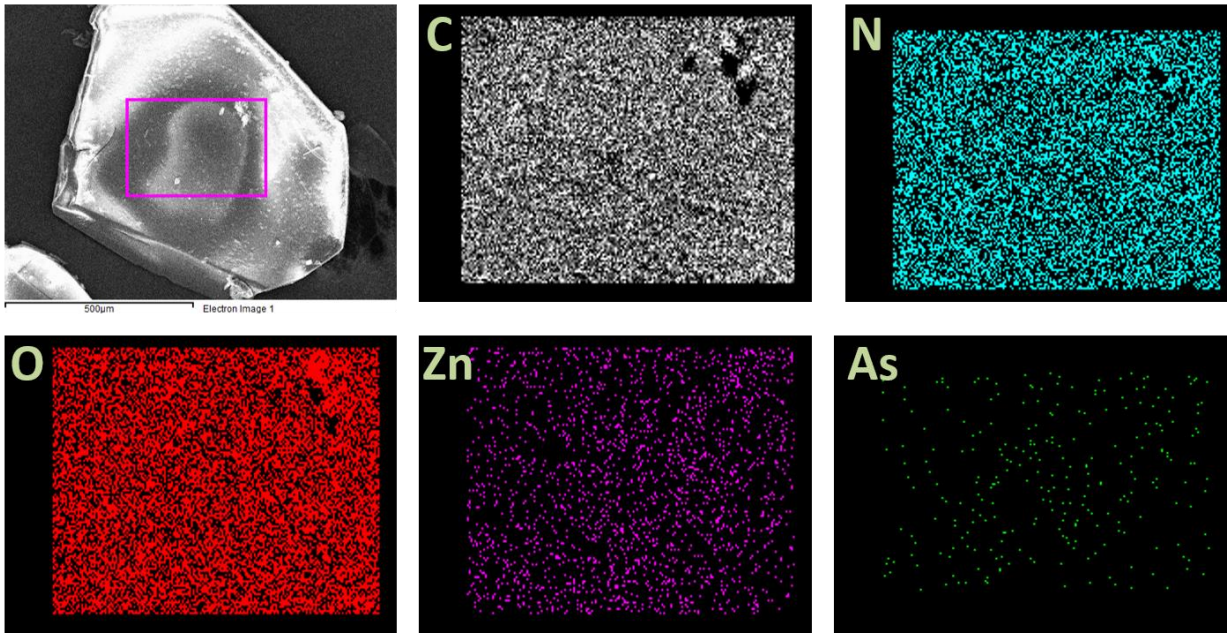

Appendix 4.31. Elemental mapping of iMOF-4C@$HAsO_4^{2-}$.

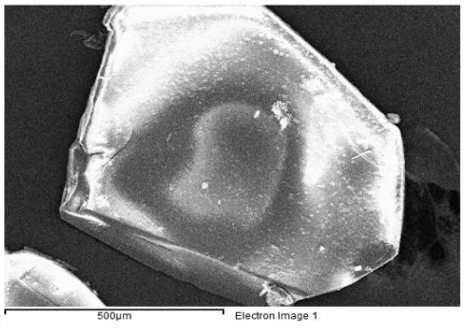

Element	Weight%	Atomic%
C K	66.79	75.78
N K	13.45	13.08
O K	10.99	9.36
Zn L	6.64	1.38
As L	2.14	0.39
Totals	100.00	

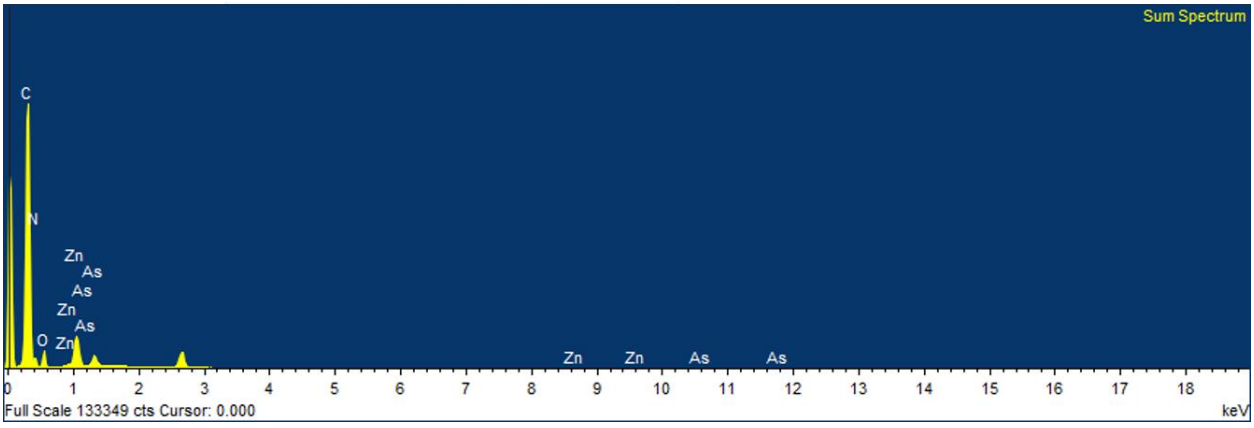

Appendix 4.32. EDX analysis of iMOF-4C@$HAsO_4^{2-}$.

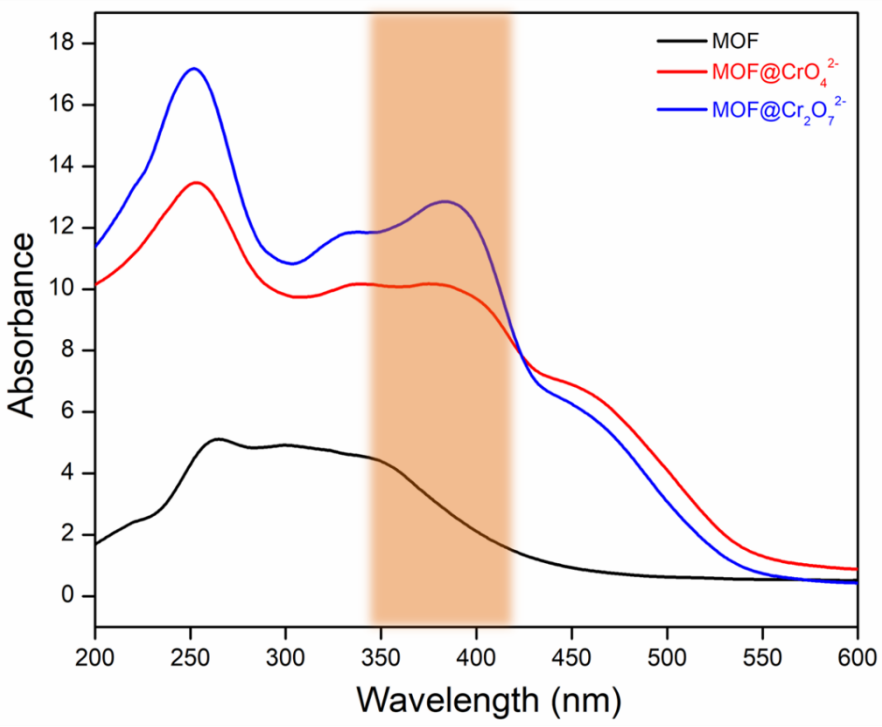

Appendix 4.33. solid state UV-vis spectra of iMOF-4C.

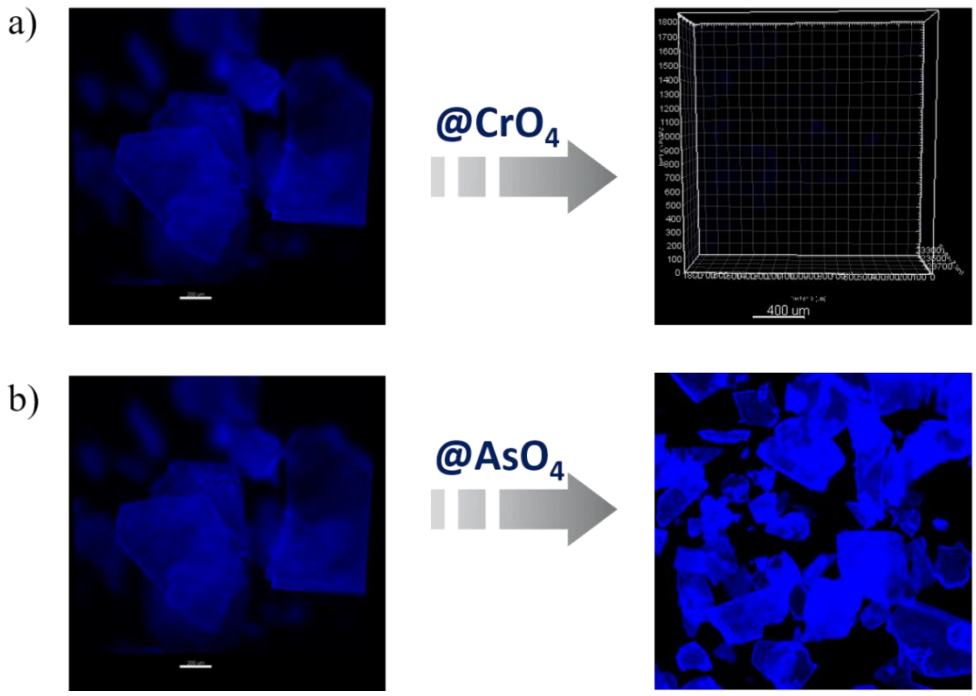

Appendix 4.34. Change in confocal fluorescence imaging of iMOF-4C upon addition of (a) CrO_4^{2-}, (b) $HAsO_4^{2-}$.

Anion exchange studies

The cationic nature of iMOF-4C prompted us to check its potential toward sequestration of these oxo-anions. For this, we have carried out an *in-situ* titration under UV−vis spectroscopy with aqueous solution of CrO_4^{2-} anions (2 mL, 0.5 mM) and 1 mg of iMOF-4C via monitoring absorption maxima (λ_{max}) at 372 nm (Appendix 4.33). A gradual decremental trend in absorption profile was observed with increasing time intervals affirmed the capture of CrO_4^{2-} anions by iMOF-4C. The anion trapping process was found to be kinetically rapid which is further advocated from the % removal vs time plot (Appendix 4.34-4.35). Additionally, the anion capture process was found to follow the pseudo second order kinetics (Figure S36).

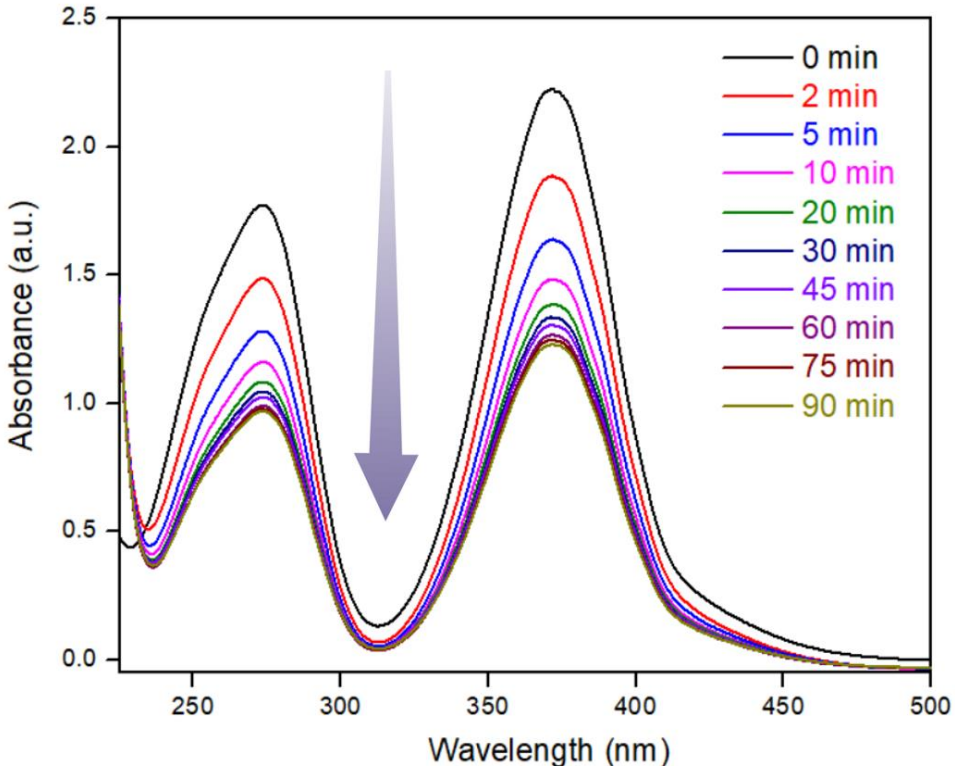

Appendix 4.35. UV−vis spectra in the presence of iMOF-4C for CrO_4^{2-}.

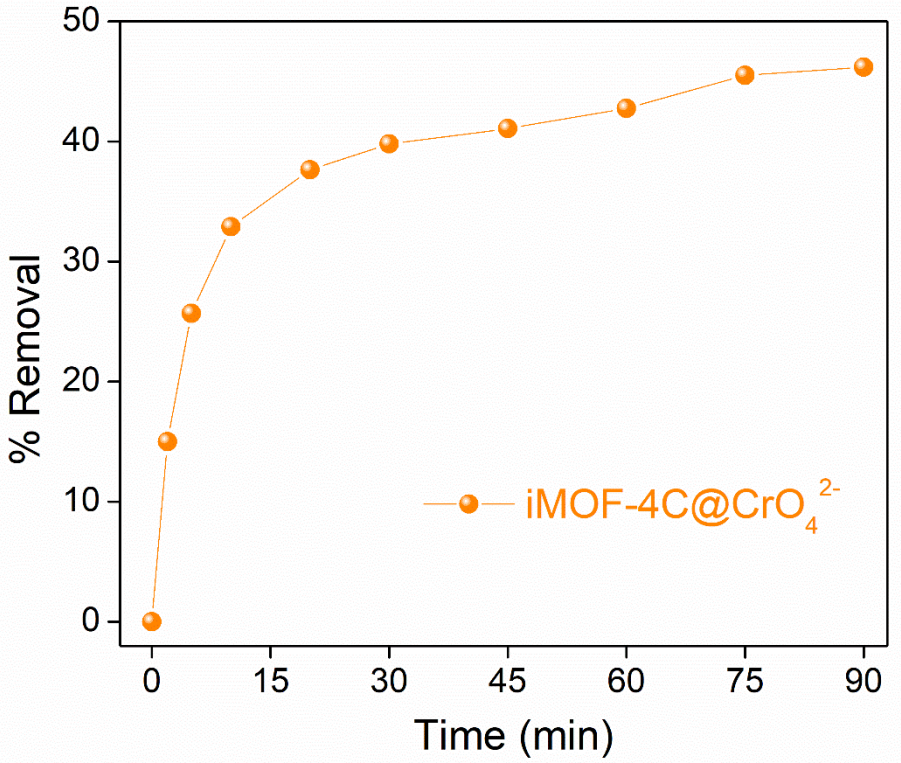

Appendix 4.36. Removal (in %) of CrO_4^{2-} with iMOF-4C at different time intervals.

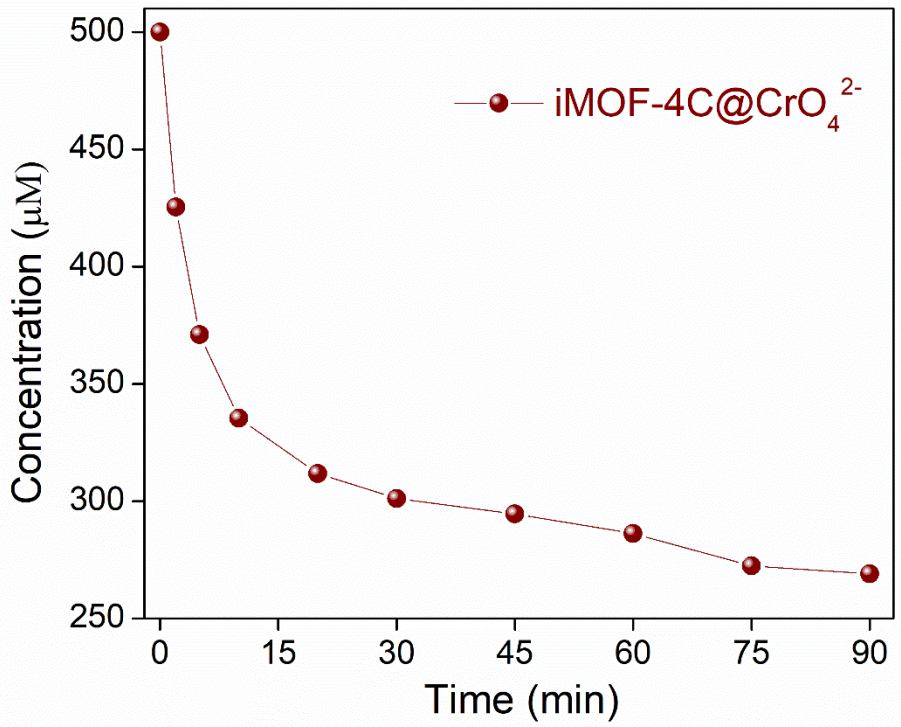

Appendix 4.37. Decrease in concentration of CrO_4^{2-} with iMOF-4C at different time intervals.

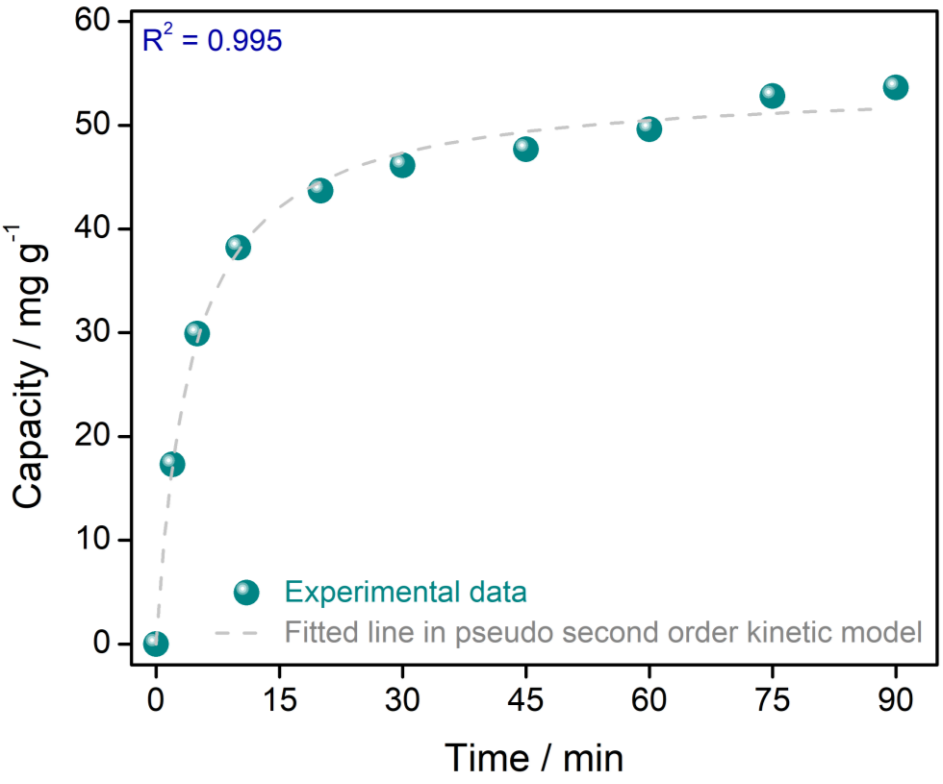

Appendix 4.38. Kinetic study of CrO_4^{2-} ion capture with iMOF-4C.

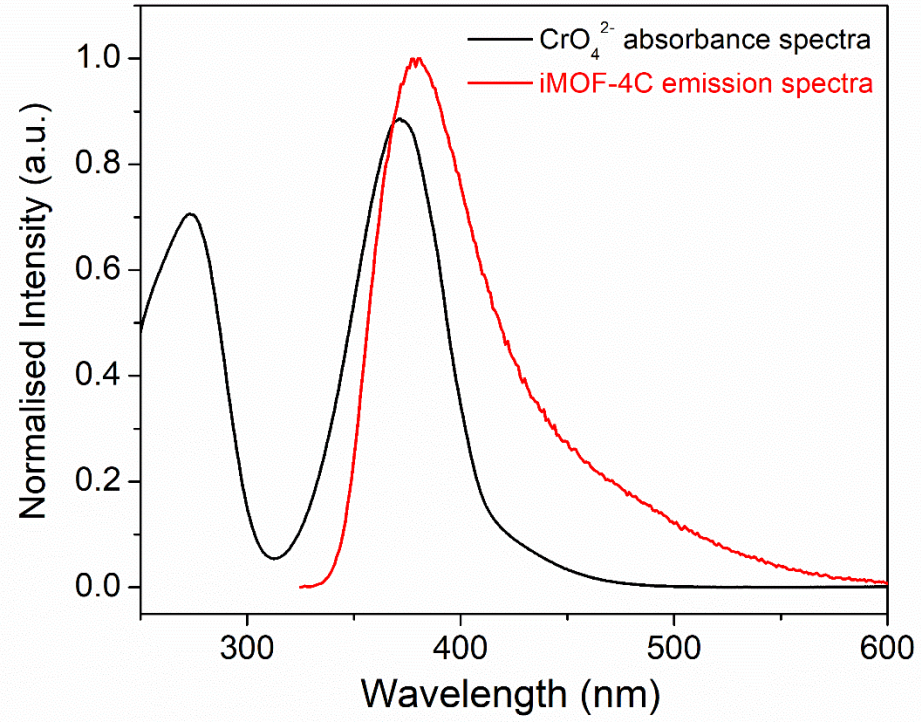

Appendix 4.39. Absorbance and emission spectra of CrO_4^{2-} and iMOF-4C respectively.

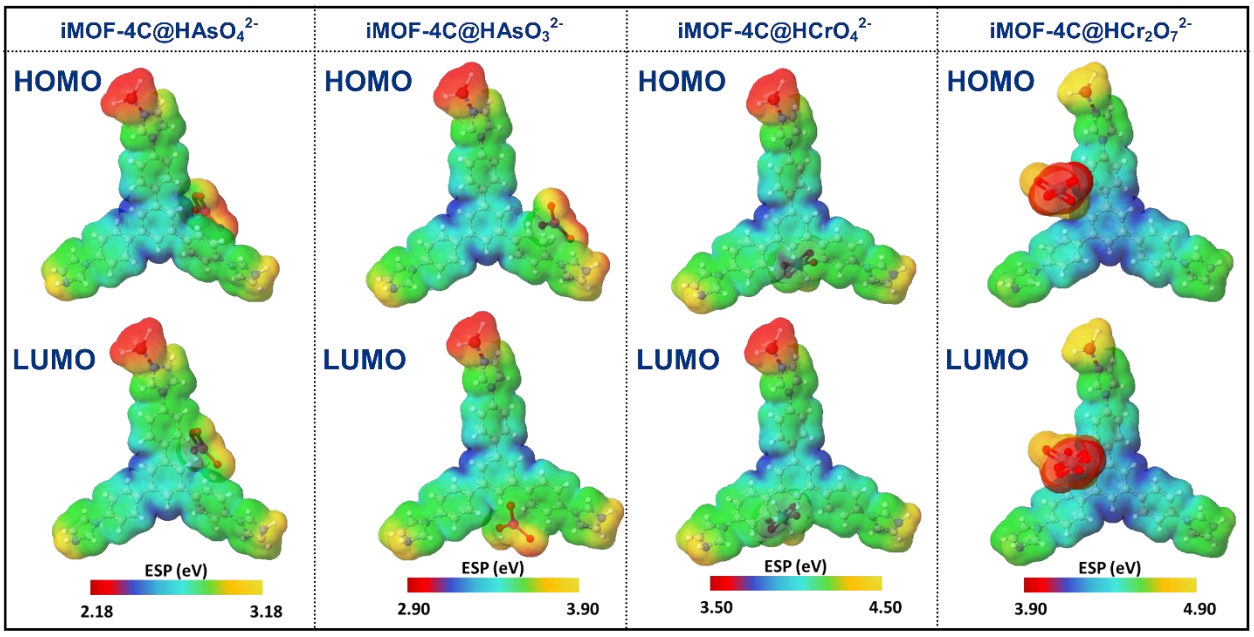

Appendix 4.40. Electron density map of HOMO and LUMO energy state of iMOF-4C showing the change in electronic properties of the framework in presence of different oxo-anions.

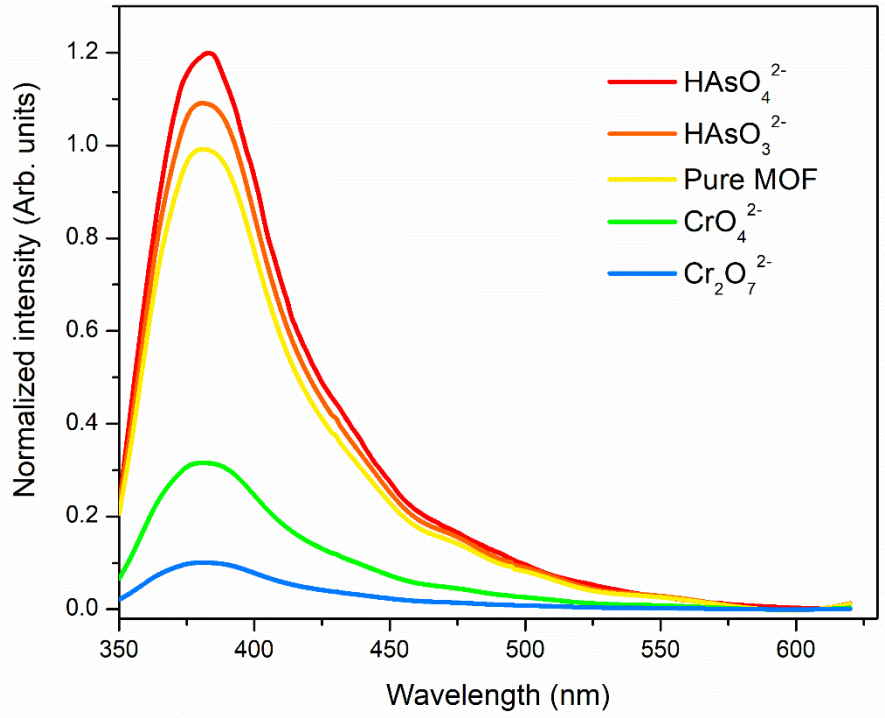

Appendix 4.41. Theoretically predicted emission profiles for iMO-4C and change in emission upon interacting with different anions based on DFT calculations on single unit.

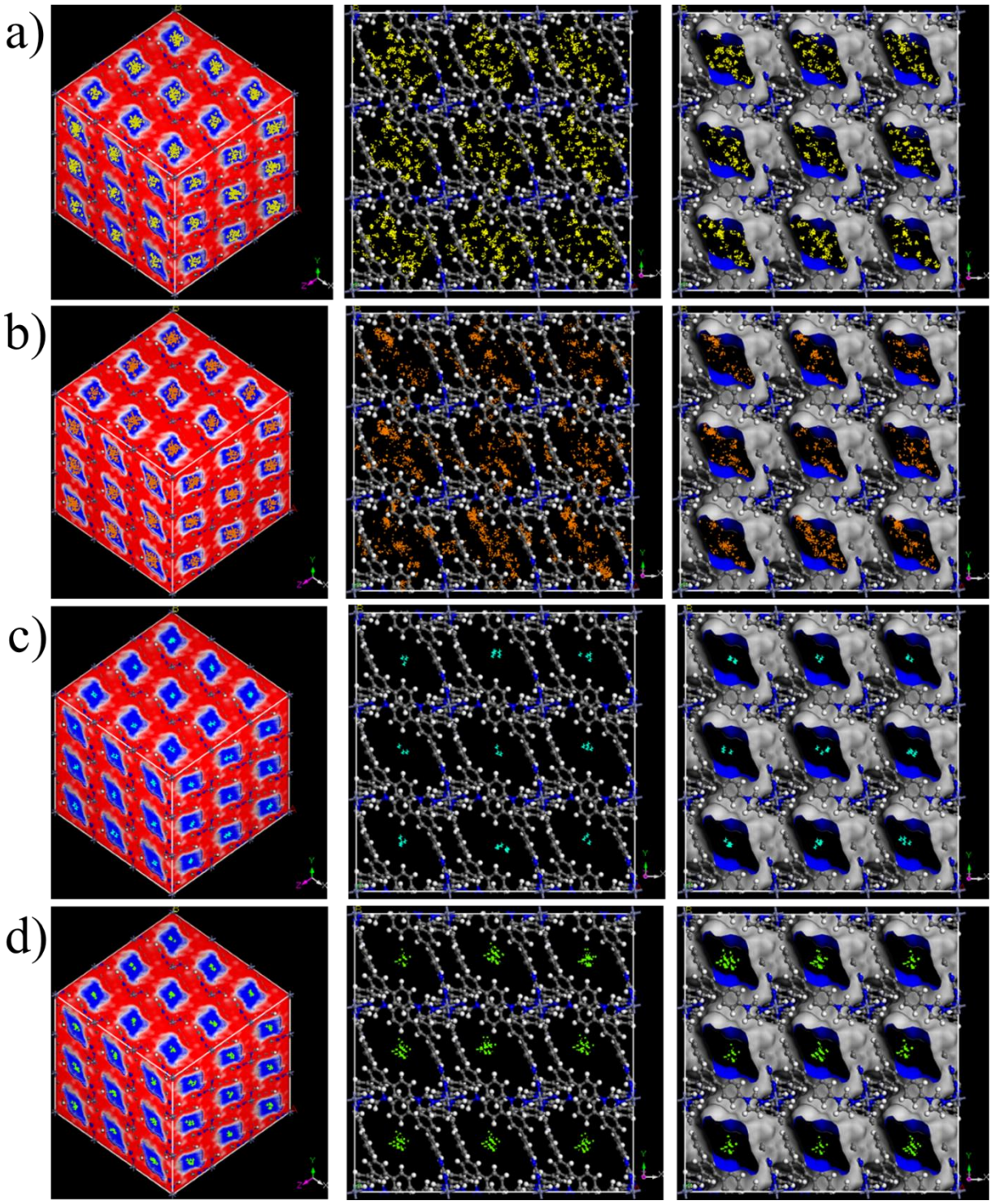

Appendix 4.42. Electron density map for (a) $Cr_2O_7^{2-}$, (b) CrO_4^{2-}, (c) $HAsO_4^{2-}$ and (d) $HAsO_3^{2-}$.

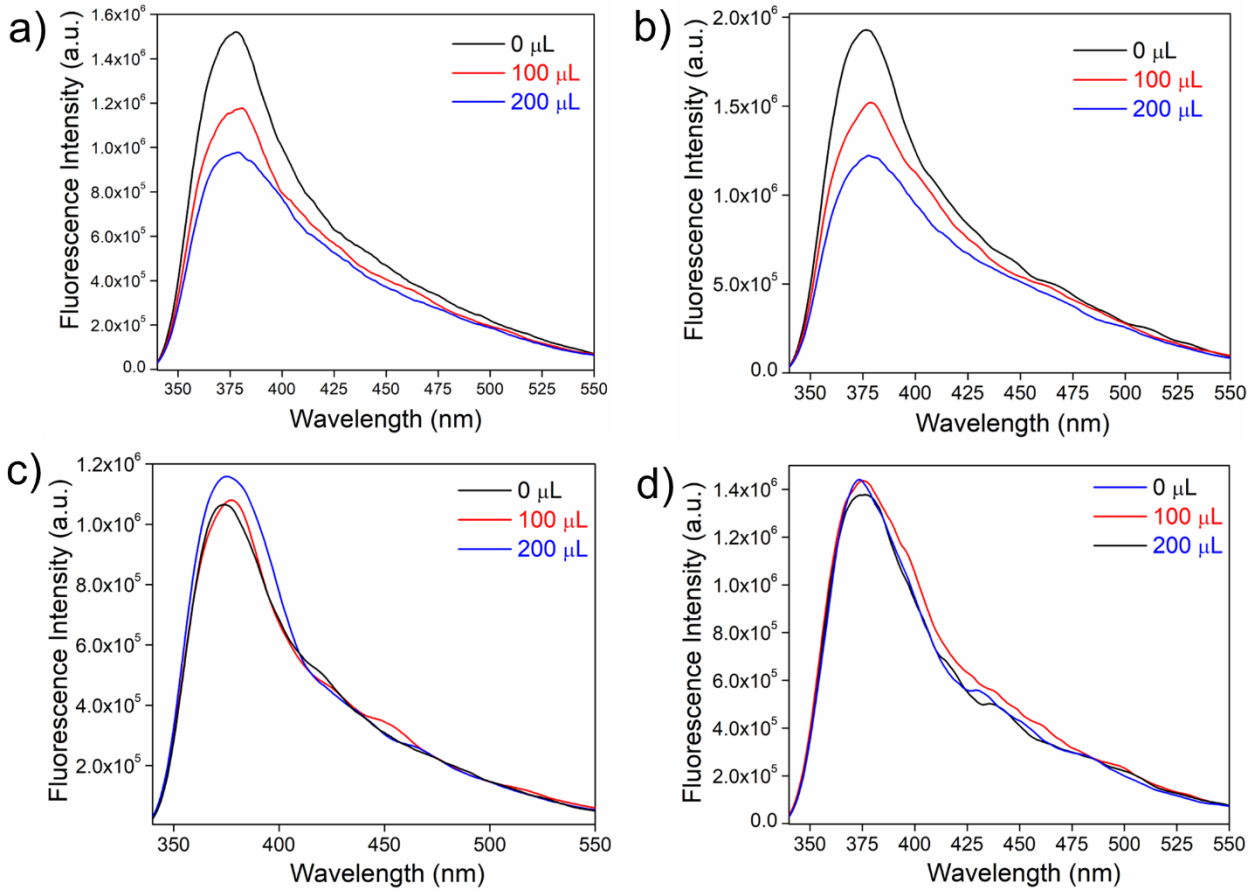

Appendix 4.43. Fluorescence responses of the only ligand (L) in presence (a) CrO_4^{2-}, (b) $Cr_2O_7^{2-}$, (c) $HAsO_4^{2-}$ and (d) $HAsO_3^{2-}$.

Appendix Table 4.1. A comparison table of Sensing performance in MOF based materials for CrO_4^{2-} and $Cr_2O_7^{2-}$ with some well-studied examples in the literature.

MOF	Analyte	K_{sv} (M^{-1})	LOD (mol/L)	Medium	Mode of Sensing	Reference
Comparison with other MOFs based CrO_4^{2-} sensors						
iMOF-4C	**CrO_4^{2-}**	**1.31×10^5**	**3.06×10^{-6}**	**Water**	**Luminescence Quenching**	**This Work**
$[Zn_3(L)(OH)(H_2O)_5]\cdot NMP\cdot 2H_2O$	CrO_4^{2-}	1.3×10^4	4.29×10^{-4}	Water	Luminescence Quenching	40
$[Cd(L)_2(H_2O)_2]$	CrO_4^{2-}	1.1×10^4	1.75×10^{-4}	Water	Luminescence Quenching	41
$[Zn_2(TPOM)(NDC)_2]\cdot 3.5H_2O$	CrO_4^{2-}	7.81×10^3	2.5×10^{-6}	Water	Luminescence Quenching	42
[Tb(L)(HCOO)(H_2O)]	CrO_4^{2-}	1.3×10^3	1.8×10^{-6}	Water	Luminescence Quenching	43
[Eu(L)(HCOO)(H_2O)]n	CrO_4^{2-}	1.5×10^3	1.2×10^{-6}	Water	Luminescence Quenching	44
$[Zn_2(TPOM)(NH_2\text{–}BDC)_2]\cdot 4H_2O$	CrO_4^{2-}	$4.45X10^3$	4.8×10^{-6}	DMF	Luminescence Quenching	45
$[Zn(btz)]_n$	CrO_4^{2-}	$3.19X10^3$	1×10^{-5}	Water	Luminescence Quenching	46
$[Zn_2(ttz)H_2O]_n$	CrO_4^{2-}	$2.35X10^3$	2×10^{-5}	Water	Luminescence Quenching	46
$[Zn(L)(H_2O)]\cdot H_2O$	CrO_4^{2-}	1.02×10^4	4.8×10^{-6}	Water	Luminescence Quenching	47
[Eu(L)(H_2O)(DMA)]	CrO_4^{2-}	5.33×10^4	7.30×10^{-6}	Water	Luminescence Quenching	48
Comparison with other MOFs based $Cr_2O_7^{2-}$ sensors						
iMOF-4C	**$Cr_2O_7^{2-}$**	**4.85×10^5**	**4.15×10^{-6}**	**Water**	**Luminescence Quenching**	**This Work**
$[Zn_3(L)(OH)(H_2O)_5]\cdot NMP\cdot 2H_2O$	$Cr_2O_7^{2-}$	6.6×10^4	6.05×10^{-5}	Water	Luminescence Quenching	40
$[Cd(L)_2(H_2O)_2]$	$Cr_2O_7^{2-}$	5.1×10^4	3.41×10^{-5}	Water	Luminescence Quenching	41
$[Tb(TBOT)(H_2O)](H_2O)_4(DMF)(NMP)_{0.5}$	$Cr_2O_7^{2-}$	1.37×10^4	1.4×10^{-4}	Water	Luminescence Quenching	49
$[Zn(L)(H_2O)]\cdot H_2O$	$Cr_2O_7^{2-}$	2.07×10^4	3.53×10^{-6}	Water	Luminescence Quenching	47
$[Zn_2(TPOM)(NH_2\text{–}BDC)_2]\cdot 4H_2O$	$Cr_2O_7^{2-}$	$7.59X10^3$	3.9×10^{-6}	DMF	Luminescence Quenching	45
Eu_4L_3	$Cr_2O_7^{2-}$	$1.52X10^3$	10×10^{-6}	DMF	Luminescence Quenching	50
$[Tb(TATAB)(H_2O)_2]\cdot NMP$	$Cr_2O_7^{2-}$	$1.11X10^4$	1×10^{-6}	Water	Luminescence Quenching	51

Eu^{3+}@MIL-121	$Cr_2O_7^{2-}$	$4.34X10^3$	0.05×10^{-6}	Water	Luminescence Quenching	52
$[Zn(btz)]_n$	$Cr_2O_7^{2-}$	$4.23X10^3$	2×10^{-6}	Water	Luminescence Quenching	46
$[Zn_2(ttz)H_2O]_n$	$Cr_2O_7^{2-}$	$2.19X10^3$	2×10^{-5}	Water	Luminescence Quenching	46

Appendix Table 4.2. Crystal data and structure refinement for iMOF-4C.

Identification code	iMOF-4C	
CCDC Number	2073931	
Empirical formula	C66 H48 N12 Zn	
Formula weight	1074.53	
Temperature	296(2) K	
Wavelength	0.71073 Å	
Crystal system	Trigonal	
Space group	R -3 :H	
Unit cell dimensions	a = 18.7016(16) Å	α= 90°.
	b = 18.7016(16) Å	β= 90°.
	c = 23.159(2) Å	γ = 120°.
Volume	7014.7(14) $Å^3$	
Z	3	
Density (calculated)	0.763 Mg/m^3	
Absorption coefficient	0.294 mm^{-1}	
F(000)	1674	
Crystal size	0.120 x 0.100 x 0.100 mm^3	
Theta range for data collection	2.162 to 26.531°.	
Index ranges	-22<=h<=23, -23<=k<=23, -29<=l<=29	
Reflections collected	26733	
Independent reflections	3224 [R(int) = 0.0494]	
Completeness to theta = 25.242°	99.6 %	
Refinement method	Full-matrix least-squares on F^2	
Data / restraints / parameters	3224 / 0 / 120	
Goodness-of-fit on F^2	1.016	
Final R indices [I>2sigma(I)]	R1 = 0.0722, wR2 = 0.2106	
R indices (all data)	R1 = 0.1162, wR2 = 0.2577	
Extinction coefficient	n/a	
Largest diff. peak and hole	0.300 and -0.544 $e.Å^{-3}$	

4.6 References

[1] L. H. Keith, W. A. Teillard, *Environ. Sci. Technol.* **1979**, *13*, 416.

[2] Resolution A/RES/64/292; *United Nations General Assembly*, July **2010**.

[3] (a) M. Palmer, E. Bernhardt, E. Chornesky, S. Collins, A. Dobson, C. Duke, B. Gold, R. Jacobson, S. Kingsland, R. Kranz, M. Mappin, M. L. Martinez, F. Micheli, J. Morse, M. Pace, M. Pascual, S. Palumbi, A. Simons, A. Townsend, M. Turner, *Science* **2004**, *304*, 1251–1252; (b) S. Mukherjee, D. Sensharma, O. T. Qazvini, S. Dutta, L. K. Macreadie, S. K. Ghosh, R. Babarao, *Coord. Chem. Rev.* **2021**, *437*, 213852.

[4] D. R. Godschalk, *Nat. Hazards Rev.* **2003**, *4*, 166.

[5] Resolution Adopted by the General Assembly on 25 September **2015**, United Nations, A/RES/70/1.

[6] (a) M. B. Luo, Y. Y. Xiong, H. Q. Wu, X. F. Feng, J. Q. Li, F. Luo, *Angew.Chem. Int. Ed.* **2017**, *56*, 16376 –16379; (b) H.-R. Fu, Y. Zhao, Z. Zhou, X.-G. Yang, L.-F. Ma, *Dalton Trans.* **2018**, *47*, 3725–3732; (c) H.-Ru Fu, N. Wang, J.-H. Qin, M.-L. Han, L.-F. Ma and F. Wang, *Chem. Commun.* **2018**, *54*, 11645--11648.

[7] (a) G. T. Pan, S. Chong, H. J. Tsai, W. H. Lu and T. C. K. Yang, *Adv. Polym. Technol.* **2018**, *37*, 1176–1184; (b) P. Samanta, P. Chandra, S. Dutta, A. V. Desai and S. K. Ghosh, *Chem. Sci.* **2018**, *9*, 7874 –7881.

[8] W. Liu, Y.Wang, Z. Bai, Y. Li, Y. Wang, L. Chen, L. Xu, J. Diwu, Z. Chai and S. Wang, *ACS Appl. Mater. Interfaces* **2017**, *9*, 16448–16457.

[9] (a) United States Environmental Protection Agency Publication. EPA816-F-01004, (accessed Sept 24, 2011). http://www.epa.gov/safewater/arsenic/compliance.html, (b) S. Sharma, S. Let, A. V. Desai, S. Dutta, G. Karuppasamy, M. M. Shirolkar, R. Babarao and S. K. Ghosh, *J. Mater. Chem. A* **2021**, *9*, 6499-6507, (c) S. Dutta, S. Let, S. Sharma, D. Mahato and S. K. Ghosh, Chem. Rec. **2021**, DOI: *10.1002/tcr.202100127*.

[10] M. F. Hughes, B. D. Beck, Y. Chen, A. S. Lewis and D. J. Thomas, *Toxicol. Sci.* **2011**, *123*, 305–332.

[11] E. Munoz and S. Palmero, *Talanta* **2005**, *65*, 613–620.

[12] S. Chatterjee, S. Sarkar and S. Bhattacharya, *Chem. Res. Toxicol.* **2014**, *27*, 1887-1900.

[13] M. A. Rahman, H. Hasegawa and R. P. Lim, *Environ. Res.* **2012**, *116*, 118-132.

[14] (a) B. Booth, *Environ. Sci. Technol.* **2009**, *43*, 1243–1244; (b) N. Mogihimi, M. Mohapatra and K. T. Leung, *Anal. Chem.* **2015**, *87*, 5546–5552; (c) S. Lohar, A. Sahana, A. Banerjee, A. Banik, S. K. Mukhopadhyay, J. S. Matalobos, D. Das, *Anal. Chem.* **2013**, *85*, 1778–1783.

[15] (a) M. Derbyshire, A. Lamberty, P. H. E. Gardiner, *Anal. Chem.* **1999**, *71*, 4203−4207; (b) B. Gammelgaard, Y. P. Liao, O. Jons, *Anal. Chim. Acta* **1997**, *354*, 107−113.

[16] B. Wen, X. Q. Shan, J. Lian, *Talanta* **2002**, *56*, 681−687.

[17] A. Syty, R. G. Chridtensen, T. C. Rains, *J. Anal. At. Spectrom.* **1988**, *3*, 193−197.

[18] (a) J. G. Navarette, M. I. Toral, A. Leiva, M. Y. Pedram, H. E Ríos, X. B. Olarán, M. D. Urzúa, *React. Funct. Polym.* **2016**, *109*, 112–119; (b) T. S. Y. Choonga, T. G. Chuaha, Y. Robiaha, F. L. G. Koaya, I. Azni, *Desalination* **2007**, *217*, 136–166; (c) M. B. Baskan, A. Pala, *Desalination* **2010**, *254*, 42–48; (d) X. Ge, J. T. Liu, X. Y. Song, G. Z. Wang, H. M. Zhang, Y.X. Zhang, H. J. Zhao, *Chem. Eng. J.* **2016**, *301*, 139–148. ; (e) J. Das, P. Sarkar, *Environ. Sci.: Water Res. Technol.* **2016**, *2*, 693–704.

[19] (a) E. Barea, C. Montoro, J. A. R. Navarro, *Chem. Soc. Rev.* **2014**, *43*, 5419-5430; (b) J.Cui, Y. -L. Wong, M. Zeller, A. D. Hunter, Z. Xu, *Angew. Chem. Int. Ed.* 2014, *53***,** 14438-14442. ; (c) D. –G. Cho, J. L. Sessler, *Chem. Soc. Rev.* **2009**, *38*, 1647-1662. ; (d) J. Du, M. Hu, J. Fan, X. Peng, *Chem. Soc. Rev.* **2012**, *41*, 4511-4535.

[20] (a) L. E. Kreno, K. Leong, O. K. Farha, M. Allendorf, R. P. Van Duyne, J. T. Hupp, *Chem. Rev.* **2012**, *112*, 1105-1125; (b) M. D. Allendorf, C. A. Bauer, R. K. Bhakta, R. J. T. Houk, *Chem. Soc. Rev.* **2009**, *38*, 1330-1352; (c) Y. Cui, Y. Yue, G. Qian, B. Chen, *Chem. Rev.* **2012**, *112*, 1126-1162; (d) R. Dalapati, S. Biswas, *Chem. Asian J.* **2019**, *14*, 2822 –2830; (e) S. Let, P. Samanta, S. Dutta, S. K. Ghosh, *Inorganica Chimica Acta* **2019**, *500*, 119205.

[21] (a) Metal-Organic Frameworks (MOFs) for Environmental Applications (Book Edited by: Dr. Sujit K. Ghosh, Elsevier Publication, **2019** DOI: https://doi.org/10.1016/C2017-0-01721-4;

(b) J. Li, G. Zhao, C. Chen, Z. Chai, A. Alsaedi, T. Hayat, X. Wang, *Chem. Soc. Rev.* **2018**, *47*, 2322-2356; (c) W. P. Lustig, S. Mukherjee, N. D. Rudd, A. V. Desai, J. Li, S. K. Ghosh, *Chem. Soc. Rev.* **2017**, *46*, 3242-3285; (d) P.Samanta, A. V. Desai, S. Let and S. K. Ghosh, *ACS Sustainable Chem. Eng.* **2019**, *7*, 7456-7478; (e) P. Samanta, S. Let, W. Mandal, S. Dutta, S. K. Ghosh, *Inorg. Chem. Front.* **2020**, *7*, 1801-1821; (f) A. Karmakar, P. Samanta, S. Dutta, S. K. Ghosh, *Chem.Asian J.* **2019**, *14*, 4506 – 4519; (g) H.-R. Fu, X.-X. Wu, L.-F. Ma, F. Wang, J. Zhang, *ACS Appl. Mater. Interfaces* **2018**, *21*, 18012–18020; (h) T. He, Y.-Z. Zhang, X.-J. Kong, J. Yu, X.-L. Lv, Y. Wu, Z.-Ji Guo, J.-R. Li, *ACS Appl. Mater. Interfaces* **2018**, *19*, 16650–16659.

[22] (a) X. Wang, L. Zhang, J. Yang, F. Liu, F. Dai, R. Wang, D. Sun, *J. Mater. Chem. A* **2015**, *3*, 12777−12785; (b) S. Khatua, S. Goswami, S. Biswas, K. Tomar, H. S. Jena, S. Konar, *Chem. Mater.* **2015**, *27*, 5349−5360; (c) A. V. Desai, S. Sharma, A. Roy, M. M. Shirolkar, S. K. Ghosh, *Mol. Syst. Des. Eng.* **2020**, *5*, 469-476.

[23] (a) Y. Lu, B. Yan, J. L. Liu, *Chem. Commun.* **2014**, *50*, 9969−9972; (b) S.Fajal, P. Samanta, S. Dutta, S. K. Ghosh, *Inorganica Chimica Acta* **2019**, *502*, 1193592; (c) M. Zheng, H. Tan, Z. Xie, L. Zhang, X. Jing, Z. Sun, *ACS Appl.Mater. Interfaces* **2013**, *5*, 1078−1083; (d) P. Samanta, A. V. Desai, S. Sharma, P. Chandra, S. K. Ghosh, *Inorg. Chem* **2018**, *57*, 2360-2364.

[24] (a) W. -T. Koo, S. –J. Choi, S. –J. Kim, J. –S. Jang, H. L. Tuller, I. –D. Kim, *J. Am. Chem. Soc.* **2016**, *138*, 13431−13437; (b) M. Drobek, J. H. Kim, M. Bechelany, C. Vallicari, A. Julbe, S. S. Kim, *ACS Appl. Mater. Interfaces* **2016**, *8*, 8323−8328; (c) A. V. Deasi, B. Joarder, A. Roy, P. Samanta, R. Babarao, S. K. Ghosh, *ACS Appl. Mater. Interfaces* **2018**, *10*, 39049–39055; (d) C. Gogoi, A. Kumar, M. SK, S. Biswas, *Microporous Mesoporous Mater.* **2021**, *311*, 110725; (e) A. Karmakar, B. Joarder, A. Mallick, P. Samanta, A. V. Desai, S. Basu, S. K. Ghosh, *Chem. Commun.* **2017**, *53*, 1253-1256; (f) R. Dalapati, S. Nandi, S. Biswas, *Dalton Trans.* **2020**, *49*, 8684-8692.

[25] (a) D. Xie, Y. Ma, Y. Gu, H. Zhou, H. Zhang, G. Wang, Y. Zhang, H. Zhao, *J. Mater. Chem. A* **2017**, *5*, 23794–23804; (b) L. Esrafili, A. Morsali, M. –L. Hu, A. A. Tehrani, L. Carlucci, P. Mercandelli, D. M. Proserpio, *Inorg. Chem.* **2020**, *59*, 16421−16429; (c) X. Xu, Z. Luo, K. Ye, X. Zou, X. Niu, J. Pan, https://doi.org/10.1016/j.jhazmat.2020.124407. ; (d) C. -X.

Wang, Y. –P. Xia, Z. –Q. Yao, J. Xu, Z. Chang, X. –H. Bu, *Dalton Trans.* **2019**, *48*, 387–394; (e) Z. Chen, X. Mi, J. Lu, S. Wang, Y. Li, J. Dou, D. Li, *Dalton Trans.* **2018**, *47*, 6240–6249; (f) P. Li, X. –M. Yin, L. –L. Gao, S. –L. Yang, Q. Sui, T, Gong, E. –Q. Gao, *ACS Appl. Nano Mater.* **2019**, *2*, 4646−4654; (g) Z. J. Lin, H. –Q. Zheng, H. –Y. Zheng, L. –P. Lin, Q. Xin, R. Cao, *Inorg. Chem.* **2017**, *56*, 14178−14188.

[26] (a) R. Goswami, S. C. Mandal, B. Pathak, S. Neogi, *ACS Appl. Mater. Interfaces* **2019**, *43*, 40134–40150; (b) W. Liu, Y. Wang, Z. Bai, Y. Li, Y. Wang, L. Chen, L. Xu, J. Diwu, Z. Chai, S. Wang, *ACS Appl. Mater. Interfaces* **2017**, *9*, 16448−16457; (c) Z. Li, W. Cai, X. Yang, A. Zhou, Y. Zhu, H. Wang, X. Zhou, K. Xiong, Q. Zhang, Y. Gai, *Cryst. Growth Des.* **2020**, *5*, 3466–3473.

[27] A. V. Desai, A. Roy, P. Samanta, B. Manna, S. K. Ghosh, *iScience* **2018**, *3*, 21-30

[28] (a) S. Dutta, P. Samanta, B. Joarder, S. Let, D. Mahato, R. Babarao, S. K. Ghosh, *ACS Appl. Mater. Interfaces* **2020**, *37*, 41810–41818; (b) D. Sheng, L. Zhu, X. Dai, C. Xu, P. Li, C. I. Pearce,C. Xiao,J. Chen, R. Zhou, T. Duan, O. K. Farha, Z. Chai, S. Wang, Angew.Chem. Int. Ed. **2019**, *58*, 4968 –4972.

[29] SAINT Plus; Bruker AXS Inc.: Madison, WI, **2004**.

[30] L. Krause, R. Herbst-Irmer, G. M. Sheldrick, D. Stalke, *J. Appl. Crystallogr*. **2015**, *48*, 3−10.

[31] G. M. Sheldrick, SHELXTL, Reference Manual, version 5.1; Bruker AXS Inc.: Madison, WI, **1997**.

[32] G. M. Sheldrick, *Acta Crystallogr., Sect. A: Found. Crystallogr*. **2008**, *64*, 112−122.

[33] G. M. Sheldrick, *Acta Crystallogr., Sect. C: Struct. Chem*. **2015**, *71*, 3−8.

[34] L. Farrugia, WinGX; University of Glasgow: Glasgow, Scotland, **2009**.

[35] A. L. Spek, *Acta Crystallogr., Sect. C: Struct. Chem*. **2015**, *71*, 9−18.

[36] P. Samanta, A. V. Desai, S. Sharma, P. Chandra, S. K. Ghosh, *Inorg. Chem*. **2018**, *57*, 2360–2364.

[37] Dassault Systèmes BIOVIA, Materials Studio, **2017**, San Diego: Dassault Systèmes.

[38] (a) M. Wang, L. Guo, D. Cao, *Anal. Chem*. **2018**, *90*, 3608−3614; (b) R. Goswami, S. C. Mandal, N. Seal, B. Pathak, S. Neogi, *J. Mater. Chem. A* **2019**, *7*, 19471–19484.

[39] M. M. Shirolkar, R. Athavale, S. Ravindran, V. Rale, A. Kulkarni, R. Deokar, *Nano-Structures & Nano-Objects* **2021**, *25*, 100657.

[40] Y.-T. Yan, W.-Y. Zhang, F. Zhang, F. Cao, R.-F. Yang, Y.-Y. Wang, L. Hou, *Dalton Trans.* **2018**, *47*, 1682-1692.

[41] Y.-T. Yan, F. Cao, W.-Y. Zhang, S.-S. Zhang, F. Zhanga, Y.-Y. Wang, *New J. Chem*. **2018**, *42*, 9865-9875.

[42] R. Lv, H. Li, J. Su, X. Fu, B. Yang, W. Gu, X. Liu, *Inorg. Chem*. **2017**, *56*, 12348–12356.

[43] Z. Sun, M. Yang, Y. Ma, L. Li, *Cryst. Growth Des.* **2017**, *17*, 4326–4335.

[44] Z. Sun, M. Yang, Y. Ma, L. Li, *Cryst. Growth Des.* **2017**, *17*, 4326–4335.

[45] R. Lv, J. Wang, Y. Zhang, H. Li, L. Yang, S. Liao, W. Gu, X. Liu, *J. Mater. Chem. A* **2016**, *4*, 15494-15500.

[46] C.-S. Cao, H.-C. Hu, H. Xu, W.-Z. Qiao, B. Zhao, *CrystEngComm* **2016**, ***18***, 4445-4451.

[47] X.-Y. Guo, F. Zhao, J.-J. Liu, Z.-L. Liu, Y.-Q. Wang, *J. Mater. Chem. A* **2017**, *5*, 20035-20043.

[48] J.-J. Zhao, P.-Y. Liu, L.-J. Song, L. Zhang, Z.-L. Liu, Y.-Q. Wang, *Dalton Trans.* **2021**, Advance Article, DOI:*10.1039/D1DT00112D*.

[49] M. Chen, W.-M. Xu, J.-Y. Tian, H. Cui, J.-X. Zhang, C.-S. Liu, M. Du, *J. Mater. Chem. C* **2017**, *5*, 2015-2021.

[50] W. Liu, X. Huang, C. Xu, C. Chen, L. Yang, W. Dou, W. Chen, H. Yang, W. Liu, *Chem. Eur.J.* **2016**, *22*, 18769 –18776.

[51] G.-X. Wen, M.-L. Han, X.-Q. Wu, Y.-P. Wu, W.-W. Dong, J. Zhao, D.-S. Li, L.-F. Ma, *Dalton Trans.* **2016**, *45*, 15492-15499.

[52] J.-N. Hao, B. Yan, *New J. Chem.* **2016**, *40*, 4654-4661.

Chapter 5

A Water Stable Cationic MOF with Hydrophobic Pore Surface as Efficient Scavenger of Oxo-anion Pollutants from Water

5.1 Introduction

Water pollution in the recent past has escalated to be a pressing problem globally that threatens the development and survival of human civilization. The intensifying impact of widespread growing urbanization and industrialization across the world prevails to be the foremost reason for water pollution.[1-2] Such enormous water pollution has led to the huge depletion of drinking water. In the same context, the United Nations have predicted that by the year 2025, at least one billion people will encounter the ultimate crisis of access to clean water.[3] Water pollution can occur through various sources, amongst which pollution due to heavy metals (metals having density greater than 5 g cm^{-3}) or heavy metal based oxo-anions (AsO_4^{3-}, CrO_4^{2-}, SeO_3^{2-}, TcO_4^{-} etc.) have certainly become a pertinent problem as the bio-accumulation of such elements within living organisms causes severe toxicity.[4] The US Environment Protection Agency (EPA) has listed several inorganic pollutants including these aforementioned oxo-anions as priority pollutants.[5-6] In recent years, immense research attention has been devoted towards the sequestration of Cr (VI) based oxo-anions owing to their mutagenic and carcinogenic impacts on living systems.[7-8] Industries like steel manufacturing, leather tanning, wood preservation, textile pigments and dyes etc. have been found to use chromate in huge quantities for various applications. Among them, tanning based industries solely release 30–35 liters of chromium contaminated water for the production of one kilogram of leather.[9-10] Moreover, the vitrification process of nuclear waste is found to be affected by Cr(VI) oxo-anions as it weakens the integrality of waste glass by forming crystalline spinels along with the waste glass.[11-12] Furthermore, several nations across the globe have witnessed various calamities of ground water contamination owing to the inappropriate disposal of Cr (VI) anions, for example, groundwater contamination in Hinkley, California is one such incident, which has drawn attention globally.[13] Apart from these heavy metal-based water contamination issues, radioactive waste generated from nuclear power generating fission process is another genuine concern.[14] To address this pertinent problem, sequestration of pertechnetate (TcO_4^-) ion has become a pressing concern as the major nuclear fission product of technetium, (^{99}Tc) is found to be radioactive in nature with a very long half-life of 2.1×10^5 years. Nuclear fission processes of ^{239}Pu or ^{235}U produce radioactive ^{99}Tc with a high fission yield and it has been estimated that until the year of 2010, nearly 305 metric tons of ^{99}Tc has been released from various nuclear reactors and weapons testing operations.[15] The high mobility of TcO_4^- in water combined with it‘s high stability, non-complexing property and high water solubility induces it to exist as low-level waste material.[16] Although, various techniques, such as photocatalytic reduction, adsorption, ion exchange, chemical precipitation etc. have been employed to counter this issue, ion exchange process scores over other techniques owing to their relatively easy and

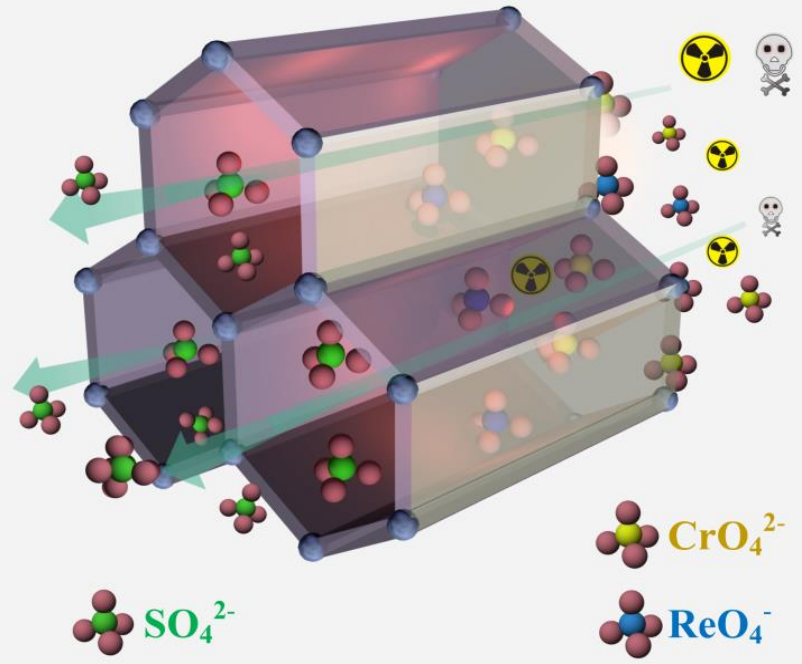

Scheme 5.1. Schematic representation of oxo-anion capture by a cationic MOF.

safe handling, high sensitivity and selectivity, high efficiency in low concentration waste solution etc.[17-22] However, the use of contemporary ion-exchangers encompasses impediments such as poor kinetics, lower selectivity, inferior efficiency which in turn propels the need for seeking novel materials.[23-24]

Over the past two decades, metal-organic frameworks (MOFs) have proliferated as one of the most significant classes of porous materials due to their wide range of applications.[25-39] Amongst them, cationic metal-organic frameworks (iMOF-C) have attracted enormous attention due to their applicability as anion receptors as well as ion exchange materials.[40-41] Existing cationic materials such as layered double hydroxides, cationic polymeric materials, cationic lanthanide hydroxide etc. have already been explored towards capture anions with higher charge density as the electrostatic interaction exclusively dictates the entire host-guest interaction.[42-45] Consequently, due to this kind of general trend, namely, Hofmeister bias selectivity, the capture of toxic anionic pollutants having lower charge density is extremely tortuous.[46-48] To counter this dilemma, we have adopted a strategy to synthesize a robust cationic MOF with a built-in hydrophobic cavity inside which can effectively interact, selectively recognize anions having lower charge density through hydrogen bonding with the hydrophobic cavity assisted by anion exchange. Additionally, the strategic choice of uncoordinated anions having tetrahedral geometry such as (SO_4^{2-} or PO_4^{3-}) can facilitate the anion exchange process, e.g. fast kinetics, selectivity owing to the shape template effect.

In one of our recent report, we have shown strategically selective capture study of permanganate (MnO_4^-) and dichromate ($Cr_2O_7^{2-}$) ions by a 3D water-stable cationic MOF. However, this work encounters issues regarding the chemical stability of the MOF as the central metal center is coordinated by four ligands along with one solvent molecule (water) and one SO_4^{2-} anion. On account of such structural restrictions, the compound was found to present limited chemical stability. Additionally, the unexchangeability of the coordinated SO_4^{2-} anions results into a partial exchange of the SO_4^{2-} anions inside of the porous network with the incoming anions and consequently illustrates lower uptake capacity of the material, which is one of the most important aspect for an efficient sorbent material in toxic anion capture processes.[23]

Taking all these aspects into account, herein we report a new robust chemically stable, cationic MOF $[\{Ni(L)_2\}\cdot(SO_4)\cdot x(G)]_n$ (iMOF-2C; L= ligand); G= DMF, H_2O), crafted from a neutral tripodal linker containing free exchangeable sulfate ions inside the pores. The guest free phase of iMOF-2C was found to act as a rapid and selective scavenger for both oxo-anions, namely chromate (CrO_4^{2-}) and perrhenate (ReO_4^-) ions, while the later being employed as a surrogate analogue for radioactive TcO_4^- anions (Scheme 1).

5.2 Experimental

5.2.1. Materials: All reagents and solvents were commercially accessible and used without any further purification.

5.2.2. Synthesis

Synthesis of Ligand 1,1'-(5'-(4-(1H-imidazol-1-yl)phenyl)-[1,1':3',1''-terphenyl]-4,4''-diyl)bis(1H-imidazole): The ligand was synthesized following a reported protocol.[49] A mixture of 4,4''-dibromo-5'-(4-bromophenyl)-1,1':3',1''-terphenyl (1 gm, 0.92 mmol), imidazole (752 mg, 5.3 mmol), K_2CO_3 (1.02 gm, 3.6 mmol) and $CuSO_4$ (6.5 mg, 0.041 mmol) was heated at 160^{o}C under inert atmosphere for 120 hours. After cooling to room temperature, the reaction mixture was dissolved with CH_2Cl_2 (60 ml) and washed several times with water. The organic layer was brought to dryness to give a white powder. The ligand was recyrstallized from a mixture of MeOH:CH_2Cl_2 (1:1) in yield of 75%.

Synthesis of iMOF-2C: A mixture of the ligand (L) (10.15 mg, 0.02 mmol), $NiSO_4\cdot xH_2O$ (5.60mg, 0.02 mmol), water (1 ml) and N,N-dimethylformamide (2 ml) was kept in a teflon capped glass vial and was heated for 48 hours at 120^{o}C followed by cooling down to room temperature. The compound was separated by filtration and washed with methanol and water for

several times. Off white color crystals of compound iMOF-2C were obtained in ~58% yield. Further the obtained crystals were dipped in MeOH for 2 days prior to heating it under high vacuum at 90^{o}C to acquire guest free phase iMOF-2C. Additionally, we could not locate the highly disordered guest molecules in the structure crystallographically. The formula of iMOF-2C was determined from PLATON SQUEEZE function and estimated to be $\{[Ni_1(L)_1\}]\cdot(SO_4)_2.x(G)\}$.

5.2.3. Physical Measurements: Powder X-ray diffraction patterns were recorded on Bruker D8 Advanced X-Ray diffractometer using Cu Kα radiation (λ= 1.5406 Å) in 5° to 40° 2θ range with a scan speed of 0.6omin^{-1}. All infra-red (IR) spectra were recorded using a NICOLET 6700 FT-IR spectrophotometer, using KBr pellets in the range of 400– 4000 cm^{-1}. Thermogravimetric analysis (TGA) was recorded on a Perkin-Elmer STA 6000 TGA analyser under an N_2 atmosphere with a heating rate of 10^{o}C min^{-1}. Gas adsorption measurements were carried out using a Bel Sorp-max instrument from Bel Japan. FESEM was performed using a FEI Quanta 3D dual beam ESEM at 30 kV. UV spectra were acquired on a Shimadzu UV 2600 Spectrophotometer. HRTEM images were recorded on JEOL USA JEM-2200 FS Transmission Electron Microscope.

5.2.4. X-ray Structural Studies: Single-crystal X-ray data of iMOF-2C was collected at 150 K on a Bruker KAPPA APEX II CCD Duo diffractometer (operated at 1500 W power: 50 kV, 30 mA) using graphite-monochromated Mo Kα radiation (λ = 0.71073 Å). Crystal was on nylon CryoLoops (Hampton Research) with Paraton-N (Hampton Research). The data integration and reduction were processed with SAINT software.[50] A multi-scan absorption correction was applied to the collected reflections. The structure was solved by the direct method using SHELXTL[51] and was refined on F2 by fullmatrix least-squares technique using the SHELXL-97[52] program package within the WINGX[53] program. All non-hydrogen atoms were refined anisotropically. All hydrogen atoms were located in successive difference Fourier maps, and they were treated as riding atoms using SHELXL default parameters. The structures were examined using the Adsym subroutine of PLATON[54] to ensure that no additional symmetry could be applied to the models. It should be noted that the guest and anion molecules in **iMOF-2C** are highly disordered and could not be modeled properly, so the diffused electron densities resulting from them were removed by the SQUEEZE routine in PLATON[55] and the results were

appended in the CIF files. The SQUEEZE option was used to eliminate the contribution of disordered guest molecules. Crystallographic data for iMOF-2C: **CCDC 1980127** contains the supplementary crystallographic data for this paper.

5.2.5. Oxo-anion capture study:

5.2.5.1. Time dependent oxo-anion removal study: For the CrO_4^{2-} removal study, we have taken 0.5 mM 2 mL aqueous solution of CrO_4^{2-} anion in a UV cuvette and collected the initial absorbance reading by UV-Vis spectroscopy. 1 mg of activated iMOF-2C has been added to the cuvette and then we have recorded the absorbance spectra of the supernatant solution accordingly at several time intervals. Similar experimental procedure was followed to carry out the UV-Vis spectroscopy for ReO_4^- anion with a solution of 0.5 mM ReO_4^- ion. Furthermore, the % removal of oxo-anions with respect to time and time vs decrease in concentration of oxo-anions data were calculated from this time dependent study by using the following equation,

$$D_t = \frac{C_0 - C_t}{C_0} \text{ x } 100\% = \frac{A_0 - A_t}{A_0} \text{ x } 100\%$$

$$i.e., \quad C_t = C_0 - \frac{A_0 - A_t}{A_0} \text{x } C_0$$

Where, D_t is the exchange capacity of iMOF-2c, A_0 and C_0 are the absorbance and initial concentration of the supernatant solution, A_t and C_t, are the absorbance and concentration of the supernatant solution at particular times.

5.2.5.2. Oxo-anion capture study in presence of concurrent anions:

We have taken Br^-, Cl^-, ClO_4^-, SO_4^{2-} and NO_3^- ions as the contending anions in this study, which are ubiquitous to any regular water sources, particularly in waste water. Further, we have done the capture experiments with a equimolar (2.5 mM aqueous solution; 1:1) of competing anion with the targeted oxo-anion. 2 mg of activated iMOF-2C was added to the aqueous solution mixture with stirring condition for 24 hours. The solution was further filtered off after 24 hours to separate the compound iMOF-2C from the mixture. Thus acquire oxo-anion solution was further diluted 10 times to characterize by UV-Vis spectroscopy. Additionally, the oxo-anion

removal efficiency in presence of other competing anions of iMOF-2C was calculated by comparing the different concentrations with blank solution (Blank solution: 2.5 mM of only oxo-anion was taken instead of mixture).

5.2.5.3. Calculation of capacity:

5 mg of activated iMOF-2C was dipped into 5 mM 5 mL of oxo-anion solution at stirring condition for 24 hours. After 24 hours, the solution dipped iMOF-2C compound was separated by filtration and the filtrate was further used for characterisation. UV-Vis experiment has been carried out by diluting (0.2 mM each solution has been analysed for UV-Vis) the solution.

We have calculated the saturation uptake capacity of the compound iMOF-2C in 24 hours from the initial absorbance and final absorbance data of the oxo-anion solutions by using the following equation,

$$\boldsymbol{Q_t = \frac{(C_0 - C_t) * V}{m}}$$

Where, C_t, C_0, Q_t, m and V are the concentration of the oxo-anion solution at particular times, initial concentration of oxo-anion solution, capacity of adsorbent, mass and volume of the solution applied for the adsorbent respectively. Furthermore, the concentration dependent oxo-anion capture experiments were performed several times to obtain the accuracy in the adsorption isotherm plots.

5.2.5.4. Reversibility Studies:

iMOF-2C was regenerated by keeping the oxo-anion loaded compound (10 mg) for 24 hours in tetrabutylammonium sulfate solution ($[[CH_3(CH_2)_3]_4N]_2SO_4$) (10ml). Recyclability of the regenerated compound was performed with 5 mL, 1 mM of the oxo-anion solutions (CrO_4^{2-} and ReO_4^-). After 1 day, the concentrations of the post capture oxo-anion solutions were obtained by UV-Vis spectroscopy. Similar experiment was repeatedly performed for up to ten cycles in case of both the anions (CrO_4^{2-} and $ReO4^-$). Furthermore, the compound loaded column bed was regenerated employing similar method where tetrabutylammonium sulfate solution was allowed to pass through the stationary phase column bed to regenerate the pristine compound. Then, 1 mM aqueous solution of CrO_4^{2-} anion was poured through the column bed to check the capture performance.

5.2.5.5. Adsorption isotherm experiment: iMOF-2C (5 mg) was immersed in 2 mL water solution of oxo-anion having different concentration (in case of CrO_4^{2-} ion concentration was taken in the range of 29-580 ppm and for ReO_4^- ion the range of concentration is 62.5-1251 ppm). After 2 hours UV-Visible spectroscopy was carried out with the supernatant solution and further fitted with following equation,

$$\underline{\text{Langmuir model,}} \qquad \boldsymbol{Q_e = \frac{Q_m C_e}{K_d + C_e}}$$

where, Ce (ppm) and Q_e (mg gm^{-1}) are the oxo-anion concentration at equilibrium and amount of oxo-anion adsorbed at equilibrium respectively. Q_m (mg gm^{-1}) is the maximum amount of oxo-anion per unit mass of adsorbent to form a complete monolayer. K_d (mg/L) is a constant related to the affinity of the binding sites.

$$\underline{\text{Freundlich Model,}} \qquad \boldsymbol{Q_e = K_F C_e^{1/n}}$$

where, K_F and 1/n are the Freundlich model constants, indicating capacity and intensity of adsorption, respectively.

5.2.5.6. pH-dependent capture study: iMOF-2C (2 mg) was immersed in 2 mL solution of 2.5 mM oxo-anion (in case of CrO_4^{2-} ion pH-4, pH-9, pH-10 and pH-12.4 were used, whereas for ReO_4^- ion pH-9 and pH-12.4 were used) and stirred for 24 hours. After 1-day UV-Vis study was carried out to check the removal efficiency of iMOF-2C. Following equation has been used for calculation and compared with the data at pH-7 for relative performance,

$$\boldsymbol{D_t = \frac{C_0 - C_t}{C_0} \text{ x } 100\% = \frac{A_0 - A_t}{A_0} \text{ x } 100\%}$$

Where, D_t is the exchange capacity, C_0 and A_0 are initial concentration and absorbance of the oxo-anion solution respectively, C_t and A_t, are concentration and absorbance of the oxo-anion solution at specific times respectively.

5.2.6. Simulation Details:

The lowest energy configuration of each anion in the primitive cell of iMOF-2C MOF structure was obtained from the classical simulated annealing technique using classical force field as implemented in sorption module in *Materials Studio*.[56] The framework atoms are kept frozen

during simulation. The interactions of gas-adsorbent and gas-gas were modeled as a combination of pairwise site-site Lennard-Jones (LJ) and Coulombic potentials. The LJ potential parameters of both the framework atoms and the adsorbates are adopted from the Universal force field (UFF).[57] The charges for the framework atoms were assigned based on the Qeq charges as implemented in *Materials Studio* package.

In the simulated annealing method, the temperature was lowered stepwise, allowing the gas molecule to reach a desirable configuration based on different moves such as rotation, translation and repositioning with preset probabilities of occurrence. This process of heating and cooling the system was repeated in several heating cycles to find the local minima. Forty heating cycles were performed where the maximum temperature and the final temperature were 10^5 K and 100 K, respectively.

5.2.6.1. DFT calculations: Periodic geometric optimization and the static binding energies for each anion in iMOF-2C frameworks were calculated using density functional theory (DFT) as implemented in the software package VASP 5.4.4.[58] It is well-known that standard DFT methods based on generalized gradient approximation do not fully account for the energies for each anion with the framework, we implemented dispersion corrections using DFT-D3 method .[59] Electron exchange and correlation were described using the generalized gradient approximation Perdew, Burke, and Ernzerhof (PBE) [60] form and the projector-augmented wave potentials were used to treat core and valence electrons.[61] In all cases, we used a plane-wave kinetic energy cutoff of 800 eV and a Gamma-point mesh for sampling the Brillouin zone. The ionic coordinates were relaxed until the Hellman-Feynman ionic forces were less than 0.01 eV/Å.

5.2.6.2. Electrostatic Potential Surface (ESP): Density functional theory (DFT) computations were performed using the Gaussian program [62] to derive the ESP surface of iMOF-2C cluster model. Based on the periodic DFT optimised structure of iMOF-2c, a cluster model which contains one Ni^{2+} cation and six ligands were constructed. Each ligand contains one imidazole ring and one benzene ring and the terminal sp^3 carbon atom of each ligand was saturated by three H atoms. Geometry optimization of fragment were carried out in the liquid phase at (SMD) B3LYP-D3/SDD~6-31G(d) level. The SMD implicit solvent model (3) with water as the solvent was used to include the solvation effects. The hybrid B3LYP exchange-correlation functional (4)

combined with the D3 version of Grimme's dispersion (5) were employed. The Stuttgart/Dresden relativistic effective core potential and the associated valence basis set (SDD) were applied for Ni (6), while the 6-31G(d) basis sets were used for C, H, O, and N (7). During

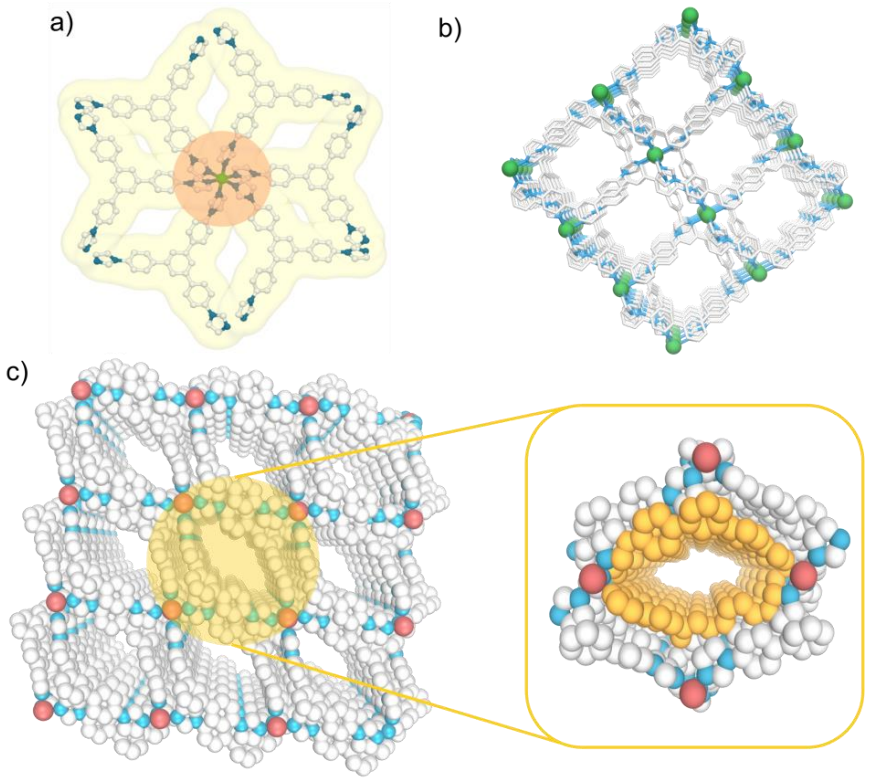

Figure 5.1. (a) Coordination environment in iMOF-2C (Hydrogen atoms have been omitted for clarity, color: Gray - C, Blue - N, Green - Ni), (b) Perspective view of packing in iMOF-2C along *c*-axis (color: Gray - C, Blue - N, Red - Ni), (c) Packing diagram of iMOF-2C and zoomed view highlighting (in yellow) the hydrophobic channel inside the MOF.

optimizations, the Ni^{2+} cations, the N and C atoms of the imidazole rings, and the terminal sp^3 carbons were fixed. The electrostatic potential (ESP) on the van der Waals (VDW) surfaces (isodensity = 0.001 a.u.) of iMOF-2Cfragment was derived based on its ground state electron density.

5.2.6.3. Binding Energies: The initial location of the anion in the primitive cell of iMOF-2C was obtained from the classical simulated annealing technique as described above. Static binding energies (ΔE) at 0 K in vacuum were calculated using the following expression

$$\Delta E = E_{MOF+Anion} - E_{MOF+} - E_{Anion}$$

where E_x refers, respectively, to the total energies of the MOF + Anion complex, the charged MOF^+ alone, and the anion molecule respectively.

4.3 Results and discussion

iMOF-2C was synthesized by a solvothermal reaction from a mixture of $NiSO_4.xH_2O$ and ligand (L) (Appendix Scheme 5.1) (1:1), with a solvent combination of water and N,N'-dimethylformamide (DMF) (1:2) at 130^oC (Appendix Scheme 5.2). Single crystal X-ray diffraction (SC-XRD) analysis of the trigonal pyramidal-shaped crystals revealed that the two dimensional (2D) framework crystallizes in the R -3 space group. The asymmetric unit consists of one Ni (II) cation with 1/6 occupancy and one ligand (L) unit with 1/3 occupancy and disordered anions and solvent molecules (Appendix 5.2-5.3). The central metal center is coordinated by six nitrogen atoms of six individual ligand units resulting in octahedral geometry around the Ni (II) center (Figure 5.1a, Appendix 5.4-5.5). The average N-Ni bond length was found to be 2.083Å. iMOF-2C was found to be bi-porous in nature having one small pore and one large pore, with highly hydrophobic environment inside the pore originating from the hydrophobic benzene rings of the ligand (Figure 5.1c, Appendix 5.6-5.7). The overall positive charge of the framework was neutralized by the free disordered tetrahedral sulfate anions residing inside the pores. However, the anions could not be located in the pristine crystal structure which is a well-known phenomenon for framework materials having large voids. Further, presence of the sulfate anion was confirmed by Fourier-transform infrared (FTIR) spectra and Energy-dispersive X-ray (EDX) spectra. The topology analysis affirmed that the compound possess a (3, 6)-connected bi-nodal kgd topology. The highlighting characteristic of kgd topology is in the generation of intrinsical porosity, originating from the non-planar 2D sheets.[63-65] PLATON study calculations affirmed that the total empty volume of iMOF-2C is 2191 $Å^3$, which corresponds to 24.6% of the total volume.It should be noted that the guest and anion molecules in iMOF-2C are highly disordered and could not be modeled properly. Powder X-ray diffraction (PXRD) reveals a slight change in the as-synthesized phase originating from the loss of occluded labile solvent molecules but confirms the overall structural integrity of the bulk phase (Appendix 5.11). Thermogravimetric analysis (TGA) corroborated well with the initial loss of free guest molecules, DMF and water within the framework (Appendix 5.12).

Fourier transform infrared (FTIR) spectrum of iMOF-2C confirmed the presence of all the peaks corresponding to the ligand as well as a peak at ~1100 cm^{-1} attributed to the free SO_4^{2-} anions inside the pore (Appendix 5.36). Field emission scanning electron microscopy (FESEM) and High-resolution transmission electron microscopy (HRTEM) images of iMOF-2C endorsed the trigonal pyramidal morphology of the crystals, and EDX spectra confirmed the elemental purity of the compound

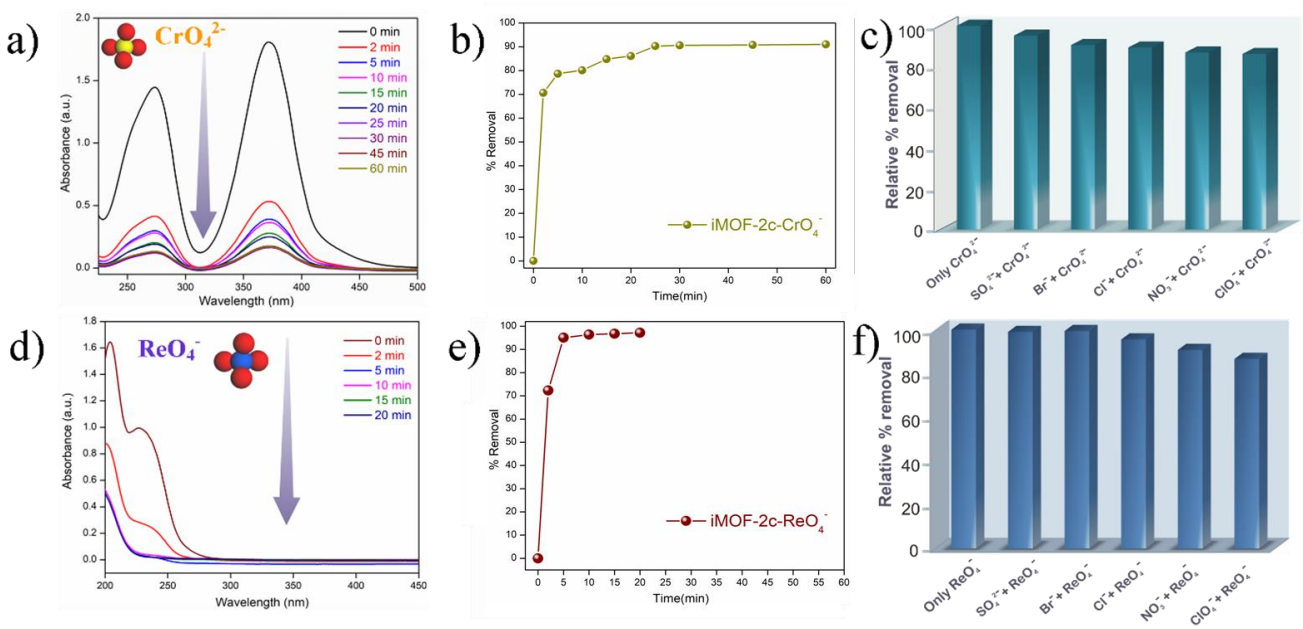

Figure 5.2. (a) UV-Vis spectra in presence of iMOF-2C for CrO_4^{2-}, (b) Removal (in %) of CrO_4^{2-} with iMOF-2C at different time intervals, (c) Bar diagram for removal efficiency of iMOF-2C in presence of Br^-, Cl^-, NO_3^- and SO_4^{2-} ions for CrO_4^{2-}, (d) UV-Vis spectra in presence of iMOF-2C for ReO_4^- (e) Removal (in %) of ReO_4^- with iMOF-2C at different time intervals, (f) Bar diagram for removal efficiency of iMOF-2C in presence of Br^-, Cl^-, NO_3^- and SO_4^{2-} ions for ReO_4^-.

(Appendix 5.15-5.18). iMOF-2C illustrated excellent hydrolytic stability owing to its shielded metal nodes as all the coordination sites of Ni center are occupied by the ligands (Appendix 5.13). Furthermore, the compound was found to display excellent chemical stability even in wide range of pH solutions (pH = 4 to 12.45) as PXRD patterns confirmed the retention of structural integrity at different pH conditions (Appendix 5.14). To validate the porosity of iMOF-2C, low temperature N_2 (77K) adsorption was performed. A very less uptake was observed for iMOF-2C

which indicates the inherent non-porous nature of the cationic framework as the porous void space is occupied by free SO_4^{2-} anions inside (Appendix 5.19).

Such chemical stability of the cationic framework actuated us to check the trapping ability of iMOF-2C toward toxic oxo-anions in the water medium. As both forms of the Chromium (VI) oxo-anions, namely, chromate (CrO_4^{2-}) and dichromate ($Cr_2O_7^{2-}$) remain at interchangeable equilibrium depending upon pH of the medium, we have carried out the Cr (VI) oxo-anion capture experiments with chromate anion. Crystals of iMOF-2C were dipped into an aqueous K_2CrO_4 solution and the capture process was monitored by UV/Vis absorption spectroscopy, PXRD and FTIR. Initially we observed that the yellow colored solution became colorless with time and the color of the crystals turned yellow (Appendix 5.20-5.21). Furthermore, this observation propelled us to perform the capture study of CrO_4^{2-} ion in water monitored through UV-Visible spectroscopy. We performed the in-situ titration study in UV-Vis spectroscopy with 0.5 mM aqueous solution of CrO_4^{2-} ion (2 mL) and 1 mg of iMOF-2C by monitoring absorption maxima at 372 nm (λ_{max} of CrO_4^{2-}) (Figure 2a). The gradual decrease of the peak at 372 nm in UV-Vis spectra with increasing time intervals confirmed the capture of CrO_4^{2-} ion by the crystals of iMOF-2C. The anion exchange process found to be kinetically very rapid as almost 72% of CrO_4^{2-} ions were captured by 1 mg of iMOF-2C within only 2 mins and removal of almost ~99 % concentration of CrO_4^{2-} within 30 mins (Appendix 5.26). The % removal with time plot affirmed the fast capture of CrO_4^{2-} ion by iMOF-2C (Figure 2b). The uptake capacity of iMOF-2C for CrO_4^{2-} ion was calculated (476.3 mg g^{-1}) from UV-Vis spectroscopy, which was further assured by ICP-MS studies (Appendix 5.27). Notably, the uptake capacity of iMOF-2C was found to be among the highest reported values in the regime of MOF-based materials (Appendix Table 5.1). No change in PXRD patterns of the chromate exchange phase iMOF-2C-(CrO_4^{2-}) validated the retention of the structural integrity of the framework (Appendix 5.28). EDX spectra and FTIR spectroscopy further affirmed the presence of chromate ions as a homogeneous distribution of chromium was observed in the elemental mapping profiles and a peak at 894 cm^{-1} corresponding to CrO_4^{2-} in the FT-IR spectra of iMOF-2C-(CrO_4^{2-}) was obtained (Appendix 5.29-5.31, 5.36-5.37).

Along this line, another toxic oxo-anion, TcO_4^- is accounted as a significant hazardous radioactive water pollutant owing to β-emitting radioactive nature of ^{99}Tc. We took an alternative

way to avoid the safety and handling issues of radioactive TcO_4^- in a common chemical laboratory by choosing the non-radioactive surrogate ReO_4^- as model oxo-anion. Additionally, ReO_4^- have almost identical chemical properties and charge densities with the analogues TcO_4^- ion (Both Re and Tc reside in the same group of the periodic table) which can help in replicating the real-time scenario. Similar studies as chromate ion capture have been performed for the removal of ReO_4^- from water. Here also, the crystals of iMOF-2C were dipped into 2 ml of 0.5 mM ReO_4^- solution and the capture process was monitored by UV/Vis absorption spectroscopy, PXRD and FTIR as stated previously. The in situ titration study in UV/Vis absorption spectroscopy revealed a gradual decrease in the intensity maxima of ReO_4^- ion at 208 nm (λ_{max}) at different time intervals (Figure 2d). Notably, the sequestration process showed very fast kinetics and almost 70% ReO_4^- ions were captured within just 2 mins despite the bigger size of ReO_4^- anion and almost ~99% of the initial concentration was found to reduce within just 20 mins (Appendix 5.33). The % removal with time plot supported the fast capture of ReO_4^- ion by iMOF-2C (Figure 2e). The uptake capacity of iMOF-2C for ReO_4^- ion was calculated (691 mg g^{-1}) from UV-Vis spectroscopy, which found to be among the highest reported values particularly in the regime of MOF-based materials (Appendix 5.34, Appendix Table 5.2). No change in PXRD patterns of the perrhenate exchanged phase iMOF-2C-(ReO_4^-) affirmed the retention of the structural integrity of the framework (Appendix 5.35). FESEM images of both iMOF-2C-(CrO_4^{2-}) and iMOF-2C-(ReO_4^-) confirmed the morphology and structural integrity of the crystals remained the same as iMOF-2C (Appendix 5.22, 5.29). EDX analysis of iMOF-2C-(ReO_4^-) indicated the inclusion of ReO_4^- as a homogeneous distribution of Re was observed in the elemental mapping profiles and the absence of SO_4^{2-} anion assured the anion exchange process which was further affirmed by FT-IR spectroscopy and EDX analysis (Appendix 5.30-5.31, 5.36-5.37). The appearance of a new peak in FT-IR spectra at ~918 cm^{-1} was observed in iMOF-2C-(ReO_4^-) corresponding to ReO_4^- ion. Moreover, it was affirmed that anion sequestration process for both CrO_4^{2-} and ReO_4^- anions with iMOF-2C follows the pseudo-second-order kinetics as the kinetics profile of the capture process is only dependent upon the amount of adsorbate and the amount of adsorbent (Appendix 5.43 to 5.48). The R^2 values were found to be 0.992 for CrO_4^{2-} and 0.993 for ReO_4^- capture process. The rate constant k_2 has been found to be 0.015 mg/g min for CrO_4^{2-} and 0.0052 mg/g min for ReO_4^-.

On account of the robust nature of the MOF crystals, our major focus was turned toward monitoring the capture studies in a single crystal to single crystal (SC-SC) manner. Notably, in case of both the anions, the quality of the crystals were found to be very good in both stages of post-oxo-anion capture and release. Although we were able to solve the crystal structure of iMOF-2C-(CrO_4^{2-}) properly, but due to very weak diffraction and high disorderliness, despite several attempts, the oxo-anions could not be located inside the pores of the MOF. Additionally, we have provided a comparison table between the cell parameters of iMOF-2C and iMOF-2C-(CrO_4^{2-}), from which it is clearly evident that the overall structure parameters are almost remaining unchanged but the volume of the unit cell is getting increased by a small margin in case of iMOF-2C-(CrO_4^{2-}) (Appendix Table 5.3).

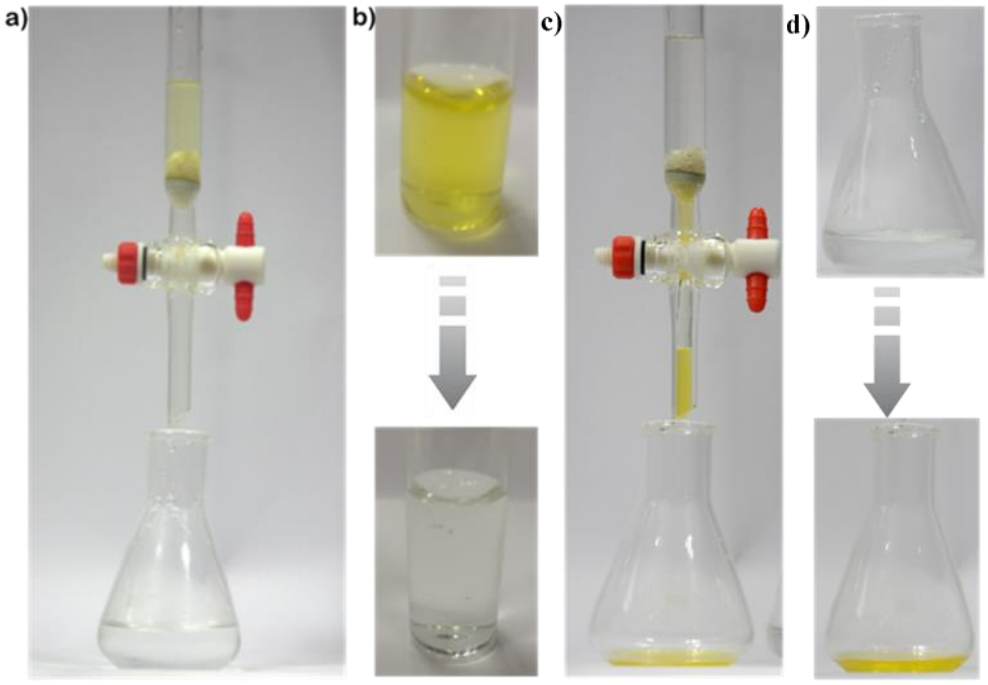

Figure 5.3. (a) Representation of the iMOF-2C loaded column used for column chromatographic separation of oxo-anion from water, (b) Capture of CrO_4^{2-} by iMOF-2C bed in column (c) Regeneration of the iMOF-2C loaded column by an aqueous solution of tetrabutylammonium sulfate, (d) Release of captured CrO_4^{2-} from iMOF-2C bed.

In a real-time scenario, the coexistence of various competing anions (such as SO_4^{2-}, NO_3^-, Cl^- etc.) are found in waste water along with the concerning oxo-anions. Enthused from the high

loading capacity of iMOF-2C for CrO_4^{2-} and ReO_4^- anions, we checked the affinity of oxo-anions towards iMOF-2C in the presence of other competing anions. To verify the selectivity, we took several competing anions (Br^-, Cl^-, ClO_4^-, SO_4^{2-} and NO_3^-) in a binary mixture for both the oxo-anions. In the case of both the anions, iMOF-2C performed efficiently as in each case of binary mixtures, the removal efficiency was found to be ≥ 90% (Figure 2c, 2f). Indeed, such analysis demonstrated the efficiency of iMOF-2C in selectively trapping the concerned oxo-anions in presence of other contending anions.

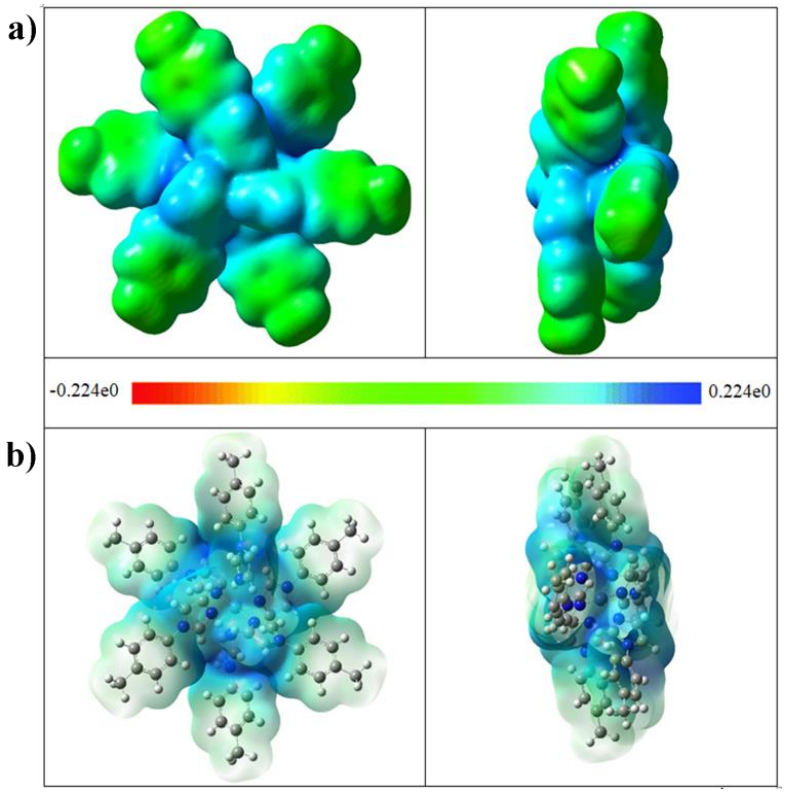

Figure 5.4. Fragment of iMOF-2C showing the electrostatic potential isosurface (isodensity = 0.001 a.u.) at (SMD)B3LYP-D3/SDD~6-31G(d) level of theory (a) Top view and Side view, (b) ESP diagram of the iMOF-2C cluster model using the Gaussian program showing Top view and Side view.

Reusability is another crucial aspect of a material to be used in real-time applicability of such a capture process. To validate the regeneration, we dipped 10 mg of the chromate exchanged iMOF-2C-(CrO_4^{2-}) and perrhenate anion exchanged iMOF-2C-(ReO_4^-) in an aqueous solution of tetrabutylammonium sulfate solution (10 ml, 50% weight percentage solution in water)

(Appendix 5.40-5.42, 5.53). In case of iMOF-2C-(CrO_4^{2-}), the color of the solution became yellow within 10

mins and the compound gradually became colorless as the CrO_4^{2-} ions were replaced by SO_4^{2-} ions inside the porous network of iMOF-2C, which was further confirmed from UV-Vis spectra of the supernatant solution. Notably, iMOF-2C was found to perform even up to 10 cycles without losing its efficiency for both chromate and perrhenate anions, which is very rarely reported in the regime of porous materials.

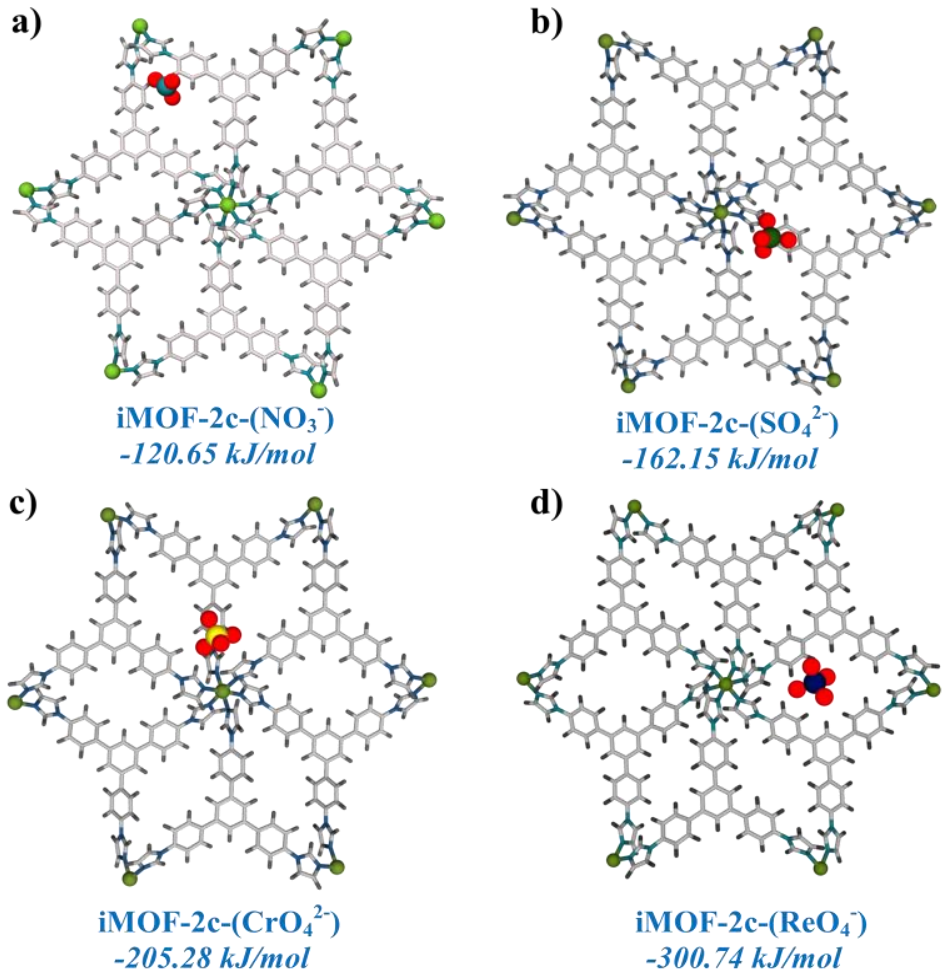

Figure 5.5. Optimized structures of iMOF-2C with different binding anions and the corresponding binding energies calculated based on DFT-D3 method, (a) iMOF-2C-(NO_3^-), (b) iMOF-2C-(SO_4^{2-}), (c) iMOF-2C-(CrO_4^{2-}), (d) iMOF-2C-(ReO_4^-).

Convenient rational utilization of the laboratory performing materials is always of high demand for further implementation toward real-time applicability. In this context, we have constructed a stationary phase column with iMOF-2C which was utilized to trap oxo-anions from water (Figure 3a-3b). Both oxo-anion solutions of 2.5 mM were allowed to run through the column where, in case of chromate solution, the prominent color change was evidenced in the eluent as the chromate ions got trapped into the cavity of iMOF-2C (supplementary video in the ESI). The UV-Vis spectra of the column eluent confirmed the absence of CrO_4^{2-} (Appendix 5.49). The oxo-anion loaded column was further washed with water to discard the possibility of surface adsorption during the oxo-anion capture. The anion exchange process was confirmed from the colourless eluent from the column. Furthermore, the oxo-anion loaded column was regenerated by aqueous solution of tetrabutylammonium sulfate as described previously (Figure 3c-3d).

To get further insights regarding the higher affinity and selectivity towards CrO_4^{2-} and ReO_4^- over other anions, we have performed density functional theory (DFT) calculations. Based on the periodic DFT optimized structure of iMOF-2C, a cluster model that contains one Ni^{2+} cation and six ligands were constructed. Each ligand contains one imidazole ring and one benzene ring and the terminal sp^3 carbon atom of each ligand was saturated by three H atoms. The electrostatic potential (ESP) distribution profiles corroborate with the uniform delocalization of positive charge of the Ni^{2+} over the surrounding imidazole moieties of the six ligand molecules which further acts as the recognition sites toward the incoming oxo-anions particularly with the anions having lower charge density (Figure 4a-4b).

Moreover, the lowest energy configuration of each anion in the primitive cell of iMOF-2C structure was obtained from the classical simulated annealing technique using the classical force field as implemented in the sorption module in Materials Studio [66] (Figure 5a-5d). In this study, we have selected a periodic model of iMOF-2C and optimized the structure with different anions (NO_3^-, SO_4^{2-}, CrO_4^{2-}, ReO_4^-) to calculate the respective binding energies. It is notable that the binding energy of iMOF-2C-(CrO_4^{2-}) (- 205.28 kJ mol^{-1}) was found to be much higher than that of the respective binding energies of iMOF-2C-(NO_3^-) and iMOF-2C-(SO_4^{2-}) analogues, (-120.65 kJ mol^{-1}) and (-162.15 kJ mol^{-1}) respectively as implemented in the software package VASP 5.4.4 [52] (See SI for more simulation details) (Figure 5a-5c). The binding energy of the iMOF-2C-(ReO_4^-) structure was found to be (-300.74 kJ mol^{-1}), which is twice the binding

energy of NO_3^- and significantly higher than that of the binding energy of SO_4^{2-}. The binding energy calculations corroborated perfectly with the experimental observations of the compound iMOF-2C in terms of high selectivity towards CrO_4^{2-} and ReO_4^- over other anions. Furthermore, the strategic choice of hydrophobic core inside the MOF can be justified significantly as the interaction between the more hydrophobic anions (having less hydration energy, e.g. CrO_4^{2-}, ReO_4^-) and the hydrophobic core of the MOF was found to be much preferential compared with other anions having higher energy of hydration (e.g. NO_3^-, SO_4^{2-}), resulting in high uptake capacities as well as an excellent selectivity for both the oxo-anions.

5.4 Conclusions:

In conclusion, we have synthesized a novel robust cationic metal-organic framework, iMOF-2C, which exhibits remarkable kinetics towards toxic oxo-anion removal along with excellent selectivity, and a high loading capacity for both CrO_4^{2-} and ReO_4^-. The capacities of iMOF-2C for both oxo-anions were found to be among the highest values reported in the field of porous materials. Moreover, the density functional theory studies evidently reveal the origin of the excellent efficiency and selectivity towards the oxo-anion capture process and also the potential oxo-anion recognition sites. Furthermore, the compound exhibited exceptional recycling ability (upto 10 cycles), which is one of the most important feature for a material to be considered in real-time applicability. This work, we believe, promises to contribute significantly toward rational designing and development of stable cationic MOFs for remediation of toxic anionic water pollutants and will open a new avenue to counter such challenging environmental issues in the future.

5.5 Appendix section

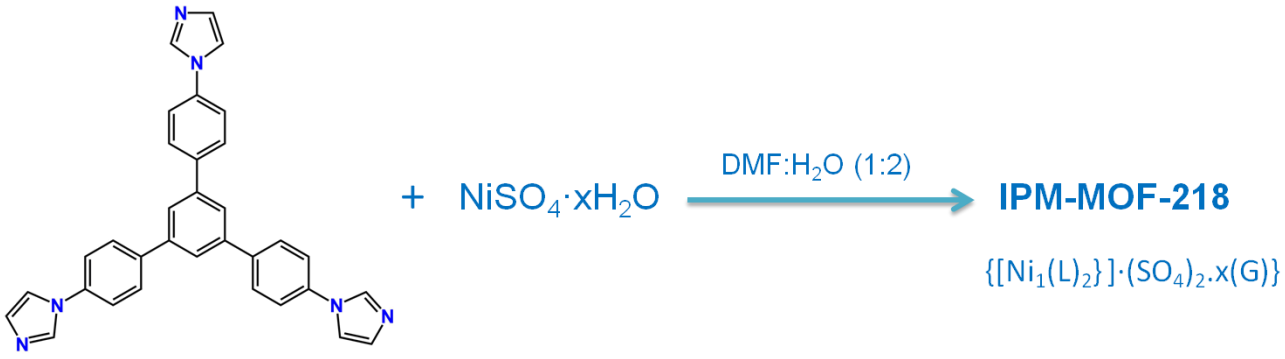

Appendix Scheme S1: Representation of the protocol employed for the synthesis of iMOF-2C.

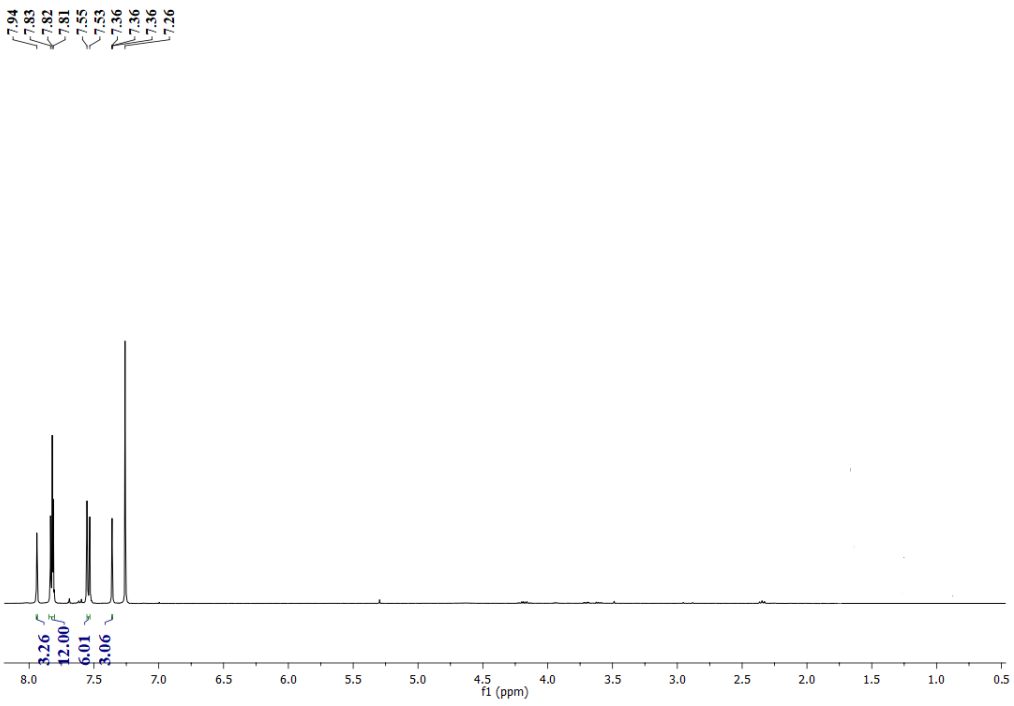

Appendix 5.1: ^{1}H NMR spectra of ligand (L).

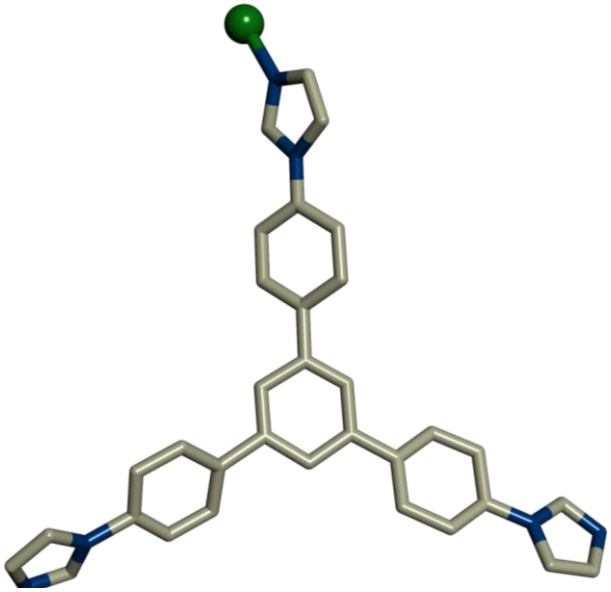

Appendix 5.2: Asymmetric unit of **iMOF-2C** (Hydrogen atoms have been omitted for clarity, colour: Gray - C, Blue - N, Green - Ni).

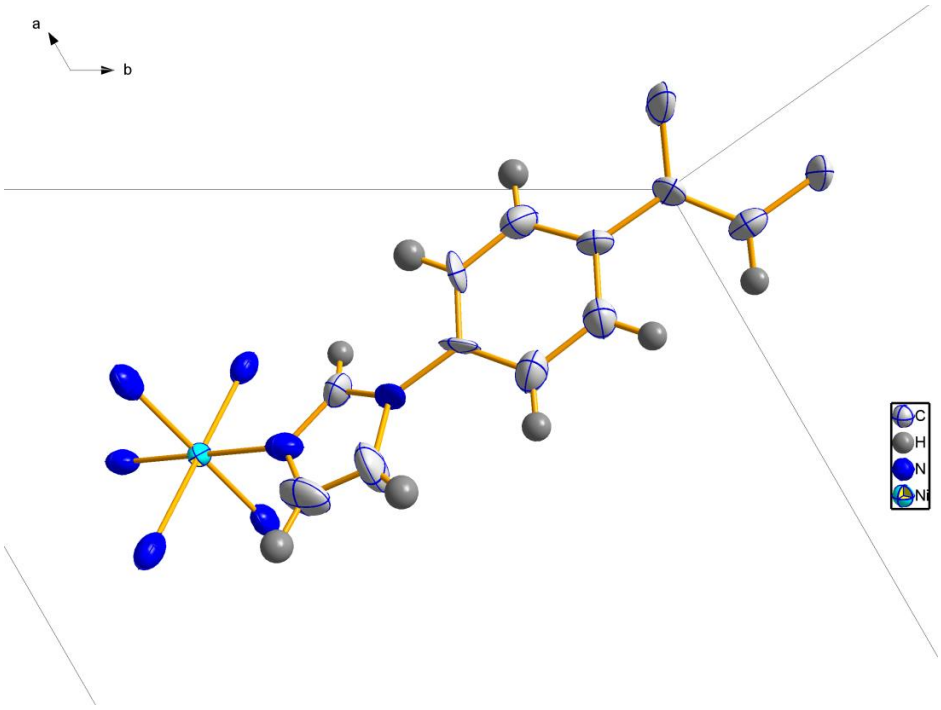

Appendix 5.3: ORTEP diagram of asymmetric unit fragment in **iMOF-2C** in thermal ellipsoids (50% probability).

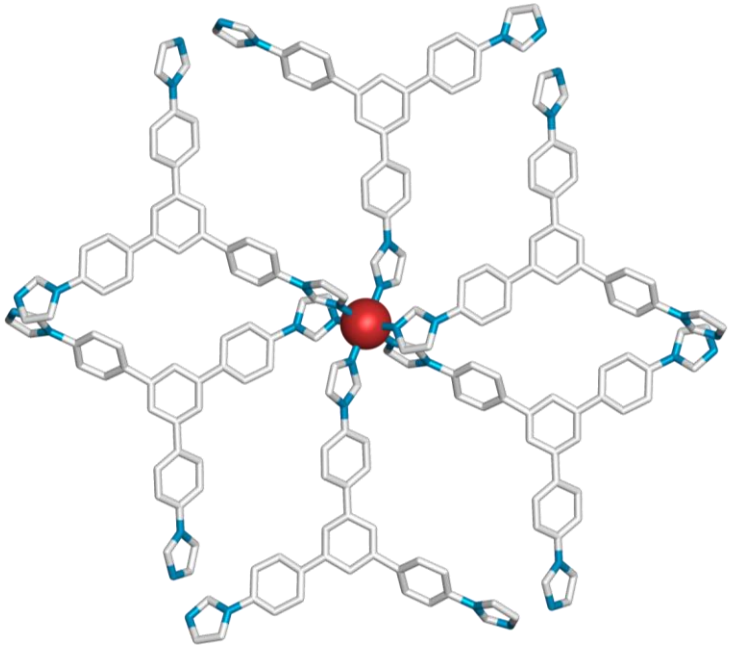

Appendix 5.4: Coordination environment of **iMOF-2C** (Hydrogen atoms have been omitted for clarity, colour: Gray - C, Blue - N, Red - Ni).

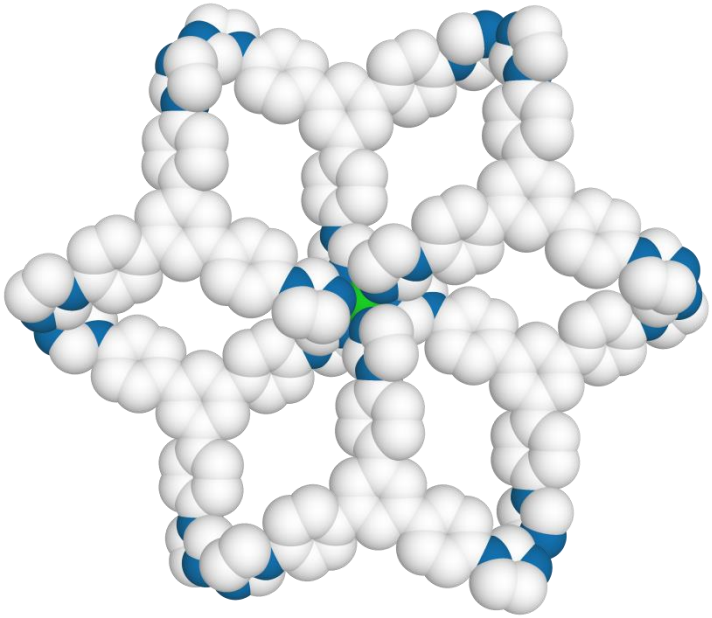

Appendix 5.5: Coordination environment of **iMOF-2C** (Hydrogen atoms have been omitted for clarity, colour: Gray - C, Blue - N, Green - Ni).

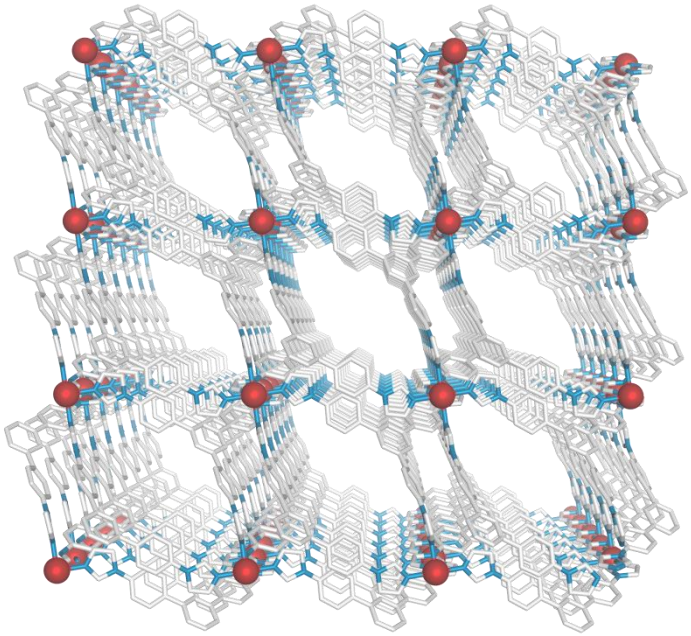

Appendix 5.6: Perspective view of over all packing of **iMOF-2C** along c-axis. (Hydrogen atoms and disordered anions have been omitted for clarity, colour: Gray - C, Blue - N, Red – Ni).

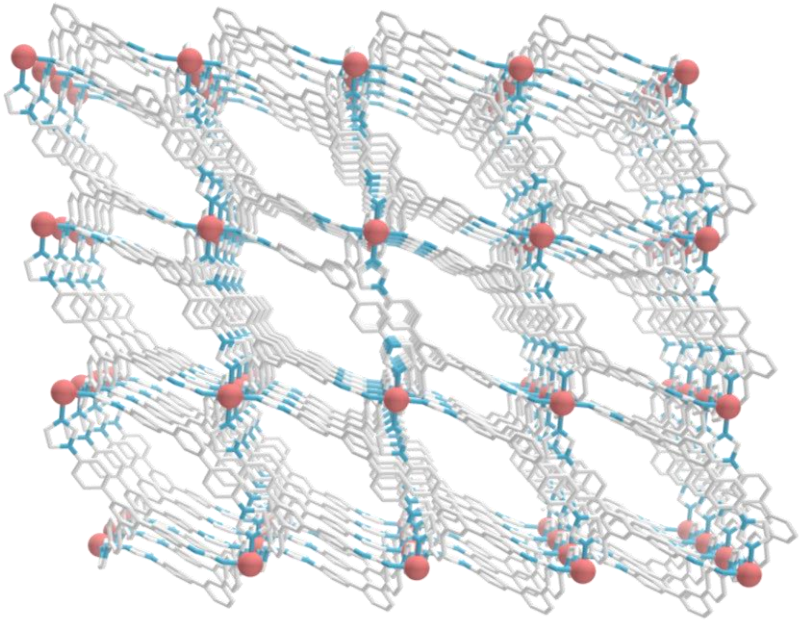

Appendix 5.7: Perspective view of overall packing of **iMOF-2C** along b-axis. (Hydrogen atoms and disordered anions have been omitted for clarity, colour: Gray - C, Blue - N, Red – Ni).

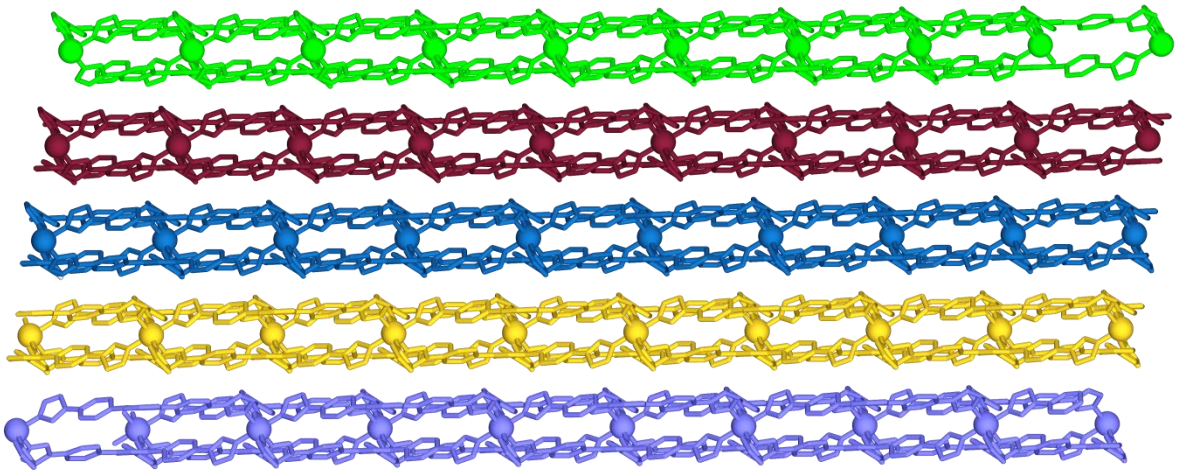

Appendix 5.8: packing diagram showing construction of a 2D nonplanar sheet like structure of all three compounds.

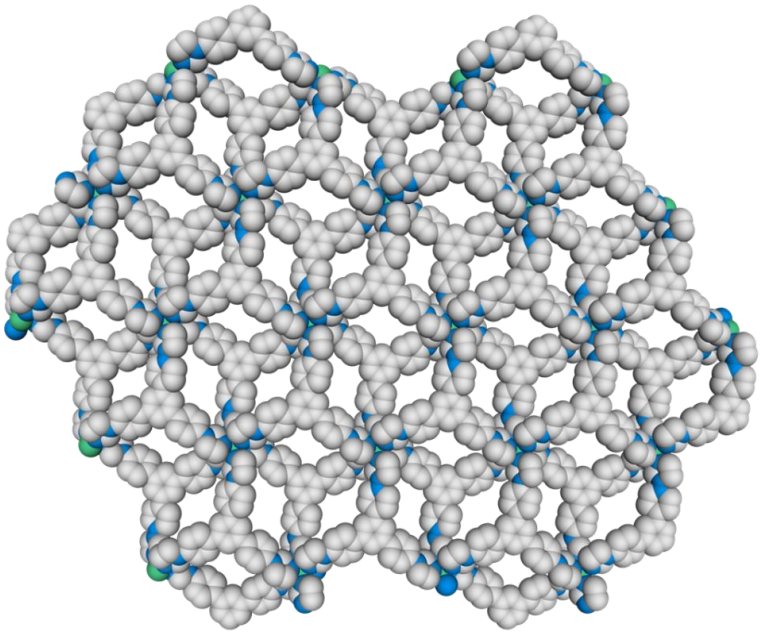

Appendix 5.9: Packing diagram of **iMOF-2C** showing the coordination environment of the metal node. (Hydrogen atoms and disordered anions have been omitted for clarity, colour: Gray - C, Blue - N, Green - Ni).

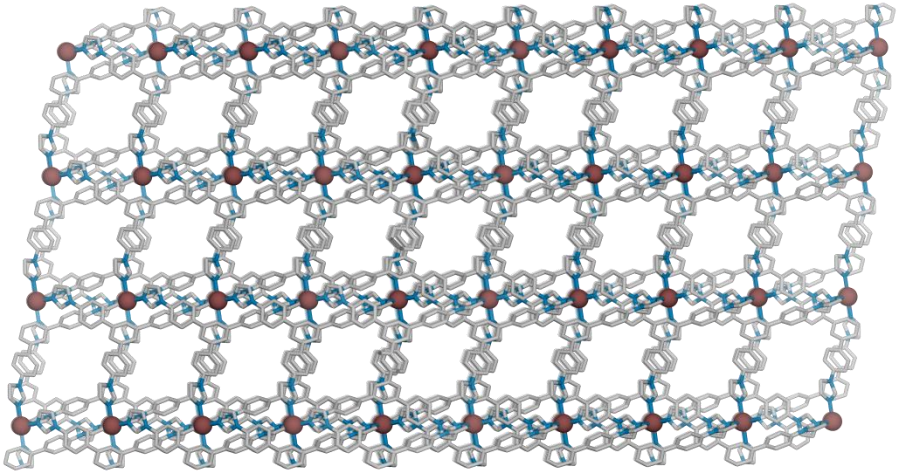

Appendix 5.10: Perspective view of over all packing of **iMOF-2C**along c-axis. (Hydrogen atoms and disordered anions have been omitted for clarity, colour: Gray - C, Blue - N, Red – Ni).

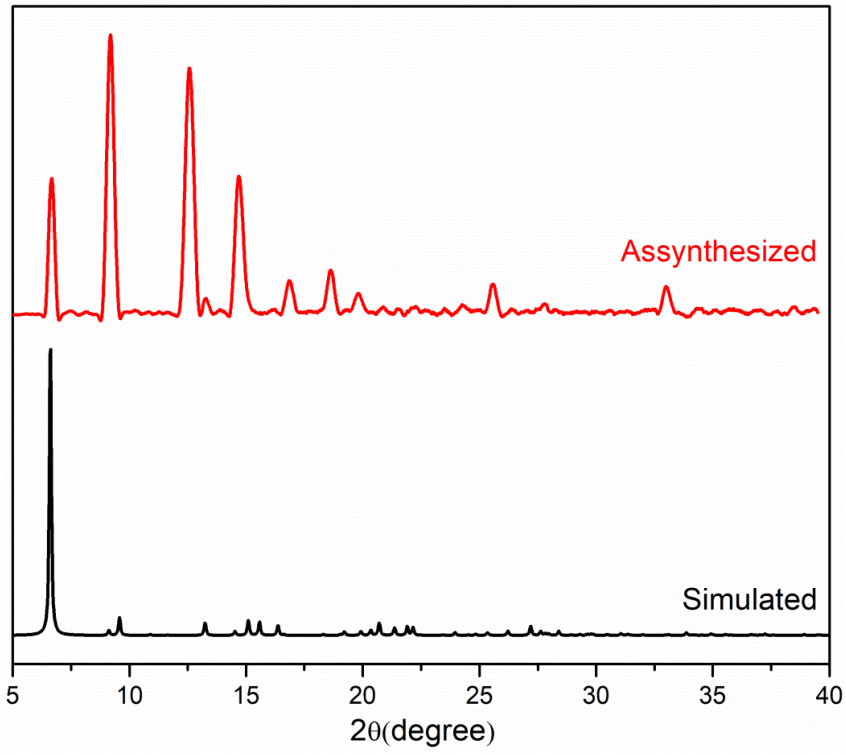

Appendix 5.11: Powder X-ray diffraction patterns of simulated **iMOF-2C** (black) and the assynthesized phase of **iMOF-2C** (red).

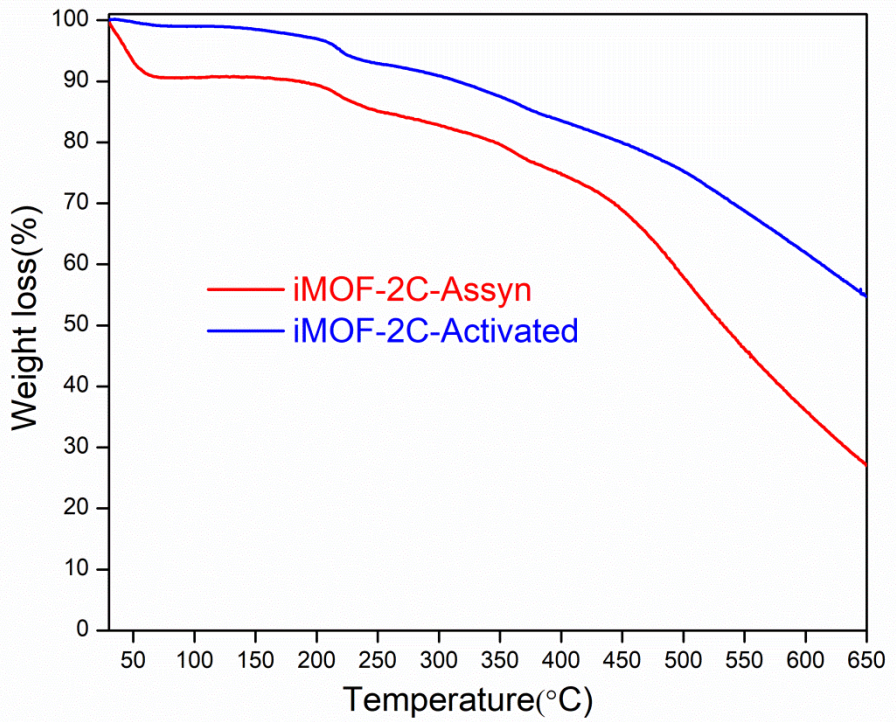

Appendix 5.12: TGA profiles for compound **iMOF-2C**.

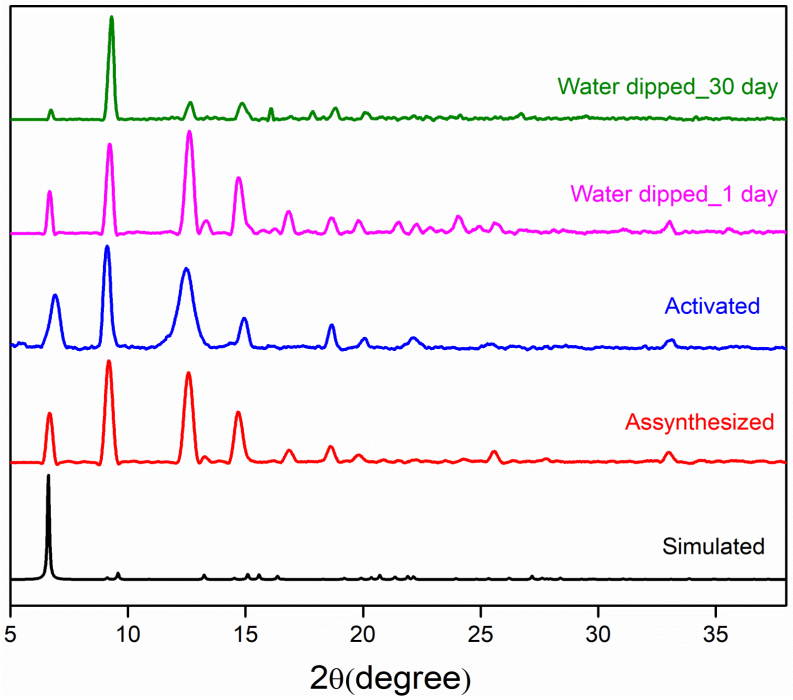

Appendix 5.13: Powder X-ray diffraction patterns of **iMOF-2C;** simulated (black), as-synthesized (red), activated (blue) and water dipped phases (pink and green).

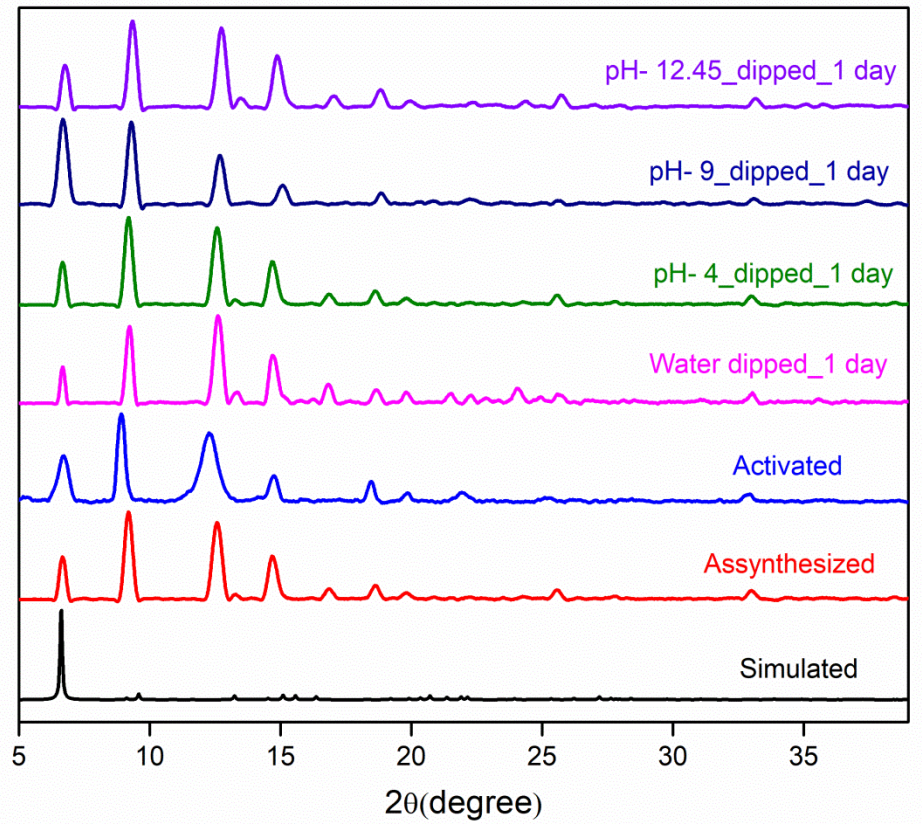

Appendix 5.14: Powder X-ray diffraction patterns of iMOF-2C illustrating hydrolytic stability.

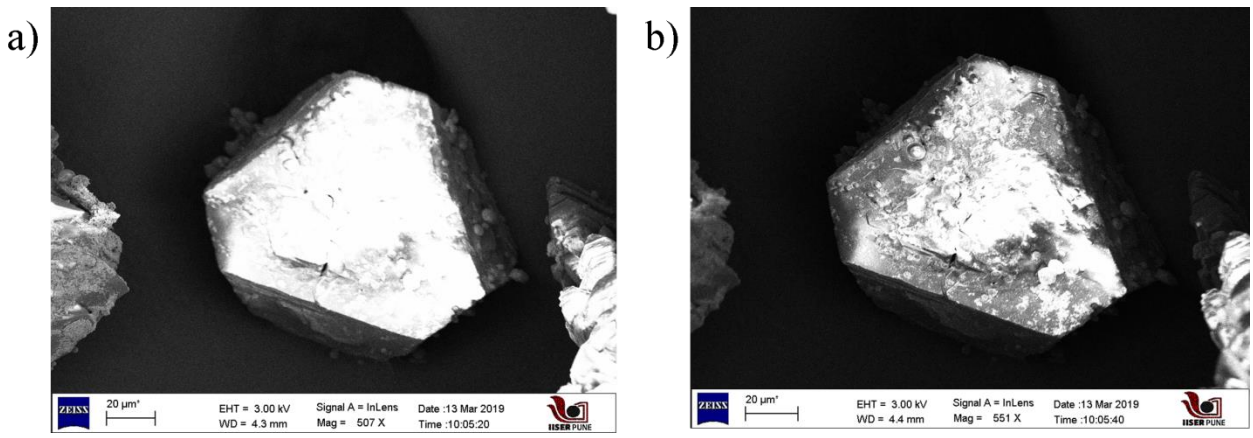

Appendix 5.15: FESEM images of **iMOF-2C**.

Element	% weight
C	56.19
N	9.75
O	21.09
S	3.55
Ni	9.41
Total	100

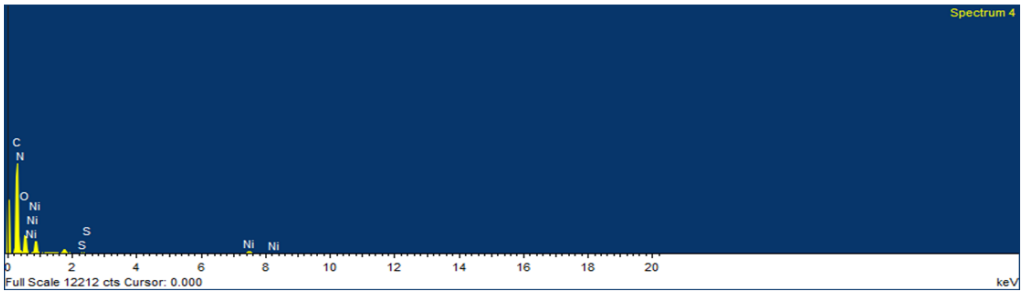

Appendix 5.16: EDX analysis of **iMOF-2C**.

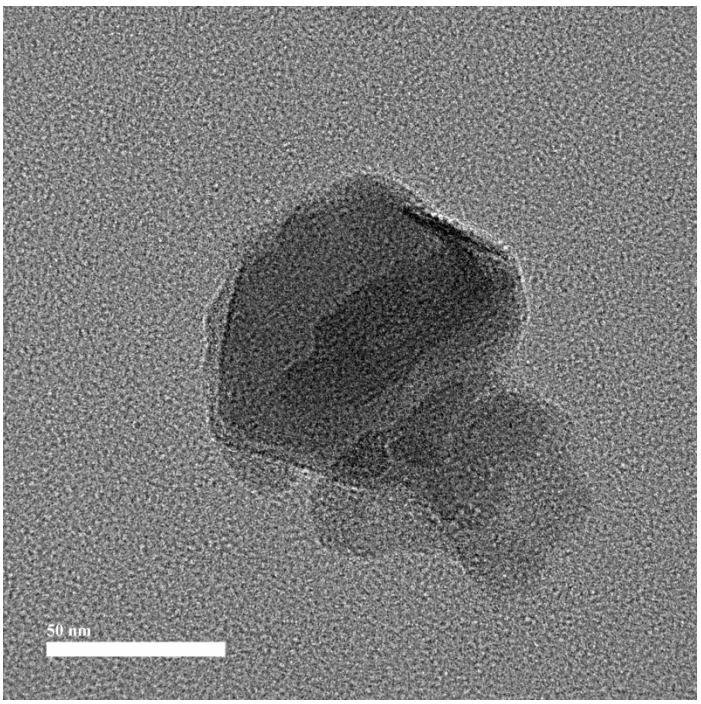

Appendix 5.17: HRTEM image of **iMOF-2C**.

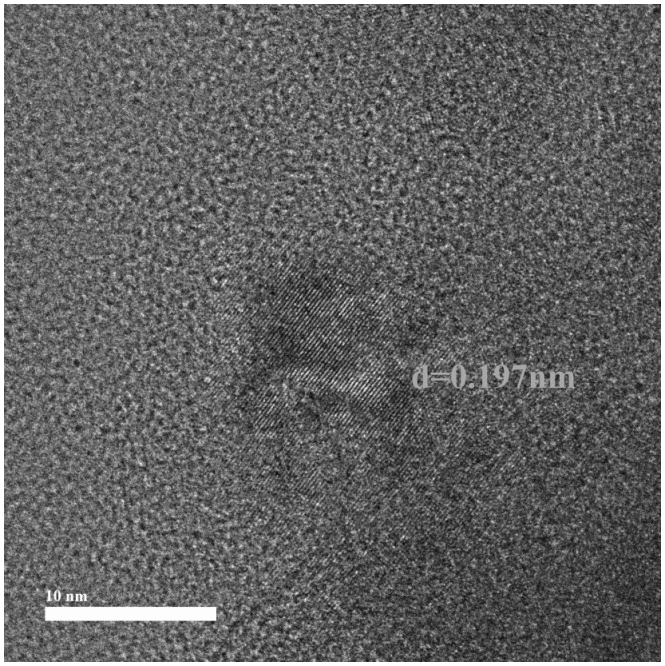

Appendix 5.18: HR-TEM image of **iMOF-2C** showing lattice fringe within the crystals.

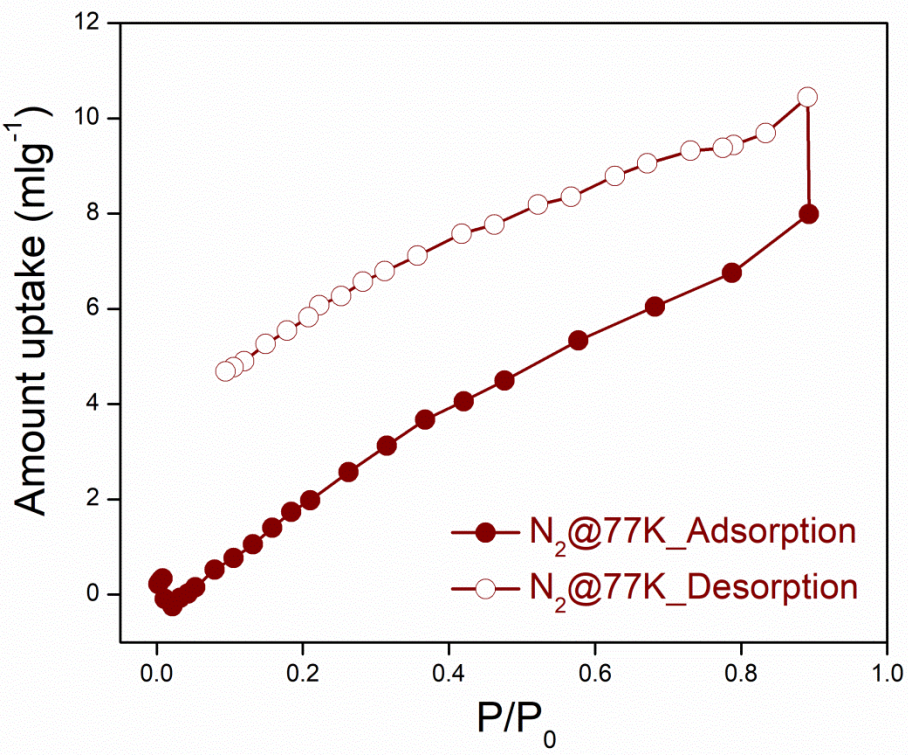

Appendix 5.19: Low temperature gas adsorption isotherm for iMOF-2c.

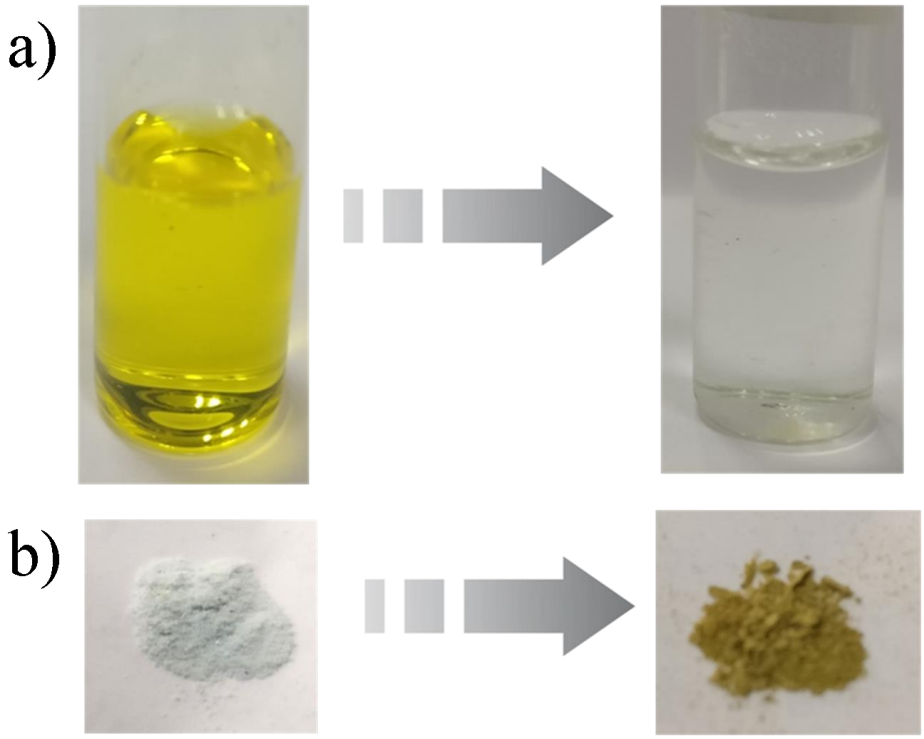

Appendix 5.20: (a) Images of CrO_4^{2-} ion solution and (b) solid **iMOF-2C** before and after of capture study.

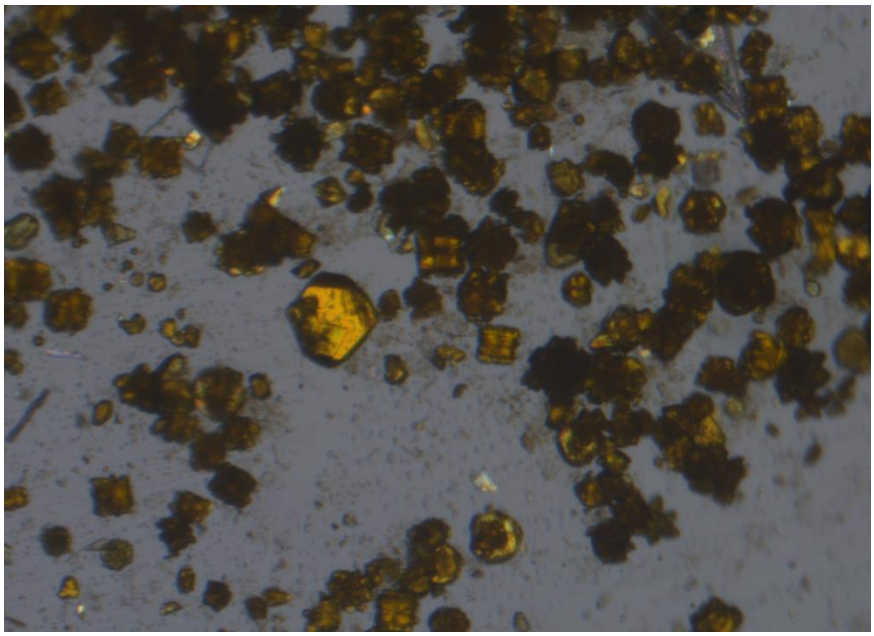

Appendix 5.21: Image of single crystals of **iMOF-2C** after CrO_4^{2-} exchange.

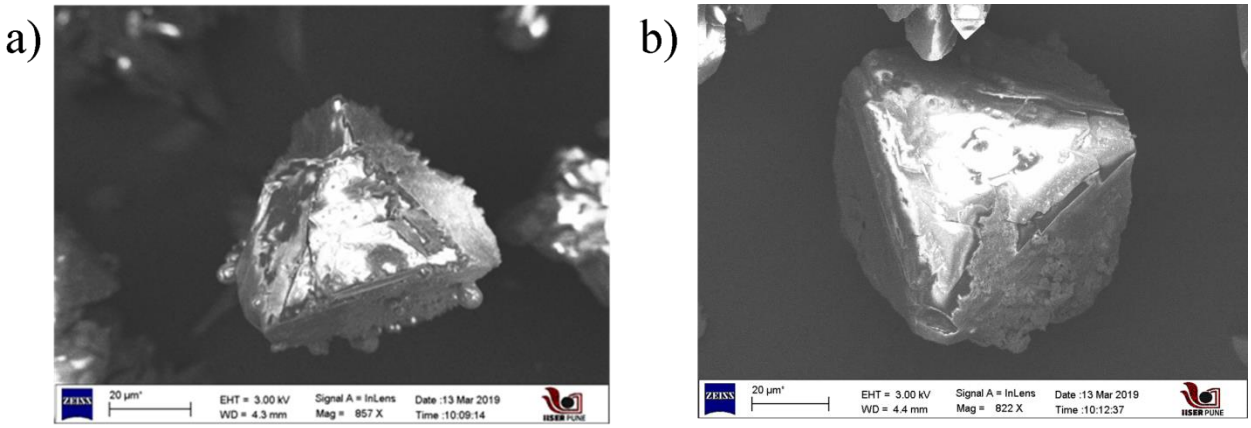

Appendix 5.22: FESEM images of **iMOF-2C** after CrO_4^{2-} exchange.

Element	% weight
C	63.5
N	5.84
O	25.57
Cr	2.72
Ni	2.37
Total	100

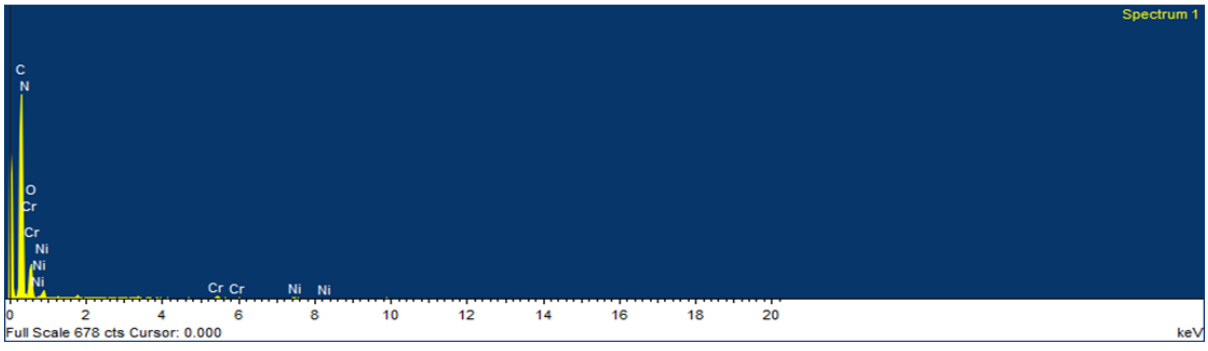

Appendix 5.23: EDX analysis of **iMOF-2C** after CrO_4^{2-} exchange.

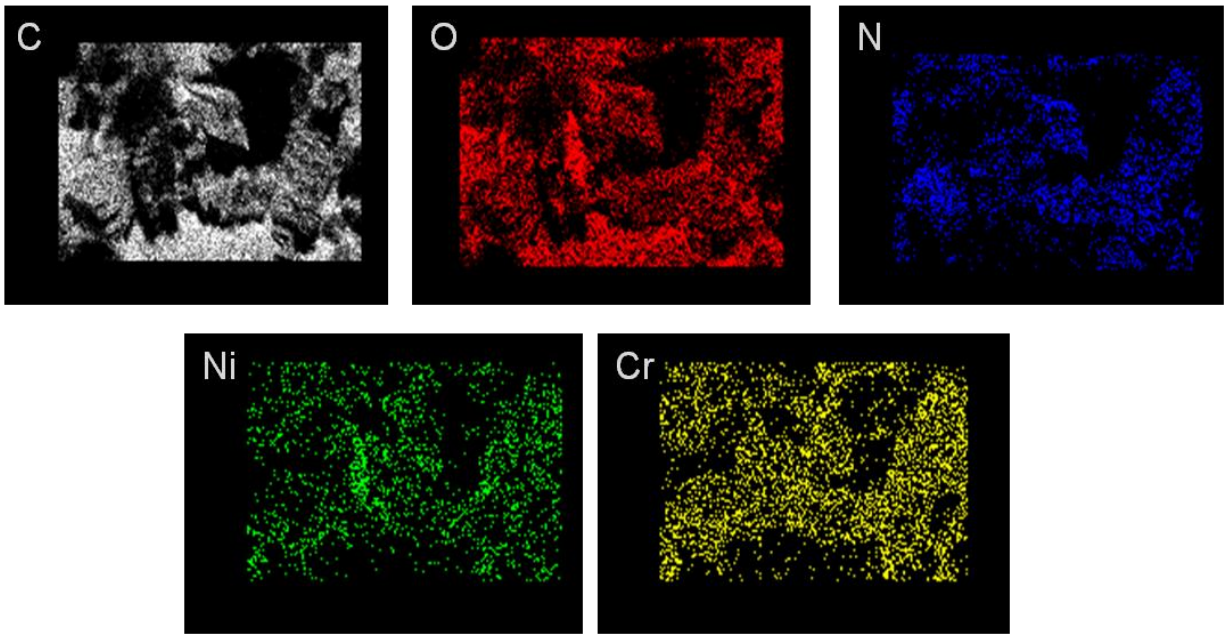

Appendix 5.24: Elemental mapping of **iMOF-2C** after CrO_4^{2-} exchange.

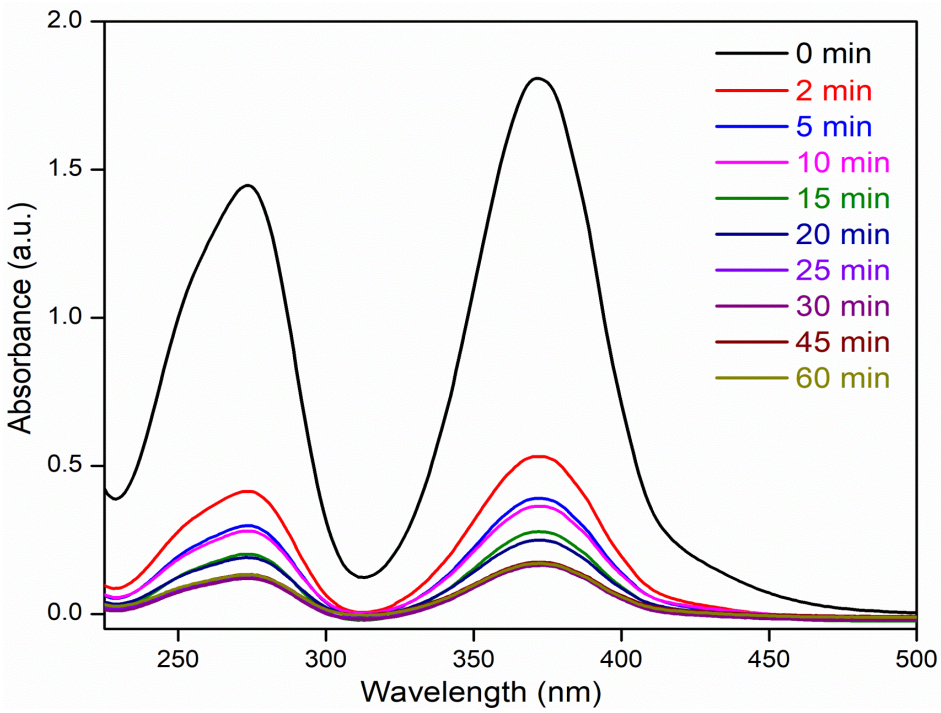

Appendix 5.25: UV-Vis spectroscopy of CrO_4^{2-} ion solution in water in presence of **iMOF-2C** at different time intervals.

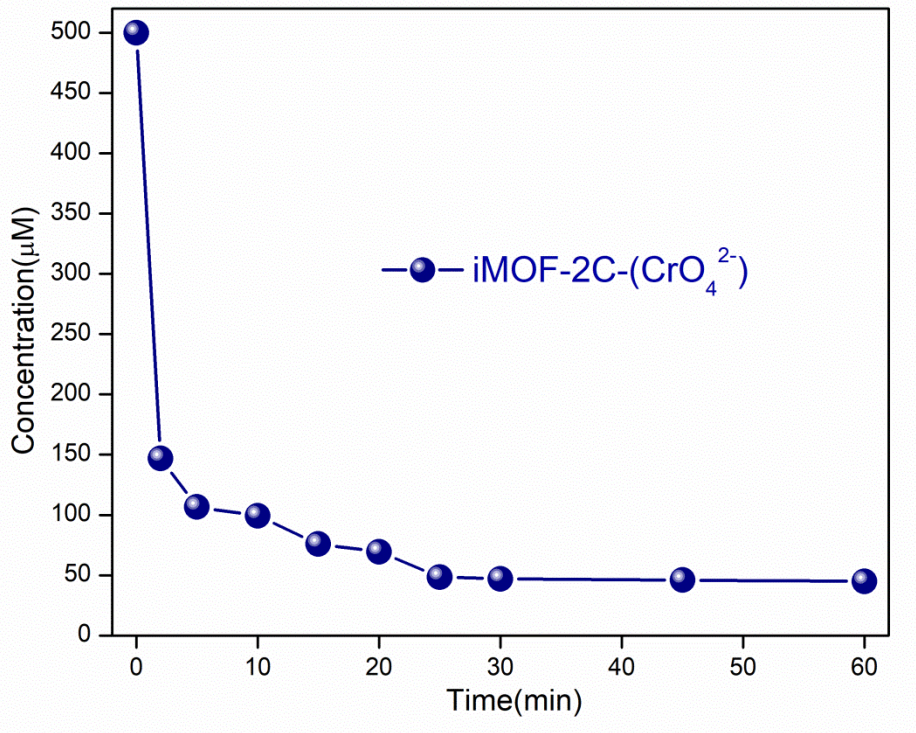

Appendix 5.26: Decrease in the concentration of the CrO_4^{2-} ion from water solution on addition of **iMOF-2C**.

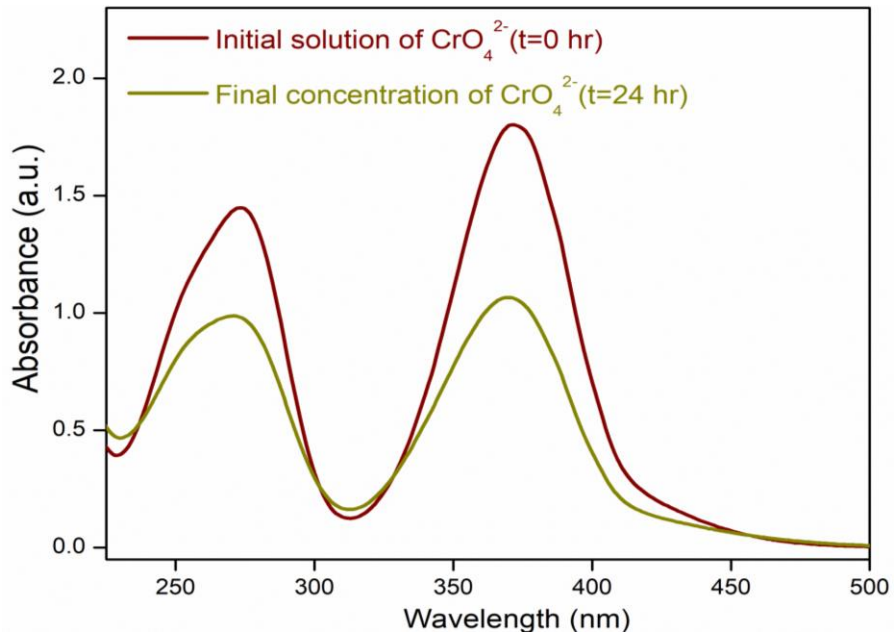

Appendix 5.27: UV-Vis spectra of only CrO_4^{2-} before (wine red) and after (dark yellow) addition of **iMOF-2C**(time duration: 24hrs); capacity of **iMOF-2C** for CrO_4^{2-} ion has been calculated from this data.

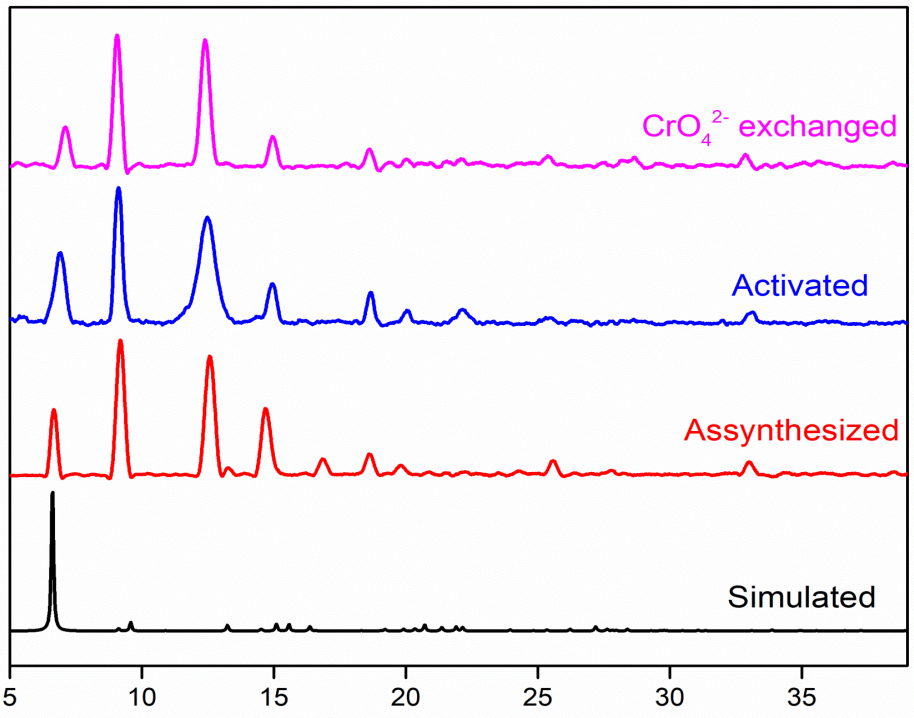

Appendix 5.28: Powder X-ray diffraction patterns of **iMOF-2C** simulated (gray), assynthesized (red), activated (blue), CrO_4^{2-} exchange (pink).

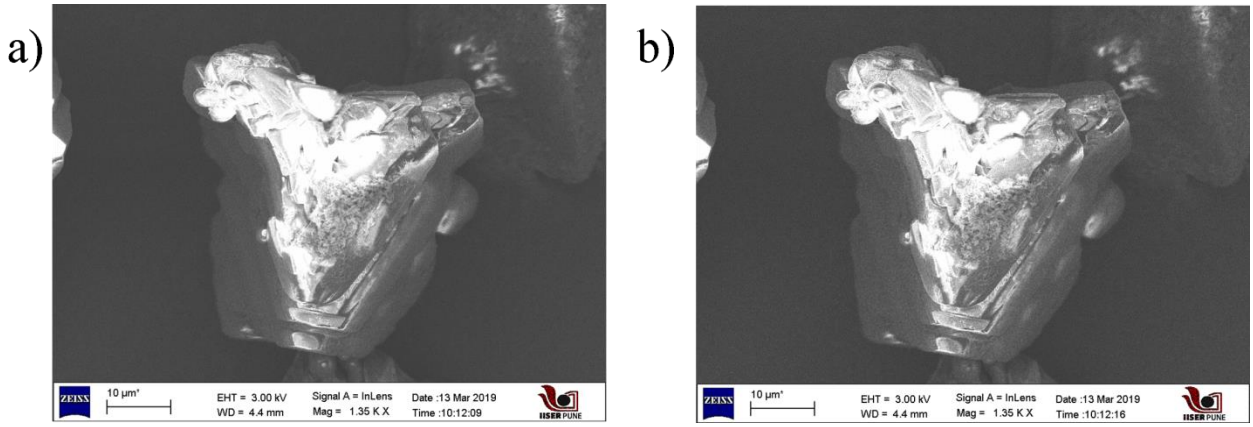

Appendix 5.29: FESEM images of **iMOF-2C** after ReO_4^- exchange.

Element	% weight
C	64.85
N	7.62
O	20.75
Re	4.66
Ni	2.12
Total	100

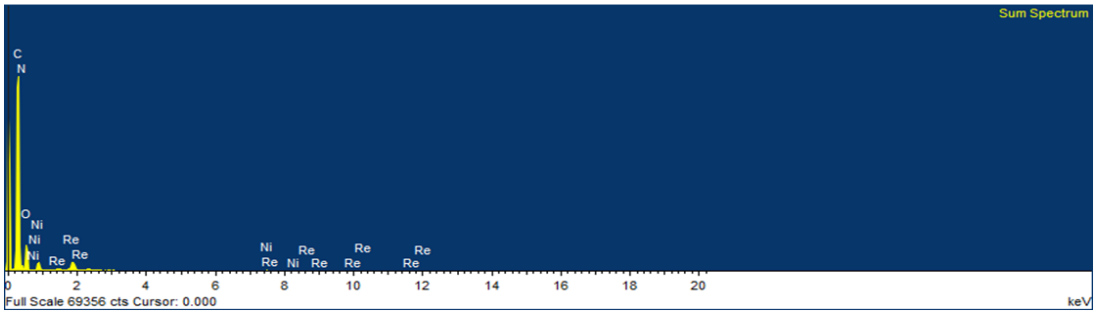

Appendix 5.30: EDX analysis of **iMOF-2C** after ReO_4^- exchange.

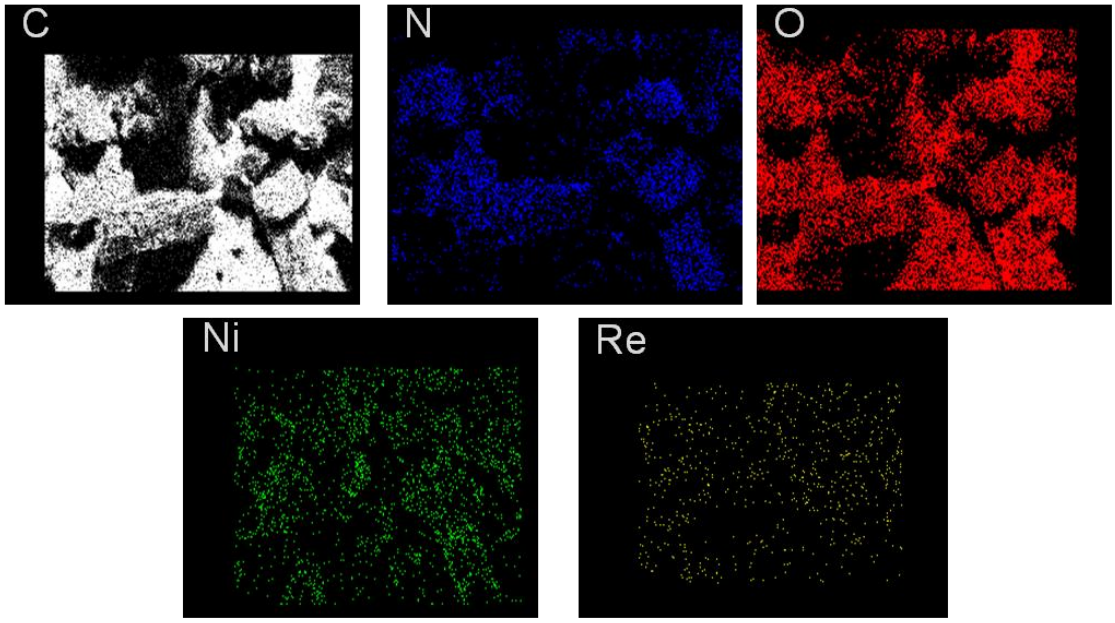

Appendix 5.31: Elemental mapping of **iMOF-2C** after ReO_4^- exchange.

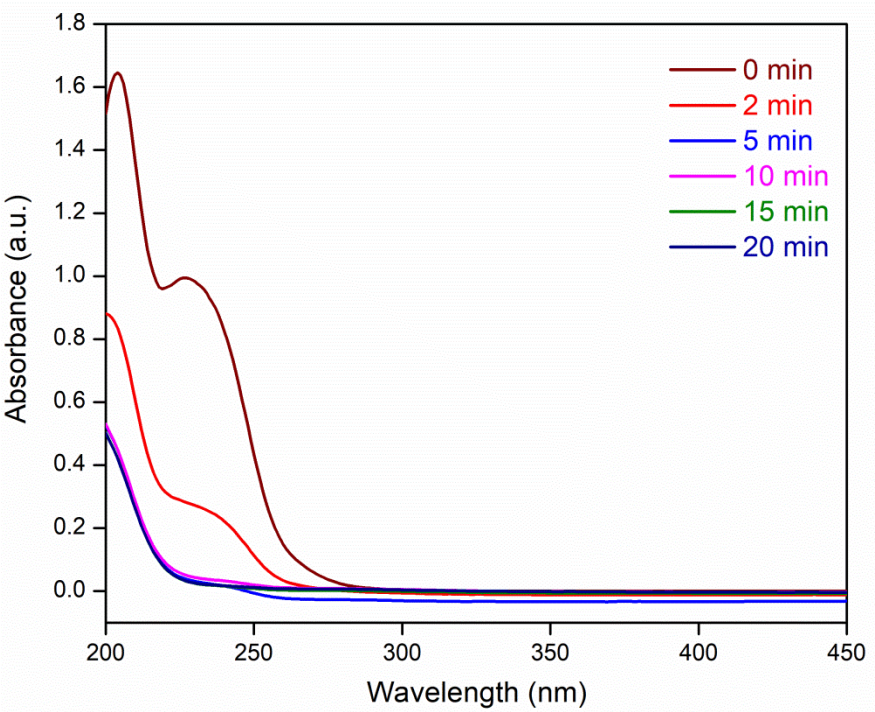

Appendix 5.32: UV-Vis spectroscopy of ReO_4^- ion solution in water in presence of **iMOF-2C** at different time intervals.

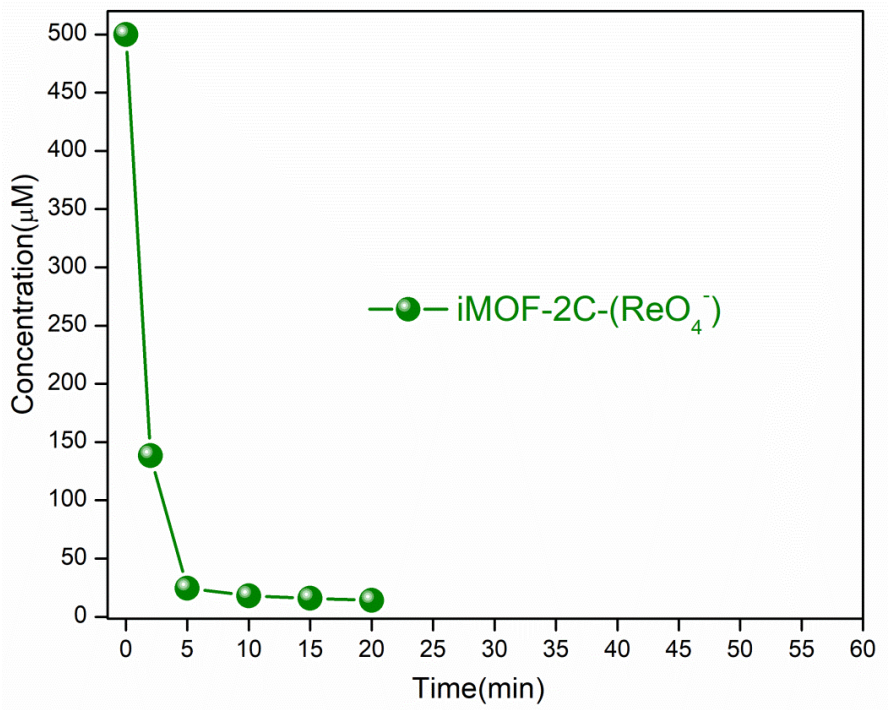

Appendix 5.33: Decrease in the concentration of the ReO_4^- ion from water solution on addition of **iMOF-2C**.

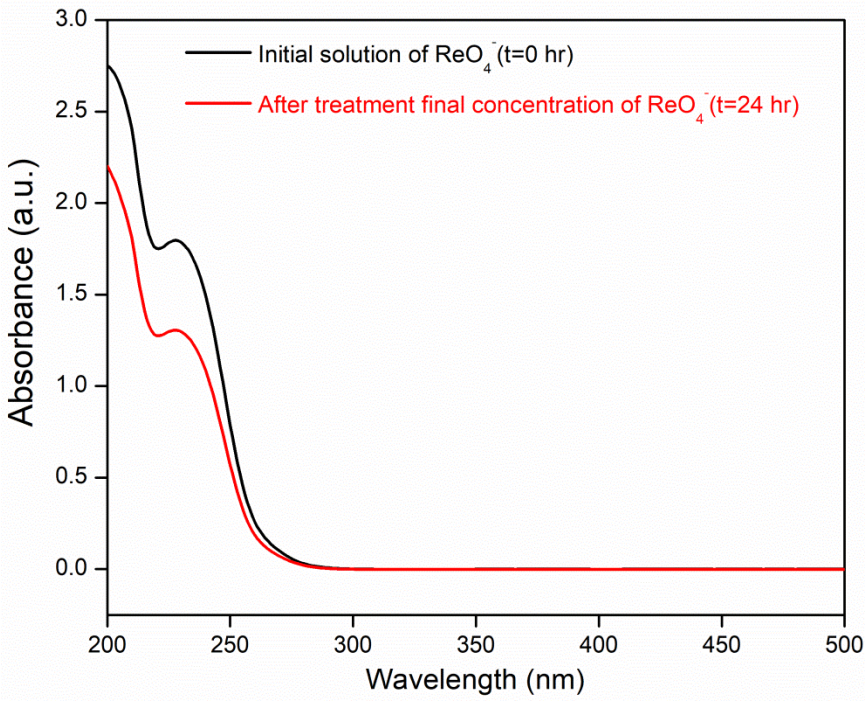

Appendix 5.34: UV-Vis spectra of only ReO_4^- before (black) and after (red) addition of iMOF-2C(time duration: 24hrs); capacity of **iMOF-2C** for ReO_4^- ion has been calculated from this data.

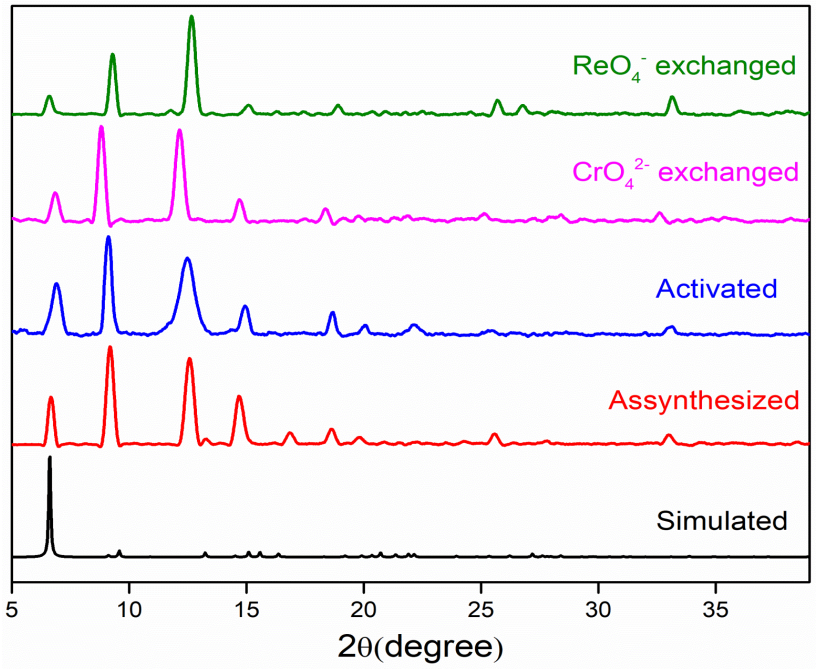

Appendix 5.35: Powder X-ray diffraction patterns of **iMOF-2C** simulated (gray), assynthesized (red), activated (blue), CrO_4^{2-} exchange (pink) and ReO_4^- exchange (green).

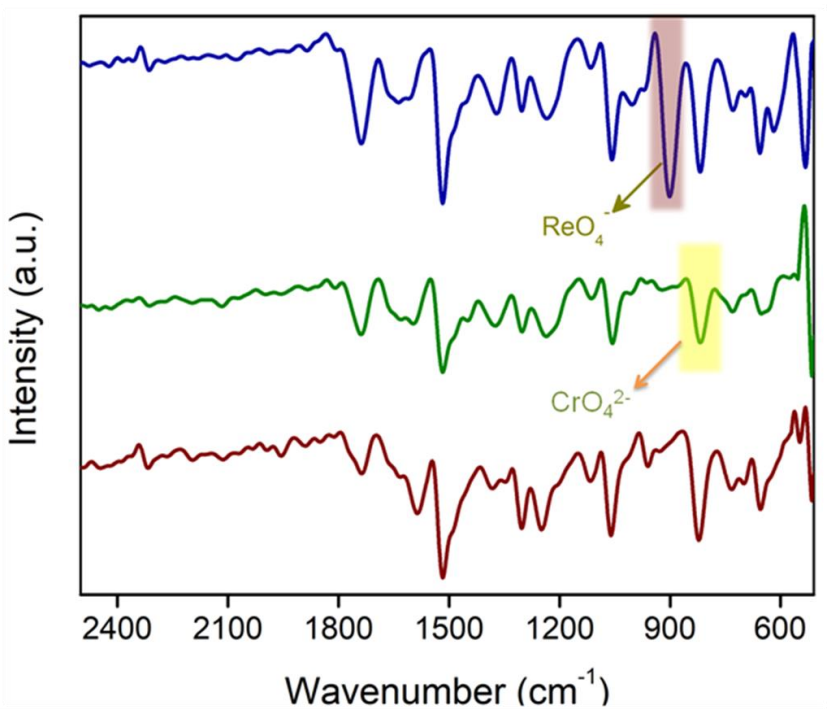

Appendix 5.36: Infra-red (IR) spectroscopy of **iMOF-2C** (wine red), **iMOF-2C-(CrO_4^{2-})** (green) and **iMOF-2C-(ReO_4^-)** (blue).

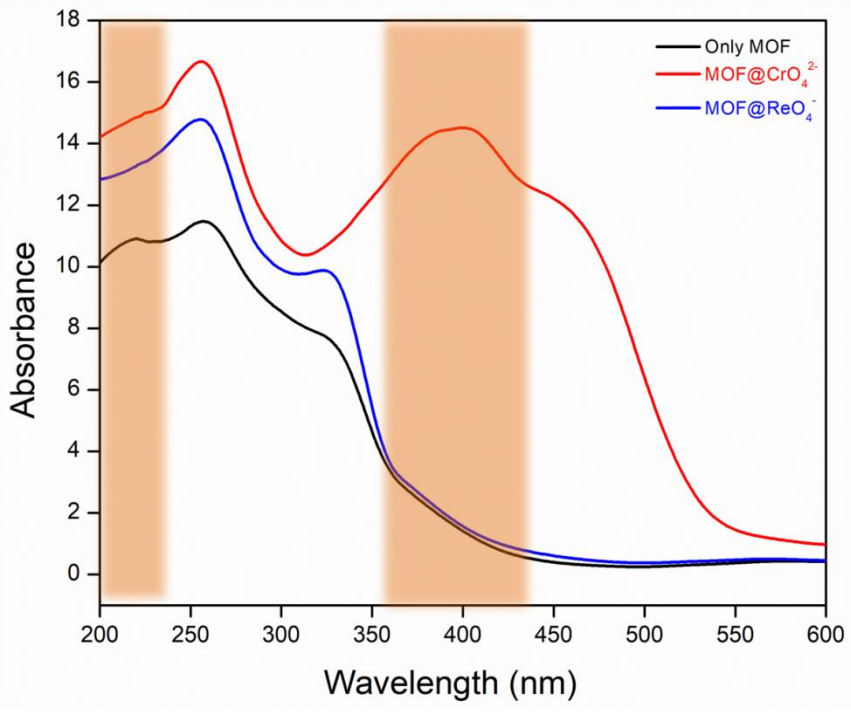

Appendix 5.37: Solid state UV-Vis spectra of **iMOF-2C** (black), **iMOF-2C-(CrO_4^{2-})** (red) and **iMOF-2C-(ReO_4^-)** (blue).

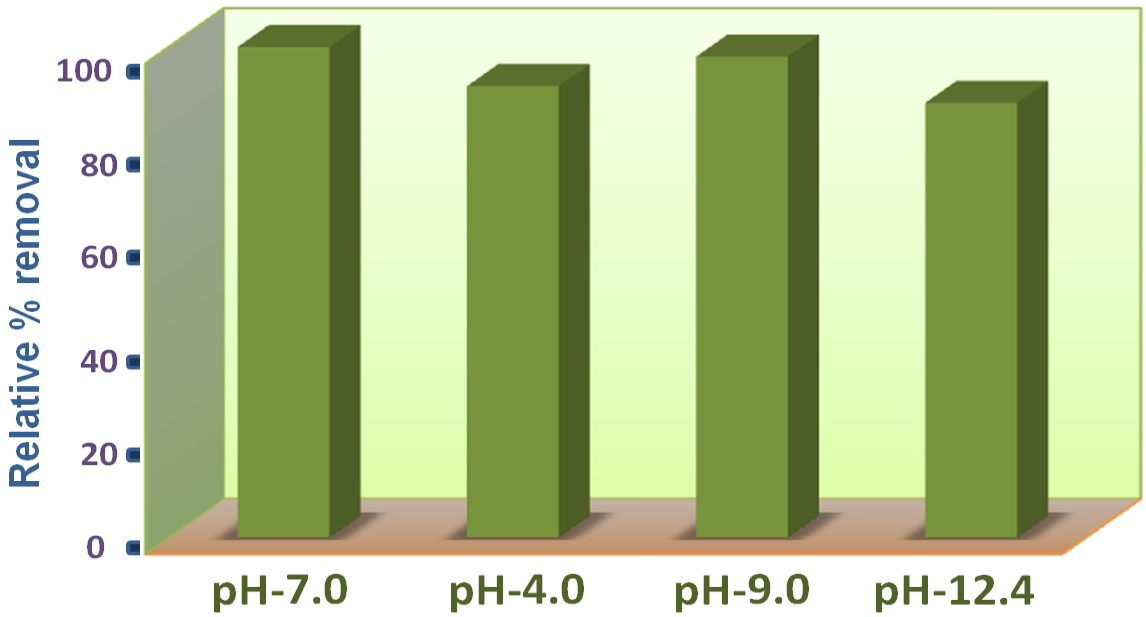

Appendix 5.38: Bar diagram representing relative % removal of CrO_4^{2-} ion from water by **iMOF-2C** at different pH-medium.

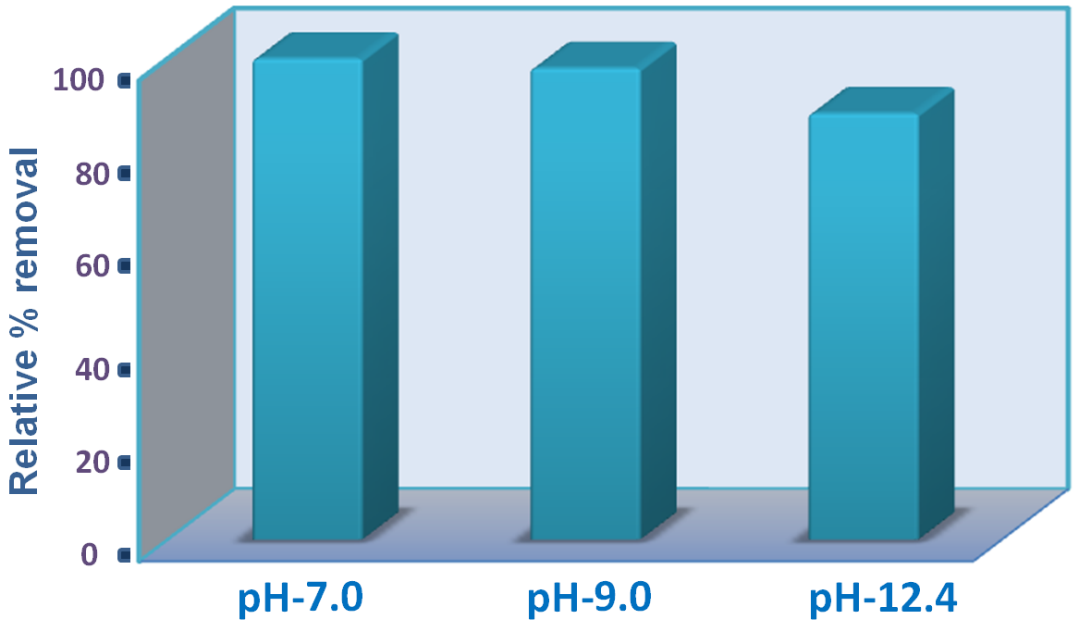

Appendix 5.39: Bar diagram representing relative % removal of ReO_4^{-} ion from water **iMOF-2C** at different pH-medium.

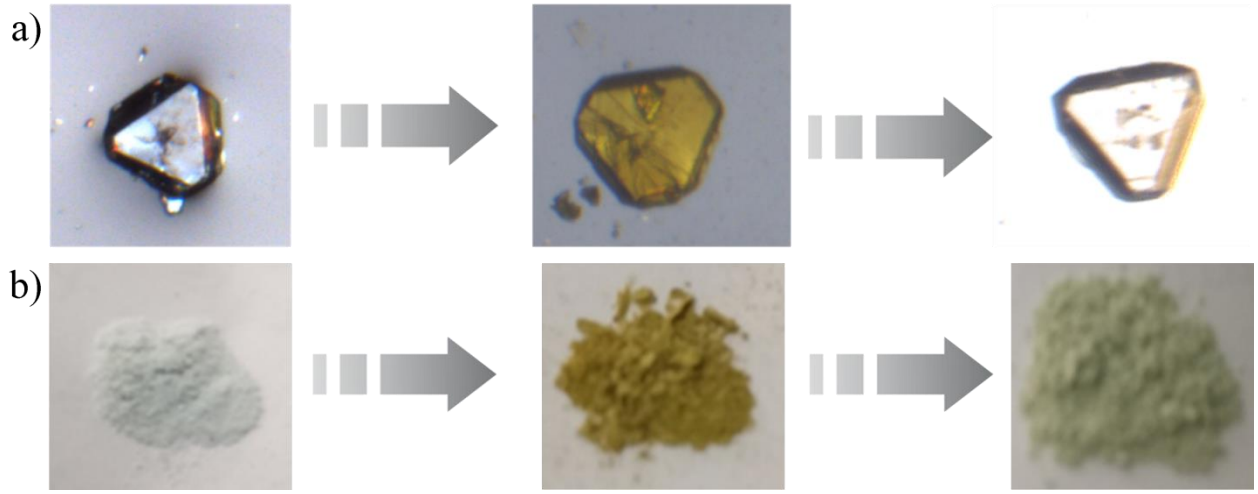

Appendix 5.40: (a) images of **iMOF-2C** single crystal before CrO_4^{2-} exchange, after CrO_4^{2-} exchange and after CrO_4^{2-} release; (b) images of **iMOF-2C** before CrO_4^{2-} exchange, after CrO_4^{2-} exchange and after CrO_4^{2-} release.

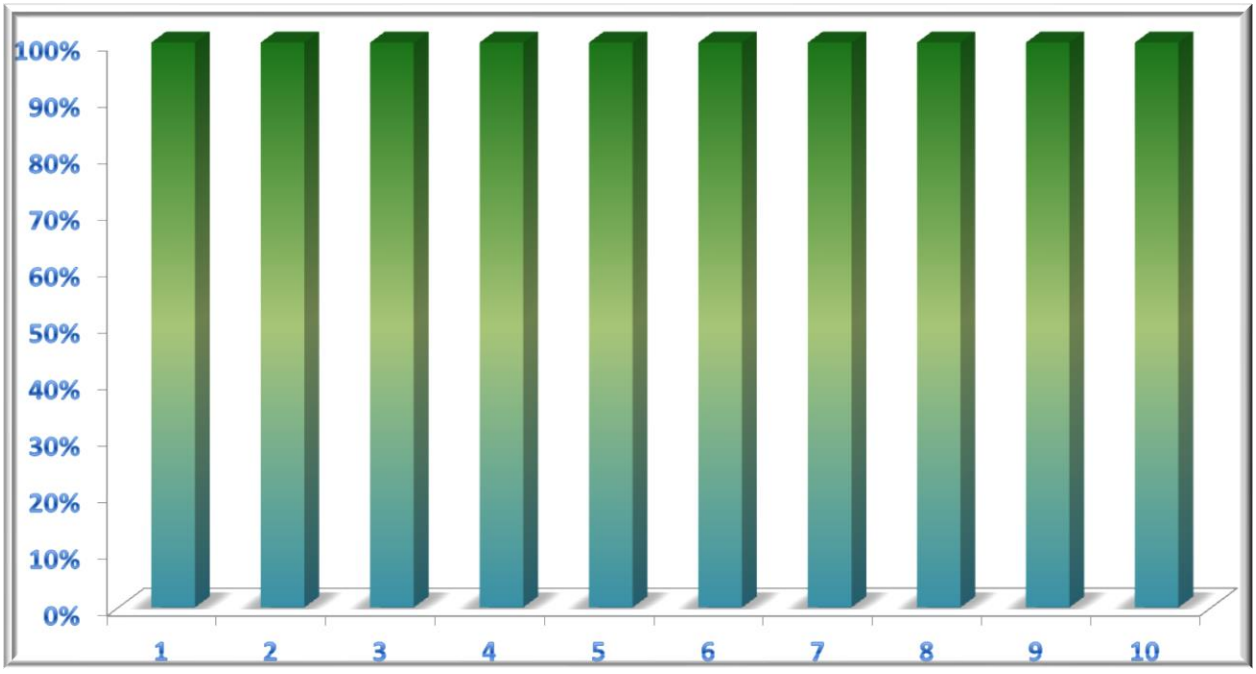

Appendix 5.41: Recyclability test of **iMOF-2C** for CrO_4^{2-} ion.

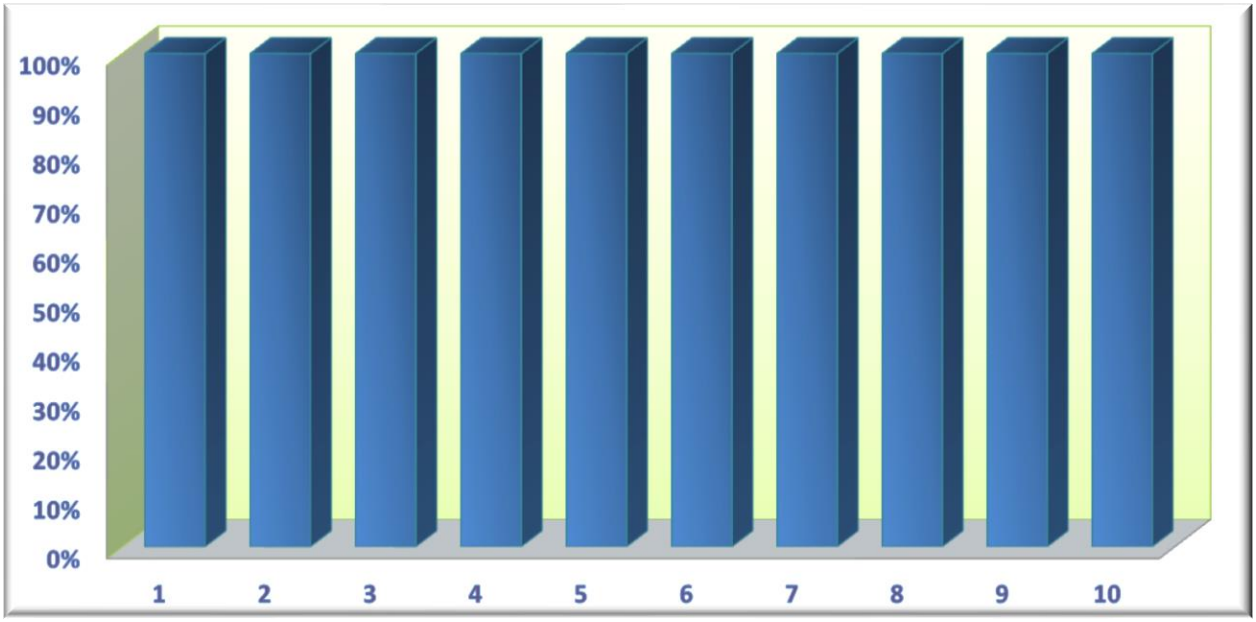

Appendix 5.42: Recyclability test of **iMOF-2C** for ReO_4^- ion.

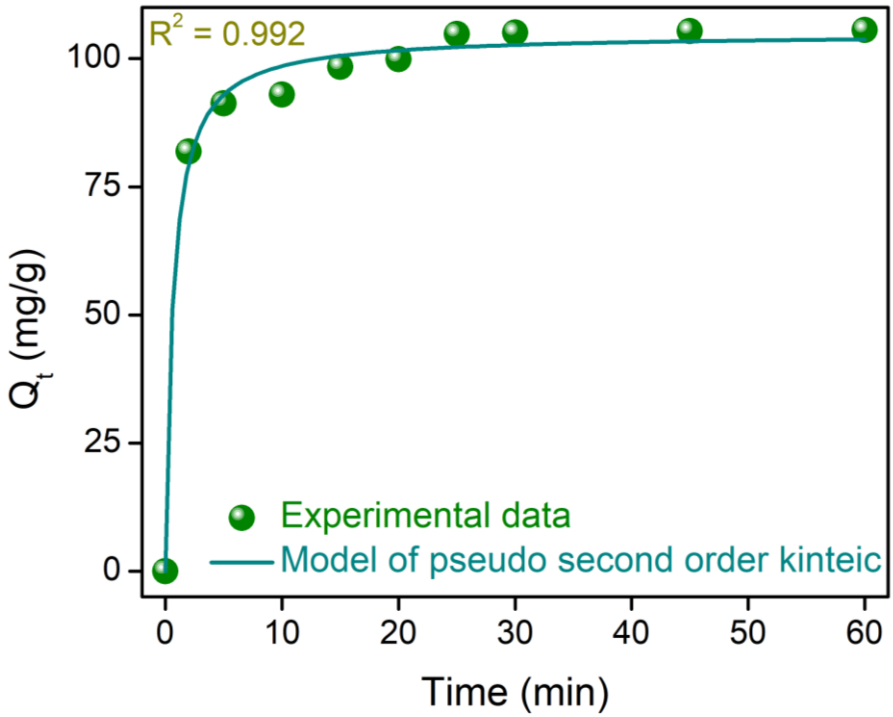

Appendix 5.43: Kinetic study of CrO_4^{2-} ion capture with **iMOF-2C**.

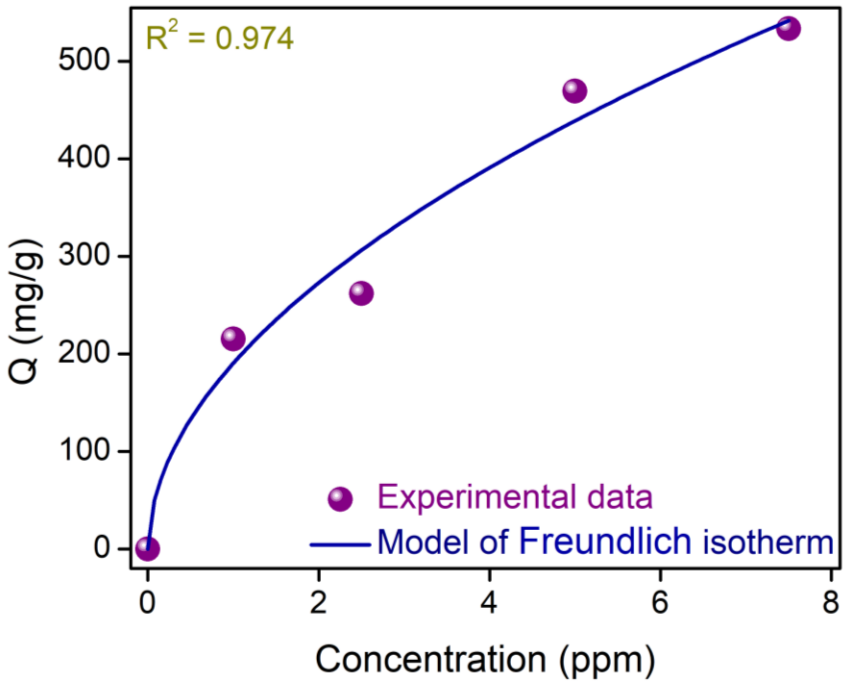

Appendix 5.44: Freundlich model of CrO_4^{2-} ion capture study with **iMOF-2C**.

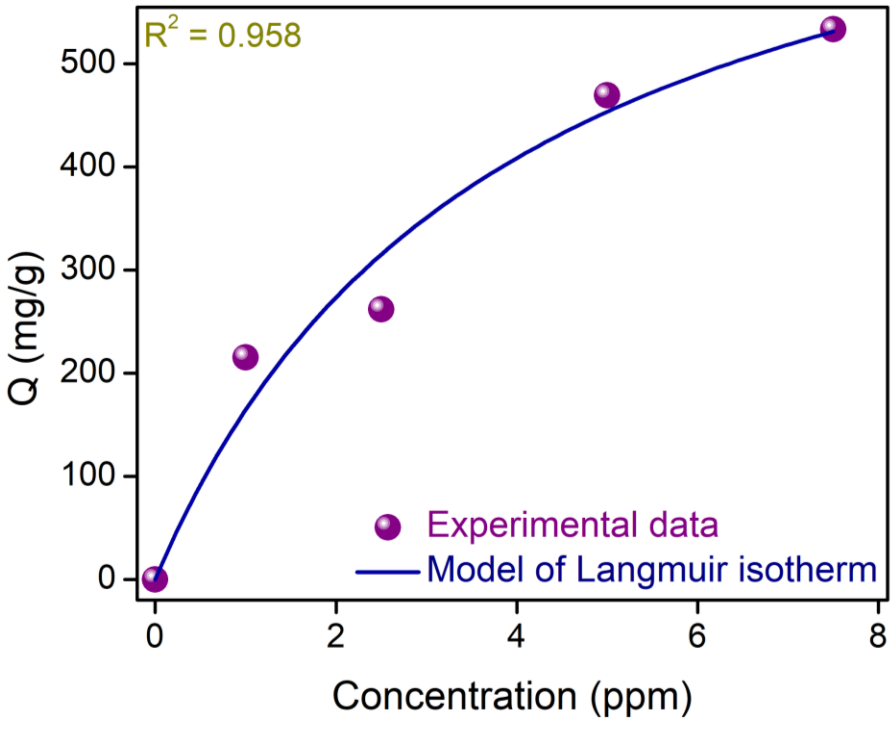

Appendix 5.45: Langmuir model of CrO_4^{2-} ion capture study with **iMOF-2C**.

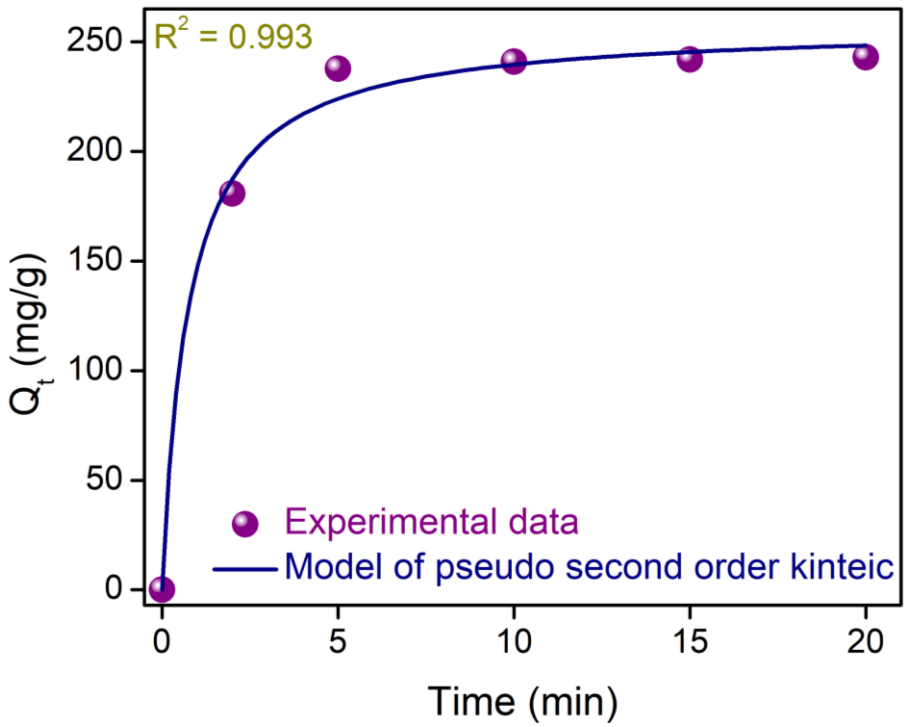

Appendix 5.46: Kinetic study of ReO_4^- ion capture with **iMOF-2C**.

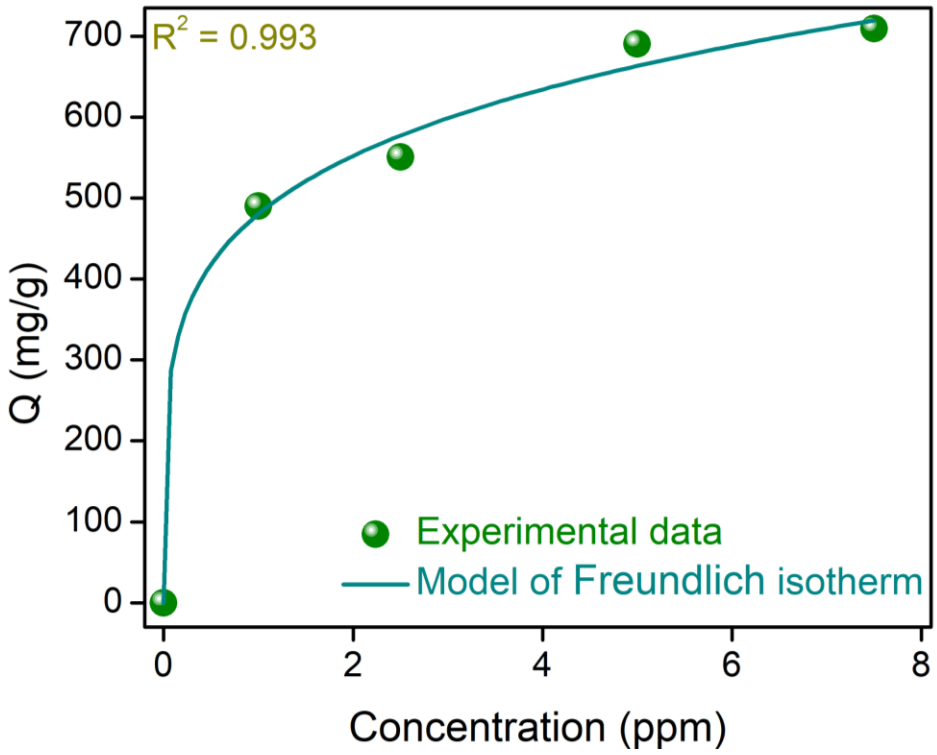

Appendix 5.47: Freundlich model of ReO_4^- ion capture study with **iMOF-2C**.

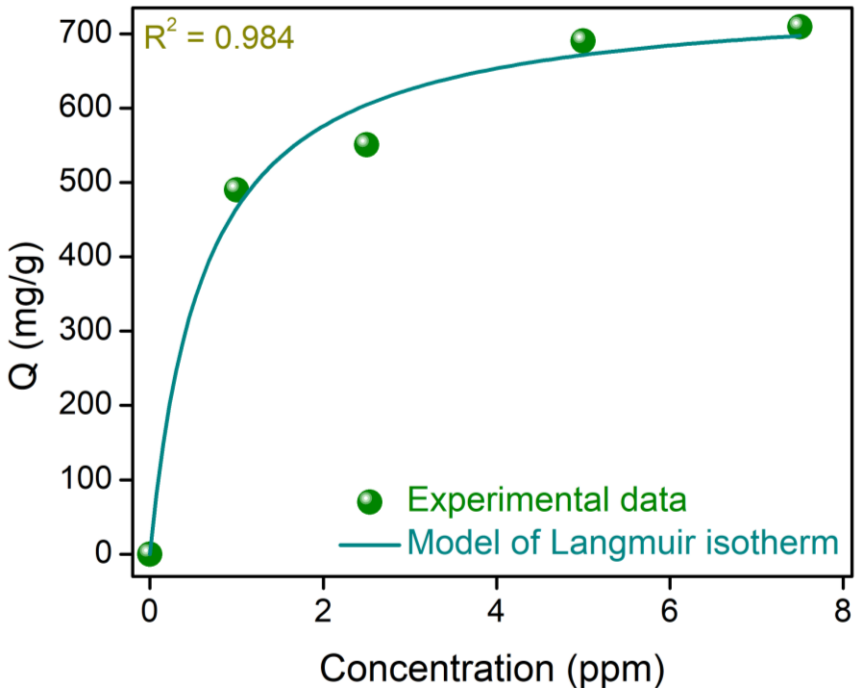

Appendix 5.48: Langmuir model of ReO_4^- ion capture study with **iMOF-2C**.

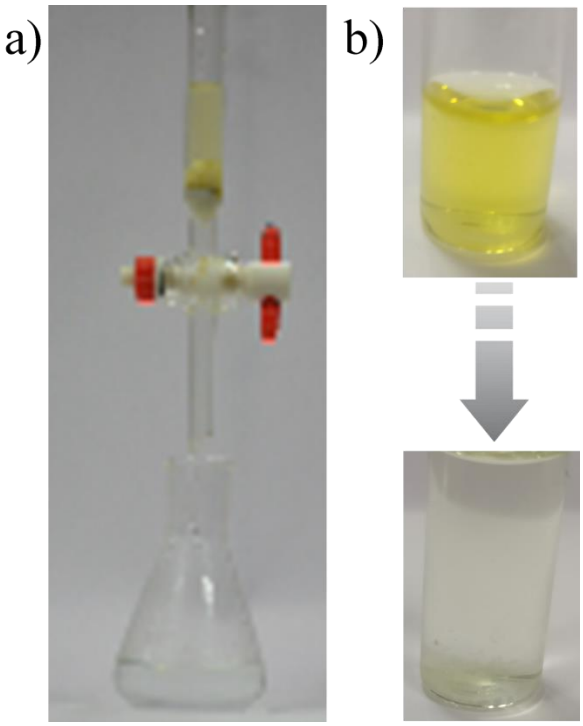

Appendix 5.49: Images of CrO_4^{2-} solution (top) and after (bottom) passing through the **iMOF-2C** loaded column.

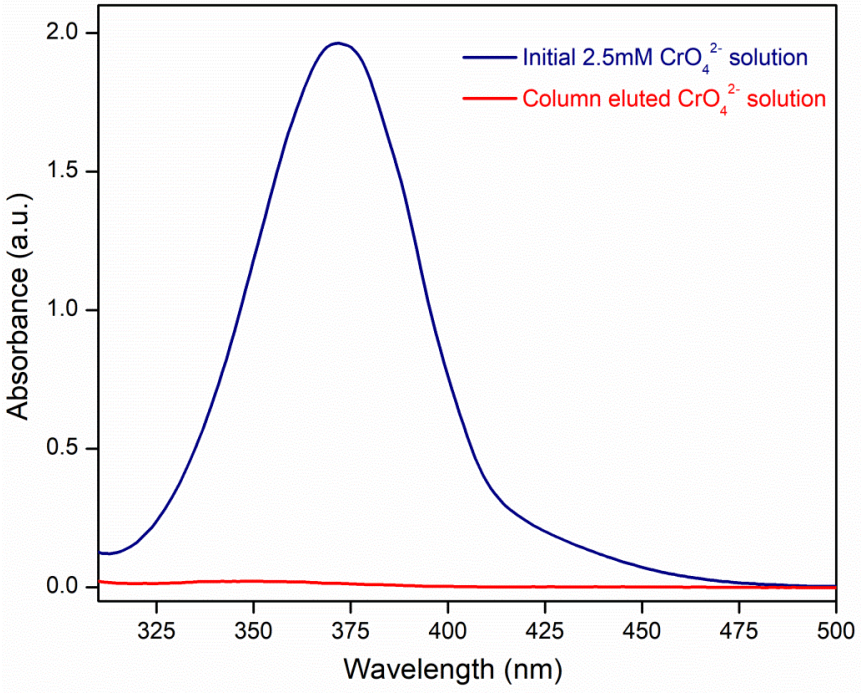

Appendix 5.50: UV-Vis spectra of the 2.5 mM CrO_4^{2-} solution before (blue) and after (red) passing through the **iMOF-2C** loaded column.

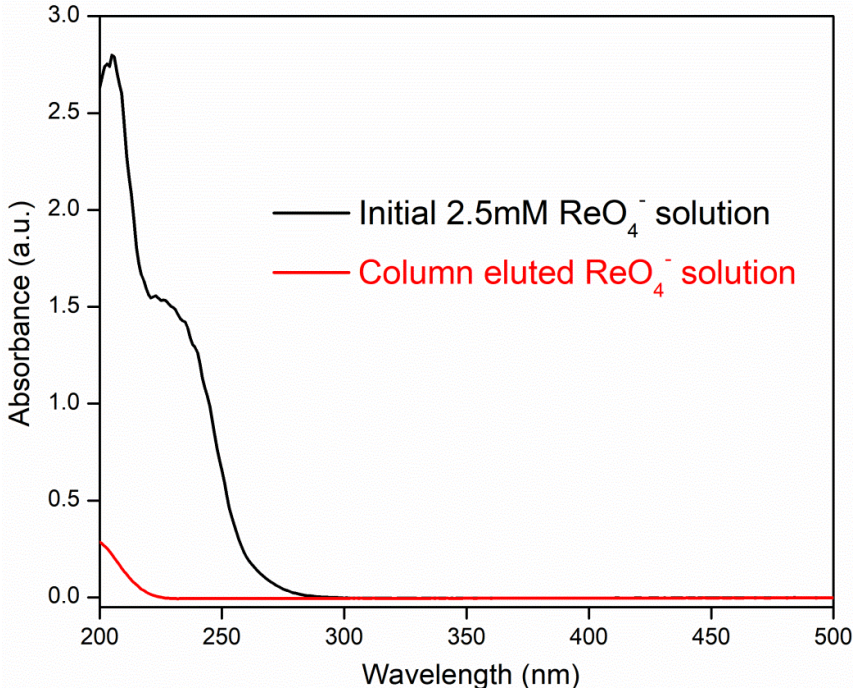

Appendix 5.51: UV-Vis spectra of the 2.5 mM ReO_4^- solution before (black) and after (red) passing through the **iMOF-2C** loaded column.

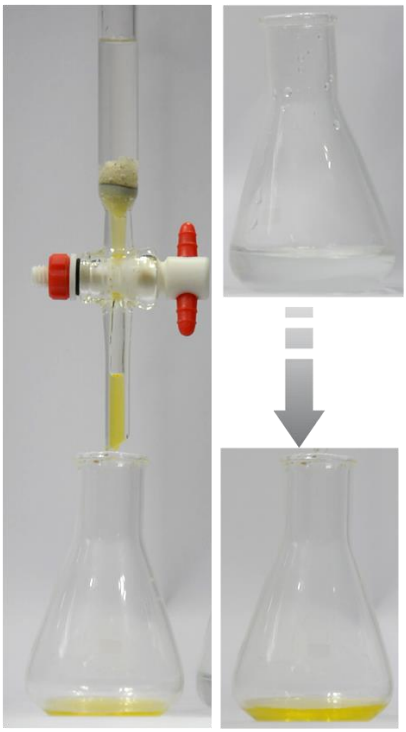

Appendix 5.52: Regeneration of the column with tetrabutylammonium sulfate solution.

No of Cycles	Cycle-1	Cycle-2	Cycle-3	Cycle-4	Cycle-5
Initial solution					
After capture					
Release					
No of Cycles	**Cycle-6**	**Cycle-7**	**Cycle-8**	**Cycle-9**	**Cycle-10**
Initial solution					
After capture					
Release					

Appendix 5.53: Images of the supernatant solution of different cycles of CrO_4^{2-} capture and release.

Appendix Table 5.1: A comparison table of CrO_4^{2-} capture (CrO_4^{2-} mg/gm) with some well-studied examples in the literature (N.D.: Not done)

MOF Based Materials			
Compound	**Capacity (mg/gm)**	**Selectivity**	**Reference**
iMOF-2C	**476.3**	**Cl^-, NO_3^-, Br^-, SO_4^{2-}, ClO_4^-**	**This work**
TJU-1	279	Cl^-, HCO_3^-, NO_3^-, SO_4^{2-}	67
MOR-2	263	Cl^-, NO_3^-, HCO_3^-, etc.	68
1-NO_3	82.5	NO_3^-, CO_3^{2-}	69
Zn–Co-SLUG-35	68.5	NO_3^-, SO_4^{2-}	70
1-ClO_4	62.9	halide anions	71
SLUG-21	60	NO_3^-, CO_3^{2-}	72
Other Porous Materials			
Compound	**Capacity (mg/gm)**	**Selectivity**	**Reference**
Compound-1	133	Cl^-, NO_3^-, Br^-, SO_4^{2-}	73
MgAl-LDHs	112	N.D.	74
Fe nanoparticles	109	N.D.	75
ED-rGO	100	N.D.	76
Polyaniline	18.1	N.D.	77

Appendix Table 5.2: A comparison table of ReO_4^- capture (ReO_4^- mg/gm) with some well-studied examples in the literature (N.D.: Not done)

MOF Based Materials			
Compound	**Capacity (mg/gm)**	**Selectivity**	**Reference**
iMOF-2C	**691**	**Cl^-, NO_3^-, Br^-, SO_4^{2-}, ClO_4^-**	**This Work**
Th-MOF	807	Cl^-, OAc^-, SO_4^{2-}	78
SBN	786	N.D.	84
SLUG-21	602	NO_3^-, CO_3^{2-}	79
SCU-100	553	CO_3^{2-}, SO_4^{2-}, PO_4^{3-}	80
SCU-101	217	various anions	81
NU-1000	210	Cl^-, NO^{3-}, Br^-, I^-, SO_4^{2-},	82
UIO-66-NH_2	159	NO_3^-, SO_4^{2-}, PO_4^{3-}	83
Other Porous Materials			
Compound	**Capacity (mg/gm)**	**Selectivity**	**Reference**
PQA-pN(Me)2Py-Cl	1127	NO_3^-, SO_4^{2-}	85
PQA-Py-Cl	849	NO_3^-, SO_4^{2-}	85
PQA-pNH2Py-Cl	642	NO_3^-, SO_4^{2-}	85
Compound-1	517	Cl^-, NO_3^-, Br^-, SO_4^{2-}	73
PAF-1-F	420	SO_4^{2-}, PO_4^{3-}	86
LDHs	130	N.D.	87
Dowex1x8	98.1	N.D.	86
Purolite 530E	96	N.D.	86
PolyDMAEMA hydrogels	30.5	N.D.	88

Appendix Table 5.3: A comparison table of cell parameters of iMOF-2C and iMOF-2C-CrO_4^{2-}

Parameters	iMOF-2C	iMOF-2C-(CrO_4^{2-})
a (A^0)	18.59 (10)	18.64 (11)
b (A^0)	18.59 (10)	18.473 (11)
c (A^0)	23.04 (19)	24.195(11)
α (degree)	90	89.406
β (degree)	90	89.507
ɣ (degree)	120	120.156
Cell Volume ($A^{0\,3}$)	7125.29	7184.09

Appendix Table 5.4. Crystal data and structure refinement for imof-2C.

Identification code	iMOF-2C	
CCDC Number	1980127	
Empirical formula	C66 H48 N12 Ni	
Formula weight	1067.87	
Temperature	296(2) K	
Wavelength	0.71073 Å	
Crystal system	Triclinic	
Space group	R -3	
Unit cell dimensions	a = 12.554(9) Å	□= 91.887(16)°.
	b = 12.876(9) Å	□= 90.589(18)°.
	c = 13.703(10) Å	□ = 98.136(16)°.
Volume	2191(3) $Å^3$	
Z	1	
Density (calculated)	0.809 Mg/m^3	
Absorption coefficient	0.255 mm^{-1}	
F(000)	556	
Crystal size	0.120 x 0.100 x 0.100 mm^3	
Theta range for data collection	2.221 to 26.542°.	
Index ranges	-15<=h<=13, -16<=k<=15, -17<=l<=17	
Reflections collected	25718	
Independent reflections	8947 [R(int) = 0.2033]	
Completeness to theta = 25.242°	99.7 %	
Refinement method	Full-matrix least-squares on F^2	
Data / restraints / parameters	8947 / 0 / 358	
Goodness-of-fit on F^2	0.890	
Final R indices [I>2sigma(I)]	R1 = 0.1141, wR2 = 0.2891	
R indices (all data)	R1 = 0.2621, wR2 = 0.3343	
Extinction coefficient	n/a	
Largest diff. peak and hole	0.708 and -0.519 $e.Å^{-3}$	

5.6 References

[1] R. P. Schwarzenbach, B. I. Escher, K. Fenner, T. B. Hofstetter, C. A. Johnson, U. Gunten, B. Wehrli, *Science* **2006,** *313*, 1072–1077.

[2] J. B. Derraik, *Mar. Pollut. Bull.*, **2002,** *44*, 842–852.

[3] E. M. Dias, C. Petit, *J. Mater. Chem. A* **2015**, *3*, 22484 –22506.

[4] L. H. Keith, W. A. Teillard, *Environ. Sci. Technol.* **1979**, *13*, 416–423.

[5] H. Fei, D. L. Rogow, S. R. J. Oliver, *J. Am. Chem. Soc.* **2010**, *132*, 7202–7209.

[6] R. Cao, B. D. McCarthy, S. J. Lippard, *Inorg. Chem.* **2011**, *50*, 9499–9507.

[7] Toxicological Profile for Chromium, Public Health Service Agency for Toxic Substances and Diseases Registry U.S. Department of Health and Human Services, *Atlanta, GA*, **2012**.

[8] R. Vonburg, D. Liu, *J. Appl. Toxicol*, **1993**, *13*, 225–230.

[9] L. Khezami, R. Capart, *J. Hazard. Mater.*, **2005**, *123*, 223–231.

[10] M. B. Luo, Y. Y. Xiong, H. Q. Wu, X. F. Feng, J. Q. Li, F. Luo, *Angew. Chem., Int. Ed.*, **2017**, *56*, 16376–16379.

[11] W. Liu, Y. Wang, Z. Bai, Y. Li, Y. Wang, L. Chen, L. Xu, J. Diwu, Z. Chai, S. Wang, *ACS Appl. Mater. Interfaces*, **2017**, *9*, 16448–16457.

[12] S. R. J. Oliver, *Chem. Soc. Rev.*, **2009**, *38*, 1868–1881.

[13] C. Pellerin, S. M. Booker, *Environ. Health Perspect.*, **2000**, *108*, A402–A407.

[14] C. Xiao, A. Khayambashi, S. Wang, *Chem. Mater.*, **2019**, *31*, 3863−3877.

[15] S. Wang, P. Yu, B. A. Purse, M. J. Orta, J. Diwu, W. H. Casey, B. L. Phillips, E. V. Alekseev, W. Depmeier, D. T. Hobbs, T. E. Albrecht-Schmitt, *Adv. Funct. Mater.*, **2012**, *22*, 2241– 2250.

[16] Q. Sun, L. Zhu, B. Aguila, P. K. Thallapally, C. Xu, J. Chen, S. Wang, D. Rogers, S. Ma, *Nat. Commun.*, **2019**, *DOI: 10.1038/s41467-019-09630*.

[17] T. H. Boyer, P. C. Singer, *Environ. Sci. Technol.*, **2008**, *42*, 608–613.

[18] B. Gammelgaard, Y. P. Liao, O. Jons, *Anal. Chim. Acta,* **1997**, *354*, 107–113.

[19] B. Wen, X. Q. Shan, J. Lian, *Talanta,* **2002**, *56*, 681–687.

[20] A. Syty, R. G. Christensen, T. C. Rains, *J. Anal. At. Spectrom.,* **1988**, *3*, 193–197.

[21] D. Sheng, L. Zhu, C. Xu, C. Xiao, Y. Wang, Y. Wang, L. Chen, J. Diwu, J. Chen, Z. Chai, T. E. Albrecht-Schmitt, S. Wang, *Environ. Sci. Technol,* **2017**, *51*, 3471–3479.

[22] D. Banerjee, D. Kim, M. J. Schweiger, A. A. Kruger, P. K. Thallapally, *Chem. Soc. Rev.,* **2016**, *45*, 2724–2739.

[23] A. V. Desai, B. Manna, A. Karmakar, A. Sahu, S. K. Ghosh, *Angew. Chem. Int. Ed.,* **2016**, *55*, 7811–7815.

[24] J. Li, X. Dai, L. Zhu, C. Xu, D. Zhang, M. A. Silver, P. Li, L. Chen, Y. Li, D. Zuo, H. Zhang, C. Xiao, J. Chen, J. Diwu, O. K. Farha, T. E. Albrecht-Schmitt, Z. Chai, S. Wang, *Nat Commun* **2018**, 9, 3007. doi.org/10.1038/s41467-018-05380-5.

[25] R. J. Kuppler, D. J. Timmons, Q.-R. Fang, J.-R. Li, T. A. Makal, M. D. Young, D. Yuan, D. Zhao, W. Zhuang, H.-C. Zhou, *Coord. Chem. Rev.,* **2009**, *253*, 3042−3066.

[26] P. Horcajada, R. Gref, T. Baati, P. K. Allan, G. Maurin, P. Couvreur, G. Ferey, R. E. Morris, C. Serre, *Chem. Rev.,* **2012**, *112*, 1232−1268.

[27] W. P. Lustig, S. Mukherjee, N. D. Rudd, A. V. Desai, J. Li, S. K. Ghosh, *Chem. Soc. Rev.,* **2017**, *46*, 3242−3285.

[28] N. S. Bobbitt, M. L. Mendonca, A. J. Howarth, T. Islamoglu, J. T. Hupp, O. K. Farha R. Q. Snurr, *Chem. Soc. Rev.,* **2017**, *46*, 3357−3385.

[29] P. Samanta, S. Let, W. Mandal, S. Dutta, S. K. Ghosh, *Inorg. Chem. Front.,* **2020**,*7*, 1801-1821.

[30] S. Sharma, A. V. Desai, B. Joarder, S. K. Ghosh, *Angew. Chem. Int. Ed.,* **2020**, *59*, 7788-7792.

[31] Metal-organic frameworks (MOFs) for Environmental Applications, 1st edition, (Ed.: S. K. Ghosh), *Elsevier*, **2019**, *doi: 10.1016/C2017-0-01721-4*.

[32] J. Li, X. Wang, G. Zhao, C. Chen, Z. Chai, A. Alsaedi, T. Hayat, X. Wang, *Chem. Soc. Rev.*, **2018**, 47, 2322-2356.

[33] M. Mon, R. Bruno, J. Ferrando-Soria, D. Armentano, E. Pardo, *J. Mater. Chem. A*, **2018**, *6*, 4912-4947.

[34] L. Zhu, V. Sheng, C. Xu, X. Dai, M. A. Silver, J. Li, P. Li, Y. Wang, Y. Wang, L. Chen, C. Xiao, J. Chen, R. Zhou, C. Zhang, O. K. Farha, Z. Chai, T. E. Albrecht-Schmitt, S. Wang, *J. Am. Chem. Soc.*, **2017**, *139*, 14873–14876.

[35] Y. Li, Z. Yang, Y. Wang, Z. Bai, T. Zheng, X. Dai, S. Liu, D. Gui, W. Liu, M. Chen, L. Chen, J. Diwu, L. Zhu, R. Zhou, Z. Chai, T. E. Albrecht-Schmitt,; S. Wang, *Nat Commun* **2017**, 8, 1354. https://doi.org/10.1038/s41467-017-01208-w.

[36] A. Karmakar, P. Samanta, S. Dutta, S. K. Ghosh, *Chem. Asian J.*, **2019**, *14*, 4506 –4519.

[37] S.-Q. Deng, Y.-L. Miao, Y.-L. Tan, H.-N. Fang, Y.-T. Li, X.-J. Mo, S.-L. Cai, J. Fan, W.-G. Zhang, S.-R. Zheng, *Inorg. Chem.*, **2019**, 58, 20, 13979-13987.

[38] D. Banerjee, S. K. Elsaidi, B. Aguila, B. Li, D. Kim, M. J. Schweiger, A. A. Kruger, C. J. Doonan, S. Ma, P. K. Thallapally, Chem. Eur. J., 2016, 22, 17581 – 17584.

[39] D. Banerjee, W. Xu, Z. Nie, L. E. V. Johnson, C. Coghlan, M. L. Sushko, D. Kim, M. J. Schweiger, A. A. Kruger, C. J. Doonan, P. K. Thallapally, Inorg. Chem., 2016, 55, 8241−8243.

[40] A. Karmakar, A. V. Desai, S. K. Ghosh, *Coord. Chem. Rev.*, **2016**, *307*, 313–341.

[41] A. V. Desai, A. Roy, P. Samanta, B. Manna, S. K. Ghosh, *iScience*, **2018**, *3*, 21-30.

[42] H.W. Olfs, L. O. Torres-Dorante, R. Eckelt, H. Kosslick, *Appl. Clay Sci.*, **2009**, *43*, 459 – 464.

[43] L. J. McIntyre, L. K. Jackson, A. M. Fogg, *Chem. Mater.* **2008**, *20*, 335 – 340.

[44] H. V. Goulding, S. E. Hulse, W. Clegg, R. W. Harrington, H. Y. Playford, R. I. Walton, A. M. Fogg, *J. Am. Chem. Soc.* **2010**, *132*, 13618 – 13620.

[45] P. Samanta, P. Chandra, S. Dutta, A. V. Desai, S. K. Ghosh, *Chem. Sci.* **2018**, *9*, 7874 – 7881.

[46] D. Banerjee, D. Kim, M. J. Schweiger, A. A. Kruger, P. K. Thallapally, *Chem. Soc. Rev.* **2016**, *45*, 2724 – 2739.

[47] N. Busschaert, C. Caltagirone, W. Van Rossom, P. A. Gale, *Chem. Rev.* **2015**, *115*, 8038 – 8155.

[48] D. Sheng, L. Zhu, X. Dai, C. Xu, P. Li, C. I. Pearce, C. Xiao, J. Chen, R. Zhou, T. Duan, O. K. Farha, Z. Chai, S. Wang, *Angew. Chem. Int. Ed.* **2019**, *58*, 4968–4972.

[50] *SAINT Plus, version 7.03; Bruker AXS Inc*.: Madison, WI, 2004.

[51] G. M. Sheldrick, SHELXTL, *Reference Manual, version 5.1; Bruker AXS Inc*.: Madison, WI, 1997.

[52] G. M. Sheldrick, *Acta. Crystallogr. Sect. A* **2008**, 64, 112-122.

[53] L. Farrugia, *WinGX, version* 1.80.05; University of Glasgow: Glasgow, Scotland, 2009.

[54] A. L. Spek, PLATON, a Multipurpose Crystallographic Tool; Utrecht University: Utrecht, The Netherlands, 2005.

[55] A. L. Spek, *J. Appl. Crystallogr*., 2003, **36**, 07-13.

[56] Dassault Systèmes BIOVIA, Material Studio, San Diego: Dassault Systèmes, **2019**.

[57] A. K. Rappe, C. J. Casewit, K. S. Colwell, W. A. Goddard, W. M. Skiff, *J. Am. Chem. Soc.* **1992**, *114*, 10024-10035.

[58] G. Kresse, J. Hafner, J. *Phys. Rev. B* **1993**, *48*, 13115-13118.

[59] S. Grimme, S. Ehrlich, L. Goerigk, J. *Comp. Chem.* **2011**, *32*, 1456-1465.

[60] J. P. Perdew, K. Burke, M. Ernzerhof, *Phys. Rev. Lett.* **1996** *77*, 3865-3868.

[61] G. Kresse, D. Joubert, *Phys. Rev. B* **1999**, *59*, 1758-1775**.**

[62] M. J. Frisch, G. W. Trucks, H. B. Schlegel, G. E. Scuseria, M. A. Robb, J. R. Cheeseman, G. Scalmani, V. Barone, B. Mennucci, G. A. Petersson, H. Nakatsuji, M.

Caricato, X. Li, H. P. Hratchian, A. F. Izmaylov, J. Bloino, G. Zheng, J. L. Sonnenberg, M. Hada, M. Ehara, K. Toyota, R. Fukuda, J. Hasegawa, M. Ishida, T. Nakajima, Y. Honda, O. Kitao, H. Nakai, T. Vreven, J. A. Jr. Montgomery, J. E. Peralta, F. Ogliaro, M. Bearpark, J. J. Heyd, E. Brothers, K. N. Kudin, V. N. Staroverov, R. Kobayashi, J. Normand, K. Raghavachari, A. Rendell, J. C. Burant, S. S. Iyengar, J. Tomasi, M. Cossi, Gaussian 09, Revision E.01.

[63] S. -R. Zheng, Q. -Y. Yang, Y. -R. Liu, J. -Y. Zhang, Y. -X. Tong, C. -Y. Zhao, C. -Y. Su, *Chem. Commun.* **2008**, *0*, 356–358.

[64] T. G. Mitina, V. A. Blatov, *Cryst. Growth Des.* **2013**, *13*, 1655–1664.

[65] S. -S. Liu, S. Yuan, X. -Y. Li, S. Miao, Z. -W. Yu, X. -P. Wang, D. Sun, *Inorg. Chim. Acta* **2014**, *416*, 195–199.

[66] Dassault Systèmes BIOVIA, Material Studio, San Diego: Dassault Systèmes, **2019**.

[67] H. Yang, H. Fei, *Chem. Commun.* **2017**, *53*, 7064−7067.

[68] S. Rapti, D. Sarma, S. A. Diamantis, E. Skliri, G. S. Armatas, A. C. Tsipis, Y. S. Hassan, M. Alkordi, C. D. Malliakas, M. G. Kanatzidis, T. Lazarides, J. C. Plakatouras, M. J. Manos, *J. Mater. Chem. A* **2017**, *5*, 14707–14719.

[69] L. Li, X. Feng, R. Han, S. Zang, G. Yang, *J. Hazard. Mater.* **2017**, *321*, 622−628.

[70] H. Fei, C. S. Han, J. C. Robins, S. R. J. Oliver, *Chem. Mater.* **2013**, *25*, 647−652.

[71] P. Shi, B. Zhao, G. Xiong, Y. Hou, P. Cheng, *Chem. Commun.* **2012**, *48*, 8231−8233.

[72] H. Fei, M. R. Bresler, S. R. J. Oliver, *J. Am. Chem. Soc.* **2011**, *133*, 11110−11113.

[73] P. Samanta, P. Chandra, S. Dutta, A. V. Desai, S. K. Ghosh, Chem. Sci. **2018**, *9*, 7874–7881.

[74] Y. Li, B. Gao, T. Wu, D. Sun, X. Li, B. Wang, F. Lu, *Water Res.* **2009**, *43*, 3067−3075.

[75] J. Cao, W. -X. Zhang, *J. Hazard. Mater.* **2006**, *132*, 213−219.

[76] H. -L. Ma, Y. Zhang, Q. -H. Hu, D. Yan, Z. -Z. Yu, M. Zhai, *J. Mater. Chem.* **2012**, *22*, 5914−5916.

[77] B. Qiu, C. Xu, D. Sun, H. Wei, X. Zhang, J. Guo, Q. Wang, D. Rutman, Z. Guo, S. Wei, *RSC Adv.* **2014**, *4*, 29855–29865.

[78] Y. Li, B. Gao, T. Wu, D. Sun, X. Li, B. Wang, F. Lu, *Water Res.* **2009**, *43*, 3067−3075.

[79] H. Xu, C.-S. Cao, H.-S. Hu, S.-B. Wang, J.-C. Liu, P. Cheng, N. Kaltsoyannis, J. Li, B. Zhao, Angew. Chem. Int. Ed. **2019**, *131*, 6083-6088.

[80] H. Fei, D. L. Rogow, S. R. J. Oliver, *J. Am. Chem. Soc.* **2010**, *132*, 7202−7209.

[81] D. Sheng, L. Zhu, C. Xu, C. Xiao, Y. Wang, Y. Wang, L. Chen, J. Diwu, J. Chen, Z. Chai, S. Wang, *Environ. Sci. Technol.* **2017**, *51*, 3471−3479.

[82] L. Zhu, V. Sheng, C. Xu, X. Dai, M. A. Silver, J. Li, P. Li, Y. Wang, Y. Wang, L. Chen, C. Xiao, J. Chen, R. Zhou, C. Zhang, O. K. Farha, Z. Chai, T. E. Albrecht-Schmitt, S. Wang, *J. Am. Chem. Soc.* **2017**, *139*,14873–14876.

[83] R. J. Drout, K. Otake, A. J. Howarth, T. Islamoglu, L. Zhu, C. Xiao, S. Wang, O. K. Farha, *Chem. Mater.* **2018**, *30*, 1277–1284.

[84] D. Banerjee, W. Q. Xu, Z. M. Nie, L. E. V. Johnson, C. Cogh-lan, M. L. Sushko, D. Kim, M. J. Schweiger, A. A. Kruger, C. J. Doonan, P. K. Thallapally, *Inorg. Chem.* **2016**, *55*, 8241–8243.

[85] L. Zhu, C. Xiao, X. Dai, J. Li, D. Gui, D. Sheng, L. Chen, R. Zhou, Z. Chai, T. E. Albrecht-Schmitt, S. Wang, *Environ. Sci. Technol. Lett.* **2017**, *4*, 316−322.

[86] Q. Sun, L. Zhu, B. Aguila, P. K. Thallapally, C. Xu, J. Chen, S. Wang, D. Rogers, S. Ma, Nat. Commun. **2019**, DOI: 10.1038/s41467-019-09630.

[87] D. Banerjee, S. K. Elsaidi, B. Aguila, B. Li, D. Kim, M. J. Schweiger, A. A. Kruger, C. J. Doonan, S. Ma, P. K. Thallapally, *Chem. Eur. J.* **2016**, *22*, 17581−17584.

[88] H. Fei, C. S. Han, J. C. Robins, S. R. J. Oliver, *Chem. Mater.* **2013**, *25*, 647−652.

[89] Y. Yan, M. Yi, M. L. Zhai, H. F. Ha, Z. F. Luo, X. Q. Xiang, *React. Funct. Polym.* **2004**, *59*, 149-154.

Chapter 6

Summary and Perspectives

6.1 Summary and Perspectives

In summary, various target specific cationic MOFs were designed and synthesized during the course of this thesis for in-depth studies and basic understandings toward industrial and environmental applications. The main objective of the works covered in this thesis was to exploration of functional cationic MOFs having various counter anions inside toward selective light hydrocarbon separation and remediation of toxic water pollutants. Further, structure-property correlation driven development of cationic MOFs has been further emphasized and utilized for specific targeted applications. Hitherto, lack of stability of the cationic frameworks restricted its' applicability severely and remained unexplored in most of the domain of practical applications. Particularly, the rational approaches in tuning the counter functional anions for target-specific applications in the cationic frameworks is a take-away outcome of this present thesis work. This is absolutely important for the development of cationic MOFs as next generation functional ionic porous material towards practical implementation.

Although basic understanding and scientific exploration of these materials at the molecular level is important, the actual challenges still remain in converting them into workable form. MOFs are generally obtained in crystalline powder-forms which are difficult to be applied in real-time applications directly as solid-state sorbent materials. Apart from this, another major aspect is retention of performance and efficiency of the material from molecular level to the practical workable scale which need to be addressed prior to real-time implementation of these materials. In addition to these issues, scalability, cost-energy footprint and reusability of the materials are the other challenges which researchers are currently looking into thoroughly. Thus, during the next few years, researchers will concentrate on the simultaneous development of functional ionic MOFs for industrial and environmental applications along with enhancing their stability and efficiency aspect in workable form under the operational conditions.

Check for updates

How to cite: Angew. Chem. Int. Ed. 2022, 61, e202114132
International Edition: doi.org/10.1002/anie.202114132
German Edition: doi.org/10.1002/ange.202114132

Metal-Organic Frameworks

Three-in-One C_2H_2-Selectivity-Guided Adsorptive Separation across an Isoreticular Family of Cationic Square-Lattice MOFs

Subhajit Dutta[+], Soumya Mukherjee[+], Omid T. Qazvini, Arvind K. Gupta, Shivani Sharma, Debanjan Mahato, Ravichandar Babarao, and Sujit K. Ghosh**

Abstract: *Energy-efficient selective physisorption driven C_2H_2 separation from industrial C2-C1 impurities such as C_2H_4, CO_2 and CH_4 is of great importance in the purification of downstream commodity chemicals. We address this challenge employing a series of isoreticular cationic metal-organic frameworks, namely iMOF-nC (n = 5, 6, 7). All three square lattice topology MOFs registered higher C_2H_2 uptakes versus the competing C2-C1 gases (C_2H_4, CO_2 and CH_4). Dynamic column breakthrough experiments on the best-performing iMOF-6C revealed the first three-in-one C_2H_2 adsorption selectivity guided separation of C_2H_2 from 1:1 C_2H_2/CO_2, C_2H_2/C_2H_4 and C_2H_2/CH_4 mixtures. Density functional theory calculations critically examined the C_2H_2 selective interactions in iMOF-6C. Thanks to the abundance of square lattice topology MOFs, this study introduces a crystal engineering blueprint for designing C_2H_2-selective layered metal-organic physisorbents, previously unreported in cationic frameworks.*

Introduction

Separation and purification of light hydrocarbons in an energy-efficient manner is of fundamental relevance to petrochemical industries.[1,2] Typically, light hydrocarbons such as acetylene (C_2H_2) and ethylene (C_2H_4) are utilized to produce several commodity chemicals, such as plastics, fibers, rubber, vinyl compounds, acrylic acid derivatives, α-ethynyl alcohols, among others.[3,4] Industrial production of C_2H_2 continue to rely upon energy-intensive state-of-the-art, including methane (CH_4) combustion and/or steam cracking of naphtha. Exacerbating the energy footprint and producing waste, these processes often co-produce other C_2-C_1 gases such as CH_4, C_2H_4 and carbon dioxide (CO_2).[5] Even when present in trace concentrations, C_2H_2 is a catalytic poison in C_2H_4 polymerization, therefore its presence blocks the desired C_2H_4 flow, inadvertently leading to explosions. Flammability of C_2H_2, with the widest range among flammables, 2.5–81%, compounds this problem.[6] In this context, it is rather unsurprising to notice the recent upsurge in research interest to develop porous physisorbents for energy-efficient C_2H_2 capture driven adsorptive separation from mixtures of industrial relevance, including but not limited to C_2H_2/CO_2, C_2H_2/C_2H_4, C_2H_2/CH_4.[7] Traditional purification methods *viz.* chemisorption, solvent extraction, azeotropic and/or fractional and/or cryogenic distillation albeit can separate these gases, but they bear huge energy footprint, for instance, around 10–15% of the global energy is consumed in separation processes. Moreover, the demand for these commodities is estimated to be tripled by 2050.[8,9] This underscores the need to replace the existing energy-intensive purification technologies that majorly suffer from high energy footprint with energy-efficient alternatives such as recyclable/regenerable physisorption.[2a,10] Despite recent advances, the oft-encountered handicaps to achieve such small molecule separations primarily stems from their close physicochemical properties, such as similar kinetic diameters and boiling/melting points.[2a,11] In this context, porous framework solids, metal-organic frameworks (MOFs) have recently emerged with benchmark early performance indicators for C_2H_2 separation.[5,12] Nevertheless, combining multiple binary selectivities to achieve C_2H_2 separation from more than one gas mixtures is a task yet unaddressed by MOFs, despite the high efficiency entailed. Considering C_2H_2/CO_2, C_2H_2/C_2H_4, C_2H_2/CH_4 mixtures, hereinafter denoted as C2-C1 separations, MOFs have established several new benchmarks in the past

[*] S. Dutta,[+] S. Mukherjee,[+] S. Sharma, D. Mahato, S. K. Ghosh
Department of Chemistry, Indian Institute of Science Education and Research (IISER), Pune
Dr. Homi Bhabha Road, Pashan, Pune-411008 (India)
E-mail: sghosh@iiserpune.ac.in
S. Mukherjee[+]
Catalysis Research Center, Technical University of Munich Ernst-Otto-Fischer Straße 1, 85748 Garching b. München (Germany)
and
Department of Chemistry, Technical University of Munich
Lichtenbergstraße 4, 85748 Garching b. München (Germany)
O. T. Qazvini
Department of Chemical Engineering and Analytical Science, The University of Manchester
Oxford Road, Manchester M13 9PL (UK)
R. Babarao
School Science, RMIT University
Melbourne 3001 (Australia)
and
Commonwealth Scientific and Industrial Research Organisation (CSIRO) Manufacturing
Clayton, Victoria 3169 (Australia)
E-mail: ravichandar.babarao@rmit.edu.au
A. K. Gupta
Centre for Analysis and Synthesis, Department of Chemistry, Lund University
Box 124, 22100 Lund (Sweden)
[+] These authors contributed equally to this work.
Supporting information and the ORCID identification number(s) for the author(s) of this article can be found under: https://doi.org/10.1002/anie.202114132.

© 2021 Wiley-VCH GmbH

Dalton Transactions

ROYAL SOCIETY OF CHEMISTRY

PAPER

View Article Online
View Journal | View Issue

Published on 08 June 2021. Downloaded by Indian Institute of Science Education & Research Pune on 12/20/2021 10:17:20 AM.

Check for updates

Cite this: Dalton Trans., 2021, 50, 10133

A luminescent cationic MOF for bimodal recognition of chromium and arsenic based oxo-anions in water†

Subhajit Dutta,‡[a] Sumanta Let,‡[a] Mandar M. Shirolkar,[b] Aamod V. Desai,[a] Partha Samanta,[a] Sahel Fajal,[a] Yogeshwar D. More[a] and Sujit K. Ghosh *[a]

Water pollution from heavy metals and their toxic oxo-anionic derivatives such as CrO_4^{2-}, $Cr_2O_7^{2-}$, $HAsO_4^{2-}$, and $HAsO_3^{2-}$ has become one of the most critical environmental issues. To address this, herein, we report a new hydrolytically stable luminescent Zn(II) based cationic metal organic framework (MOF), iMOF-4C, which further successfully exhibited a rare dual "turn off/on" fluorescence response toward Cr(VI), As(V) and As(III) based oxo-anions respectively in water medium. In addition, iMOF-4C was found to maintain its superior selectivity in the presence of other concurrent anions (e.g. SO_4^{2-}, Cl^-, Br^-, ClO_4^-, NO_3^-, SCN^- and CO_3^{2-}). More importantly, iMOF-4C exhibited an excellent selective and sensitive luminescence "turn-off" response towards CrO_4^{2-} and $Cr_2O_7^{2-}$ anions in water medium with the quenching constant (K_{sv}) values as high as 1.31×10^5 M^{-1} (CrO_4^{2-}) and 4.85×10^5 M^{-1} ($Cr_2O_7^{2-}$), which are found to be the highest among the values reported in the regime of MOFs. Interestingly, iMOF-4C showed fluorescence "turn-on" response toward $HAsO_4^{2-}$ and $HAsO_3^{2-}$ with an enhancement coefficient (K_{ec}) of 1.98×10^4 M^{-1} and 3.56×10^3 M^{-1} respectively. The high sensitivity and low detection limits make iMOF-4C more feasible for real-time sensing of such toxic oxo-anions in an aqueous medium. Furthermore, the probable sensing mechanism has been investigated by DFT calculation studies and discussed in detail.

Received 1st April 2021,
Accepted 4th June 2021

DOI: 10.1039/d1dt01097b

rsc.li/dalton

Introduction

Water pollution has become a pressing problem in the 21st century for the global population.[1] The access to clean and fresh aquatic systems is acknowledged as indispensable to entirely discern human rights.[2] A compelling upsurge in world population in combination with increasing urbanization and energy consumption poses a direct threat to sustainable life on the Earth for generations to come.[3] Consequently, the generation of enormous amounts of hazardous waste and overexploitation of natural resources are apparent on earth's ecosystem and water bodies.[4] Acknowledging this fact, universal accessibility to clean freshwater remains the main objective of the "Sustainable Development Agenda" of the United Nations.[5] In particular, water pollution from heavy metals (density >5 g cm^{-3}) and their corresponding oxo-anions (*e.g.*, AsO_4^{3-}, CrO_4^{2-}, SeO_3^{2-}) have emerged as a persisting problem that leads to acute toxicity when accumulated in living organisms.[6] Chromium (Cr), on account of its hardness and corrosion resistance ability, is of huge industrial relevance and is extensively utilized in electroplating, metallurgy and printing.[7] In wastewater, the usual abundance of chromium is in its highly soluble hexavalent oxo-anionic forms (CrO_4^{2-} and $Cr_2O_7^{2-}$) depending on the pH.[8] It is a well-known fact that these anions are mutagenic and carcinogenic in nature and are highly toxic to living organisms and the environment. To this end, pollution due to chromium has attracted considerable attention amongst researchers worldwide.

On the other hand, arsenic (As), known as a slow death mineral, stands high among the most carcinogenic and lethal elements,[9] and is largely abundant in water, soil, atmosphere and organisms.[10] Inorganic arsenic [As(III) and As(V)] generally accumulates in keratin-rich tissues, viz., hair, skin, body fluids,[11,12] and impedes ATP production and energy transduction reactions along with endothelial damage.[13] The toxicity is punctuated by the fact that the U.S. EPA (Environmental Protection Agency, United States) and WHO have lowered the maximum contaminant level (MCL) of arsenic from 50 to 10

[a]Department of Chemistry, Indian Institute of Science Education and Research (IISER), Pune, Dr Homi Bhabha Road, Pashan, Pune-411008, India. E-mail: sghosh@iiserpune.ac.in; Tel: +91 20 2590 8076
[b]Symbiosis Center for Nanoscience and Nanotechnology (SCNN), Symbiosis International (Deemed University) (SIU), Lavale, Pune-412115, Maharashtra, India

†Electronic supplementary information (ESI) available. CCDC: 2073931. For ESI and crystallographic data in CIF or other electronic format see DOI: 10.1039/d1dt01097b

‡These authors contributed equally to this work.

ACS APPLIED MATERIALS & INTERFACES

www.acsami.org

Research Article

A Water-Stable Cationic Metal–Organic Framework with Hydrophobic Pore Surfaces as an Efficient Scavenger of Oxo-Anion Pollutants from Water

Subhajit Dutta, Partha Samanta,[#] Biplab Joarder,[#] Sumanta Let, Debanjan Mahato, Ravichandar Babarao, and Sujit K. Ghosh*

Cite This: *ACS Appl. Mater. Interfaces* 2020, 12, 41810–41818

Read Online

ACCESS | Metrics & More | Article Recommendations | Supporting Information

ABSTRACT: Water contamination due to heavy metal-based toxic oxo-anions (such as CrO_4^{2-} and TcO_4^-) is a critical environmental concern that demands immediate mitigation. Herein, we present an effort to counter this issue by a novel chemically stable cationic metal–organic framework (iMOF-2C) with strategic utilization of a ligand with hydrophobic core, known to facilitate such oxo-anion capture process. Moreover, the compound exhibited very fast sieving kinetics for such oxo-anions and a very high uptake capacity for CrO_4^{2-} (476.3 mg g^{-1}) and ReO_4^- (691 mg g^{-1}), while the latter being employed as a surrogate analogue for radioactive TcO_4^- anions. Notably, the compound showed excellent selectivity even in the presence of other competing anions such as NO_3^-, Cl^-, SO_4^{2-}, ClO_4^-, etc.. Furthermore, the compound possesses excellent reusability (up to 10 cycles) and is also employed to a stationary phase ion column to decontaminate the aforementioned oxo-anions from water.

KEYWORDS: *ionic metal–organic frameworks (iMOFs), cationic MOFs, oxo-anion, anion exchange, hydrophobic surface, pollutant capture, column chromatographic separation*

Downloaded via IISER PUNE on January 21, 2022 at 07:25:34 (UTC).
See https://pubs.acs.org/sharingguidelines for options on how to legitimately share published articles.

INTRODUCTION

Water pollution in the recent past has escalated to be a pressing problem globally that threatens the development and survival of human civilization. The intensifying impact of widespread growing urbanization and industrialization across the world prevails to be the foremost reason for water pollution.[1,2] Such enormous water pollution has led to the huge depletion of drinking water. In the same context, the United Nations have predicted that by the year 2025, at least one billion people will encounter the ultimate crisis of access to clean water.[3] Water pollution can occur through various sources, among which pollution due to heavy metals (metals having density greater than 5 g cm^{-3}) or heavy metal-based oxo-anions (AsO_4^{3-}, CrO_4^{2-}, SeO_3^{2-}, TcO_4^-, etc.) have certainly become a pertinent problem as the bioaccumulation of such elements within living organisms causes severe toxicity.[4] The US Environment Protection Agency (EPA) has listed several inorganic pollutants including these aforementioned oxo-anions as priority pollutants.[5,6] In recent years, immense research attention has been devoted toward the sequestration of Cr(VI)-based oxo-anions owing to their mutagenic and carcinogenic impacts on living systems.[7,8] Industries such as steel manufacturing, leather tanning, wood preservation, textile pigments and dyes etc. have been found to use chromate in huge quantities for various applications. Among them, tanning-based industries solely release 30–35 L of chromium contaminated water for the production of 1 kg of leather.[9,10] Moreover, the vitrification process of nuclear waste is found to be affected by Cr(VI) oxo-anions as it weakens the integrality of waste glass by forming crystalline spinels along with the waste glass.[11,12] Furthermore, several nations across the globe have witnessed various calamities of ground water contamination owing to the inappropriate disposal of Cr(VI) anions, for example, groundwater contamination in Hinkley, California is one such incident, which has drawn attention globally.[13] Apart from these heavy metal-based water contamination issues, radioactive waste generated from the nuclear power generating fission process is another genuine concern.[14] To address this pertinent problem, sequestration of pertechnetate (TcO_4^-) ions has become a pressing concern as the major nuclear fission product of technetium, (^{99}Tc), is found to be radioactive in nature with a very long half-life of 2.1×10^5 years. Nuclear fission processes of ^{239}Pu or ^{235}U produce radioactive ^{99}Tc with a high fission yield, and it has been estimated that until the year of 2010, nearly 305 metric

Received: July 28, 2020
Accepted: August 24, 2020
Published: August 24, 2020

ACS Publications

© 2020 American Chemical Society

https://dx.doi.org/10.1021/acsami.0c13563
ACS Appl. Mater. Interfaces 2020, 12, 41810–41818